

Development of Luminescent Dendrimeric Metallacrowns from Lanthanide-based Metallacrowns

by

Beatriz Abril Lopez Bermudez

A dissertation submitted in partial fulfillment
of the requirements for the degree of
Doctor in Philosophy
(Chemistry)
in the University of Michigan
2021

Doctoral Committee:

Professor Vincent L. Pecoraro, Chair
Associate Professor Julie Biteen
Professor Nicolai Lehnert
Professor Stephen C. Rand

Beatriz Abril Lopez Bermudez

lopezbea@umich.edu

ORCID iD: 0000-0003-0536-1035

© Beatriz Abril Lopez Bermudez 2021
All Rights Reserved

Dedication

To my family. You all made this possible one way or another.

Acknowledgements

I would like to thank all the people who have supported, helped, and mentored me throughout my time at the University of Michigan. I would first like to thank my advisor Prof. Vincent Pecoraro. I have learned a lot from you and truly appreciate the research freedom that you provided me throughout this past five years in your lab. Your guidance and advice have helped me grow tremendously as a scientist, and I will always be grateful for that. I would also like to thank each member of my committee, Prof. Julie Biteen, Prof. Nicolai Lehnert, and Prof. Stephen Rand. I am grateful for the insight and advice that you have provided me at candidacy, data meetings, and now reading this long document. Your help has ultimately made my thesis work better.

To all of my labmates, past and present, thank you. Berni, Elvin, Tyler, Karl, Winston, Jake, and Audrey, you all made my time at the lab invaluable, enriching, and fun. I learned a great deal from each one of you about how to be a better scientist and how to have fun at the lab. I consider myself truly lucky for having some of the best labmates a person could wish for. To my first group of friends in Ann Arbor, Shiba, Curly, Molly, and Kwan. You all graduated before me, leaving me to miss you dearly. You are all amazing people who I look up to. Thank you for your friendship and all of your encouragement. I would also like to give special thanks to Berni, Elvin, and Jill for not only being very supportive of my work, but also for becoming some of my closest friends. Gradschool without you three would have been just too boring.

There are many others I would like to thank for their support. From when I was an undergrad at USC, Dr. Brent Melot, Dr. Wolfgang Zeier, Dr. Shiliang Zhou, and Dr. Abbey Neer. You were the first ones to mentor me as a true scientist and inspired me to pursue a PhD. To my collaborators Dr. Svetlana Eliseeva, Prof. Stéphane Petoud, and Dr. Guillaume Collet for all of their help collecting and interpreting data, while also teaching me a great deal about luminescence. And to the amazing staff in the Chemistry department, Katie Foster, Liz Oxford, James Windak, Roy Wentz, and Tracy Stevenson. I sincerely appreciate all the work you all have done for me and the department.

Lastly, I would like to thank my family. I would not be the person I am now or be where I am at without all of you. All the struggles and sacrifices made me strong and appreciative of your love. Thank you for pushing me to be better, thank you for showing me how to be better, and thank you for everything you have done for me. And to Ethan, there are no words that can truly convey how grateful I am to you. You have not only provided me with unconditional love, but you have also given me the strength needed whenever I was doubtful of myself. Thank you for always being there, and thank you for making me a better person and helping me grow as a scientist.

Table of Contents

Dedication	ii
Acknowledgements	iii
List of Tables	viii
List of Figures	x
List of Appendices	xxii
Abstract	xxiii
Chapter 1 Dendrimers, Metallodendrimers, and Luminescent Metallacrowns	1
1.1 Introduction	1
1.2 Dendrimers	1
1.2.1 Synthesis	3
1.2.2 Families and Applications	5
1.2.3 PAMAM Dendrimers	9
1.3 Metallodendrimers	12
1.3.1 Classification and Examples	13
1.4 Metallacrowns	18
1.4.1 Structural Design, Synthesis, and Applications	19
1.4.2 Lanthanide Ion Luminescence	23
1.4.3 Ln ^{III} -Based Luminescent Metallacrowns	27
1.4.4 Luminescent Metallacrowns as Optical Imaging Probes	32
1.4.5 Expansion of Metallacrown Functionalization	36
1.5 Thesis Aims	38
Chapter 2 Toroidal Dendrimeric Metallacrowns from Luminescent Ln₂Ga₈Shi₈Mip₄ Scaffolds	39
2.1 Introduction	39
2.2 Experimental	41
2.2.1 Chemical and Materials	41
2.2.2 General Characterization Methods	42
2.2.3 Synthetic Procedures	42
2.2.4 Solution Stability	54

2.2.5 Luminescence Studies	55
2.2.6 Cell Studies.....	57
2.3 Results.....	58
2.3.1 Ln ₂ Ga ₈ Shi ₈ Mip ₄ Metallacrown	58
2.3.2 Ln ₂ Ga ₈ Shi ₈ Mip ₄ Functionalization.....	64
2.3.3 Toroidal Dendrimeric Metallacrowns (T-DMCs)	66
2.3.4 Cell studies	76
2.4 Discussion.....	78
2.4.1 Synthesis, Characterization, and Small Molecule Functionalization of Ln ₂ Ga ₈ Shi ₈ Mip ₄ Metallacrowns	78
2.4.2 Toroidal Dendrimeric Metallacrowns	83
2.4.3 Cell Studies.....	91
2.5 Conclusion	92
Chapter 3 Light-Catalyzed Functionalization of Luminescent Metallacrowns and Hyperboloidal Dendrimeric Metallacrowns	94
3.1 Introduction.....	94
3.2 Experimental.....	95
3.2.1 Chemical and Materials.....	95
3.2.2 General Characterization Methods.....	96
3.2.3 X-Ray Crystallography.....	97
3.2.4 UV Photocatalytic Setup	97
3.2.5 Synthetic Procedures	98
3.2.6 Luminescence Studies	113
3.3 Results.....	114
3.3.1 LnGa ₄ xShi ₄ (Benzoate) ₄ and Ln ₂ Ga ₈ xShi ₈ Ip ₄ Metallacrowns.....	114
3.3.2 LnGa ₄ xShi ₄ (Benzoate) ₄ and Ln ₂ Ga ₈ xShi ₈ Ip ₄ Functionalization	129
3.3.3 Hyperboloidal Dendrimeric Metallacrowns (H-DMCs)	136
3.4 Discussion.....	150
3.4.1 Synthesis and Characterization of LnGa ₄ xShi ₄ (benzoate) ₄ and Ln ₂ Ga ₈ xShi ₈ Ip ₄ Metallacrowns (Ln: Yb ^{III} , Sm ^{III} , and Gd ^{III} ; x: pYne, mYne, pAl, and pAl).....	150
3.4.2 Small Molecule Functionalization of LnGa ₄ xShi ₄ (benzoate) ₄ and Ln ₂ Ga ₈ xShi ₈ Ip ₄ Metallacrowns (Ln: Yb ^{III} and Sm ^{III} ; x: pYne, mYne, pAl, and pAl)	156
3.4.3 Hyperboloidal Dendrimeric Metallacrowns.....	159
3.5 Conclusion	169
Chapter 4 Bifunctional Luminescent Metallacrowns and Symmetric/Asymmetric Dendrimeric Metallacrowns	171
4.1 Introduction.....	171
4.2 Experimental.....	172
4.2.1 Chemical and Materials.....	172
4.2.2 General Characterization Methods.....	173

4.2.3 UV Photocatalytic Setup	173
4.2.4 Synthetic Procedures	174
4.2.5 Luminescence Studies	185
4.2.6 Cell Studies.....	185
4.3 Results.....	186
4.3.1 Ln ₂ Ga ₈ xShi ₈ Mip ₄ Metallacrowns.....	186
4.3.2 Ln ₂ Ga ₈ xShi ₈ Mip ₄ Functionalization.....	190
4.3.3 Symmetric and Asymmetric Dendrimeric Metallacrowns.....	194
4.3.4 Redshifted Toroidal Dendrimeric Metallacrowns	202
4.4 Discussion.....	208
4.4.1 Synthesis, Characterization, and Small Molecule Functionalization of Ln ₂ Ga ₈ xShi ₈ Mip ₄ (Ln: Yb ^{III} ; x: pYne, mYne, pAl, and pAl.....	210
4.4.2 Symmetric and Asymmetric (Janus Dendrimeric Metallacrowns)	214
4.4.3 Redshifted Dendrimeric Metallacrowns (Redshifted-DMCs).....	224
4.5 Conclusions.....	226
Chapter 5 Conclusions and Future Work	229
5.1 Preparation of DMCs	229
5.2 Effect of functional group position	232
5.3 Enhancement of luminescence.....	236
5.4 Cellular uptake	239
5.5 Summary	241
Appendices.....	243
Bibliography	291

List of Tables

Table 1.1 Luminescent lifetimes (τ_{obs}) and Ln ^{III} -centered quantum yields under ligand excitation (ϕ_{LnL}) for LnZn ₁₆ L ₁₆ (Ln: Yb, Nd, Er; L: picHa, quinHa, and pyzHa) in the solid and solution state (methanol: 1 mg/mL and water 200 μ M) ^a 101,118,128	29
Table 1.2 Absorbance maximum (Abs_{max}) of MCs and energy levels of the singlet (S [*]), triplet (T [*]) and inter-/intra ligand charge transfer (ILCT).....	29
Table 1.3 Luminescent lifetimes (τ_{obs}) and Yb ^{III} -centered quantum yields under ligand excitation (ϕ_{LnL}) for each MC scaffold in solid and solution state (50 μ M in methanol) ^a 102,119,124	32
Table 2.1 Luminescence lifetimes (τ_{obs}) and Yb ^{III} -centered quantum yields collected under ligand excitation (ϕ_{YbL}) ^a	63
Table 2.2 Luminescence lifetimes (τ_{obs}) and Yb ^{III} -centered quantum yields collected under ligand excitation (ϕ_{YbL}) ^a	73
Table 2.3. Luminescence lifetimes (τ_{obs}) and Ln ^{III} -centered quantum yields collected under ligand excitation (ϕ_{LnL}) ^a	76
Table 2.4 Calculated solvent molecules encapsulated or associated with samples in DLS.	88
Table 3.1 Crystallographic details for YbGa ₄ pYneShi ₄ (Benzoate) ₄ , YbGa ₄ mYneShi ₄ (Benzoate) ₄ , and YbGa ₄ AlShi ₄ (Benzoate) ₄ metallacrowns	118
Table 3.2 Luminescence lifetimes (τ_{obs}) and Sm ^{III} -centered quantum yields collected under ligand excitation (ϕ_{LnL}) ^a	126
Table 3.3 Luminescence lifetimes (τ_{obs}) and Yb ^{III} -centered quantum yields collected under ligand excitation (ϕ_{LnL}) ^a	129
Table 3.4 Reaction conditions for coupling HS-G1.0 PAMAM dendrons to Yb ₂ Ga ₈ pYneShi ₈ Ip ₄ under UV light-catalyzed Approach A. Each of the trials is color coded to match the ESI-MS results on Figure 3.20.	137
Table 3.5 Reaction conditions for coupling HS-G1.5 PAMAM dendrons to Yb ₂ Ga ₈ pYneShi ₈ Ip ₄ under UV light-catalyzed Approach A. Each of the trials is color coded to match the ESI-MS results on Figure 3.21.	138
Table 3.6 Reaction conditions for coupling HS-G1.0 PAMAM dendrons to Yb ₂ Ga ₈ pYneShi ₈ Ip ₄ under UV light-catalyzed Approach B (Green) and heat-catalyzed Approach C (Yellow and Pink). Each of the trials is color coded to match the ESI-MS results on Figure 3.22.	140
Table 3.7 Reaction conditions for coupling HS-G1.5 PAMAM dendrons to Yb ₂ Ga ₈ pYneShi ₈ Ip ₄ under UV light-catalyzed Approach B. Each of the trials is color coded to match the ESI-MS results on Figure 3.23.	141
Table 3.8 Reaction conditions for coupling HS-G1.0 PAMAM dendrons to YbGa ₄ pAlShi ₄ (benzoate) ₄ under UV-light catalyzed Approach A.	142

Table 3.9 Reaction conditions for coupling HS-G0.5 PAMAM dendrons to Yb ₂ Ga ₈ AlShi ₈ Ip ₄ under UV- light catalyzed Approach A. Each of the trials is color coded to match the ESI-MS results on Figure 3.25	143
Table 3.10 Reaction conditions for coupling HS-G1.0 PAMAM dendrons to Yb ₂ Ga ₈ AlShi ₈ Ip ₄ under UV- light catalyzed Approach A. A. Each of the trials is color coded to match the ESI-MS results on Figure 3.26.	144
Table 3.11 Reaction conditions for coupling HS-G1.0 PAMAM dendrons to Yb ₂ Ga ₈ mAlShi ₈ Ip ₄ under UV- light catalyzed Approach A.....	145
Table 3.12 Reaction conditions for coupling HS-G1.0 PAMAM dendrons to Yb ₂ Ga ₈ mAlShi ₈ Ip ₄ under Heat-catalyzed Approach C.	146
Table 3.13 Luminescence lifetimes (τ_{obs}) and Yb ^{III} -centered quantum yields collected under ligand excitation (ϕ_{YbL}) ^a	150
Table 3.14 Absorbance maximum (Abs_{max}) of MCs, energy levels of their singlet (S [*]) triplet (T [*]), and lanthanide (Ln [*]) energies, and energy difference (ΔE) between states.	153
Table 3.15 Luminescence lifetimes (τ_{obs}) and Yb ^{III} -centered quantum yields (ϕ_{LnL}) in DMSO of MCs described in this chapter. Compounds have been listed in order of decreasing quantum yields, and divided between monomeric and dimeric scaffolds.....	156
Table 3.16 Calculated solvent molecules encapsulated or associated with samples in DLS.	166
Table 4.1 Luminescence lifetimes (τ_{obs}) and Yb ^{III} -centered quantum yields collected under ligand excitation (ϕ_{YbL}) ^a	190
Table 4.2 DMSO solution luminescence lifetimes (τ_{obs}) and Yb ^{III} -centered quantum yields collected under ligand excitation (ϕ_{YbL}) ^a	202
Table 4.3 DMSO solution luminescence lifetimes (τ_{obs}) and Yb ^{III} -centered quantum yields collected under ligand excitation (ϕ_{YbL}) ^a	207
Table 4.4 List of MC and DMC prepared for this chapter. Each of the different classifications are highlighted with different color, with the small molecule coupling in yellow, S-DMC in green, Janus-DMC in blue, biotinylated Janus-DMCs in gray and white, and the redshifted-DMCs in orange.	208
Table 5.1 Luminescent paraments of Yb ^{III} -based MCs and DMCs collected under ligand excitation (ϕ_{LnL}).	237
Table 5.2 List of NIR-emitting probes reposted it the past five years with attractive photophysical properties and investigated for cell imaging.	239

List of Figures

Figure 1.1	Architecture of a third-generation dendrimer (left) and dendron (right), with multiple end groups, several internal cavities, and color-coded structural features.	2
Figure 1.2	Traditional dendrimer synthesis approaches. In the divergent approach (a), reactive surfaces are shown in purple, while monomer reactive sites are shown in red and protected ones in magenta. In the convergent approach (b), monomer reactive sites are shown in orange and its deactivated focal point is shown in cyan. As for the dendron, reactive focal point is shown in red.	4
Figure 1.3	Building blocks of the most highly referenced dendrimers. Without any further surface functionalization, these would be the dendrimer surfaces.	6
Figure 1.4	Multiple applications of dendrimers by surface modification or cavity encapsulation.	7
Figure 1.5	Ethylendiamine (EDA) cored PAMAM dendrimer. Synthesis follows two repetitive steps: i) Michael addition of EDA to Methyl acrylate; followed by, ii) ester amidation with EDA. Steps are repeated until the desired generation is achieved.....	10
Figure 1.6	PAMAM dendrimer structural defects.	12
Figure 1.7	Different metal unit positions in metallodendrimers. a) Dendrimer with a metal ion core; b) dendrimer with a macrocyclic metal complex core; c) dendrimer with metal units encapsulated in cavities; d) dendrimer with metal ions coordinated to cavities with ligand centers; e) dendrimers with metals at the periphery; and f) dendrimers with metal complexes as branching units.	13
Figure 1.8	Schematic representation of a) meso-porphyrin-cored and b) cyclam-cored metallodendrimers.....	16
Figure 1.9	Structural comparison of crowns ethers (left) and metallacrowns (right). Both named based on their ring size and number of oxygen atoms. Both structures as representing a 12-membered ring with [C-C-O] ₄ repeating units for the crown ether and [M-N-O] ₄ repeating units for the MC.	18
Figure 1.10	Diagram showing ring ligand coordination and its influence on ring geometry. Salicylhydroxamate ligand (middle top) templates a square-shaped 12-MC-4, while picoline hydroxamate ligand (middle bottom) generates a pentagonal-shaped 15-MC-5. ¹⁰³	20
Figure 1.11	Crystal structures of different MCs illustrating the different bridges (or lack of) needed to complete the coordination sphere of their lanthanide cores. ^{101,102,106,107}	21
Figure 1.12	Diagram of the antenna effect (top). Simplified Jablonsky diagram representing (bottom) energy absorption, transfer, and radiative emissions of the lanthanide ion. S ⁰ and S [*] : ground and excited singlet states, respectively. T [*] : excited triplet state. ISC: intersystem crossing. ET: energy transfer.....	23
Figure 1.13	Partial energy diagram of Ln ^{III} ion highlighting the emissive states of each metal ion and the singlet and triplet energy position of an efficient Ln[12-MC _{Ga(III)N(shi)-4}] ₂ scaffold, ¹¹⁹ with the following emissive states for each lanthanide: Pr(³ P ₀): 20475cm ⁻¹ ,	

	Nd(⁴ F _{3/2}): 11460cm ⁻¹ , Sm(⁴ G _{5/2}): 17900cm ⁻¹ , Eu(⁵ D ₀): 17260cm ⁻¹ , Tb(⁵ D ₄): 20400cm ⁻¹ , Dy(⁴ F _{9/2}): 21100cm ⁻¹ , Ho(⁵ F ₅): 155000cm ⁻¹ , Er(⁴ I _{13/2}): 6700cm ⁻¹ , Tm(¹ G ₄): 21350cm ⁻¹ , and Yb(² F _{5/2}): 10300cm ⁻¹ . ^{137,138}	25
Figure 1.14	Crystal structure of Nd[12-MC _{Zn(II)N(pyZHa)-4}] ₂ [24-MC _{Zn(II)N(pyZHa)-8}] metallacrown (top left), showing the host(host-guest) motif (right), and the three different ring ligands used to prepare LnZn ₁₆ L ₁₆ MCs. Figure adapted from ref. 125 and 126. ^{128,129}	27
Figure 1.15	X-ray crystal structures of the three members of the Ga-family. (Top) Top view and (bottom) side view of the three MCs. Blue: Ln ^{III} , pink: Ga ^{III} , red: O, purple: N, and gray: C. Solvent molecules, counterions, and hydrogen atoms have been omitted for clarity. ^{102,106,119}	30
Figure 1.16	PGSE-DOSY on (a) YGa ₄ miShi ₄ (benzoate ₄), (b) Y ₂ Ga ₈ Shi ₈ (iip ₄), and (c) YGa ₈ L ₈ (OH ₄) MCs showing diffusion rates of the bridge (red, a and b) and ring (blue, a and b; multiple colors in c) protons in methanol solutions. The black (a and b) or purple (c) trace is from a TMMS standard. ^{119,140}	31
Figure 1.17	(Top) Comparison of necrotic cell labeling with YbZn ₁₆ pyZHa ₁₆ (b, blue) and PI (c, red). White arrows on (a) point at necrotic cells. (d) Overlap of both images showing colocalized labeling. (d) Merge of all images. (Bottom) Images comparing photostability of PI (red) and MC (blue) after (a) 10sec, (b) 50sec, (c) 100sec, (d) 200sec, and (e) 500sec. Most of the luminescent signal of PI is gone while the MC's remains. ¹²⁸	33
Figure 1.18	Epifluorescence microscopy images of fixed HeLa cells. (a) brightfield, (b) NIR emission of YbZn ₁₆ pyZHa ₁₆ MC, (c) visible emission of PI, (d) merged of (b) and (c) to demonstrate colocalization of both complexes, and (d) merge with brightfield. ¹²⁹	34
Figure 1.19	Luminescent intensities of a 1:1 mixture of Sm ₂ Ga ₈ Shi ₈ (ip) ₄ /Tb ₂ Ga ₈ Shi ₈ (ip) ₄ suspended in amino functionalized polystyrene nanobeads. Tb ^{III} transitions are labeled in black, while Sm ^{III} transitions are labeled in blue. ¹²¹	35
Figure 1.20	Selection of ligands used to prepare metallacrowns. Abbreviated names are color coded to determine original ligand (blue), commercially available carboxylic acid starting material (green), synthetically modified (red). (top) Ring ligands for LnZn ₁₆ MCs. (middle) Ring ligands and (bottom) bridge ligands for Ga-family MCs.	36
Figure 2.1	Exemplified notations required for the absolute quantum yield measurements.....	56
Figure 2.2	(Top) ESI-MS of Y ₂ Ga ₈ Shi ₈ Mip ₄ metallacrown in negative ion mode. (Bottom) (Bottom) expansion of the major peak corroborating the -2 isotopic distribution of the complex.....	58
Figure 2.3	¹ H NMR spectrum of Y ₂ Ga ₈ Shi ₈ (Mip) ₄ in d ₆ -DMSO. Labeled peaks from ring and bridging ligands. Pyridine peaks labeled separately.	59
Figure 2.4	ESI-MS spectra of Y ₂ Ga ₈ Shi ₈ Ip ₄ and Y ₂ Ga ₈ Shi ₈ Mip ₄ MC mixture dissolved in DMF. Top spectrum collected immediately after mixing (Day 0), and bottom spectrum taken after five days.....	60
Figure 2.5	ESI-MS spectra of Y ₂ Ga ₈ Shi ₈ Ip ₄ and Y ₂ Ga ₈ Shi ₈ Mip ₄ MC mixture in DMF/H ₂ O (1:1 v/v%). Top spectrum collected immediately after mixing (Day 0), and bottom spectrum taken after one day.	60
Figure 2.6	UV-Vis absorbance spectrum of 39.5 μM Yb ₂ Ga ₈ Shi ₈ Mip ₄ MC in DMSO at room temperature. Absorbance maxima is at 317 nm, and an extinction coefficient of 4.1x10 ⁴ M ⁻¹ cm ⁻¹	61

- Figure 2.7 Solid state phosphorescence spectrum of $Gd_2Ga_8Shi_8Mip_4$ MC (black trace), and 0-0, 0-1 and 0-2 phonon transitions (colored traces) fitted with multiple Gaussian functions and Origin9 program. Data collected upon excitation at 340 nm, and after a 200-500 μs time delay at 77K. Fits differ in bandwidth due to the complexity of the ligand system, with several inter- and intramolecular interactions. Some distortion of the widths is also observed since the fits are plotted against wavelength. Subsequent fits (e.g., 0-3, 0-4, etc.) are less reliable, and in general omitted from these analyses. 62
- Figure 2.8 Corrected and normalized excitation (left, λ_{em} : 980 nm) and emission (right, λ_{ex} : 320–340 nm) spectra of $Yb_2Ga_8Shi_8Mip_4$ in the solid state (dashed traces) and 50 μM solutions in DMSO (solid traces) at room temperature. 63
- Figure 2.9. Experimental luminescence decay curves (black) of $Yb_2Ga_8Shi_8Mip_4$ MC in the (a) solid state and (b) in 50 μM DMSO solutions. Experimental excitation at 355 nm and monitoring the Yb^{III} emission at 980 nm at room temperature. Both curves are fitted to biexponential decay with adjusted R^2 parameters of >0.99 for both fittings..... 64
- Figure 2.10 (Top) ESI-MS of $Sm_2Ga_8Shi_8Mip_4(Cys)_4$ metallacrown in negative ion mode (m/z calcd. $Sm_2Ga_8C_{112}H_{80}N_{16}O_{48}S_4$: 1704.2 $[M]^{2-}$; found: 1703.7 $[M]^{2-}$). (Bottom) expansion of the major peak corroborating the -2 isotopic distribution of the complex. The mass spectrum confirms the lack of any uncoupled MC..... 64
- Figure 2.11 (left) Solution state excitation (λ_{em} : 595 nm) and (right) emission (λ_{ex} : 315 nm) spectra of $Sm_2Ga_8Shi_8Mip_4$ and $Sm_2Ga_8Shi_8Mip_4(cysteamine)_4$ compounds collected in $\sim 2 \mu M$ solutions in methanol at room temperature. Background spectrum was subtracted to remove second harmonic artifacts. 65
- Figure 2.12. Normalized ESI-MS spectra of $Yb_2Ga_8Shi_8Mip_4$ Core and G:0.5-2.0 DMCs in methanol solutions. Core and G0.5 are -2 species, while G1-1.5 are +2 and G2 is +3 species. 66
- Figure 2.13 DLS size distribution of $Yb_2Ga_8Shi_8Mip_4$ MC core and each dendrimeric metallacrown generation (G0.5-2.0) in DMSO and at room temperature. 67
- Figure 2.14 DLS size distribution of G1.0-2.0 toroidal-DMCs in 99:1 H_2O :DMSO solutions at concentrations of 30-68 μM at room temperature and at pH: 7.5..... 68
- Figure 2.15 Average hydrodynamic diameter (D_{av}) difference of $Yb_2Ga_8Shi_8Mip_4$ G1.5 dendrimeric metallacrowns due to aggregation arising from different sample preparation approaches. 69
- Figure 2.16 ESI-MS spectra of $Tb_2Ga_8Shi_8Mip_4$ MC and $Tb_2Ga_8Shi_8Mip_4$ G0.5 dendrimeric metallacrown in DMF/ H_2O (1:1, v/v%). Top spectrum collected immediately after mixing (Day 0), and bottom spectrum taken after seven days..... 70
- Figure 2.17 UV-Vis absorption of $Yb_2Ga_8Shi_8Mip_4$ MC and $Yb_2Ga_8Shi_8Mip_4$ G0.5-2.0 DMCs dissolved in DMSO. Solutions made of 1-20 μM at room temperature. Absorbance maxima is at 317 nm with an extinction coefficient of $4.1 \times 10^4 M^{-1}cm^{-1}$ 71
- Figure 2.18 Solid state phosphorescence spectrum of $Gd_2Ga_8Shi_8Mip_4$ G0.5 DMC (black traces). 0-0, 0-1, and 0-2 transitions (colored traces) for the DMC are fitted with multiple Gaussian functions and Origin9 program. Data collected upon excitation at 300 nm, and after 100 μs time delay at 77K. Fits differ in bandwidth due to the complexity of the ligand system, with several inter- and intramolecular interactions. Some distortion of the widths is also observed since the fits are plotted against wavelength. Subsequent fits (e.g., 0-3, 0-4, etc.) are less reliable, and in general omitted from these analyses. 71

Figure 2.19 Corrected and normalized (left) excitation ($\lambda_{em} = 980$ nm), and (right) emission ($\lambda_{ex} = 320$ nm) spectra of 50 μ M DMSO solution of Yb ₂ Ga ₈ Shi ₈ Mip ₄ core and G:0.5 – 2.0 at room temperature.	72
Figure 2.20 Experimental luminescent decay curves (black) and monoexponential fits (cyan) of 50 μ M Yb ₂ Ga ₈ Shi ₈ Mip ₄ DMCs G: 0.5 – 2.0 in DMSO at room temperature. Excitation at 355 nm and Yb ^{III} emissions at 980 nm. a) Yb ₂ Ga ₈ Shi ₈ Mip ₄ G0.5, b) Yb ₂ Ga ₈ Shi ₈ Mip ₄ G1.0, and c) Yb ₂ Ga ₈ Shi ₈ Mip ₄ G1.5. Adjusted R ² parameters of >0.99 for all fittings.	73
Figure 2.21. Corrected and normalized excitation spectra of G0.5 DMCs in the solid state (dashed traces) and in 200 μ M H ₂ O/DMSO (96%/4%) solutions (solid traces) upon monitoring the main transitions Ln ^{III} ion at room temperature.	75
Figure 2.22. Corrected and normalized emission spectra of G0.5 DMCs in the solid state (dashed traces) and in 200 μ M H ₂ O/DMSO (96%/4%) solutions (solid traces) under ligand excitation (320-340 nm) at room temperature.	75
Figure 2.23. Microscopy images of HeLa cells incubated with 100 μ M of Yb ₂ Ga ₈ Shi ₈ Mip ₄ G0.5 and G1.5 DMCs in aqueous solutions with 1% DMSO. (Top) Yb ^{III} NIR epifluorescence image for G0.5 (λ_{ex} : 377 nm, band pass 50 nm; λ_{em} : 805 nm, long pass; 40 s of exposure) and G1.5 (λ_{ex} : 377 nm, band pass 50 nm; λ_{em} : 805 nm, long pass; 10s of exposure).	77
Figure 2.24. Microscopy images of HeLa cells incubated with 100 μ M of Yb ₂ Ga ₈ Shi ₈ Mip ₄ G1.0 DMC in saline solution with 1% DMSO. A) Brightfield image, and B) NIR epifluorescence image ($\lambda_{ex} = 377$ nm, band pass 50nm; $\lambda_{em} = 785$ nm, long pass; 2s of exposure). Objective 40 ^X . Scale bar = 20 μ m.	77
Figure 2.25 Possible set of isomer for a single thiol-Michale addition to a maleimide group. Thiol coupling can yield two sets of isomer, and each isomer has a 180° of rotational freedom.	82
Figure 3.1 Photograph of LED Box highlighting key components. Coupling reaction using this set up were performed by covering the box with a lid (not shown in picture) and placing the assembly inside a hood.	98
Figure 3.2 (Top) ESI-MS of YbGa ₄ pAlShi ₄ (Benzoate) ₄ MC in negative ion mode. (Bottom) expansion of the major peak corroborating the -1 isotopic distribution of the complex.	115
Figure 3.3 ¹ H NMR spectrum of SmGa ₄ pAlShi ₄ (Benzoate) ₄ in d ₆ -DMSO. Labeled peaks from the ring ligands. Pyridine and benzoate peaks labeled separately.	116
Figure 3.4 Top-down views of molecular structures of YbGa ₄ pYneShi ₄ (Benzoate) ₄ , YbGa ₄ mYneShi ₄ (Benzoate) ₄ , and YbGa ₄ mAlShi ₄ (Benzoate) ₄ scaffolds obtained from X-ray diffraction. Hydrogen atoms, counterions, and solvent molecules haven been omitted for clarity. Color code: Yb ^{III} , blue; Ga ^{III} , pink; N, violet; O, red; C, gray... ..	117
Figure 3.5 (Top) ESI-MS of Yb ₂ Ga ₈ pAlShi ₈ Ip ₄ MC in negative ion. (Bottom) expansion of the major peak corroborating the -1 isotopic distribution of the complex.....	119
Figure 3.6 ¹ H NMR spectrum of Sm ₂ Ga ₈ pAlShi ₈ Ip ₄ in d ₆ -DMSO. Labeled peaks are from the ring and bridge ligands. Pyridine peaks are labeled separately.....	120
Figure 3.7 Comparison of the UV-Vis absorption spectra of the four new hydroxamic acid derivatives and the salicyl hydroxamic acid. All spectra were recorded at room temperature in DMSO at concentration of 50-200 μ M.....	121
Figure 3.8 UV-Vis absorbance spectra of YbGa ₄ xShi ₄ (benzoate) ₄ (x: pYne, mYne, pAl, and mAl) recorded at room temperature in DMSO at concentrations of 2-25 μ M.....	122

Figure 3.9 UV-Vis absorbance spectra of $\text{Yb}_2\text{Ga}_8\text{xShi}_4\text{Ip}_4$ (x: pYne, mYne, pAl, and mAl) recorded at room temperature in DMSO at concentrations of 3-50 μM	122
Figure 3.10 Solid state phosphorescence spectrum of $\text{GdGa}_4\text{pYneShi}_4(\text{Benzoate})_4$, $\text{GdGa}_4\text{mYneShi}_4(\text{Benzoate})_4$, $\text{GdGa}_4\text{pAlShi}_4(\text{Benzoate})_4$, $\text{GdGa}_4\text{mAlShi}_4(\text{Benzoate})_4$, $\text{Gd}_2\text{Ga}_8\text{mYneShi}_8\text{Ip}_4$, $\text{Gd}_2\text{Ga}_8\text{pAlShi}_8\text{Ip}_4$, and $\text{Gd}_2\text{Ga}_8\text{mAlShi}_8\text{Ip}_4$ MCs (black traces). 0-0, 0-1, and 0-2 transitions (colored traces) for each MC are fitted with multiple Gaussian functions and Origin9 program. Data collected upon excitation at 340 nm, and after 200-500 μs time delay at 77K. Fits differ in bandwidth due to the complexity of the ligand system, with several inter- and intramolecular interactions. Some distortion of the widths is also observed since the fits are plotted against wavelength. Subsequent fits (e.g., 0-3, 0-4, etc.) are less reliable, and in general omitted from these analyses.	123
Figure 3.11 Corrected and normalized excitation (left, λ_{em} : 597 nm) and (right, λ_{ex} : 320–360 nm) spectra of $\text{SmGa}_4\text{pYneShi}_4(\text{Benzoate})_4$, $\text{Sm}_2\text{Ga}_8\text{pYneShi}_8\text{Ip}_4$, $\text{SmGa}_4\text{mYneShi}_4(\text{Benzoate})_4$, $\text{Sm}_2\text{Ga}_8\text{mYneShi}_8\text{Ip}_4$, $\text{SmGa}_4\text{pAlShi}_4(\text{Benzoate})_4$, $\text{Sm}_2\text{Ga}_8\text{mYneShi}_8\text{Ip}_4$, $\text{SmGa}_4\text{mAlShi}_4(\text{Benzoate})_4$, and $\text{Sm}_2\text{Ga}_8\text{mAlShi}_8\text{Ip}_4$ in the solid state (dashed traces) and 50 μM solutions in DMSO (solid traces) at room temperature.	125
Figure 3.12 Corrected and normalized excitation (left, λ_{em} : 980 nm) and (right, λ_{ex} : 320–375 nm) spectra of $\text{YbGa}_4\text{pYneShi}_4(\text{Benzoate})_4$, $\text{Yb}_2\text{Ga}_8\text{pYneShi}_8\text{Ip}_4$, $\text{YbGa}_4\text{mYneShi}_4(\text{Benzoate})_4$, $\text{Yb}_2\text{Ga}_8\text{mYneShi}_8\text{Ip}_4$, $\text{YbGa}_4\text{pAlShi}_4(\text{Benzoate})_4$, $\text{Yb}_2\text{Ga}_8\text{mYneShi}_8\text{Ip}_4$, $\text{YbGa}_4\text{mAlShi}_4(\text{Benzoate})_4$, and $\text{Yb}_2\text{Ga}_8\text{mAlShi}_8\text{Ip}_4$ in the solid state (dashed traces) and 50 μM solutions in DMSO (solid traces) at room temperature.	128
Figure 3.13 ESI-MS spectra of UV-light catalyzed coupling of β -Mercaptoethanol (β ME) to $\text{YbGa}_4\text{pYneShi}_4(\text{benzoate})_4$ (top) and $\text{Yb}_2\text{Ga}_8\text{pYneShi}_8\text{Ip}_4$ (bottom). Six to eight thiol-yne couplings to the monomeric MC are observed, while fourteen to sixteen coupling to the dimeric MC are observed.	130
Figure 3.14 ESI-MS spectra of UV-light catalyzed coupling of β -Mercaptoethanol (β ME) to $\text{YbGa}_4\text{mYneShi}_4(\text{benzoate})_4$ with zero to six couplings (top) and $\text{Yb}_2\text{Ga}_8\text{mYneShi}_8\text{Ip}_4$ with eleven to sixteen couplings (bottom). The meta-functionalized MCs show lower reactivity toward thiol-yne coupling compared to the para-functionalized counterpart.	131
Figure 3.15 ESI-MS spectra of UV-light catalyzed coupling of β -Mercaptoethanol (β ME) to $\text{YbGa}_4\text{pAlShi}_4(\text{benzoate})_4$ (top) and $\text{Yb}_2\text{Ga}_8\text{pAlShi}_8\text{Ip}_4$ (bottom). Four thiol-yne couplings to the monomeric MC, while six to eight to the dimeric MC.	132
Figure 3.16 ESI-MS spectra of UV-light catalyzed coupling of β -Mercaptoethanol (β ME) to $\text{YbGa}_4\text{pAlShi}_4(\text{benzoate})_4$ (top) and $\text{Yb}_2\text{Ga}_8\text{pAlShi}_8\text{Ip}_4$ (bottom). Four thiol-yne couplings to the monomeric MC, while six to eight to the dimeric MC.	133
Figure 3.17 ESI-MS spectra of UV-light catalyzed coupling of β -Mercaptoethanol (β ME) to $\text{SmGa}_4\text{pAlShi}_4(\text{benzoate})_4$ (top) and $\text{SmGa}_4\text{mAlShi}_4(\text{benzoate})_4$ (bottom). In both cases, complete coupling of four small molecules to each MC was observed.	134
Figure 3.18 UV-Vis Absorbance spectra of $\text{YbGa}_4\text{pYneShi}_4(\text{benzoate})_4$, $\text{Yb}_2\text{Ga}_8\text{pYneShi}_8\text{Ip}_4$, $\text{YbGa}_4\text{pAlShi}_4(\text{benzoate})_4$, and $\text{Yb}_2\text{Ga}_8\text{pAlShi}_8\text{Ip}_4$ post β -mercaptoethanol coupling recorded at room temperature in DMSO at concentrations of 0.1 mg/mL.	135

Figure 3.19 Solution state emission (λ_{ex} : 310 nm) spectra of $\text{YbGa}_4\text{pYneShi}_4(\text{benzoate})_4$, $\text{Yb}_2\text{Ga}_8\text{pYneShi}_8\text{Ip}_4$, $\text{YbGa}_4\text{pAlShi}_4(\text{benzoate})_4$, and $\text{Yb}_2\text{Ga}_8\text{pAlShi}_8\text{Ip}_4$ post β -mercaptoethanol coupling recorded at room temperature in DMSO at concentrations of 0.1 mg/mL.....	135
Figure 3.20. ESI-MS spectra of the synthetic trials to prepare hyperboloidal DMC with $\text{Yb}_2\text{Ga}_8\text{pYneShi}_8\text{Ip}_4$ MC cores and HS-G1.0 PAMAM dendrons under Approach A.	137
Figure 3.21. ESI-MS spectra of the synthetic trials to prepare hyperboloidal DMC with $\text{Yb}_2\text{Ga}_8\text{pYneShi}_8\text{Ip}_4$ MC cores and HS-G1.5 PAMAM dendrons under Approach A.	138
Figure 3.22 ESI-MS spectra of the synthetic trials to prepare hyperboloidal DMC with $\text{Yb}_2\text{Ga}_8\text{pYneShi}_8\text{Ip}_4$ MC cores and HS-G1.0 PAMAM dendrons under Approach B (Green) and Approach C (Yellow and Pink).	139
Figure 3.23 ESI-MS spectra of the synthetic trials to prepare hyperboloidal DMC with $\text{Yb}_2\text{Ga}_8\text{pYneShi}_8\text{Ip}_4$ MC cores and HS-G1.5 PAMAM dendrons under Approach B.	141
Figure 3.24 ESI-MS spectra of DMC G1.0 with $\text{YbGa}_4\text{Shi}_4(\text{benzoate})_4$ MC core under Approach A.....	142
Figure 3.25 ESI-MS spectra of the synthetic trials to prepare hyperboloidal DMC with $\text{Yb}_2\text{Ga}_8\text{pAlShi}_8\text{Ip}_4$ MC cores and HS-G0.5 PAMAM dendrons under Approach A.	143
Figure 3.26 ESI-MS spectra of the synthetic trials to prepare hyperboloidal DMC with $\text{Yb}_2\text{Ga}_8\text{pAlShi}_8\text{Ip}_4$ MC cores and HS-G1.0 PAMAM dendrons under Approach A.	144
Figure 3.27 ESI-MS spectra of the synthetic trials to prepare hyperboloidal DMC with $\text{Yb}_2\text{Ga}_8\text{mAlShi}_8\text{Ip}_4$ MC cores and HS-G1.0 PAMAM dendrons under Approach A.	145
Figure 3.28 ESI-MS spectra of the synthetic trials to prepare hyperboloidal DMC with $\text{Yb}_2\text{Ga}_8\text{mAlShi}_8\text{Ip}_4$ MC cores and HS-G1.0 PAMAM dendrons under Approach C.	146
Figure 3.29 DLS size distribution of $\text{Yb}_2\text{Ga}_8\text{pAlShi}_8\text{Ip}_4$ MC and G1.0 DMC at 5 mg/mL and 3.2 mM, respectively, in DMSO and at room temperature.....	147
Figure 3.30 DLS size distribution of $\text{Yb}_2\text{Ga}_8\text{pAlShi}_8\text{Ip}_4$ G1.0 hyperboloidal-DMC at 34.1 μM solution in 99:1 H_2O :DMSO at room temperature and at pH: 7.5.	147
Figure 3.31 UV-Vis absorption spectrum of 12 μM $\text{Yb}_2\text{Ga}_8\text{pAlShi}_8\text{Ip}_4$ MC (top) and 11 μM $\text{Yb}_2\text{Ga}_8\text{pAlShi}_8\text{Ip}_4$ G1.0 DMC (bottom) dissolved in DMSO and at room temperature. Absorbance maxima for both compounds is at 310 nm with an extinction coefficient of $6.8 \times 10^4 \text{ M}^{-1}\text{cm}^{-1}$	148
Figure 3.32 Corrected and normalized excitation (left, $\lambda_{\text{em}} = 980 \text{ nm}$), and emission ($\lambda_{\text{ex}} = 320 \text{ nm}$) spectra of 50 μM DMSO solution of $\text{Yb}_2\text{Ga}_8\text{pAlShi}_8\text{Ip}_4$ G1.0 DMC at room temperature.	149
Figure 3.33 Plot of singlet energy vs. triplet energy for the parent MCs and all of the measured monomeric and dimeric Gd^{III} -MC with thiol-ene/yne appendages.	154
Figure 3.34 DLS size distribution of $\text{Yb}_2\text{Ga}_8\text{Shi}_8\text{Mip}_4$ G1.0 T-DMC and $\text{Yb}_2\text{Ga}_8\text{pAlShi}_8\text{Ip}_4$ G1.0 H-DMC in DMSO at room temperature.	165
Figure 4.1 Photograph of LED Box highlighting key components. Coupling reaction using this set up were performed by covering the box with a lid (not shown in picture) and placing the assembly inside a hood.	174

Figure 4.2 (Top) ESI-MS of Yb ₂ Ga ₈ pAlShi ₈ Mip ₄ metallacrown in negative ion mode. (Bottom) expansion of the major peak corroborating the -2 isotopic distribution of the complex.	187
Figure 4.3 UV-Vis absorbance spectra of Yb ₂ Ga ₈ xShi ₄ Mip ₄ (x: pYne, mYne, pAl, and mAl) recorded at room temperature in DMSO at concentrations of 8.5-10.5 μM.	188
Figure 4.4 Corrected and normalized excitation (left, λ _{em} : 980 nm) and emission (right, λ _{ex} : 320–375 nm) spectra of Yb ₂ Ga ₈ pAlShi ₈ Mip ₄ and Yb ₂ Ga ₈ mYneShi ₈ Mip ₄ in the solid state (dashed traces) and 50 μM solutions in DMSO (solid traces) at room temperature.	189
Figure 4.5 (Top) ESI-MS of Yb ₂ Ga ₈ pAlShi ₈ Mip ₄ βME ₁₂₋₁₁ metallacrown in negative ion mode. (Bottom) expansion of the major peak corroborating the -2 isotopic distribution of the complex.	192
Figure 4.6 (Top) ESI-MS of Yb ₂ Ga ₈ mAlShi ₈ Mip ₄ βME ₁₂₋₁₁ metallacrown in negative ion mode. (Bottom) expansion of the major peak corroborating the -2 isotopic distribution of the complex.	192
Figure 4.7 (Top) ESI-MS of Yb ₂ Ga ₈ pYneShi ₈ Mip ₄ βME ₂₀₋₁₈ metallacrown in negative ion mode. (Bottom) expansion of the major peak corroborating the -2 isotopic distribution of the complex.	193
Figure 4.8 UV-Vis Absorbance spectra of Yb ₂ Ga ₈ pAlShi ₈ Mip ₄ , Yb ₂ Ga ₈ mAlShi ₈ Mip ₄ , and Yb ₂ Ga ₈ pYneShi ₈ Mip ₄ post symmetric β-mercaptoethanol coupling recorded at room temperature in DMSO at concentrations of 10-18 uM.	193
Figure 4.9 (Top) ESI-MS of Yb ₂ Ga ₈ pAlShi ₈ Mip ₄ (G0.5) ₄ DMC in negative ion mode. Dendrons (D _x) are only coupled to the four maleimide appendages of the metallacrown core. (Bottom) ESI-MS of Yb ₂ Ga ₈ pAlShi ₈ Mip ₄ (G0.5) ₁₂₋₁₀ in positive ion mode. This time, G0.5 dendrons are attached to both the maleimide appendages and the ring ligands of the MC core.	194
Figure 4.10 (Top) ESI-MS of Yb ₂ Ga ₈ pAlShi ₈ Mip ₄ (G1.0) ₄ DMC, and (Bottom) Yb ₂ Ga ₈ pAlShi ₈ Mip ₄ (G1.0) ₄ (G0.5) ₇₋₄ in positive ion mode. G1.0 dendrons are only coupled to the four maleimide appendages, while the G0.5 dendrons are coupled only to the ring ligands of the MC core.	195
Figure 4.11 UV-Vis absorption spectra of 2.60 μM Yb ₂ Ga ₈ pAlShi ₈ Mip ₄ MC (top) and 2.75 μM Yb ₂ Ga ₈ pAlShi ₈ Mip ₄ (G1.0) ₄ (G0.5) ₇₋₄ Janus-DMC (bottom) dissolved in DMSO and at room temperature. Absorbance maxima for both compounds is at 310 nm with an extinction coefficient of 8.67x10 ⁴ M ⁻¹ cm ⁻¹ . The slight decrease in absorbance intensity of the Janus-DMC is due to the small difference in solution concentration between the two samples.	196
Figure 4.12 ESI-MS of Yb ₂ Ga ₈ pAlShi ₈ Mip ₄ (Bt) ₄ DMC in negative ion mode, and (Bottom) Yb ₂ Ga ₈ pAlShi ₈ Mip ₄ (Bt) ₄ (G1.0) ₈₋₅ in positive ion mode. Biotin groups are only coupled to the four maleimide appendages, while the G1.0 dendrons are coupled only to the ring ligands of the MC core.	197
Figure 4.13 Absorption spectra of 2.64 μM Yb ₂ Ga ₈ pAlShi ₈ Mip ₄ (G1.0) ₄ (Bt) ₈₋₅ Janus-DMC dissolved in DMSO and at room temperature. Absorbance maximum located at 310 nm with an extinction coefficient of 8.67x10 ⁴ M ⁻¹ cm ⁻¹	198
Figure 4.14 ESI-MS of Yb ₂ Ga ₈ pAlShi ₈ Mip ₄ (G1.0) ₄ (Bt) ₈₋₆ DMC in positive ion mode. G1.0 dendrons are only coupled to the four maleimide appendages, while the Biotin groups are coupled only to the ring ligands of the MC core.	199

Figure 4.15 DLS size distribution of Yb ₂ Ga ₈ pAlShi ₈ Mip ₄ (G1.0) ₄ (Bt) ₈ Janus-DMC at 1.5 μM solution in DMSO at room temperature.....	200
Figure 4.16 DLS size distribution of Yb ₂ Ga ₈ pAlShi ₈ Mip ₄ (G1.0) ₄ (Bt) ₈ Janus-DMC at 4.6 μM solution in 99:1 H ₂ O:DMSO at room temperature and at pH: 7.5.	200
Figure 4.17 UV-Vis absorption spectrum of 3.4 μM Yb ₂ Ga ₈ pAlShi ₈ Mip ₄ (G1.0) ₄ (Bt) ₈₋₆ Janus-DMC dissolved in DMSO and at room temperature. Absorbance maximum at 310 nm with an extinction coefficient of 8.67x10 ⁴ M ⁻¹ cm ⁻¹	201
Figure 4.18 Corrected and normalized excitation (left, λ _{em} = 980 nm), and emission (λ _{ex} = 320 nm) spectra of 50 μM DMSO solution of Yb ₂ Ga ₈ pAlShi ₈ Mip ₄ (G1.0) ₄ (Bt) ₈ Janus-DMC at room temperature.	202
Figure 4.19 Normalized ESI-MS spectra of DMCs with Yb ₂ Ga ₈ mYneShi ₈ Mip ₄ cores and G: 1.0, 1.0 -OH, and 1.5 in methanol solutions. Dendrons are only coupled to the maleimide appendages of the MC core.....	203
Figure 4.20 DLS size distribution of Yb ₂ Ga ₈ mYneShi ₈ Mip ₄ T-DMC with G1.0, 1.0 -OH, and 1.5 at 1.5 μM concentrations dissolved in DMSO at room temperature.	204
Figure 4.21 DLS size distribution of Yb ₂ Ga ₈ mYneShi ₈ Mip ₄ T-DMC with G1.0 (50.4 μM) , 1.0 -OH (27.5 μM) , and 1.5 (15 μM) in 99:1 H ₂ O:DMSO at room temperature and at pH: 7.5.....	205
Figure 4.22 UV-Vis absorption spectra of redshifted T-DMCs Yb ₂ Ga ₈ mYneShi ₈ Mip ₄ G1.0 (25.1 μM) , 1.0 -OH (19.7 μM) , and 1.5 (9.36 μM) dissolved in DMSO and at room temperature. Absorbance maxima at 340 nm and with an extinction coefficient of 4.36x10 ⁴ M ⁻¹ cm ⁻¹	206
Figure 4.23 Corrected and normalized excitation (left, λ _{em} = 980 nm), and emission (λ _{ex} = 320 nm) spectra of 50 μM DMSO solution of redshifted T-DMC Yb ₂ Ga ₈ mYneShi ₈ Mip ₄ G1.0, G1.0 -OH, and G1.5 at room temperature.	206
Figure 4.24 Microscopy images of HeLa cells incubated with Yb ₂ Ga ₈ mYneShi ₈ Mip ₄ G1.0, 1.0 -OH, 1.5 T-DMC in cell culture media solution with 1% DMSO. A) Brightfield image, and B) NIR epifluorescence image (λ _{ex} = 377nm, band pass 50nm; λ _{em} = 785nm, long pass; 2s of exposure).....	208
Figure 4.25 DLS size distribution comparing Yb ₂ Ga ₈ pAlShi ₈ Mip ₄ (G1.0) ₄ (Bt) ₈ J-DMC, Yb ₂ Ga ₈ Shi ₈ Mip ₄ G1.0 T-DMC and Yb ₂ Ga ₈ pAlShi ₈ Ip ₄ G1.0 H-DMC in DMSO at room temperature.	220
Figure 4.26 DLS size distribution comparing Yb ₂ Ga ₈ pAlShi ₈ Mip ₄ (G1.0) ₄ (Bt) ₈ J-DMC, Yb ₂ Ga ₈ Shi ₈ Mip ₄ G1.0 T-DMC and Yb ₂ Ga ₈ pAlShi ₈ Ip ₄ G1.0 H-DMC in solution in 99:1 H ₂ O:DMSO at room temperature and at pH: 7.5.....	221
Figure 5.1 Plot of singlet vs. triplet energies of synthetically functionalized metallacrowns prepared for this thesis (GdGa ₄ pYneShi ₄ , GdGa ₄ mYneShi ₄ , GdGa ₄ pAlShi ₄ , GdGa ₄ mAlShi ₄ , Gd ₂ Ga ₈ mYneShi ₈ , Gd ₂ Ga ₈ pAlShi ₈ , Gd ₂ Ga ₈ mAlShi ₈), and previously reported scaffolds (GdGa ₄ Shi ₄ , GdGa ₄ Cl-Shi ₄ , GdGa ₄ Br-Shi ₄ , Gd ₂ Ga ₈ Shi ₈ , Gd ₂ Ga ₈ l-Shi ₈ , Gd ₂ Ga ₈ MoShi ₈ , and Gd ₂ Ga ₈ MeShi ₈) ^{102,106,124,178} with appendages at the para- and meta-positions. Para-substituted MCs are in red, meta-substituted are in blue, and unsubstituted are in gray. LnGa ₄ are depicted with filled symbols, while Ln ₂ Ga ₈ scaffolds are half-filled. Legend: unsubstituted MCs with rectangles (Shi); propargyl-appended MCs with circles (p/mYeneShi); allyl-appended MCs with stars (p/mAlShi); halogenated-appended MCs with triangles (x-Shi); alkoxy-appended MC with a diamond (MoShi); and methyl-appended MC with a hexagon (MeShi).	233

Figure 5.2 Plots showing dependence of DMC configuration on quantum yield (a) and brightness (b). Yb ₂ Ga ₈ Shi ₈ Ip ₄ represents a MC with zero dendron arms and with no ring/bridge functionalization, Toroidal-DMC has four dendron arms, Hyperboloidal-DMC has eight dendron arms, and Janus-DMC has twelve dendron arms. Data used to make both plots was collected in DMSO solutions and with G1.0 PAMAM DMCs only.	238
Figure A1 ¹ H NMR spectrum of 5-(3-carboxylacrylamide)isophthalic acid. Unlabeled peaks are left over solvent molecule, such as acetone, DMF, and water.....	244
Figure A2 ¹ H NMR spectrum of 5-maleimideisophthalic acid. Unlabeled peaks are left over solvent molecule, such as water.....	245
Figure A3 ¹ H NMR spectrum of YbGa ₄ Shi ₄ (benzoate) ₄ . Labeled peaks are from ring ligand. Pyridine and benzoate peaks labeled separately. Unlabeled peaks are solvents.....	245
Figure A4 ¹ H NMR spectrum of 1. Small impurity peaks at 2.73 ppm and 2.97 ppm are from cystamine byproduct (~2%).	246
Figure A5 ¹ H NMR spectrum of 2. Small impurity peaks at 2.80-3.20 ppm and 3.70 ppm are from disulfide byproduct (~5%).	246
Figure A6 ¹ H NMR spectrum of 3.....	247
Figure A7 ¹ H NMR spectrum of 4.....	247
Figure A8 ¹ H NMR spectrum of 5.....	248
Figure A9 ¹ H NMR spectra of deprotected 6.....	248
Figure A10 ¹ H NMR spectra of deprotected 7. Left over trityl salt seen between 7.00-7.50 ppm accounts for ≤1%.	249
Figure A11 ¹ H NMR spectra of deprotected 8. Left over trityl salt seen between 7.00-7.50 ppm accounts for ≤1%.	249
Figure A12 ¹ H NMR spectra of deprotected 9.....	250
Figure A13 (Top) ESI-MS of SmGa ₄ Shi ₄ (benzoate) ₄ metallacrown in negative ion. (Bottom) -1 isotopic distribution.	251
Figure A14 (Top) ESI-MS of YbGa ₄ Shi ₄ (benzoate) ₄ metallacrown in negative ion. (Bottom) -1 isotopic distribution.	251
Figure A15 (Top) ESI-MS of GdGa ₄ Shi ₄ (benzoate) ₄ metallacrown in negative ion. (Bottom) -1 isotopic distribution.	252
Figure A16 (Top) ESI-MS of TbGa ₄ Shi ₄ (benzoate) ₄ metallacrown in negative ion. (Bottom) -1 isotopic distribution.	252
Figure A17 (Top) ESI-MS of YGa ₄ Shi ₄ (benzoate) ₄ metallacrown in negative ion. (Bottom) -1 isotopic distribution.	253
Figure A18 (Top) ESI-MS of Sm ₂ Ga ₈ Shi ₈ (Mip) ₄ metallacrown in negative ion. (Bottom) -2 isotopic distribution.	253
Figure A19 (Top) ESI-MS of Yb ₂ Ga ₈ Shi ₈ Mip ₄ metallacrown in negative ion. (Bottom) -2 isotopic distribution.	254
Figure A20. (Top) ESI-MS of Gd ₂ Ga ₈ Shi ₈ (Mip) ₄ metallacrown in negative ion. (Bottom) -2 isotopic distribution.	254
Figure A21. (Top) ESI-MS of Tb ₂ Ga ₈ Shi ₈ (Mip) ₄ metallacrown in negative ion. (Bottom) -2 isotopic distribution.	255
Figure A22 ESI mass spectrum of Sm ₂ Ga ₈ Shi ₈ (Mip) ₄ G0.5 dendrimeric metallacrown in negative ion.	255
Figure A23 ESI mass spectrum of Tb ₂ Ga ₈ Shi ₈ (Mip) ₄ G0.5 dendrimeric metallacrown in negative ion.	256

Figure A24 ESI mass spectrum of Gd ₂ Ga ₈ Shi ₈ (Mip) ₄ G0.5 dendrimeric metallacrown in negative ion.	256
Figure A25 ESI mass spectrum of Yb ₂ Ga ₈ Shi ₈ (Mip) ₄ G0.5 dendrimeric metallacrown in negative ion.	257
Figure A26. ESI mass spectrum of Yb ₂ Ga ₈ Shi ₈ (Mip) ₄ G1.0 dendrimeric metallacrown in positive ion.	257
Figure A27 ESI mass spectrum of Yb ₂ Ga ₈ Shi ₈ (Mip) ₄ G1.5 dendrimeric metallacrown in positive ion.	258
Figure A28 ESI mass spectrum of Yb ₂ Ga ₈ Shi ₈ (Mip) ₄ G2.0 dendrimeric metallacrown in positive ion.	258
Figure A29 UV-Vis absorbance spectra in MeOH of Sm ₂ Ga ₈ Shi ₈ Mip ₄ prior and after cysteamine coupling in at room temperature and with 2-3 μM concentrations.	259
Figure C30 ¹ H NMR spectrum of Methyl 2-hydroxy-4-(prp-2-yn-1-yloxy)benzoate (1).....	262
Figure C31 ¹ H NMR spectrum of N,2-dihydroxy-4-(prop-2-yn-1-yloxy)benzamide (pYneShi, 2).	263
Figure C32 ¹ H NMR spectrum of Methyl 2-hydroxy-5-(prp-2-yn-1-yloxy)benzoate (3).....	263
Figure C33 ¹ H NMR spectrum of N,2-dihydroxy-5-(prop-2-yn-1-yloxy)benzamide (mYneShi, 4).	264
Figure C34 ¹ H NMR spectrum of Methyl 4-(allyloxy)-2-hydroxybenzoate (5).	264
Figure C35 ¹ H NMR spectrum of 4-(allyloxy)-N,2-dihydroxybenzamide (pAlShi, 6).....	265
Figure C36 ¹ H NMR spectrum of Methyl 5-(allyloxy)-2-hydroxybenzoate (7).	265
Figure C37 ¹ H NMR spectrum of 5-(allyloxy)-N,2-dihydroxybenzamide (mAlShi, 8)	266
Figure C38 ¹ H NMR spectrum of SmGa ₄ pYneShi ₄ (Benzoate) ₄ in d ₆ -DMSO. Labeled peaks from the ring ligands. Pyridine peaks labeled separately.	266
Figure C39 ¹ H NMR spectrum of SmGa ₄ mYneShi ₄ (Benzoate) ₄ in d ₆ -DMSO. Labeled peaks from the ring ligands. Pyridine peaks labeled separately.	267
Figure C40 ¹ H NMR spectrum of SmGa ₄ mAlShi ₄ (Benzoate) ₄ in d ₆ -DMSO. Labeled peaks from the ring ligands. Pyridine and benzoate peaks labeled separately.	267
Figure C41 ¹ H NMR spectrum of Sm ₂ Ga ₈ pYneShi ₈ Ip ₄ in d ₆ -DMSO. Labeled peaks from the ring and bridge ligands. Pyridine peaks labeled separately.....	268
Figure C42 ¹ H NMR spectrum of Sm ₂ Ga ₈ mYneShi ₈ Ip ₄ in d ₆ -DMSO. Labeled peaks from the ring and bridge ligands. Pyridine peaks labeled separately.....	268
Figure C43 ¹ H NMR spectrum of Sm ₂ Ga ₈ mAlShi ₈ Ip ₄ in d ₆ -DMSO. Labeled peaks from the ring and bridge ligands. Pyridine peaks labeled separately.....	269
Figure C44 (Top) ESI-MS of YbGa ₄ pYneShi ₄ (Formate) ₄ MC in negative ion. (Bottom) -1 isotopic distribution.	269
Figure C45 (Top) ESI-MS of SmGa ₄ pYneShi ₄ (Formate) ₄ MC in negative ion. (Bottom) -1 isotopic distribution.	270
Figure C46 (Top) ESI-MS of GdGa ₄ pYneShi ₄ (Formate) ₄ MC in negative ion. (Bottom) -1 isotopic distribution.	270
Figure C47 (Top) ESI-MS of YbGa ₄ mYneShi ₄ (Benzoate) ₄ MC in negative ion. (Bottom) -1 isotopic distribution.	271
Figure C48 (Top) ESI-MS of SmGa ₄ mYneShi ₄ (Formate) ₄ MC in negative ion. (Bottom) -1 isotopic distribution.	271
Figure C49 ESI-MS of GdGa ₄ mYneShi ₄ (Formate) ₄ MC in negative ion. (Bottom) -1 isotopic distribution.	272

Figure C50 (Top) ESI-MS of SmGa ₄ pAlShi ₄ (Formate) ₄ MC in negative ion. (Bottom) -1 isotopic distribution.	272
Figure C51 (Top) ESI-MS of GdGa ₄ pAlShi ₄ (Formate) ₄ MC in negative ion. (Bottom) -1 isotopic distribution.	273
Figure C52 (Top) ESI-MS of YbGa ₄ mAlShi ₄ (Formate) ₄ MC in negative ion. (Bottom) -1 isotopic distribution.	273
Figure C53 (Top) ESI-MS of SmGa ₄ mAlShi ₄ (Formate) ₄ MC in negative ion. (Bottom) -1 isotopic distribution.	274
Figure C54 (Top) ESI-MS of GdGa ₄ mAlShi ₄ (Formate) ₄ MC in negative ion. (Bottom) -1 isotopic distribution.	274
Figure C55 (Top) ESI-MS of Yb ₂ Ga ₈ pYneShi ₈ Ip ₄ MC in negative ion. (Bottom) -2 isotopic distribution.	275
Figure C56 (Top) ESI-MS of Sm ₂ Ga ₈ pYneShi ₈ Ip ₄ MC in negative ion. (Bottom) -2 isotopic distribution.	275
Figure C57. (Top) ESI-MS of Gd ₂ Ga ₈ pYneShi ₈ Ip ₄ MC in negative ion. (Bottom) -2 isotopic distribution.	276
Figure C58 ESI-MS of Yb ₂ Ga ₈ mYneShi ₈ Ip ₄ MC in negative ion. (Bottom) -2 isotopic distribution.	276
Figure C59 ESI-MS of Sm ₂ Ga ₈ mYneShi ₈ Ip ₄ MC in negative ion. (Bottom) -2 isotopic distribution.	277
Figure C60 ESI-MS of Gd ₂ Ga ₈ mYneShi ₈ Ip ₄ MC in negative ion. (Bottom) -2 isotopic distribution.	277
Figure C61 (Top) ESI-MS of Sm ₂ Ga ₈ pAlShi ₈ Ip ₄ MC in negative ion. (Bottom) -2 isotopic distribution.	278
Figure C62 (Top) ESI-MS of Gd ₂ Ga ₈ pAlShi ₈ Ip ₄ MC in negative ion. (Bottom) -2 isotopic distribution.	278
Figure C63 (Top) ESI-MS of Yb ₂ Ga ₈ mAlShi ₈ Ip ₄ MC in negative ion. (Bottom) -2 isotopic distribution.	279
Figure C64 (Top) ESI-MS of Sm ₂ Ga ₈ mAlShi ₈ Ip ₄ MC in negative ion. (Bottom) -2 isotopic distribution.	279
Figure C65 (Top) ESI-MS of Gd ₂ Ga ₈ mAlShi ₈ Ip ₄ MC in negative ion. (Bottom) -2 isotopic distribution.	280
Figure C66 (Top) ESI-MS of YbGa ₄ pYneShi ₄ (βME) ₈₋₆ in negative ion. (Bottom) -1 isotopic distribution.	280
Figure C67 ESI-MS of YbGa ₄ mYneShi ₄ (βME) ₆₋₄ in negative ion. (Bottom) -1 isotopic distribution.	281
Figure C68 ESI-MS of YbGa ₄ pAlShi ₄ (βME) ₄ in negative ion. (Bottom) -1 isotopic distribution.	281
Figure C69 ESI-MS of YbGa ₄ mAlShi ₄ (βME) ₄ in negative ion. (Bottom) -1 isotopic distribution.	282
Figure C70 ESI-MS of SmGa ₄ pAlShi ₄ (βME) ₄ in negative ion. (Bottom) -1 isotopic distribution.	282
Figure C71. ESI-MS of SmGa ₄ mAlShi ₄ (βME) ₄ in negative ion. (Bottom) -1 isotopic distribution.	283
Figure C72. ESI-MS of Yb ₂ Ga ₈ pYneShi ₈ Ip ₄ (βME) ₁₆₋₁₄ in negative ion. (Bottom) -2 isotopic distribution.	283

Figure C73 ESI-MS of $\text{Yb}_2\text{Ga}_8\text{mYneShi}_8\text{Ip}_4(\beta\text{ME})_{16-11}$ in negative ion. (Bottom) -2 isotopic distribution.	284
Figure C74 ESI-MS of $\text{Yb}_2\text{Ga}_8\text{pAlShi}_8\text{Ip}_4(\beta\text{ME})_{8-6}$ in negative ion. (Bottom) -2 isotopic distribution.	284
Figure C75 ESI-MS of $\text{Yb}_2\text{Ga}_8\text{mAlShi}_8\text{Ip}_4(\beta\text{ME})_{8-5}$ in negative ion. (Bottom) -2 isotopic distribution.	285
Figure D76 (Top) ESI-MS of $\text{Yb}_2\text{Ga}_8\text{mAlShi}_8\text{Mip}_4$ MC in negative ion. (Bottom) expansion of the major peak corroborating the -2 isotopic distribution of the complex.....	286
Figure D77 (Top) ESI-MS of $\text{Yb}_2\text{Ga}_8\text{pYneShi}_8\text{Mip}_4$ MC in negative ion. (Bottom) expansion of the major peak corroborating the -2 isotopic distribution of the complex.....	287
Figure D78 (Top) ESI-MS of $\text{Yb}_2\text{Ga}_8\text{mYneShi}_8\text{Mip}_4$ MC in negative ion. (Bottom) expansion of the major peak corroborating the -2 isotopic distribution of the complex.....	287
Figure D79 ^1H NMR spectrum of Trityl-G1.0-OH dendron.	288
Figure D80 ^1H NMR spectrum of HS-G1.0-OH dendron. Signals at ~6.9-7.7 ppm are left over trityl salt.	288
Figure D81 ^1H NMR spectrum of 1. Small impurity peaks at 2.73 ppm and 2.97 ppm are from cystamine byproduct (~2%).	289
Figure D82 ^1H NMR spectrum of 2. Unlabeled peaks at 2.50 ppm, 2.73 ppm, and 2.89 ppm are from dmsd-d ₆ and leftover DMF.....	289
Figure D83 ^1H NMR spectrum of 3.	290
Figure D84 ^1H NMR spectrum of 3. Peaks at above 7.0 ppm are residual trityl salt.	290

List of Appendices

Appendix A Supplemental Information for Chapter 2	244
Appendix B Calculations for the Estimation of Encapsulated/Associated Solvent Molecules to MCs and DMCs by DLS.....	260
Appendix C Supplemental Information for Chapter 3.....	262
Appendix D Supplemental Information for Chapter 4	286

Abstract

Dendrimeric metallacrowns (DMCs) combine both dendrimers and metallacrowns as viable luminescent probes. Three approaches were investigated, these included functionalizing luminescent Ln₂Ga₈ metallacrowns at either the bridging or ring sites, or simultaneously at both positions, to then use them as the core of dendrimers. Investigation of the physical and optical properties of each DMC was performed, their solution behavior characterized, and in some cases their ability to label cells was investigated.

Ln₂Ga₈ metallacrowns were functionalized with maleimide appendages at the bridging ligands to undergo thiol-coupling reactions. Complete coupling of cysteamine to the functionalized metallacrown confirmed thiol-coupling reactivity and that there was no degradation of the luminescent signal. Toroidal-DMCs could then be prepared by coupling poly(amidoamine) dendrons (G0.5-2.0) to Yb₂Ga₈ metallacrown-cores. Increased solution stability in mixed-aqueous/organic media was observed in DMCs compared to metallacrowns. Yb^{III}-sensitization yielded long lifetimes (62-64μs) and high quantum yields (7.03-9.38%) in solution. The observed luminescent enhancement of the metallacrown core was attributed to the solvent protection by the dendrons. Depending on the solvent, generation size, and sample preparation, these DMCs showed various degrees of self-aggregation as determined by dynamic light scattering. HeLa cells incubated with G0.5- and G1.5-DMCs exhibited strong luminescence from non-specific binding at the cell membrane, while G1.0 toroidal-DMCs were internalized with luminescent signals localized at cell nucleoli. Altogether, these results show that toroidal-DMCs are more viable as imaging probes than non-functionalized metallacrowns.

The more challenging functionalization occurred at the ring position. Four new ligands with allyl- and propargyl-appendages at the *para*- or *meta*-position were synthesized, and then LnGa₄ and Ln₂Ga₈ metallacrowns were prepared (Sm^{III} and Yb^{III}) with each ring ligand. It was shown that the functionalization position (*para* vs. *meta*) had an effect on the ligand-centric singlet (29412 vs 26667cm⁻¹) and triplet (23450 vs 21630cm⁻¹) energies, as well as on thiol-coupling

reactivity (*para*>*meta*). The Sm^{III} and Yb^{III} metallacrowns exhibited quantum yields in solution ranging 1.4-2.9% and 3.7-8.1%, which includes the highest value among Yb^{III}-compounds (e.g., DMSO: F₁₅TPPYb-H (Yb-2) 3.5% and PAN-DOTA(Yb) 0.054%). Synthetic trials revealed that Yb₂Ga₈ metallacrowns with *para*-allyl ring ligands were the best cored for the photocatalytic synthesis of hyperboloidal-DMCs with G1.0 poly(amidoamine) dendrons based on completeness of coupling. Photophysical characterization confirmed sensitization of Yb^{III}-emission and enhancement of the luminescent properties, resulting in long lifetimes (69 μ s) and high quantum yields (8.7%) in solution.

Since the templating ligands were functionalized independently, bifunctional metallacrowns could be prepared, and the synthesis of symmetric and asymmetric molecules to form more versatile dendrimers constructs was achieved. Three different DMCs were prepared using bifunctionalized Yb-metallacrowns. The first was a symmetric-DMC with twelve poly(amidoamine) dendrons coupled to both ligand positions, matching the highest number of dendron-growth/attachment sites in the literature. Asymmetric coupling was then investigated by preparing Janus-DMCs with orthogonally-positioned biotin and G1.0-dendrons. Finally, controlling the degree of thiol-coupling by selecting redshifted ring ligands with low thiol-reactivity was investigated, yielding a redshifted Yb-metallacrown that selectively coupled thiol-groups at the bridges. Photophysical characterization of the Janus- and redshifted-DMCs exhibited excellent Yb^{III}-emission, with long lifetimes (62-66 μ s) and high quantum yields (7.4-8.8%).

In summary, functionalization of metallacrowns at the templating ring and bridging ligands with thiol-active groups allowed the preparation of DMCs, which have high quantum yields and long luminescent lifetimes for this molecular class. Altogether, this work provides a new strategy toward the versatile design of luminescent DMCs, metallacrowns, and dendrimers.

Chapter 1

Dendrimers, Metallodendrimers, and Luminescent Metallacrowns

1.1 Introduction

In this section, I begin by introducing the concepts of dendrimers, metallodendrimers, and metallacrowns (MCs), focusing on their synthesis, families, and applications. I then concentrate on the luminescent behavior of metallacrowns, by first going over the basics of lanthanide luminescence, as well as the structural requirements for the design of lanthanide scaffolds. This is followed by the introduction of the zinc and gallium family metallacrowns, and their applications as optical imaging probes. I additionally describe the synthetic evolution of metallacrowns by ligand functionalization and incorporation of coupling sites to the scaffold. I also highlight the versatile, but delicate, ligand design requirements necessary to ensure formation of metallacrowns and the conservation of their photophysical properties. Finally, this section ends with a brief overview of the thesis aims.

1.2 Dendrimers

The design and development of novel nanostructures (≤ 100 nm) with polymeric backbones, well-defined topologies, and attractive properties is a challenging endeavor, but synthetically attainable. While polymers with traditional morphologies (i.e., linear, cross-linked, and branched) have been prepared with nanoscale dimensions in one-pot reactions, they produce highly polydisperse complexes that can hinder their utility as nanocomposites. Furthermore, the precise structural control over the size, shape, and end-group functionality and location, which influence the overall properties of the complex, can be hard to fine-tune with traditional synthetic methods.¹ Thus, hyperbranched polymers such as dendrimers, with tunable structural control and high monodispersity, have attracted much attention from synthetic chemists and material scientists over the past several decades.

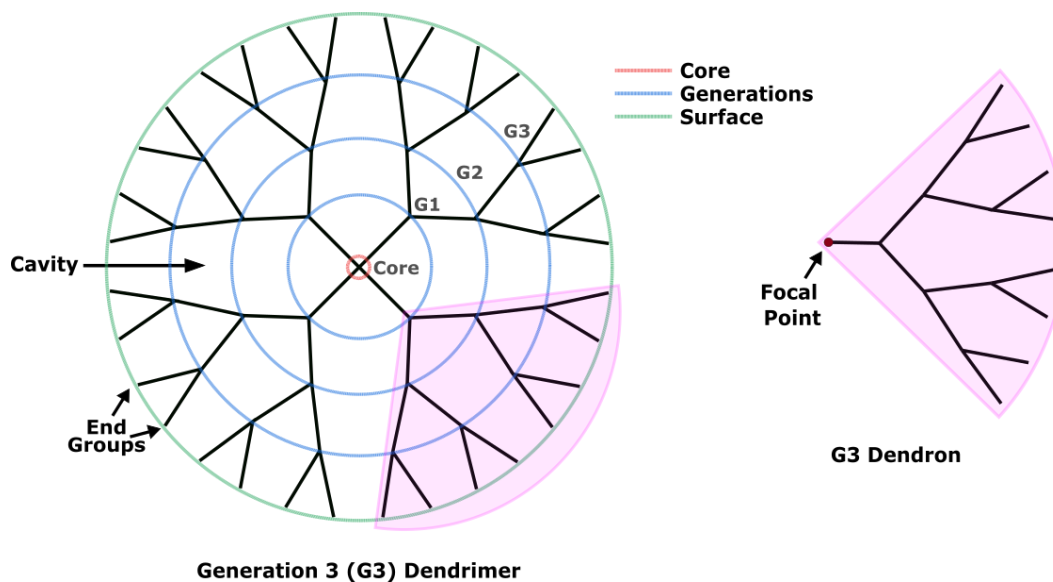


Figure 1.1 Architecture of a third-generation dendrimer (left) and dendron (right), with multiple end groups, several internal cavities, and color-coded structural features.

First reported in the late 1970's and early 1980's by Vögtle et al.² and Tomalia et al.,³ dendrimers are highly branched spherical nanostructures unique among polymeric nanoparticles. As seen in Figure 1.1, the molecular architectures of dendrimers consist of multivalent *surfaces* that control their solubility and coupling ability, covalently linked branching interiors called *generations (G)*, and a multifunctional *core* out of which the dendrimer grows.⁴ The shape of a dendrimer is mainly dictated by both the type, size, and functionality of the templating core, and the type and number of generations. Small dendrimers tend to be more open and flexible, while large ones are more spherical. This is explained by the fact that dendrimer diameter increases linearly with increasing generation while the number of surface groups increases exponentially. Thus, at a given generation, steric crowdedness at the periphery determines the final globular shape.³ Furthermore, based on the radial growth and expansion of the internal generations, cavities form within the dendrimer architecture. The cavities' shape, size, and flexibility are also influenced by both the core morphology and generation size. Under optimal conditions, the cavities can be utilized to host smaller molecular complexes. However, generations that are too small or too large would be too flexible or too stiff to allow encapsulation of guest molecules.⁵

1.2.1 Synthesis

The distinctive structural features, multivalency, and narrow polydispersity (measure of ideal size deviation) of dendrimers arises from the precise control over their preparation. Dendrimers are traditionally prepared in a stepwise fashion in one of two ways: divergently or convergently. The *divergent* approach was first introduced by the seminal work of Vögtle et al.,² and optimized by Tomalia et al.³ In this method, dendrimer growth starts from the center outward, with multifunctional cores that can react with multivalent monomeric units to form generations, as seen in Figure 1.2a. Monomers must have a readily active site that can couple to the core, and a protected (or less reactive) site that can later be activated to continue growth at the dendrimer periphery. This difference in reactivity from the monomers' extremities is what prevents uncontrolled hyperbranched polymerizations from happening.⁶ To achieve a given generation, monomers have to be added in a repetitive sequential fashion and in a large excess to drive the additions to completion. The generation number of the final product can be calculated by counting the number of synthetic additions to form the dendrimer.

Because of its gradual synthetic approach, the divergent method is well suited for both large-scale and large-generation synthesis – with dendrimers up to generation eleven previously reported.⁷ However, that same attractive exponential increase of surface groups with increasing generation catalyzes the formation of defects (imperfections) within the dendrimer shell during synthesis. Generational defects (e.g. trailing generations and oligomers) and branching imperfections (e.g. incomplete monomer addition, missing dendrons, and cyclization) are the major culprits behind dendrimer irregularities.⁸ Special care should be taken to help mitigate the formation of defects in the first place since their removal can be very challenging due to the structural similarities between the intended dendrimer and its flawed counterparts.^{3,4,6} For example, the addition of a large excess of monomer must be followed by extensive purification steps, and careful temperature control (<50°C) must be ensured at all times. For this reason, while dendrimers are well-known to be polymers with low polydispersities (~1.01), they should not be mistaken for defect-free polymers.

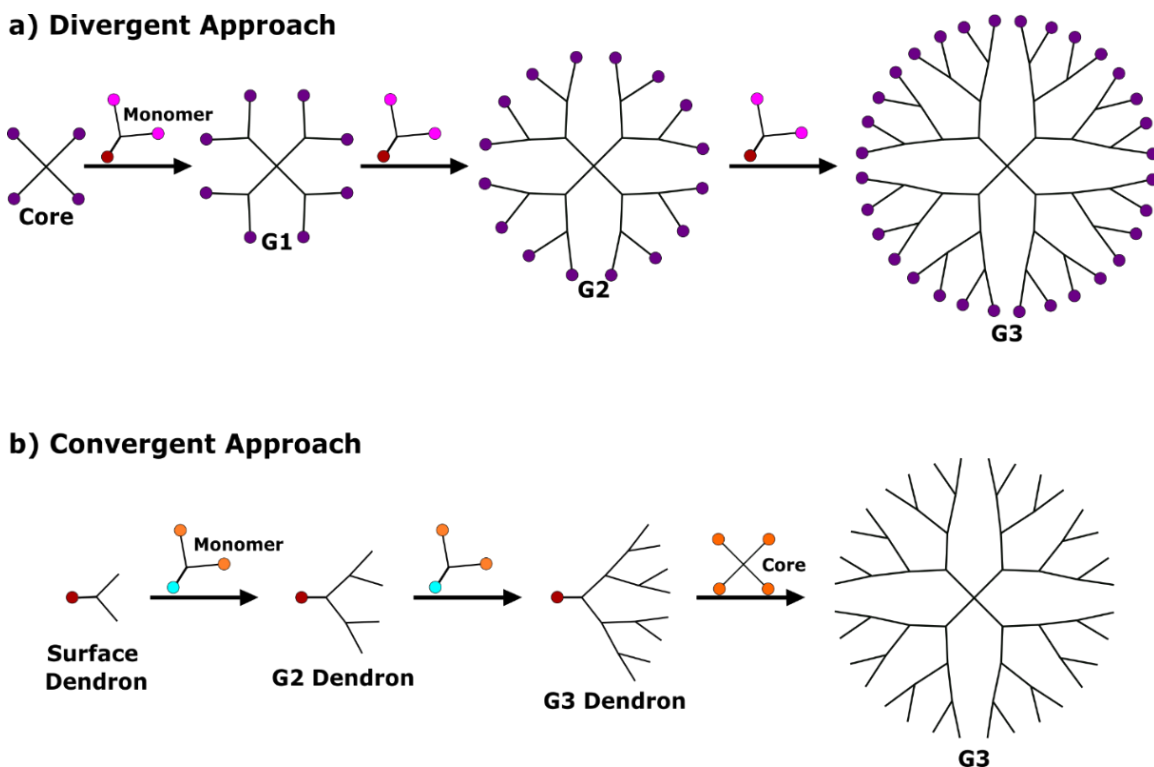


Figure 1.2 Traditional dendrimer synthesis approaches. In the divergent approach (a), reactive surfaces are shown in purple, while monomer reactive sites are shown in red and protected ones in magenta. In the convergent approach (b), monomer reactive sites are shown in orange and its deactivated focal point is shown in cyan. As for the dendron, reactive focal point is shown in red.

The *convergent* approach was first reported a few years later in 1990 by Fréchet et al.⁹ Unlike the divergent approach, it proceeds from the periphery inward. In this case, dendrons (i.e., dendrimer branches) are prepared first with repeating cycles of monomer addition. Monomers must have an unreactive focal point, which can later be activated, and at least two reactive sites for dendritic growth. Once the desired generation is achieved, the final step is the attachment of the preformed dendrons to a functional core, as seen in Figure 1.2b. In general, relatively purer dendrimers are prepared with this approach over the divergent one. This is because there is a significant reduction of generational defects and branch imperfection during synthesis since fewer active sites are present per reaction. Additionally, purification steps are more efficient since coupling reactions only require slight excess of starting materials to drive them to completion.^{6,10} However, while less imperfect material can be made, the convergent approach limits the assembly of large generations ($G > 6$) and in large scales.⁶ This is due to the steric hindrance that dendrons

develop with increasing size, which makes coupling to relatively small cores more challenging. Therefore, the convergent approach is better suited for smaller ($G \leq 5$) dendrimer synthesis.

Two other less popular dendrimer synthesis pathways are the *double stage convergent* and the *double exponential* approaches.^{11,12} In the former, small generation dendrimers are used as multifunctional cores to which small dendrons are coupled. In the latter approach, small dendrons are treated as monomeric units by selectively activating or deactivating them at their focal points or surfaces. They are then coupled together to produce larger dendrons. In the final step, these dendrons are convergently coupled to multifunctional cores. Both approaches are considered to be hybrids of the traditional protocols since the dendrons (and the cores, in the case of the double stage convergent method) can be synthesized convergently or divergently, and are coupled to the cores in a convergent fashion. Since these approaches produce dendrimers of a given generation in fewer coupling steps, they are regarded as accelerated synthetic protocols. However, the tedious preparation of its parts or the rapid steric crowding, for the case of double stage convergent and double exponential, respectively, have limited their applicability compared to the original approaches.¹¹

1.2.2 Families and Applications

Since first developed over forty years ago, numerous dendrimer families have been prepared with various chemical compositions and multiple applications.^{13,14} The most referenced dendrimer families in the literature include the following: Tomalia's poly(amidoamine) (PAMAM);³ Fréchet's poly(arylether) (Fréchet's dendrimer);⁹ Denkewalter's poly(L-lysine) (PLL);¹⁵ Vögtle's/Meijer's poly(propylenimine) (PPI);^{2,16} Hult's aliphatic polyester (bis-MPA);¹⁷ Grinstaff's polyester (PGLSA-OH);¹⁸ Newkome's polyamide;¹⁹ Simanek's poly(melamine);²⁰ and glycodendrimers.²¹ The monomeric units of these families are shown in Figure 1.3. Their tunability, chemical stability, monodispersity, and host-guest capability at their cavities, make dendrimers interesting structures with broad applications in chemical, physical, and biological processes.¹³

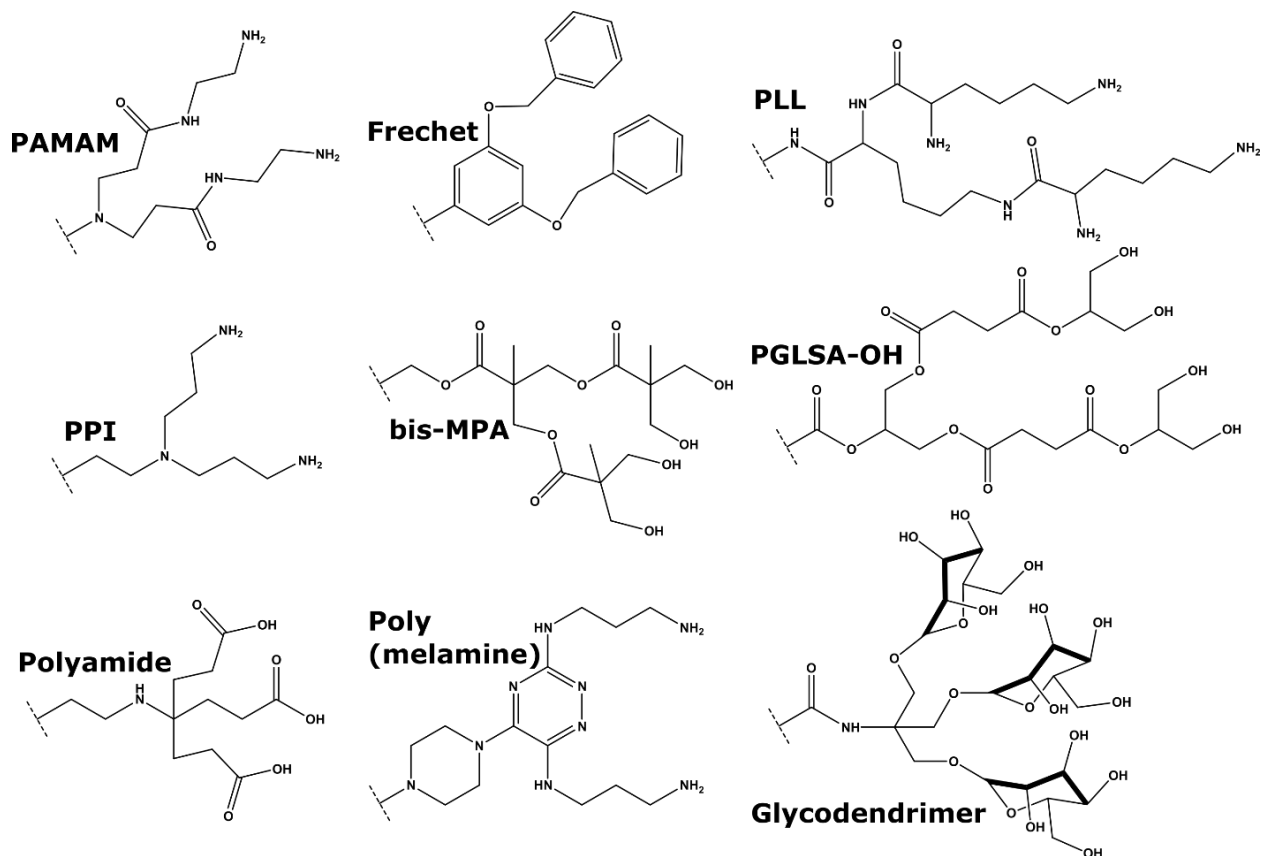


Figure 1.3 Building blocks of the most highly referenced dendrimers. Without any further surface functionalization, these would be the dendrimer surfaces.

The structural diversity, supramolecular properties, and surface multivalency in dendrimers have catalyzed their role in biomedical applications,^{14,18} overviewed in Figure 1.4. The structural diversity is easily exploited since dendrimer synthesis can be based virtually on any type of chemistry. One can imagine utilizing dendrimers made with backbones that resemble those of proteins (i.e., PAMAM, PPI, or PLL), or with biodegradable groups, (i.e., bis-MPA or PGLSA-OH) for any number of biological applications.²² As for their supramolecular properties, dendrimers can form host-guest complexes with substrates within their cavities via H-bonding, ionic interactions, hydrophobic solvation, or coordination with any of the monomeric units within the dendrimer shell. This feature has been exploited in biomedical research by encapsulation of hydrophobic drugs or imaging agents by water-soluble dendrimers.¹³ Furthermore, since multiple guests can be encapsulated in a single dendrimer, high concentrations of payload can be rapidly achieved, which is an important feature for drug delivery systems in therapeutic applications.²³

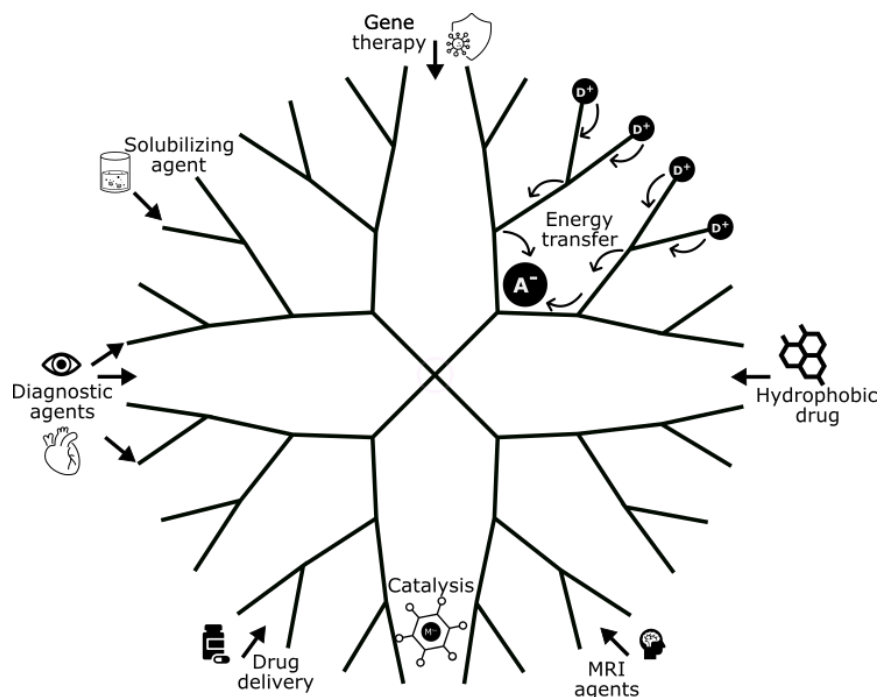


Figure 1.4 Multiple applications of dendrimers by surface modification or cavity encapsulation.

Lastly, the surface multivalency of dendrimers is probably their most exploited feature in the biomedical field, given the nature and number of groups that dendrimers can have at the periphery. Molecules of biological interest, such as targeting agents, detection labels, or affinity ligands, can be covalently attached to one or all of the surface groups of dendrimers. For example, coupling of multiple gadolinium complexes to one dendrimer resulted in sharper and more detailed MRI images, and because of its large size (compared to commercially available MRI contrast agents), longer retention times were possible.⁴ The chemistry of surface modification depends on the functional group at the dendrimer periphery and on the molecule of choice, with most dendrimers requiring common coupling methods, like amine coupling to PAMAM or PPI dendrons.⁵ Additionally, dendrimer multivalency on its own, without further functionalization, allows for multipoint-membrane interactions, which further highlights the utility of dendrimers as macromolecular carriers in therapeutic applications.¹⁰

The multiple available dendrimer families also open up the possibility to develop asymmetric structures, better known as Janus dendrimers. Named after Janus the god of duality in ancient Roman religion, asymmetric dendrimers enable the development of structures with contrasting chemical or physical properties on the same molecule.²⁴ Typically, Janus dendrimers

are prepared in one of two ways: *i*) by coupling together two dendrons of different families or generation size with a multifunctional core in a convergent fashion; or, *ii*) by coupling two different dendrons with complementary focal points (e.g., azide and alkyne) together.²⁵ Since the synthesis of Janus dendrimers tends to be more involved than the synthesis of standard dendrimers, there are fewer published examples of asymmetric dendrimers. Nevertheless, the possibility of developing dendrimers with heterofunctionality on the same complex is still an attractive feature in fields such as material science and biology.

Even though dendrimers seem to be the perfect nanopolymer for biomedical research, their progress toward clinical trials is moving at a slow pace. This is because their toxicity – which is dependent on their concentration, surface charge, and size – remains an area requiring great improvement.^{26,27} Nevertheless, there are two commercially- and FDA-approved dendrimers currently in the market: VivaGel® (Starpharma),²⁸ a PLL dendrimer-based microbicide for the prevention and treatment of bacterial vaginosis, HIV, and other sexually transmitted infections; and Stratus® CS (Siemens),²⁹ a diagnostic system for quantitative cardiac assays made with G5 PAMAM dendrimers. However, dendrimer technology still needs more time to mature to clinical applications.

While the majority of dendrimer research has focused on their development as biological agents, fundamental research has also been done in areas of catalysis^{30–32} and photophysics.^{33,34} In the former, homogenous catalysts have been incorporated within the dendrimer or at the surface, providing increased solubility (depending on the dendrimer family); unique microenvironments that resemble those of enzymes with buried catalytic centers; and multiple catalytic sites in the same molecule.¹³ Also, due to the large diameters of dendrimers compared to small molecule catalysts, they can more easily be recovered, and thus recycled. As for the photophysical studies, this is the second most researched application of dendrimers. Some examples include light harvesting^{35,36} through the dendrimer architecture, organic light-emitting diodes (OLED),^{37,38} photovoltaic devices,^{39,40} and fundamental energy transfer studies.^{41,42} Pioneer work with Fréchet-type dendrimers encapsulating an accepting species (e.g., a chromophore or metal complex),¹³ confirmed that energy transfer through the dendrimer can occur via Dexter or Förster processes.

Additionally, dendrimers can enhance the development of microenvironments that protect the accepting species from non-radiative quenchers during energy transfer events; this is collectively termed “dendrimer effect”. Furthermore, the larger the dendrimer, the more potent the

“dendrimer effect” since there is a higher density of absorbing and donor species – either by having more Fréchet-type dendrons per dendrimer or more surfaces to couple donors. In total, this provides considerable advantages over small molecules and regular polymers. Further discussion of metal-based dendrimer activity is presented in later sections.

1.2.3 PAMAM Dendrimers

PAMAM dendrimers are the most studied dendrimer family since they had the first well-detailed synthesis protocol among dendrimers, and were commercially available soon after being published for the first time. Their research has heavily focused on biomedical applications^{43,44} due to their intrinsic biocompatibility and water solubility. As seen in Figure 1.5, PAMAM dendrimers have ethylenediamine (EDA) and methyl acrylate repeating units that together make up each generation. The internal generations are prepared by sequential reaction of methyl acrylate with EDA in a two-step repeating fashion: first, alkylation of an EDA with methyl acrylate by Michael addition; and second, amide coupling to the ester from the previous step with more EDA. Each reaction cycle requires both steps to form a new generation. Ester-terminated dendrimers, after methyl acrylate addition, are designated as half-generation, while full generations are obtained after the EDA introduction. PAMAM dendrimers have also been prepared with ammonia or cystamine (both with amine reactive sites) as initiator cores to provide different branch multiplicity, and with other linear diamines with longer carbon chains (e.g., dodecamethylenediamine) to manipulate the size of internal cavities.^{12,43}

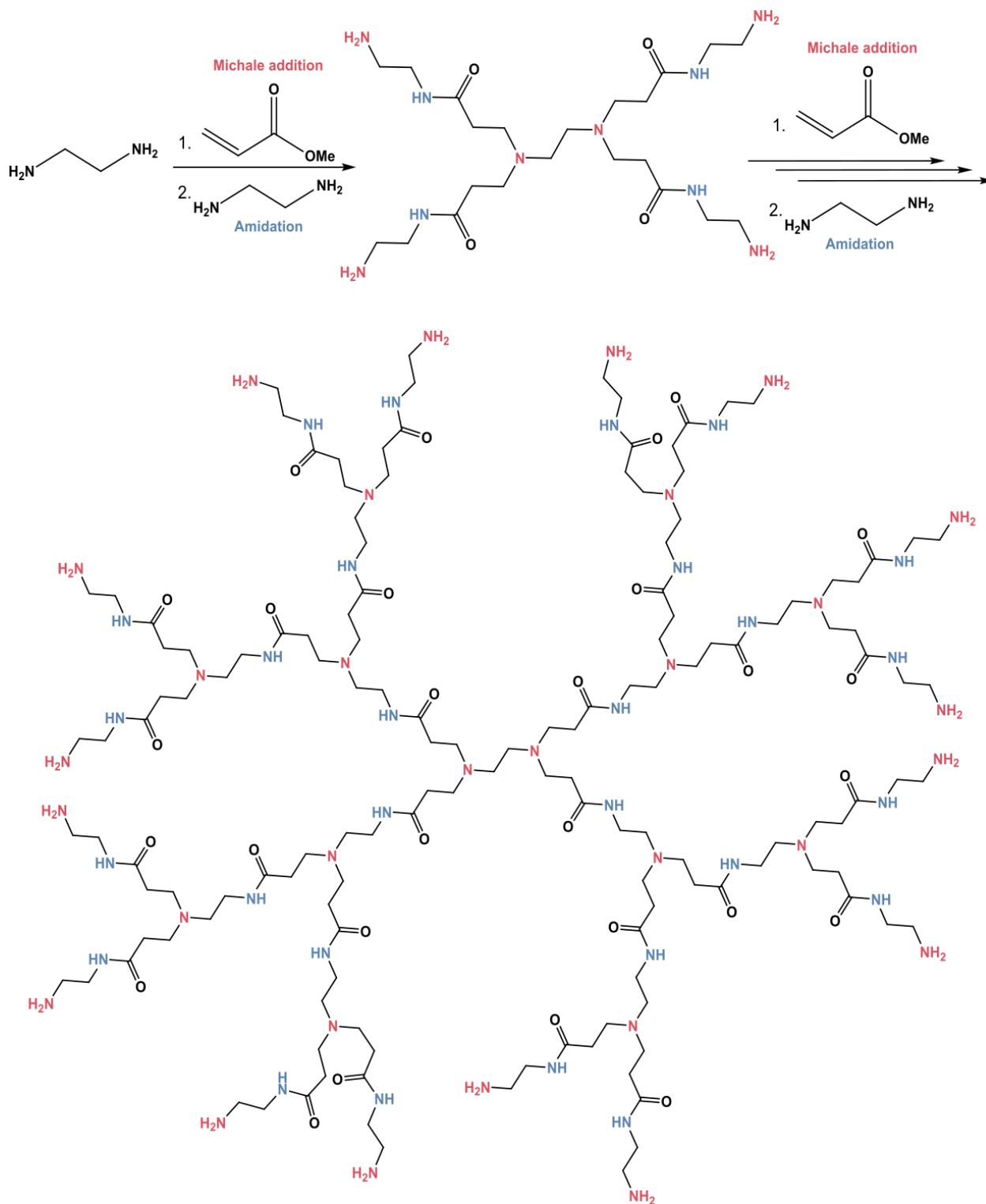


Figure 1.5 Ethylenediamine (EDA) cored PAMAM dendrimer. Synthesis follows two repetitive steps: i) Michael addition of EDA to Methyl acrylate; followed by, ii) ester amidation with EDA. Steps are repeated until the desired generation is achieved.

PAMAM dendrimer divergent growth results in a linear increase of diameter (~1 nm per generation), an exponential increase on the number of peripheral groups, and doubling of the overall molecular weight with every new generation.⁴³ As a result of this, and its chemical composition, PAMAM dendrimers can have a large number of internal amides and tertiary amine groups, as well as a high number of primary amine groups open for further functionalization. The basic interiors of PAMAM dendrimers have a great influence on their structural behavior in solution. In low pH environments ($\text{pH} \leq 4$), PAMAM dendrimers tend to have extended conformations due to the electrostatic repulsion of the internal ammonium groups. At neutral pH, moderate dendrimer back-folding (i.e., dendrons folding into the interior of the dendrimer) arises as a result of H-bonding of tertiary amine groups in the interior with the ammonium groups at the surfaces. As for high pH solutions ($\text{pH} \geq 10$), high levels of back-folding occur due to the lack of any electrostatic repulsion since dendrimers become more neutral. At this pH, PAMAM dendrimers have their most globular shape.⁴⁵ Furthermore, buffer interaction can also influence the hydrodynamic radius of PAMAM dendrimers. With phosphate-based buffers, such as PBS, $\text{HPO}_4^{2-}/\text{H}_2\text{PO}_4^-$ ions can penetrate the dendritic shell, and form H-bonds with internal amine groups at pH 5-8. The buffer-dendrimer interaction then catalyzes back-folding, which results in a decrease of hydrodynamic diameter (~1 nm reduction in G5 dendrimers).⁴⁶ The high concentration of primary amine groups at the periphery of PAMAM dendrimers are positively charged at physiological pH (7.35-7.40). Thus, they tend to have high cytotoxicity levels when compared to anionic or neutral multivalent compounds.²⁷ However, simple surface modification to suppress dendrimer toxicity is routinely employed. This is most commonly done with hydroxyl (-OH) and carboxylic (-COOH) groups, or with more elaborate groups such as long hydrocarbons or polyethylene glycol (PEG) chains.

Another important aspect to highlight about PAMAM dendrimers is their tendency to have imperfections with increasing generation. As previously explained, divergent synthesis opens up sites for defect formation, but high temperature ($>40^\circ\text{C}$), or drastic changes in pH and/or concentration can also result in further defect formation of premade PAMAM dendrimers. The most common events are due to retro-Michael reactions. But in the presence of impurities due to inadequate purification, intramolecular lactam formation and dimerization can potentially also arise, as seen in Figure 1.6.^{4,12} However, these post-synthesis defect events are not limited to only

PAMAM – dendrimers such as PPI and PLL can have similar shortcomings. Thus, proper storage and handling precautions must be followed to avoid structural defect formation.

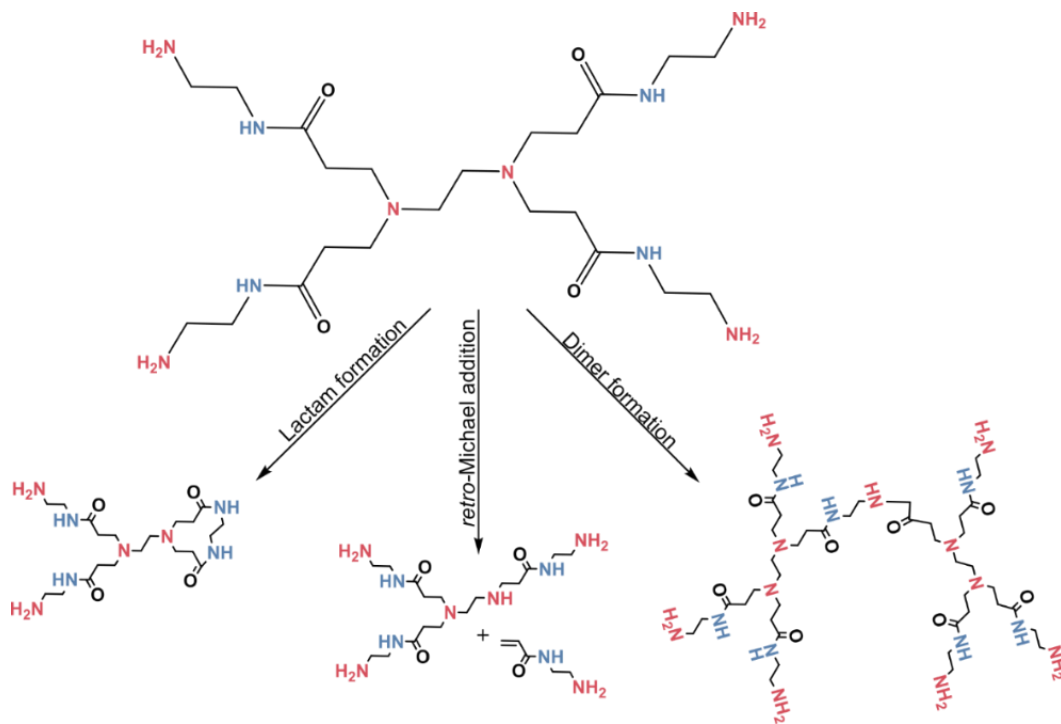


Figure 1.6 PAMAM dendrimer structural defects.

1.3 Metallodendrimers

Pioneering dendrimer research began with the development of effective synthetic methodologies, followed by their exploitation as payload carriers and delivery systems. However, over the years their utility flourished from the incorporation of metal ions into their structures. Metallated dendrimers, or metallodendrimers, are dendrimers that have one or multiple metal ions or metal clusters encapsulated, coordinated, or coupled to any part of a dendrimer.^{13,47–50} They are capable of exploiting the intrinsic physical and chemical properties of metal ions, while also exploiting those of dendrimers – such as dendrimer effects. In metallodendrimers, generation dependent dendrimer effects⁵¹ manifest as enhanced metal reactivity due to: metal cooperativity of species placed in close proximity; high and localized densities of metal ions within nanoscopic scaffolds; and, the formation of microenvironments that isolate and protect metal species within the dendrimer shell. Thus, a growing subfield of dendrimer research, and an expansion on both

metal coordination and nanomaterial synthesis, is the complexation of dendrimers with metals, and in particular, transition and rare-earth metals.

1.3.1 Classification and Examples

Metallodendrimers can have metal units incorporated at different positions within the dendritic shell (core,^{52–56} cavities,^{30,57–61} and branching units^{62–64}) or around it (surfaces^{65–71}). Additionally, albeit less common due to its synthetic complexity, multiple positions can be coordinated to metal ions at the same time (e.g., core + branching units,⁷² branching units + surface,⁷³ and core + branching units + surface^{72,74}). Preparation of the different classes of metallodendrimers is dictated by the location of the metal ion. Metal ions can be surrounded by dendrons (Figure 1.7a), incorporated into dendrimers (Figure 1.7b-d), chelated at the surface (Figure 1.7e), or synthetically included during dendrimer growth (Figure 1.7f).

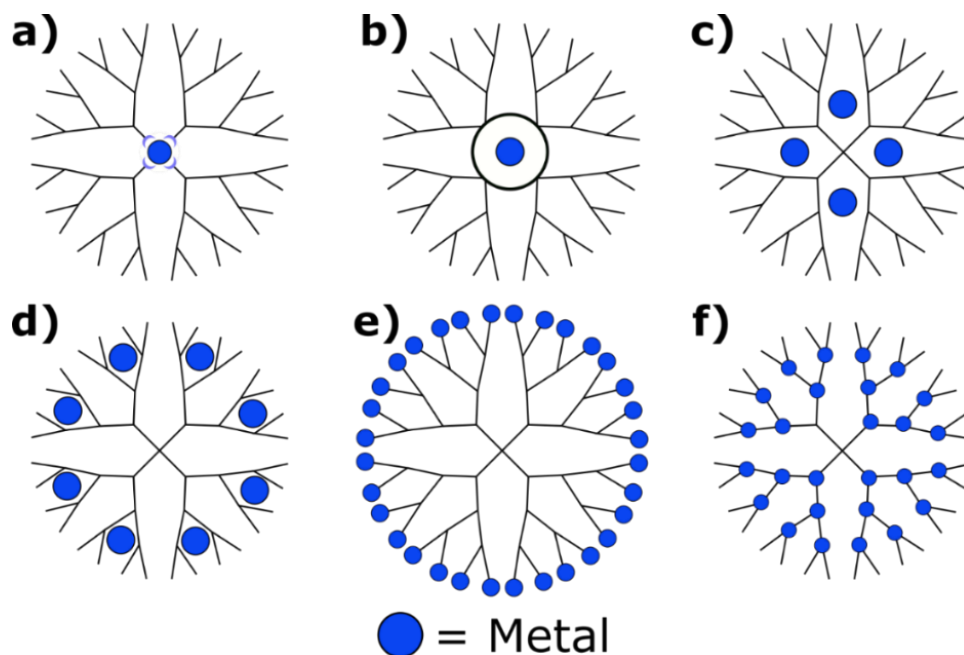


Figure 1.7 Different metal unit positions in metallodendrimers. a) Dendrimer with a metal ion core; b) dendrimer with a macrocyclic metal complex core; c) dendrimer with metal units encapsulated in cavities; d) dendrimer with metal ions coordinated to cavities with ligand centers; e) dendrimers with metals at the periphery; and f) dendrimers with metal complexes as branching units.

From a structural and synthetic point of view, metallodendrimers are most commonly assembled by placing metals at either the surface, at the ligand sites within generations, or at the

core. Metal incorporation at the surface, shown in Figure 1.7e, is usually done with preformed and prefunctionalized dendrimers. Surfaces with chelating ligand centers are able to bind multiple metal ions within a limited space. The proximity and number of metal centers per dendrimer can lead to cooperation and enhanced metal reactivity – a feature rarely seen in smaller metallic complexes. As an example, PAMAM and PLL dendrimers (G4-10) decorated at the surface with multiple gadolinium chelators, such as DOTA or DTPA groups, demonstrated enhanced sensitivity of detection and excellent imaging contrast, as well as high relaxivity (up to sixfold) compared to single Gd(III)-ion chelators.^{75,76} This was both due to an increase in concentration of Gd-chelators per dendrimer, and the high molecular weight of the compounds. In a more fundamental study, G1-3 PPI dendrimers were functionalized at the surface with 17-electron pentamethylamidoferrocenyl $[\text{Fe}(\eta^5\text{-C}_5\text{Me}_5)(\text{CO})_3](\text{PF}_6)$ species to study their molecular recognition capabilities as a function of size.⁷⁷ The metallodendrimers behaved as photoredox sensors for anion recognition of $\text{H}_2\text{PO}_4^-/\text{HSO}_4^-$ species in solution. The study concluded that generation-dependent effects on the anion recognition were observed, with increasing interaction going from G1 to G3. This can be attributed to the increasing number of $[\text{Fe}(\eta^5\text{-C}_5\text{Me}_5)(\text{CO})_3](\text{PF}_6)$ groups per dendrimer (G1:4ferrocenyls, G2:8ferrocenyls, and G3:16ferrocenyls).

Metallation is also commonly done by chelation of metal ions at the multiple ligand centers in the interior of dendrimers such as PAMAM, PLL, or PPI, as seen in Figure 1.7d. With metallodendrimers of this class, metal ion concentration can be somewhat controlled by adjusting the molar ratios of the metal and the dendrimer. But due to the multiple chelating centers, the exact location of metal species cannot be accurately determined, which can become more problematic with bigger dendrimers. Nevertheless, this metallation approach is an advantageous one since the dendrimer architecture offers an isolated environment that shields the chelated metal ions from the surrounding environment (e.g., solvent molecules). Furthermore, just as with dendrimers with metallated surfaces, multiple metal ions can be coordinated within the same complex in a limited space.³⁰ Numerous photophysical and energy transfer studies have been done utilizing this class of metallodendrimers. By first functionalizing PLL dendrimers with 24 dansyl chromophores, Vicinelli et al.⁵⁹ investigated the energy transfer from the periphery to the interior of the dendrimer chelated with a single lanthanide ion (Ln: Nd^{III} , Eu^{III} , Gd^{III} , Tb^{III} , Er^{III} , and Yb^{III}). Quenching of the fluorescent excited states of the dansyl units was observed, accompanied with the sensitization of near-infrared (NIR) emissions of Nd^{III} , Er^{III} , and Yb^{III} . When utilizing a PAMAM dendrimer

decorated with 32 naphthalimide groups, Petoud et al.^{57,58} prepared a polymetallic complex capable of chelating approximately eight lanthanide ions (Ln: Eu^{III} and Sm^{III}). The dendrimer demonstrated good sensitization of both lanthanide ions in the visible range, as well as the ability to label HeLa cells capable of emitting in the NIR when using the Sm^{III} metallodendrimer.

Dendrimers with metallated cores can be prepared by coordinating dendrons with suitable focal points around a metal ion (Figure 1.7a), or by having a well-defined metal macrocycle from which dendrons grow outward (Figure 1.7b). For metal ion-cored metallodendrimers, dendrons with appropriate focal points can self-assemble around a metal ion. Classic examples include Ru^{II}- and Ln^{III}-cored metallodendrimers. Ru^{II}-cored metallodendrimers have been prepared with bipyridine focal point dendrons (Fréchet-type) to yield luminescent and redox active dendrimers.^{55,78} Photophysical studies of these compounds with naphthyl peripheral units in organic solutions (e.g., acetonitrile or dichloromethane) demonstrated excellent (~90%) energy transfer from the naphthyl chromophores, through the polyaryl dendritic shell, and into the [Ru(bpy)₃]²⁺ core. As a result, the [Ru(bpy)₃] cored metallodendrimers exhibited strong luminescent signal in the visible region (λ_{max} : 610 nm) upon excitation in the UV region. Furthermore, in aerated solutions or solutions with dissolved methylviologen, the rate of quenching events was significantly reduced due to the protection of the core by the dendritic shell. In fact, luminescent intensities twice as large as compared to the nondendritic [Ru(bpy)₃]²⁺ complex were observed.⁷⁹

Similar energy transfer and luminescent sensitization was observed when three carboxylic acid focal point polyaryl dendrons were self-assembled around Ln^{III} ions (Ln: Er^{III}, Tb^{III}, and Eu^{III}).⁵⁶ Photophysical experiments in toluene solutions and in the solid state irradiated with UV-light (280-290nm), demonstrated that strong luminescent signal arises from the Ln^{III}-cored metallodendrimers. The dendrimer shell offered good chelating sites only at the core, and protection from self-quenching events (Ln-Ln) by coordinating only one metal ion per dendrimer, while also protecting the metal ion from the surrounding environment. Generation-dependent effects were also observed, with larger dendrimers having enhanced luminescent properties. This was attributed to the antenna effect of the dendrimer framework (described in detailed in later sections). Therefore, the dendrimer served as a good chelating and sensitizing ligand system.

In general, metal ion-cored dendrimers offer better control of the location and concentration of metal species compared to surface or cavity metallation. However, well-defined

macrocyclic units as the core of dendrimers offers a more secure encapsulation of the metal ion. Examples of macrocyclic-cored metallodendrimers are scarce, with porphyrin- and cyclam-core complexes as the leading standards (Figure 1.8). Porphyrin-cored dendrimers were intended to resemble hemoproteins.⁸⁰ In order to protect the heme activity from the surrounding environment, the hemoprotein active site is buried within a protein matrix. Likewise, the core of porphyrin metallodendrimers is buried within the dendritic shell offering similar protection. Furthermore, due to the tunability of dendrimers, this class of metallodendrimers offers significant advantages over smaller systems.⁵² Pioneering work from Aida et al. utilizing G4 Fe(II) porphyrin-cored dendrimers demonstrated that the metallodendrimers were capable of carrying O₂ in a similar fashion to hemoproteins.⁸¹ The O₂-Fe adduct was long lived ($t_{1/2}$: +2 months) and when N₂ (g) was bubbled into the reaction solution, deoxygenation occurred. The study concluded that oxygenation and deoxygenation cycles could be repeated due to the dendritic shell protection of the porphyrin core. Additionally, they observed low gas permeability, which signifies that the Fe^{II} core has high resistance to carbonylation in a CO atmosphere. Thus, this early study confirmed the ability to combine the intrinsic properties of the macrocyclic core with those of the surrounding dendrimer. Many more studies have been performed ever since with an array of dendrimer families (Fréchet-type, PAMAM, polyamide, etc.), and have investigated multiple areas of porphyrin chemistry (luminescence,^{54,82} spectroscopy,^{63,83} energy transfer,^{42,84} and biological applications⁸⁵).

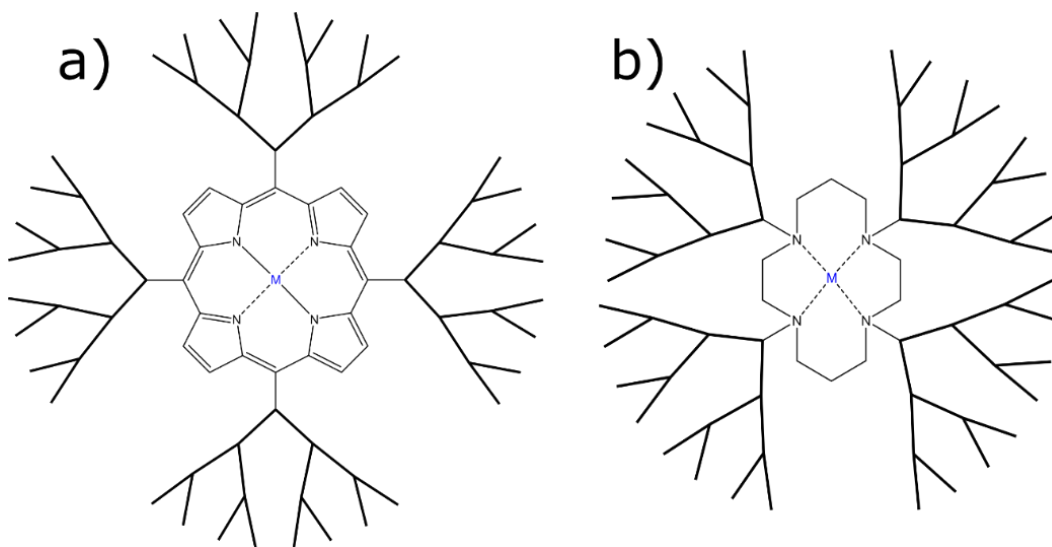


Figure 1.8 Schematic representation of a) meso-porphyrin-cored and b) cyclam-cored metallodendrimers.

Metallodendrimers with a 1,4,8,11-tetraazacyclodecane (cyclam) cores are capable of coordinating an array of transition metals (Co^{II} - Zn^{II}) and lanthanide ions with large stability constants.⁸⁶ Just as with the porphyrin-cored dendrimers, these metallodendrimers have a well-defined metal-coordinating macrocyclic center. But unlike the porphyrin complexes, cyclam-cored dendrimers tend to form dimers when metallated with transition metals⁸⁷ and trimers with lanthanide ions.⁸⁸ This structural conformation is driven by the steric hindrance of the surrounding dendrons, and the need to fulfill the metal ion coordination sphere.

As for their application, cyclam-cored metallodendrimers have been studied for their spectroscopic properties as sensors^{86,89,90} and molecular antennae.^{91,92} Interestingly, while lanthanide ions are securely encapsulated at the core of cyclam metallodendrimers, luminescent sensitization has not been observed. This seems to be due to inefficient energy transfer from the excited states of the surrounding dendrons to the emissive states of the lanthanide core.⁸⁸ This is true even when prepared with Fréchet-type dendrons (known for their excellent energy transfer) or with multiple naphthyl units at the surfaces. Thus, the energy transfer efficiency and the nature of the Ln^{III} coordination sphere are closely related to each other.

Generally, metallodendrimers have been heavily exploited as multivalent ligand systems for transition-metals and lanthanide ions. This is because the dendritic architecture offers (i) a shielded environment for metals from quenching processes (when encapsulated or at the core); (ii) metal-signal amplification due to high concentrations or close proximity (or both); and (iii) light harvesting and energy transfer pathways to the metal ions. Their synthesis depends on the location and number of the metal ions, while its application is determined by the position, nature, and concentration of metal species. Moreover, while metallodendrimers with metal ion only at the core limit the amount of metal concentration per dendrimer, they offer stoichiometric and more stable (in the case of macrocyclic-cored) metal incorporation, which results in an overall higher synthetic control of the complex. From these qualities and the examples described above, it is apparent that the complexation of dendrimers with metal ions has inspired (and continuous to inspire) the development of a variety of novel compounds – from catalysts, to spectroscopic probes, to optical materials.

1.4 Metallacrowns

Metallacrowns (MCs), inorganic analogues of crown ethers with a $[\text{Metal-N-O}]_n$ repeating unit, are polymetallic macrocycles inspired by the molecular topology and chelating properties of crown ethers, as well as by the ligand coordination principles and ease of self-assembling systems.⁹³ MCs' composition arises from hydroxamic acid ligands (M-N-O) coordinating to two metal ions (M-N-O) in the hydroximate form (the doubly deprotonated form of a hydroxamic acid) to generate a macrocyclic ring. As seen in Figure 1.9, the oxygen atoms in the MC ring point inward, creating a metal chelating site at its cavity. Therefore, just like crown ethers, MCs are able to encapsulate a wide range of metal ions in their cores.⁹⁴ As for their nomenclature, MCs also follow crown ethers' approach, but with added details to describe the type of ring metal ions (M) and central metal ions (M'), the heteroatom in the ring (Z), the hydroxamate ligand (L), the bound anions or bridging ligands (L'), the counter ions (X), and the solvent molecules (Y) that template the MC scaffold.⁹⁵ Thus, the explicit MC nomenclature in this thesis is as follows: $M'[\text{ring size-MC}_{M(n)Z(L)\text{-ring oxygens}}]L' \cdot X^{n+} \cdot Y$. However, since this nomenclature is rather long, a shorthand version is used in which ions and solvent molecules that are not essential are omitted. For example, the scaffold $\text{Ln}[12\text{-MC}_{\text{Ga(III)N(shi)4}}](\text{benzoate})_4(\text{pyridinium})(\text{MeOH})(\text{Pyridine})_2$ is written as $\text{LnGa}_4\text{Shi}_4(\text{benzoate})_4$.

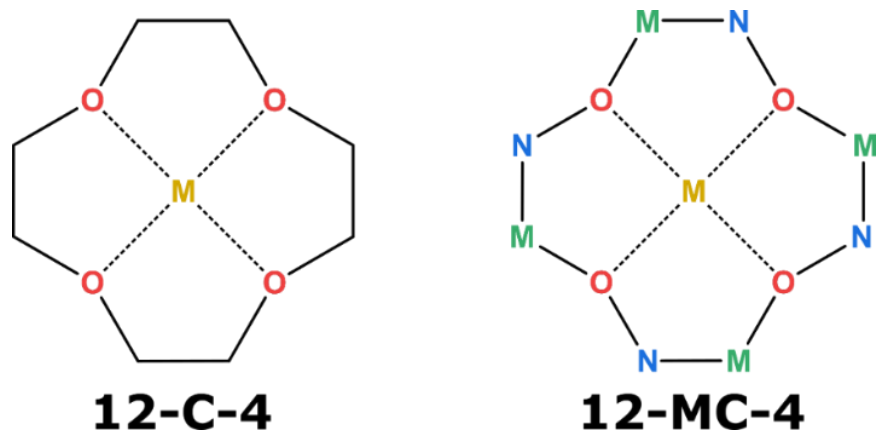


Figure 1.9 Structural comparison of crown ethers (left) and metallacrowns (right). Both named based on their ring size and number of oxygen atoms. Both structures as representing a 12-membered ring with $[\text{C-C-O}]_4$ repeating units for the crown ether and $[\text{M-N-O}]_4$ repeating units for the MC.

1.4.1 Structural Design, Synthesis, and Applications

To narrow down the discussion regarding the design and synthesis of MCs, this section mainly focuses on heterometallic 12-MC-4 scaffolds with $3d+4f$ metal ions or group-13+ $4f$ metal ions (ring metal + central metal, respectively). Brief references to 15-MC-5 scaffolds are done to emphasize their structural differences and stability compared to 12-MC-4 complexes. Ample discussion on the selection of $4f$ metals is done in later sections.

Since being first discovered in 1989,⁹⁶ a wide array of MC sizes^{95,97,98} with a variety of metal combinations^{93,94,99–102} have been prepared. When developing novel MC scaffolds, their design requires delicate control of all of the synthetic variables (i.e., ligands, metals, solvent, counterions, stoichiometry, and crystallization conditions). However, with careful attention to the principles of coordination chemistry, one can successfully design and predict specific structures⁹³ – an attribute that is sought after in any self-assembled complex. The high degree of geometric and structural control of MCs arises from the templating ring ligands. As seen in Figure 1.10, with MCs such as 12-MC-4 and 15-MC-5 (the two most commonly studied scaffolds), ligands such as salicylhydroxamic acid (H_3Shi) and picoline hydroxamic acid ($picHa$), can coordinate metal ions at 90° and 108° , respectively. This coordination arrangement generally results in a squared-shaped 12-MC-4 and a pentagonal 15-MC-5.¹⁰³ However, in some instances, and under specific reaction conditions mainly driven by the metal ion of choice, this ring arrangement can be partially circumvented. For example, 12-MC-4 structures with $picHa$ or α -amino hydroxamic acids have been prepared with Ni^{II} , Cu^{II} , or Zn^{II} as both the ring and central metal ions. The templating ligands adopt a 90° conformation over the preferred 108° to compensate for the encapsulation of the relatively small central metal ions. In other words, since the cavity radius of a 15-MC-5 is too large ($\sim 1.05 \text{ \AA}$) to securely encapsulate the divalent transition metal ions (Ni^{II} : 0.70 \AA , Cu^{II} : 0.74 \AA , and Zn^{II} : 0.74 \AA), the ring ligands must endure structural adjustments at each metal site to accommodate the four-fold symmetry assembly of the 12-MC-4 scaffold.¹⁰⁴ However, these MC scaffolds are not stable in solution, and have been identified as the primary intermediate in the assembly of $M^{III}15-MC-5$ compounds, where M^{III} is a trivalent metal ion with a larger ionic radius. This was proven by adding lanthanide salts (Ln^{III} : Nd-Yb) to the preformed $M^{II}12-MC-4$ scaffolds, and observing the formation of the new 15-MC-5 species with Ln^{III} as the central metal.^{104,105}

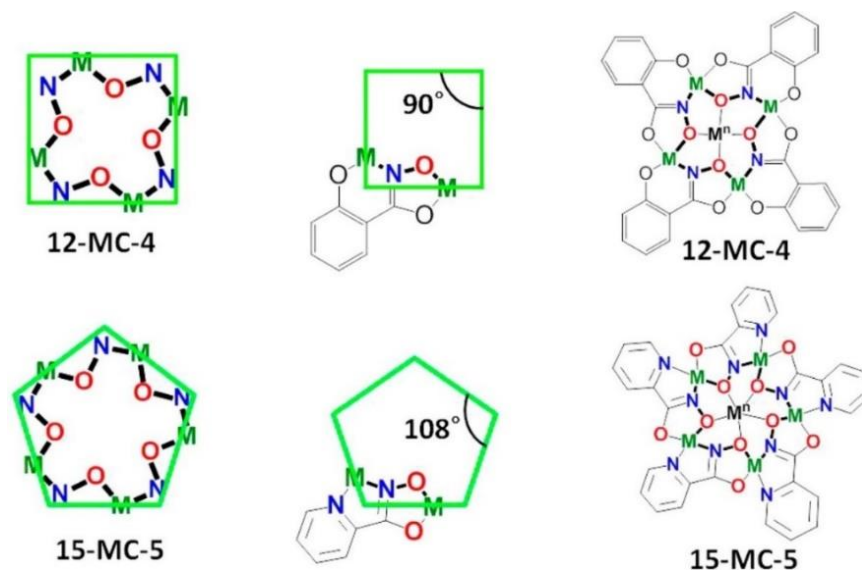


Figure 1.10 Diagram showing ring ligand coordination and its influence on ring geometry. Salicylhydroxamate ligand (middle top) templates a square-shaped 12-MC-4, while picoline hydroxamate ligand (middle bottom) generates a pentagonal-shaped 15-MC-5.¹⁰³

As for their syntheses, given the fact that MCs are self-assembled structures, their preparation simply requires the mixture of their components in an appropriate solvent system. Stoichiometric addition of bases, such as sodium hydroxide or pyridine, are often added to ensure full deprotonation of the organic ligands, and as counterions for charge balance. MC crystals then precipitate as a result of slow solvent evaporation; vapor diffusion of solvents; or delicate layering with water on top of the dissolved reaction. Either approach can be used to ensure supersaturation of the solution that then foments MC crystallization. With regard to the solvent of choice, one has to keep in mind different factors: (a) it must be able to dissolve all of the individual ingredients; (b) it should not interfere with MC formation (i.e., strongly bind to reaction components); (c) it should non solvate the MC too well as to inhibit crystallization; and ideally, (d) it should only produce one type of MC. Regarding the last point, an interesting study by Jankolovits et al. demonstrated the solvent-dependence behind the assembly of MC with picoline hydroxamic acid (picHa), Zn^{II} , and Ln^{III} ions with a series of different solvent systems (DMF, MeOH, Pyridine, H_2O /Pyridine, and DMF/Pyridine).¹⁰³ This study suggested that both the metal ions' polarization and geometries are determining factors behind solvent-dependent effects in MC formation. This reinforces the ease of MC self-assembly synthesis, while also highlighting the importance of thoughtful design.

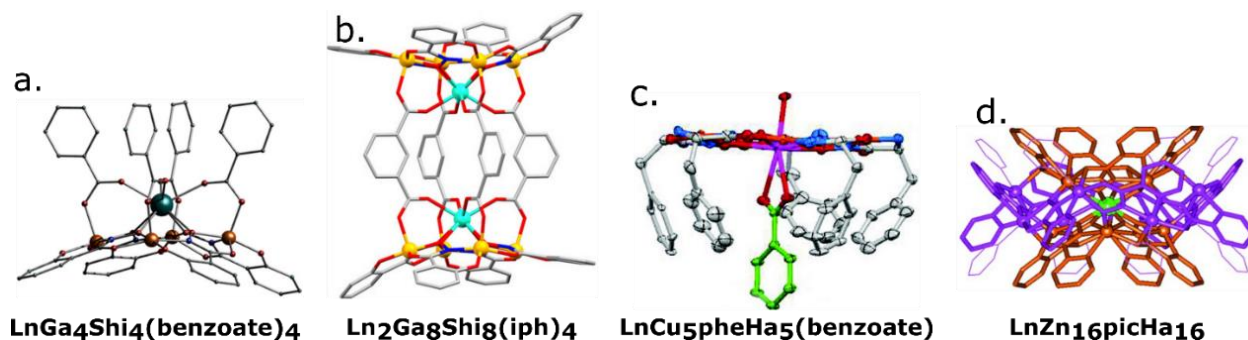


Figure 1.11 Crystal structures of different MCs illustrating the different bridges (or lack of) needed to complete the coordination sphere of their lanthanide cores.^{101,102,106,107}

The metal selection, nature, valency, geometry, and intrinsic properties of the ring and central metal ions must be taken into consideration when preparing MC complexes. The ring metal ions in MCs are most commonly 3*d* transition metal ions or group-13 metal ions (Al–In). In order to provide charge balance to the MC scaffold, trivalent metal ions are commonly paired up with triprotic ring ligands (such as H₃Shi). Similarly, divalent metal ions and diprotic ligands (such as picHa) are combined together.⁹³ As for the central metal ion, the first MCs consisted of homometallic complexes with 3*d* metal ions encapsulated in their cavities.¹⁰⁸ But this was soon expanded to make heterometallic complexes with different metal groups.^{93–95,109} Depending on the central metal ionic radius, MC scaffolds arrange their configuration to ensure a cavity size of matching diameter. Furthermore, if necessary, bridging ligands (or sometimes counter ions or solvent molecules) can complete the coordination sphere of the central metal. For example, in Ln[12-MC_{Ga(III)N(shi)-4}](benzoate)₄(pyridinium)(MeOH)(Pyridine)₂ (shorthand: LnGa₄Shi₄(benzoate)₄)¹⁰² and dimeric Ln₂[[12-MC_{Ga(III)N(shi)-4}]₂(isophthalate)₄(ammonium)(DMF)₂ (shorthand: Ln₂Ga₈Shi₈(Ip)₄)¹⁰⁶ metallacrowns, the benzoate and isophthalate ligands coordinate to each of the four ring metals and the central lanthanide metal to fulfill the eight-coordinate sphere of the ring metals and the lanthanide core (Figure 1.11a and b). In the case of the Ln₂Ga₈Shi₈(Ip)₄, the isophthalate ligands are also bridging two LnGa₄Shi₄ MCs together. As for 15-MC-5 motifs with Ln^{III} at their core, metallacrowns such as Ln[15-MC_{Cu(II)N(pheHa)-5}](NO₃)₃ (shorthand: LnCu₅pheHa₅, pheHa: phenylalanine hydroxamate),¹¹⁰ three nitrate groups complete the coordination sphere of the Ln^{III} ion (Figure 1.11c). However, the solvents can be easily displaced and leave behind open coordination sites for other ligands, such as carboxylates. For this reason, Ln^{III}15-MC-5 motifs have been extensively

studied as molecular recognition agents.¹⁰⁹ In instances where the MC scaffold is able to fulfill the coordination sphere, no extra ligands or solvent molecules are required. This is the case of Ln[12-MC_{Zn(II)N(picHa)-4}]₂[24-MC_{Zn(II)N(picHa)-8}](triflate)₃(pyridine)₈ (shorthand: LnZn₁₆picHa₁₆), where the Ln^{III} ion is coordinated to two 12-MC-4 scaffolds and surrounded by a 24-MC-8 belt (Figure 1.11d).¹⁰¹ In this MC, the eight-coordination sphere of the metal core is completely fulfilled by the MC's ring ligands. It should be also noted that, in many cases, solvent molecules still coordinate to MCs through the secondary coordination sphere. Additionally, counter ions can also coordinate, and in most cases are necessary to provide charge balance to the overall structure.

Due to their broad structural diversity, the ease of their self-assembling construction, and the wide variety of metal ions that can be used to template their rings, MCs have been studied for a broad range of applications. To narrow down the discussion of these applications, emphasis is given to scaffolds with lanthanide ions as the central metal, and 3*d* transition metal ions at the ring. The first MCs were studied for their metal ion sequestration capabilities, and proven early on to be able to encapsulate transition, alkali, lanthanides, and a few actinide metal ions in solution.¹⁰⁹ Eventually, heterometallic MCs were prepared with the aim to further exploit the intrinsic chemical and physical properties of 3*d* transition metals and rare-earth metal ions.

Host-guest and molecular recognition applications of MCs have been best studied with 15-MC-5 scaffolds where the central ion is a lanthanide metal (Ln^{III}: La^{III}, Gd^{III}), and the ring ligands are either Cu^{II} or Ni^{II}. With these scaffolds, dimeric compartments assemble for selective recognition of carboxylate guests coordinated to the Ln^{III} core. This host-guest behavior and selective recognition has been observed in both solution and solid state.^{107,110,111}

The magnetic properties of several MC scaffolds with lanthanide ions (Ln^{III}: Dy^{III}, Gd^{III}, Tb^{III}, Sm^{III}) and Mn^{III}, Cu^{III}, or Ga^{III} have also been of great interest.^{112–117} Since MCs are able to accommodate multiple metal ions within a small volume and at well-defined locations, metal-metal interactions can be enhanced. This is of special interest in the field of single-molecule magnets (SMM), where such interactions result in large spin densities. Furthermore, their well-defined and varied topologies allow to better control and study the magnetic anisotropy of MCs.⁹⁵ Lastly, in the past decade, the application of lanthanide-based MCs as luminescent probes has grown drastically. With numerous publications,^{101,102,106,118–124} patents,^{125–127} and preliminary biological studies,^{128,129} luminescence has become one of the most sought-after applications in MC research.

1.4.2 Lanthanide Ion Luminescence

Before going into more detail about lanthanide-based luminescent metallocrowns, a brief review on the basics of lanthanide (Ln^{III}) ion luminescence and probe design, is presented. The interesting luminescent properties of Ln^{III} ions arise from their characteristic electronic configuration ($[\text{Xe}]4f^n$ (n : 0-14)). These metals exhibit sharp emission bands, long luminescent lifetimes, and strong resistance to photobleaching. Luminescent emission occurs from intra-configurational f-f transitions that, because they are shielded by their outer $5s^25p^6$ subshells, are minimally perturbed by their surrounding crystal field environment. This translates into well-defined and narrow emission spectra characteristic of each Ln^{III} ion, and that are mainly unaffected by the metal coordinating environment.^{130,131} With the exception of La^{III} ($4f^0$), Ce^{III} (impending 4f-5d transitions), Pm^{III} (radioactive), Gd^{III} (UV emission), and Lu^{III} ($4f^{14}$), Ln^{III} ion luminescence can be observed with a wide range of colors, and throughout the visible (Pr^{III} - Tm^{III}) and near-infrared (Pr^{III} - Sm^{III} , Dy^{III} - Yb^{III}) spectrum,¹¹⁹ making them interesting metal ions for tailorable luminescent spectroscopy.

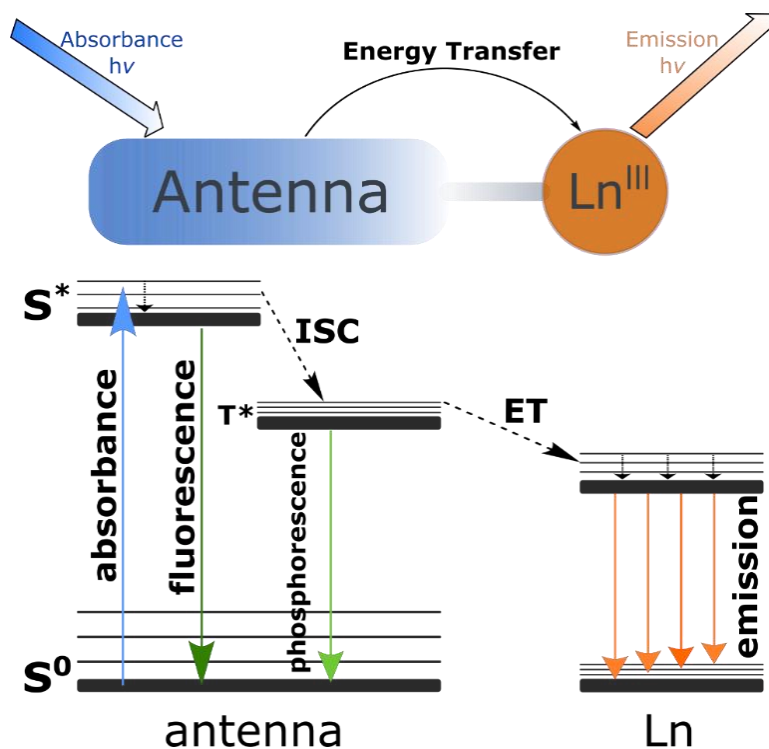


Figure 1.12 Diagram of the antenna effect (top). Simplified Jablonski diagram representing (bottom) energy absorption, transfer, and radiative emissions of the lanthanide ion. S^0 and S^* : ground and excited singlet states, respectively. T^* : excited triplet state. ISC: intersystem crossing. ET: energy transfer.

The same electronic configuration that endows Ln^{III} ions with their unique spectroscopic attributes and long luminescent lifetimes, is also responsible for their low molar absorptivity (<10 M⁻¹cm⁻¹) due to the Laporte and spin selection rules. Therefore, direct excitation of the Ln^{III} ions into their 4f excited states is inefficient, and rarely yields strongly luminescent signals unless excited by a high-power source (like a laser). However, indirect excitation of Ln^{III} emission can be done by placing highly absorbing ligands in close proximity to the metal ion, followed by energy transfer to the Ln^{III} ion emissive state.^{132,133} Illustrated in Figure 1.12, this sensitization mechanism, known as the antenna effect, features a main energy transfer pathway that starts at the ligand-centered absorption through the singlet states ($S^0 \rightarrow S^*$), followed by intersystem crossing to the ligand-centered triplet state ($S^* \rightarrow T^*$). From there, the final energy transfer to the Ln^{III} emissive states occurs ($T^* \rightarrow Ln^*$), ending with the relaxation to the J ground state of the Ln^{III} ion, and its luminescent emission. Metal to ligand charge transfer (MLCT) and inter/intra-ligand charge transfer (ILCT) events can also contribute to the lanthanide sensitization. Lastly, it is important to mention that the intramolecular energy transfer from antennas to Ln^{III} ions can follow either Förster (through space) or Dexter (through bond) processes depending on the ligand system surrounding the metal ion.¹³¹ The excitation and emission bands of Ln^{III} ions excited through the antenna effect tend to have very large separations, known as pseudo-Stokes shifts. This is because the antenna usually absorbs in the 300-400 nm range, while the Ln^{III} emission is always above 400 nm extending up to the NIR. This simplifies signal quantification and experimental design by allowing obvious spectra discrimination of the absorbed and emitted light.

Competitive energy transfer can also occur, hindering the overall energy transfer and luminescent intensity of the lanthanide. Nonradiative deactivation by the ligand system or solvent molecules are most commonly attributed to the vibrational overtones of X-H (X: O, N, C).¹³⁴ To minimize such vibrational quenching, careful design of the lanthanide probe is needed to keep X-H groups away. For example, encapsulating the Ln^{III} ion in a sterically bulky ligand system where solvent molecules cannot access the metal ion, such as a metallodendrimer, or a rigid metallated ligand system with limited X-H groups at a fixed distance from the Ln^{III} ion, such as a MC. Low-lying ILCT states can also nonradiatively quench the luminescent signal through photo-induced electron transfer, mainly affecting the more redox-sensitive Ln^{III} ions (i.e., Sm^{III}, Eu^{III}, and Yb^{III}).^{135,136} As for radiative quenching processes (e.g., ligand fluorescence or phosphorescence), careful ligand design is also necessary to minimize their effects. Since the energy difference (ΔE)

between the antenna's T^* and the Ln^{III} emissive state is a well-established parameter influencing sensitization efficiencies,¹³¹ one common approach is to design ligands with triplet states that are between 2500-3000 cm^{-1} away from the emissive states of the Ln^{III} ion, as shown in Figure 1.13. If the ΔE is too small, energy back transfer events occur ($T^* \leftarrow \text{Ln}^*$), which often results in molecular phosphorescence and lower quantum yields (ϕ). Similarly, the ΔE between the S^* and T^* ligand states should be close to 5000 cm^{-1} from each other to ensure efficient intersystem crossing.

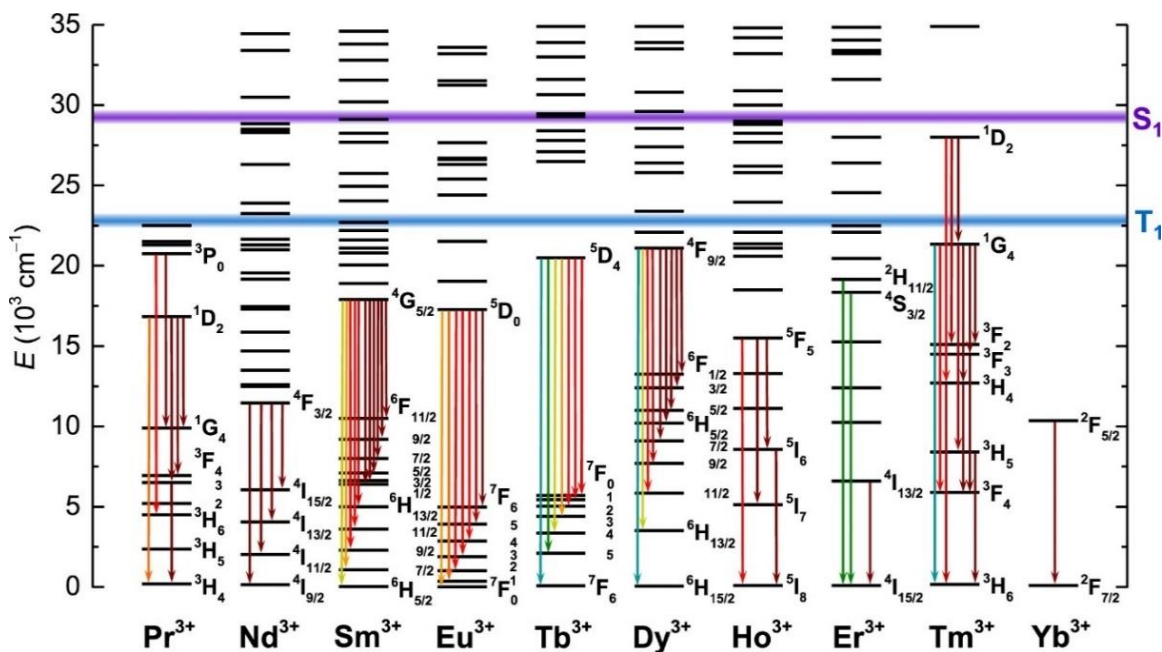


Figure 1.13 Partial energy diagram of Ln^{III} ion highlighting the emissive states of each metal ion and the singlet and triplet energy position of an efficient $\text{Ln}[12\text{-MCGa}(\text{III})\text{N}(\text{shi})\text{-4}]_2$ scaffold,¹¹⁹ with the following emissive states for each lanthanide: $\text{Pr}({}^3\text{P}_0)$: 20475 cm^{-1} , $\text{Nd}({}^4\text{F}_{3/2})$: 11460 cm^{-1} , $\text{Sm}({}^4\text{G}_{5/2})$: 17900 cm^{-1} , $\text{Eu}({}^5\text{D}_0)$: 17260 cm^{-1} , $\text{Tb}({}^5\text{D}_4)$: 20400 cm^{-1} , $\text{Dy}({}^4\text{F}_{9/2})$: 21100 cm^{-1} , $\text{Ho}({}^5\text{F}_5)$: 155000 cm^{-1} , $\text{Er}({}^4\text{I}_{13/2})$: 6700 cm^{-1} , $\text{Tm}({}^1\text{G}_4)$: 21350 cm^{-1} , and $\text{Yb}({}^2\text{F}_{5/2})$: 10300 cm^{-1} .^{1,137,138}

Two important parameters for the quantification and basic understanding of luminescence are quantum yield (ϕ) and luminescent lifetime (τ_{obs}).^{130,131} Luminescent quantum yield is the measurement of emission efficiency of any luminescent complex, and in simple terms it is defined as

$$\phi = \frac{\text{number of emitted photons}}{\text{number of absorbed photons}} \quad (1.1)$$

For the overall quantum yield of lanthanide complexes (φ_{Ln}^L), defined as the Ln^{III} luminescence under ligand excitation, the following equation is used,

$$\varphi_{Ln}^L = \eta_{sens} \varphi_{Ln}^{Ln} . \quad (1.2)$$

Here η_{sens} is the efficiency of sensitization of the ligand system, and φ_{Ln}^{Ln} is the intrinsic quantum yield of the Ln^{III} ion. This latter term is the yield of the metal-centered luminescence upon direct excitation. The φ_{Ln}^{Ln} is directly related to rate constant of radiative (k_{rad}) and nonradiative (k_{nrad}) deactivation processes, as follows:

$$\varphi_{Ln}^{Ln} = \frac{k_{rad}}{k_{rad} + k_{nrad}} = \frac{k_{rad}}{k_{obs}} . \quad (1.3)$$

While the radiative (τ_{rad}) and luminescent (τ_{obs}) lifetimes relate to each other, as follows:

$$\varphi_{Ln}^{Ln} = \frac{\tau_{obs}}{\tau_{rad}} . \quad (1.4)$$

And τ_{obs} is defined as $1/k_{obs}$.

Understanding the basics of lanthanide ion luminescence is important when developing new ligand systems as luminescent probes. To design an effective Ln^{III} ion probe, the antenna must absorb and transfer energy efficiently, as well as secure the metal ion in place, and minimize nonradiative quenching events. If the Ln^{III} probe were to be used in solution state, solvent protection and solution stability are also required. Lastly, for biological imaging applications, Ln^{III} probes should be soluble, stable, and luminescent in aqueous environments. As well as excitable at >400 nm in order to avoid photoinduced damage of biological samples in *in vitro* analysis or at NIR for *in vivo* experiments. Furthermore, sensitization of the NIR Ln^{III} ion emitters would be of great interest since this wavelength range is well suited for biological imaging applications.^{134,139}

1.4.3 Ln^{III}-Based Luminescent Metallacrowns

Careful design of the surrounding Ln^{III} environment is key to obtain: secure metal ion encapsulation; large molar absorptivity; efficient energy transfer; solvent protection; reduction of nonradiative deactivating pathways; intense luminescent signal; and sensitization of a variety of Ln^{III} ions. To this end, MCs provide an ideal environment for Ln^{III} ion luminescence. This is due to several unique features: oxime rings that securely encapsulation the metal ion; bridging ligands that complete the coordination sphere of the Ln^{III} and further stabilize it in place; a framework with multiple antennas resulting in large extinction coefficients; a rigid polymetallic architecture with limited bonded X-H vibrational oscillators; and a scaffold able to sensitize a wide range of Ln^{III} while nullifying the need to synthesize different scaffolds for different Ln^{III} ions.

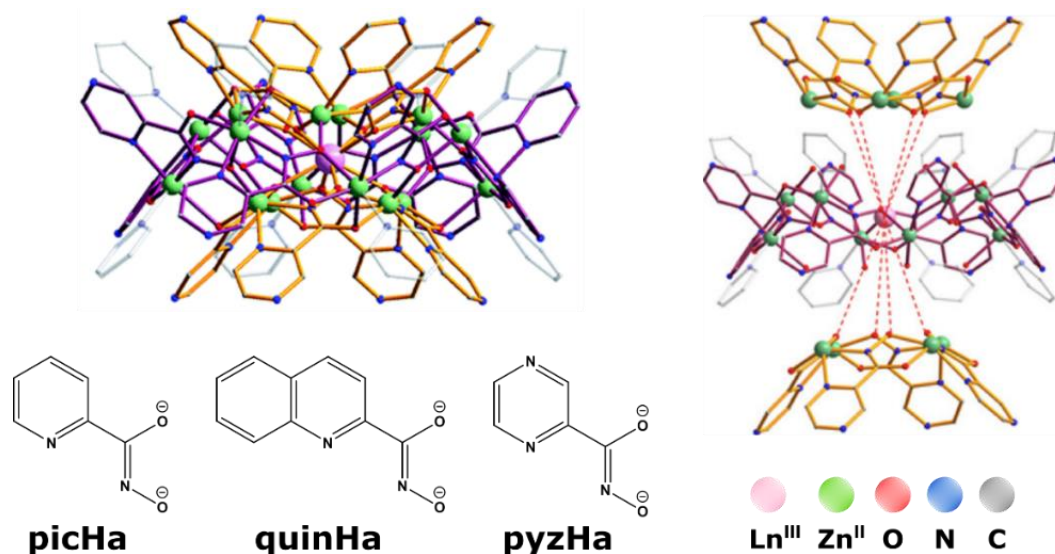


Figure 1.14 Crystal structure of Nd[12-MC_{Zn(II)N(pyZHa)-4}]₂[24-MC_{Zn(II)N(pyZHa)-8}] metallacrown (*top left*), showing the host(host-guest) motif (*right*), and the three different ring ligands used to prepare **LnZn₁₆L₁₆** MCs. Figure adapted from ref. 125 and 126.^{128,129}

Luminescent MCs can be divided into the zinc family and the gallium family based on the ring metal ions. The Zn-family was the first reported example of MCs exhibiting NIR luminescence by efficiently sensitizing Nd^{III}, Er^{III}, and Yb^{III}.^{101,118,128} As previously described, these MCs have an overall chemical formula of Ln[12-MC_{Zn(II)N(L)-4}]₂[24-MC_{Zn(II)N(L)-8}] (shorthand: LnZn₁₆L₁₆, L: ring ligand), where a single Ln^{III} ion is surrounded by sixteen antennas. The LnZn₁₆L₁₆ scaffold was also the first reported MC prepared with Zn^{II} metal ions as the ring metal, and the first MC with a host(host-guest) like scaffold as seen in Figure 1.14. The closed-

shell Zn^{II} was selected as the ring metal since its full $3d^{10}$ shell prevents luminescent quenching through d-d transitions, and it is optically transparent in the visible and NIR spectrum. The first $LnZn_{16}L_{16}$ MC was prepared with picHa as the ring ligand, but in an effort to red-shift the absorbance maxima, the second member of the Zn-family utilized quinaldichydroxamate (quinHa), which shifted the absorption to 380nm. The next generation aimed to improve the water solubility of the MC, so the ring ligand was switched to pyrazinehydroximate (pyzHa). With this ligand, $LnZn_{16}pyzHa_{16}$ became the first luminescent water-soluble MC. Furthermore, all of these MCs have the same host(host-guest) like conformation, are highly stable in solution, and have the special structural feature that no O-H or N-H vibrational oscillators are in close proximity to the Ln^{III} metal, and that the nearest C-H bond is at 6.7 Å with picHa and pyzHa, and at 7.0 Å with quinHa.

As for their photophysical properties, the presence of sixteen absorbing antennas resulted in high molar absorptivity (ϵ : $5.5 \times 10^4 \text{ M}^{-1}\text{cm}^{-1}$ at 380 nm in methanol for $LnZn_{16}quinHa_{16}$; and ϵ : $4.8 \times 10^4 \text{ M}^{-1}\text{cm}^{-1}$ at 360 nm in water for $LnZn_{16}pyzHa_{16}$), and absorption bands in the range of 200-450 nm – well into the minimum range to avoid photoinduced damage of biological samples. Luminescent sensitization of visible Ln^{III} emitters was not observed, and attributed to inefficient antenna sensitization. This is because the MC's T^* is located at about 21000 cm^{-1} , which is too close to the emissive state of most Ln^{III} ions. The emissive level of each Ln^{III} can be seen in Figure 1.13. However, excellent sensitization of the NIR Ln^{III} emitters was observed. The photophysical data detailed in Table 1.1 shows a significant increase in the solid and solution state quantum yields (ϕ_{Ln}^L), as well as luminescent lifetimes of $LnZn_{16}quinHa_{16}$ compared to $LnZn_{16}picHa_{16}$. This can be attributed to better overlap of the antenna T^* state and Ln^* states as seen in Table 1.2, as well as the presence of inter- and intraligand CT states. Additionally, the 4.4% increase in distance of C-H oscillator to the Ln^{III} core of $LnZn_{16}quinHa_{16}$ also reduces quenching through nonradiative vibrational coupling. Of equal importance is the solution state quantum yield (ϕ_{Ln}^L) of $YbZn_{16}pyzHa_{16}$ fully dissolved in water, which made it the brightest Yb^{III} compound in water at the time of its report. Furthermore, the quantum yields of all the MCs in deuterated solvents (D_2O and CD_3OD) are significantly higher than those dissolved in protonated solvents (H_2O and CH_3OH), demonstrating that the O-H high-energy vibration from small solvent molecules can still get close enough to the Ln^{III} ion.

Table 1.1 Luminescent lifetimes (τ_{obs}) and Ln^{III}-centered quantum yields under ligand excitation (φ_{Ln}^L) for LnZn₁₆L₁₆ (Ln: Yb, Nd, Er; L: picHa, quinHa, and pyzHa) in the solid and solution state (methanol: 1 mg/mL and water 200 μ M)^a 101,118,128

Compound	State/Solvent	τ_{obs} [μ s] ^b	φ_{Ln}^L [%] ^c
YbZn ₁₆ picHa ₁₆	Solid	34.5(1)	0.40(2)
	CH ₃ OH	12.1(1)	0.13(1)
	CD ₃ OD	133(1)	1.60(3)
YbZn ₁₆ quinHa ₁₆	Solid	47.8(4)	2.44(4)
	CH ₃ OH	14.88(1)	0.25(1)
	CD ₃ OD	150.7(2)	2.88(2)
YbZn ₁₆ pyzHa ₁₆	Solid	45.6(3)	0.659(4)
	CH ₃ OH	5.57(1)	0.0112(7)
	CD ₃ OD	81.3(1)	0.257(3)
NdZn ₁₆ picHa ₁₆	Solid	1.18(2)	0.40(1)
	CH ₃ OH	0.90(1)	0.22(2)
	CD ₃ OD	3.52(2)	0.98(1)
NdZn ₁₆ quinHa ₁₆	Solid	1.79(2)	1.13(4)
	CH ₃ OH	1.16(1)	0.38(1)
	CD ₃ OD	4.11(3)	1.35(1)
NdZn ₁₆ pyzHa ₁₆	Solid	1.71(1)	0.444(9)
	CH ₃ OH	0.214(4)	0.0077(1)
	CD ₃ OD	1.29(1)	0.0617(9)
ErZn ₁₆ picHa ₁₆	Solid	5.73(2)	1.042(1)
	CH ₃ OH	1.25(1)	0.00099(3)
	CD ₃ OD	11.40(3)	0.036(1)

^a At room temperature. ^b Standard deviation (2σ) between parentheses. Estimated experimental error: τ_{obs} , $\pm 2\%$; φ_{Ln}^L $\pm 10\%$. ^c Under excitation at 370 nm.

Table 1.2 Absorbance maximum (Abs_{max}) of MCs and energy levels of the singlet (S*), triplet (T*) and inter-/intra ligand charge transfer (ILCT)

Compound	Absorbance _{max}	S* [cm^{-1}] ^a	T* [cm^{-1}] ^b	ILCT [cm^{-1}] ^c
GdZn ₁₆ picHa ₁₆	325 nm	31250	24250	25000
GdZn ₁₆ quinHa ₁₆	380 nm	29850	21000	21560
GdZn ₁₆ pyzHa ₁₆	360 nm	28570	25035	22220

^a Determined as the edge of absorption spectrum of the corresponding ligand. ^b Determined as 0-0 transition of the phosphorescence spectrum of the corresponding Gd^{III} MC. ^c Determined as the edge of the absorption spectrum of the corresponding Gd^{III} MC.

The Ga-MCs are currently the most studied of the luminescent MC families due to their functionalization potential (further discussed in later sections), and ability to sensitize both the visible and NIR Ln^{III} emitting ions.^{102,106,119,122} This family consists of 12-MC-4 scaffolds with optically transparent Ga^{III} as their ring metal. Just like with Zn^{II} , Ga^{III} has a full $3d^{10}$ shell which prevents d-d luminescent quenching. The Ga-family has three independent members: the monomeric $\text{Ln}[12\text{-MC}_{\text{Ga}(\text{III})\text{N}(\text{L})-4}]\text{L}'_4$ (shorthand: $\text{LnGa}_4\text{L}_4(\text{L}')_4$, L: ring ligand, L': bridge ligand); the dimeric $\text{Ln}[12\text{-MC}_{\text{Ga}(\text{III})\text{N}(\text{L})-4}]_2\text{L}'_4$ (shorthand: $\text{LnGa}_8\text{L}_8(\text{L}')_4$); and, the recently reported $\text{Ln}_2[12\text{-MC}_{\text{Ga}(\text{III})\text{N}(\text{L})-4}]_2\text{OH}_4$ (shorthand: $\text{Ln}_2\text{Ga}_8\text{L}_8(\text{OH})_4$). As seen in Figure 1.15, the $\text{LnGa}_4\text{L}_4(\text{L}')_4$ is a canonical 12-MC-4 structure with salicylhydroxamate derivatives as the ring ligands, carboxylate derivatives as the bridging ligands, and a Ln^{III} ion core. The $\text{Ln}_2\text{Ga}_8\text{L}_8(\text{L}')_4$ consists of two 12-MC-4 scaffolds bridged together by four isophthalate derivatives. Lastly, the $\text{LnGa}_8\text{L}_8(\text{OH})_4$ is also a dimeric 12-MC-4, but with four bridging hydroxides. A major attribute of the Ga-family over the Zn-family is the luminescent sensitization of a broader spectrum of Ln^{III} (both in the solid and solution state) due to having an antenna with a T^* ($\sim 22200\text{-}22620\text{ cm}^{-1}$) that better overlaps with the emissive Ln^* states of each metal ion (Figure 1.13). $\text{LnGa}_4\text{Shi}_4(\text{benzoate})_4$ is capable of sensitizing Sm, Tb–Yb, while $\text{Ln}_2\text{Ga}_8\text{Shi}_8(\text{ip})_4$ can sensitize Pr–Sm, Tb–Er, and Yb, and $\text{LnGa}_8\text{L}_8(\text{OH})_4$ is able to efficiently sensitize the entire series of luminescent trivalent ions from Pr to Yb.

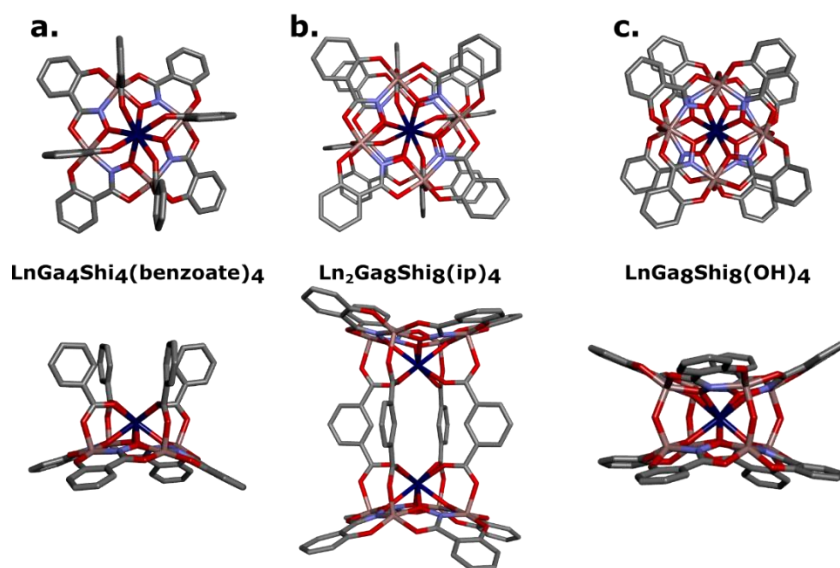


Figure 1.15 X-ray crystal structures of the three members of the Ga-family. (Top) Top view and (bottom) side view of the three MCs. Blue: Ln^{III} , pink: Ga^{III} , red: O, purple: N, and gray: C. Solvent molecules, counterions, and hydrogen atoms have been omitted for clarity.^{102,106,119}

Pulse gradient spin echo diffusion ordered spectroscopy (PGSE-DOSY) done in methanol solutions of the three MCs^{119,140} demonstrated that the monomeric LnGa₄Shi₄(benzoate)₄ scaffold is significantly less stable than the other two MCs. This was determined by comparing the diffusion of a ring ligand proton and a bridge ligand proton (benzoate, isophthalate, or hydroxyls depending on the MC under study). As seen in Figure 1.16a, the carboxylate proton and Shi proton of a YGa₄Shi₄(benzoate)₄ MC diffuse at different rates; therefore, it was determined that the benzoate bridges in the metallacrown dissociate in methanol. To further test this, excess of benzoate ligand was added to the MC solution which then resulted on an even larger disparity of the diffusion rates. This suggested that the instability of the YGa₄Shi₄(benzoate)₄ MC was due to a continuous and rapid exchange between bound and free benzoates. Similar experiments were performed on a Y₂Ga₈Shi₈(ip)₄ MC and YGa₈L₈(OH)₄. In the case of both MC dimers, the diffusion coefficient of their ring and bridge ligands were similar, suggesting no instabilities (Figure 1.16b and c).

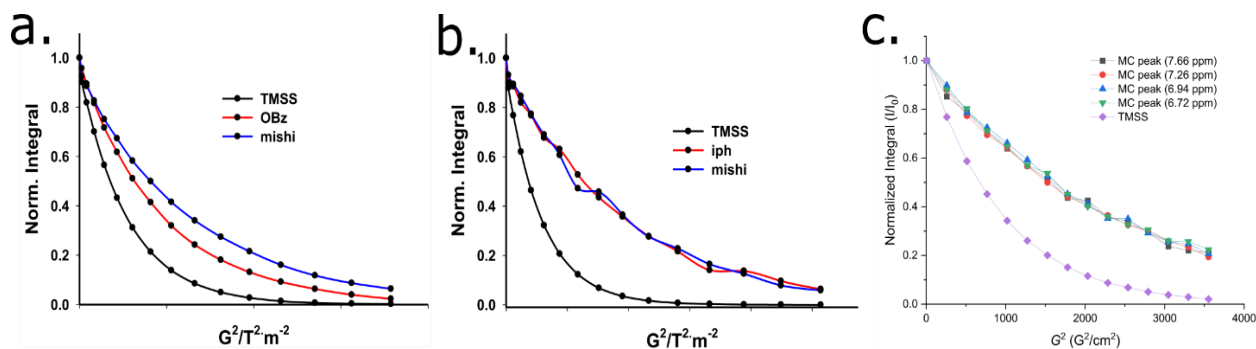


Figure 1.16 PGSE-DOSY on (a) YGa₄miShi₄(benzoate)₄, (b) Y₂Ga₈Shi₈(iip)₄, and (c) YGa₈L₈(OH)₄ MCs showing diffusion rates of the bridge (red, a and b) and ring (blue, a and b; multiple colors in c) protons in methanol solutions. The black (a and b) or purple (c) trace is from a TMMS standard.^{119,140}

As for their photophysical properties, the three members of the Ga-family are one of the few examples to date capable of sensitizing a broad spectrum of Ln^{III} ions. Of special interest is the fact that Ln^{III} such as Tm^{III} and Ho^{III} were sensitized, as well as the rarely seen NIR emission of Sm^{III} and Dy^{III}.^{133,141,142} The presence of multiple absorbing antennas (4 or 8) per lanthanide translates into good molar absorptivity (ϵ : 3.9×10^4 M⁻¹cm⁻¹ for LnGa₄Shi₄(benzoate)₄; ϵ : 4.1×10^4 M⁻¹cm⁻¹ for Ln₂Ga₈Shi₈(ip)₄; and ϵ : 3.6×10^4 M⁻¹cm⁻¹ for LnGa₈Shi₈(OH)₄) in methanol, with absorption bands between 200-350 nm, and a maximum at ~310 nm. Compared to the LnZn₁₆ MCs, these values are only slightly smaller, but a significant blue shift on the absorption bands takes over. However, by preparing the MC scaffold with a more conjugated system, such as a

naphthalene hydroxamic acid (Nha), the excitation energy can be redshifted, as in the case of $\text{Ln}_2[12\text{-MCGa(III)N(Nha)-4}]_2(\text{ip})_4$, (shorthand: $\text{Ln}_2\text{GaNha}_8(\text{ip})_4$) with an excitation energy at 380 nm.

Table 1.3 lists the photophysical measurements of the Yb^{III} -based MCs of the Ga-family. When first reported, $\text{YbGa}_4\text{Shi}_4(\text{benzoate})_4$ scaffold had the highest quantum yield for a Yb^{III} complex with C-H bonds. A significant increase in both solution and solid-state quantum yields is observed when compared to the Zn-family MCs. This is due to the larger ΔE values ($\sim 11900\text{-}12300\text{ cm}^{-1}$) of the ligand T^* and Yb^* states. The decrease in quantum yield in the solid state of the dimeric $\text{YbGa}_8\text{Shi}_8(\text{ip})_4$ is attributed to self-quenching due to the proximity of the Ln^{III} ions to each other. While the decrease in $\text{YbGa}_8\text{Shi}_8(\text{OH})_4$ is attributed to its bridging ligands being high energy oscillators. Excitation of the deuterated MC solutions once again show a large increase of luminescence sensitization, which is especially large with $\text{YbGa}_8\text{Shi}_8(\text{OH})_4$. This makes sense since this MC, compared to $\text{YbGa}_4\text{Shi}_4(\text{benzoate})_4$, has twice as many antennas. From this, it is obvious that nonradiative and solvent quenching are a bigger problem with the Ga-family than the Zn-family due to a less protective architecture. Nonetheless, meticulous ligand design can offer the opportunity to build a more protective MC scaffold capable of effectively sensitizing Ln^{III} luminescence.

Table 1.3 Luminescent lifetimes (τ_{obs}) and Yb^{III} -centered quantum yields under ligand excitation ($\phi_{\text{Ln}}^{\text{L}}$) for each MC scaffold in solid and solution state (50 μM in methanol) ^{a 102,119,124}

Compound	State/Solvent	τ_{obs} [μs] ^b	$\phi_{\text{Ln}}^{\text{L}}$ [%] ^c
$\text{YbGa}_4\text{Shi}_4(\text{benzoate})_4$	Solid	55.7(3)	5.88(2)
	CH_3OH	2.06(4)	0.26(1)
	CD_3OD	36.6(1)	4.29(1)
$\text{YbGa}_8\text{Shi}_8(\text{ip})_4$	Solid	37.1	4.82(4)
$\text{YbGa}_8\text{Shi}_8(\text{OH})_4$	Solid	27.4(9)	2.8(1)
	CH_3OH	15.6(2)	0.78(4)
	CD_3OD	196(1)	8.4(1)

^a At room temperature. ^b Standard deviation (2σ) between parentheses. Estimated experimental error: τ_{obs} , $\pm 2\%$; $\phi_{\text{Ln}}^{\text{L}}$, $\pm 10\%$. ^c Under excitation at 355nm. Under excitation at 340nm for the sampled in the solid state and at 310nm for solution.

1.4.4 Luminescent Metallacrowns as Optical Imaging Probes

Due to their remarkable Ln^{III} sensitization abilities, their retention of luminescent signal in solution (even in protic solvents), and their distinctive synthetic modularity, MCs have the

potential to become attractive optical imaging probes. To be considered a suitable luminescent imaging agent, any probe must meet the following requirements: water solubility and colloidal stability at physiological conditions; retention of luminescent properties in solution; and biocompatibility.²³ To this end, Martinic et al. utilized the fully water soluble YbZn₁₆pyzHa₁₆ MC to image HeLa cells, as shown in Figure 1.17.¹²⁸ It was shown that this MC has the following properties: noncytotoxic at concentrations required for cell imaging (45 μM and >90% cell viability); chemically stable and photostable under physiological conditions; and, of even greater interest, and an ability to selectively accumulate and label the cytoplasm and nucleus of necrotic HeLa cells. The latter point was confirmed with epifluorescence microscopy images of incubated cell with the MC, and were also compared to those incubated with propidium iodide (PI) – the standard dye for this type of cell labeling. From this it was confirmed that both compounds image the cells similarly. Furthermore, the intrinsic resistance to photobleaching of Ln^{III} ions is of great importance for biological imaging that requires long or repeated period of illumination. Once again comparing the HeLa cells labeled with YbZn₁₆pyzHa₁₆ and the organic-based PI, it was shown that after 500s of constant illumination, the MC remained photostable while the PI signal decreased over time due to photodecomposition. Thus, LnZn₁₆pyzHa₁₆ MC has the potential to be a better alternative to commercially available organic dyes for necrotic cell labeling.

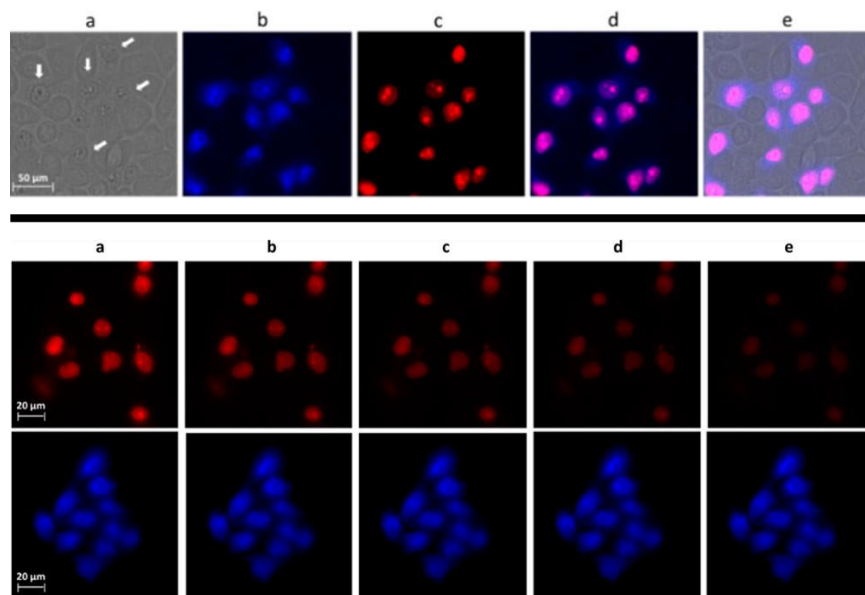


Figure 1.17 (Top) Comparison of necrotic cell labeling with YbZn₁₆pyzHa₁₆ (b, blue) and PI (c, red). White arrows on (a) point at necrotic cells. (d) Overlap of both images showing colocalized labeling. (e) Merge of all images. (Bottom) Images comparing photostability of PI (red) and MC (blue) after (a) 10sec, (b) 50sec, (c) 100sec, (d) 200sec, and (e) 500sec. Most of the luminescent signal of PI is gone while the MC's remains.¹²⁸

A follow up study on the same $\text{LnZn}_{16}\text{pyzHa}_{16}$ (Ln: Nd^{III} and Yb^{III}) MC demonstrated its ability to simultaneously fix and counter stain the nucleus and cytoplasm of HeLa Cells.¹²⁹ Cell fixation, which is the preservation of cell morphology, is a valuable first step when labeling cells. While several fixation approaches have been developed,¹⁴³ no single perfect technique works for all cells, and often numerous ones have to be combined, adding extra steps to an already delicate experiment setup. Furthermore, often a counter staining agent is used to increase labeling contrast. Counter staining can be problematic if it overlaps with the excitation and emission bands of the main cell dye. Thus, it was noteworthy when Martinć et al. reported the simultaneous counter staining and fixation of HeLa cells with MCs, as shown in Figure 1.18. The cells were fixed by incubation with 150 μM $\text{YbZn}_{16}\text{pyzHa}_{16}$ for fifteen minutes, followed by illumination with UV-A for ten minutes. Staining was then performed after UV-A illumination by further incubation for one hour. Incubation with PI was also done to have a comparison of colocalization in the nucleus and localization in the cytoplasm. The adequacy of fixation and labeling of cells by the MC, combined with the intrinsic luminescent properties of Ln^{III} ions, and great sensitization of luminescent signal in solution and cell conditions, corroborated once again the utility of $\text{LnZn}_{16}\text{pyzHa}_{16}$ as imaging probes.

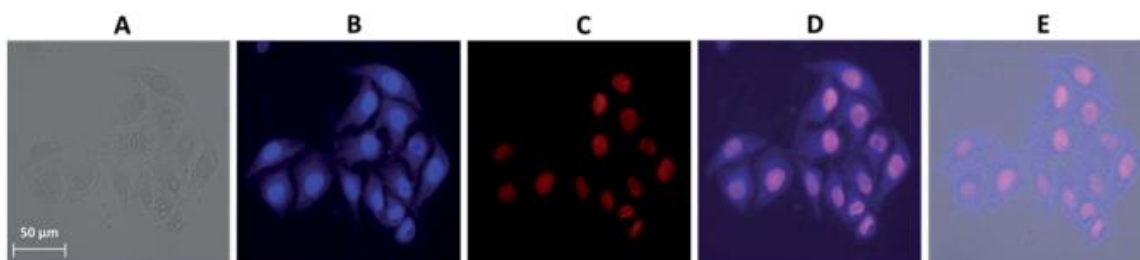


Figure 1.18 Epifluorescence microscopy images of fixed HeLa cells. (a) brightfield, (b) NIR emission of $\text{YbZn}_{16}\text{pyzHa}_{16}$ MC, (c) visible emission of PI, (d) merged of (b) and (c) to demonstrate colocalization of both complexes, and (e) merge with brightfield.¹²⁹

While the water solubility and great photostability of $\text{LnZn}_{16}\text{pyzHa}_{16}$ are attractive features of this MC family, its utility is limited to NIR emitters. However, as previously discussed, the Ga-family can expand MC utility as imaging probes. Since the monomeric $\text{LnGa}_4\text{Shi}_4(\text{benzoate})_4$ demonstrated limited solution stability in the presence of excess carboxylate, which is abundant in biological samples, the dimeric $\text{Ln}_2\text{Ga}_8\text{Shi}_8(\text{ip})_4$ was chosen to perform preliminary cell studies. As reported by Nguyen et al.,¹⁰⁶ incubation of HeLa cells with $\text{Yb}_2\text{Ga}_8\text{Shi}_8(\text{ip})_4$ was proven to be

noncytotoxic up to 200 μM concentrations. Furthermore, epifluorescence microscopy images showed strong Yb^{III} ion luminescent signal from non-specific interactions of MC aggregates at the surface of the cells. Unfortunately, internalization of the MC into the cell was not observed due to the poor water solubility of the $\text{Ln}_2\text{Ga}_8\text{Shi}_8(\text{ip})_4$ in both cell culture media and water.

One way around the limited aqueous solubility and biocompatibility of $\text{Ln}_2\text{Ga}_8\text{Shi}_8(\text{ip})_4$ is to insert them into biocompatible matrixes, such as polystyrene nanobeads.¹⁴⁴ This approach was partially investigated by Salerno et al.¹²¹ where $\text{Sm}_2\text{Ga}_8\text{Shi}_8(\text{ip})_4$ and $\text{Tb}_2\text{Ga}_8\text{Shi}_8(\text{ip})_4$ MCs were embedded in amino-functionalized polystyrene nanobeads. The main focus of the study was to investigate the ratiometric luminescent behavior of each MC and a 1:1 MC-mixture as molecular nanothermometers. This report demonstrated a larger temperature dependence on the emission of the Tb^{III} - based MC over the Sm^{III} one due to smaller $T^*-\text{Tb}^*$ ΔE , which led to greater Boltzmann dependent back transfer ($T^* \leftarrow \text{Tb}^*$), and temperature dependent emissions. Thus, as seen in Figure 1.19, back transfer events are even more prevalent with increasing temperature, where the Tb^{III} luminescent intensities decrease with increasing temperature (300-328 K), while the Sm^{III} intensities remain constant. While no cell studies were done to test the ability of the polystyrene beads to enhance the MC uptake by cells, the luminescent studies were performed in aqueous suspension of the nanobeads loaded with the MCs. Given the very low water solubility of $\text{Ln}_2\text{Ga}_8\text{Shi}_8(\text{ip})_4$, similar data collection would have been unattainable without the nanobead matrix.

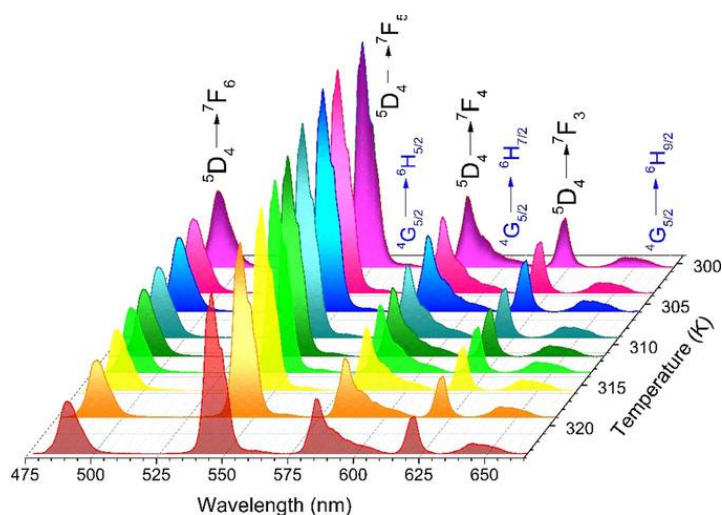


Figure 1.19 Luminescent intensities of a 1:1 mixture of $\text{Sm}_2\text{Ga}_8\text{Shi}_8(\text{ip})_4/\text{Tb}_2\text{Ga}_8\text{Shi}_8(\text{ip})_4$ suspended in amino functionalized polystyrene nanobeads. Tb^{III} transitions are labeled in black, while Sm^{III} transitions are labeled in blue.¹²¹

1.4.5 Expansion of Metallacrown Functionalization

A lot of work has been done to expand the functionality of MCs. Ring ligand alternation of the Zn-family MCs, shown in Figure 1.14 (top), resulted in enhanced luminescent sensitization and the red-shift of the excitation energy of $\text{LnZn}_{16}\text{quinHa}_{16}$; while with $\text{LnZn}_{16}\text{pyzHa}_{16}$, it enhanced water solubility that promoted its application as a cell imaging agent. With the Ga-family, a broader range of ring and bridge ligands variation can be expected since numerous salicylic acid derivatives (parent material of the hydroxamic acid ligands) and isophthalic acid derivatives are commercially available. Furthermore, a step beyond is the synthetic modification of the ligands to introduce new functionalities, such as new coupling sites, absorbance shifting, or enhanced water solubilization. To this end, several ligands have been prepared from commercially available sources or synthetically modified in order to prepare MC scaffolds with increase functionalization potentials. Figure 1.20 illustrates some of the numerous ligands that have been used to prepared MCs.^{109,118,122,128,140,145–147}

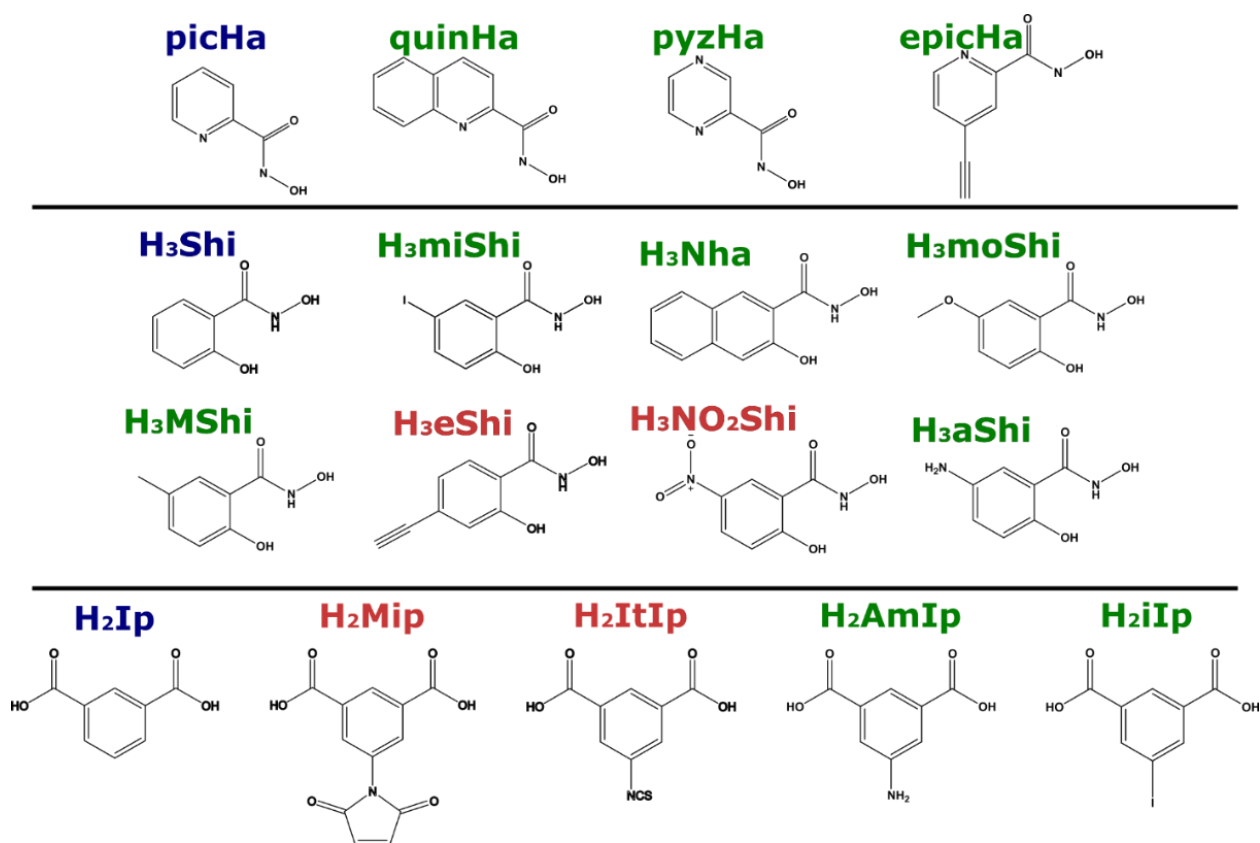


Figure 1.20 Selection of ligands used to prepare metallacrowns. Abbreviated names are color coded to determine original ligand (blue), commercially available carboxylic acid starting material (green), synthetically modified (red). (top) Ring ligands for LnZn_{16} MCs. (middle) Ring ligands and (bottom) bridge ligands for Ga-family MCs.

Red shifting of the excitation energy can be achieved with MCs prepared with ring ligands such as Nha, moShi, eShi, and MShi for Ga MCs (Abs. max: 380 nm, 345 nm, 340 nm, and 325 nm respectively), or quinHa for Zn MCs (Abs. max: 380 nm); however, aqueous solubility is hindered with these ligands. MCs made with NO₂Shi are very water soluble, but Ln^{III} sensitization is quenched. Therefore, careful selection of the ligand system based on the desired application is required. For example, Lutter et al.¹²⁴ utilized the iodinated H₃miShi ring and H₂iip bridge ligand to prepare Ln₂[12-MC_{Ga(III)N(miShi)-4}]₂(iip)₄ (shorthand: Ln₂Ga₈miShi₈(Ip)₄) and Ln₂[12-MC_{Ga(III)N(miShi)-4}]₂(iip)₄ (shorthand: Ln₂Ga₈miShi₈(iIp)₄) MCs. The goal was to produce a scaffold capable of multimodal imaging by combining the Ln^{III} luminescent sensitization with the X-ray attenuation properties of the halogen appendage. NIR emission from each scaffold prepared with Yb^{III} was observed both in the solid state and in DMF solutions. X-ray attenuation characterization, which is an analysis of the reduction of x-ray intensity as it passes through a medium,¹⁴⁸ demonstrated competitive attenuation concentrations (14.10 and 17.62 HUmol⁻¹, respectively) that were almost 40-45 times higher than the commercially available contrast agent iobitridol (0.38 HUmol⁻¹). This is due to the fact that the two Ln^{III} metal ions are great absorbers of X-rays.

Incorporation of coupling sites (or attachment points) to the ring ligands was also investigated. Lutter et al.^{122,140} and Plenk et al.¹⁴⁷ independently reported the synthetic introduction of alkyne groups to the ring ligands of the dimeric and monomeric (respectively) 12-MC-4 scaffold via Sonogashira cross-coupling.¹⁴⁹ While Plenk's Cu^{II}-based MC was studied for SMM development, Lutter prepared Ga^{III} MCs for luminescent studies. However, both exploited the copper-catalyzed alkyne-azide cycloaddition (CuAAC) by clicking small azide molecules onto the MC scaffold. The luminescent Sm₂[12-MC_{Ga(III)N(eshi)-4}]₂(ip)₄ (shorthand: Sm₂Ga₈eShi₈(Ip)₄) was prepared and characterized for both its luminescent properties and its coupling ability. The excitation and emission characterization of the MC showed a redshift of the absorbance maxima to ~335 nm (compared to Shi, ~310 nm), as well as excellent sensitization of the Sm^{III} ion in the visible range. Next, benzyl azide was clicked via CuAAC. Mass spectrometry analysis corroborated complete coupling of eight equivalents of the small azide to the MC. Luminescent characterization was once again done to corroborate that the click reaction did not affect the sensitization ability of the MC. Luminescence of the Sm^{III} was once again observed. This report demonstrated the ability to synthetically incorporate coupling sites for further functionalization, while maintaining the luminescent signal of the lanthanide core. These results are an encouraging

path to overcome some of the limitations of luminescent metallacrowns, such as poor water solubility or limited solution stability, that have historically delayed their practical applications as optical imaging probes. Furthermore, this opens up the possibility of investigating the synthetic incorporation of other coupling groups (e.g., thiol-ene coupling, radical bond formation, Michael addition), and the attachment of other interesting groups (e.g., small molecules, antenna, bioactive molecules) to expand the application of MCs into other material chemistry fields.

1.5 Thesis Aims

While understanding the limitation of luminescent metallacrowns and metallodendrimers, but also taking advantage of their modularity and synthetic variability, this thesis aims to exploit the functionalization potential of both dendrimer and MCs further. This is done by utilizing the dimeric Ln_2Ga_8 MC as the new polymetallic core of dendrimers, creating a new class of metallodendrimers: dendrimeric metallacrowns (DMCs). The hypothesis behind this work is that lanthanide-based dendrimeric metallacrowns will combine the photophysical properties of MC with those of dendrimers, specifically PAMAM dendrimers.

Chapter 2 will focus on the synthetic development and characterization of toroidal dendrimeric metallacrowns, where PAMAM dendrons are coupled to the bridging ligands of Ln_2Ga_8 MCs. Photophysical characterization and luminescent cell imaging studies are presented as well. In Chapter 3, the intricate and meticulous design of ring ligands is presented, with emphasis on the synthetic methodologies to develop effective thiol-ene and -yne coupling site to Ln_2Ga_8 MCs. Synthesis and characterization of hyperboloidal dendrimeric metallacrowns with PAMAM dendrons coupled to the ring ligands is discussed. As well and photophysical and luminescent characterization of the dendrimers. In Chapter 4, incorporation of bifunctional coupling sites at the bridge and ring ligands of Ln_2Ga_8 MCs is presented. Synthesis and characterization of PAMAM dendrons coupled to both ligand positions, as well as Janus dendrimers are presented. Lastly, in Chapter 5 concluding remarks on this thesis work, as well as the numerous future directions of dendrimeric metallacrowns are discussed.

Chapter 2

Toroidal Dendrimeric Metallacrowns from Luminescent $\text{Ln}_2\text{Ga}_8\text{Shi}_8\text{Mip}_4$ Scaffolds

2.1 Introduction

As introduced in Chapter 1, the well-defined architecture of dendrimers can be tailored to have specific applications depending on the dendrimer family, size, surface functionality, and core. When combined with metal ion species, dendrimers are better known as metallodendrimers. Metallodendrimers are capable of exploiting the intrinsic properties of metal ions while exhibiting distinct behaviors (e.g., colloidal, electronic, and optical properties) from their small molecule or linear polymer counterparts. Metal coordination in metallodendrimers can happen at the surface, within generations, and at the core. While metalation only at the core reduces the amount of metal species within the dendrimer, it is an advantageous approach since it offers better control of the position and concentration of metal ions.

Regarding their photophysical properties, metal free luminescent dendrimers have been prepared with organic chromophores at the periphery or within the dendrimer shells.^{34,150,151} But like with any other organic-based luminescent compounds, this type of functionalized luminescent dendrimer is prone to photobleaching.^{152,153} Furthermore, narrow Stoke shifts, and emission signals that are altered by the surrounding chemical environment can reduce the quality of the collected data. Therefore, metallodendrimers, especially the ones prepared with Ln^{III} ions, can have a significant advantage over traditional organic-based luminescent dendrimers.

Unfortunately, the unique intrinsic luminescent properties of Ln^{III} ions (i.e., long lifetimes, photostability, and sharp emissions bands in the visible and NIR) have been exploited only by a handful of metallodendrimers. The main mechanism of metalation has been either incorporating one or several Ln^{III} ions in the cavities of dendrimers functionalized with absorbing antennas, or by coordination of a single Ln^{III} ion with carboxylate focal point Fréchet-type dendrons. In the

former example, work by Vicinelli et al.⁵⁹ and Petoud et al.,^{57,58} demonstrated that Ln^{III} ions encapsulated by dendrimers can be sensitized through the antenna effect. In the study by Vicinelli, only one Ln^{III} ion was incorporated into the framework of a G2 PLL dendrimer that was previously functionalized with twenty-four dansyl antennas. Of the several Ln^{III} ions tested, only the NIR emitters were sensitized. This was due to the poor energy overlap of the dansyl excited states (S* or T*) with the visible Ln^{III} ion (Ln*) emissive states. Since no photophysical data was reported, it is difficult to make a direct comparison with this system. Moreover, the exact concentration and location of the Ln^{III} could not be determined. Studies by Petoud et al. showed an average of eight Ln^{III} ions (Sm^{III} or Eu^{III}) incorporated into the cavities of a G3 PAMAM dendrimer functionalized with thirty-two naphthalene antennas. With this metallodendrimer, both visible and NIR (in the case of Sm^{III}) emission was observed. However, each Ln-metallodendrimer had moderately low quantum yields – 0.06% for Eu^{III}, and 0.022(2)% in the visible and 0.00085(5)% in the NIR for Sm^{III}. Emission spectra plots corroborated that the low quantum yields were due to inefficient energy-transfer of the antennas since naphthalene fluorescence was also observed. The radiative quenching of the Ln^{III} emission was attributed to the large distance between the antennas and the Ln^{III} metals.

With the carboxylate focal point Fréchet-type dendrons, metallodendrimers can assemble around a single Ln^{III} ion. The aryl dendrons work both as a protective dendritic shell and as the absorbing antenna. The work of Kawa et al.⁵⁶ and Pitois et al.¹⁵⁴ is representative of this type of metallodendrimers. Both demonstrated luminescence signals characteristic of Ln^{III} ions (Eu^{III}, Tb^{III}, and Er^{III}), and showed efficient energy transfer through the dendrimer architecture. However, the self-assembled metallodendrimers were incredibly fragile since the Ln^{III} core is held by relatively weak coordinating sites. Thus, solution state characterization such as NMR or mass spectrometry could not be performed without destroying the dendrimers. In other words, while sensitization seemed to be effective, secure encapsulation was not.

Inefficient sensitization, concentration, undefined location, and unsecured encapsulation of the Ln^{III} ion are the main problems of Ln-based metallodendrimers. The concentration, location, and encapsulation issues can be overcome by using a well-defined coordinating macrocycle as the core of metallodendrimers, such as porphyrin- or cyclam-cored dendrimers. However, while efficient energy harvesting and transfer has been observed with both when prepared with Fréchet-type dendrimers, sensitization of Ln^{III} luminescence has not been reported with either core.^{88,155}

Furthermore, even if either metallodendrimer was capable of sensitizing Ln^{III} luminescence, their application would still be somewhat limited by the dendron family of choice since aromatic dendritic systems are necessary for optimal energy transfer. Therefore, metallodendrimers with cores that can be stimulated independently of the dendrimer family would offer more flexibility in the synthesis and application of the system – for example, a more biocompatible dendrimer like PAMAM could be utilized.

To this end, this thesis chapter presents the development and characterization of toroidal-shaped dendrimeric metallacrowns prepared with dimeric Ln₂[12-MC_{Ga(III)N_(shi)-4}]₂(5-maleimide isophthalate)₄ (shorthand: Ln₂Ga₈Shi₈Mip₄) MC cores. This report is the first study to utilize metallacrowns as the core of metallodendrimers, affording a new class of metallodendrimers capable of sensitized lanthanide luminescence. This is also the first report of toroidal shaped metallodendrimers. I first demonstrate the effective synthetic introduction of thiol-active maleimide coupling sites to the bridging ligands of Ln₂Ga₈ MCs. I then show the efficient thiol coupling capabilities of Ln₂Ga₈Shi₈Mip₄ with small molecules, and the luminescence characterization pre- and post-thiol coupling. I follow this by presenting data that shows conclusively the formation of dendrimeric metallacrowns, as well as their luminescence properties. Lastly, I investigate the potential of toroidal dendrimeric metallacrowns to become luminescent imaging probes. Altogether, this chapter investigates and exploits both the functionalization potential and photophysical properties of metallacrowns.

2.2 Experimental

2.2.1 Chemical and Materials

All reagents and chemicals were purchased from commercial sources and used without further purification. Cysteamine (Sigma-Aldrich, 95%), cysteamine hydrochloride (Alfa Aesar, 98+%), Extra dry dichloromethane (Acros, 99.9%), Trifluoro acetic acid (Fisher, Peptide synthesis grade), Trityl chloride (Acros, 98%), Chloroform (Fisher, ACS grade), Sodium hydroxide (Fisher, ACS grade), Magnesium sulfate anhydrous (Fisher), Methanol (Fisher, ACS grade), Methyl acrylate (Acros, 99%), Ethylenediamine (Alfa Aesar, 99%), Toluene (LabChem, ACS grade), Dichloromethane (Fisher, ACS grade), Triethylsilane (TCI, 98+%), Petroleum ether (Fisher, ACS grade), Gallium (III) nitrate hydrate (Acros, 99.9998%), Ytterbium nitrate pentahydrate (Sigma Aldrich, 99.9%), Samarium nitrate hexahydrate (Sigma Aldrich, 99.9%), Terbium nitrate

pentahydrate (Sigma-Aldrich 99.9%), Gadolinium nitrate hexahydrate (Sigma-Aldrich. 99.999%), Yttrium nitrate hexahydrate (Alfa Aesar, 99.9%), Salicylhydroxamic acid (Alfa Aesar, 99%), Sodium benzoate (Fisher), Pyridine (Fisher, ACS certified), 5-Amino isophthalic acid (Chem-Impex International), Maleic anhydride (Sigma-Aldrich, 99%), N,N-dimethylformamide (Fisher, Sequencing grade), Acetone (Fisher), Acetic anhydride (Fisher, ACS certified), Sodium acetate trihydrate (Sigma-Aldrich, 99.5%), 4-(Dimethylamine)pyridine (**DMAP**, Acros, 99%), Dialysis membrane Spectra/Por 7 (MWCO 2 kDa, regenerated cellulose), Dialysis membrane Spectra/Por 7 (MWCO 3.5 kDa, regenerated cellulose), Dimethyl sulfoxide (Fisher, HPLC grade), Chloroform-d 0.03% v/v% TMS (Acros, 99.8+%), Dimethyl sulfoxide-d₆ 0.03% TMS (Acros, 99.9%), Methanol-d₄ (Acros, 99.8%), Methanol (Sigma-Aldrich HPLC Plus, 99.9%), and NanoStar Disposable MicroCuvette (Wyatt).

2.2.2 General Characterization Methods

Electrospray Ionization Mass Spectrometry (ESI-MS) was performed on an Agilent 6230 TOF HPLC-MS in negative or positive ion mode with fragmentation voltage of 250-350V. Samples were prepared by dissolving approximately 0.5-1 mg of compound in 2 mL of HPLC grade methanol. Samples of 5-10 μ L were manually injected. Methanol was employed as eluent in negative ion, and acetonitrile with 0.1% formic acid in positive ion. The flow rate was 0.5-1 mL/min. Data were processed with Agilent MassHunter Qualitative Analysis Software.

CHN elemental analysis was performed in a Carlo Erba 1108 elemental analyzer and a PerkinElmer 2400 elemental analyzer by Atlantic Microlab.

¹H NMR spectra were acquired on a 400 MHz Varian MR400 or 500 MHz Varian VNMR500 NMR Spectrometer. Samples were prepared in Chloroform-d, Dimethyl sulfoxide-d₆, or Methanol-d₄, and spectra were processed using MestraNOVA software.

Dynamic Light Scattering (DLS) was performed on a DynaPro NanoStar instrument at 25°C with a scattering angle of 90°. Samples were prepared by dilution in DMSO, followed by centrifugation for five minutes at twelve rpm. Scans were done with five second acquisition time seta and twenty runs. Data was plotted using OriginPro 2020 software.

2.2.3 Synthetic Procedures

I now describe the synthetic procedures followed in this chapter. All reactions were

completed under aerobic conditions and at room temperature, unless otherwise noted. Characterization figures (ESI-MS, NMR, and DLS) not shown under the result section can be found in Appendix (Appx.) A.

Metallacrown bridge ligand:

5-(3-carboxylacrylamide)isophthalic acid was prepared by dissolving 5-aminoisophthalic acid (19.92 g, 100 mmol, 1 eq.) and maleic anhydride (10.79 g, 110 mmol, 1.1 eq) in DMF (200 mL). The mixture was stirred for 6-12 hours at room temperature. Then, the DMF was removed with a stream of N₂ (g) over the reaction mixture. The solid was then washed with copious amounts of acetone to yield a tan color powder (70% yield, >99% pure). ¹H NMR (Figure appx. A1, 400 MHz, dms_o-d₆) δ 13.18 (s, 3H), 10.66 (s, 1H), 8.46 (d, *J* = 1.5 Hz, 2H), 8.18 (t, *J* = 1.6 Hz, 1H), 6.33 (d, *J* = 12.7 Hz, 0H), 6.33 (d, *J* = 11.9 Hz, 1H). Elemental analysis calcd. (%) for C₁₂H₉NO₇: C 49.10, H 3.92, N 5.45; found: C 49.09, H 4.13, N 5.33.

5-maleimidoisophthalic acid (H₂Mip) was prepared by adding 5-(3-carboxylacrylamide)isophthalic acid (2.79 g, 10.0 mmol, 1 eq) and sodium acetate trihydrate (0.68 g, 5.0 mmol, 0.5 eq) into acetic anhydride (15.0 mL). The mixture was refluxed while stirring at 60°C for 2.5 hours. Acetic anhydride was then removed under reduced pressure at 50-60°C. Water (20.0 mL) was then added and the slurry mixture was stirred at 70°C for another 2 hours. The reaction was then cooled to room temperature, filtered, and rinsed with copious amounts of water. The product was dried under vacuum overnight to yield a white powder (80% yield, >99% pure). ¹H NMR (Figure appx. A2 400 MHz, dms_o-d₆) δ 8.46 (t, *J* = 1.7 Hz, 1H), 8.23 (d, *J* = 1.6 Hz, 3H), 7.23 (s, 3H). Elemental analysis calcd. (%) for C₁₂H₇NO₆: C 55.18, H 2.70, N 5.36; found: C 55.10, H 2.71, N 5.48.

LnGa₄Shi₄(benzoate)₄ Metallacrowns:

General synthesis procedure for Ln[12-MC_{Ga(III)N(shi)-4](benzoate)₄(pyridinium)(pyridine)₂(MeOH)₂ metallacrowns} (Ln^{III}: Y^{III}, Sm^{III}, Gd^{III}, Tb^{III}, or Yb^{III}), LnGa₄Shi₄(benzoate)₄. MCs were prepared by slight modification of previous literature procedures¹⁰² that follow three different protocols depending on the nature on the Ln^{III} ion. The synthetic yields were 20-40%.

SmGa₄Shi₄(benzoate)₄ was prepared by fully dissolving salicylhydroxamic acid (H₃Shi,

0.1531 g, 1.0 mmol, 4 eq), sodium benzoate (0.4323 g, 3.0 mmol, 12 eq), and pyridine (2 mL) in methanol (20 mL). Then $\text{Sm}(\text{NO}_3)_3 \cdot x\text{H}_2\text{O}$ (0.5 mmol, 2 eq) and $\text{Ga}(\text{NO}_3)_3 \cdot x\text{H}_2\text{O}$ (1.0 mmol, 4 eq) were dissolved in methanol (20 mL) separately. The three methanol solutions were combined and stirred at room temperature for 5 – 10 minutes. The mixture was then filtered, and let to slowly evaporate in a glass jar covered with aluminum foil with several holes. Crystals were collected by gravity filtration and rinsed with methanol. MS (Figure appx. A13, ESI): m/z calcd. for $\text{C}_{56}\text{H}_{36}\text{N}_4\text{O}_{20}\text{SmGa}_4$: 1519.8 [M]⁻; found: 1519.8 [M]⁻. Elemental analysis calcd. (%) for $\text{SmGa}_4\text{C}_{73}\text{H}_{60}\text{N}_7\text{O}_{22}$: C 48.27, H 3.33, N 5.40; found: C 48.29, H 3.16, N 5.51.

$\text{YbGa}_4\text{Shi}_4(\text{benzoate})_4$ was prepared by fully dissolving salicylhydroxamic acid (H_3Shi , 0.1531 g, 1.0 mmol, 4 eq), sodium benzoate (0.5764 g, 4.0 mmol, 12 eq), and pyridine (2 mL) in methanol (20 mL). Then $\text{Yb}(\text{NO}_3)_3 \cdot x\text{H}_2\text{O}$ (0.25 mmol, 1 eq) and $\text{Ga}(\text{NO}_3)_3 \cdot x\text{H}_2\text{O}$ (1.0 mmol, 4 eq) were dissolved in methanol (20 mL) separately. The three methanol solutions were combined and stirred at room temperature for 5 – 10 minutes. The mixture was then filtered, and let to slow evaporate in a glass jar covered with aluminum foil with several holes. Crystals were collected by gravity filtration and rinsed with methanol. MS (Figure appx. A14, ESI): m/z calcd. for $\text{C}_{56}\text{H}_{36}\text{N}_4\text{O}_{20}\text{YbGa}_4$: 1535.8 [M]⁻; found: 1535.8 [M]⁻. Elemental analysis calcd. (%) for $\text{YbGa}_4\text{C}_{73}\text{H}_{60}\text{N}_7\text{O}_{22}$: C 47.67, H 3.29, N 5.33; found: C 47.69, H 3.10, N 5.49.

$\text{LnGa}_4\text{Shi}_4(\text{benzoate})_4$ (Ln: Gd, Tb, Y) was prepared by fully dissolving salicylhydroxamic acid (H_3Shi , 0.1531 g, 1.0 mmol, 4 eq), sodium benzoate (0.4323 g, 3.0 mmol, 12 eq), and pyridine (2 mL) in methanol (20 mL). Then $\text{L}(\text{NO}_3)_3 \cdot x\text{H}_2\text{O}$ (0.25 mmol, 1 eq) and $\text{Ga}(\text{NO}_3)_3 \cdot x\text{H}_2\text{O}$ (1.0 mmol, 4 eq) were dissolved in methanol (20 mL) separately. The three methanol solutions were combined and stirred at room temperature for 5 – 10 minutes. The mixture was then filtered, and let to slow evaporate in a glass jar covered with aluminum foil with several holes. Crystals were collected by gravity filtration and rinsed with methanol.

$\text{GdGa}_4\text{Shi}_4(\text{benzoate})_4$ MS (Figure appx. A15, ESI): m/z calcd. for $\text{C}_{56}\text{H}_{36}\text{N}_4\text{O}_{20}\text{GdGa}_4$: 1519.8 [M]⁻; found: 1519.8 [M]⁻. Elemental analysis calcd. (%) for $\text{GdGa}_4\text{C}_{73}\text{H}_{60}\text{N}_7\text{O}_{22}$: C 48.09, H 3.32, N 5.38; found: C 48.18, H 3.07, N 5.59.

$\text{TbGa}_4\text{Shi}_4(\text{benzoate})_4$. MS (Figure appx A16, ESI): m/z calcd. for $\text{C}_{56}\text{H}_{36}\text{N}_4\text{O}_{20}\text{TbGa}_4$: 1522.8 [M]⁻; found: 1522.8 [M]⁻. Elemental analysis calcd. (%) for $\text{TbGa}_4\text{C}_{73}\text{H}_{60}\text{N}_7\text{O}_{22}$: C 48.04, H 3.31, N 5.37; found: C 48.33, H 3.12, N 5.54.

YGa₄Shi₄(benzoate)₄. ¹H NMR (Figure appx. A3 400 MHz, cd₃od) δ 8.57 (dt, J = 4.4, 1.7 Hz, 6H), 8.12 (d, J = 7.4 Hz, 4H), 8.04 (s, 8H), 7.90 (tt, J = 7.7, 1.8 Hz, 3H), 7.48 (ddd, J = 7.7, 4.4, 1.5 Hz, 7H), 7.31 (t, J = 7.8 Hz, 6H), 7.02 (d, J = 8.3 Hz, 4H), 6.82 (t, J = 7.5 Hz, 4H). MS (Figure appx. A17, ESI): *m/z* calcd. for C₅₆H₃₆N₄O₂₀YGa₄: 1450.9 [M]⁻; found: 1450.9 [M]⁻.

Ln₂Ga₈Shi₈Mip₄ Metallacrowns:

General synthesis procedure for Ln₂[12-MC_{Ga(III)N(shi)-4}]₂(Mip)₄ metallacrowns (Ln^{III}: Y^{III}, Sm^{III}, Gd^{III}, Tb^{III}, or Yb^{III}), Ln₂Ga₈Shi₄(Mip)₄. MCs were synthesized according to previous literature procedures.¹²² LnGa₄Shi₄(benzoate)₄ (1.0 mmol, 1 eq) and H₂Mip (2.1 mmol, 2.1 eq) were dissolved in DMF (10-20 mL) and stirred at room temperature for 6-12 hours. DMF was then removed with a stream of N₂ (g) over the reaction mixture. The product was then rinsed with cold methanol to yield a pale orange to yellow MC powder. The synthetic yields were 80-90% based on the metallacrown.

Sm₂Ga₈Shi₈(Mip)₄. MS (Figure appx. A18, ESI): *m/z* calcd. for Sm₂Ga₈C₁₀₄H₅₂N₁₂O₄₈: 1549.7 [M]²⁻; found 1547.7 [M]²⁻. Elemental analysis calcd. (%) for Sm₂Ga₈C₁₇₀H₁₀₂N₁₂O₇₀Na₂: C 35.89, H 2.89, N 4.69; found: C 35.94, H 2.84, N 4.76.

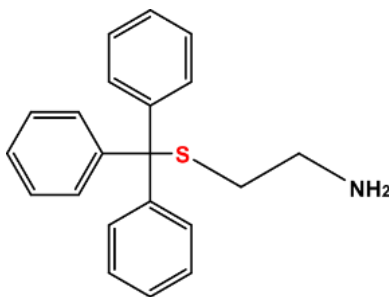
Yb₂Ga₈Shi₈(Mip)₄. MS (Figure appx. A19, ESI): *m/z* calcd. for Yb₂Ga₈C₁₀₄H₅₂N₁₂O₄₈: 1569.7 [M]²⁻; found 1570.7 [M]²⁻. Elemental analysis calcd. (%) for Yb₂Ga₈C₁₁₂H₇₆N₁₄O₅₅Na₂: C 39.02, H 2.22, N 5.69; found: C 39.15, H 2.24, N 5.71.

Gd₂Ga₈Shi₈(Mip)₄. MS (Figure appx. A20, ESI): *m/z* calcd. for Gd₂Ga₈C₁₀₄H₅₂N₁₂O₄₈: 1554.7 [M]²⁻; found 1570.7 [M]²⁻. Elemental analysis calcd. (%) for Gd₂Ga₈C₁₁₇H₈₉N₁₅O₅₉Na₂: C 39.39, H 2.51, N 5.89; found: C 39.36, H 2.53, N 5.90.

Tb₂Ga₈Shi₈(Mip)₄. MS (Figure appx. A21, ESI): *m/z* calcd. for Tb₂Ga₈C₁₀₄H₅₂N₁₂O₄₈: 1556.2 [M]²⁻; found 1556.7 [M]²⁻. Elemental analysis calcd. (%) for Tb₂Ga₈C₁₁₇H₈₉N₁₅O₅₉Na₂: C 39.36, H 2.51, N 5.88; found: C 39.36, H 2.53, N 5.90.

Y₂Ga₈Shi₈(Mip)₄. ¹H NMR (Figure 2.3, 400 MHz, dms_o-d₆) δ 8.92 (d, J = 35.7 Hz, 4H), 8.18, 8.02 (dd, J = 15.1, 1.5 Hz, 8H), 7.87 (t, J = 6.9 Hz, 8H), 7.22 (t, J = 7.6 Hz, 8H), 7.07 (d, J = 1.2 Hz, 8H), 6.89 – 6.82 (m, 8H), 6.69 (t, J = 7.4 Hz, 8H). MS (Figure 2.2, ESI): *m/z* calcd. for Y₂Ga₈C₁₀₄H₅₂N₁₂O₄₈: 1486.2 [M]²⁻; found 1486.7 [M]²⁻.

Trityl-protected PAMAM dendrons:

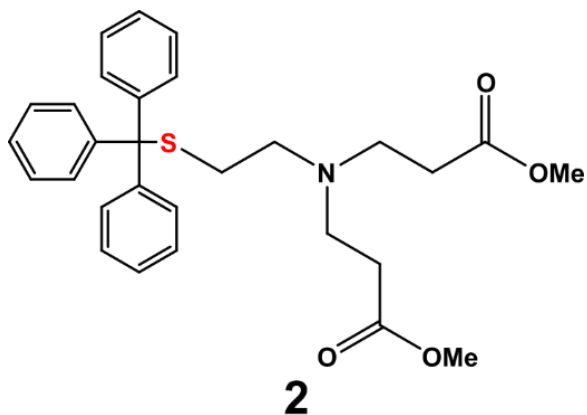


1

Chemical Formula: C₂₁H₂₁NS

MW: 319.47 g/mol

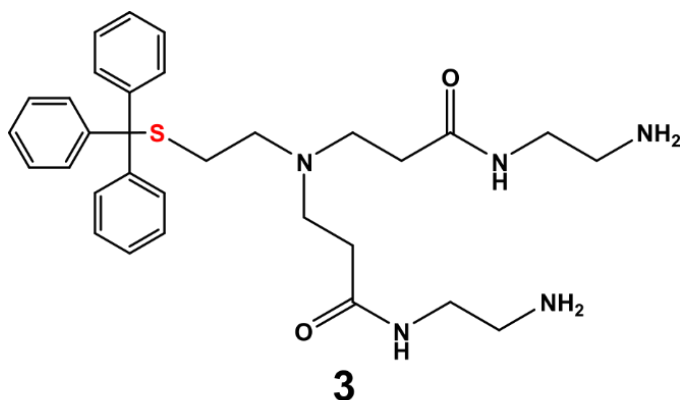
2-(tritylthio)ethanamine (**1**), was prepared by adding anhydrous dichloromethane (DCM) (25 mL) to cysteamine hydrochloride (5.00 g, 44 mmol) under N₂ (g), and placed in an ice bath. Then, while stirring TFA (10 mL) was added to the mixture dropwise, followed by the addition of trityl chloride (8.70 g, 44 mmol) at once. The solution turned dark yellow, and was stirred under N₂ (g) atmosphere at 0°C for 2 hours. After this time, the reaction was concentrated under reduced pressure, and then redissolved in chloroform (25 mL). While vigorously stirring the redissolve reaction, 10 M NaOH (15 mL) was added to it, and stirred at room temperature for one hour. The reaction solution turned clear and was then successively extracted 3 x 50 mL chloroform. The organic layers were combined, and then washed with 3 x 50 mL brine. Finally, the organic layer was dried over anhydrous MgSO₄, and concentrated to yield a colorless oil (12.7 g, 98.0% yield, ~98% pure). ¹H NMR (Figure appx. A4, 400 MHz, CDCl₃): δ=7.53 – 7.49 (d, 6H), 7.30 (t, *J* = 8.8, 6.8 Hz, 6H), 7.25 – 7.20 (t, 3H), 2.57 (t, *J* = 6.6 Hz, 2H), 2.35 (t, *J* = 6.6 Hz, 2H), 1.47 (s, 2H).



Chemical Formula: C₂₉H₃₃NO₄S

MW: 491.65 g/mol

Trityl-G0.5 dendron (2) was prepared by dissolving **1** (11.50 g, 36 mmol) in methanol (25 mL). The solution was then added dropwise to a stirring solution of methyl acrylate (17 mL, 180 mmol, 5 eq per amine) in methanol (50 mL) placed in an ice bath. Addition was done over a period of thirty minutes. Then, the reaction was stirred at room temperature for three days. After this time, the reaction was concentrated under reduced pressure at a maximum of 35°C. The product was re-dissolved in methanol and concentrated once again to remove any leftover excess of methyl acrylate. This yielded a colorless to light-yellow oil (99.0% yield, 95% Pure).¹H NMR (Figure appx. A5, 400 MHz, CDCl₃): δ=7.46 (d, *J* = 8.2, 1.2 Hz, 6H), 7.32 (t, 6H), 7.24 (t, 3H), 3.66 (s, 6H), 2.64 (t, *J* = 7.2 Hz, 4H), 2.35 (t, 8H).

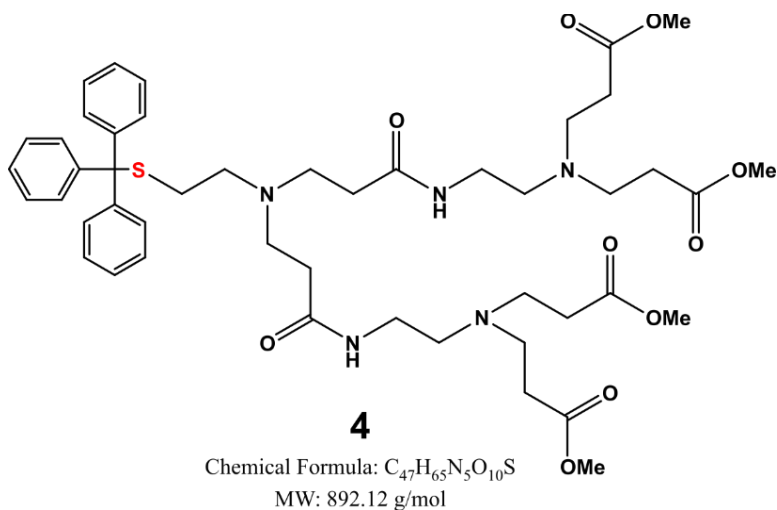


Chemical Formula: C₃₁H₄₁N₅O₂S

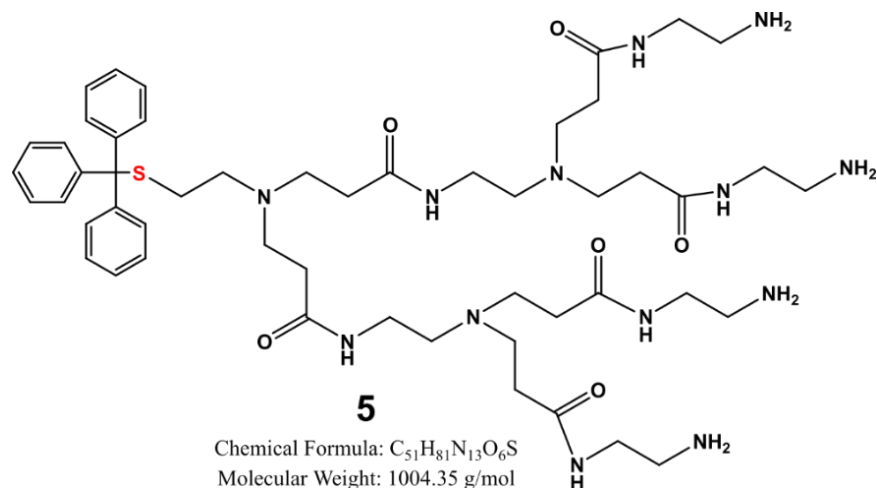
MW 547.76 g/mol

Trityl-G1.0 dendron (3) was prepared by first dissolving **2** (17.70 g, 36.0 mmol) in methanol (50 mL), and ethylenediamine (EDA) (67.0 mL, 1 mol, 12.5 eq per ester) in methanol (150 mL) separately. The EDA solution was placed in an ice bath, and while stirring, the **2** solution

was added dropwise. The addition of **2** was slow enough such that the reaction's temperature was kept under 40°C. The reaction was allowed to warm up to room temperature, and the stirred for four days. After this time, the reaction was concentrated under reduced pressure at 35°C maximum. To remove the excess of EDA, azeotropic distillation with Toluene:Methanol (9:1, 150 mL) was performed using a rotary evaporator at 35-40°C. Distillation was repeated until the EDA peak ($\delta=2.74$ ppm) was no longer seen by NMR. After purification, the product was a light-orange oil (98.7% yield, 94.0% Pure). ^1H NMR (Figure appx. A6, 400 MHz, CDCl_3): $\delta=7.54$ (t, 2H), 7.42 (d, 6H), 7.35 (t, $J=7.0$ Hz, 6H), 7.28 (t, 3H), 3.26 (q, $J=5.9$ Hz, 4H), 2.78 (t, 4H), 2.63 (t, $J=6.3$ Hz, 4H), 2.40 (t, 4H), 2.30 (t, $J=6.3$ Hz, 4H), 2.03 (s, 8H).



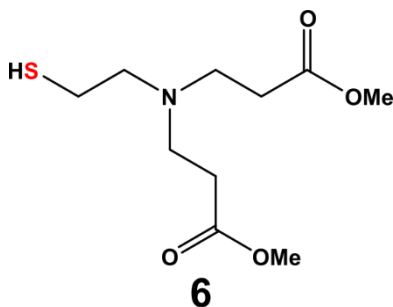
Trityl-G1.5 dendron (**4**) was prepared following the same steps as in **2**. The product was a yellow oil (97.0% yield, 94% Pure). ^1H NMR (Figure appx. A7, 400 MHz, CDCl_3) $\delta=7.39$ (d, 6H), 7.27 (t, 10H), 7.21 (t, 3H), 7.11 (t, $J=5.4$ Hz, 2H), 3.65 (s, 12H), 3.25 (q, $J=5.9$ Hz, 4H), 2.73 (t, $J=6.8$ Hz, 8H), 2.63 (t, $J=6.8$ Hz, 4H), 2.50 (t, $J=6.1$ Hz, 4H), 2.43 – 2.33 (m, 12H), 2.25 (t, $J=6.8$ Hz, 4H).



Trityl-G2.0 dendron (5) was prepared following the same steps as **3**. The product was a yellow oil (97.0% yield, 94% Pure). ¹H NMR (Figure appx. A8, 400 MHz, CDCl₃) δ 7.90 (t, *J* = 5.8 Hz, 2H), 7.69 (t, *J* = 5.3 Hz, 3H), 7.30 (d, 6H), 7.21 (t, 6H), 7.15 (t, 3H), 3.18 (q, *J* = 5.8 Hz, 8H), 3.11 (q, *J* = 6.2 Hz, 4H), 2.70 (t, *J* = 5.9 Hz, 7H), 2.63 (t, *J* = 6.4 Hz, 14H), 2.50 (t, *J* = 6.5 Hz, 3H), 2.41 (t, *J* = 6.4 Hz, 3H), 2.26 (q, *J* = 7.7, 6.3 Hz, 12H), 2.16 (t, *J* = 6.4 Hz, 4H).

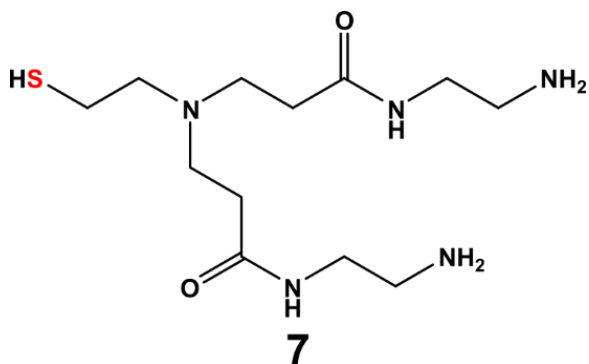
PAMAM dendron deprotection:

General synthesis procedure for deprotection of trityl-protected dendrons. Trityl protected dendron of a given generation was dissolved in a round bottom flask with dry DCM. TFA was added slowly dropwise while stirring and with N₂ (g) blowing over the flask. This was followed by a one-shot addition of triethylsilane. The reaction was left stirring at room temperature for four hours under N₂ (g) atmosphere. The solvent was removed under reduced pressure at a maximum of 35°C, followed by trituration with petroleum ether five times for fifteen minutes each. Final product was once again dried under reduced pressure and stored at -80°C.



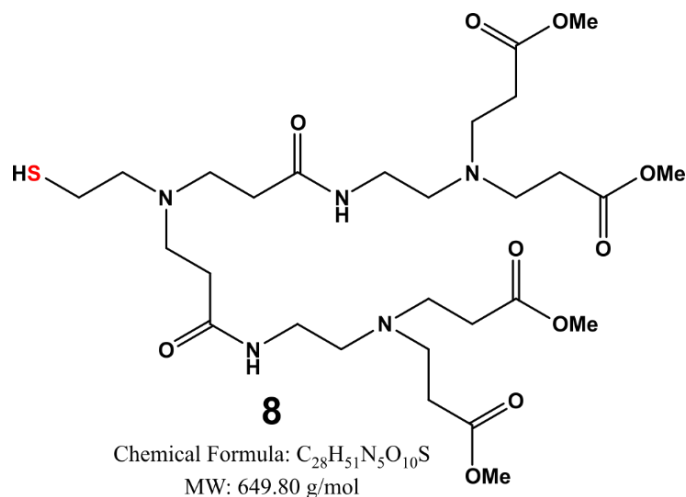
Chemical Formula: C₁₀H₁₉NO₄S
Molecular Weight: 249.33

HS-G0.5 dendron (6) was prepared by dissolving **2** (0.51g, 1.04 mmol, 1 eq) in 10 mL of DCM. The reaction required 0.597 mL of TFA (7.80 mmol, 7.5eq) and 1.25 mL of triethylsilane (7.80 mmol, 7.5eq) for proper deprotection. For the trituration step, five 10 mL aliquots of petroleum ether were used. The product was a light-yellow oil (1.03 mmol, 99% yield). ¹H NMR (Figure appx. A9 400 MHz, CDCl₃) δ 3.72 (s, 6H), 3.45 (t, *J* = 6.9 Hz, 4H), 3.30 (dd, *J* = 9.1, 6.4 Hz, 2H), 2.90 (dt, *J* = 9.7, 7.2 Hz, 6H).

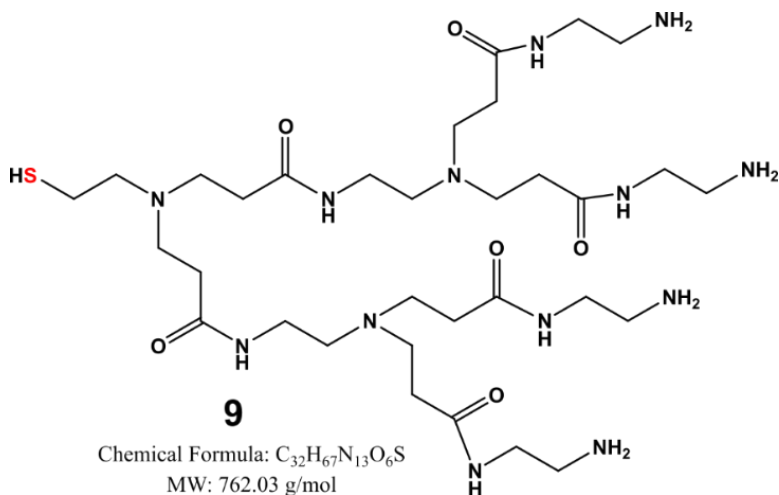


Chemical Formula: C₁₂H₂₇N₅O₂S
MW: 305.44 g/mol

HS-G1.0 dendron (7) was prepared by dissolving **3** (1.10g, 2.0 mmol, 1 eq) in 20 mL of DCM. The reaction required 2.30 mL of TFA (30.0 mmol, 15eq) and 2.40 mL of triethylsilane (15 mmol, 7.5eq) for proper deprotection. For the trituration step, five 20 mL aliquots of petroleum ether were used. The product was a light-amber oil (1.03 mmol, 99% yield). ¹H NMR (Figure appx. A10, 400 MHz, CD₃OD) δ 3.48 (q, *J* = 5.2, 4.5 Hz, 8H), 3.41 (t, *J* = 6.8 Hz, 2H), 3.08 (t, *J* = 6.0 Hz, 4H), 2.96 (t, *J* = 6.8 Hz, 2H), 2.82 (t, *J* = 6.1 Hz, 4H).



HS-G1.5 dendron (8) was prepared by dissolving **4** (0.32g, 0.36 mmol, 1 eq) in 10 mL of DCM. The reaction required 0.85 mL of TFA (10.8 mmol, 30eq) and 0.90 mL of triethylsilane (5.4 mmol, 15eq) for proper deprotection. For the trituration step, five 10 mL aliquots of petroleum ether were needed. The product was a light-orange oil (0.94 mmol, 99% yield). 1H NMR (Figure appx. A11, 400 MHz, CD_3OD) δ 3.70 (s, 12H), 3.62 (t, $J = 5.9$ Hz, 4H), 3.52 (t, $J = 6.8$ Hz, 8H), 3.47 (t, $J = 6.2$ Hz, 4H), 3.39 (t, $J = 6.9$ Hz, 2H), 3.35 (t, $J = 5.9$ Hz, 4H), 2.91 (q, $J = 6.8, 5.3$ Hz, 10H), 2.80 (t, $J = 6.2$ Hz, 4H).



HS-G2.0 dendron (9) was prepared by dissolving **5** (1.42g, 1.37 mmol, 1 eq) in 20 mL of DCM. The reaction required 4.7 mL of TFA (62 mmol, 60eq) and 1.2 mL of triethylsilane (7.78 mmol, 7.5eq) for proper deprotection. For the trituration step, five 20 mL aliquots of petroleum ether were used. The product was an amber oil (1.2 mmol, 90% yield). 1H NMR (Figure appx. A12, 400 MHz, $dms\text{-}d_6$) δ 8.61 (t, $J = 5.8$ Hz, 2H), 8.51 (t, $J = 5.9$ Hz, 4H), 3.62 – 3.55 (m, 4H),

3.53 – 3.45 (m, 12H), 3.44 – 3.34 (m, 8H), 3.31 (t, $J = 8.5, 6.6$ Hz, 4H), 2.98 (q, $J = 6.0$ Hz, 8H), 2.92 (t, $J = 8.8$ Hz, 2H), 2.80 – 2.70 (m, 12H), 2.59 (d, $J = 4.8$ Hz, 2H).

Small molecule coupling to Ln₂Ga₈Shi₈Mip₄:

Sm₂Ga₈Shi₈Mip₄(Cys)₄ was prepared by dissolving Sm₂Ga₈Shi₈Mip₄ (0.020 mmol, 1 eq) and cysteamine (0.18 mmol, 9 eq) in degassed DMF (5-10 mL). The reaction was stirred for 6-12 hours, and the DMF was removed with a stream of N₂ (g) over the solution. Once dried, the product was rinsed with cold methanol to yield an off-white product (>95% yield). MS (Figure 2.10, ESI): m/z calcd. Sm₂Ga₈C₁₁₂H₈₀N₁₆O₄₈S₄: 1704.2 [M]²⁻; found: 1702.2 [M]²⁻. Elemental analysis calcd. (%) for Sm₂Ga₈C₁₁₆H₁₄₈N₁₆O₇₈S₄Na₂: C 34.43, H 3.69, N 5.54; found: C 34.38, H 3.56, N 5.45.

Toroidal Dendrimeric Metallacrown (DMC) synthesis and purification:

Synthetic details: Ln₂Ga₈Shi₈Mip₄ was dissolved in degassed DMF to a final concentration of 10 mg/mL. This was followed by the addition of dendron dissolved in minimum amount of degassed DMF. DMAP was added to solutions prepared with dendrons **HS G1-2**. Reaction was stirred in a sealed vial flushed with N₂ (g) for 1-10 days depending on the dendron generation. Completion of the reaction was corroborated by ESI-MS. If partial completion, ¼ of the initial dendron concentration was added to the reaction, and stirred for 2 more days as previously described. Once completed, the reaction was concentrated with a stream of N₂ (g) prior purification.

Purification details: Ln₂Ga₈Shi₈Mip₄ **G0.5** was purified by rinsing a concentrated solution with copious amount of water, followed by overnight drying under vacuum at room temperature. For Ln₂Ga₈Shi₈Mip₄ **G1-2**, purification was done using RC dialysis bags with a MWCO of 2 or 3.5 kDa, depending on the complex's molecular weight. Once all of the initial DMF was removed, the DMC was redissolved in DMSO, and dialysis was done against DMSO as the dialysate. The volume of dialysate was 200 times the volume of the sample inside the dialysis bag. To avoid dialysis bag decomposition, new bags were used every 24 hrs and dialysate was also exchanged daily. Mass spectra of the sample was taken daily to monitor the removal of free dendron. Once the dendron peak was not observed by ESI-MS, the dialysis was stopped, and the sample was slowly concentrated to about ¼ of the original volume with a stream of N₂ (g). Sample concentration was determined by UV-Vis spectrometry by using the extinction coefficient of the

metallacrown core. *It is important to avoid complete removal of all the solvent, or temperatures above 35°C so as to avoid defect formation.* DMCs were stored as DMSO solutions for further characterization.

General synthesis procedure for Ln₂Ga₈Shi₈Mip₄ G0.5 DMCs: **Ln₂Ga₈Shi₈Mip₄** (0.050 mmol, 1 eq) and **6** (0.50 mmol, 10 eq) were dissolved in degassed DMF. The solution was stirred for 24 hours at room temperature. After purification, the final product was an off-white powder with quantitative yields based on metallacrown.

Sm₂Ga₈Shi₈Mip₄ G0.5. MS (Figure appx. A22, ESI): *m/z* calcd. for Sm₂Ga₈C₁₄₄H₁₂₈N₁₆O₆₄S₄: 2047.43 [M]²⁻; found: 2046.92 [M]²⁻. Elemental analysis calcd. (%) for Sm₂Ga₈C₁₄₄H₁₃₈N₁₆Na₂O₆₉S₄: C 40.89, H 3.29, N 5.30; found: C 39.90, H 3.26, N 5.42.

Tb₂Ga₈Shi₈Mip₄ G0.5. MS (Figure appx. A23, ESI): *m/z* calcd. for Tb₂Ga₈C₁₄₄H₁₂₈N₁₆O₆₄S₄: 2054.44 [M]²⁻; found: 2054.93 [M]²⁻. Elemental analysis calcd. (%) for Tb₂Ga₈C₁₄₄H₁₄₀N₁₆Na₂O₇₀S₄: C 40.56, H 3.31, N 5.26; found: C 40.64, H 3.36, N 5.23.

Gd₂Ga₈Shi₈Mip₄ G0.5. MS (Figure appx. A24, ESI): *m/z* calcd. for Gd₂Ga₈C₁₄₄H₁₂₈N₁₆O₆₄S₄: 2053.43 [M]²⁻; found: 2053.32 [M]²⁻. Elemental analysis calcd. (%) for Gd₂Ga₈C₁₄₀H₁₃₆N₁₆O₆₈S₄: C 40.70, H 3.32, N 5.42; found: C 40.63, H 3.31, N 5.38.

Yb₂Ga₈Shi₈Mip₄ G0.5. MS (Figure appx. A25, ESI): *m/z* calcd. for Yb₂Ga₈C₁₄₄H₁₂₈N₁₆O₆₄S₄: 2068.45 [M]²⁻; found: 2068.94 [M]²⁻. Elemental analysis calcd. (%) for Yb₂Ga₂C₁₄₈H₁₅₀N₁₆O₇₁Na₂S₄: C 40.71, H 3.46, N 5.13; found: C 40.73, H 3.46, N 4.83.

Yb₂Ga₈Shi₈Mip₄ G1.0 was prepared by dissolving Yb₂Ga₈Shi₈Mip₄ (0.050 mmol, 1 eq), **7** (1.00 mmol, 20 eq), and DMAP (0.050 mmol, 1 eq) in DMF. The solution was stirred for four days under N₂ (g) atmosphere. After purification and concentration, the product was a bright orange solution. MS (Figure appx. A26, ESI): *m/z* calcd. Yb₂Ga₈C₁₅₂H₁₆₄N₃₂O₅₆S₄: 2183.13 [M+2H]²⁺; found 2183.71 [M+2H]²⁺. Reaction yield post purification ~80% as determined by UV-Vis concentration.

Yb₂Ga₈Shi₈Mip₄ G1.5 was prepared by dissolving Yb₂Ga₈Shi₈Mip₄ (0.014 mmol, 1 eq), **8** (0.29 mmol, 20 eq), and DMAP (0.014 mmol, 1 eq) in DMF. The solution was stirred for six days under N₂ (g) atmosphere. After purification and concentration, the product was a dark orange

solution. MS (Figure appx. A27, ESI): m/z calcd. $\text{Yb}_2\text{Ga}_8\text{C}_{216}\text{H}_{260}\text{N}_{32}\text{O}_{88}\text{S}_4$: 2871.43 $[\text{M}+2\text{H}]^{2+}$, and $\text{C}_{216}\text{H}_{261}\text{Ga}_8\text{N}_{32}\text{O}_{88}\text{S}_4\text{Yb}_2$: 1914.62 $[\text{M}+3\text{H}]^{3+}$; found 2872.52 $[\text{M}+2\text{H}]^{2+}$, and 1915.36 $[\text{M}+3\text{H}]^{3+}$. Reaction yield post purification ~70% as determined by UV-Vis concentration.

Yb₂Ga₈Shi₈Mip₄ **G2.0** was prepared by dissolving $\text{Yb}_2\text{Ga}_8\text{Shi}_8\text{Mip}_4$ (0.011 mmol, 1 eq), **9** (0.23 mmol, 20 eq), and DMAP (0.011 mmol, 1 eq) in DMF. The solution was stirred for 10 days under N_2 (g) atmosphere. After purification and concentration, the product was a dark orange solution. MS (Figure appx. A28, ESI): m/z calcd. $\text{Yb}_2\text{Ga}_8\text{C}_{232}\text{H}_{325}\text{N}_{64}\text{O}_{72}\text{S}_4$: 2063.85 $[\text{M}+3\text{H}]^{3+}$; found 2064.81 $[\text{M}+3\text{H}]^{3+}$. Reaction yield post purification ~70% as determined by UV-Vis concentration.

2.2.4 Solution Stability

Mixtures of $\text{Y}_2\text{Ga}_8\text{Shi}_8\text{Ip}_4/\text{Y}_2\text{Ga}_8\text{Shi}_8\text{Mip}_4$, and $\text{Tb}_2\text{Ga}_8\text{Shi}_8\text{Mip}_4/\text{Tb}_2\text{Ga}_8\text{Shi}_8\text{Mip}_4$ **G0.5** were dissolved in *i*) DMF or *ii*) a mixture of DMF/ H_2O to assess their solution stability over time. ESI-MS was used to monitor the mixtures stability over a period of several hours or days. Experimental details are described below.

Y₂Ga₈Ip + Y₂Ga₈Mip Organic Solvent Mixture: 1.5 μmol of each MC were dissolved separately in 1 mL of DMF. Solutions of 50 μL of each were then mixed together and diluted with 1 mL of methanol. Analysis of the mixture by ESI-MS was done daily over a period of five days. MS (Figure 2.4, ESI): m/z calcd. for $\text{Y}_2\text{Ga}_8\text{C}_{88}\text{H}_{48}\text{N}_8\text{O}_{40}$: 1295.71 $[\text{M}]^{2-}$; found 1296.71 $[\text{M}]^{2-}$; and for m/z calcd. $\text{Y}_2\text{Ga}_8\text{C}_{104}\text{H}_{52}\text{N}_{12}\text{O}_{48}$: 1486.21 $[\text{M}]^{2-}$; found 1486.70 $[\text{M}]^{2-}$, respectively.

Y₂Ga₈Ip + Y₂Ga₈Mip Mixed Media Mixture: 1.5 μmol of each MC were dissolved separately in 0.5 mL of DMF, followed by the addition of 0.5 mL of DI H_2O . Solutions of 50 μL of each were then mixed together and diluted with 1 mL of methanol. Analysis of the mixture by ESI-MS was done daily over a period of two days. MS (Figure 2.5, ESI): m/z calcd. for $\text{Y}_2\text{Ga}_8\text{C}_{88}\text{H}_{48}\text{N}_8\text{O}_{40}$: 1295.71 $[\text{M}]^{2-}$; found 1296.71 $[\text{M}]^{2-}$; m/z calcd. for $\text{Y}_2\text{Ga}_8\text{C}_{92}\text{H}_{49}\text{N}_9\text{O}_{42}$: 1343.21 $[\text{M}]^{2-}$; found 1344.20 $[\text{M}]^{2-}$; m/z calcd. for $\text{Y}_2\text{Ga}_8\text{C}_{96}\text{H}_{50}\text{N}_{10}\text{O}_{44}$: 1391.21 $[\text{M}]^{2-}$; found 1391.70 $[\text{M}]^{2-}$; m/z calcd. for $\text{Y}_2\text{Ga}_8\text{C}_{100}\text{H}_{51}\text{N}_{11}\text{O}_{46}$: 1438.71 $[\text{M}]^{2-}$; found 1439.20 $[\text{M}]^{2-}$; and for m/z calcd. $\text{Y}_2\text{Ga}_8\text{C}_{104}\text{H}_{52}\text{N}_{12}\text{O}_{48}$: 1486.21 $[\text{M}]^{2-}$; found 1486.70 $[\text{M}]^{2-}$, respectively.

Tb₂Ga₈Mip + Tb₂Ga₈Mip G:0.5 Mixed Media Mixture: 1.5 μmol of the MC and DMC were dissolved separately in 0.5 mL of DMF, followed by the addition of 0.5 mL of DI H_2O . 50 μL of

each solution were then mixed together and diluted with 1 mL of methanol. Analysis of the mixture by ESI-MS was done daily over a period of seven days. MS (Figure 2.16, ESI): m/z calcd. for $\text{Tb}_2\text{Ga}_8\text{C}_{104}\text{H}_{52}\text{N}_{12}\text{O}_{48}$: 1556.23 $[\text{M}]^{2-}$; found 1556.72 $[\text{M}]^{2-}$; and m/z calcd. for $\text{Tb}_2\text{Ga}_8\text{C}_{144}\text{H}_{128}\text{N}_{16}\text{O}_{64}\text{S}_4$: 2054.44 $[\text{M}]^{2-}$; found 2054.93 $[\text{M}]^{2-}$, respectively.

2.2.5 Luminescence Studies

Solution state absorbance was collected using a Cary 100Bio UV-Vis spectrometer in absorbance mode. MC samples were prepared by dissolving them in 3 mL of DMSO with a final concentration of 1-20 μM , while DMC samples were recorded as DMSO solutions post purification. Data were processed using OriginPro 2020 software.

Solution state emission of MC coupled to small molecules was collected using a Horiba Quanta Master spectrometer in emission state mode. Samples were prepared by dissolving them in 3 mL of DMSO or methanol with a final concentration of 1-20 μM . Data were processed using OriginPro 2020 software.

Photophysical measurements were performed and analyzed by Dr. Svetlana Eliseeva at the Centre de Biophysique Moléculaire, Orleans, France. Luminescence data of MCs and G0.5 DMCs were collected on freshly prepared solutions in DMSO, in $\text{H}_2\text{O}/\text{DMSO}$ (96:4), or in the solid state placed into 2.4 mm i.d. quartz capillaries, while G1.0-2.0 DMC samples were diluted to 50 μM solutions and only recorded in solution state. Emission and excitation spectra were measured on a Horiba-Jobin-Yvon Fluorolog 3 spectrofluorimeter equipped with either a visible photomultiplier tube (PMT) (220-800 nm, R928P; Hamamatsu), a NIR solid-state InGaAs detector cooled to 77 K (800-1600 nm, DSS-IGA020L; ElectroOptical Systems, Inc., USA), or a NIR PMT (950-1650 nm, H10330-75; Hamamatsu). All spectra were corrected for the instrumental functions. Luminescence lifetimes were determined under excitation at 355 nm provided by a Nd:YAG laser (YG 980; Quantel). Luminescent signals were detected in the visible or NIR ranges with a R928 or H10330-75 PMTs connected to the iHR320 monochromator (Horiba Scientific), respectively. The output signals from the detectors were fed into a 500 MHz bandpass digital oscilloscope (TDS 754C; Tektronix) and transferred to a PC for data processing with the Origin 8 software. Luminescence lifetimes are reported as the average of three or more independent measurements. Quantum yields were determined with a Fluorolog 3 spectrofluorimeter based on the absolute method using an integration sphere (GMP SA). Quantum yield measurements were performed utilizing the

modified de Mello et al.^{131,156} approach which requires three individual measurements: *i*) the exiting integrated light intensity of an empty capillary (L_a) irradiated at the excitation wavelength (i.e., the Rayleigh scattering band); *ii*) the exiting integrated light intensity of the sample (L_c); and *iii*) the exiting integrated light intensity of the entire emission spectrum (E_c). A simplified diagram of the set up is shown in Figure 2.1.

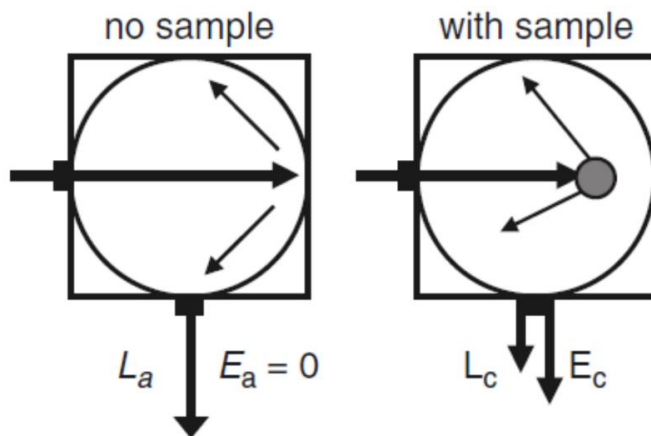


Figure 2.1 Exemplified notations required for the absolute quantum yield measurements.¹³¹

The absolute quantum yield (ϕ_{Ln}^L) can then be calculated with the following equation,

$$\phi_{Ln}^L = \frac{E_c}{[L_c(\lambda_{ex}) - L_a(\lambda_{ex})]F_{att}(\lambda_{ex})} \quad (1)$$

Where $F_{att}(\lambda_{ex})$ represents the correction for the attenuators used in the measurements. To ensure careful correction the instrument was regularly calibrated using quartz tungsten halogen lamp (45W, Newport). Each sample was measured several times varying the position of samples. Estimated experimental error for the determination of quantum yields is estimated as ~10%. Determination of the quantum yields for each chapter in this thesis follows the same methodology.

2.2.6 Cell Studies

Cell studies were performed and interpreted by Dr. Guillaume Collet at the Centre de Biophysique Moléculaire, Orleans, France.

Cell culture: HeLa cells (human cervical cancer cells collected from Henrietta Lacks) were cultured in EMEM medium (Sigma) supplemented with 10% (vol:vol) fetal bovine serum (FBS, Sigma), 100 U/mL penicillin (Sigma), and 100 µg/mL streptomycin (Sigma). Cells were routinely cultured at 37 °C in a humidified incubator in a 95% air/5% CO₂ atm and passaged by detaching cells with trypsin/EDTA 0.25% (Gibco). HeLa cells were seeded in an eight chambers Lab-Tek (1.0 borosilicate coverglass system) at 10 000 cells/chamber in a final volume of 400 µL of complete EMEM medium. After 48 h, cell culture medium was removed and after three washes with 500 µL of saline (9 g/L NaCl), Yb₂Ga₈Shi₈Mip₄ DMC was added to cells at a dilution of 100 µM in saline with 1 % DMSO (vol:vol) for 2 hours of incubation. Prior collecting images, HeLa cells were washed three times with 500 µL of saline. For the microscopy imaging, HeLa cells were kept in 200 µL of OptiMEM (Gibco) without phenol red, supplemented with 2% (vol:vol) fetal bovine serum (FBS, Sigma), 100 U/mL penicillin (Sigma), and 100 µg/mL streptomycin (Sigma).

Optical microscopy imaging: Epifluorescence microscopy was performed with an inverted Nikon Eclipse Ti microscope equipped with an EMCCD Evolve camera from Photometrics. The Nikon Intensilight C-HGFIE mercury-halide lamp was used as the excitation source. For imaging of Yb₂Ga₈Shi₈Mip₄ DMC, the Yb^{III} signal was observed using the following set of filters: a 377 nm with 50 nm bandwidth in the pass band excitation filter, a 506 nm dichroic beam splitter, and a long pass 785 nm emission filter. Fluorescent images were obtained with Nikon Plan Fluor 40x objective after two seconds of exposure time. An Okolab incubation chamber adapted to the microscope allowed the incubation parameters to be maintained at a constant 37 °C with a humidified atmosphere of 95% air/5% CO₂. All microscopy images were acquired and processed with Nikon NIS Elements AR software.

2.3 Results

2.3.1 $\text{Ln}_2\text{Ga}_8\text{Shi}_8\text{Mip}_4$ Metallacrown

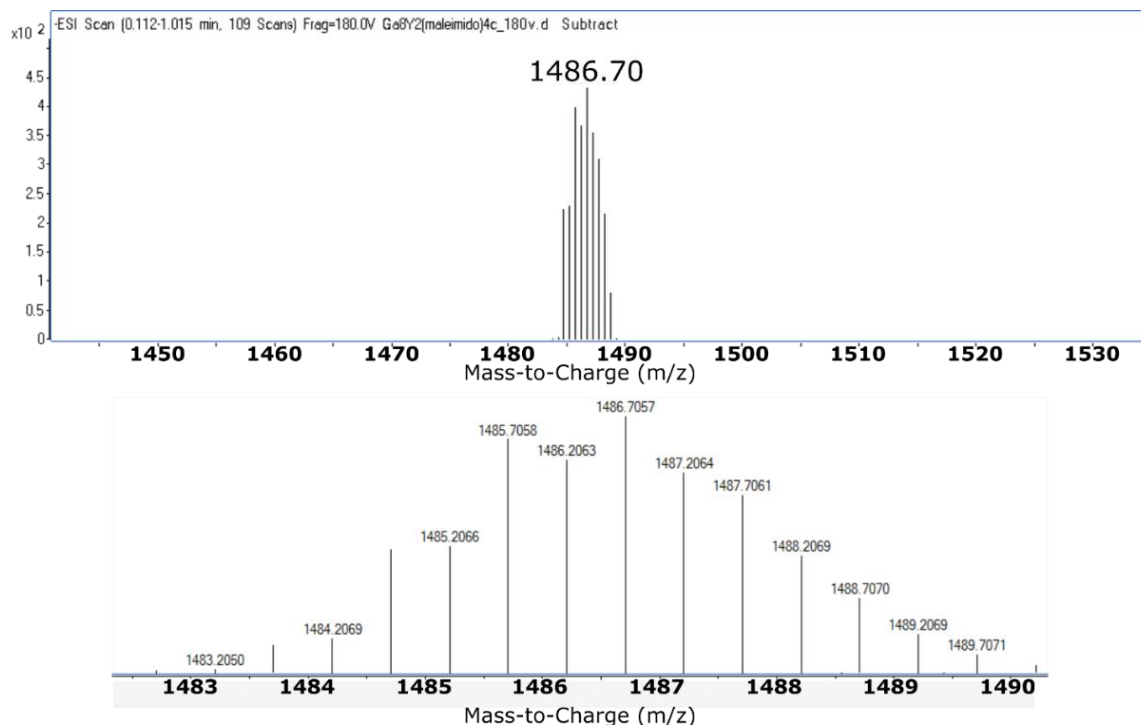


Figure 2.2 (Top) ESI-MS of $\text{Y}_2\text{Ga}_8\text{Shi}_8\text{Mip}_4$ metallacrown in negative ion mode. (Bottom) (Bottom) expansion of the major peak corroborating the -2 isotopic distribution of the complex.

Synthesis and physical characterization of $\text{Ln}_2\text{Ga}_8\text{Shi}_8\text{Mip}_4$. The reaction between $\text{LnGa}_4\text{Shi}_4(\text{benzoate})_4$ ($\text{Ln} = \text{Y}^{\text{III}}$, Sm^{III} , Gd^{III} , Tb^{III} , and Yb^{III}) and 5-maleimidoisophthalic acid (H_2Mip) in DMF led to the formation of $\text{Ln}_2\text{Ga}_8\text{Shi}_8\text{Mip}_4$ with the general formula $\text{Ln}_2[12\text{-MC}_{\text{Ga}(\text{III})\text{N}(\text{shi})\text{-4}}]_2(\text{Mip})_4$. Solids were collected as crystalline powder material, and characterized by ESI-MS, ^1H NMR (for Y^{III} compounds), and elemental analysis. As seen in Figure 2.2, the ESI-MS spectrum of $\text{Y}_2\text{Ga}_8\text{Shi}_8\text{Mip}_4$ shows a single distribution with a -2 charge of consistent mass for the MC scaffold. Figures in Appendix (appx.) A18-21 show the ESI-MS spectra of the same MC prepared with different Ln^{III} ions. Figure 2.3 shows the ^1H NMR spectrum of $\text{Y}_2\text{Ga}_8\text{Shi}_8\text{Mip}_4$, suggesting a fourfold symmetry where integration gives a 2:1 ratio between Shi and Mip ligands.

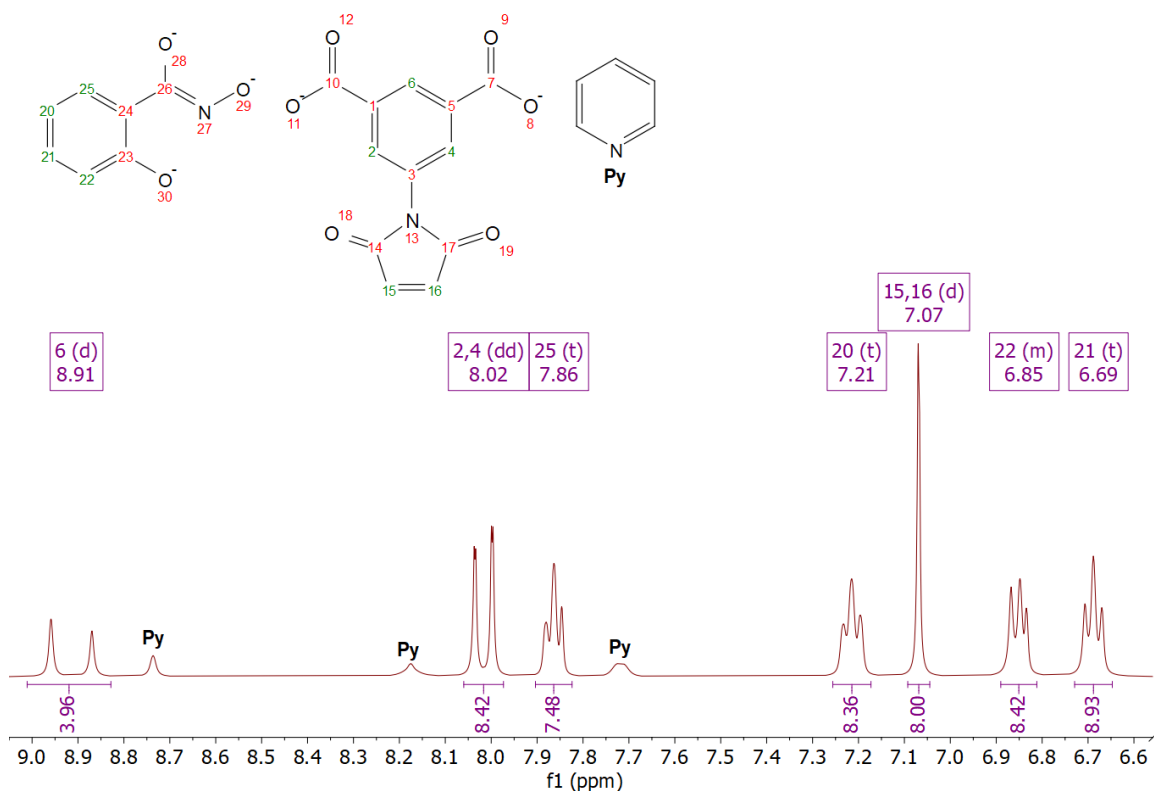


Figure 2.3 ^1H NMR spectrum of $\text{Y}_2\text{Ga}_8\text{Shi}_8(\text{Mip})_4$ in d_6 -DMSO. Labeled peaks from ring and bridging ligands. Pyridine peaks labeled separately.

Solution stability of $\text{Ln}_2\text{Ga}_8\text{Shi}_8\text{Mip}_4$. The solution stability of these MCs was investigated using ESI-MS. Mixtures of $\text{Y}_2\text{Ga}_8\text{Shi}_8\text{Ip}_4$ (m/z :1295.7) and $\text{Y}_2\text{Ga}_8\text{Shi}_8\text{Mip}_4$ (m/z :1486.2), which are MCs with similar structures but different bridging ligands and molecular weights, were dissolved in *i*) DMF solely or *ii*) in a mixture of DMF/ H_2O (1:1 v/v%). Mass spectrometry analysis was used to monitor the mixture's stability over a period of several hours or days. Both solutions were diluted in methanol to equal concentrations to ensure proper desolvation in the mass spectrometer. If unstable, gradual bridge ligand exchange was observed by ESI-MS. As seen in Figure 2.4, bridge ligand exchange was not observed in the MC mixture for several days when dissolved only in DMF. On the other hand, when dissolved in DMF/ H_2O , the MC mixture underwent bridge exchange immediately after mixed. Complete exchange was observed after one day, as seen in Figure 2.5.

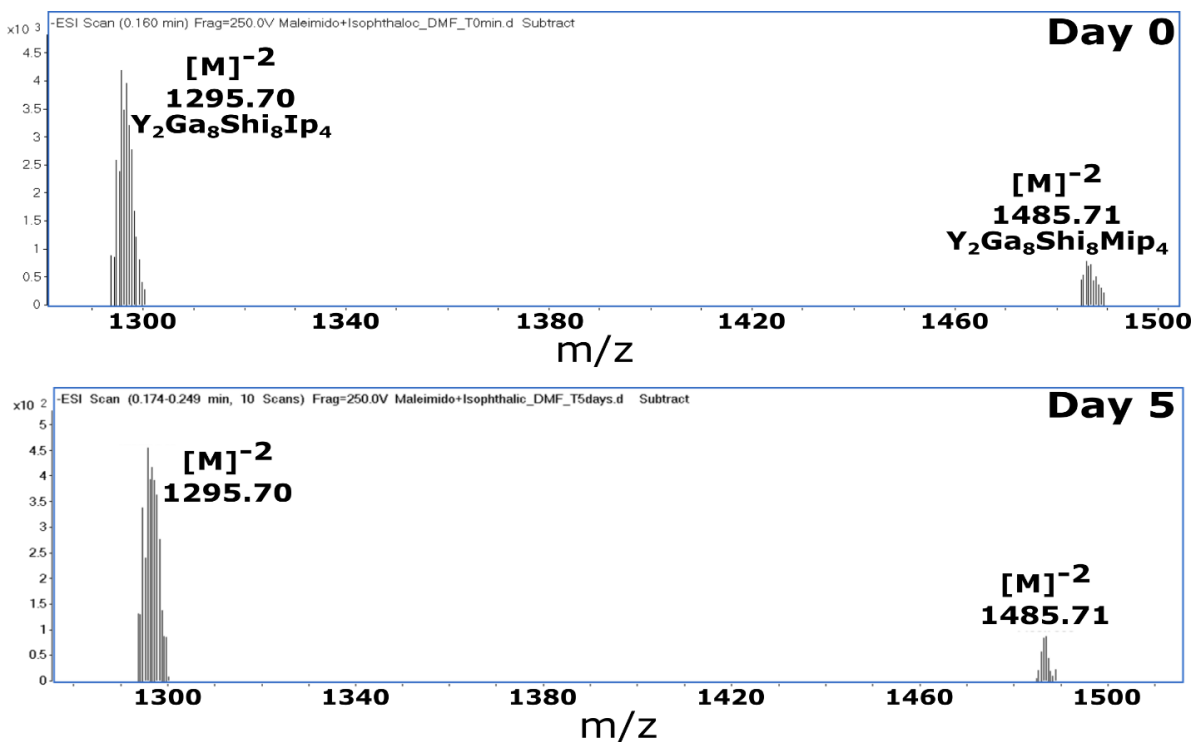


Figure 2.4 ESI-MS spectra of $Y_2Ga_8Shi_8Ip_4$ and $Y_2Ga_8Shi_8Mip_4$ MC mixture dissolved in DMF. Top spectrum collected immediately after mixing (Day 0), and bottom spectrum taken after five days.

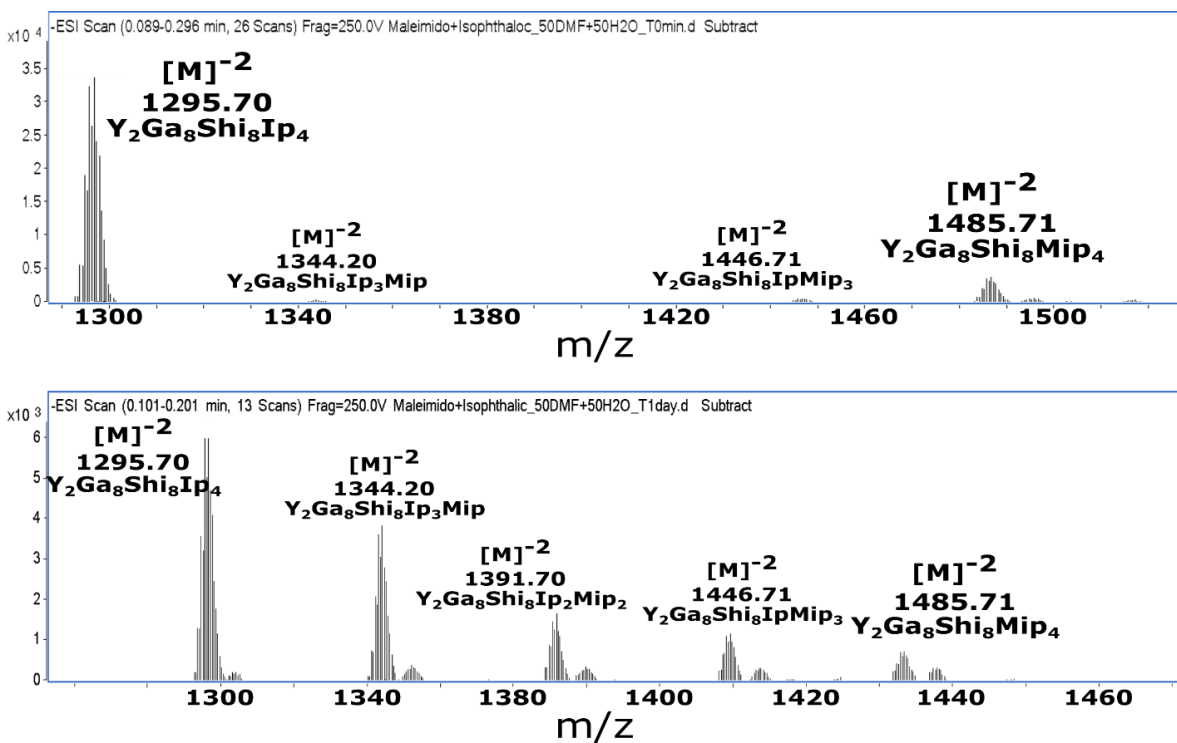


Figure 2.5 ESI-MS spectra of $Y_2Ga_8Shi_8Ip_4$ and $Y_2Ga_8Shi_8Mip_4$ MC mixture in DMF/ H_2O (1:1 v/v%). Top spectrum collected immediately after mixing (Day 0), and bottom spectrum taken after one day.

Photophysical properties of Ln₂Ga₈Shi₈Mip₄ (Ln: Yb^{III} and Gd^{III}). As seen in Figure 2.6, the DMSO solution of Yb₂Ga₈Shi₈Mip₄ MC exhibits a broad absorption band attributed to the $\pi \rightarrow \pi^*$ transitions located in the range of 250-350 nm. A low-energy maximum is located between 317-319 nm, with an absorption coefficient of $\sim 4.1 \times 10^4 \text{ M}^{-1} \text{ cm}^{-1}$. The energy of the ligand singlet (S^*) determined from the edge of the absorption spectrum is located at about 349 nm (28650 cm^{-1}). Figure 2.7 shows that the energy position of the ligand triplet state (T^*) is located at 430 nm (23280 cm^{-1}). The T^* value was determined from the phosphorescence spectrum of the Gd^{III}-MC as the 0-0 transition which is the lowest energy fit shown in red. Bandwidth of the fits differ due to the complexity of the sensitizing ligand system which has several inter- and intramolecular interactions. Additionally, some distortions of the widths are also observed since the spectra are plotted against wavelength. Fits for the subsequent transitions (e.g., 0-3, 0-4, etc.) are less reliable, and therefore, have been excluded from these analyses.

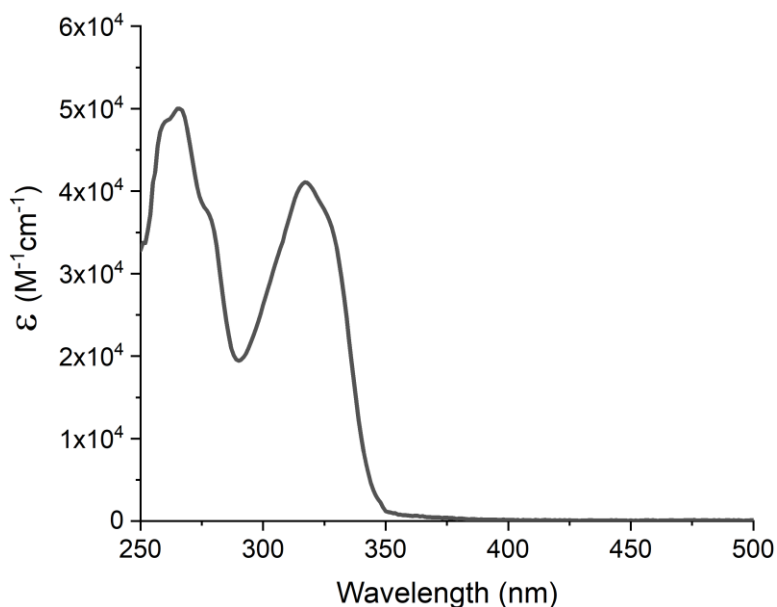


Figure 2.6 UV-Vis absorbance spectrum of 39.5 μM Yb₂Ga₈Shi₈Mip₄ MC in DMSO at room temperature. Absorbance maxima is at 317 nm, and an extinction coefficient of $4.1 \times 10^4 \text{ M}^{-1} \text{ cm}^{-1}$.

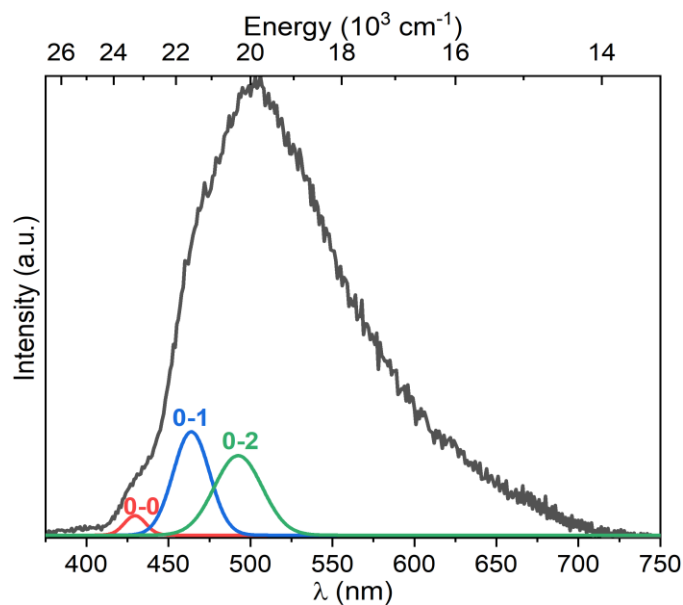


Figure 2.7 Solid state phosphorescence spectrum of $\text{Gd}_2\text{Ga}_8\text{Shi}_8\text{Mip}_4$ MC (black trace), and 0-0, 0-1 and 0-2 phonon transitions (colored traces) fitted with multiple Gaussian functions and Origin9 program. Data collected upon excitation at 340 nm, and after a 200-500 μs time delay at 77K. Fits differ in bandwidth due to the complexity of the ligand system, with several inter- and intramolecular interactions. Some distortion of the widths is also observed since the fits are plotted against wavelength. Subsequent fits (e.g, 0-3, 0-4, etc.) are less reliable, and in general omitted from these analyses.

Solution and solid-state excitation and emission spectra of $\text{Yb}_2\text{Ga}_8\text{Shi}_8\text{Mip}_4$ are shown in Figure 2.8. The excitation spectra collected upon monitoring the Yb^{III} -centered emission at 980 nm show broad ligand-centered bands up to 350-400 nm. Due to saturation effects,¹⁵⁷ a slight expansion of the excitation bands is observed for the solid-state data compared to the solution data. Upon excitation in the ligand centered region (320 or 340 nm), the characteristic emission of Yb^{III} is observed at the range of 920-1100 nm with a maximum at 980 nm in the solution-state, and at 1010 nm in the solid-state arising from the $^2\text{F}_{5/2} \rightarrow ^2\text{F}_{7/2}$ transition. Luminescent lifetimes (τ_{obs}) and the lanthanide's quantum yields upon ligand excitation (ϕ_{Ln}^L) were also acquired and summarized in Table 2.1. For the sake of comparison, values of other previously reported Yb^{III} -MCs are also shown. Shown in Figure 2.9 are the luminescent decay curves of $\text{Yb}_2\text{Ga}_8\text{Shi}_8\text{Mip}_4$ in both solid and solution state. Both curves demonstrate biexponential decay with the dominating contribution arising from the long-lived components (23 and 49 μs , respectively). Both the τ_{obs} and ϕ_{Ln}^L values for $\text{Yb}_2\text{Ga}_8\text{Shi}_8\text{Mip}_4$ in DMSO are 2.1 and 22.1 times higher than those in the solid state. Furthermore, comparing the ϕ_{Ln}^L of the parent $\text{Yb}_2\text{Ga}_8\text{Shi}_8\text{Ip}_4$ MC to the functionalized $\text{Yb}_2\text{Ga}_8\text{Shi}_8\text{Mip}_4$, a significant decreased is observed in both solid state (~97% decrease) and in

DMSO (~63% decrease). This is likely due to the quenching effects of the pyridinium counter ions (that the parent material lacks), and the quenching effects of the maleimide groups.

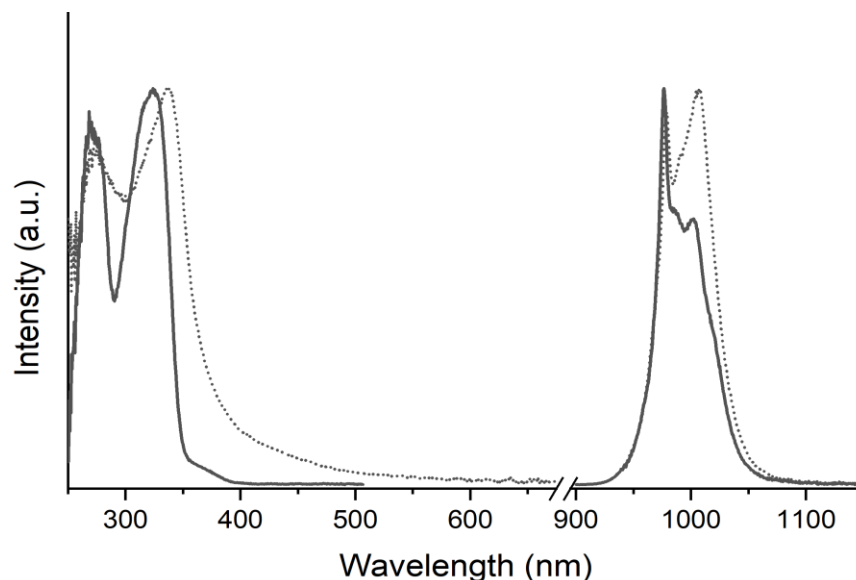


Figure 2.8 Corrected and normalized excitation (left, λ_{em} : 980 nm) and emission (right, λ_{ex} : 320–340 nm) spectra of $\text{Yb}_2\text{Ga}_8\text{Shi}_8\text{Mip}_4$ in the solid state (dashed traces) and 50 μM solutions in DMSO (solid traces) at room temperature.

Table 2.1 Luminescence lifetimes (τ_{obs}) and Yb^{III} -centered quantum yields collected under ligand excitation (ϕ_{Yb}^L)^a

Compound	State/Solvent	τ_{obs} [μs] ^b	τ_{av} [μs] ^c	ϕ_{Ln}^L [%] ^d
$\text{Yb}_2\text{Ga}_8\text{Shi}_8\text{Mip}_4$	Solid	23.2(3) : 89.8(4)% 4.75(7) : 10.2(4)%	22.7(8)	0.126(3)
	DMSO	48.7(6) : 84.6(5)% 6.9(2) : 15.4(5)%	45.3(9)	2.78(6)
$\text{Yb}_2\text{Ga}_8\text{Shi}_8\text{Ip}_4$	Solid ^e	37.1(1) : 100%	--	4.82(4)
	DMSO	60.9(4) : 100%	--	7.56(3)
$\text{YbGa}_4\text{Shi}_4(\text{benzoate})_4$	Solid ^f	55.7(3) : 100%	--	5.88(2)
	DMSO	33(2) : 34(5)% 15.4(5) : 66(5)%	24(1)	2.2(1)

^a For samples in the solid state or for 50 μM solutions in DMSO, at room temperature, 2σ values between parentheses. Estimated experimental errors: τ_{obs} , $\pm 2\%$; Q_{Yb}^L , $\pm 10\%$. ^b Under excitation at 355 nm. If biexponential decay was observed, population parameters $P_i = \frac{B_i\tau_i}{\sum_{i=1}^n B_i\tau_i}$ in % are given after the colon. ^c Lifetime averages calculated as: $\tau_{av} = \frac{\sum_i B_i\tau_i^2}{\sum_i B_i\tau_i}$; B_i are the population parameters given in % after the lifetime values. ^d Quantum yield under excitation at 320–360 nm. ^e J. Am. Chem. Soc. 2016, 138, 5100–5109. ^f Chem. Eur. J. 2018, 24, 1031–1035.

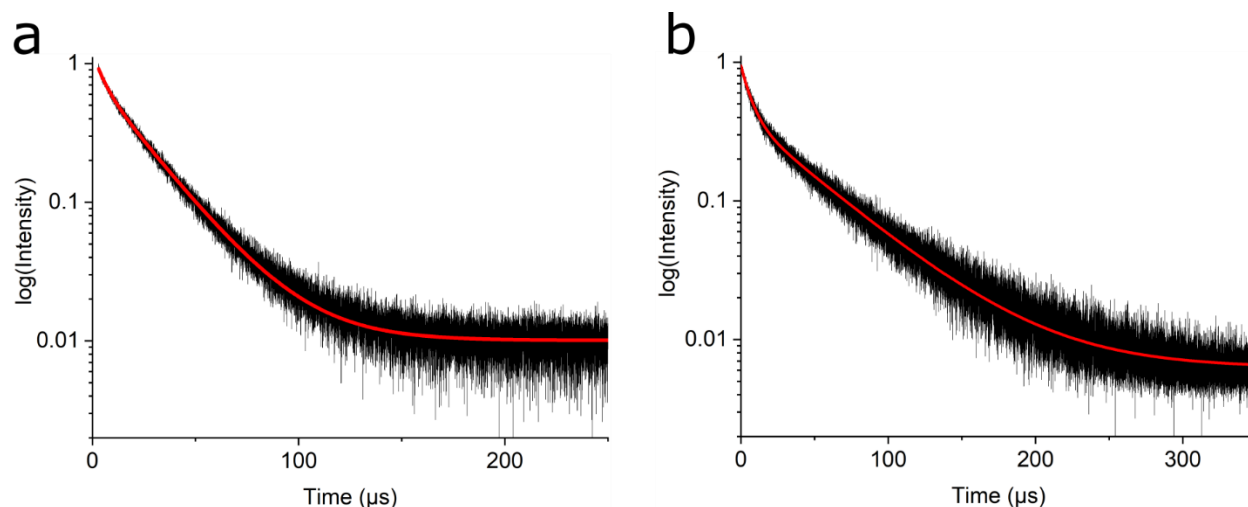


Figure 2.9. Experimental luminescence decay curves (black) of $\text{Yb}_2\text{Ga}_8\text{Shi}_8\text{Mip}_4$ MC in the (a) solid state and (b) in $50 \mu\text{M}$ DMSO solutions. Experimental excitation at 355 nm and monitoring the Yb^{III} emission at 980 nm at room temperature. Both curves are fitted to biexponential decay with adjusted R^2 parameters of >0.99 for both fittings.

2.3.2 $\text{Ln}_2\text{Ga}_8\text{Shi}_8\text{Mip}_4$ Functionalization.

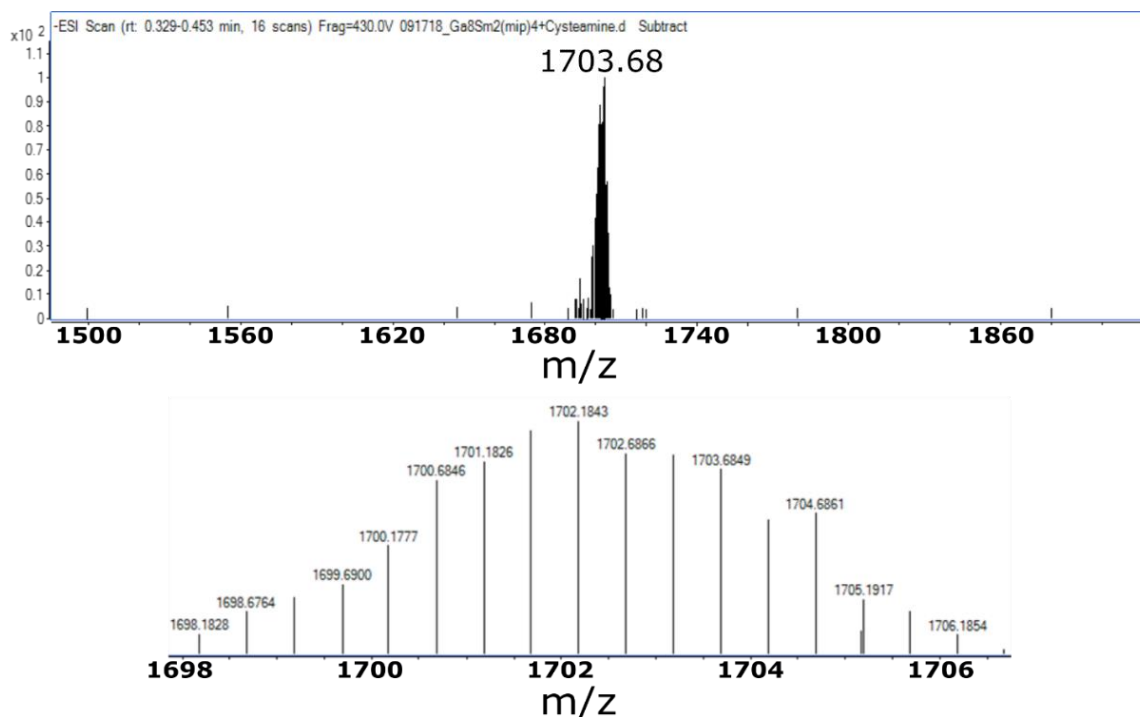


Figure 2.10 (Top) ESI-MS of $\text{Sm}_2\text{Ga}_8\text{Shi}_8\text{Mip}_4(\text{Cys})_4$ metallacrown in negative ion mode (m/z calcd. $\text{Sm}_2\text{Ga}_8\text{C}_{112}\text{H}_{80}\text{N}_{16}\text{O}_{48}\text{S}_4$: 1704.2 [M]^{2-} ; found: 1703.7 [M]^{2-}). (Bottom) expansion of the major peak corroborating the -2 isotopic distribution of the complex. The mass spectrum confirms the lack of any uncoupled MC.

Small molecule coupling to Sm₂Ga₈Shi₈Mip₄. The reaction between Sm₂Ga₈Shi₈Mip₄ and cysteamine in DMF led to the coupling of four equivalents of the small molecule to the Sm^{III}-MC – with the shorthand formula of Sm₂Ga₈Shi₈Mip₄(Cys)₄. Product was collected as an off-white powder that was characterized by ESI-MS, elemental analysis, UV-Vis absorbance spectroscopy, and fluorescence spectroscopy. Figure 2.10 shows the ESI-MS spectrum of Sm₂Ga₈Shi₈Mip₄(Cys)₄ as a single peak and with an isotopic distribution of 0.5 m/z, corroborating the intrinsic -2 charge of the metallacrown

The UV-Vis absorbance spectra of Sm₂Ga₈Shi₈Mip₄ in methanol before and after cysteamine coupling is shown in Figure appx. A29. Both scaffolds display a $\pi \rightarrow \pi^*$ transition band extending up to 350 nm. The absorbance maxima (λ_{max}) are located at about 310–315nm, and have molar absorption coefficients of $\sim 4.4\text{E}+4 \text{ M}^{-1}\text{cm}^{-1}$ in methanol. Solution state excitation and emission spectra in methanol are shown in Figure 2.11. Excitation spectra of both Sm₂Ga₈Shi₈Mip₄ and Sm₂Ga₈Shi₈Mip₄(Cys)₄ upon monitoring the Sm^{III} emission at 595 nm are dominated by broad ligand-centered bands in the UV region between 250-360 nm. The emission spectra excited at 315 nm exhibit sharp characteristic emission bands in the visible range at 560 nm ($^4\text{G}_{5/2} \rightarrow ^6\text{H}_{5/2}$), 595 nm ($^4\text{G}_{5/2} \rightarrow ^6\text{H}_{7/2}$), 645 nm ($^4\text{G}_{5/2} \rightarrow ^6\text{H}_{9/2}$), and 700 nm ($^4\text{G}_{5/2} \rightarrow ^6\text{H}_{11/2}$). All of which are specific to Sm^{III} f-f transitions.

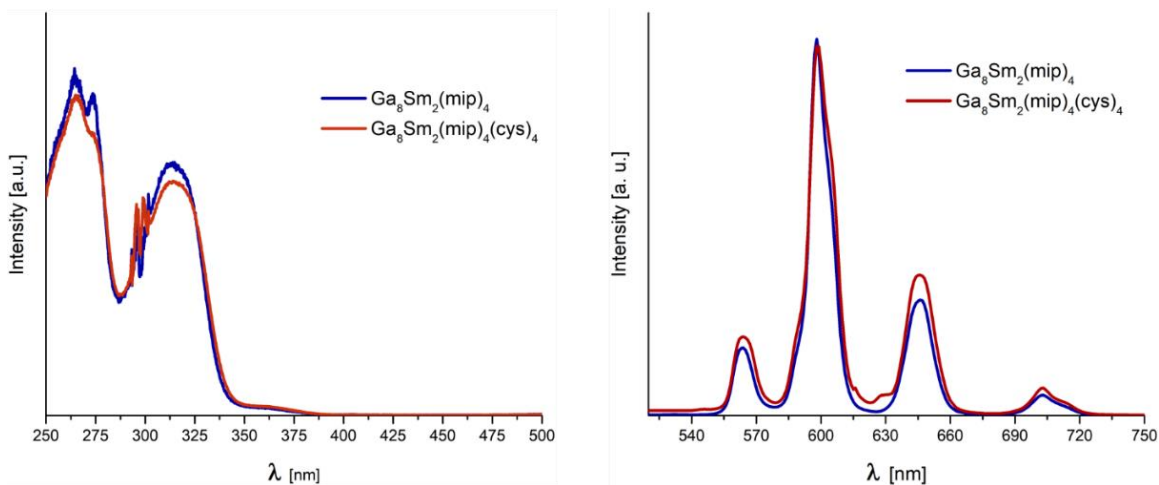


Figure 2.11 (left) Solution state excitation (λ_{em} : 595 nm) and (right) emission (λ_{ex} : 315 nm) spectra of Sm₂Ga₈Shi₈Mip₄ and Sm₂Ga₈Shi₈Mip₄(cysteamine)₄ compounds collected in $\sim 2 \mu\text{M}$ solutions in methanol at room temperature. Background spectrum was subtracted to remove second harmonic artifacts.

2.3.3 Toroidal Dendrimeric Metallacrowns (T-DMCs)

Synthesis and physical characterization of Toroidal DMCs. The reaction between $\text{Ln}_2\text{Ga}_8\text{Shi}_8\text{Mip}_4$ and thiol-focal point PAMAM dendrons (HS-G: 0.5-2.0) in DMF led to the formation of T-DMCs of multiple generations. Referred with the general formula $\text{Ln}_2\text{Ga}_8\text{Shi}_8\text{Mip}_4\text{GX}$ (X: 0.5-2.0), DMCs were purified by dialysis, and characterized by ESI-MS and dynamic light scattering (DLS). $\text{Ln}_2\text{Ga}_8\text{Shi}_8\text{Mip}_4$ dendrimeric metallacrowns can be prepared with numerous Ln^{III} ions (Sm^{III} , Tb^{III} , Gd^{III} , and Yb^{III}) as seen in Figure appx. A22-24, but emphasis was placed on preparing Yb^{III} -based complexes of larger generations. DMCs were characterized by ESI-MS to corroborate complete coupling of four dendrons to the four maleimide appendages of the MC core. Figure 2.12 shows the increasing m/z ratios of Yb^{III} -DMCs with increasing generation. The MC core and DMC G0.5 were seen as -2 charged complexes, while the next three larger generations were better characterized in positive ion mode and seen as +2 or +3 charged complexes. Structural imperfections arising from synthetic protocols or ESI-MS characterization can be observed as peaks with smaller m/z values (Figure appx. A25-28).

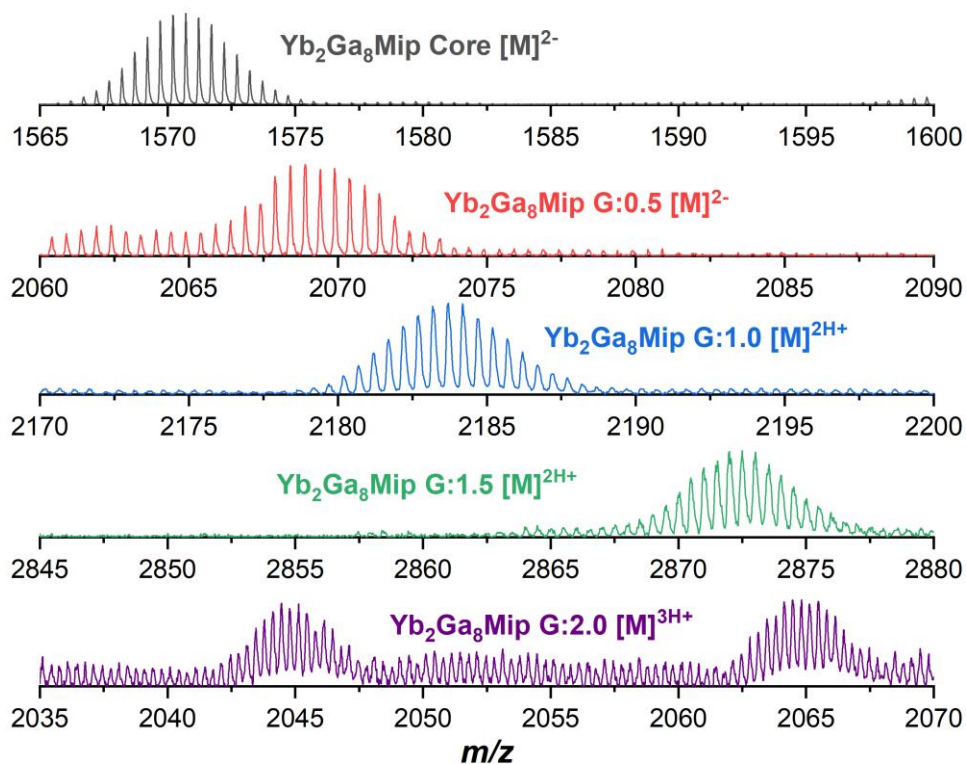


Figure 2.12. Normalized ESI-MS spectra of $\text{Yb}_2\text{Ga}_8\text{Shi}_8\text{Mip}_4$ Core and G:0.5-2.0 DMCs in methanol solutions. Core and G0.5 are -2 species, while G1-1.5 are +2 and G2 is +3 species.

Size distribution analysis of samples in DMSO using DLS confirmed increasing diameters with increasing generations, as seen on Figure 2.13. The average measured hydrodynamic diameters (D_{av}), polydispersity indexes (PDI), and diffusion coefficients (D_c) of the MC core and each DMC generation are the following: 2.19 nm (PDI: 0.20, D_c : $9.98 \times 10^{-7} \text{ cm}^2 \text{ s}^{-1}$); 2.50 nm (PDI: 0.18, D_c : $8.75 \times 10^{-7} \text{ cm}^2 \text{ s}^{-1}$); 4.00 nm (PDI: 0.34, D_c : $5.47 \times 10^{-7} \text{ cm}^2 \text{ s}^{-1}$); 4.12 nm (PDI: 0.23, D_c : $5.35 \times 10^{-7} \text{ cm}^2 \text{ s}^{-1}$); and 4.62 nm (PDI: 0.59, D_c : $4.73 \times 10^{-7} \text{ cm}^2 \text{ s}^{-1}$). The increasing diameters and decreasing D_c values confirm an increase in size, volume, and weight of each complex. Low intensity peaks to the right of the DLS graphs shows that the MC core and DMC G1.0 have a small degree of aggregation in solution, most likely due to sample concentration (5-10 mg/mL) or solvent interaction.

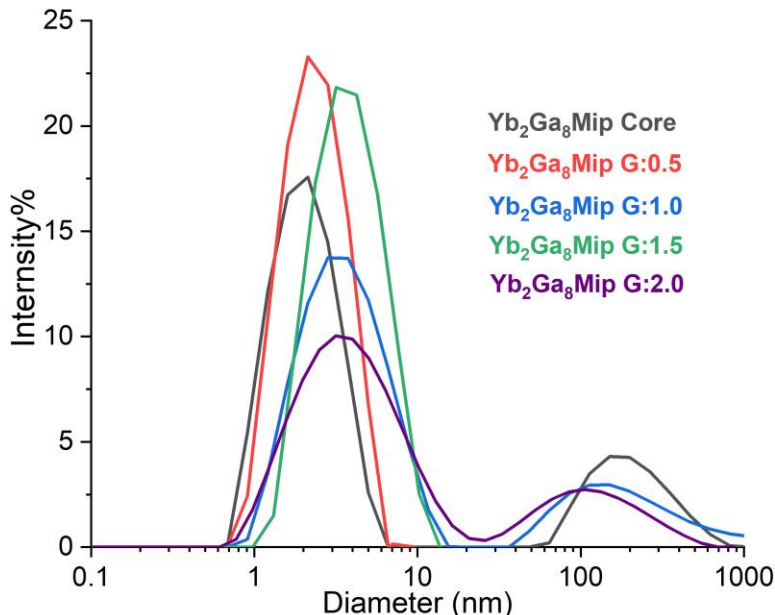


Figure 2.13 DLS size distribution of Yb₂Ga₈Shi₈Mip₄ MC core and each dendrimeric metallacrown generation (G0.5-2.0) in DMSO and at room temperature.

The solution behavior of G1.0-2.0 DMCs in more aqueous environments was also investigated through DLS. Each of the T-DMCs were diluted with water to a final solution mixture of 99:1 H₂O:DMSO (v/v%) at pH 7.5. Under such conditions, the DLS plots shown in Figure 2.14, display two sets of peaks for each DMC. The G1.0- and G1.5-DMCs each have a small D_{av} values of 8.5 and 3.1 nm, respectively, which match closely the D_{av} values in DMSO solutions. This suggest that some of the DMC in aqueous solution remain as single particles or undergo mild

aggregation. In addition to this, larger diameter aggregates with narrow polydispersities are observed for the three DMCs, with G2.0-DMC having the largest diameter aggregates. In contrast to what is observed with the DLS in DMSO, the large aggregates in aqueous solutions have higher intensities than the smaller diameter species. The D_{av} , PDI, and D_c of each DMC generation and each of its peaks are as follows: G1.0-DMC D_{av} : 8.5/278.4 nm, PDI: 0.14/0.09 and D_c : 5.65e-7/1.73e-8 cm²s⁻¹; G1.5 D_{av} : 3.1/159.6 nm, PDI: 0.02/0.04 and D_c : 1.57e-6/3.02e-8 cm²s⁻¹; and G2.0 D_{av} : 87.1/404.8 nm, PDI: 0.04/0.05 and D_c : 5.53e-8/1.19e-8 cm²s⁻¹.

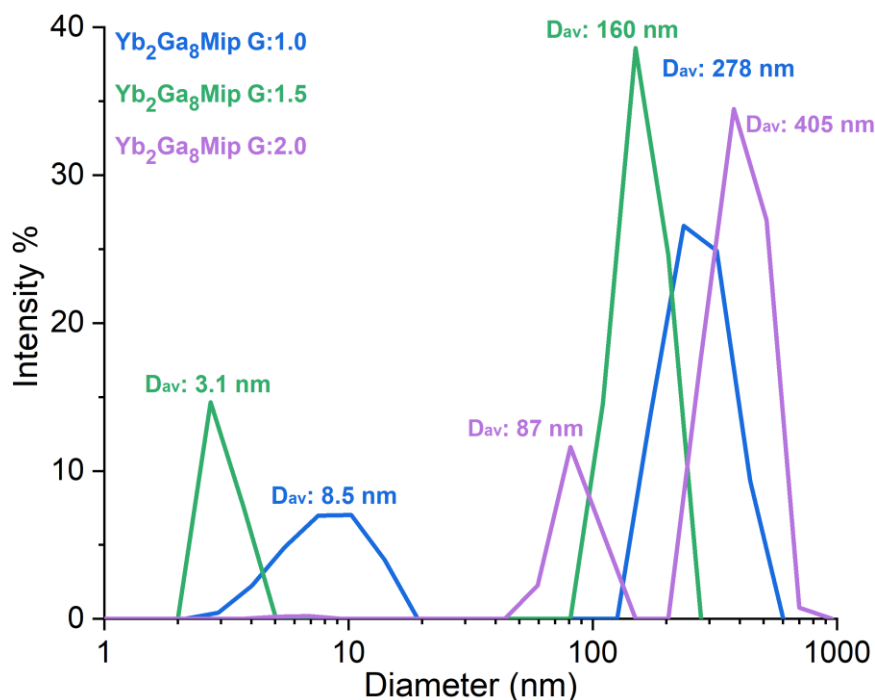


Figure 2.14 DLS size distribution of G1.0-2.0 toroidal-DMCs in 99:1 H₂O:DMSO solutions at concentrations of 30-68 μ M at room temperature and at pH: 7.5.

Sample aggregation was also observed to increase based on sample preparation for DLS analysis. Figure 2.15 shows the DLS plot of the same Yb₂Ga₈Shi₈Mip₄ G1.5 complex, but with two different diameters. Both sample A and B had the same concentration (\sim 1.5 mM) and were characterized under similar conditions, but prepared for DLS analysis differently. Sample A, with the larger average hydrodynamic diameter, was prepared by first drying the sample to completion and then redissolving it in DMSO. Sample B, with the smaller diameter, was never dried. In the timescale of sample preparation and analysis, sample A's aggregates are stable in solution and show narrower polydispersity.

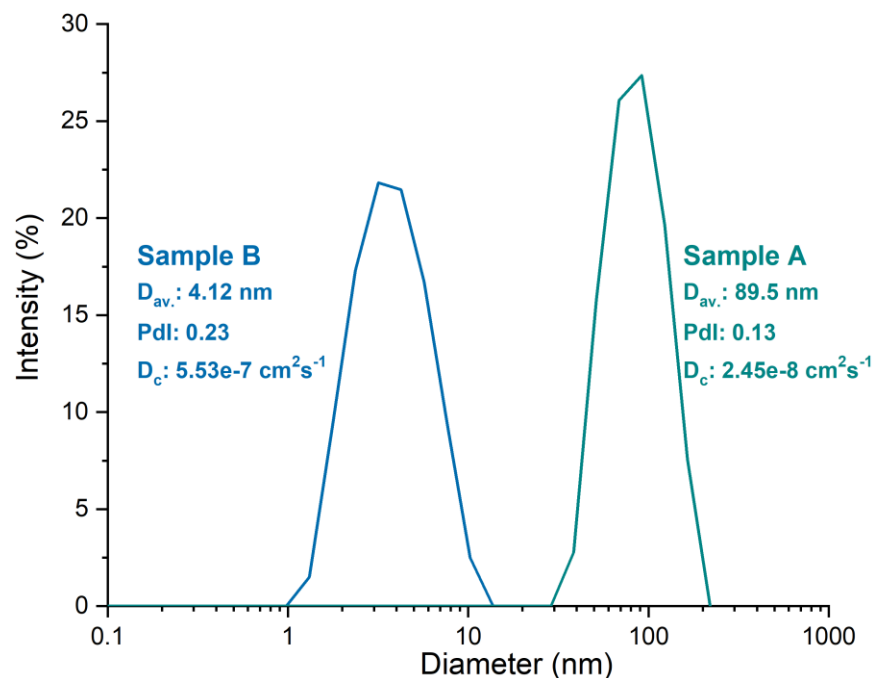


Figure 2.15 Average hydrodynamic diameter (D_{av}) difference of $\text{Yb}_2\text{Ga}_8\text{Shi}_8\text{Mip}_4$ G1.5 dendrimeric metallacrowns due to aggregation arising from different sample preparation approaches.

Solution stability of $\text{Ln}_2\text{Ga}_8\text{Shi}_8\text{Mip}_4$ dendrimeric metallacrowns. The solution stability of DMCs was investigated using ESI-MS. Mixtures of $\text{Tb}_2\text{Ga}_8\text{Shi}_8\text{Mip}_4$ (m/z : 1556.23) and $\text{Tb}_2\text{Ga}_8\text{Shi}_8\text{Mip}_4$ G0.5 (m/z : 2054.94) were dissolved in DMF/ H_2O (1:1 v/v%) and monitored daily by mass spectrometry. As seen in Figure 2.16, bridge ligand exchange was not observed for the seven days the sample was monitored. This suggests that in mixed aqueous media, the DMC is stable in solution and does not undergo ligand exchange with the MC core.

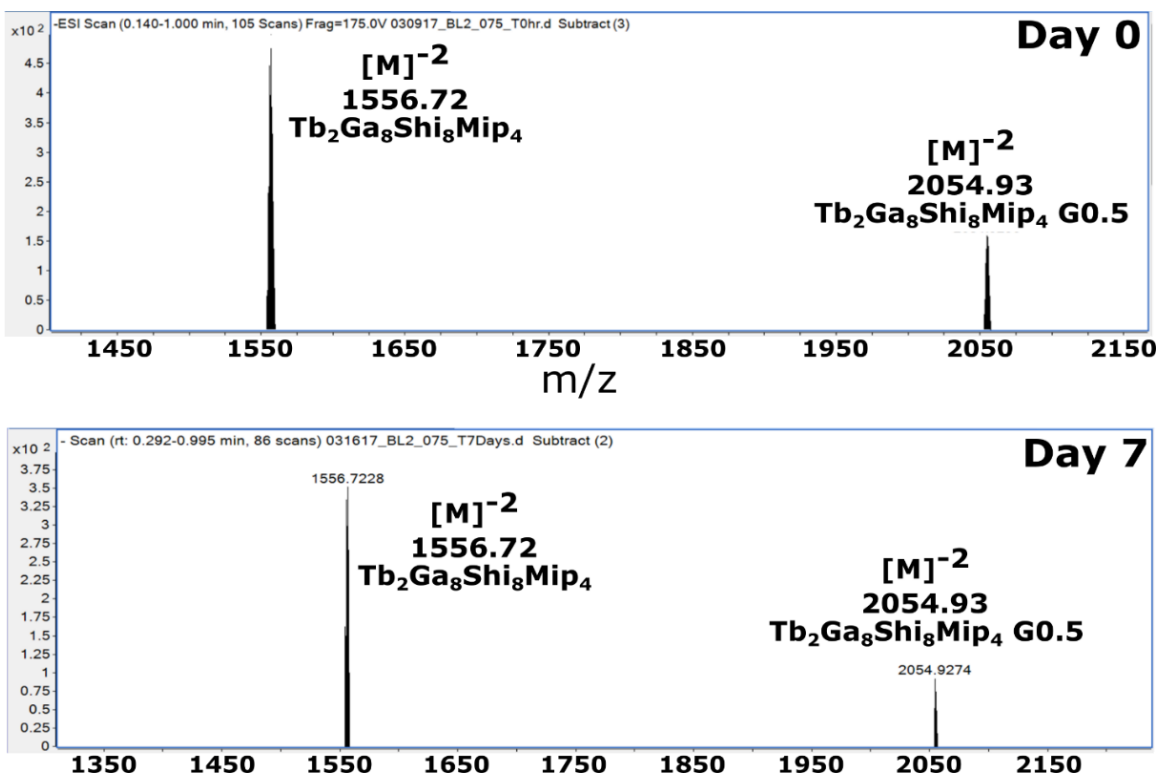


Figure 2.16 ESI-MS spectra of $\text{Tb}_2\text{Ga}_8\text{Shi}_8\text{Mip}_4$ MC and $\text{Tb}_2\text{Ga}_8\text{Shi}_8\text{Mip}_4$ G0.5 dendrimeric metallacrown in DMF/ H_2O (1:1, v/v%). Top spectrum collected immediately after mixing (Day 0), and bottom spectrum taken after seven days.

Photophysical properties of $\text{Ln}_2\text{Ga}_8\text{Shi}_8\text{Mip}_4$ G:0.5 – 2.0 DMCs (Ln : Sm^{III} , Tb^{III} , Gd^{III} , Yb^{III}). As seen in Figure 2.17, the DMSO solution of each of the four DMC generations ($\text{Yb}_2\text{Ga}_8\text{Shi}_8\text{Mip}_4$ G:0.5-2.0) exhibit a broad absorption band attributed to the $\pi \rightarrow \pi^*$ transition located in the range of 250 -350 nm, with a low-energy maximum between 317-319 nm, just like the parent $\text{Yb}_2\text{Ga}_8\text{Shi}_8\text{Mip}_4$ MC core. The energy of the ligand singlet (S^*), determined from the edge of the absorption spectra, is identical to that of the MC core alone, 349 nm (28650 cm^{-1}). As for the triplet state (T^*), it was determined as the 0-0 transition at about 447.5 nm (22350 cm^{-1}) of the $\text{Gd}_2\text{Ga}_8\text{Shi}_8\text{Mip}_4$ G:0.5 DMC phosphorescence. The Gaussian decomposition of the spectrum of for this DMC is shown in Figure 2.18. Bandwidth of the fits differ due to the complexity of the sensitizing ligand system which has several inter- and intramolecular interactions. Additionally, some distortions of the widths are also observed since the spectra are plotted against wavelength. Fits for the subsequent transitions (e.g., 0-3, 0-4, etc.) are less reliable, and therefore, have been excluded from these analyses.

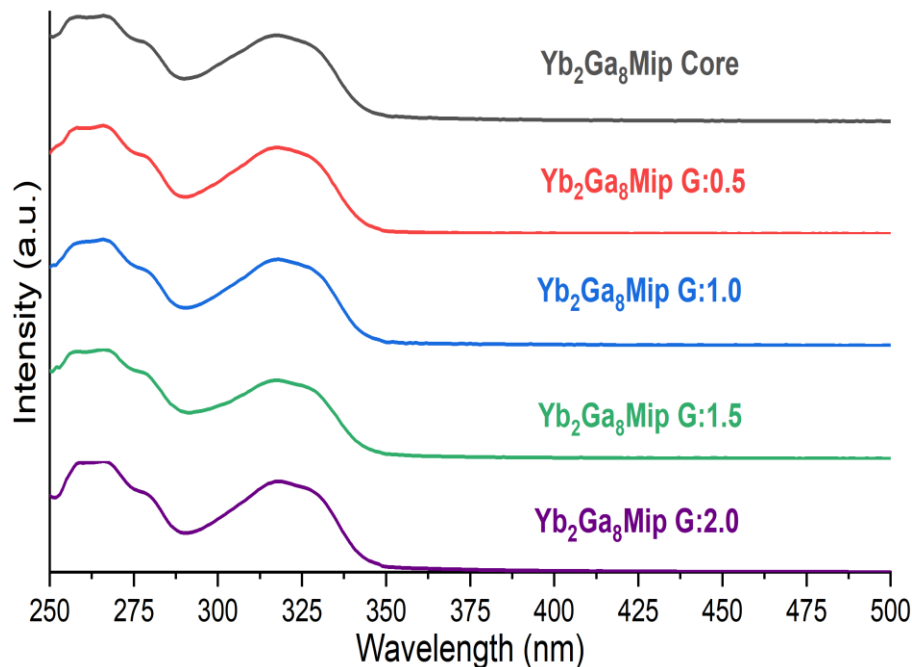


Figure 2.17 UV-Vis absorption of $\text{Yb}_2\text{Ga}_8\text{Shi}_8\text{Mip}_4$ MC and $\text{Yb}_2\text{Ga}_8\text{Shi}_8\text{Mip}_4$ G0.5-2.0 DMCs dissolved in DMSO. Solutions made of 1-20 μM at room temperature. Absorbance maxima is at 317 nm with an extinction coefficient of $4.1 \times 10^4 \text{ M}^{-1}\text{cm}^{-1}$.

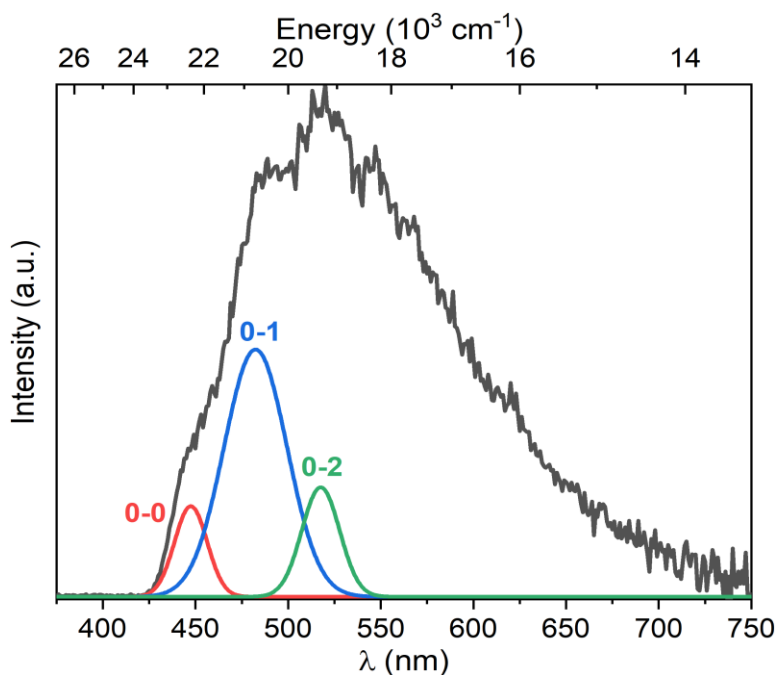


Figure 2.18 Solid state phosphorescence spectrum of $\text{Gd}_2\text{Ga}_8\text{Shi}_8\text{Mip}_4$ G0.5 DMC (black traces). 0-0, 0-1, and 0-2 transitions (colored traces) for the DMC are fitted with multiple Gaussian functions and Origin9 program. Data collected upon excitation at 300 nm, and after 100 μs time delay at 77K. Fits differ in bandwidth due to the complexity of the ligand system, with several inter- and intramolecular interactions. Some distortion of the widths is also observed since the fits are plotted against wavelength. Subsequent fits (e.g, 0-3, 0-4, etc.) are less reliable, and in general omitted from these analyses.

The excitation and emission spectra shown in Figure 2.19 of $\text{Yb}_2\text{Ga}_8\text{Shi}_8\text{Mip}_4$ G:0.5 - 2.0 DMCs were collected as DMSO solutions. Solid state measurements were not collected since sample concentration induces undesired dendritic defects – such as trailing generations, oligomers, incomplete monomer addition, missing dendrons, and cyclization. The excitation spectra collected upon monitoring the Yb^{III} emission at 980 nm show broad ligand-centered bands up to 350 nm. As for the emission spectra, upon excitation in the ligand-center region (320 nm), characteristic Yb^{III} luminescent signal was observed for all generations. Emissions are located at the range of 900-1200 nm, with a maximum at 980 nm arising from the $^2\text{F}_{5/2} \rightarrow ^2\text{F}_{7/2}$ transition. Luminescent lifetimes (τ_{obs}) and absolute quantum yields (ϕ_{Ln}^L) in DMSO were also acquired and are summarized in Table 2.2. Luminescent decay curves of $\text{Yb}_2\text{Ga}_8\text{Shi}_8\text{Mip}_4$ G:0.5-1.5 DMCs in Figure 2.20 show that all compounds are monoexponential, with τ_{obs} between 62-64 μs . Compared to the $\text{Yb}_2\text{Ga}_8\text{Shi}_8\text{Mip}_4$ core, the DMCs have τ_{obs} and ϕ_{Yb}^L values that are ~ 1.3 and ~ 2.5 - 3.4 times higher, respectively.

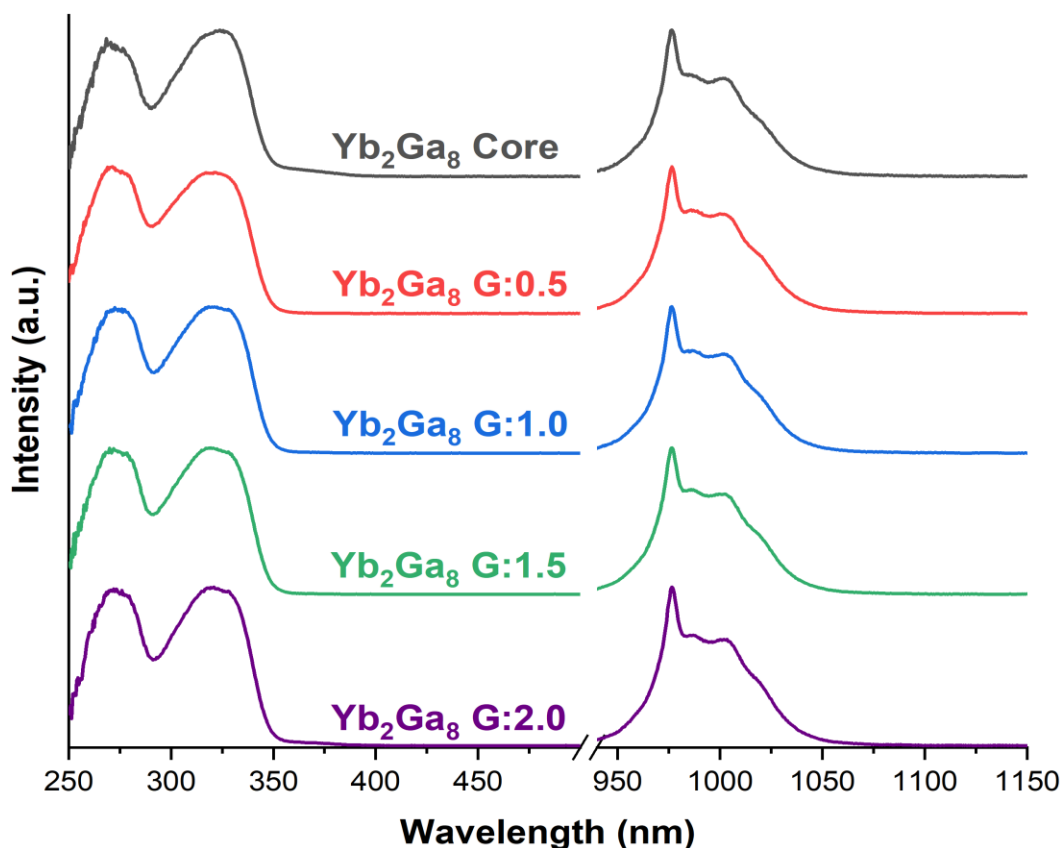


Figure 2.19 Corrected and normalized (left) excitation ($\lambda_{\text{em}} = 980$ nm), and (right) emission ($\lambda_{\text{ex}} = 320$ nm) spectra of 50 μM DMSO solution of $\text{Yb}_2\text{Ga}_8\text{Shi}_8\text{Mip}_4$ core and G:0.5 – 2.0 at room temperature.

Table 2.2 Luminescence lifetimes (τ_{obs}) and Yb^{III}-centered quantum yields collected under ligand excitation (ϕ_{Yb}^L)^a

Compound	State/Solvent	τ_{obs} [μs] ^b	ϕ_{Yb}^L [%] ^c
Yb ₂ Ga ₈ Shi ₈ Mip ₄	DMSO	48.7(6) : 84.6(5)% 6.9(2) : 15.4(5)%	2.78(6)
Yb ₂ Ga ₈ Shi ₈ Mip ₄ G0.5	DMSO	62.3(4)	7.03(1)
Yb ₂ Ga ₈ Shi ₈ Mip ₄ G1.0	DMSO	63.8(8)	9.38(2)
Yb ₂ Ga ₈ Shi ₈ Mip ₄ G1.5	DMSO	62.9(3)	9.02(8)
Yb ₂ Ga ₈ Shi ₈ Mip ₄ G2.0	DMSO	63.6(4)	8.73(8)

^a For 50 μM solutions in DMSO at room temperature and with 2σ values between parentheses. Estimated experimental errors: τ_{obs} , $\pm 2\%$; Q_{Yb}^L , $\pm 10\%$. ^b Under excitation at 355 nm. If biexponential decay was observed, population parameters $P_i = \frac{B_i\tau_i}{\sum_{i=1}^n B_i\tau_i}$ in % are given after the colon. ^c Under excitation at 320 nm.

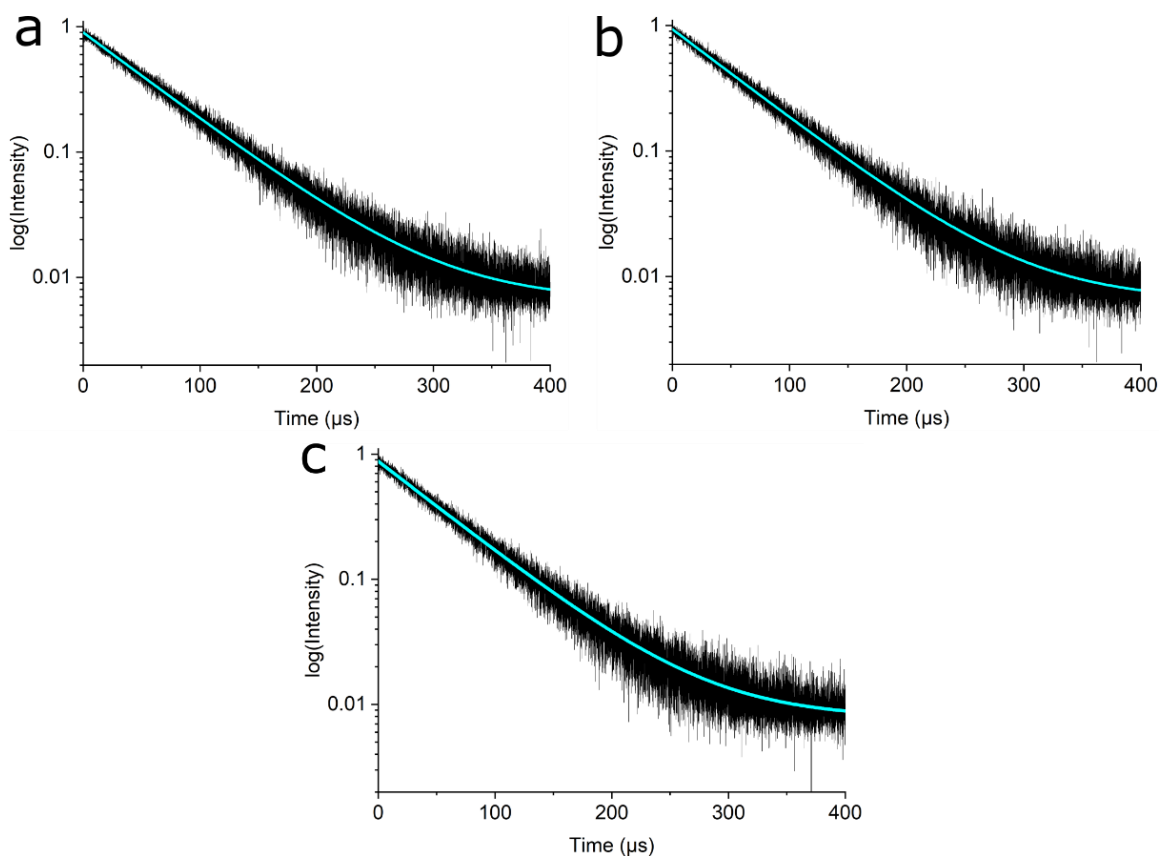


Figure 2.20 Experimental luminescent decay curves (black) and monoexponential fits (cyan) of 50 μM Yb₂Ga₈Shi₈Mip₄ DMCs G: 0.5 – 2.0 in DMSO at room temperature. Excitation at 355 nm and Yb^{III} emissions at 980 nm. a) Yb₂Ga₈Shi₈Mip₄ G0.5, b) Yb₂Ga₈Shi₈Mip₄ G1.0, and c) Yb₂Ga₈Shi₈Mip₄ G1.5. Adjusted R^2 parameters of >0.99 for all fittings.

Toroidal dendrimeric metallacrowns were also prepared with Sm^{III} and Tb^{III} ions and their luminescence was investigated. Solution and solid-state excitation and emission spectra of

Ln₂Ga₈Shi₈Mip₄ G0.5 DMCs (Ln: Sm^{III}, Tb^{III}, and Yb^{III}) are shown in Figure 2.21 and Figure 2.22. Luminescent lifetimes (τ_{obs}) and absolute quantum yields (φ_{Ln}^L) were also acquired and are summarized in Table 2.3. Excitation spectra in the solid state upon monitoring the main emission bands of the corresponding Ln^{III} ion (Tb^{III}: 545 nm, Sm^{III}: 640 nm, and Yb^{III} 980 nm) show broad ligand-centered bands up to ~375 nm. For the Sm^{III}-DMC, sharp features that correspond to the f-f transitions are observed at ~376 nm (${}^6P_{7/2} \leftarrow {}^6H_{5/2}$), ~404.5 nm (${}^6P_{3/2} \leftarrow {}^6H_{5/2}$), ~417-420 nm (${}^6P_{5/2} \leftarrow {}^6H_{5/2}$), ~442 nm (${}^4G_{9/2} \leftarrow {}^6H_{5/2}$), ~465 nm (${}^4I_{13/2} \leftarrow {}^6H_{5/2}$), ~475 nm (${}^4I_{11/2} \leftarrow {}^6H_{5/2}$), ~480 nm (${}^4I_{9/2} \leftarrow {}^6H_{5/2}$), and ~500 nm (${}^4G_{7/2} \leftarrow {}^6H_{5/2}$). Excitation spectra measured in solutions of H₂O/DMSO (96%:4%) present only broad ligand-centered bands up to 350 nm. Once again, due to saturation effects,¹⁵⁷ the solid state spectra is slightly broader than the solution state data. Upon excitation in the ligand-centered region (320-340 nm), characteristic Ln^{III} emission was observed in both solution and solid state.

For the Sm₂Ga₈Shi₈Mip₄ G0.5 DMC, solid and solution state emission in the visible range is observed between 550-725 nm arising from the ${}^4G_{5/2}$ level. The multiple sharp emission bands can be assigned to ${}^4G_{5/2} \rightarrow {}^6H_J$ ($J = 5/2-11/2$) transitions as follows: ${}^4G_{5/2} \rightarrow {}^6H_{5/2}$ at ~560 nm; ${}^4G_{5/2} \rightarrow {}^6H_{7/2}$ at ~595 nm; ${}^4G_{5/2} \rightarrow {}^6H_{9/2}$ at ~640 nm; and ${}^4G_{5/2} \rightarrow {}^6H_{11/2}$ at ~700 nm. The most intense emission band at ~595 nm is responsible for the distinctive pink-orange emission of the complex. Both the solid state τ_{obs} and φ_{Ln}^L values for Sm₂Ga₈Shi₈Mip₄ G0.5 are 1.2 and 2.1 higher than those in solution state, respectively.

For the Tb₂Ga₈Shi₈Mip₄ G0.5 DMC, solid and solution state emission in the visible range is observed between 480-685 nm and displays a vibrant green color. The multiple sharp emission bands can be assigned to ${}^5D_4 \rightarrow {}^7F_J$ ($J = 6-0$) transitions as follows: ${}^5D_4 \rightarrow {}^7F_6$ at ~490 nm; ${}^5D_4 \rightarrow {}^7F_5$ at ~540 nm; ${}^5D_4 \rightarrow {}^7F_4$ at ~580 nm; ${}^5D_4 \rightarrow {}^7F_3$ at ~620 nm; ${}^5D_4 \rightarrow {}^7F_2$ at ~650 nm; ${}^5D_4 \rightarrow {}^7F_1$ at ~660 nm; and ${}^5D_4 \rightarrow {}^7F_0$ at ~490 nm. Experimental luminescent decays of this complex in solution and solid state are best fitted with biexponential functions, with dominating contributions arising from the long-lived components (980 and 1090 μs , respectively). Both the τ_{obs} and φ_{Ln}^L values for Tb₂Ga₈Shi₈Mip₄ G0.5 in the solid state are 1.1 and 2.0 times higher than those in the solution state, respectively.

The luminescent description of Yb₂Ga₈Shi₈Mip₄ G0.5 DMC in H₂O/DMSO and solid state are similar to those previously described in just DMSO. As for the τ_{obs} and φ_{Ln}^L , values in the solid state are 2.7 and 3.7 higher than those in the solution state, respectively.

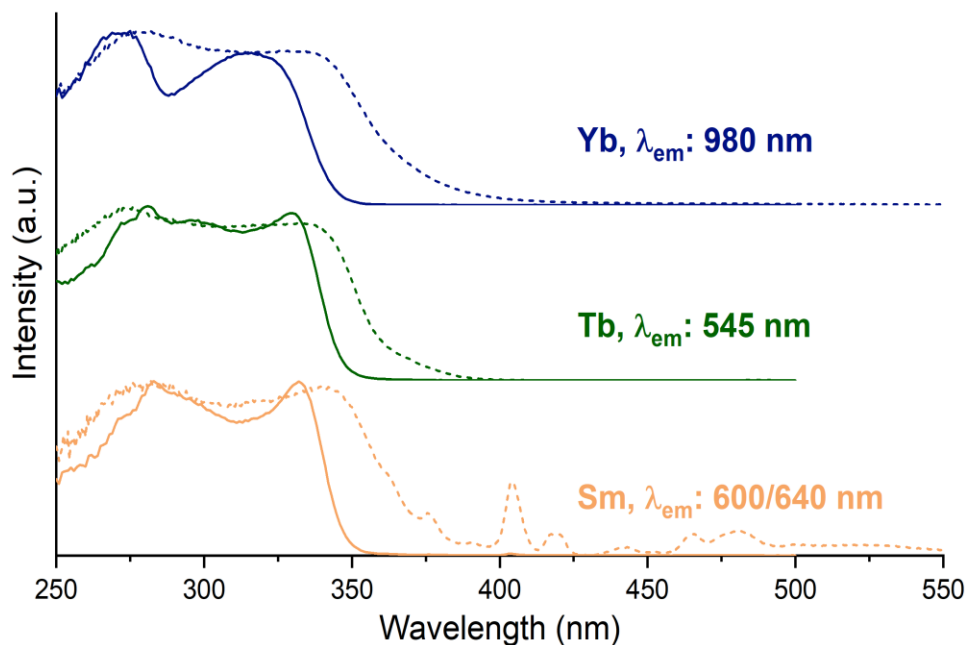


Figure 2.21. Corrected and normalized excitation spectra of G0.5 DMCs in the solid state (dashed traces) and in 200 μM $\text{H}_2\text{O}/\text{DMSO}$ (96%/4%) solutions (solid traces) upon monitoring the main transitions Ln^{III} ion at room temperature.

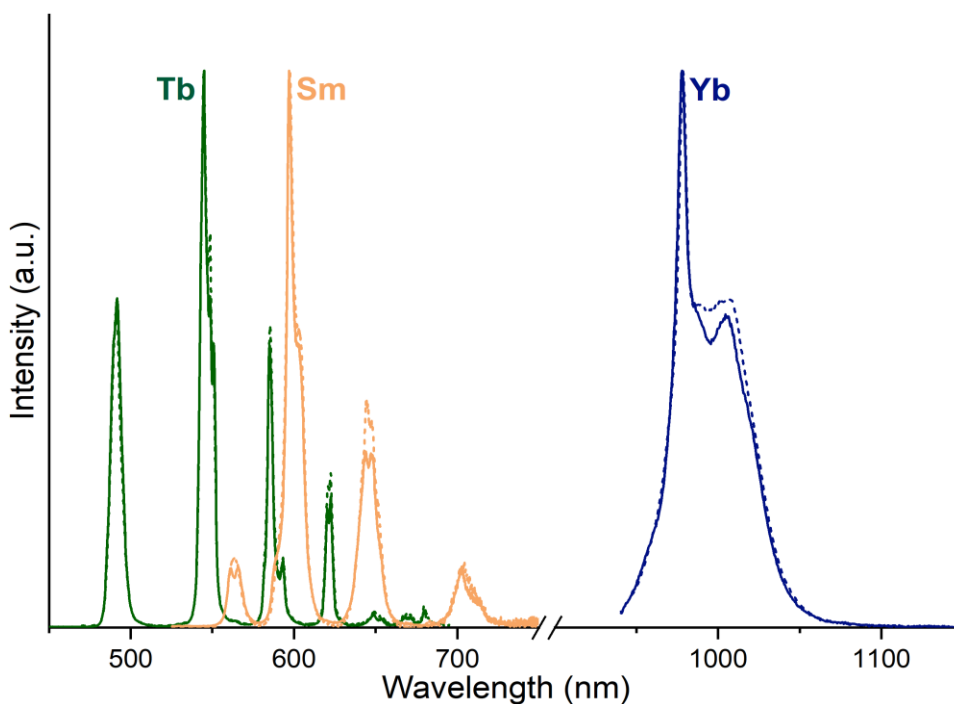


Figure 2.22. Corrected and normalized emission spectra of G0.5 DMCs in the solid state (dashed traces) and in 200 μM $\text{H}_2\text{O}/\text{DMSO}$ (96%/4%) solutions (solid traces) under ligand excitation (320-340 nm) at room temperature.

Table 2.3. Luminescence lifetimes (τ_{obs}) and Ln^{III}-centered quantum yields collected under ligand excitation (φ_{Ln}^L)^a

Compound	State/Solvent	τ_{obs} [μs] ^b	φ_{Ln}^L [%] ^c
Yb ₂ Ga ₈ Shi ₈ Mip ₄ G0.5	Solid	35.3(6)	3.24(9)
	H ₂ O/DMSO (96%/4)	13.2(1)	0.868(9)
Tb ₂ Ga ₈ Shi ₈ Mip ₄ G0.5	Solid	1090(12) : 88(1)% 258(6) : 12(1)%	11.9(3)
	H ₂ O/DMSO (96%/4)	980(30) : 89.7(8)% 170(10) : 10.3(8)%	6.1(3)
Sm ₂ Ga ₈ Shi ₈ Mip ₄ G0.5	Solid	112(1)	2.31(2)
	H ₂ O/DMSO (96%/4)	96.2(9)	1.1(1)

^a For samples in the solid state or 1 mg/mL in H₂O/DMSO, at room temperature, 2 σ values between parentheses. Estimated experimental errors: τ_{obs} , $\pm 2\%$; Q_{Yb}^L , $\pm 10\%$. ^b Under excitation at 355 nm. If biexponential decay was observed, population parameters $P_i = \frac{B_i \tau_i}{\sum_{i=1}^n B_i \tau_i}$ in % are given after the colon. ^c Under excitation at 340 nm for samples in the solid state and 320 nm for solutions.

2.3.4 Cell studies

Yb₂Ga₈Shi₈Mip₄ G0.5 - 1.5 DMC were used to investigate their ability to label cells. To this end, HeLa cells were incubated with 100 μM solutions of each DMC dissolved in water/DMSO (99:1%, v/v%) or saline/DMSO (99:1%, v/v%) mixtures. Epifluorescence microscopy images of the cells exhibit strong Yb^{III} luminescent signal arising from the core of each DMC; however, as seen in Figure 2.23, G0.5 and G1.5 DMC images show significant aggregation and localization mostly at the surfaces of the cells – with some substrate interaction when incubated with G0.5 DMC. As for G1.0 DMC, non-specific interaction with cell membranes can be seen as an intense luminescent signal at the edges of the cells. Additional labeling can be also observed at the nucleoli of several cells, as seen in Figure 2.24.

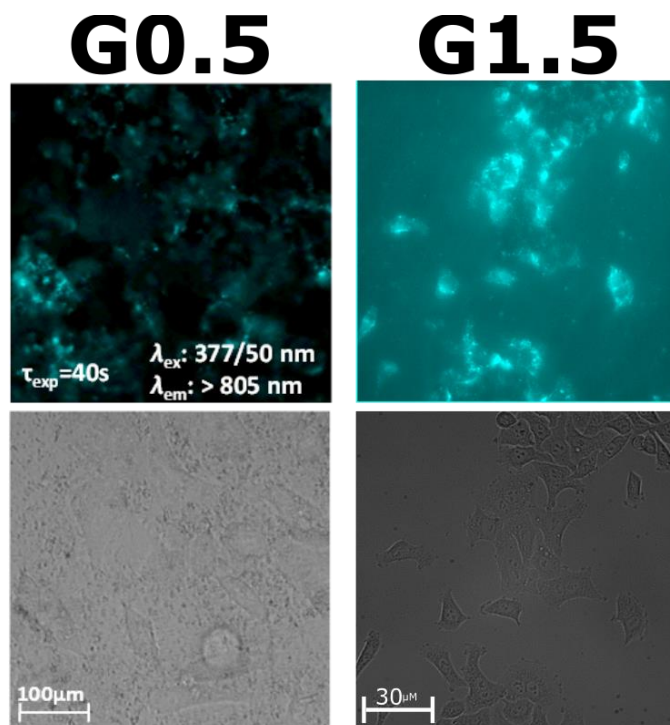


Figure 2.23. Microscopy images of HeLa cells incubated with 100 μM of $\text{Yb}_2\text{Ga}_8\text{Shi}_8\text{Mip}_4$ G0.5 and G1.5 DMCs in aqueous solutions with 1% DMSO. (Top) Yb^{III} NIR epifluorescence image for G0.5 (λ_{ex} : 377 nm, band pass 50 nm; λ_{em} : 805 nm, long pass; 40 s of exposure) and G1.5 (λ_{ex} : 377 nm, band pass 50 nm; λ_{em} : 805 nm, long pass; 10s of exposure).

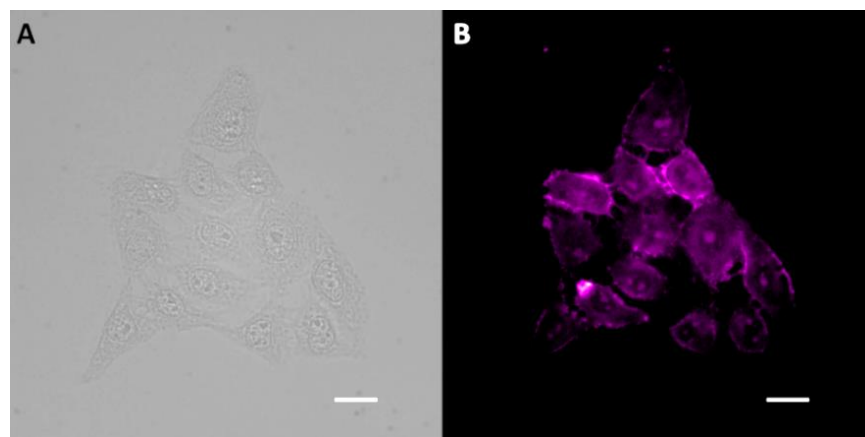


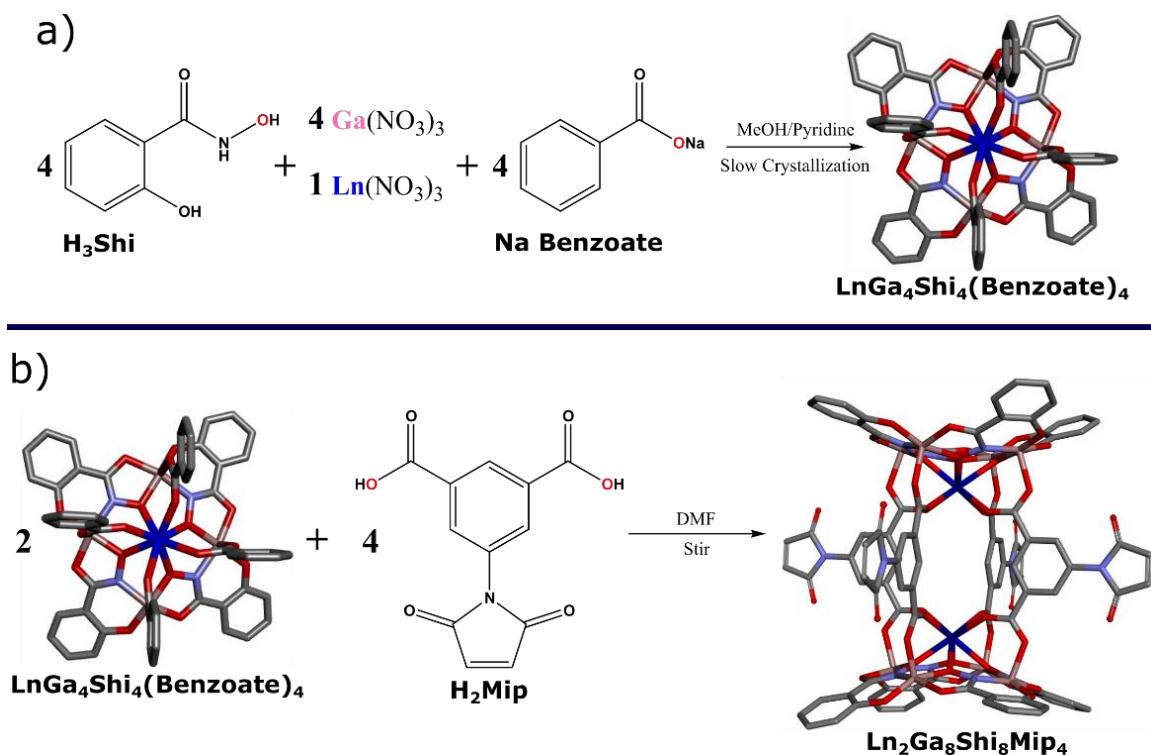
Figure 2.24. Microscopy images of HeLa cells incubated with 100 μM of $\text{Yb}_2\text{Ga}_8\text{Shi}_8\text{Mip}_4$ G1.0 DMC in saline solution with 1% DMSO. A) Brightfield image, and B) NIR epifluorescence image (λ_{ex} = 377nm, band pass 50nm; λ_{em} = 785nm, long pass; 2s of exposure). Objective 40 \times . Scale bar = 20 μm .

2.4 Discussion

2.4.1 Synthesis, Characterization, and Small Molecule Functionalization of $\text{Ln}_2\text{Ga}_8\text{Shi}_8\text{Mip}_4$ Metallocrowns

The $\text{Ln}_2\text{Ga}_8\text{Shi}_8\text{Mip}_4$ scaffold represents the first MC with coupling sites at the bridging ligands. The maleimide appendage was chosen as the coupling group for this scaffold due to its ease of synthesis, and high reactivity towards thiol-coupling under mild conditions. The reaction between maleimide and thiols is driven by the withdrawing effects of its two carbonyl groups, along with the enhanced reactivity of the alkene site due to ring strain.¹⁵⁸ Unlike previously reported Ln_xGa_y (x : 1 or 2; y : 4 or 8) MCs,^{102,106,119} this scaffold was not prepared by slow crystallization, but rather by carboxylate substitution on the $\text{LnGa}_4\text{Shi}_4(\text{benzoate})_4$ with 5-maleimide isophthalic acid. This approach was adopted due to the maleimide group's sensitivity to alkaline reaction conditions. Under basic conditions, the maleimide ring can be hydrolyzed resulting in the opening of the ring and a significant decrease of its thiol-coupling reactivity. Therefore, since Ln_xGa_y MC synthesis requires addition of bases, such as NaOH or NH_4HCO_3 , a different synthetic methodology was adopted for the preparation of $\text{Ln}_2\text{Ga}_8\text{Shi}_8\text{Mip}_4$ scaffolds. Taking advantage of the difference in pKa between benzoic acid (~4.20) and isophthalic acid derivative (~3.46, ~4.46), the four benzoate bridging ligands of the monomeric $\text{LnGa}_4\text{Shi}_4(\text{benzoate})_4$ can be replaced by four 5-maleimide isophthalate ligands, yielding the dimeric $\text{Ln}_2\text{Ga}_8\text{Shi}_8\text{Mip}_4$ MC, as shown in Scheme 2.1

Since $\text{Ln}_2\text{Ga}_8\text{Shi}_8\text{Mip}_4$ was not isolated as a crystalline material, crystallographic data was not collected. However, the structural morphology is expected to be analogous to the $\text{Ln}_2\text{Ga}_8\text{Shi}_8\text{Ip}_4$ MC¹⁰⁶ where the two $\text{LnGa}_4\text{Shi}_4$ subunits are crystallographically inequivalent, but virtually similar. Furthermore, they are structurally similar to the monomeric $\text{LnGa}_4\text{Shi}_4(\text{benzoate})_4$. Each of the 12-MC_{Ga(III)N(shi)-4} scaffolds have a slightly concave ring morphology, and contains four d¹⁰ Ga^{III} metal ions linked together by four Shi³⁻ ring ligands. Each of the Ln^{III} ions are located at the center of each of the two 12-MC_{Ga(III)N(shi)-4} scaffolds, and are bridge together by four Mip²⁻ ligands. The Ln^{III} ions are eight-coordinate, where the four oxime oxygens from the MC and the four carboxylate oxygens from the bridging ligands complete the coordination sphere of each Ln^{III}.



Scheme 2.1. a) Synthesis of $\text{LnGa}_4\text{Shi}_4(\text{benzoate})_4$ from free ligands and metal salts via slow crystallization. b) Synthesis of $\text{Ln}_2\text{Ga}_8\text{Shi}_8\text{Mip}_4$ by carboxylate substitution of benzoate with H_2Mip on the monomeric MC.

Due to the lack of crystallography data, the chemical composition of $\text{Ln}_2\text{Ga}_8\text{Shi}_8\text{Mip}_4$ was corroborated by ESI-MS and ^1H NMR, as shown in Figure 2.2 and Figure 2.3. With both techniques, the exclusive presence of the dimeric MC scaffold was observed, thus confirming the composition and purity of the compound. Looking at the isotopic distribution of the MC's mass spectrum, the overall charge of the complex was confirmed to be -2 – just as expected based on the crystallographic composition of the $\text{Ln}_2\text{Ga}_8\text{Shi}_8\text{Ip}_4$ scaffold. Charge neutrality, however, is likely achieved with pyridinium counter ions. This can be expected since charge neutrality of the precursor $\text{LnGa}_4\text{Shi}_4(\text{benzoate})_4$ is maintained with a single pyridinium ion, as confirmed by crystallographic data. But potentially more convincing is the fact that in the ^1H NMR spectrum of $\text{Y}_2\text{Ga}_8\text{Shi}_8\text{Mip}_4$, pyridine peaks can be seen with higher ppm values (δ : 8.75, 8.19, 7.70) from the expected ones (δ : 8.58, 7.76, 7.35) in d_6 -DMSO. The NMR also further confirms the presence of a 2:1 ratio of Shi:Mip ligands, as expected for the $\text{Ln}_2\text{Ga}_8\text{Shi}_8\text{Mip}_4$ scaffold. Peak splitting of the bridging ligand protons (labeled 13,17, and 15 on Figure 2.3) arises from the non-equivalence between the two $12\text{-MC}_{\text{Ga(III)N}(\text{shi})-4}$ scaffolds in the dimeric MC. This has also been observed in previously reported analogous Ln_2Ga_8 complexes.^{106,122,124}

As for the MC behavior in solution, the scaffold is fully soluble in polar aprotic solvents such as DMSO and DMF, but insoluble in water. The solution stability in organic solvents was investigated by mixing together equimolar solutions of $Y_2Ga_8Shi_8Mip_4$ and $Y_2Ga_8Shi_8Ip_4$ solely dissolved in DMF. The mixture was monitored by ESI-MS daily over a period of five days. As seen in Figure 2.4, no bridge exchange events are observed, and each of the MC mass spectrum signals are seen as discrete species; thus, confirming that under such conditions both MC scaffolds are stable in solution. However, when the same experiment was done under more aqueous conditions (DMF/H₂O 1:1, v/v%), bridge ligand exchange between $Y_2Ga_8Shi_8Mip_4$ and $Y_2Ga_8Shi_8Ip_4$ occurs rapidly. As shown in Figure 2.5, exchange events are seen as low intensity signals of a single bridge ligand exchange between both compounds immediately after mixing. The entire spectrum of ligand exchange events (3:1, 2:2, 1:3; Mip:Ip) is seen just after one day. Therefore, making the solution mixture more aqueous decreases the unsubstituted $Y_2Ga_8Shi_8Ip_4$ and unfactionalized $Y_2Ga_8Shi_8Mip_4$ MCs' solution stability by catalyzing bridge ligand exchange events. It is important to highlight that other MC scaffolds, such as $LnZn_{16p}YzHA_{16}$ is stable in both organic and aqueous environments. Thus, it seems that the aqueous instability of $Y_2Ga_8Shi_8Ip_4$ and unfactionalized $Y_2Ga_8Shi_8Mip_4$ MCs arise from their structural morphology. Furthermore, as detailed in later sections, aqueous instability of the $Y_2Ga_8Shi_8Mip_4$ MC is deterred once functionalized with dendrons.

The solution ligand-centered optical properties of $Ln_2Ga_8Shi_8Mip_4$ in DMSO demonstrated that the scaffold has an absorbance between 250-350 nm, with a low energy maximum at ~317 nm. The MC's singlet state (S^* : 28650 cm⁻¹) and triplet state (T^* : 23280 cm⁻¹) have a favorable energy difference (5370 cm⁻¹) that ensures good ligand intersystem crossing ($S^* \rightarrow T^*$). This is of great importance for Ln^{III} ion sensitization since the T^* state of the antenna is regarded as the main feeding level to the metal ion emissive state.¹³¹ Regarding the T^* calculation for $Ln_2Ga_8Shi_8Mip_8$, its energy position was determined using the Gd^{III}-based scaffold since that Ln^{III} has an accepting energy level located at 32000 cm⁻¹. Such energy level is too high to be populated by the T^* , thus the phosphorescent emission upon excitation at the ligand-centered region is determined to be the T^* state of the MC.¹⁵⁹ The T^* value of $Gd_2Ga_8Shi_8Mip_8$ was found to be close to values of previously reported Ln_xGa_y (x: 1 or 2; y: 4 or 8) MCs: $GdGa_4Shi_4(benzoate)_4$ with 22170 cm⁻¹;¹⁰² $GdGa_4Shi_8(OH)_4$ with 22620 cm⁻¹;¹¹⁹ and $Gd_2Ga_8Shi_8Ip_4$ with 21980 cm⁻¹.¹⁰⁶

As for the Ln^{III}-centered photophysical properties, the good spectral overlap between the absorbance and excitation spectra of the Yb₂Ga₈Shi₈Mip₄ scaffold, seen in Figure 2.6 and Figure 2.8, further demonstrates the favorable antenna effect of the MC scaffold to the Ln^{III} ions. Additionally, the T* state is located at a higher energy level than the main emissive state of all luminescent Ln^{III} ions. However, significant back transfer should be expected for Ln^{III} ions with emissive states too close to the T* level, such as Tb^{III} (20400 cm⁻¹), Dy^{III} (21100 cm⁻¹), and Tm^{III} (21350 cm⁻¹). Other electronic events, such as ligand-to-metal charge transfer (LMCT), can also impede Ln^{III} ion sensitization, just as with the LnGa₄ and Ln₂Ga₈ scaffolds where many, but not all, Ln^{III} ions can be sensitized by these MCs.

Upon excitation into the ligand-centered bands at 320-340 nm of Yb₂Ga₈Shi₈Mip₄, characteristic Yb^{III} luminescence emission in the NIR is observed in both solution and solid state, as seen in Figure 2.8. Quantitative photophysical data listed in Table 2.1, show that τ_{obs} and ϕ_{Yb}^L in the solid state of Yb₂Ga₈Shi₈Mip₄ are significantly lower compared to the previously reported Yb^{III}-based MCs of the Ga-family. The large drop in both values in the solid state can be attributed to two effects: *i*) the presence of the pyridinium counter ions (with N-H oscillators); and, *ii*) the quenching behavior of maleimide. In the former, the vibronic oscillator of pyridinium counter ions can be in close enough proximity when in solid state to quench the luminescence of Yb^{III}. This is corroborated by the fact that in DMSO (an aprotic solvent) solutions, τ_{obs} and ϕ_{Yb}^L values increase likely due to the dissociation/solvation of the pyridinium ions. For the latter, unsubstituted maleimide groups are known to be efficient quenchers of luminescent emission.^{160,161} Quenching arises from direct conjugation of maleimide groups to fluorophores due to the low lying n \rightarrow π^* transition of the ring, and through photoinduced electron transfer (PET) to the C=C bond. Thus, the presence of such LMCT states provide a favorable environment for non-radiative decay and are responsible for the pale orange to yellow color of the compound. Lastly, the biexponential nature of the scaffold's τ_{obs} is also due such quenching effects. Fortunately, the quenching effects of maleimide rings are improved once the C=C bonds becomes saturated – e.g., by thiol coupling.

The Michael addition of cysteamine was carried out onto the four maleimide appendages of Sm₂Ga₈Shi₈Mip₄ by simply reacting a small excess of cysteamine (9 eq) to the MC (1 eq) dissolved in DMF. Complete coupling of four cysteamine per MC was corroborated by ESI-MS as seen in Figure 2.10. The luminescent characterization of Sm₂Ga₈Shi₈Mip₄ and Sm₂Ga₈Shi₈Mip₄(Cys)₄ (pre- and post-functionalization, respectively) demonstrated that Sm^{III}

emission is sensitized in both scenarios. The solution state absorbance and excitation spectra of $\text{Sm}_2\text{Ga}_8\text{Shi}_8\text{Mip}_4$ and $\text{Sm}_2\text{Ga}_8\text{Shi}_8\text{Mip}_4(\text{Cys})_4$ are identical and have a low energy maximum at ~ 311 nm in methanol. The same is observed for the emission spectra, where the f-f transition remain identical in both complexes. Thus, these results demonstrate the efficient and simple thiol coupling of small molecules onto MCs, and, even more importantly, that Ln^{III} sensitization is still observed after coupling.

An important structural aspect of $\text{Ln}_2\text{Ga}_8\text{Shi}_8\text{Mip}_4$ scaffolds is the fact that the thiol-Michael addition to each of the four maleimide appendages can happen at either of two carbon positions in the maleimide's C=C bond. Thus, resulting in the possibility of forming two different isomers per appendage. In the case of a $\text{Ln}_2\text{Ga}_8\text{Shi}_8\text{Mip}_4$ MC, the four maleimide appendages each can have four possible configurations. As seen in Figure 2.25, each maleimide group has the potential to have two different isomers (A and B), each with a 180° of rotational freedom. The presence of several potential isomers could influence the overall chirality of the complex, which could also have an influence on the behavior as an imaging agent – e.g., cell uptake or polarized luminescence. Furthermore, the presence of multiple isomers can also have an influence on the measured polydispersity of the complex by DLS. While having multiple chiral centers in a single molecule results in an ensemble of diastereomers, each potentially possessing different physical properties, at this point there is no method for separating these distinct complexes. Therefore, for the remainder of this thesis each generation of DMCs is largely treated as if it corresponds to a single isomer; however, the reader should be aware of this added complexity.

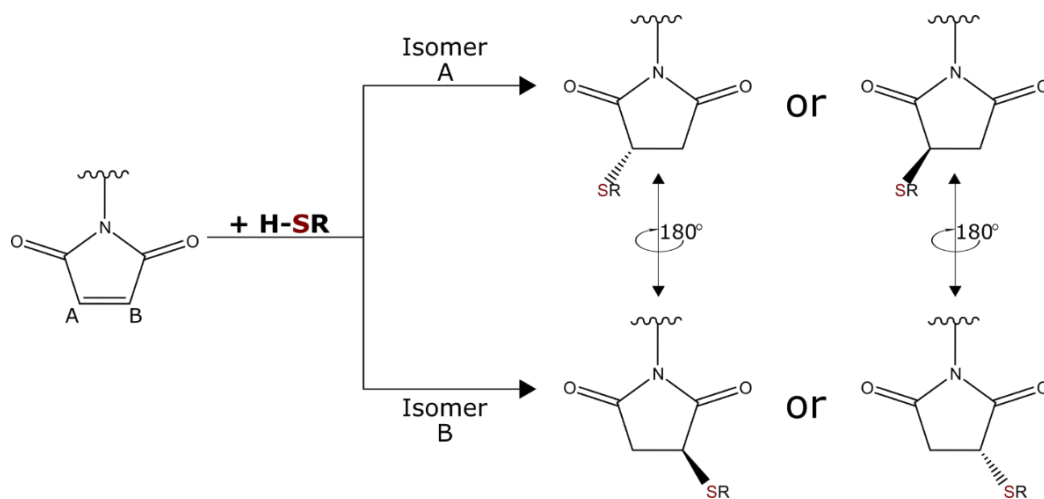
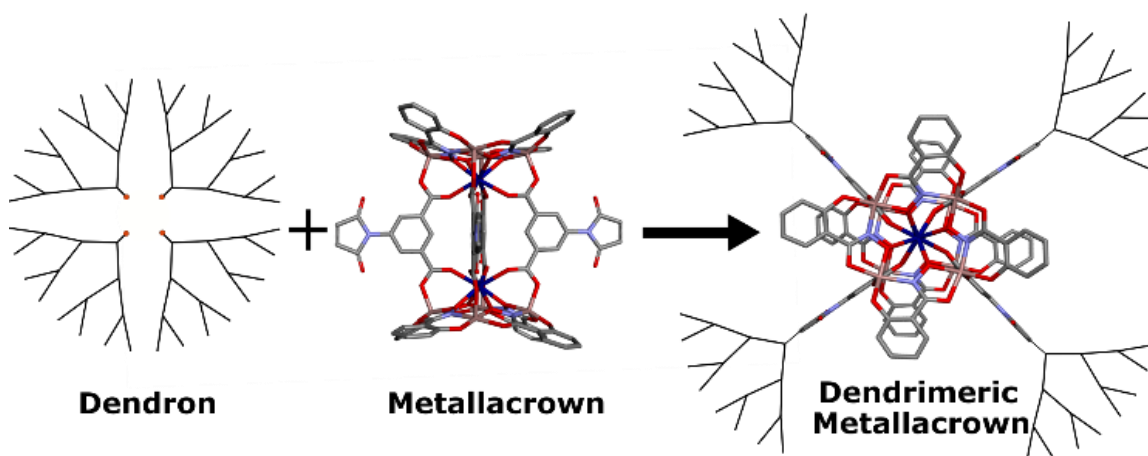


Figure 2.25 Possible set of isomer for a single thiol-Michale addition to a maleimide group. Thiol coupling can yield two sets of isomer, and each isomer has a 180° of rotational freedom.

2.4.2 Toroidal Dendrimeric Metallacrowns

After corroborating that luminescent sensitization is still possible with functionalized MCs, the next step was to exploit such functionalization potential to expand the application of luminescent MC into the field of dendrimers. To this end, $\text{Yb}_2\text{Ga}_8\text{Shi}_8\text{Mip}_4$ MCs were used as the core of PAMAM dendrimers, as shown in Scheme 2.2, in order to develop a new class of Ln^{III} ion luminescent metallodendrimers.

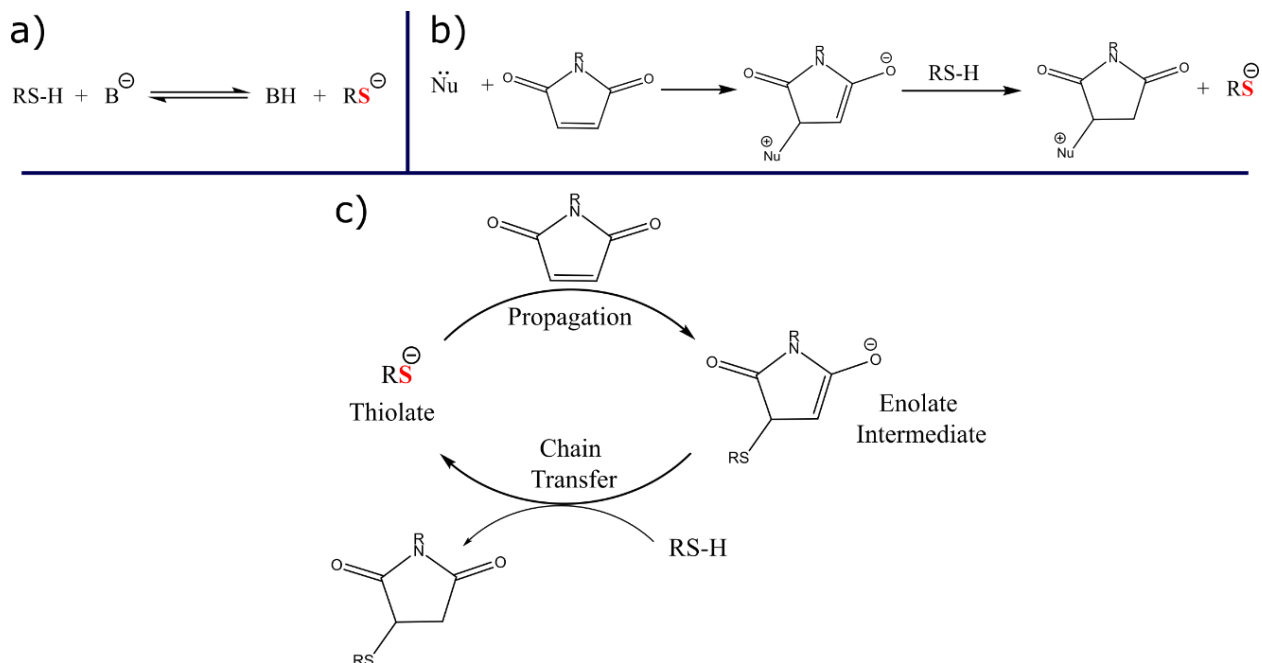


Scheme 2.2. Simplified representation of dendrimeric metallacrown preparation. Left, thiol-focal point dendron. Middle, model of $\text{Ln}^{\text{III}}_2[12\text{-MC}_{\text{Ga}(\text{III})\text{N}(\text{shi})\text{-}4}]_2(\text{Mip})_4$ MC. Right, top view of toroidal dendrimeric metallacrowns.

To start, thiol-focal point PAMAM dendrons of four generations (G:0.5-2.0) were prepared with modified standard procedures.¹⁶² Briefly, dendron synthesis began with thiol trityl protection of cysteamine, followed by sequential reaction with methyl acrylate and ethylenediamine in methanol. Once the desired generation was achieved, deprotection was done under acidic conditions to yield free thiol focal point dendrons to couple readily to $\text{Yb}_2\text{Ga}_8\text{Shi}_8\text{Mip}_4$ MCs. The trityl protection and deprotection for PAMAM dendron synthesis is a relatively uncommon synthetic approach. So far only two papers published by Wängler et al.^{163,164} have used such an approach, but instead of cysteamine used as the thiol source, they used long polyethylene glycol (PEG) linkers with a thiol-focal point. The synthetic methodology described in this chapter was developed independently of Wängler et al.'s work, and follows more of a peptide protecting and deprotecting approach. More commonly, disulfide compounds, such as cystamine ($\text{H}_2\text{NCH}_2\text{CH}_2\text{S-SCH}_2\text{CH}_2\text{NH}_2$),^{165,166} are employed for the dendron synthesis. This synthetic approach requires the reduction of the disulfide bond with reducing agents such as dithiothreitol (DTT) or tris(2-

carboxyethyl)phosphine) (TCEP) to yield free thiol-focal point dendrons. However, for the synthesis of DMCs, this approach was not suitable. This is because both DTT and TCEP have been shown to interfere with thiol-maleimide coupling.^{167,168} Thus, in order to avoid complicated oxygen free purification methods (as to avoid the re-oxidation of the free thiol dendron) to remove DTT and TCEP, the trityl protection-and-deprotection approach was used instead.

DMCs were then prepared by reacting an excess of freshly deprotected thiol-focal point dendrons with $\text{Yb}_2\text{Ga}_8\text{Shi}_8\text{Mip}_4$ under mildly basic conditions and an inert atmosphere. The addition of 4-dimethylaminopyridine (DMAP) as base to the reaction solution was to ensure the formation of thiolate ions of dendrons to start the catalytic cycle of Michael addition.¹⁵⁸ The maleimide coupling mechanism has largely been explained as first needing the formation of some thiolate anion that then further deprotonates other thiols. As seen in Scheme 2.3, two methods to form the initial enolate are widely accepted: base-initiated and nucleophile-initiated. Since DMAP is nucleophilic base, either mechanism can play a role. Addition of DMAP was not required when the MC was only coupled to cysteamine. This is most likely since the thiolate formed from the amine site deprotonating the thiol site in cysteamine.



Scheme 2.3. (Top) Formation of thiolate anion from a) acid-base equilibrium reaction, and b) nucleophile-initiated pathway. (Bottom) Accepted Michael addition of thiolates to maleimides by catalytic formation of thiolate.

Reaction length between dendrons and the MC increased with increasing dendron generation, requiring 7-10 days for complete coupling with the largest dendron (G2.0). Purification of G1.0 - 2.0 DMCs was done by dialysis against DMSO for over a week. Dialysate and dialysis bags were changed every 24 hours, and removal of excess uncoupled dendron was monitored by ESI-MS daily. The samples were deemed pure once the free dendron peak was no longer visible by mass spectrometry. However, it is important to remember that dendrimer defects (e.g. incomplete monomer addition, missing dendrons, and cyclization) are not removed by this method, since their removal is almost impossible due to the structural similarities between perfect and imperfect dendrons.^{3,4,6} Thus, “pure product” is defined as a fully coupled MC center with four dendrons, and with no left over unreactive material -such as Ln₂Ga₈Shi₈Mip₄ MC or unreacted dendrons. Purification of G0.5 DMC only required solvent concentration, followed by rinsing with copious amounts of water due to the significantly lower water solubility of this DMC compared to the other generations.

As seen in Figure 2.12 characterization by ESI-MS corroborated complete coupling of four dendrons to the MC core, and the lack of unreacted MC. The increasing molecular weight of DMC with increasing generation was corroborated by ESI-MS seen as increasing *m/z* values. Interestingly, as the number of internal amide and amine groups increased with each generation, protonation of the compounds was more easily achieved; thus, DMC of G1.0-2.0 were better detected by the mass spectrometer in positive mode, and with multiple protonation states – unlike the MC core and G0.5 DMC which were only visible in negative ion mode, as a -2 species.

Analysis by DLS also confirmed increasing size of the DMC since the approximated hydrodynamic diameters increased with increasing generation. Compared to standard PAMAM dendrimers, DMC are shown to be more polydisperse. The four DMCs (G0.5-2.0) had polydispersity index (PDI) values ranging from 0.18-0.59, while regular PAMAM dendrimers tend to have narrow polydispersities of 0.0 – 0.1 by DLS (or 1.0-1.1 by GPC). Since polydispersity is a measure of homogeneity of compounds in solution, the greater the PDI, the more heterogeneous the sample (i.e., more variation in particle size). However, while by DLS standards these DMCs have moderate polydispersity, this is not necessarily a reflection of heterogeneity – which could be interpreted as samples with varying particle size due to incomplete dendron coupling to the MC core, or as high degrees of aggregation. This is because the DLS instrument calculates a PDI and average hydrodynamic diameter from the measured diffusion coefficient with the assumption that

particles in solution are perfect spheres. In other words, the DLS delivers diameters of spheres that diffuse the same way as the DMC particles. Thus, since the toroidal DMCs are not spherical and depending on the angle of diffusion measure by the instrument, the calculated diameter can moderately vary in size – thus, yielding larger PDI values. Furthermore, the presence of isomers arising from the two different coupling sites in a maleimide appanage could be interpreted as a measure of low homogeneity by the DLS; thus, yielding broader polydispersities. Yet, more importantly is the fact that the measured diffusion coefficient of each DMC generation decreases with increasing generation, further confirming, in conjunction with ESI-MS characterization, that the complexes increase both in size and molecular weight. If future applications of DMCs required greater definition of the size distribution, there are further experimental¹⁶⁹ and mathematical¹⁷⁰ analyses that could be employed to approximate the dendrimer diameters better based on shape and diffusion rates.

Another important piece of information observed by DLS is the aggregation behavior of particles in solution dependent on solvent composition and sample preparation, and depicted as larger diameter values than expected. Solvent dependent aggregation was clearly observed when comparing the DLS plots of the DMCs in DMSO and in H₂O/DMSO (99:1, v/v%) solutions (Figure 2.13 and Figure 2.14). While in DMSO solutions a small degree of aggregation was observed, in H₂O/DMSO solutions large aggregates (160-405 nm) were more prominent. The G1.5 DMC had the smallest size aggregates in H₂O/DMSO compared to the G1.0 and G2.0 DMCs. This is likely due to the less hydrophilic surface groups (-OMe) of the G1.5-DMC which make the dendritic shell contract in the more aqueous environment. This contraction is common among standard dendrimers, and its heavily dependent on dendron composition (i.e., surface and family), solvent composition, and overall solution pH.^{45,46} This contraction behavior is also observed when looking at the smaller diameter peak of the same G1.5-DMC plot, which has a smaller average hydrodynamic diameter (~3 nm) in water than in DMSO (~4 nm). As for the full generation toroidal-DMCs, G2.0 has significantly larger aggregates than the G1.0 DMC. The fact that G2.0-DMC has twice as many -NH₂ surface groups (16) compared to G1.0-DMC (8) suggests that the observed aggregation behavior in water is not due to the lack of solubility. This is because the higher the number of hydrophilic surface groups in a dendrimer, the higher its water solubility. Thus, other self-aggregation mechanisms, such as dendron entanglement or enhanced hydrogen bonding, may be the main reason behind the larger diameter species. More extensive DLS analysis

is needed to understand such aggregation behavior better and minimize its effects.

As for sample preparation aggregation, as seen in Figure 2.15, two G1.5 DMC samples dissolved in DMSO and with similar concentrations have different hydrodynamic diameters (4.12 nm and 89.5 nm). The main difference between Sample A and Sample B is the way they were prepared for analysis. Sample A was concentrated to completion (i.e., all its solvent was removed) and then redissolved in DMSO, while Sample B was always dissolved in DMSO. The large difference in diameters is attributed to aggregation that is catalyzed when samples are concentrated. As solvent volume is reduced and the solution becomes more concentrated, the dendrimer arms are more likely to interlink with each other and form oligomers (dimer, trimer, etc.). Interestingly, the PDI values are also different with the larger diameter sample having a much narrower polydispersity. This is most likely due to the fact that as the DMCs particles aggregate, they take on more globular shapes. Overall, this solution behavior further exemplifies the need to not over concentrate dendrimer solutions as to avoid defects formation and unwanted aggregation.

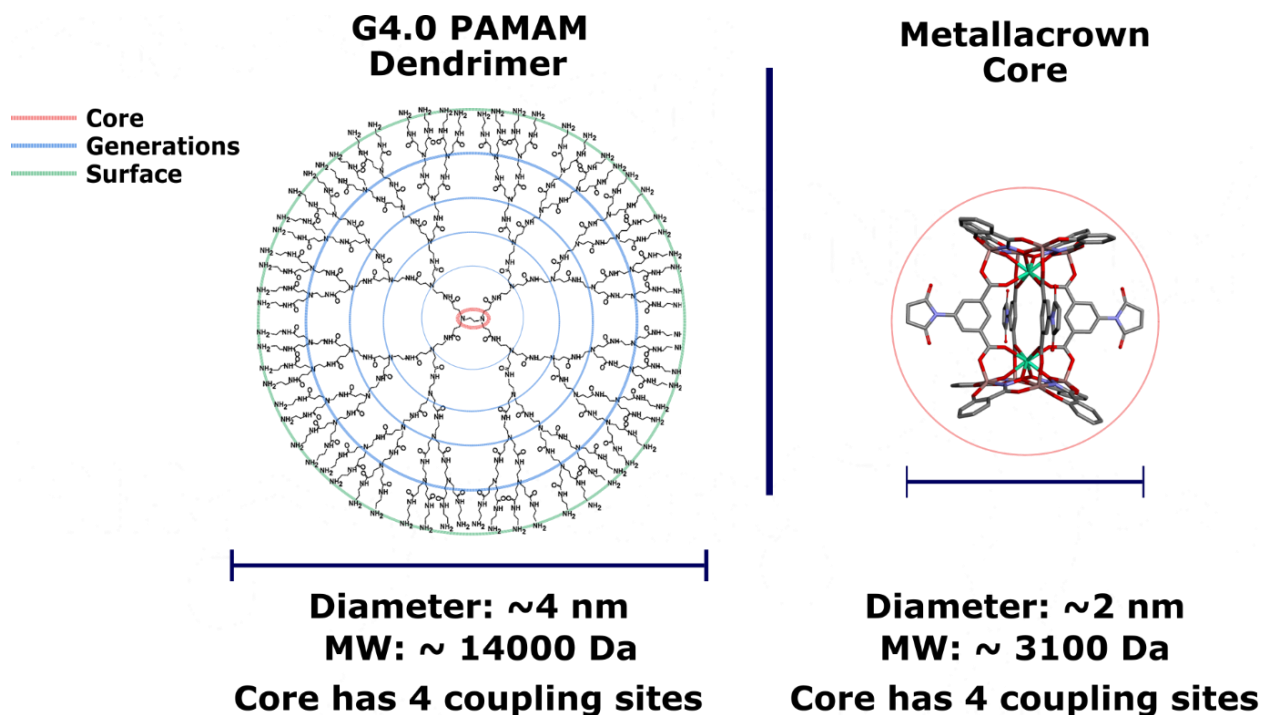
One more piece of information that can be subtracted from the DLS data is an approximation of the maximum number of solvent molecules encapsulated/associated to the DMC and the MC. This can be extrapolated from the density (ρ_m) of the measured sample by DLS, and comparing it to the maximum density of the sample, which can be determined from the crystal structure of a given scaffold. Three assumptions would be made in this case: *i*) the density of the $\text{Yb}_2\text{Ga}_8\text{Shi}_8\text{Mip}_4$ would be assumed to be the same as the one measured for the $\text{Yb}_2\text{Ga}_8\text{Shi}_8\text{Ip}_4$ MC from crystallographic data¹⁰⁶ (ρ :1.445); *ii*) the density of each DMC is extrapolated from the difference in the measured values of the MC and the DMC, and the assumed MC density; and *iii*) the molecules associated/encapsulated are only DMSO (MW: 78 g/mol). Values to perform the calculations are listed in Table 2.4, and detailed step-by-step calculations are shown in Appendix B. With this approach, a reasonable estimation for the maximum level of solvation of the MC and each of the DMCs can be determined. The increase in DMSO molecules associated with the DMCs is to be expected since the addition of four sets of dendrons arms with increasing generation size also increases the number of cavities and sites for solvent encapsulation.

Table 2.4 Calculated solvent molecules encapsulated or associated with samples in DLS.

Sample	R ^a (nm)	V ^b (mL)	MW ^c (g/mol)	Mass ^d (g)	ρ _m ^e (g/mL)	ρ (g/mL)	#DMSO molecules
MC	1.10	5.58e-21	3140	5.21e-21	0.93	1.445 ^f	14
DCM G0.5	1.25	8.18e-21	4140	6.87e-21	0.84	1.31	19
DMC G1.0	2.00	33.51e-21	4360	7.24e-21	0.22	0.34	20
DCM G1.5	2.06	36.62e-21	5740	9.53e-21	0.26	0.40	26
DCM G2.0	2.31	51.63e-21	6190	10.28e-21	0.20	0.31	28

^a From DLS estimated hydrodynamic radius. ^b Volume assuming sample is a sphere; $V=3/4\pi R^3$. ^c From ESI-MS. ^d MW/Avogadro's number. ^e Calculated density. ^f From crystal structure.¹⁰⁶

Both the ESI-MS and DLS data highlight the structural and morphological difference of regular dendrimers and dendrimeric metallacrowns. For example, with relatively small dendron generations, DMCs reach diameter sizes comparable to those of larger PAMAM dendrimers made with EDA cores – with G1-2 toroidal DMS close in size to standard G4-5 PAMAM dendrimers.^{171–173} The same is true for the molecular weight as seen by mass spectroscopy. The four DMCs generations range from 3.1 kDa to 6.2 kDa, which is comparable to G2-3 PAMAM dendrimers.¹⁷³ The obvious size difference arises from the much larger DMC cores compared to EDA-cored PAMAM dendrimers, which are about five times smaller (EDA, 0.38nm), as seen in Scheme 2.4. This influences the overall shape of DMCs as well as the cavity formation within the dendritic shell. With more massive cores but shorter dendron length, PAMAM DMC cavities are expected to be more open and flexible. However, depending on the desired application, cavity size can be tailored by the chosen dendrimer family coupled to the core, with more sterically hindered dendrons making less flexible DMCs. Shell tailoring with different dendron families, and large diameter in conjunction with high molecular weight after fewer synthetic cycles are qualities sought when developing nanomaterials, especially for those with biomedical application where cell uptake and retention times are factors driven by size and weight.²³



Scheme 2.4 Comparison between a G4.0 EDA-cored PAMAM dendrimer with a $\text{Ln}_2\text{Ga}_8\text{Shi}_8\text{Mip}_4$ MC highlighting that the MC has a diameter (measured by DLS) half as large as a large PAMAM dendrimer. Also, the MC used as the core of DMCs has the same amount of coupling sites for dendron grow, as EDA-cored PAMAM dendrimers.

Furthermore, compared to EDA-cored PAMAM dendrimers, $\text{Ln}_2\text{Ga}_8\text{Shi}_8\text{Mip}_4$ -cored DMCs have a more toroidal, or disk-like, shape. This is as a result of dendron attachment taking place at the waist of the MC core, which already has protruding maleimide appendages pointing out from the midsection. The location of the dendrimer arms also offers the benefit of protecting the core from undesirable solvent interaction even with the smallest dendrimer. As seen in Figure 2.16, when combining $\text{Tb}_2\text{Ga}_8\text{Shi}_8\text{Mip}_4$ with $\text{Tb}_2\text{Ga}_8\text{Shi}_8\text{Mip}_4$ G0.5 in DMF/ H_2O (1:1, %v/v), bridge exchange does not occur even after several days. Since ligand exchange occurred rapidly under similar conditions between $\text{Y}_2\text{Ga}_8\text{Shi}_8\text{Ip}_4$ and $\text{Y}_2\text{Ga}_8\text{Shi}_8\text{Mip}_4$, the increase in solution stability was attributed to the added protection that the dendrons arms offer to the MC core from solvent molecules. This is of particular importance not only for the solution stability of the DMCs, but also for the efficient sensitization of the core that can be hindered by solvents with non-radiative quenchers.

Since luminescent PAMAM dendrimers most often rely on surface modification or encapsulation of organic-based chromophores, their emission is limited by their photostability and surrounding chemical environment. Metallodendrimers have expanded this avenue, but still very

few examples of Ln^{III}-based luminescent dendrimers exist.^{56-59,88,155} To evaluate the luminescent properties of DMCs and the influence of the dendrimer shell on the core sensitization, the photophysical properties of each Yb^{III}-based DMC generation were investigated. Absorption spectra of each generation in DMSO exhibit $\pi \rightarrow \pi^*$ transition bands in the range of 250-350 nm, with a low-energy maximum between 317-319 nm ($\epsilon \approx 4.1 \times 10^4 \text{ M}^{-1} \text{ cm}^{-1}$). Just as with the unfunctionalized MC core, the singlet state (S^* : 28650 cm⁻¹) and the triplet state (T^* : 22350 cm⁻¹) are 6300 cm⁻¹ apart, which is favorable for efficient intersystem crossing. The T^* energy level was measured using G0.5 Gd^{III} DMC and is not expected to change much between dendrimer generations since the absorbance contribution of the complex arises from the ring ligands, with little or no contribution from the bridging ligands. Furthermore, PAMAM dendrons are poor antennas – i.e., they are not particularly good at energy transfer.

Based on the Figure 2.17, the size of the dendron generation does not seem to affect the electronic properties of the organic ligands in the MC scaffold since the absorbance spectra is identical for each generation. The good overlap of the absorbance spectra and excitation spectra indicates effective energy absorbance and transfer by the MC rings. Excitation at 320 nm exhibited characteristic Yb^{III} emission from 950-1150 nm for all generations, as seen in Figure 2.19. Photophysical data shown in Table 2.2 demonstrates that, as expected, the quenching effects of the maleimide rings are eliminated when coupled with dendrons. Both the values of Yb^{III} DMCs' τ_{obs} and ϕ_{Yb}^L increase significantly (by a factor of ~1.3, and ~2.5 – 3.4, respectively) compared to the MC core. The lifetimes are also best fitted with monoexponential decay, unlike the MC core, most likely due to the elimination of the maleimide rings' quenching behavior. Increasing quantum yield could also be due to solvent protection by the dendritic shell; however, longer generations can also have the hindering effect of encapsulating solvent molecules within cavities. This may explain why going from G0.5 to G1.0 the ϕ_{Yb}^L increases by a factor of ~25%, but going to longer generations slightly reduce such values by ~4% and ~7%, respectively. Nevertheless, the high quantum yields, and longer lifetimes are exciting results for the first Yb^{III}-based DMCs.

As seen in Figure 2.21, Figure 2.22, and Table 2.3, solid state and H₂O/DMSO photophysical data of G0.5 Ln₂Ga₈Shi₈Mip₄ DMCs (Ln: Yb^{III}, Tb^{III}, and Sm^{III}) were collected. Sharp emission bands corresponding to each of the Ln^{III} ions' f-f transitions are observed in the visible and NIR regions under excitation at 320-340 nm. In general, these DMCs have comparable quantum yields and luminescent lifetimes to other MCs.^{102,106,119,129} The solid state ϕ_{Yb}^L of 3.24%

for Yb₂Ga₈Shi₈Mip₄ G0.5 DMC is higher than most Yb^{III}-based MCs – with the exception of the monomeric parent MC YbGa₄Shi₄(benzoate)₄ with 5.88%. The Sm^{III}-based DMC has similar ϕ_{Sm}^L (2.31%) values to other Sm^{III}-based MCs, with the exception of SmGa₈Shi₈(OH)₄ (10.4%). Lastly, the Tb^{III}-based DMC has the lowest ϕ_{Tb}^L (11.9%) value of all published MCs. This is due to energy back-transfer events (T* ← Tb*) since the DMC's T* and emissive Tb* levels are too close to each other (ΔE : 1950 cm⁻¹). Such back energy transfer is likely also responsible for the biexponential character of the Tb^{III}-DMC luminescent decay. To study the luminescent behaviors of these DMC in more aqueous environments, solution state data in H₂O/DMSO (~96:4, v/v%) was collected. This solvent ratio was found to be the solubility limit in water with 1 mg/mL concentrations of each DMC. As expected, the τ_{obs}/ϕ_{Yb}^L decreased by a factor of ~2.7/~3.7 for Yb^{III}, ~1.2/~2.1 for Sm^{III}, and ~1.1/~1.9 for Tb^{III}; nevertheless, luminescent emission was still strong enough to be detected. Additionally, compared to the only fully water soluble YbZn₁₆PyzHa₁₆ MC with a ϕ_{Yb}^L of 0.0112%, the ϕ_{Yb}^L of the Yb^{III}-DMC is ~77.5 times larger. This is due in part to the better ΔE between the T* and Yb* states and the lack of ILCT levels of the DMC compared to the YbZn₁₆PyzHa₁₆ MC, but is also due to the solvent protection by the dendron arms, as seen in the ESI-MS stability experiments. It is important to point out that solid state luminescent characterization was only performed on the smallest of the DMCs as so avoid defect formation from solvent concentration with the larger generations.

2.4.3 Cell Studies

PAMAM dendrimers have been extensively researched in areas of nanomedicine as payload carriers of agents, such as therapeutic drugs, contrast agents, and imaging probes.¹⁷⁴ Therefore, due to the nature of the dendrimer shell, and the improvement of water stability and luminescent sensitization, DMCs were used to label HeLa cells in order to assess their luminescent imaging potential. As seen in Figure 2.23, while bright luminescent signal was detected with cells incubated with Yb₂Ga₈Shi₈Mip₄ G0.5 and G1.5 DMCs, cell uptake was not observed. Instead, both compounds form aggregates, and have non-specific interaction with the cells surfaces. Since aggregate formation was not observed in DMSO solutions by DLS, this behavior must arise from their interaction with a more aqueous environment and the fact that both DMC have methyl ester (-OMe) surfaces. Improved behavior was observed when cells were incubated with Yb₂Ga₈Shi₈Mip₄ G1.0 DMC. A strong epifluorescence signal in the NIR was detected arising from

the MC core. The localization of an intense signal around cells suggests non-specific labeling interactions of the DMC to the cell membrane. But a bright signal localized at the nucleoli of most cells, as seen in Figure 2.24, indicate that part of the G1.0 DMC was internalized by the cells – with a cell trafficking up to the nucleus. Furthermore, cells images also demonstrate the three DMC generations are stable, and capable of sensitizing the Yb^{III} luminescence under cell culture conditions. Thus, DMCs, especially full generation ones, have the potential to become NIR luminescent payload delivery systems with photostable cores. This would be a great improvement to standard PAMAM dendrimers that require functionalization with organic luminescent probes. Furthermore, the toroidal shape of DMCs could offer an advantage over spherical dendrimers when adhering to cells since elongated shapes would have higher surface areas that can facilitate multivalent interactions with cell surfaces.¹⁷⁵ Altogether, this demonstrates the great imaging potential of DMCs.

2.5 Conclusions

The work presented in this chapter demonstrates the functionalization potential of Ln^{III}-based metallacrowns, and their expansion into the dendrimer field. I described the synthetic incorporation of thiol-active maleimide groups to the bridging ligands of dimeric Ln₂Ga₈ MCs. The Ln₂Ga₈Shi₈Mip₄ MC scaffold was characterized by ESI-MS and NMR to corroborate chemical and structural composition. Solid state photophysical characterization demonstrated that the maleimide groups have a strong quenching effect on the luminescence of the Yb^{III}-based scaffold, with its τ_{obs} and ϕ_{Yb}^l values drastically decreasing compared to the parent monomeric MC YbGa₄Shi₄(benzoate)₄ and the structurally analogous dimeric MC Yb₂Ga₈Shi₈Ip₄. Fortunately, such quenching effects are eliminated once the maleimide groups are coupled to thiol-bearing compounds. The functionalization ability of Ln₂Ga₈Shi₈Mip₄ was corroborated by coupling four cysteamine groups to the four maleimide appendages of the MC. The Sm^{III} emission of the pre- and post-cysteamine coupled event corroborated that the luminescence signal is not hindered by such functionalization. However, the limited solution stability and insolubility of this scaffold in water restricts its application to non-aqueous environments.

To exploit the optical properties of MCs, improve their aqueous stability, and expand their applications, Ln₂Ga₈Shi₈Mip₄ were used as the core of dendrimeric metallacrowns, combining the photophysical characteristic of MC with those of dendrimers. For this, I showed the synthesis and

characterization of a new family of dendrimeric metallacrowns with $\text{Ln}_2\text{Ga}_8\text{Shi}_8\text{Mip}_4$ MC cores and PAMAM dendritic shells. ESI-MS and DLS corroborated the formation of DMCs of four different generations, while the photophysical characterization in DMSO solution demonstrated excellent sensitization of the Yb^{III} ions and high $\phi_{\text{Yb}}^{\text{I}}$. Furthermore, the distinct structural features of DMCs, such as the toroidal shape, large diameters, and high molecular weight with smaller generations, offer an ample opportunity to investigate their physiochemical properties. An increase in solution stability in aqueous mixed media (DMF/ H_2O) was observed, with nullification of bridge ligand exchange events once the MC core is functionalized with four PAMAM dendrons. This corroborates the solvent protection that the dendrimer shell offers to MC cores, as it has been observed with other macrocyclic cored metallodendrimers. Photophysical analysis and cell studies demonstrated excellent Ln^{III} sensitization, as well as robust stability in cell culture conditions. Furthermore, it could be expected that $\text{Ln}_2\text{Ga}_8\text{Shi}_8\text{Mip}_4$ MC undergoing thiol-Michael addition has an array of isomer combinations based on the fact that each of the maleimide appendages can yield two sets of isomers upon thiol coupling. This could have interesting pharmacokinetic properties since depending on the cell, cell uptake can be selective based on chirality. Additionally, interesting polarizable luminescent signals could be obtained if the chirality of the system can be somewhat controlled or diastereomers separated.

With this work, I was able to demonstrate that by combining dendrimers with Ln^{III} -base MC, it is possible to combine the photophysical properties of the core and the properties of dendrimers, while developing a new class of metallodendrimers. Additionally, the tunability of dendrimers and MCs opens up the possibility to customize the application of dendrimeric metallacrowns by attaching the dendrons to other positions on the MC core or coupling biologically interesting molecules such as antibodies or vitamins to the core and/or dendrimer architecture.

Chapter 3

Light-Catalyzed Functionalization of Luminescent Metallacrowns and Hyperboloidal Dendrimeric Metallacrowns

3.1 Introduction

As introduced in Chapter 1, lanthanide-based luminescent metallacrowns have been prepared with an array of Zn(II) picolinehydroxamate and Ga(III) salicylhydroxamate derivatives in order to enhance their optical properties (e.g., energy transfer or absorbance red-shifting). However, synthetic modification of their templating ring ligands in order to increase their functionalization is still at an early stage. Chapter 2 examined the functionalization of the bridging ligands of Ln₂Ga₈ MCs to introduce efficient coupling sites for thiol-bearing molecules. This functionalization then led to the development of Ln₂Ga₈ MCs capable of being used as the core of dendrimers. In this chapter, emphasis is placed on the modification of the ring ligands of LnGa₄ and Ln₂Ga₈ MCs in order to introduce coupling sites to each scaffold (four and eight, respectively).

Previous work by Plenck et al.,¹⁴⁷ and Lutter et al.^{122,140} demonstrated that via Sonogashira coupling, alkyne groups capable of undergoing copper-catalyzed alkyne-azide cycloaddition (CuAAC) can be incorporated to the ring ligands of LnGa₄ and Ln₂Ga₈ MCs. Both authors were able to couple small azide-bearing molecules onto the MCs, and study the luminescent and magnetic properties of the functionalized scaffolds. Additionally, with the Ln₂Ga₈ MCs, Lutter et al.^{122,140} also observed a red-shift of the scaffold's excitation energy that was retained pre- and post-azide coupling. However, while CuAAC is a well-studied coupling approach, its synthetic requirements, such as a Cu^I source and aqueous solvent system, can limit their application as a functionalization approach – especially with systems with limited aqueous solubility or with copper chelating sites. Furthermore, since azide compounds can be heat- and shock-sensitive with the potential of explosively decomposing,¹⁷⁶ the application of CuAAC coupling is further limited to small scale reactions, and small azide compounds. Thus, in order to further expand the

functionalization capabilities of LnGa_4 and Ln_2Ga_8 MCs at their ring ligands, a more synthetically flexible and safe approach is required.

To this end, this thesis chapter presents the synthesis and characterization of light-catalyzed metal-free thiol-yne and -ene coupling systems incorporated into two different positions on the ring ligands of luminescent LnGa_4 and Ln_2Ga_8 MCs. A total of four different ring ligands capable of undergoing thiol coupling were prepared and investigated for their coupling and luminescent properties. This report is the first study to utilize light-catalyzed coupling methods to functionalized metallacrowns. Furthermore, Ln_2Ga_8 MCs prepared with the most reactive ring ligand were utilized as the core of a new class of luminescent metallodendrimer, hereon known as hyperboloidal dendrimeric metallacrowns (H-DMCs). The hyperboloidal description arises from the fact that dendrons are attached to the ring ligands of dimeric Ln_2Ga_8 MCs, making the complex take on the shape of a hyperboloid (or hourglass) where the “top” and “bottom” of the DMC are wider than its “waist”. This is also to distinguish them from the toroidal dendrimeric metallacrowns (T-DMCs) described in Chapter 2.

For this chapter, I first describe the synthetic requirement to develop thiol-active ring ligands for 12-MC-4 metallacrowns. I then demonstrate the thiol-coupling capabilities of both LnGa_4 and Ln_2Ga_8 scaffolds prepared with each of the four new ring ligands, and their luminescence characterization pre- and post-thiol coupling. Lastly, I follow this by presenting data on the formation of DMCs, as well as their luminescent properties. Altogether, this chapter investigates the functionalization requirements of metallacrowns at an orthogonal position to that described in chapter 2, which focused on isophthalate bridges, and their photophysical properties.

3.2 Experimental

3.2.1 Chemical and Materials

All reagents and chemicals were purchased from commercial sources and used without further purification. Cysteamine (Sigma-Aldrich, 95%), cysteamine hydrochloride (Alfa Aesar, 98+%), Extra dry dichloromethane (Acros, 99.9%), Trifluoro acetic acid (Fisher, Peptide synthesis grade), Trityl chloride (Acros, 98%), Chloroform (Fisher, ACS grade), Sodium hydroxide (Fisher, ACS grade), Magnesium sulfate anhydrous (Fisher), Methanol (Fisher, ACS grade), Methyl acrylate (Acros, 99%), Ethylenediamine (Alfa Aesar, 99%), Toluene (LabChem, ACS grade), Dichloromethane (Fisher, ACS grade), Triethylsilane (TCI, 98+%), Petroleum ether (Fisher, ACS

grade), Gallium (III) nitrate hydrate (Acros, 99.9998%), Ytterbium nitrate pentahydrate (Sigma Aldrich, 99.9%), Samarium nitrate hexahydrate (Sigma Aldrich, 99.9%), Gadolinium nitrate hexahydrate (Sigma-Aldrich, 99.999%), Methyl-2,4-dihydroxy benzoate (TCI America, 98.0%), Methyl-2,5-dihydroxy benzoate (TCI America, 98.0%), Allyl bromide (Acros Organics, 99% stabilized), Propargyl bromide 80% toluene (Alfa Aesar, stabilized with MgO), Anhydrous potassium carbonate (Fisher, Certified ACS), Acetone (Fisher), Diethyl ether (Fisher), Hydroxylamine hydrochloride (Alfa Aesar, 99%), Potassium hydroxide pellets (Alfa Aesar, 85%), Ethyl acetate (Fisher, ACS grade), Hydrochloric acid (Fisher, 36.5-38.0%), Sodium benzoate (Fisher), Pyridine (Fisher, ACS certified), Isophthalic acid (Alfa Aesar, 99%), N,N-dimethylformamide (Fisher, Sequencing grade), 2-Mercapto ethanol (Fisher), 2,2-Dimethoxy-2-phenylacetophenone (DMPA, Sigma, 99%), 4,4'-Bis(dimethylamino)benzophenone (Michler's Ketone, Sigma, 98%), Azobisisobutyronitrile (AIBN, Sigma, 98%), SnakeSkin Dialysis Tubing 3.5 MWCO 22 mm (Thermo Scientific), Dimethyl sulfoxide (Fisher, HPLC grade), Chloroform-d₃ 0.03% v/v% TMS (Acros, 99.8+%), Dimethyl sulfoxide-d₆ 0.03% TMS (Acros, 99.9%), Methanol-d₄ (Acros, 99.8%), Methanol (Sigma-Aldrich HPLC Plus, 99.9%), NanoStar Disposable MicroCuvette (Wyatt), LED Emitter UV 365 nm flat lens 14 W (Digikey), AC/DC Wall mount adapter (Digikey), Computer fan (Newark), Aluminum foil tape (Newark).

3.2.2 General Characterization Methods

Electrospray Ionization Mass Spectrometry (ESI-MS) was performed on an Agilent 6230 TOF HPLC-MS in negative or positive ion mode with fragmentation voltage of 250-350V. Samples were prepared by dissolving approximately 0.5-1 mg of compound in 2 mL of HPLC grade methanol. Samples of 5-10 μ L were manually injected. Methanol was employed as eluent in negative ion, and acetonitrile with 0.1% formic acid in positive ion. The flow rate was 0.5-1 mL/min. Data were processed with Agilent MassHunter Qualitative Analysis Software.

CHN elemental analysis was performed in a Carlo Erba 1108 elemental analyzer and a PerkinElmer 2400 elemental analyzer by Atlantic Microlab.

¹H NMR spectra were acquired on a 400 MHz Varian MR400 or 500 MHz Varian VNMRS500 NMR Spectrometer. Samples were prepared in Chloroform-d, Dimethyl sulfoxide-d₆, or Methanol-d₄, and spectra were processed using MestraNOVA software.

Dynamic Light Scattering (DLS) was performed on a DynaPro NanoStar instrument at

25°C with a scattering angle of 90°. Samples were prepared by dilution in DMSO, followed by centrifugation for five minutes at twelve thousand rpm. Scans were done with five second acquisition time seta and twenty runs. Data was plotted using OriginPro 2020 software.

3.2.3 X-Ray Crystallography

Data collection and structural refinement was performed by Dr. Jeff W. Kampf at the University of Michigan. Collection was done on single crystals mounted on a Rigaku AFC10K Saturn 944+ CCD-based X-ray diffractometer equipped with a low T device and Micromax-007HF Cu-target micro-focus rotating anode ($\lambda = 1.54187 \text{ \AA}$) operated at 1.2 kW power (40 kV, 30 mA). The X-ray intensities were measured at 85(1) K with the detector placed at a distance 42.00 mm from the crystal. The structure was solved and refined with the Bruker SHELXTL (version 2018/3) software package. All non-hydrogen atoms were refined anisotropically with the hydrogen atoms placed in idealized positions. The SQUEEZE subroutine of the PLATON program suite was used to address the disordered solvent contained in solvent accessible voids present in the structure.

3.2.4 UV Photocatalytic Setup

UV-light catalyzed thiol-yne and -ene coupling of small molecules and dendrons to metallocrown was done using the set up (LED Box) shown below in Figure 3.1. The LED Box and lid (not shown in the picture) were made using fiberboard, and all of its interior was coated with aluminum tape or foil as to increase light reflectance. An aluminum coating was chosen for its high reflectivity (>85%) in the UV region¹⁷⁷ and its low cost. The light source is a UV LED emitter with a 15 Watts of output power and a narrow emission at 365 nm. To avoid overheating of the LED emitter, a copper metal plate was used as a heat sink with a computer fan placed in the back to expel hot air. Vials with samples were placed at 5-7 cm from the light source.

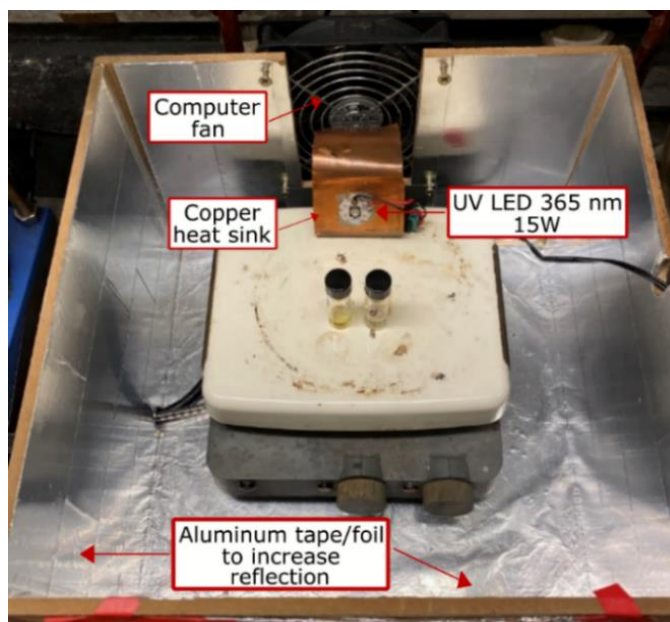


Figure 3.1 Photograph of LED Box highlighting key components. Coupling reaction using this set up were performed by covering the box with a lid (not shown in picture) and placing the assembly inside a hood.

3.2.5 Synthetic Procedures

I now describe the synthetic procedures followed in this chapter. All reactions were completed under aerobic condition and at room temperature, unless otherwise noted. Characterization figures (ESI-MS, NMR, and DLS) not shown under the result section can be found in Appendix (Appx.) C.

Metallacrowns ring ligands:

Methyl 2-hydroxy-4-(prop-2-yn-1-yloxy)benzoate (**1**) was prepared by adding methyl 2,4-dihydroxy benzoate (10.00 g, 59.5 mmol, 1 eq.), propargyl bromide (7.50 mL, 82 mmol, 1.4 eq.), and anhydrous potassium carbonate (32.9 g, 238 mmol, 4.0 eq.) to acetone (150 mL) in a round bottom flask. The mixture was refluxed while stirring for five hours at 65°C. After this time, the reaction mixture was cooled down to room temperature and concentrated under reduced pressure with a rotary evaporator at 40°C. The product was then redissolved with DI water (100 mL) and extracted thrice with diethyl ether (3 x 100 mL). The organic layers were combined and extracted thrice with a solution of 1M NaOH (3 x 50 mL). The aqueous layers were combined and then acidified to pH~1 with concentrated HCl. The precipitate was filtered off and rinsed with copious amounts of water. If a precipitate did not form after acidifying the solution, the reaction mixture

was extracted thrice with ethyl acetate, dried over magnesium sulfate, and concentrated under reduced pressure. The product was an off-white to yellow powder (39.5 mmol, 66.3% yield) that was dried over vacuum overnight. ¹H NMR (Figure Appx. C30, 500 MHz, dms_o-d₆) δ 10.76 (s, 1H), 7.73 (d, *J* = 8.5 Hz, 1H), 6.57 (d, *J* = 7.9 Hz, 2H), 4.87 (d, *J* = 2.5 Hz, 2H), 3.87 (s, 3H), 3.64 (t, *J* = 2.4 Hz, 1H).

N,2-dihydroxy-4-(*prop*-2-yn-1-yloxy)benzamide (**H_{3p}YneShi, 2**) was prepared by first dissolving hydroxylamine hydrochloride (21.89 g, 315.0 mmol, 8 eq.) in methanol (100 mL), and potassium hydroxide (20.99 g, 374.1 mmol, 9.5 eq.) in methanol (50 mL) separately. Once fully dissolved, both solutions were combined, and the potassium chloride was removed by filtration. This solution mixture was then added to a solution of **1** (8.14 g, 39.5 mmol, 1 eq.) in methanol (50 mL). The reaction mixture was then stirred for 7-10 days at room temperature. After this time, the mixture was concentrated under reduced pressure with a rotary evaporator at 35°C. To this, water (100 mL) was added, followed by the addition of concentrated HCl until the solution pH was close to 1. This was followed by filtration under vacuum and rinsed with copious amounts of water. The precipitate was then triturated twice with DCM (2 x 100 mL) for 15 minutes each time, filtered again, and dried under vacuum overnight. If after acidifying the reaction mixture no precipitate formed, the solution was extracted thrice with ethyl acetate (3 x 50 mL), dried over magnesium sulfate, concentrated under reduced pressures, and triturated twice with DCM. The product was an off-white powder (16.6 mmol, 42.1% yield). ¹H NMR (Figure Appx. C31, 400 MHz, dms_o-d₆) δ 12.72 (s, 1H), 11.35 (s, 1H), 9.24 (d, *J* = 10.9 Hz, 1H), 7.66 – 7.57 (m, 1H), 6.47 (dt, *J* = 7.6, 1.9 Hz, 2H), 4.82 (d, *J* = 2.3 Hz, 2H), 3.62 (q, *J* = 2.3 Hz, 1H).

*Methyl 2-hydroxy-5-(*prp*-2-yn-1-yloxy)benzoate (3) was prepared in the same fashion as **1**. The final product was an off-white to orange powder (31.5 mmol, 57.0% yield). ¹H NMR (Figure Appx. C32 400 MHz, dms_o-d₆) δ 10.14 (s, 1H), 7.33 (dd, *J* = 3.3, 1.5 Hz, 1H), 7.21 (ddd, *J* = 9.1, 3.4, 1.5 Hz, 1H), 6.95 (dd, *J* = 9.0, 1.6 Hz, 1H), 4.77 (d, *J* = 2.1 Hz, 2H), 3.90 (d, *J* = 1.6 Hz, 3H), 3.56 (q, *J* = 2.1 Hz, 1H).*

N,2-dihydroxy-5-(*prop*-2-yn-1-yloxy)benzamide (**H_{3m}YneShi, 4**) was prepared in the same fashion as **2**, but with **3** as the starting material. The final product was an off-white powder (~13 mmol, ~40% yield). ¹H NMR (Figure Appx. C33 400 MHz, dms_o-d₆) δ 11.75 (s, 1H), 11.36 (s, 1H), 9.38 – 9.33 (m, 1H), 7.31 (d, *J* = 2.8 Hz, 1H), 7.07 (dd, *J* = 9.1, 2.9 Hz, 1H), 6.89 – 6.83 (m,

1H), 4.72 (t, $J = 2.2$ Hz, 2H), 3.55 (t, $J = 2.5$ Hz, 1H).

Methyl 4-(allyloxy)-2-hydroxybenzoate (5) was prepared by adding methyl 2,4-dihydroxy benzoate (15.5 g, 92.4 mmol, 1 eq.), allyl bromide (10.0 mL, 115.6 mmol, 1.25 eq.), and anhydrous potassium carbonate (51.1 g, 370.0 mmol, 4.0 eq.) to acetone (250 mL) in a round bottom flask. The mixture was refluxed while stirring for five hours at 65°C. After this time, the reaction was cooled down to room temperature and concentrated under reduced pressure with a rotary evaporator at 40°C. The product was then redissolved with DI water (200 mL) and extracted thrice with diethyl ether (3 x 150 mL). The organic layers were combined and extracted thrice with a solution of 1M NaOH (3 x 100 mL). The aqueous layers were combined and then acidified to pH~1 with concentrated HCl. The precipitate was filtered off and rinsed with copious amounts of water. If a precipitate did not form after acidifying the solution, the reaction mixture was extracted thrice with ethyl acetate, dried over magnesium sulfate, and concentrated under reduced pressure. The product was an off-white to pale amber powder (30.4 mmol, 32.9% yield) that was dried over vacuum overnight. ¹H NMR (Figure Appx. C34, 500 MHz, dms_o-d₆) δ 10.78 (d, $J = 1.5$ Hz, 1H), 7.73 – 7.65 (m, 1H), 6.56 – 6.49 (m, 2H), 6.11 – 5.95 (m, 1H), 5.39 (dt, $J = 17.3, 1.7$ Hz, 1H), 5.31 – 5.23 (m, 1H), 4.61 (dd, $J = 5.3, 2.0$ Hz, 2H), 3.85 (d, $J = 1.6$ Hz, 3H).

4-(allyloxy)-N,2-dihydroxybenzamide (H_{3p}AlShi, 6) was prepared by first dissolving hydroxylamine hydrochloride (16.90 g, 243.2 mmol, 8 eq.) in methanol (150 mL), and potassium hydroxide (16.20 g, 288.8 mmol, 9.5 eq.) in methanol (100 mL) separately. Once fully dissolved, both solutions were combined, and the potassium chloride was removed by filtration. This solution mixture was then added to a solution of **5** (6.33 g, 30.4 mmol, 1 eq.) in methanol (30 mL). The mixture was then stirred for 7-10 days at room temperature. After this time, the solution was concentrated under reduced pressure with a rotary evaporator at 35°C. To this, water (100 mL) was added, followed by the addition of concentrated HCl until the solution pH was close to 1. The solution mixture was then filtrated under vacuum and rinsed with copious amount of water. The precipitate was then triturated twice with DCM (2 x 100 mL) for 15 minutes each time, filtered again, and dried under vacuum overnight. If after acidifying the reaction mixture no precipitate formed, the solution was extracted thrice with ethyl acetate (3 x 50 mL), dried over magnesium sulfate, concentrated under reduced pressures, and triturated twice with DCM. The product was an off-white powder (9.76 mmol, 32% yield). ¹H NMR (Figure Appx. C35, 400 MHz, dms_o-d₆) δ

12.71 (d, $J = 5.4$ Hz, 1H), 11.32 (s, 1H), 9.23 (s, 1H), 7.60 (d, $J = 8.7$ Hz, 1H), 6.49 – 6.37 (m, 2H), 6.02 (ddd, $J = 22.4, 10.4, 5.2$ Hz, 1H), 5.38 (dd, $J = 17.3, 1.8$ Hz, 1H), 5.26 (dd, $J = 10.5, 1.7$ Hz, 1H), 4.58 (dt, $J = 5.3, 1.6$ Hz, 2H).

Methyl 5-(allyloxy)-2-hydroxybenzoate (7) was prepared in the same fashion as **5**. The final product was an off-white to pale yellow powder (26.1 mmol, 50.6% yield). ^1H NMR (Figure Appx. C36 400 MHz, dms -d_6) δ 10.12 (s, 1H), 7.31 – 7.23 (m, 1H), 7.18 (ddd, $J = 8.9, 3.2, 1.3$ Hz, 1H), 6.97 – 6.87 (m, 1H), 6.10 – 5.96 (m, 1H), 5.43 – 5.34 (m, 1H), 5.30 – 5.22 (m, 1H), 4.52 (dt, $J = 5.1, 1.8$ Hz, 2H), 3.92 – 3.87 (m, 3H).

5-(allyloxy)-N,2-dihydroxybenzamide (H₃mAlShi, 8) was prepared in the same fashion as **6**, but with **7** as the starting material. The final product was an off-white to pale yellow powder (~5 mmol, ~40% yield). ^1H NMR (Figure Appx. C37 400 MHz, dms -d_6) δ 11.76 (s, 1H), 11.39 (s, 1H), 9.34 (s, 1H), 7.27 (d, $J = 3.0$ Hz, 1H), 7.03 (dd, $J = 9.1, 2.9$ Hz, 1H), 6.83 (d, $J = 8.9$ Hz, 1H), 6.03 (ddt, $J = 16.3, 11.0, 5.4$ Hz, 1H), 5.38 (dt, $J = 17.2, 1.7$ Hz, 1H), 5.25 (dd, $J = 10.4, 2.2$ Hz, 1H), 4.49 (dd, $J = 5.6, 1.9$ Hz, 2H).

LnGa₄x-Shi₄(benzoate)₄ Metallacrowns:

General synthesis procedure for Ln[12-MC_{Ga(III)N(pYneShi)-4](benzoate)₄(pyridinium)(pyridine)₂(MeOH)₂ metallacrowns (Ln^{III}: Yb^{III}, Sm^{III}, or Gd^{III}; shorthand: LnGa₄pYneShi₄(benzoate)₄).} MCs were prepared by slight modification of previous literature procedures¹⁰² that follow three different protocols depending on the nature on the Ln^{III} ion. The synthetic yields were 10 – 25%.

YbGa₄pYneShi₄(benzoate)₄ was prepared by fully dissolving **2** (H₃pYneShi, 0.150 g, 7.24 mmol, 1 eq), sodium benzoate (4.17 g, 28.96 mmol, 4 eq), and pyridine (15 mL) in methanol (50 mL). Then Yb(NO₃)₃·xH₂O (1.81 mmol, 0.25 eq) and Ga(NO₃)₃·xH₂O (7.24 mmol, 1 eq) were dissolved in methanol (50 mL) separately. The three methanol solutions were combined and stirred at room temperature for 5 – 10 minutes. The mixture was then filtered, and left to evaporate slowly in a glass jar covered with aluminum foil with several holes. Crystals were collected by gravity filtration and rinsed with pyridine. MS (Figure Appx. C44, ESI): m/z calcd. for YbGa₄C₄₄H₂₈N₄O₂₄: 1447.75 [M]⁻; found: 1449.75 [M]⁻. Elemental analysis calcd. (%) for YbGa₄C₈₉H₆₃N₄O₃₂Na₄: C 47.63, H 2.83, N 2.50; found: C 46.90, H 2.81, N 2.50. Single-crystal

unit cell: monoclinic; space group P2(1)/n; $a = 18.14950(9) \text{ \AA}$, $b = 25.65520(11) \text{ \AA}$, $c = 18.57270(8) \text{ \AA}$; $\beta = 90.9420(4)^\circ$; $V = 8646.82(7) \text{ \AA}^3$.

SmGa_{4p}YneShi₄(benzoate)₄ was prepared by fully dissolving **4** (H_{3p}YneShi, 0.91 g, 4.19 mmol, 1 eq), sodium benzoate (1.81 g, 12.57 mmol, 3 eq), and pyridine (9 mL) in methanol (100 mL). Then Sm(NO₃)₃·xH₂O (2.10 mmol, 0.5 eq) and Ga(NO₃)₃·xH₂O (4.19 mmol, 1 eq) were dissolved in methanol (50 mL) separately. The three methanol solutions were combined and stirred at room temperature for 5 – 10 minutes. The mixture was then filtered, and left to evaporate slowly in a glass jar covered with aluminum foil with several holes. Crystals were collected by gravity filtration and rinsed with pyridine. ¹H NMR (Figure Appx. C38, 500 MHz, dms_o-d₆) δ 7.41 (d, $J = 7.3$ Hz, 4H), 7.25 (t, $J = 7.5$ Hz, 4H), 6.37 (ddd, $J = 20.1, 8.9, 2.6$ Hz, 4H), 4.79 (dd, $J = 20.6, 2.3$ Hz, 8H), 3.57 (d, $J = 6.2$ Hz, 4H). MS (Figure Appx. C45, ESI): m/z calcd. for SmGa₄C₄₄H₂₈N₄O₂₄: 1427.73 [M]⁻; found: 1427.73 [M]⁻. Elemental analysis calcd. (%) for SmGa₄C₇₈H₅₇N₆O₂₅: C 49.11, H 3.01, N 4.41; found: C 49.10, H 3.06, N 4.53.

GdGa_{4p}Yne(benzoate)₄ was prepared by fully dissolving **4** (H_{3p}YneShi, 0.11 g, 0.53 mmol, 1 eq), sodium benzoate (0.2291 g, 1.59 mmol, 3 eq), and pyridine (1 mL) in methanol (10 mL). Then Gd(NO₃)₃·xH₂O (0.13 mmol, 0.25 eq) and Ga(NO₃)₃·xH₂O (0.53 mmol, 1 eq) were dissolved in methanol (10 mL) separately. The three methanol solutions were combined and stirred at room temperature for 5 – 10 minutes. The mixture was then filtered, and left to evaporate slowly in a glass jar covered with aluminum foil with several holes. Crystals were collected by gravity filtration and rinsed with pyridine. MS (Figure Appx. C46, ESI): m/z calcd. for GdGa₄C₄₄H₂₈N₄O₂₄: 1431.73 [M]; found: 1433.73 [M]⁻. Elemental analysis calcd. (%) for GdGa₄C₉₀H₆₇N₈Na₂O₃₀: C 48.63, H 3.04, N 5.04; found: C 48.61, H 3.02, N 4.57.

General synthesis procedure for Ln[12-MC_{Ga(III)N(mYneShi)-4](benzoate)₄(pyridinium)(pyridine)₂(MeOH)₂ metallacrowns (Ln^{III}: Yb^{III}, Sm^{III}, or Gd^{III}; LnGa_{4m}YneShi₄(benzoate)₄)}. MCs were prepared following the same protocol described above. The synthetic yields were 15 – 30%.

YbGa_{4m}YneShi₄(benzoate)₄ MS (Figure Appx. C47, ESI): m/z calcd. for YbGa₄C₆₈H₄₄N₄O₂₄: 1751.87 [M]⁻; found: 1753.87 [M]⁻. Elemental analysis calcd. (%) for YbGa₄C₉₀H₆₉N₈O₃₀: C 49.26, H 3.17, N 5.11; found: C 49.25, H 3.13, N 5.20.

SmGa_{4m}YneShi₄(benzoate)₄ ¹H NMR (Figure Appx. C39, 500 MHz, dms_o-d₆) δ 7.14 –

7.09 (m, 4H), 6.95 (s, 4H), 6.79 (s, 4H), 4.71 (d, $J = 16.7$ Hz, 8H), 3.53 – 3.45 (m, 3H), 3.31 (s, 1H). MS (Figure Appx. C48, ESI): m/z calcd. for $\text{SmGa}_4\text{C}_{44}\text{H}_{28}\text{N}_4\text{O}_{24}$: 1427.73 [M]⁻; found: 1427.73 [M]⁻. Elemental analysis calcd. (%) for $\text{SmGa}_4\text{C}_{93}\text{H}_{76}\text{N}_8\text{O}_{39}\text{Na}_5$: C 45.15, H 3.10, N 4.53; found: C 45.13, H 3.03, N 4.51.

GdGa₄mYneShi₄(benzoate)₄ MS (Figure Appx. C49, ESI): m/z calcd. for $\text{GdGa}_4\text{C}_{44}\text{H}_{28}\text{N}_4\text{O}_{24}$: 1431.73 [M]⁻; found: 1433.73 [M]⁻. Elemental analysis calcd. (%) for $\text{GdGa}_4\text{C}_{93}\text{H}_{77}\text{N}_9\text{O}_{28}\text{Na}$: C 50.14, H 3.48, N 5.66; found: C 50.64; H 3.42, N 5.64.

General synthesis procedure for Ln[12-MC_{Ga(III)N(pAlShi)-4](benzoate)₄(pyridinium)(pyridine)₂(MeOH)₂ metallacrowns (Ln^{III}: Yb^{III}, Sm^{III}, or Gd^{III}); LnGa₄pAlShi₄(benzoate)₄}. MCs were prepared following the same protocol described above. The synthetic yields were 15 – 25%.

YbGa₄pAlShi₄(benzoate)₄ MS (Figure 3.2, ESI): m/z calcd. for $\text{YbGa}_4\text{C}_{68}\text{H}_{52}\text{N}_4\text{O}_{24}$: 1759.94 [M]⁻; found: 1761.93 [M]⁻. Elemental analysis calcd. (%) for $\text{YbGa}_4\text{C}_{97}\text{H}_{80}\text{N}_7\text{O}_{28}$: C 51.93, H 3.59, N 4.34; found: C 52.45, H 3.61, N 4.52.

SmGa₄pAlShi₄(benzoate)₄ ¹H NMR (Figure 3.3, 500 MHz, dms_o-d₆) δ 7.42 (t, $J = 7.3$ Hz, 4H), 7.24 (t, $J = 7.5$ Hz, 4H), 6.41 – 6.31 (m, 4H), 6.05 (tdd, $J = 18.1, 10.5, 5.2$ Hz, 4H), 5.46 – 5.18 (m, 8H), 4.67 – 4.47 (m, 8H). MS (Figure Appx. C50, ESI): m/z calcd. for $\text{SmGa}_4\text{C}_{44}\text{H}_{36}\text{N}_4\text{O}_{24}$: 1433.79 [M]⁻; found: 1435.79 [M]⁻. Elemental analysis calcd. (%) for $\text{SmGa}_4\text{C}_{78}\text{H}_{65}\text{N}_6\text{O}_{25}$: C 48.91, H 3.42, N 4.39; found: C 48.83, H 3.44, N 4.37.

GdGa₄pAlShi₄(benzoate)₄ MS (Figure Appx. C51, ESI): m/z calcd. for $\text{GdGa}_4\text{C}_{44}\text{H}_{36}\text{N}_4\text{O}_{24}$: 1441.80 [M]⁻; found: 1441.80 [M]⁻. Elemental analysis calcd. (%) for $\text{GdGa}_4\text{C}_{81}\text{H}_{74}\text{N}_6\text{O}_{27}\text{Na}$: C 48.36, H 3.60, N 4.19; found: C 48.10, H 3.69, N 4.16.

General synthesis procedure for Ln[12-MC_{Ga(III)N(mAlShi)-4](benzoate)₄(pyridinium)(pyridine)₂(MeOH)₂ metallacrowns (Ln^{III}: Yb^{III}, Sm^{III}, or Gd^{III}); LnGa₄mAlShi₄(benzoate)₄}. MCs were prepared following the same protocol described above. The synthetic yields were 15 – 40%.

YbGa₄mAlShi₄(benzoate)₄ MS (Figure Appx. C52, ESI): m/z calcd. for $\text{YbGa}_4\text{C}_{44}\text{H}_{36}\text{N}_4\text{O}_{24}$: 1455.81 [M]⁻; found: 1457.82 [M]⁻. Elemental analysis calcd. (%) for $\text{YbGa}_4\text{C}_{99}\text{H}_{81}\text{N}_8\text{O}_{36}\text{Na}_2$: C 48.40, H 3.32, N 4.56; found: C 48.33, H 3.35, N 4.53. Single-crystal

unit cell: monoclinic; space group P2(1)/n; a = 18.71481(14) Å, b = 23.81150(16) Å, c = 18.83666(11)Å; β = 90.3922(7)°; V = 8393.94(10) Å³.

SmGa₄mAlShi₄(benzoate)₄ ¹H NMR (Figure Appx. C53, 500 MHz, dms_o-d₆) δ 7.42 – 7.38 (m, 4H), 7.22 (t, *J* = 7.6 Hz, 4H), 6.91 (d, *J* = 9.0 Hz, 4H), 6.05 (tdd, *J* = 23.4, 10.2, 5.0 Hz, 4H), 5.47 – 5.16 (m, 8H), 4.51 (dd, *J* = 32.8, 5.1 Hz, 8H). (Figure Appx. C41, ESI): *m/z* calcd. for SmGa₄C₄₄H₃₆N₄O₂₄: 1433.79 [M]⁺; found: 1435.79 [M]⁺. Elemental analysis calcd. (%) for SmGa₄C₉₉H₇₉N₉O₃₉Na₅: C 46.40, H 3.11, N 4.92; found: C 46.21, H 3.11, N 4.88.

GdGa₄mAlShi₄(benzoate)₄ MS (Figure Appx. C54, ESI): *m/z* calcd. for GdGa₄C₄₄H₃₆N₄O₂₄: 1441.80 [M]⁺; found: 1441.79[M]⁺. Elemental analysis calcd. (%) for GdGa₄C₇₈H₆₅N₆O₂₅: C 48.73, H 3.41, N 4.37; found: C 48.69, H 3.47, N 4.49.

Ln₂Ga₈x-Shi₈Ip₄ Metallacrowns:

*General synthesis procedure for Ln₂[12-MC_{Ga(III)N(x-shi)-4}]₂(Ip)₄ metallacrowns (Ln^{III}: Yb^{III}, Sm^{III}, or Gd^{III}; x: *p*Yne, *m*Yne, *p*Al, and *m*Al; Shorthand: **Ln₂Ga₈xShi₄(Ip)₄**). MCs were synthesized by slight modification of previous literature procedures.¹²² LnGa₄xShi₄(Benzoate)₄ (1.0 mmol, 1 eq) and H₂Ip (2.1 mmol, 2.1 eq) were dissolved in DMF (10-20 mL) and stirred at room temperature for 6-12 hours. DMF was then removed with a stream of N₂ (g) over the reaction mixture. The product was then rinsed with cold methanol to yield off-white to pale orange MC powder depending on the ring ligand used for synthesis. The synthetic yields were ~80% based on the metallacrown.*

Ln₂Ga₈*p*YneShi₈Ip₄ Metallacrowns (Ln^{III}: Yb^{III}, Sm^{III}, or Gd^{III}):

*Yb₂Ga₈*p*YneShi₈(Ip)₄*. MS (Figure Appx. C55, ESI): *m/z* calcd. for Yb₂Ga₈C₁₁₂H₆₄N₈O₄₈: 1596.78 [M]²⁺; found 1597.28 [M]²⁺. Elemental analysis calcd. (%) for Yb₂Ga₈C₁₇₆H₁₆₆N₁₆O₆₆: C 47.34, H 3.75, N 5.02; found: C 47.34, H 3.78, N 5.04.

*Sm₂Ga₈*p*YneShi₈(Ip)₄*. ¹H NMR (Figure Appx. C42, 500 MHz, dms_o-d₆) δ 8.38 (dd, *J* = 26.7, 8.0 Hz, 8H), 8.17 (dd, *J* = 7.7, 1.8 Hz, 4H), 7.63 (t, 8H), 7.58 (t, *J* = 7.9 Hz, 4H), 6.54 (q, *J* = 4.3, 3.1 Hz, 8H), 6.40 – 6.33 (m, 8H), 4.80 (s, 16H), 3.57 (d, *J* = 2.3 Hz, 8H). MS (Figure Appx. C56, ESI): *m/z* calcd. for Sm₂Ga₈C₁₁₂H₆₄N₈O₄₈: 1575.76 [M]²⁺; found 1574.76 [M]²⁺. Elemental analysis calcd. (%) for Sm₂Ga₈C₁₄₇H₁₂₁N₁₁O₅₈: C46.12, H 3.19, N 4.02; found: C 46.09, H 3.21, N 4.04.

Ln₂Ga₈mYneShi₈Ip₄ Metallacrowns (Ln^{III}: Yb^{III}, Sm^{III}, or Gd^{III}):

Yb₂Ga₈mYneShi₈(Ip)₄. MS (Figure Appx. C58, ESI): *m/z* calcd. for Yb₂Ga₈C₁₁₂H₆₄N₈O₄₈: 1596.78 [M]²⁻; found 1596.78 [M]²⁻. Elemental analysis calcd. (%) for Yb₂Ga₈C₁₅₃H₁₂₆N₁₂O₆₁: C 45.80, H 3.17, N 4.19; found: C 45.80, H 3.15, N 4.15.

Sm₂Ga₈mYneShi₈(Ip)₄. ¹H NMR (Figure Appx. C43, 500 MHz, dms_o-d₆) δ 8.35 (d, *J* = 28.2 Hz, 8H), 8.22 (s, 4H), 7.56 (d, *J* = 8.3 Hz, 4H), 7.46 (d, *J* = 10.6 Hz, 8H), 6.92 (d, *J* = 23.1 Hz, 16H), 4.73 (s, 16H), 3.49 – 3.45 (m, 8H). MS (Figure Appx. C59, ESI): *m/z* calcd. for Sm₂Ga₈C₁₁₂H₆₄N₈O₄₈: 1575.76 [M]²⁻; found 1575.63 [M]²⁻. Elemental analysis calcd. (%) for Sm₂Ga₈C₁₄₉H₁₂₅N₁₁O₆₀: C 46.03, H 3.24, N 3.96; found: C 46.11, H 3.24, N 3.94.

Gd₂Ga₈mYneShi₈(Ip)₄. MS (Figure Appx. C60, ESI): *m/z* calcd. for Gd₂Ga₈C₁₁₂H₆₄N₈O₄₈: 1580.77 [M]²⁻; found 1581.64 [M]²⁻. Elemental analysis calcd. (%) for Gd₂Ga₈C₁₃₁H₁₀₇N₁₁O₅₈Na₂: C 42.74, H 2.93, N 4.19; found: C 42.83, H 2.92, N 4.14.

Ln₂Ga₈pAlShi₈Ip₄ Metallacrowns (Ln^{III}: Yb^{III}, Sm^{III}, or Gd^{III}):

Yb₂Ga₈pAlShi₈(Ip)₄. MS (Figure 3.5, ESI): *m/z* calcd. for Yb₂Ga₈C₁₁₂H₈₀N₈O₁₈: 1604.84 [M]²⁻; found: 1605.72 [M]²⁻. Elemental analysis calcd. (%) for Yb₂Ga₈C₁₄₁H₁₃₅N₁₁O₅₉: C 44.20, H 3.55, N 4.02; found: C 44.18, H 3.53, N 4.00.

Sm₂Ga₈pAlShi₈(Ip)₄. ¹H NMR (Figure 3.6, 500 MHz, dms_o-d₆) δ 8.37 (dd, *J* = 26.3, 8.0 Hz, 8H), 7.62 (t, *J* = 7.5 Hz, 4H), 7.59 (t, *J* = 7.9 Hz, 4H), 7.50 (t, *J* = 7.6 Hz, 8H), 6.47 (dd, *J* = 4.9, 2.4 Hz, 8H), 6.35 (dt, *J* = 8.8, 3.2 Hz, 8H), 6.05 (ddt, *J* = 16.1, 10.6, 5.2 Hz, 8H), 5.40 (d, *J* = 17.3 Hz, 8H), 5.26 (d, *J* = 10.5 Hz, 8H), 4.56 (dt, *J* = 13.1, 6.0 Hz, 16H). MS (Figure Appx. C61, ESI): *m/z* calcd. for Sm₂Ga₈C₁₁₂H₈₀N₈O₄₈: 1583.83 [M]²⁻; found 1583.70 [M]²⁻. Elemental analysis calcd. (%) for Sm₂Ga₈C₁₂₁H₁₁₁N₁₁O₅₆Na₂: C 41.29, H 3.18, N 4.38; found: C 41.23, H 3.20, N 4.39.

Gd₂Ga₈pAlShi₈(Ip)₄. MS (Figure Appx. C62, ESI): *m/z* calcd. for Gd₂Ga₈C₁₁₂H₈₀N₈O₄₈: 1588.83 [M]²⁻; found 1589.70 [M]²⁻. Elemental analysis calcd. (%) for Gd₂Ga₈C₁₂₂H₁₁₂N₁₀O₅₈: C 41.65, H 3.21, N 3.98; found: C 41.55, H 3.22, N 4.01.

Ln₂Ga₈mAlShi₈Ip₄ Metallacrowns (Ln^{III}: Yb^{III}, Sm^{III}, or Gd^{III}):

Yb₂Ga₈mAlShi₈(Ip)₄. MS (Figure Appx. C63, ESI): *m/z* calcd. for Yb₂Ga₈C₁₁₂H₈₀N₈O₁₈: 1604.84 [M]²⁻; found 1605.85 [M]²⁻. Elemental analysis calcd. (%) for Yb₂Ga₈C₁₅₁H₁₂₆N₁₀O₅₈:

C46.35, H 3.25, N 3.58; found: C 46.43, H 3.21, N 3.60.

Sm₂Ga₈AlShi₈(Ip)₄. ¹H NMR (Figure Appx. C44, 500 MHz, dms_o-d₆) δ 8.30 (d, *J* = 85.6 Hz, 8H), 7.60 (q, *J* = 9.0, 8.2 Hz, 4H), 7.50 (t, *J* = 7.6 Hz, 12H), 7.04 – 6.77 (m, 16H), 6.05 (dt, *J* = 15.5, 5.6 Hz, 8H), 5.39 (d, *J* = 17.3 Hz, 8H), 5.22 (d, *J* = 11.2 Hz, 8H), 4.55 – 4.49 (m, 16H). MS (Figure Appx. C64, ESI): *m/z* calcd. for Sm₂Ga₈C₁₁₂H₈₀N₈O₄₈: 1583.83 [M]²⁻; found 1582.83 [M]²⁻. Elemental analysis calcd. (%) for Sm₂Ga₈C₁₅₉H₁₄₆N₁₂O₆₅: C 46.31, H 3.57, N 4.08; found: C 46.39, H 23.55, N 4.07.

Gd₂Ga₈AlShi₈(Ip)₄. MS (Figure Appx. C65, ESI): *m/z* calcd. for Gd₂Ga₈C₁₁₂H₈₀N₈O₄₈: 1588.83 [M]²⁻; found 1588.69 [M]²⁻. Elemental analysis calcd. (%) for Gd₂Ga₈C₁₂₄H₁₁₈N₁₀O₅₉: C 41.78, H 3.34, N 3.93; found: C 41.77, H 3.37, N 3.99.

Small molecule coupling to LnGa₄xShi₄(Benzoate)₄ and Ln₂Ga₈xShi₈Ip₄

General coupling procedure of β-Mercaptoethanol to LnGa₄xShi₄(Benzoate)₄ (Ln^{III}: Yb^{III} and Sm^{III}; x: pYne, mYne, pAl, and mAl). The coupling reaction was done by dissolving the metallacrown (1 eq, 15-25 mg), β-Mercaptoethanol (βME, 20 eq), and 2,2-Dimethoxy-2-phenylacetophenone (DMPA, 0.16 eq) in degassed DMF to a concentration of 50 mg/mL based on the MC mass. The reaction mixture was sealed with a septum lid and then flushed with N₂ (g) for a minimum of 10 minutes. After this time, the reaction lid was wrapped with parafilm to ensure a complete seal, and placed in the LED Box for two hours. The reaction was monitored by ESI-MS. If partial coupling was observed, driving the reaction to completion was attempted by adding ¼ of the initial β-Mercaptoethanol concentration to the mixture, and stirred for two more hours as previously described. Once finished, the reaction was concentrated with a stream of N₂ (g) prior to purification. The dried product was then rinsed with copious amount of water to yield an off-white to pale orange powder that was dried under vacuum at room temperature overnight (>75% yield, post purification). *It is important to ensure that the reaction mixture is flushed with N₂ (g) prior to shining it with UV light since left over O₂ (g) can catalyzed unwanted radical formation that can interfere with the coupling reaction or induce unwanted side reactions.*

YbGa₄pYneShi₄(βME)₈₋₆. MS (Figure 3.13 (top) and Appx. C66, ESI): *m/z* calcd. for Yb₂Ga₈C₈₄H₉₂N₄O₃₂S₈: 2378.08 [M]⁻¹; found: 2378.02 [M]⁻¹. *m/z* calcd. for YbGa₄C₇₈H₈₈N₄O₃₂S₈: 2301.95 [M]⁻¹; found: 2302.00 [M]⁻¹. *m/z* calcd. for YbGa₄C₇₂H₈₀N₄O₃₂S₈: 2223.92 [M]⁻¹; found:

2223.99 [M]⁻¹. *m/z* calcd. for YbGa₄C₇₄H₇₆N₄O₃₀S₆: 2145.93 [M]⁻¹; found: 2145.97 [M]⁻¹. *m/z* calcd. for YbGa₄C₆₈H₇₂N₄O₃₀S₆: 2067.90 [M]⁻¹; found: 2067.96 [M]⁻¹.

YbGa₄mYneShi₄(βME)₆₋₀. MS (Figure 3.14 (top) and Appx. C67, ESI): *m/z* calcd. for YbGa₄C₈₀H₈₀N₄O₃₀S₆: 2220.96 [M]⁻¹; found: 2222.01 [M]⁻¹. *m/z* calcd. for YbGa₄C₇₈H₇₄N₄O₂₉S₅: 2141.95 [M]⁻¹; found: 2143.99 [M]⁻¹. *m/z* calcd. for YbGa₄C₇₆H₆₈N₄O₂₈S₄: 2065.93 [M]⁻¹; found: 2065.98 [M]⁻¹. *m/z* calcd. for YbGa₄C₇₄H₆₂N₄O₂₇S₃: 1985.92 [M]⁻¹; found: 1987.96 [M]⁻¹. *m/z* calcd. for YbGa₄C₇₂H₅₆N₄O₂₆S₂: 1907.90 [M]⁻¹; found: 1909.95 [M]⁻¹. *m/z* calcd. for YbGa₄C₇₀H₅₀N₄O₂₅S: 1831.89 [M]⁻¹; found: 1833.93 [M]⁻¹. *m/z* calcd. for YbGa₄C₆₈H₄₄N₄O₂₄: 1751.88 [M]⁻¹; found: 1753.91 [M]⁻¹.

YbGa₄pAlShi₄(βME)₄. MS (Figure 3.15 (top) and Appx. C68, ESI): *m/z* calcd. for YbGa₄C₇₆H₇₆N₄O₂₈S₄: 2073.99 [M]⁻¹; found: 2074.04 [M]⁻¹. *m/z* calcd. for YbGa₄C₇₀H₇₂N₄O₂₈S₄: 1997.96 [M]⁻¹; found: 1998.01 [M]⁻¹. *m/z* calcd. for YbGa₄C₆₄H₆₈N₄O₂₈S₄: 1921.93 [M]⁻¹; found: 1921.98 [M]⁻¹. *m/z* calcd. for YbGa₄C₅₈H₆₄N₄O₂₈S₄: 1845.90 [M]⁻¹; found: 1845.95 [M]⁻¹. *m/z* calcd. for YbGa₄C₅₃H₆₄N₄O₂₉S₄: 1799.89 [M•MeOH]⁻¹; found: 1799.94 [M•MeOH]⁻¹.

YbGa₄mAlShi₄(βME)₄. MS (Figure 3.16 (top) and Appx. C69, ESI): *m/z* calcd. for YbGa₄C₇₆H₇₆N₄O₂₈S₄: 2073.99 [M]⁻¹; found: 2074.04 [M]⁻¹. *m/z* calcd. for YbGa₄C₇₀H₇₂N₄O₂₈S₄: 1997.96 [M]⁻¹; found: 1998.04 [M]⁻¹. *m/z* calcd. for YbGa₄C₆₄H₆₈N₄O₂₈S₄: 1921.93 [M]⁻¹; found: 1922.03 [M]⁻¹. *m/z* calcd. for YbGa₄C₅₈H₆₄N₄O₂₈S₄: 1845.90 [M]⁻¹; found: 1844.02 [M]⁻¹. *m/z* calcd. for YbGa₄C₅₃H₆₄N₄O₂₉S₄: 1799.89 [M•MeOH]⁻¹; found: 1799.99 [M•MeOH]⁻¹.

SmGa₄pAlShi₄(βME)₄. MS (Figure 3.17 (top) and Appx. C70, ESI): *m/z* calcd. for SmGa₄C₇₆H₇₆N₄O₂₈S₄: 2051.97 [M]⁻¹; found: 2052.02 [M]⁻¹. *m/z* calcd. for SmGa₄C₇₀H₇₂N₄O₂₈S₄: 1975.94 [M]⁻¹; found: 1976.01 [M]⁻¹. *m/z* calcd. for SmGa₄C₆₄H₆₈N₄O₂₈S₄: 1899.91 [M]⁻¹; found: 1899.99 [M]⁻¹. *m/z* calcd. for SmGa₄C₅₈H₆₄N₄O₂₈S₄: 1823.88 [M]⁻¹; found: 1821.97 [M]⁻¹.

SmGa₄mAlShi₄(βME)₄. MS (Figure 3.17 (bottom) and Appx. C71, ESI): *m/z* calcd. for SmGa₄C₇₆H₇₆N₄O₂₈S₄: 2051.97 [M]⁻¹; found: 2052.02 [M]⁻¹. *m/z* calcd. for SmGa₄C₇₀H₇₂N₄O₂₈S₄: 1975.94 [M]⁻¹; found: 1976.01 [M]⁻¹. *m/z* calcd. for SmGa₄C₆₄H₆₈N₄O₂₈S₄: 1899.91 [M]⁻¹; found: 1898.00 [M]⁻¹. *m/z* calcd. for SmGa₄C₅₈H₆₄N₄O₂₈S₄: 1823.88 [M]⁻¹; found: 1823.99 [M]⁻¹.

General coupling procedure of β -Mercaptoethanol to $Yb_2Ga_8xShi_8(Ip)_4$ (x : $pYne$, $mYne$, pAl , and mAl). The coupling reaction was done by dissolving the metallacrown (1 eq, 10-30 mg), β -Mercaptoethanol (β ME, 40 eq), and 2,2-Dimethoxy-2-phenylacetophenone (DMPA, 0.32 eq) in degassed DMF to a concentration of 50 mg/mL based on the MC mass. The reaction mixture was sealed with a septum lid and then flushed with N_2 (g) for a minimum of 10 minutes. After this time, the reaction lid was wrapped with parafilm to ensure a complete seal, and placed in the LED Box for four hours. The reaction was monitored by ESI-MS. If partial coupling was observed, driving the reaction to completion was attempted by adding $\frac{1}{4}$ of the initial β -Mercaptoethanol concentration to the mixture, and stirred for two more hours as previously described. Once finished, the reaction was concentrated with a stream of N_2 (g) prior to purification. The dried product was then rinsed with copious amounts of water to yield an off-white to pale orange powder that was dried under vacuum at room temperature overnight (>65% yield after purification). Once again, N_2 (g) flushing is necessary to remove as much O_2 (g) as possible.

$Yb_2Ga_8pYneShi_8Ip_4(\beta ME)_{16-14}$. MS (Figure 3.13 (bottom) and Appx. C72, ESI): m/z calcd. for $Yb_2Ga_8C_{144}H_{160}N_8O_{64}S_{16}$: 2221.39 $[M]^{-2}$; found: 2221.88 $[M]^{-2}$. m/z calcd. for $Yb_2Ga_8C_{142}H_{154}N_8O_{63}S_{15}$: 2181.39 $[M]^{-2}$; found: 2183.88 $[M]^{-2}$. m/z calcd. for $Yb_2Ga_8C_{140}H_{148}N_8O_{62}S_{14}$: 2141.88 $[M]^{-1}$; found: 2160.87 $[M]^{-1}$.

$Yb_2Ga_8mYneShi_8Ip_4(\beta ME)_{16-11}$. MS (Figure 3.14 (bottom) and Appx. C73, ESI): m/z calcd. for $Yb_2Ga_8C_{144}H_{160}N_8O_{64}S_{16}$: 2221.39 $[M]^{-2}$; found: 2221.87 $[M]^{-2}$. m/z calcd. for $Yb_2Ga_8C_{142}H_{164}N_8O_{63}S_{15}$: 2181.39 $[M]^{-2}$; found: 2182.87 $[M]^{-2}$. m/z calcd. for $Yb_2Ga_8C_{140}H_{148}N_8O_{62}S_{14}$: 2141.88 $[M]^{-2}$; found: 2143.36 $[M]^{-2}$. m/z calcd. for $Yb_2Ga_8C_{138}H_{142}N_8O_{61}S_{13}$: 2104.37 $[M]^{-2}$; found: 2104.85 $[M]^{-2}$. m/z calcd. for $Yb_2Ga_8C_{136}H_{136}N_8O_{60}S_{12}$: 2064.37 $[M]^{-2}$; found: 2065.84 $[M]^{-2}$. m/z calcd. for $Yb_2Ga_8C_{135}H_{134}N_8O_{60}S_{11}$: 2041.37 $[M]^{-2}$; found: 2046.84 $[M]^{-2}$.

$Yb_2Ga_8pAlShi_8Ip_4(\beta ME)_{8-6}$. MS (Figure 3.15 (bottom) and Appx. C74, ESI): m/z calcd. for $Yb_2Ga_8C_{128}H_{128}N_8O_{56}S_8$: 1917.40 $[M]^{-2}$; found: 1916.93 $[M]^{-2}$. m/z calcd. for $Yb_2Ga_8C_{126}H_{122}N_8O_{55}S_7$: 1878.68 $[M]^{-2}$; found: 1879.43 $[M]^{-2}$. m/z calcd. for $Yb_2Ga_8C_{124}H_{116}N_8O_{54}S_6$: 1838.39 $[M]^{-2}$; found: 1841.43 $[M]^{-2}$.

$Yb_2Ga_8mAlShi_8Ip_4(\beta ME)_{8-5}$. MS (Figure 3.16 (bottom) and Appx. C75, ESI): m/z calcd. for

$\text{Yb}_2\text{Ga}_8\text{C}_{128}\text{H}_{128}\text{N}_8\text{O}_{56}\text{S}_8$: 1917.40 [M]⁻²; found: 1917.44 [M]⁻². *m/z* calcd. for
 $\text{Yb}_2\text{Ga}_8\text{C}_{126}\text{H}_{122}\text{N}_8\text{O}_{55}\text{S}_7$: 1878.39 [M]⁻²; found: 1878.94 [M]⁻². *m/z* calcd. for
 $\text{Yb}_2\text{Ga}_8\text{C}_{124}\text{H}_{116}\text{N}_8\text{O}_{54}\text{S}_6$: 1838.39 [M]⁻²; found: 1840.94 [M]⁻². *m/z* calcd. for
 $\text{Yb}_2\text{Ga}_8\text{C}_{122}\text{H}_{110}\text{N}_8\text{O}_{53}\text{S}_5$: 1798.89 [M]⁻²; found: 1802.94 [M]⁻².

Thiol focal point PAMAM dendrons:

General synthesis, protection, and deprotection procedures of thiol focal PAMAM dendrons of different generations (HS-GX; X: 1 or 1.5) are detailed in the experimental section of Chapter II of this thesis. Freshly deprotected dendrons were used for the coupling reactions to metallacrowns.

Hyperboloidal Dendrimeric Metallacrown (H-DMC) synthetic trials and purification:

This section details the different synthetic reaction conditions and approaches (UV-light catalyzed and heat catalyzed) explored in order to synthesize hyperboloidal dendrimer metallacrowns. Both thiol-yne and thiol-ene coupling reactions were explored with the four set of metallacrowns described above ($\text{Ln}_2\text{Ga}_8\text{xShi}_8\text{Ip}_4$; x: *pYne*, *mYne*, *pAl*, and *mAl*).

Purification details: Sample purification was done using RC dialysis bags with a MWCO of 3.5 kDa, and with DMSO as the dialysate. To start, DMC samples were concentrated slowly with a stream of N₂ (g) as to remove the initial DMF, and then redissolved with DMSO to the same initial concentration. The volume of dialysate was 200 times the volume of the sample inside the dialysis bag. To avoid dialysis bag decomposition, new bags were used every 24 hours, and dialysate was also exchanged daily. Mass spectra of the sample was taken daily to monitor the removal of free dendron. Once the dendron peak was not observed by ESI-MS, the dialysis was stopped, and the sample was slowly concentrated to about ¼ of the original volume with a stream of N₂ (g). Sample concentration was determined by UV-Vis spectrometry by using the extinction coefficient of the metallacrown core prior dendron coupling. *It is important to avoid complete removal of all the solvent, or temperatures above 35°C so as to avoid defect formation. DMCs were stored as DMSO solutions for further characterization.*

Thiol-yne coupling of PAMAM dendrons to Yb₂Ga₈PYneShi₈Ip₄. The general procedures for each synthetic approach are described below, with the specific reaction conditions detailed under the Result section.

UV light-catalyzed **Approach A**: This coupling reaction was done by dissolving the metallacrown (5-10 mg, 1 eq), HS-GX (X: 1.0 or 1.5) dendron (40 eq), and 2,2-Dimethoxy-2-phenylacetophenone (DMPA) in degassed DMF. The reaction mixture was sealed with a septum lid and then flushed with N₂ (g) for a minimum of 10 minutes. After this time, the reaction lid was wrapped with parafilm to ensure a complete seal, and placed in the UV LED Box for the designed number of hours. Reactions were monitored by ESI-MS. If partial coupling was observed, driving the reaction to completion was attempted by adding ¼ of the initial dendron concentration to the reaction, and stirred again under the UV light for the initially designated amount of time.

<i>Yb₂Ga₈PYneShi₈Ip₄</i>	<i>Gl.0₈₋₁</i>	MS	(Figure	3.20,	ESI):	<i>m/z</i>	calcd.	for
Yb ₂ Ga ₈ C ₂₀₈ H ₂₈₅ N ₄₈ O ₆₄ S ₈ :	1880.37	[M] ³⁺ ;	found:	1880.37	[M] ³⁺ .	<i>m/z</i>	calcd.	for
Yb ₂ Ga ₈ C ₁₉₆ H ₂₅₈ N ₄₃ O ₆₂ S ₇ :	1778.31	[M] ³⁺ ;	found:	1778.97	[M] ³⁺ .	<i>m/z</i>	calcd.	for
Yb ₂ Ga ₈ C ₁₈₄ H ₂₃₁ N ₃₈ O ₆₀ S ₆ :	1676.91	[M] ³⁺ ;	found:	1676.90	[M] ³⁺ .	<i>m/z</i>	calcd.	for
Yb ₂ Ga ₈ C ₁₇₂ H ₂₀₃ N ₃₃ O ₅₈ S ₅ :	2361.27	[M] ²⁺ ;	found:	2363.23	[M] ²⁺ .	<i>m/z</i>	calcd.	for
Yb ₂ Ga ₈ C ₁₆₀ H ₁₇₆ N ₂₈ O ₅₆ S ₄ :	2209.67	[M] ²⁺ ;	found:	2208.14	[M] ²⁺ .	<i>m/z</i>	calcd.	for
Yb ₂ Ga ₈ C ₁₄₈ H ₁₄₉ N ₂₃ O ₅₄ S ₃ :	2056.08	[M] ²⁺ ;	found:	2056.06	[M] ²⁺ .	<i>m/z</i>	calcd.	for
Yb ₂ Ga ₈ C ₁₃₆ H ₁₂₂ N ₁₈ O ₅₂ S ₂ :	1902.98	[M] ²⁺ ;	found:	1903.97	[M] ²⁺ .	<i>m/z</i>	calcd.	for
Yb ₂ Ga ₈ C ₁₂₄ H ₉₅ N ₁₃ O ₅₀ S ₁ :	1751.89	[M] ²⁺ ;	found:	1751.38	[M] ²⁺ .			

<i>Yb₂Ga₈PYneShi₈Ip₄</i>	<i>Gl.5₈₋₄</i>	MS	(Figure	3.21,	ESI):	<i>m/z</i>	calcd.	for
Yb ₂ Ga ₈ C ₃₃₆ H ₄₇₉ N ₄₈ O ₁₂₈ S ₈ :	1679.26	[M] ⁵⁺ ;	found:	1679.84	[M] ⁵⁺ .	<i>m/z</i>	calcd.	for
Yb ₂ Ga ₈ C ₃₀₈ H ₄₂₇ N ₄₃ O ₁₁₈ S ₇ :	1936.49	[M] ⁴⁺ ;	found:	1937.48	[M] ⁴⁺ .	<i>m/z</i>	calcd.	for
Yb ₂ Ga ₈ C ₂₈₀ H ₃₇₅ N ₃₈ O ₁₀₈ S ₆ :	2365.21	[M] ³⁺ ;	found:	2366.85	[M] ³⁺ .	<i>m/z</i>	calcd.	for
Yb ₂ Ga ₈ C ₂₅₂ H ₃₂₄ N ₃₃ O ₉₈ S ₅ :	2148.09	[M] ³⁺ ;	found:	2149.36	[M] ³⁺ .	<i>m/z</i>	calcd.	for
Yb ₂ Ga ₈ C ₂₂₄ H ₂₇₃ N ₂₈ O ₈₈ S ₄ :	1931.98	[M] ³⁺ ;	found:	1932.62	[M] ³⁺ .			

UV light-catalyzed **Approach B**: The coupling reaction was done by dissolving the metallacrown (5-10 mg, 1 eq), HS-GX dendron (40 eq), and 4,4'-

Bis(dimethylamino)benzophenone (Michler's Ketone, 0.32 eq), in degassed DMF to a concentration of 10 mg/mL based on the MC mass. The reaction mixture was sealed with a septum lid and then flushed with N₂ (g) for 10 minutes minimum. After this time, the reaction lid was wrapped with parafilm to ensure a complete seal, and place in the LED Box for 2 hours. Reactions were monitored by ESI-MS. If partial coupling was observed, driving the reaction to completion was attempted by adding ¼ of the initial dendron concentration to the reaction, and stirred again under the UV light for the initially designated amount of time.

Yb₂Ga₈pYneShi₈Ip₄ GI.0₆₋₄. MS (Figure 3.22, ESI): Yb₂Ga₈C₁₈₄H₂₃₁N₃₈O₆₀S₆: 1676.91 [M]³⁺; found: 1678.89 [M]³⁺. *m/z* calcd. for Yb₂Ga₈C₁₇₂H₂₀₃N₃₃O₅₈S₅: 2361.27 [M]²⁺; found: 2361.75 [M]²⁺. *m/z* calcd. for Yb₂Ga₈C₁₆₀H₁₇₆N₂₈O₅₆S₄: 2209.67 [M]²⁺; found: 2209.67 [M]²⁺.

Yb₂Ga₈pYneShi₈Ip₄ GI.5₈₋₆. MS (Figure 3.23, ESI): *m/z* calcd. for Yb₂Ga₈C₃₃₆H₄₇₉N₄₈O₁₂₈S₈: 1679.26 [M]⁵⁺; found: 1679.64 [M]⁵⁺. *m/z* calcd. for Yb₂Ga₈C₃₀₈H₄₂₇N₄₃O₁₁₈S₇: 1936.49 [M]⁴⁺; found: 1936.97 [M]⁴⁺. *m/z* calcd. for Yb₂Ga₈C₂₈₀H₃₇₅N₃₈O₁₀₈S₆: 2365.21 [M]³⁺; found: 2365.85 [M]³⁺.

Heat-catalyzed **Approach C**: The coupling reaction was done by dissolving the metallacrown (5-10 mg, 1 eq), HS-GX dendron (40 eq), and azobisisobutyronitrile (AIBN, 0.32 eq) in degassed DMF to a concentration of 25 mg/mL based on the MC mass. The reaction mixture was sealed with a septum lid and then flushed with N₂ (g) for 10 minutes minimum. After this time, the reaction lid was wrapped with parafilm to ensure a complete seal, and stirred at 80°C for 3 hours.

Yb₂Ga₈pYneShi₈Ip₄ GI.0₄₋₁. MS (Figure 3.22, ESI): *m/z* calcd. for Yb₂Ga₈C₁₆₀H₁₇₆N₂₈O₅₆S₄: 2209.67 [M]²⁺; found: 2207.65 [M]²⁺. *m/z* calcd. for Yb₂Ga₈C₁₄₈H₁₄₉N₂₃O₅₄S₃: 2056.08 [M]²⁺; found: 2056.05 [M]²⁺. *m/z* calcd. for Yb₂Ga₈C₁₃₆H₁₂₂N₁₈O₅₂S₂: 1902.98 [M]²⁺; found: 1903.98 [M]²⁺. *m/z* calcd. for Yb₂Ga₈C₁₂₄H₉₅N₁₃O₅₀S₁: 1751.89 [M]²⁺; found: 1751.89 [M]²⁺.

Thiol-ene coupling of PAMAM dendrons to YbGa₄pAlShi₄(benzoate)₄, Yb₂Ga₈pAlShi₈Ip₄, and Yb₂Ga₈mAlShi₈Ip₄. The general procedures for each synthetic approach are described below, with the specific reaction conditions detailed under the Result section.

UV light-catalyzed **Approach A**: The coupling reaction was done by dissolving the metallacrown (5-30 mg, 1 eq), HS-GX dendron (80 eq), and 2,2-Dimethoxy-2-phenylacetophenone (DMPA) in degassed DMF. The reaction mixture was sealed with a septum lid and then flushed with N₂ (g) for 10 minutes minimum. After this time, the reaction lid was wrapped with parafilm to ensure a complete seal, and place in the UV LED Box. If partial coupling was observed, driving the reaction to completion was attempted by adding ¼ of the initial dendron concentration to the reaction, and stirred again under the UV light for the initially designated amount of time.

YbGa₄pAlShi₄(benzoate)₄ G1.0₄. MS (Figure 3.24, ESI): *m/z* calcd. for YbGa₄C₁₄₆H₁₉₀N₃₀O₃₂Na₃S₄: 1763.46 [M•3Na•3Py]²⁺; found: 1764.01[M•3Na•3Py]²⁺. *m/z* calcd. for YbGa₄C₁₃₆H₁₈₃N₂₈O₃₂S₄: 1651.44 [M•4Py]²⁺; found: 1648.45 [M•4Py]²⁺. *m/z* calcd. for YbGa₄C₁₃₁H₁₇₈N₂₇O₃₂S₄: 1610.42 [M•3Py]²⁺; found: 1609.94 [M•3Py]²⁺. *m/z* calcd. for YbGa₄C₁₂₁H₁₆₆N₂₅O₃₂Na₂S₄: 1554.36 [M•2Na•Py]²⁺; found: 1554.94 [M•2Na•Py]²⁺. *m/z* calcd. for YbGa₄C₁₁₆H₁₆₂N₂₄O₃₂NaS₄: 1503.85 [M•Na]²⁺; found: 1505.91 [M•Na]²⁺. *m/z* calcd. for YbGa₄C₁₁₀H₁₅₇N₂₄O₃₂Na₂S₄: 1476.82 [M•2Na]²⁺; found: 1475.86 [M•2Na]²⁺. *m/z* calcd. for YbGa₄C₁₀₄H₁₅₃N₂₄O₃₂Na₂S₄: 1438.81 [M•2Na]²⁺; found: 1439.79 [M•2Na]²⁺. Reaction yield post purification ~70% as determined by UV-Vis concentration.

Yb₂Ga₈pAlShi₈Ip₄ G1.0₈₋₆. MS (Figure 3.25, ESI): *m/z* calcd. for Yb₂Ga₈C₁₉₂H₂₃₆N₁₆O₈₀S₈: 2602.78 [M]²⁺; found: 2604.30 [M]²⁺. *m/z* calcd. for Yb₂Ga₈C₁₈₂H₂₁₇N₁₅O₇₆S₇: 2479.72 [M]²⁺; found: 2479.75 [M]²⁺. *m/z* calcd. for Yb₂Ga₈C₁₇₂H₁₉₈N₁₄O₇₂S₆: 2354.67 [M]²⁺; found: 2355.20 [M]²⁺. *m/z* calcd. for Yb₂Ga₈C₁₆₂H₁₇₉N₁₃O₆₈S₅: 2231.13 [M]²⁺; found: 2231.65 [M]²⁺. *m/z* calcd. for Yb₂Ga₈C₁₅₂H₁₆₀N₁₂O₆₄S₄: 2106.58 [M]²⁺; found: 2106.60 [M]²⁺. Reaction yield post purification ~65-80% as determined by UV-Vis concentration.

Yb₂Ga₈mAlShi₈Ip₄ G1.0₈₋₆. MS (Figure 3.26, ESI): *m/z* calcd. for Yb₂Ga₈C₂₀₈H₃₀₁N₄₈O₆₄S₆: 1885.74 [M]³⁺; found: 1885.72 [M]³⁺. *m/z* calcd. for

Yb₂Ga₈C₁₉₆H₂₇₄N₄₃O₆₂S₇: 1783.68 [M]³⁺; found: 1784.66 [M]³⁺. *m/z* calcd. for Yb₂Ga₈C₁₈₄H₂₄₇N₃₈O₆₀S₆: 1682.29 [M]³⁺; found: 1683.61 [M]³⁺.

Yb₂Ga₈AlShi₈Ip₄ G1.0₇₋₁. MS (Figure 3.27, ESI): *m/z* calcd. for Yb₂Ga₈C₁₉₆H₂₇₃N₄₃O₆₂S₇: 2674.52 [M]²⁺; found: 2675.49 [M]²⁺. *m/z* calcd. for Yb₂Ga₈C₁₈₄H₂₄₆N₃₈O₆₀S₆: 2522.43 [M]²⁺; found: 2523.42 [M]²⁺. *m/z* calcd. for Yb₂Ga₈C₁₇₂H₂₁₉N₃₃O₅₈S₅: 2369.33 [M]²⁺; found: 2380.81 [M]²⁺. *m/z* calcd. for Yb₂Ga₈C₁₆₀H₁₉₂N₂₈O₅₆S₄: 2217.74 [M]²⁺; found: 2218.73 [M]²⁺. *m/z* calcd. for Yb₂Ga₈C₁₄₈H₁₆₅N₂₃O₅₄S₃: 2064.14 [M]²⁺; found: 2066.14 [M]²⁺. *m/z* calcd. for Yb₂Ga₈C₁₃₆H₁₃₈N₁₈O₅₂S₂: 1911.05 [M]²⁺; found: 1913.03 [M]²⁺. *m/z* calcd. for Yb₂Ga₈C₁₂₄H₁₁₁N₁₃O₅₀S₁: 1759.95 [M]²⁺; found: 1761.46 [M]²⁺.

Heat-catalyzed **Approach C**: The coupling reaction was done by dissolving the metallacrown (5-10 mg, 1 eq), HS-GX dendron (80 eq), and azobisisobutyronitrile (AIBN, 10 eq) in degassed DMF to a concentration of 10 mg/mL based on the MC mass. The reaction mixture was sealed with a septum lid and then flushed with N₂ (g) for 10 minutes minimum. After this time, the reaction lid was wrapped with parafilm to ensure a complete seal, and stirred at 80°C for 14 hours.

Yb₂Ga₈AlShi₈Ip₄ G1.0₂₋₁. MS (Figure 3.28, ESI): *m/z* calcd. for Yb₂Ga₈C₁₃₆H₁₃₈N₁₈O₅₂S₂: 1911.05 [M]²⁺; found: 1913.51 [M]²⁺. *m/z* calcd. for Yb₂Ga₈C₁₂₄H₁₁₁N₁₃O₅₀S₁: 1759.95 [M]²⁺; found: 1761.44 [M]²⁺.

3.2.6 Luminescence Studies

Solution state absorbance was collected using a Cary 100Bio UV-Vis spectrometer in absorbance mode. MC samples were prepared by dissolving them in 3 mL of DMSO with a final concentration of 1-200 μM, while DMC samples were recorded as DMSO solutions post purification. Data were processed using OriginPro 2020 software.

Solution state emission of MCs coupled to small molecules were collected using a Horiba Quanta Master spectrometer in emission state mode. Samples were prepared by dissolving them in 3 mL of DMSO or methanol with a final concentration of 1-20 μM. Data were processed using OriginPro 2020 software.

Photophysical measurements were performed and analyzed by Dr. Svetlana Eliseeva at the Centre de Biophysique Moléculaire, Orleans, France. Luminescence data of MCs were collected on freshly prepared solutions in DMSO or in the solid state placed into 2.4 mm i.d. quartz capillaries, while DMC samples were diluted to 50 μ M solutions and only recorded in solution state. Emission and excitation spectra were measured on a Horiba-Jobin-Yvon Fluorolog 3 spectrofluorimeter equipped with either a visible photomultiplier tube (PMT) (220-800 nm, R928P; Hamamatsu), a NIR solid-state InGaAs detector cooled to 77 K (800-1600 nm, DSS-IGA020L; ElectroOptical Systems, Inc., USA), or a NIR PMT (950-1650 nm, H10330-75; Hamamatsu). All spectra were corrected for the instrumental functions. Luminescence lifetimes were determined under excitation at 355 nm provided by a Nd:YAG laser (YG 980; Quantel). Luminescent signals were detected in the visible or NIR ranges with a R928 or H10330-75 PMTs connected to the iHR320 monochromator (Horiba Scientific), respectively. The output signals from the detectors were fed into a 500 MHz bandpass digital oscilloscope (TDS 754C; Tektronix) and transferred to a PC for data processing with the Origin 8 software. Luminescence lifetimes are reported as the average of three or more independent measurements. Quantum yields were determined with a Fluorolog 3 spectrofluorimeter based on the absolute method using an integration sphere (GMP SA). Each sample was measured several times varying the position of samples. Estimated experimental error for the determination of quantum yields is estimated as \sim 10%. Details on the instrument set up to measure quantum yields is described in the experimental section of Chapter 2, under luminescent studies.

3.3 Results

3.3.1 $\text{LnGa}_4\text{xShi}_4(\text{Benzoate})_4$ and $\text{Ln}_2\text{Ga}_8\text{xShi}_8\text{Ip}_4$ Metallacrowns

Synthesis and physical characterization of $\text{LnGa}_4\text{xShi}_4(\text{Benzoate})_4$. The reaction between H_3xShi (x: *p*Yne, *m*Yne, *p*Al, and *m*Al), $\text{Ga}(\text{NO}_3)_3 \cdot x\text{H}_2\text{O}$, $\text{Ln}(\text{NO}_3)_3 \cdot x\text{H}_2\text{O}$ ($\text{Ln}^{\text{III}} = \text{Yb}^{\text{III}}$, Sm^{III} , and Gd^{III}), and sodium benzoate in a mixture of methanol and pyridine resulted in the formation of metallacrown scaffolds with the general formula $\text{Ln}[12\text{-MC}_{\text{Ga}(\text{III})\text{N}(\text{xShi})\text{-4}}](\text{C}_6\text{H}_5\text{CO}_2)_4(\text{C}_5\text{H}_6\text{N})(\text{C}_5\text{H}_5\text{N})_2(\text{CH}_3\text{OH})_2$ (shorthand: $\text{LnGa}_4\text{xShi}_4(\text{Benzoate})_4$). Solids were collected as crystalline material that were characterized by ESI-MS, ^1H NMR (for Sm^{III} compounds), elemental analysis, and single crystal X-ray diffraction. As seen in Figure 3.2, the ESI-MS spectrum of $\text{YbGa}_4\text{pAlShi}_4(\text{Benzoate})_4$ is consistent with the MC structure, and displays

a single distribution with an isotopic separation of 1.0 m/z, corroborating the intrinsic -1 charge of the metallocrown. ESI-MS spectra of scaffolds prepared with each of the four ring ligands (*p*YneShi, *m*YneShi, *p*AlShi, and *m*AlShi), and three different Ln^{III}-ions (Yb^{III}, Sm^{III}, and Gd^{III}) can be found in Appendix C Figures 44-54.

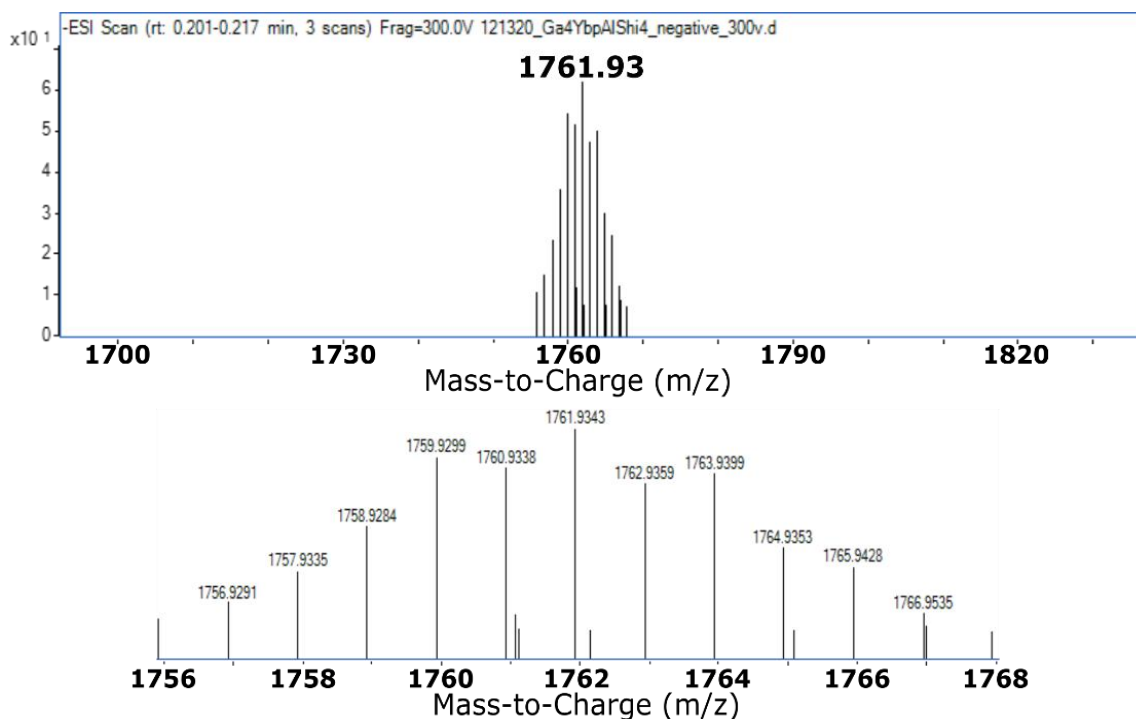


Figure 3.2 (Top) ESI-MS of YbGa₄pAlShi₄(Benzoate)₄ MC in negative ion mode. (Bottom) expansion of the major peak corroborating the -1 isotopic distribution of the complex.

Figure 3.3 shows the ¹H NMR spectrum of SmGa₄pAlShi₄(Benzoate)₄ in *d*₆-DMSO, which is consistent with a pseudo-four-fold symmetry axis within the scaffold. On the spectrum below, three signals are assigned to the aromatic protons of the *p*AlShi³⁻ ring (~6.4, 7.2, and 7.4 ppm), while three more signals are assigned to the alkene chain (~4.6, 5.3, and 6.1 ppm). For the alkyne derivatives, two signals are assigned around the same region. ¹H NMR spectra of each Sm^{III} metallocrown derivative suggest that all complexes possess the same composition – i.e., four ring ligands and four benzoate bridging ligands. The ¹H NMR spectra for the other three monomeric Sm^{III} derivatives (SmGa₄*m*AlShi₄(Benzoate)₄, SmGa₄*p*YneShi₄(Benzoate)₄, and SmGa₄*m*YneShi₄(Benzoate)₄) are shown in Appendix C Figures 38-40.

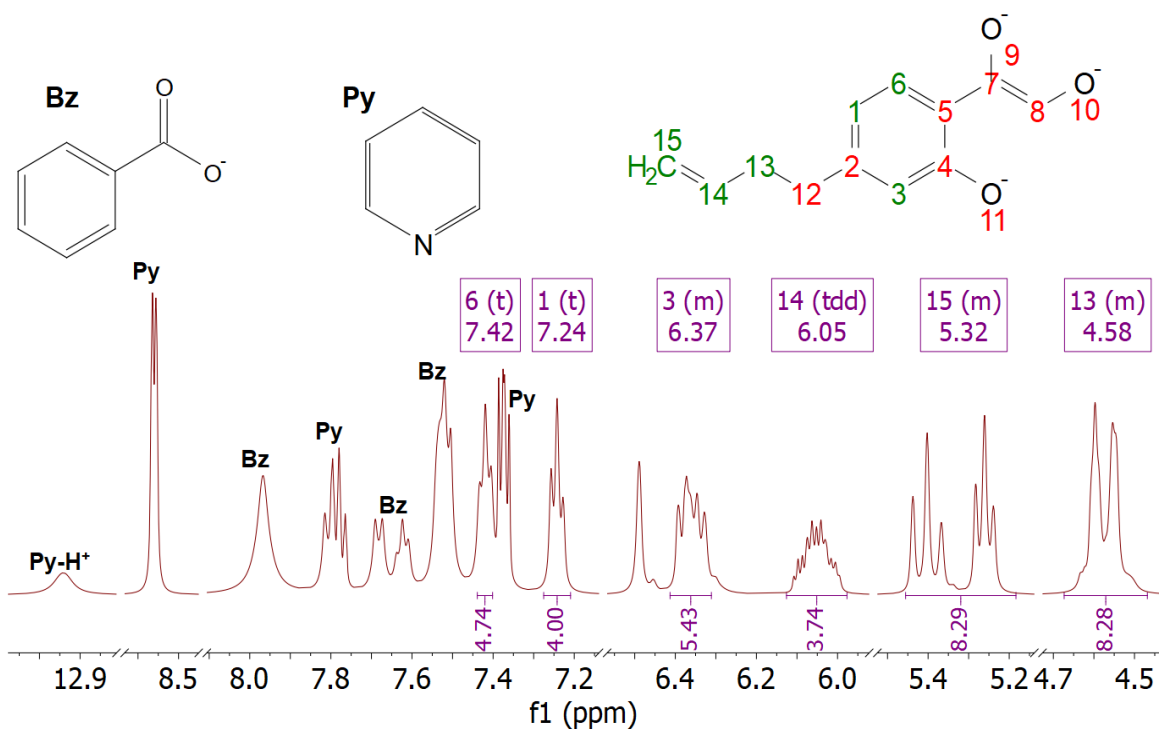


Figure 3.3 ^1H NMR spectrum of $\text{SmGa}_4\text{pAlShi}_4(\text{Benzoate})_4$ in d_6 -DMSO. Labeled peaks from the ring ligands. Pyridine and benzoate peaks labeled separately.

X-ray quality crystals were collected and analyzed for $\text{YbGa}_4\text{pYneShi}_4(\text{Benzoate})_4$, $\text{YbGa}_4\text{mYneShi}_4(\text{Benzoate})_4$ and $\text{YbGa}_4\text{mAlShi}_4(\text{Benzoate})_4$ scaffolds. The crystal structures of the three metallacrowns are shown in Figure 3.4. $\text{YbGa}_4\text{pYneShi}_4(\text{Benzoate})_4$ and $\text{YbGa}_4\text{mAlShi}_4(\text{Benzoate})_4$ scaffolds were solved using the monoclinic $P2_1/n$ space group, while $\text{YbGa}_4\text{mYneShi}_4(\text{Benzoate})_4$ was solved using the triclinic $P1$ space group. Due to the solvation of $\text{YbGa}_4\text{mYneShi}_4(\text{Benzoate})_4$, the crystal structure was solved as a dimer; however, no covalent bonds linking the two units are observed. This is further corroborated by the fact that by ESI-MS and NMR the $\text{LnGa}_4\text{mYneShi}_4(\text{Benzoate})_4$ is seen as a single monomeric unit. Structurally, the MC rings of each structure are slightly concave and are templated by four $x\text{Shi}^{3-}$ ligands bridging four Ga^{III} ions. The Yb^{III} ion is located at the center of the MC ring, bound by four hydroximate oxygen ions. The central Yb^{III} ion is also bridged to the central ring by four benzoate ligands, and adopts an 8-coordinate square antiprism geometry. Both scaffolds possess pseudo- C_4 symmetry about the Ln^{III} (as was indicated by the ^1H NMR above) and the negative charge is balanced with a single pyridinium counterion. Additional crystallographic details are provided in Table 3.1.

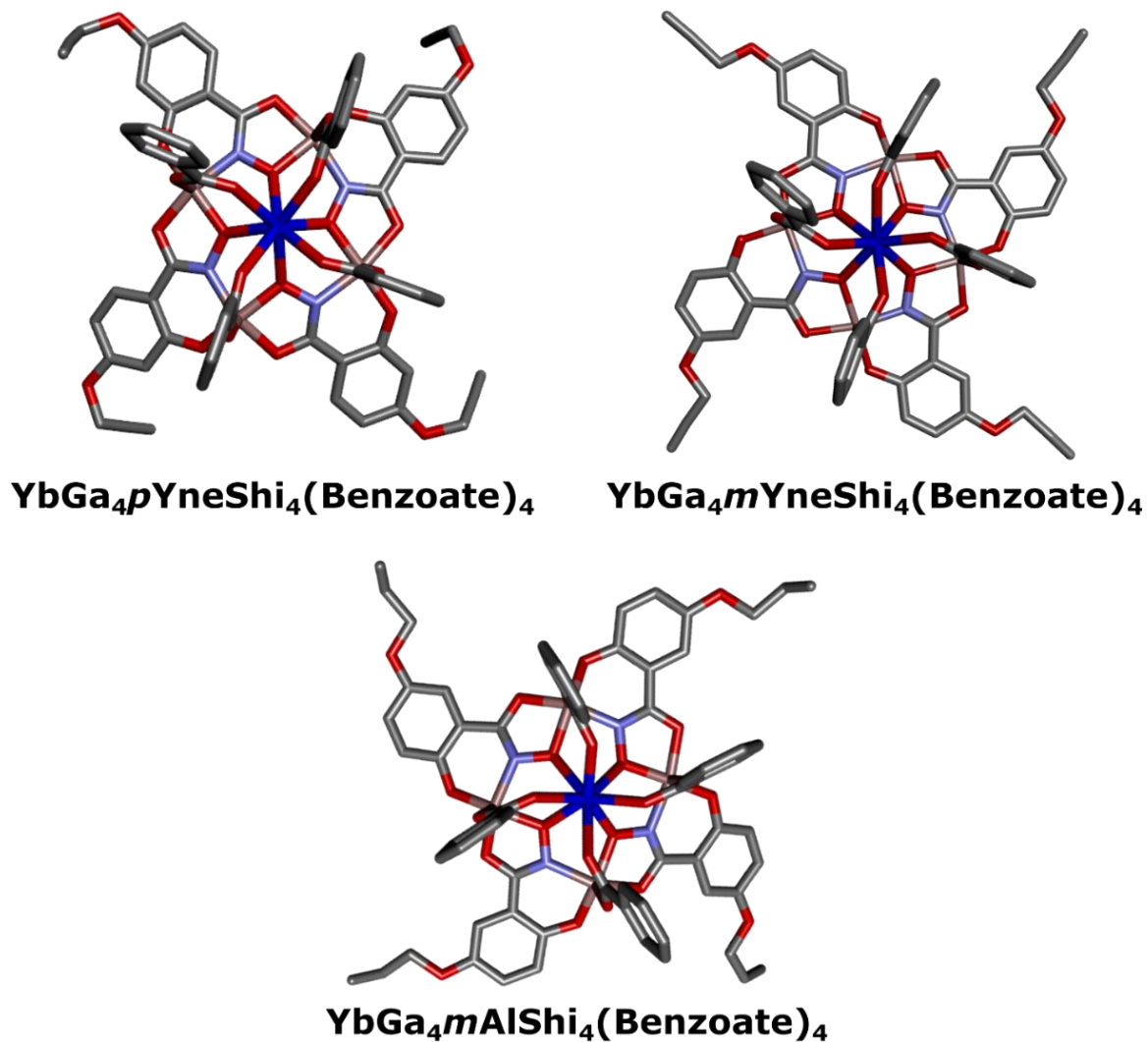


Figure 3.4 Top-down views of molecular structures of YbGa₄*p*YneShi₄(Benzoate)₄, YbGa₄*m*YneShi₄(Benzoate)₄, and YbGa₄*m*AlShi₄(Benzoate)₄ scaffolds obtained from X-ray diffraction. Hydrogen atoms, counterions, and solvent molecules have been omitted for clarity. Color code: Yb^{III}, blue; Ga^{III}, pink; N, violet; O, red; C, gray.

Table 3.1 Crystallographic details for **YbGa₄pYneShi₄(Benzoate)₄**, **YbGa₄mYneShi₄(Benzoate)₄**, and **YbGa₄mAlShi₄(Benzoate)₄** metallacrowns

	YbGa₄pYneShi₄	YbGa₄mYneShi₄	YbGa₄mAlShi₄
Formula	C ₈₅ H ₆₈ Ga ₄ N ₇ O ₂₆ Yb	C _{164.5} H _{121.5} Ga ₈ N _{13.5} O ₄₉ Yb ₂	C ₈₅ H ₇₆ Ga ₄ N ₇ O ₂₆ Yb
FW (g/mol)	2055.38	3975.08	2063.44
Crystal System/Space Group	Monoclinic, P2(1)/n	Triclinic, P1	Monoclinic, P2(1)/n
T (K)	85(2)	85(2)	85(2)
λ (Å)	1.54184	1.54184	1.54184
a (Å)	18.14950(9)	14.1115	18.71481(14)
b (Å)	25.65520(11)	18.3934	23.81150(16)
c (Å)	18.57270(8)	19.0983	18.83666(11)
α (deg.)	90	63.216(2)	90
β (deg.)	90.9420(4)	85.747(2)	90.3922(7)
γ (deg.)	90	78.619(2)	90
Volume (Å ³)	8646.82(7)	4337.65(15)	8393.94(10)
Z	4	1	4
Density, ρ (g/cm ³)	1.579	1.522	1.633
Abs. Coeff., μ (mm ⁻¹)	4.004	3.957	4.125
F(000)	4116	1983	4148
Crystal size (mm)	0.220 x 0.200 x 0.160	0.110 x 0.040 x 0.040	0.120 x 0.120 x 0.100
θ range for data coll. (deg.)	2.938 to 69.470	2.592 to 69.356	2.991 to 69.632
Limiting Indices	-22 ≤ h ≤ 21 -30 ≤ k ≤ 30 -22 ≤ l ≤ 22	-16 ≤ h ≤ 15 -22 ≤ k ≤ 22 -23 ≤ l ≤ 23	-22 ≤ h ≤ 22 -27 ≤ k ≤ 28 -22 ≤ l ≤ 22
Reflections collected/unique	130078 / 16019	62518 / 23774	118911 / 15623
Completeness to θ (%)	99.6	97.5	99.9
No. of Data/Restrain/Params	16019 / 0 / 1121	23774 / 406 / 2227	15623 / 165 / 1160
GoF on F ²	1.062	1.065	1.096
^a R ₁	0.0353 [I > 2α(I)]; 0.0363 (all data)	0.0490 [I > 2α(I)]; 0.0509 (all data)	0.0436 [I > 2α(I)]; 0.0443 (all data)
^b wR ₂	0.0900 [I > 2α(I)]; 0.0907 (all data)	0.1326 [I > 2α(I)]; 0.1420 (all data)	0.1175 [I > 2α(I)]; 0.1187 (all data)
Largest Diff. Peak, Hole (e·Å ³)	1.417 and -0.660	2.057 and -2.087	1.058 and -1.008

$$^a R_1 = \frac{\sum(|F_o| - |F_c|)}{\sum|F_o|};$$

$$^b wR_2 = \frac{[\sum[w(F_o^2 - F_c^2)^2]/\sum[w(F_o^2)]]^{1/2}}{p};$$

$$p = [\max(F_o^2, 0) + 2F_c^2]/3 \text{ (} m \text{ and } n \text{ are constants); } \sigma = [\sum[w(F_o^2 - F_c^2)^2/(n - p)]^{1/2}$$

$$w = 1/[\sigma^2(F_o^2) + (mp)^2 + np];$$

Synthesis and physical characterization of Ln₂Ga₈xShi₈Ip₄. The reaction between LnGa₄xShi₄(Benzoate)₄ (Ln = Yb^{III}, Sm^{III}, and Gd^{III}; x: *p*Yne, *m*Yne, *p*Al, and *m*Al) and isophthalic acid (H₂Ip) in DMF led to the formation of Ln₂Ga₈xShi₈Ip₄ MCs with the general formula of Ln₂[12-MC_{Ga(III)N(xshi)-4}]₂(Ip)₄. Solids were collected as crystalline powder material, and characterize by ESI-MS, ¹H NMR (for Sm^{III} compounds), and elemental analysis. As seen in Figure 3.5, the ESI-MS spectrum of Yb₂Ga₈*p*AlShi₈Ip₄ is consistent with the MC structure, and displays a single distribution with an isotopic separation of 0.5 m/z, corroborating the intrinsic -2 charge of the metallacrown. ESI-MS spectra of scaffolds prepared with each of the four ring ligands (*p*YneShi, *m*YneShi, *p*AlShi, and *m*AlShi), and three different Ln^{III}-ions (Yb^{III}, Sm^{III}, and Gd^{III}) can be found in Appendix C Figures 55-65.

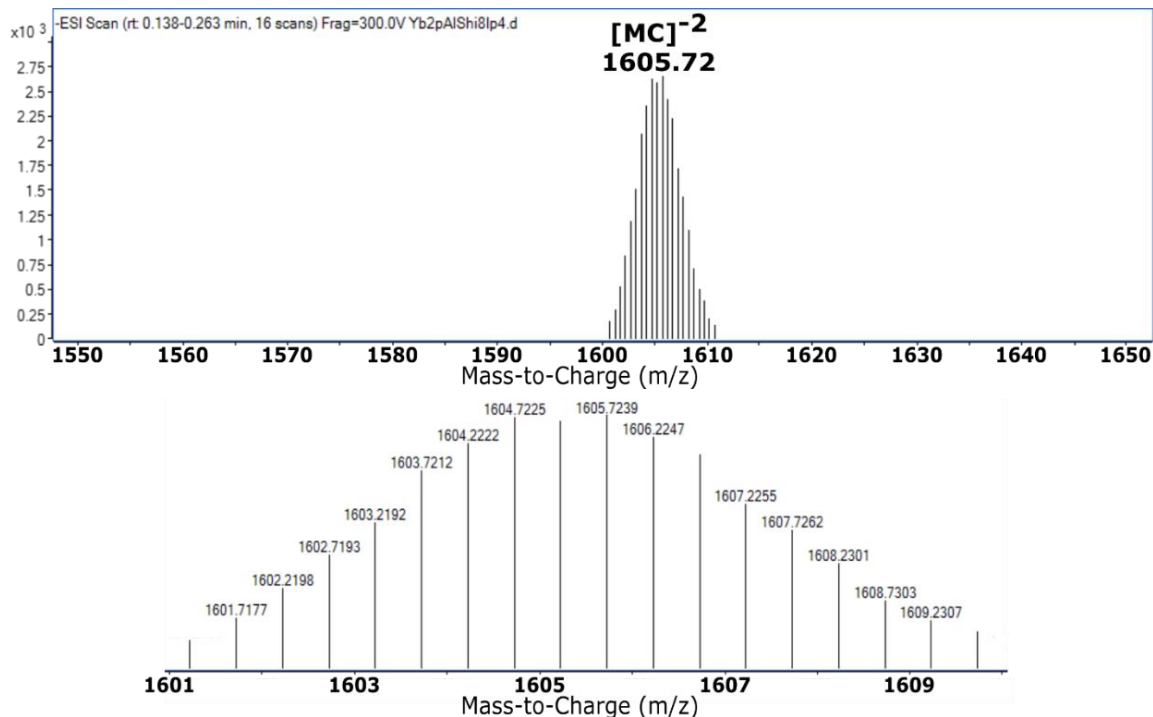


Figure 3.5 (Top) ESI-MS of Yb₂Ga₈*p*AlShi₈Ip₄ MC in negative ion. (Bottom) expansion of the major peak corroborating the -1 isotopic distribution of the complex.

The ¹H NMR characterization of Sm₂Ga₈*p*AlShi₈Ip₄ in *d*₆-DMSO shown in Figure 3.6 suggests that the metallacrown has fourfold symmetry, with an integration ratio of 2:1 between the *p*AlShi³⁻ ring ligands (~6.4, 6.5, and 7.5 ppm) and the Ip⁻² bridging ligands (~7.6 and 8.4 ppm). The ¹H NMR spectra for the other three Sm^{III} metallacrown derivatives (Sm₂Ga₈*m*AlShi₈Ip₄,

Sm₂Ga₈pYneShi₈Ip₄, and Sm₂Ga₈mYneShi₈Ip₄) are shown in Appendix C Figures 41-43. ¹H NMR spectra of each metallacrown suggests that all complexes possess the same composition – i.e., eight ring ligands and four isophthalate bridging ligands.

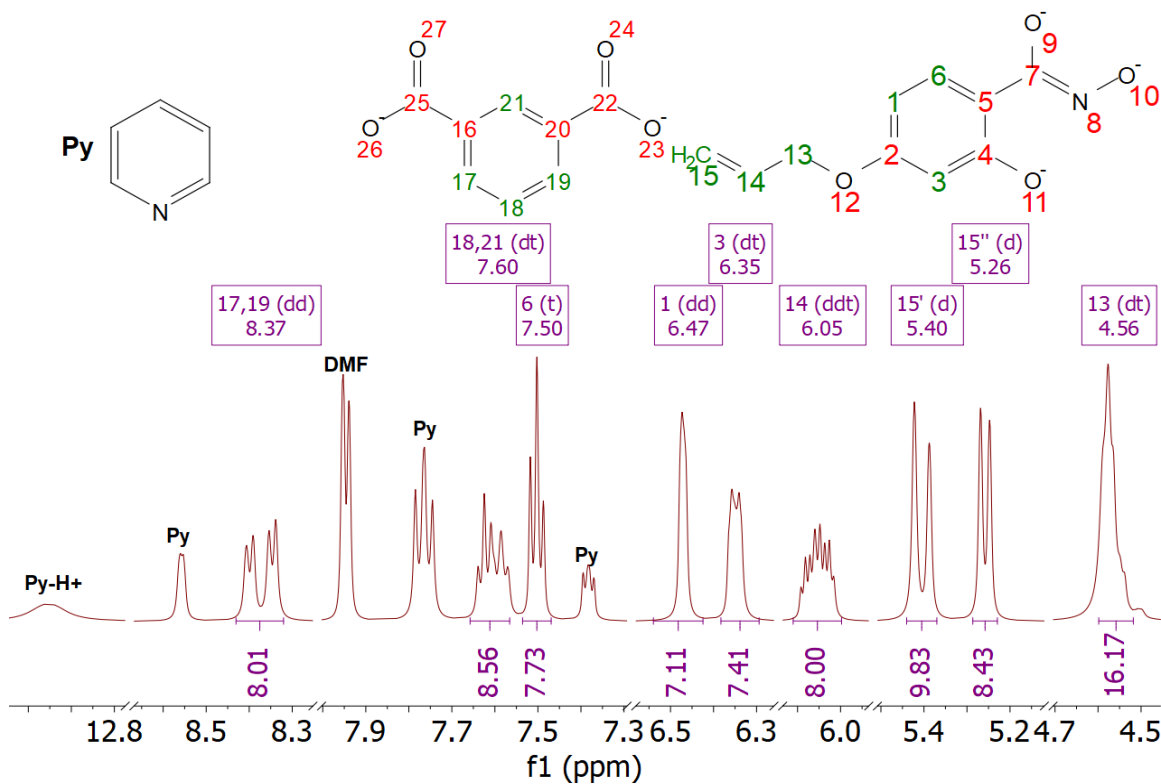


Figure 3.6 ¹H NMR spectrum of Sm₂Ga₈pAlShi₈Ip₄ in d₆-DMSO. Labeled peaks are from the ring and bridge ligands. Pyridine peaks are labeled separately.

Photophysical properties of LnGa₄xShi₄(Benzoate)₄ and Ln₂Ga₈xShi₈Ip₄ (Ln: Yb^{III}, Sm^{III}, and Gd^{III}; x: pYne, mYne, pAl, and mAl). As seen in Figure 3.7, in DMSO solutions each of the four free ring ligands (H₃pYneShi, H₃mYneShi, H₃pAlShi, and H₃mAlShi) have broad absorption bands attributed to the $\pi \rightarrow \pi^*$ transitions located between 250-325 nm for the para-substituted ligands, and 250-360 nm for the meta-substituted ligands. Compared to the parent salicylhydroxamic acid ring ligand (H₃Shi; ~301 nm, $\epsilon = 5.5 \times 10^3 \text{ M}^{-1}\text{cm}^{-1}$), the lower-energy bands of H₃pYneShi and H₃pAlShi are slightly blue-shifted to ~297 nm with both having higher extinction coefficients: $\epsilon_{\text{pYne}(297\text{nm})} = 6.9 \times 10^3 \text{ M}^{-1}\text{cm}^{-1}$ and $\epsilon_{\text{pAl}(297\text{nm})} = 8.5 \times 10^3 \text{ M}^{-1}\text{cm}^{-1}$. As for H₃mYneShi and H₃mAlShi, their lower-energy bands are red-shifted to ~324 nm, but both have lower extinction coefficients: $\epsilon_{\text{mYne}(324\text{nm})} = 4.5 \times 10^3 \text{ M}^{-1}\text{cm}^{-1}$ and $\epsilon_{\text{mAl}(326\text{nm})} = 4.7 \times 10^3 \text{ M}^{-1}\text{cm}^{-1}$.

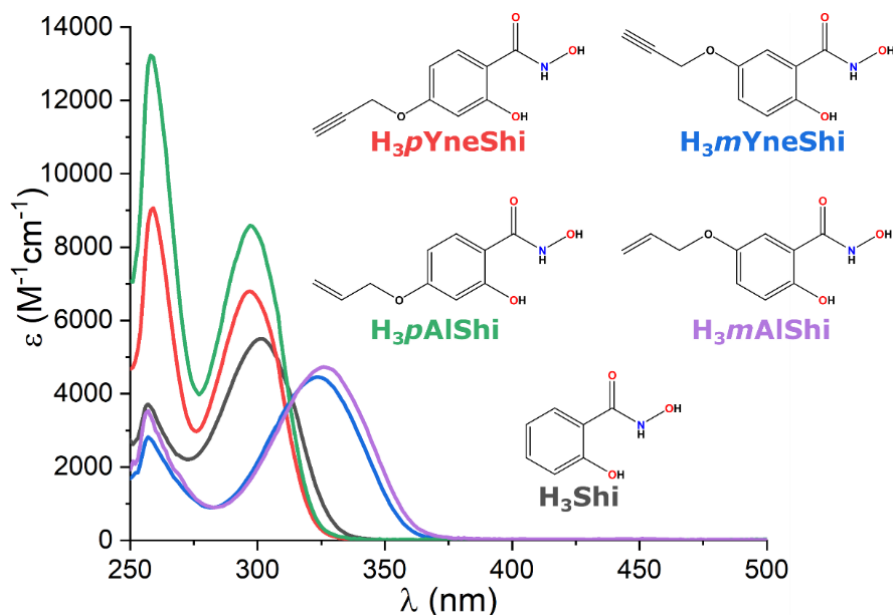


Figure 3.7 Comparison of the UV-Vis absorption spectra of the four new hydroxamic acid derivatives and the salicyl hydroxamic acid. All spectra were recorded at room temperature in DMSO at concentration of 50-200 μM .

Compared to the free ligands, the formation of the MC scaffold with each of the four ring ligands induces a redshift of the absorption bands, and an increase of the molar extinction coefficient for both the monomeric $\text{LnGa}_4\text{xShi}_4(\text{Benzoate})_4$ and dimeric $\text{Ln}_2\text{Ga}_8\text{xShi}_8\text{Ip}_4$ scaffolds. As shown in Figure 3.8, the $\text{YbGa}_4p\text{YneShi}_4(\text{Benzoate})_4$ and $\text{YbGa}_4p\text{AlShi}_4(\text{Benzoate})_4$ MCs have $\pi \rightarrow \pi^*$ transitions located between 250-340 nm. Both also have a low-energy maximum located at ~ 310 nm, with absorption coefficients of $\epsilon_{p\text{Yne}(310\text{nm})} = 4.6 \times 10^4 \text{ M}^{-1}\text{cm}^{-1}$ and $\epsilon_{p\text{Al}(310\text{nm})} = 3.8 \times 10^4 \text{ M}^{-1}\text{cm}^{-1}$, respectively. The meta-substituted $\text{YbGa}_4m\text{YneShi}_4(\text{Benzoate})_4$ and $\text{YbGa}_4m\text{AlShi}_4(\text{Benzoate})_4$ have their $\pi \rightarrow \pi^*$ transitions located between 250-360 nm, with their low-energy maximum red-shifted to ~ 340 nm. Their extinction coefficients are reduced compared to the para-substituted scaffold, with values of $\epsilon_{m\text{Yne}(337\text{nm})} = 2.6 \times 10^4 \text{ M}^{-1}\text{cm}^{-1}$ and $\epsilon_{m\text{Al}(341\text{nm})} = 2.9 \times 10^4 \text{ M}^{-1}\text{cm}^{-1}$, respectively. Lastly, $\pi \rightarrow \pi^*$ transition bands and lower-energy maximum bands of the corresponding dimeric metallacrowns are located at the same position as their monomeric counterparts, but with increasing extinction coefficient values: $\epsilon = 8.8 \times 10^4 \text{ M}^{-1}\text{cm}^{-1}$ for $\text{Yb}_2\text{Ga}_8p\text{YneShi}_8\text{Ip}_4$; $\epsilon = 6.8 \times 10^4 \text{ M}^{-1}\text{cm}^{-1}$ for $\text{Yb}_2\text{Ga}_8p\text{AlShi}_8\text{Ip}_4$; and $\epsilon = 4.9 \times 10^4 \text{ M}^{-1}\text{cm}^{-1}$ for both $\text{Yb}_2\text{Ga}_8m\text{YneShi}_8\text{Ip}_4$ and $\text{Yb}_2\text{Ga}_8m\text{AlShi}_8\text{Ip}_4$. The energy positions of the ligands' singlet states (S^*), determined from the edge of the absorption spectra, are located at ~ 340 nm (29412 cm^{-1}) for both monomeric and dimeric MCs templated with $p\text{YneShi}$ and $p\text{AlShi}$, and at ~ 375 nm (26667 cm^{-1}) for the MCs with $m\text{YneShi}$ and $m\text{AlShi}$.

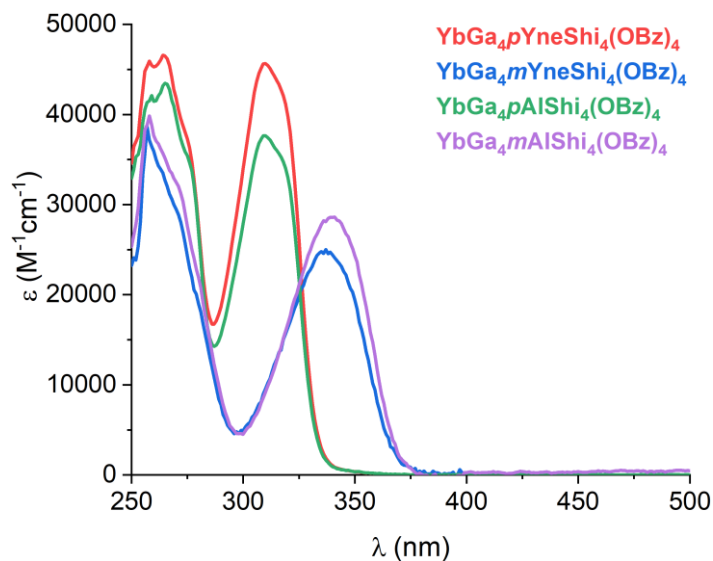


Figure 3.8 UV-Vis absorbance spectra of $\text{YbGa}_{4x}\text{Shi}_4(\text{benzoate})_4$ (x : *pYne*, *mYne*, *pAl*, and *mAl*) recorded at room temperature in DMSO at concentrations of 2–25 μM .

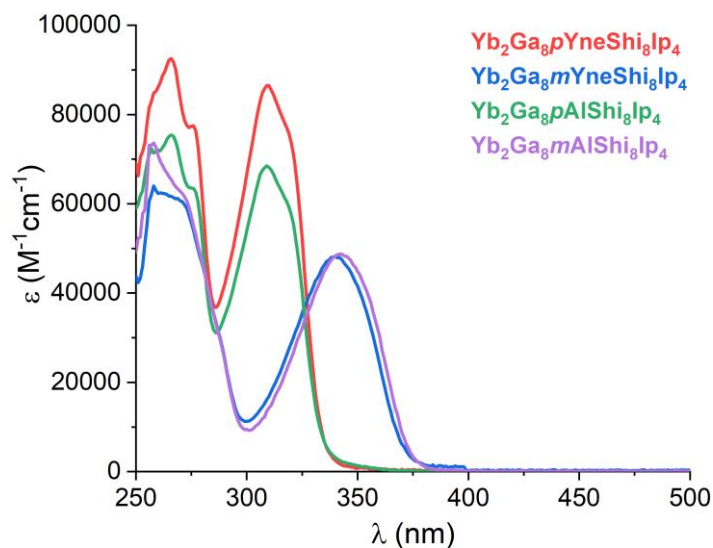


Figure 3.9 UV-Vis absorbance spectra of $\text{Yb}_2\text{Ga}_{8x}\text{Shi}_4\text{Ip}_4$ (x : *pYne*, *mYne*, *pAl*, and *mAl*) recorded at room temperature in DMSO at concentrations of 3–50 μM .

The triplet state (T^*) energy values for six of the scaffolds were determined as the 0–0 transition from the phosphorescence spectrum of the Gd^{III} -MCs. T^* calculations are determined using Gd^{III} -based MCs since the lanthanide's accepting energy levels are located at 32000 cm^{-1} , which are too high to be populated by the ligands' T^* . Therefore, the phosphorescent emission upon excitation at the ligand-centered region is determined to be the T^* state of the MC.¹⁵⁹ Data were recorded in the solid state in time-resolved mode at 77K under 340 nm pulse excitation after

a 200-500 μs delay between excitation and acquisition. Bandwidth of the fits differ due to the complexity of the sensitizing ligand system which has several inter- and intramolecular interactions. Additionally, some distortions of the widths are also observed since the spectra are plotted against wavelength. Fits for the subsequent transitions (e.g., 0-3, 0-4, etc.) are less reliable, and therefore, have been excluded from these analyses. Due to the difficulty to obtain enough crystalline product for analysis, data for $\text{Gd}_2\text{Ga}_8\text{pYneShi}_8\text{Ip}_4$ metallacrowns was not collected. Shown in Figure 3.10 are the T^* energy positions for $\text{GdGa}_4\text{pYneShi}_4(\text{Benzoate})_4$ at 426 nm (23450 cm^{-1}), $\text{GdGa}_4\text{pAlShi}_4(\text{Benzoate})_4$ at 428 nm (23360 cm^{-1}), $\text{Gd}_2\text{Ga}_8\text{pAlShi}_8\text{Ip}_4$ at 440nm (22740 cm^{-1}), $\text{GdGa}_4\text{mYneShi}_4(\text{Benzoate})_4$ at 466 nm (21480 cm^{-1}), $\text{Gd}_2\text{Ga}_8\text{mYneShi}_8\text{Ip}_4$ at 463nm (21620 cm^{-1}), $\text{GdGa}_4\text{mAlShi}_4(\text{Benzoate})_4$ at 462nm (21630 cm^{-1}), and $\text{Gd}_2\text{Ga}_8\text{mAlShi}_8\text{Ip}_4$ at 467nm (21410 cm^{-1}).

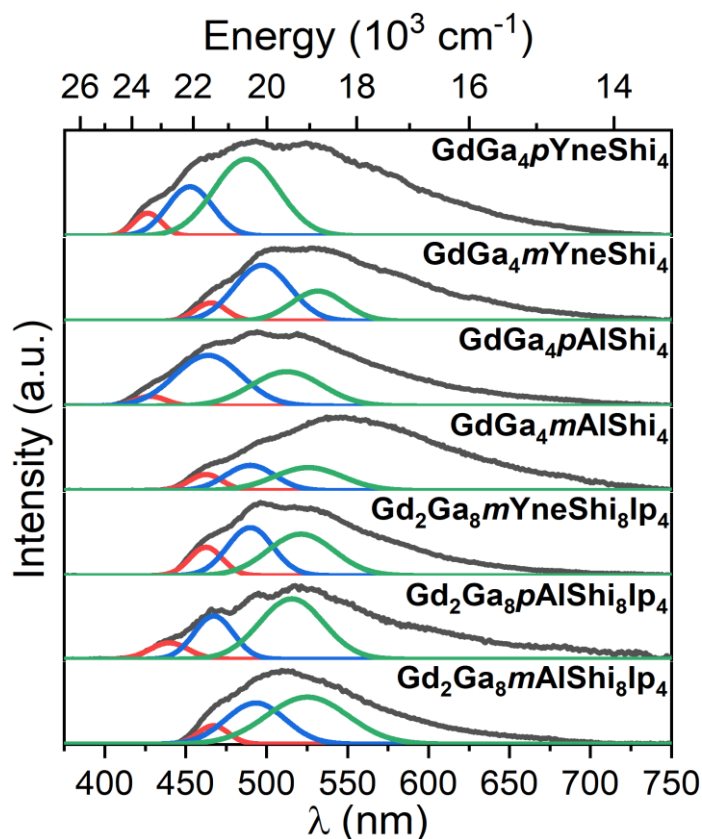


Figure 3.10 Solid state phosphorescence spectrum of $\text{GdGa}_4\text{pYneShi}_4(\text{Benzoate})_4$, $\text{GdGa}_4\text{mYneShi}_4(\text{Benzoate})_4$, $\text{GdGa}_4\text{pAlShi}_4(\text{Benzoate})_4$, $\text{GdGa}_4\text{mAlShi}_4(\text{Benzoate})_4$, $\text{Gd}_2\text{Ga}_8\text{mYneShi}_8\text{Ip}_4$, $\text{Gd}_2\text{Ga}_8\text{pAlShi}_8\text{Ip}_4$, and $\text{Gd}_2\text{Ga}_8\text{mAlShi}_8\text{Ip}_4$ MCs (black traces). 0-0, 0-1, and 0-2 transitions (colored traces) for each MC are fitted with multiple Gaussian functions and Origin9 program. Data collected upon excitation at 340 nm, and after 200-500 μs time delay at 77K. Fits differ in bandwidth due to the complexity of the ligand system, with several inter- and intramolecular interactions. Some distortion of the widths is also observed since the fits are plotted against wavelength. Subsequent fits (e.g. 0-3, 0-4, etc.) are less reliable, and in general omitted from these analyses.

Excitation and emission spectra of $\text{LnGa}_4\text{xShi}_4(\text{Benzoate})_4$ and $\text{Ln}_2\text{Ga}_8\text{xShi}_8\text{Ip}_4$ (Ln: Yb^{III} and Sm^{III} ; x: *pYne*, *mYne*, *pAl*, and *mAl*) were collected and are shown in Figure 3.11 for the Sm^{III} -MCs, and Figure 3.12 for the Yb^{III} -MCs. The excitation spectra in the solid state and in DMSO solutions collected upon monitoring the main transition of the corresponding Ln^{III} -ion show broad ligand-centered bands up to 340-400 nm for the para-substituted metallacrowns (*pYneShi* and *pAlShi*), and up to 380-430 nm for the meta-substituted metallacrowns (*mYneShi* and *mAlShi*). Due to saturation effects,¹⁵⁷ a slight expansion of the excitation bands is observed for the solid-state data compared to the solution-state data. Additionally, for the solid-state data of the Sm^{III} -MCs, sharp signals of low intensities can be observed, and are attributed to the ion's f-f transitions.

Upon excitation in the ligand centered regions (320 or 375 nm), characteristic emissions bands for Sm^{III} in the visible, and Yb^{III} in the NIR range can be observed for all MCs in both solid state and DMSO solutions. Luminescent lifetimes (τ_{obs}) and the lanthanide's quantum yields values upon ligand excitation (φ_{Ln}^L) for each of the Sm^{III} -MC and Yb^{III} -MC derivatives are summarized in Table 3.2 and Table 3.3, respectively. For the sake of comparison, values of other previously reported Yb^{III} -MCs are also shown.

For the Sm^{III} -MCs, characteristic emission of Sm^{III} in both solid state and solution is observed in the visible range for all compounds upon excitation at 320-360 nm. Emission bands are seen at 560 nm (${}^4\text{G}_{5/2} \rightarrow {}^6\text{H}_{5/2}$), 595 nm (${}^4\text{G}_{5/2} \rightarrow {}^6\text{H}_{7/2}$), 645 nm (${}^4\text{G}_{5/2} \rightarrow {}^6\text{H}_{9/2}$), and 700 nm (${}^4\text{G}_{5/2} \rightarrow {}^6\text{H}_{11/2}$), all of which are specific to Sm^{III} f-f transitions. The experimental luminescent decays of some of the compounds are best fitted with biexponential functions, and in such cases the average luminescent lifetime (τ_{av}) is reported. In all biexponential decay events, the dominating contributors are from the long-lived components. Luminescent lifetimes (τ_{obs}) of the monomeric scaffolds vary from 141(4) to 166(1) μs in the solid state, and 99(2) to 137(6) in DMSO. As for the dimeric MCs, τ_{obs} in the solid state range from 95.0(7) to 124(1) in the solid state, and from 115(6) to 127(3) in solution. The quantum yields (φ_{Sm}^L) for the monomer in solid state and in solution vary from 0.90(1) to 5.69(1)% and from 1.34(2) to 1.72(2)%, respectively. As for the dimeric MCs, the range is from 0.56 to 3.54(9)% in the solid state, and from 1.08(1) to 2.75(6)% in DMSO. Weak and broad bands can be observed in the emission spectra plots between 350-550 nm corresponding to $\pi \rightarrow \pi^*$ transitions within the organic ligands. The quantum yields of those ligand-centered (φ_L^L) emissions were found to have larger values in solution than in the solid state

in all of the eight compounds. Knowing the ϕ_L^L of the ligand-centered emissions allowed for the calculation of the total quantum yield (ϕ_T) of each complex, which showed that a significant ϕ_L^L contribution is observed for the meta-substituted dimeric metallacrowns.

Compared to the unfunctionalized $\text{SmGa}_4\text{Shi}_4^{102}$ parent MC in the solid state, ϕ_{Sm}^L values for $\text{SmGa}_4p\text{YneShi}_4$ and $\text{SmGa}_4m\text{AlShi}_4$ decreased by $\sim 50\%$ and $\sim 60\%$, respectively. Yet, $\text{SmGa}_4m\text{YneShi}_4$ and $\text{SmGa}_4p\text{AlShi}_4$ ϕ_{Sm}^L values increased by $\sim 60\%$ and $\sim 130\%$, respectively. As for the comparison with $\text{Sm}_2\text{Ga}_8\text{Shi}_8\text{Ip}_4^{106}$ solid state ϕ_{Sm}^L , only $\text{Sm}_2\text{Ga}_8p\text{YneShi}_8\text{Ip}_4$ had $\sim 70\%$ drop, while $\text{Sm}_2\text{Ga}_8m\text{YneShi}_8\text{Ip}_4$ and $\text{Sm}_2\text{Ga}_8m\text{AlShi}_8\text{Ip}_4$ had similar ϕ_{Sm}^L values to that of the parent MC. Notably, once again $\text{Sm}_2\text{Ga}_8p\text{AlShi}_8\text{Ip}_4$ had a $\sim 70\%$ increase in ϕ_{Sm}^L .

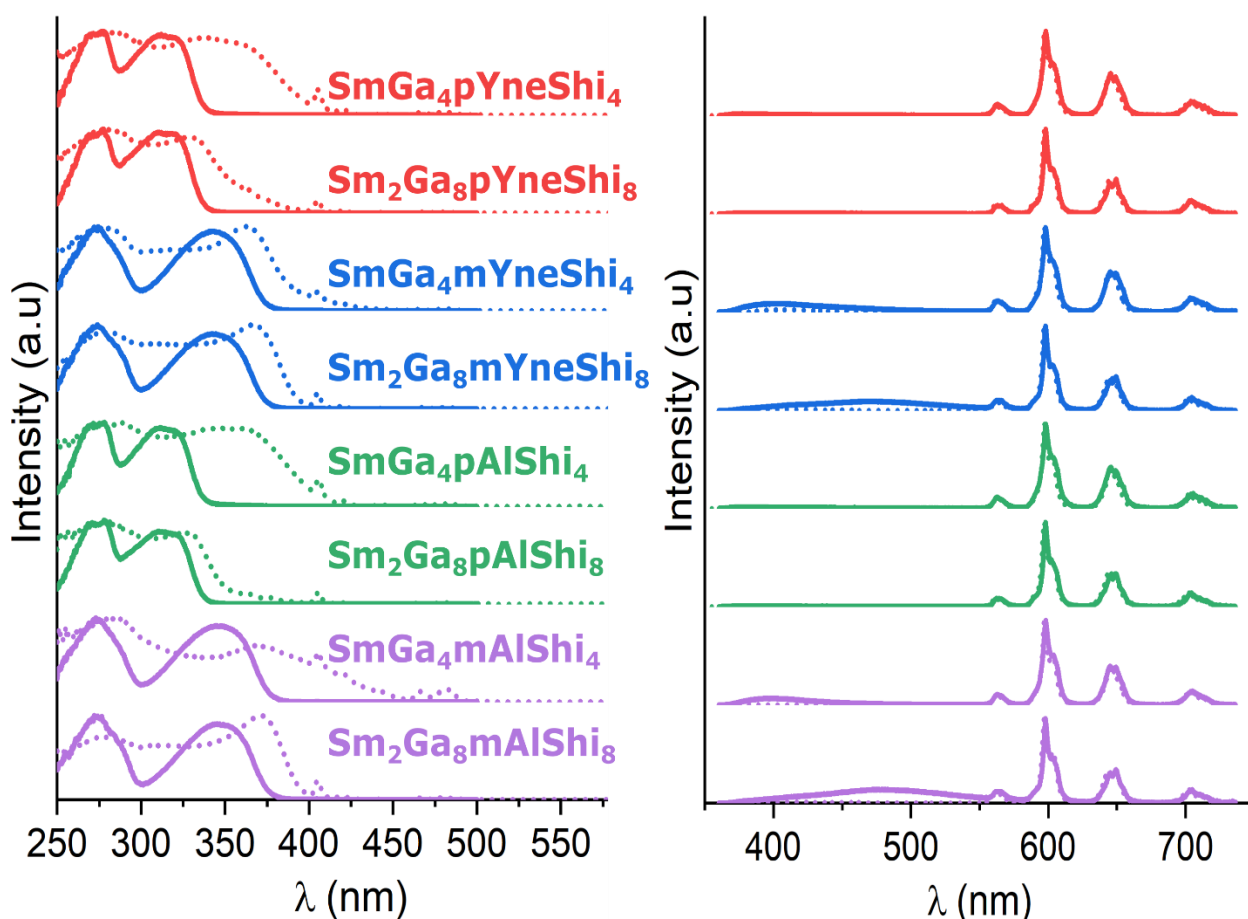


Figure 3.11 Corrected and normalized excitation (left, λ_{em} : 597 nm) and (right, λ_{ex} : 320–360 nm) spectra of $\text{SmGa}_4p\text{YneShi}_4(\text{Benzoate})_4$, $\text{Sm}_2\text{Ga}_8p\text{YneShi}_8\text{Ip}_4$, $\text{SmGa}_4m\text{YneShi}_4(\text{Benzoate})_4$, $\text{Sm}_2\text{Ga}_8m\text{YneShi}_8\text{Ip}_4$, $\text{SmGa}_4p\text{AlShi}_4(\text{Benzoate})_4$, $\text{Sm}_2\text{Ga}_8p\text{AlShi}_8\text{Ip}_4$, $\text{SmGa}_4m\text{AlShi}_4(\text{Benzoate})_4$, and $\text{Sm}_2\text{Ga}_8m\text{AlShi}_8\text{Ip}_4$ in the solid state (dashed traces) and 50 μM solutions in DMSO (solid traces) at room temperature.

Table 3.2 Luminescence lifetimes (τ_{obs}) and Sm^{III}-centered quantum yields collected under ligand excitation (ϕ_{Ln}^L)^a

Compound	State/Solvent	τ_{obs} [μs] ^b	τ_{av} [μs] ^c	ϕ_{Ln}^L [%] ^d	ϕ_L^L [%] ^e	ϕ_T [%] ^f
SmGa ₄ Shi ₄ ^g	Solid	148 : 100%	--	2.46	--	--
Sm ₂ Ga ₈ Shi ₈ Ip ₄ ^h	Solid	117 : 100%	--	2.09(5)	--	--
SmGa _{4p} YneShi ₄	Solid	166(1) : 100%	--	1.28(2)	--	1.28
	DMSO	102(2) : 89(3)% 37(2) : 11(3)%	99(2)	1.36(1)	0.106(1)	1.466
Sm ₂ Ga _{8p} YneShi ₈	Solid	124(1) : 100%	--	0.56	0.0072(2)	0.5672
	DMSO	127(3) : 100%	--	1.58	0.119(1)	1.699
SmGa _{4m} YneShi ₄	Solid	149(3) : 92(3)% 46(1) : 8(2)%	146(3)	4.0(1)	0.32(2)	4.32
	DMSO	140(6) : 86(2)% 25(1) : 14(2)%	137(6)	1.34(2)	0.65(1)	1.99
Sm ₂ Ga _{8m} YneShi ₈	Solid	102(5) : 93(4)% 24(1) : 7(4)%	101(5)	2.2(2)	0.104(7)	2.304
	DMSO	127(3) : 100%	--	1.41(5)	1.25(3)	1.66
SmGa _{4p} AlShi ₄	Solid	154(1) : 100%	--	5.69(1)	0.060(1)	6.29
	DMSO	107(2) : 81(1)% 32(1) : 19(1)%	102(1)	1.36(2)	0.113(2)	1.473
Sm ₂ Ga _{8p} AlShi ₈	Solid	95.0(7) : 100%	--	3.54(9)	--	3.54
	DMSO	115(6) : 100%	--	2.75(6)	0.141(5)	2.891
SmGa _{4m} AlShi ₄	Solid	153(3) : 100%	--	0.90(1)	0.0454(5)	0.9454
	DMSO	143(4) : 91(3)% 23.0(1) : 9(3)%	141(4)	1.72(2)	0.429(4)	2.149
Sm ₂ Ga _{8m} AlShi ₈	Solid	104(2) : 94(2)% 24.3(5) : 6(2)%	103(2)	2.1(2)	0.088(5)	2.188
	DMSO	125(9) : 100%	--	1.08(1)	1.43(1)	1.51

^a For samples in the solid state and 50 μM solutions in DMSO at room temperature, 2 σ values between parentheses. Estimated experimental errors: τ_{obs} , $\pm 2\%$; Q_{Yb}^L , $\pm 10\%$. ^b Under excitation at 355 nm, if biexponential decay was observed, population parameters $P_i = \frac{B_i \tau_i}{\sum_{i=1}^n B_i \tau_i}$ in % are given after the colon. ^c Lifetime averages calculated as: $\tau_{\text{av}} = \frac{\sum_i B_i \tau_i^2}{\sum_i B_i \tau_i}$; B_i are the population parameters given in % after the lifetime values. ^d Quantum yield under excitation at 320-360 nm. ^e Quantum yield of ligand-centered transition. ^f Total quantum yield ($\phi_{Ln}^L + \phi_L^L$). ^g J. Am. Chem. Soc. 2016, 138, 5100–5109. ^h Chem. Eur. J. 2018, 24, 1031–1035.

For the Yb^{III}-MCs, characteristic emissions of Yb^{III} in the solid state and solution are observed in the range of 940-1150 nm, with a maximum at 980 nm arising from the $^2F_{5/2} \rightarrow ^2F_{7/2}$ transitions. Biexponential decay was observed with some of the compounds, and in such cases the average lifetime (τ_{av}) was reported. Once again, the dominating contributors to such decays arise

from their long-lived components. The τ_{obs} values of the monomeric metallacrowns in DMSO solutions are ~ 1.1 - 1.6 times longer than those in the solid state – with the exception of $\text{YbGa}_4p\text{YneShi}_4$ whose value in the solid state is ~ 1.4 times longer than in solution. A similar trend is observed with the dimeric metallacrowns, where the solution state τ_{obs} values are ~ 1.7 - 3.1 times longer than those in the solid state. As for the monomeric MCs' ϕ_{Yb}^L , the solution state values are ~ 2.8 - 7.0 times large than in the solid state – with the exception of $\text{YbGa}_4p\text{YneShi}_4$ with a ϕ_{Yb}^L ~ 1.2 times larger in the solid state. In the case of the dimeric metallacrowns, the DMSO solution state ϕ_{Yb}^L are ~ 4.6 - 7.0 times larger than those in the solid state.

Compared to the τ_{obs} and ϕ_{Yb}^L values of the Yb^{III} -based parent MCs ($\text{YbGa}_4\text{Shi}_4^{102}$ and $\text{Yb}_2\text{Ga}_8\text{Shi}_8\text{Ip}_4^{124}$) shown in Table 2.1 in Chapter 2, these eight new metallacrowns display some differences. The τ_{obs} and ϕ_{Yb}^L values in the solid state for the monomeric scaffold ($\text{YbGa}_4p\text{YneShi}_4$, $\text{YbGa}_4m\text{YneShi}_4$, $\text{YbGa}_4p\text{AlShi}_4$, and $\text{YbGa}_4m\text{AlShi}_4$) are lower (~ 1.2 - 1.9 and ~ 1.3 - 11.1 times) than those of the parent material. The most drastic difference in both τ_{obs} and ϕ_{Yb}^L in the solid state to the parent $\text{YbGa}_4\text{Shi}_4$, are the values for $\text{YbGa}_4m\text{YneShi}_4$. Since the drop in both values is rather steep compared to the other monomeric scaffold, this could indicate the presence of radiative quenchers (e.g., solvent molecules) at a much closer proximity to the Ln^{III} center compared to the other MCs compounds. As for the solution state data in DMSO, both the τ_{obs} and ϕ_{Yb}^L values of the monomeric scaffolds increase by ~ 1.4 - 1.9 and ~ 1.7 times, respectively, when compared to the $\text{YbGa}_4\text{Shi}_4$ MC. In the case of the dimeric scaffolds ($\text{Yb}_2\text{Ga}_4p\text{YneShi}_8$, $\text{Yb}_2\text{Ga}_4m\text{YneShi}_8$, $\text{Yb}_2\text{Ga}_4p\text{AlShi}_8$, and $\text{Yb}_2\text{Ga}_4m\text{AlShi}_8$), solid state data show lower values for both τ_{obs} and ϕ_{Yb}^L for the four scaffolds – with a decline of ~ 1.2 - 2.4 and ~ 3.0 - 4.5 times, respectively – when compared to the parent $\text{Yb}_2\text{Ga}_8\text{Shi}_8\text{Ip}_4$. As the values in DMSO, both τ_{obs} and ϕ_{Yb}^L of the new four metallacrowns are relatively close in value to those of the $\text{Yb}_2\text{Ga}_8\text{Shi}_8\text{Ip}_4$ metallacrown.

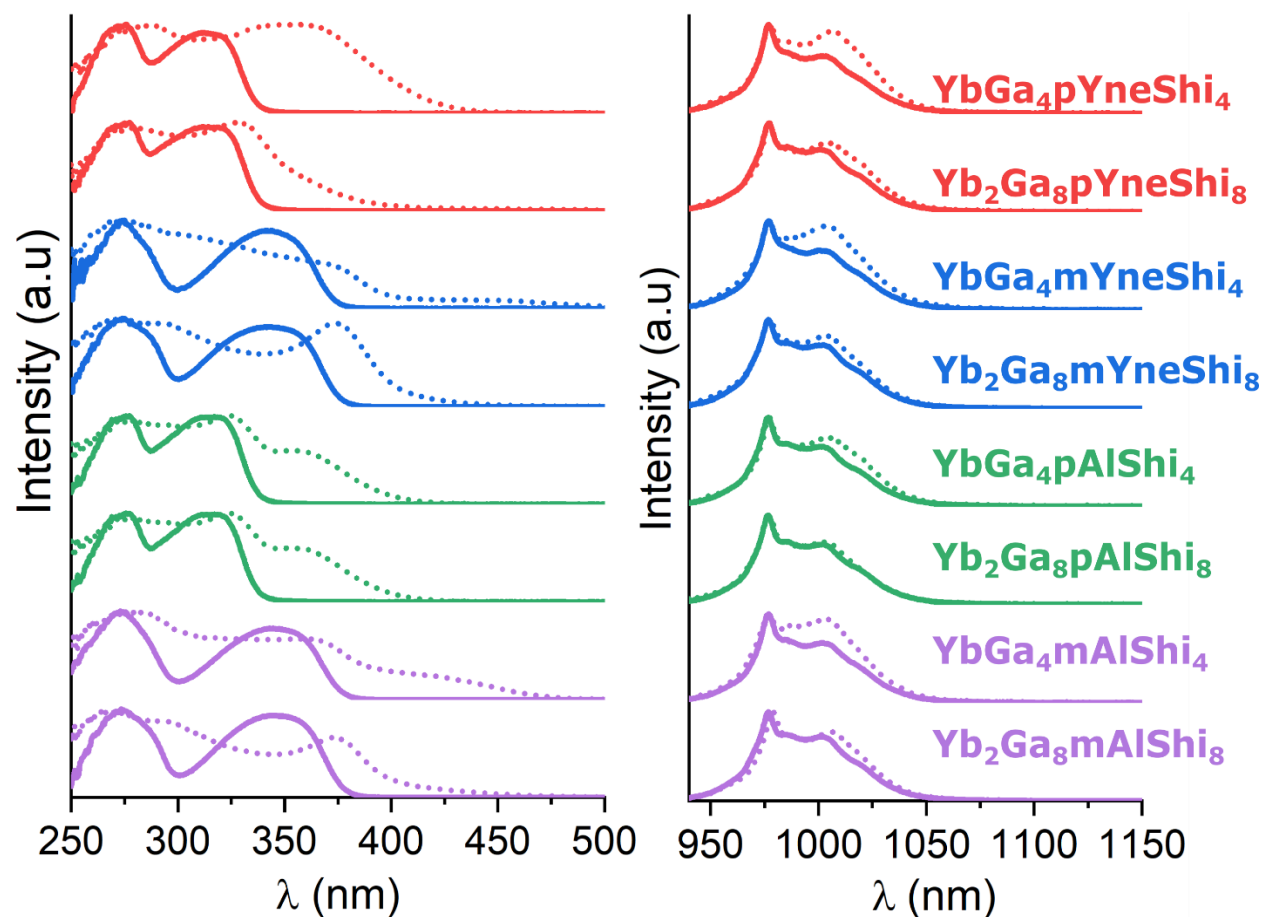


Figure 3.12 Corrected and normalized excitation (left, λ_{em} : 980 nm) and (right, λ_{ex} : 320–375 nm) spectra of $\text{YbGa}_4\text{pYneShi}_4(\text{Benzoate})_4$, $\text{Yb}_2\text{Ga}_8\text{pYneShi}_8\text{Ip}_4$, $\text{YbGa}_4\text{mYneShi}_4(\text{Benzoate})_4$, $\text{Yb}_2\text{Ga}_8\text{mYneShi}_8\text{Ip}_4$, $\text{YbGa}_4\text{pAlShi}_4(\text{Benzoate})_4$, $\text{Yb}_2\text{Ga}_8\text{mYneShi}_8\text{Ip}_4$, $\text{YbGa}_4\text{mAlShi}_4(\text{Benzoate})_4$, and $\text{Yb}_2\text{Ga}_8\text{mAlShi}_8\text{Ip}_4$ in the solid state (dashed traces) and 50 μM solutions in DMSO (solid traces) at room temperature.

Table 3.3 Luminescence lifetimes (τ_{obs}) and Yb^{III}-centered quantum yields collected under ligand excitation ($\phi_{\text{Ln}}^{\text{L}}$)^a

Compound	State/Solvent	τ_{obs} [μs] ^b	τ_{av} [μs] ^c	$\phi_{\text{Ln}}^{\text{L}}$ [%] ^d
YbGa ₄ Shi ₄	Solid ^e	55.7(30 : 100%)	--	5.88(2)
	DMSO	33(2) : 34(5)% 15.4(5) : 66(5)%	24(1)	2.2(1)
Yb ₂ Ga ₈ Shi ₈ Ip ₄	Solid ^f	37.1(1) : 100%	--	4.82(4)
	DMSO	60.9(4) : 100%	--	7.56(3)
YbGa _{4p} YneShi ₄	Solid	48.3(4) : 100%	--	4.46(1)
	DMSO	37(1) : 72(3)% 13(1):28(3)%	34(1)	3.7(2)
Yb ₂ Ga _{8p} YneShi ₈	Solid	15.3(1) : 100%	--	1.16(4)
	DMSO	47.3(3) : 100%	--	6.26(6)
YbGa _{4m} YneShi ₄	Solid	31.7(7) : 69(2)% 7.9(3):31(2)%	29.3(7)	0.53(1)
	DMSO	48(3) : 100%	--	3.73(9)
Yb ₂ Ga _{8m} YneShi ₈	Solid	20.1(2) : 83(3)% 5.4(3):27(3)%	19.4(3)	1.59(5)
	DMSO	58(4) : 100%	--	7.3(2)
YbGa _{4p} AlShi ₄	Solid	45.6(5)	--	2.42(4)
	DMSO	40(2) : 63(1)% 14(1) : 37(1)%	36(2)	8.10(7)
Yb ₂ Ga _{8p} AlShi ₈	Solid	23.2(3)	--	1.37(8)
	DMSO	53.5 : 65(1)% 8.4(1) : 35(1)%	49.9(7)	7.75(1)
YbGa _{4m} AlShi ₄	Solid	43.2(7) : 91.1(7)% 9.5(4):8.9(7)%	42.5(7)	1.37(1)
	DMSO	47(2) : 100%	--	3.80(7)
Yb ₂ Ga _{8m} AlShi ₈	Solid	28(2) : 87(6)% 5.7(3):13(6)%	27(2)	1.07(9)
	DMSO	59(5) : 100%	--	7.46(7)

^a For samples in the solid state and 50 μM solutions in DMSO at room temperature, 2σ values between parentheses. Estimated experimental errors: τ_{obs} , $\pm 2\%$; Q_{Yb}^{L} , $\pm 10\%$. ^b Under excitation at 355 nm, if biexponential decay was observed, population parameters $P_i = \frac{B_i \tau_i}{\sum_{i=1}^n B_i \tau_i}$ in % are given after the colon. ^c Lifetime averages calculated as: $\tau_{\text{av}} = \frac{\sum_i B_i \tau_i^2}{\sum_i B_i \tau_i}$; B_i are the population parameters given in % after the lifetime values. ^d Quantum yield under excitation at 320–360 nm. ^e J. Am. Chem. Soc. 2016, 138, 5100–5109. ^f Chem. Eur. J. 2018, 24, 1031–1035.

3.3.2 LnGa_{4x}Shi₄(Benzoate)₄ and Ln₂Ga_{8x}Shi₈Ip₄ Functionalization

Small molecule coupling to LnGa_{4x}Shi₄(Benzoate)₄ and Ln₂Ga_{8x}Shi₈Ip₄. The reaction between LnGa_{4x}Shi₄(Benzoate)₄ or Ln₂Ga_{8x}Shi₈Ip₄ and β -mercaptoethanol (β ME) in the presence of DMPA and UV light led to the coupling of up to four, eight, or sixteen equivalents of the small molecule to the monomeric and dimeric metallacrowns via thiol-yne coupling (for MCs with pYneShi and mYneshi) or thiol-ene coupling (for MCs with pAlShi or mAlShi). The desired product was collected as an off-white to light yellow powder that was characterized by ESI-MS,

UV-Vis absorbance spectroscopy, and fluorescence spectroscopy. Shown in Figure 3.13 and Figure 3.14 are the ESI-MS spectra of thiol-yne coupling to the para- and meta-substituted monomeric $\text{YbGa}_4\text{YneShi}_4(\text{Benzoate})_4$ and dimeric $\text{Yb}_2\text{Ga}_8\text{YneShi}_8\text{Ip}_4$ metallacrowns. Both the monomeric and dimeric scaffolds templated with *p*YneShi ligands seem to have higher reactivity towards thiol-yne coupling compared to the scaffold with *m*YneShi ligands. This is corroborated by the fact that a narrower distribution of β -mercaptoethanol molecules coupled to $\text{YbGa}_4\text{pYneShi}_4$ (six to eight coupled β MEs) and $\text{Yb}_2\text{Ga}_8\text{pYneShi}_8$ (fourteen to sixteen coupled β MEs) is observed by ESI-MS, compared to a broader distribution with $\text{YbGa}_4\text{mYneShi}_4$ (zero to six coupled β MEs) and $\text{Yb}_2\text{Ga}_8\text{mYneShi}_8$ (eleven to sixteen coupled β MEs).

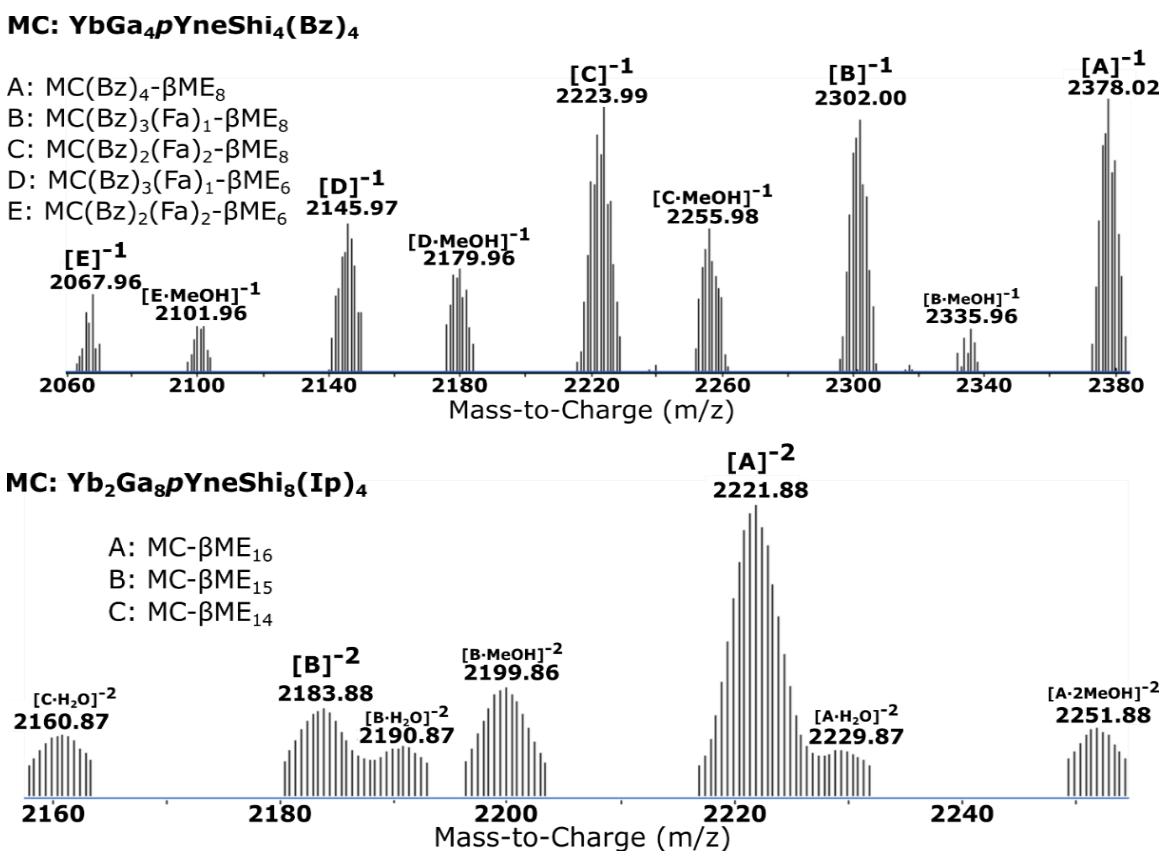


Figure 3.13 ESI-MS spectra of UV-light catalyzed coupling of β -Mercaptoethanol (β ME) to $\text{YbGa}_4\text{pYneShi}_4(\text{benzoate})_4$ (top) and $\text{Yb}_2\text{Ga}_8\text{pYneShi}_8\text{Ip}_4$ (bottom). Six to eight thiol-yne couplings to the monomeric MC are observed, while fourteen to sixteen coupling to the dimeric MC are observed.

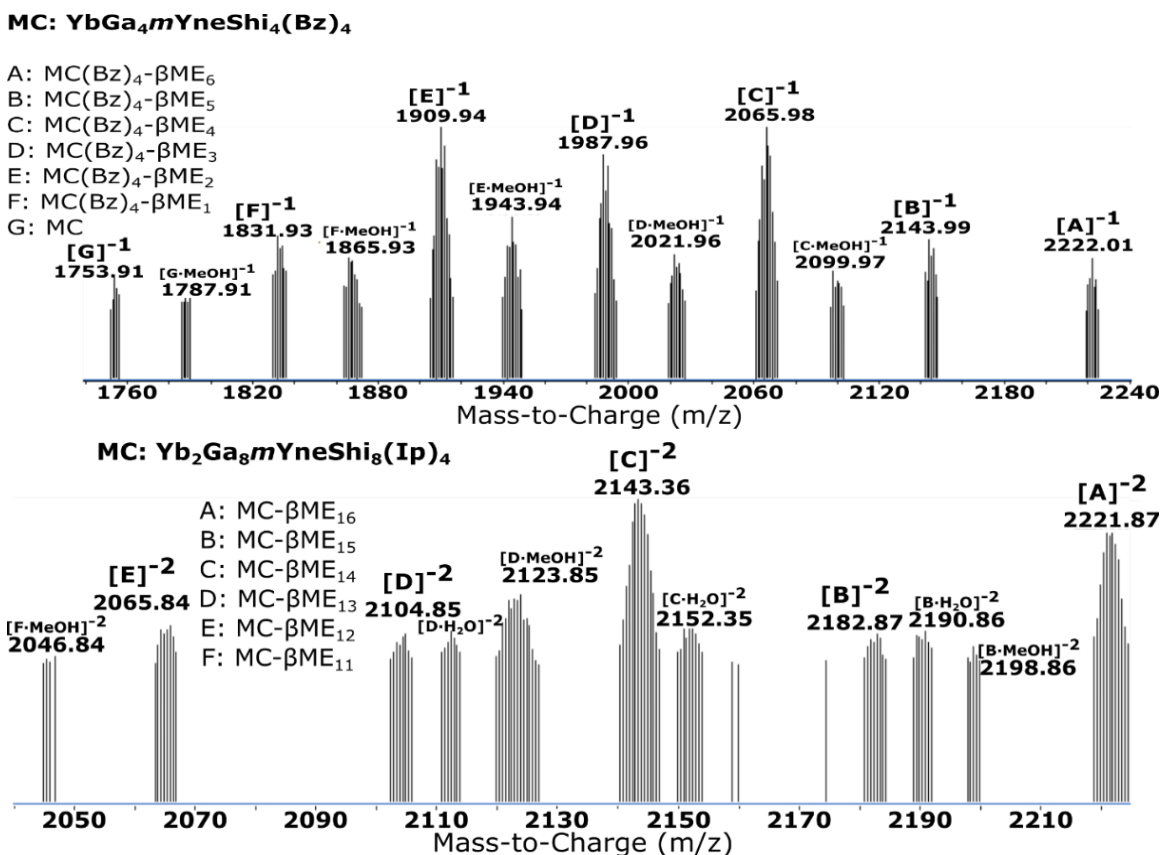


Figure 3.14 ESI-MS spectra of UV-light catalyzed coupling of β-Mercaptoethanol (βME) to YbGa₄*m*YneShi₄(benzoate)₄ with zero to six couplings (top) and Yb₂Ga₈*m*YneShi₈Ip₄ with eleven to sixteen couplings (bottom). The meta-functionalized MCs show lower reactivity toward thiol-yne coupling compared to the para-functionalized counterpart.

As for the thiol-ene active ligands, Figure 3.15 and Figure 3.16 show the ESI-MS spectra of the para- and meta-substituted monomeric and dimeric metallocrowns. Both YbGa₄*p*AlShi₄(Benzoate)₄ and YbGa₄*m*AlShi₄(Benzoate)₄ show complete coupling of four βME molecules to each scaffold. The distribution of peaks observed in both spectra arise from the exchange of benzoate (Bz) bridging ligands by formate (Fa) ligands. This is due to the solvent composition used to run the mass spectrometer (i.e. acetonitrile with 0.1% formic acid). This is commonly observed when characterizing LnGa₄xShi₄(Benzoate)₄ MCs by ESI-MS. Small molecule couplings to the dimeric Yb₂Ga₈*p*AlShi₈Ip₄ and Yb₂Ga₈*m*AlShi₈Ip₄ scaffolds show a distribution of six to eight couplings to the para-substituted MC, and five to eight couplings for the meta-substituted. The observation suggests a slight difference in reactivity based on the functionalization position. However, compared to the thiol-yne counterparts (*p*Yne and *m*Yne), the thiol-ene active ligands (*p*Al and *m*Al) seem to have higher reactivity towards thiol coupling.

This tendency is especially true when comparing the meta-functionalized scaffolds, with the $\text{Yb}_2\text{Ga}_8\text{mAlShi}_8\text{Ip}_4$ MC having a much narrower distribution of coupled βME molecules than the $\text{Yb}_2\text{Ga}_8\text{mYneShi}_8\text{Ip}_4$ scaffold.

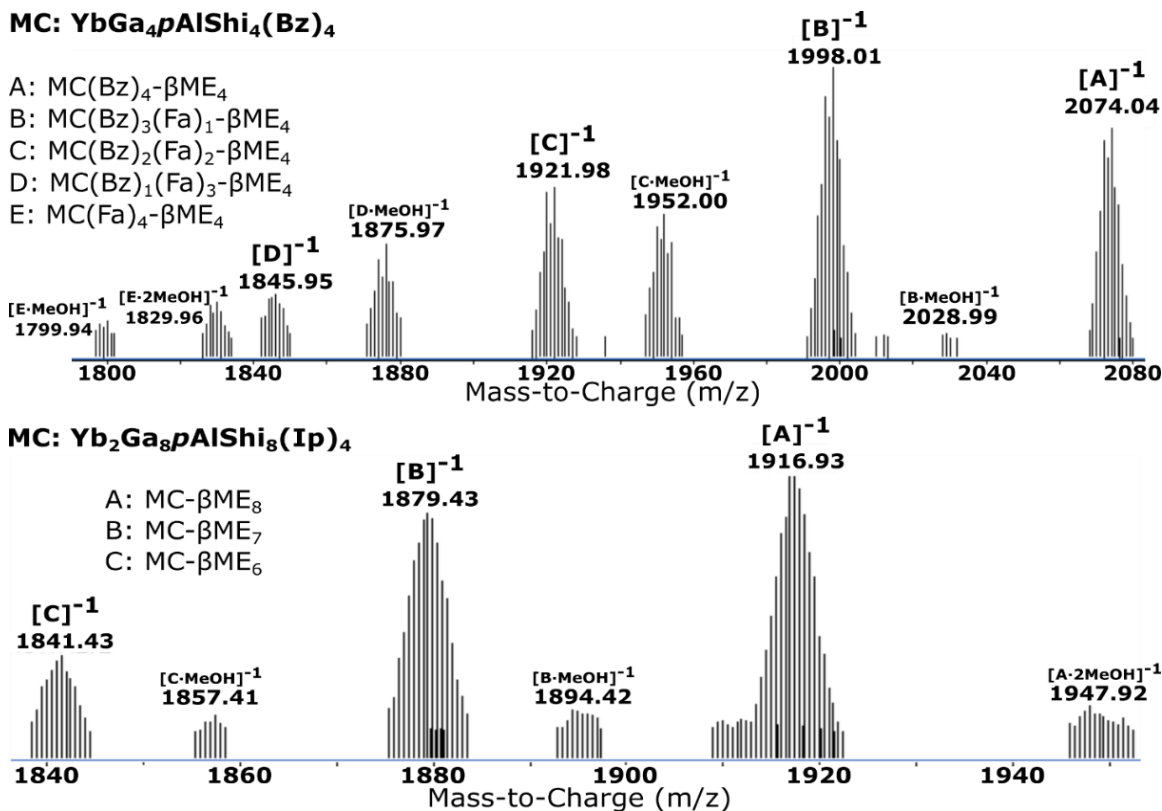


Figure 3.15 ESI-MS spectra of UV-light catalyzed coupling of β -Mercaptoethanol (βME) to $\text{YbGa}_4\text{pAlShi}_4(\text{benzoate})_4$ (top) and $\text{Yb}_2\text{Ga}_8\text{pAlShi}_8\text{Ip}_4$ (bottom). Four thiol-ene couplings to the monomeric MC, while six to eight to the dimeric MC.

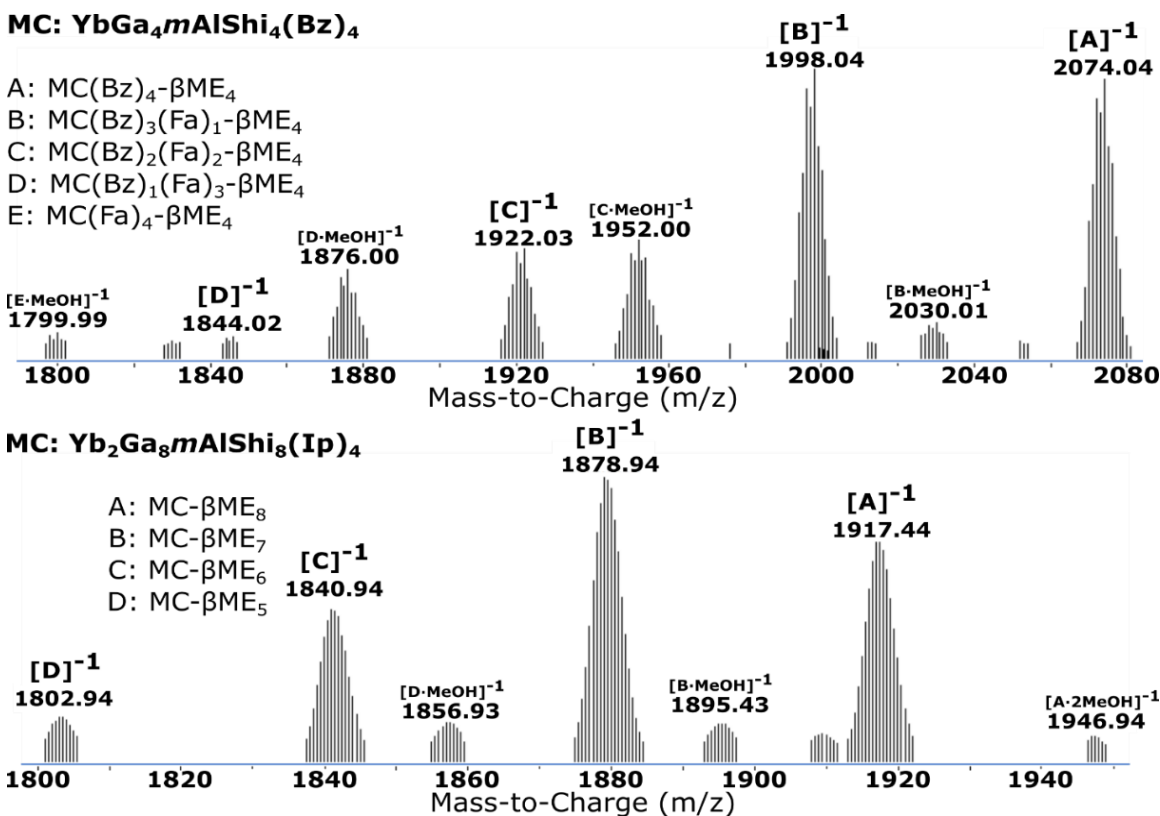


Figure 3.16 ESI-MS spectra of UV-light catalyzed coupling of β-Mercaptoethanol (βME) to YbGa₄pAlShi₄(benzoate)₄ (top) and Yb₂Ga₈pAlShi₈Ip₄ (bottom). Four thiol-ene couplings to the monomeric MC, while six to eight to the dimeric MC.

Lastly, small molecule coupling to the Sm^{III}-MC analogues of the monomeric scaffolds, SmGa₄pAlShi₄(benzoate)₄ and SmGa₄mAlShi₄(benzoate)₄, resulted in complete coupling of four βME molecules to each metallocrowns, as seen in Figure 3.17. The distribution of peaks is once again observed due to benzoate bridge exchange with formate ligands during ESI-MS characterization. As with the unfunctionalized MCs, all of the ESI-MS spectra have a 1.0 m/z isotopic distribution for the monomeric scaffolds, and a 0.5 m/z isotopic distribution for the dimeric MCs.

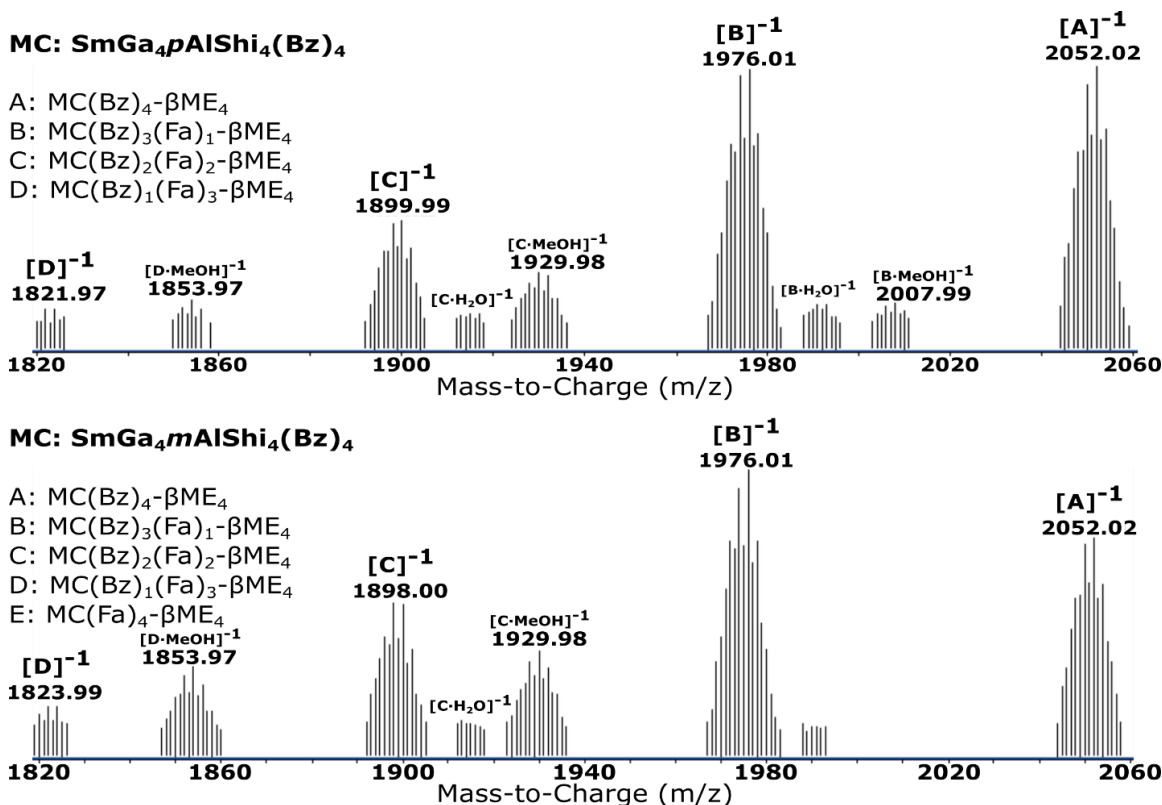


Figure 3.17 ESI-MS spectra of UV-light catalyzed coupling of β -Mercaptoethanol (β ME) to SmGa_{4p}AlShi₄(benzoate)₄ (top) and SmGa_{4m}AlShi₄(benzoate)₄ (bottom). In both cases, complete coupling of four small molecules to each MC was observed.

The UV-Vis absorbance spectra of YbGa_{4p}YneShi₄(benzoate)₄, Yb₂Ga_{8p}YneShi₈Ip₄, YbGa_{4p}AlShi₄(benzoate)₄, and Yb₂Ga_{8p}AlShi₈Ip₄ in DMSO post β ME coupling are shown in Figure 3.18. Each of the scaffolds displays a $\pi \rightarrow \pi^*$ transition bands extending up to 340 nm with absorbance maxima (λ_{\max}) located at about 310 nm. The spectral profiles overlap with the absorbance bands of the unfunctionalized MCs shown in Figure 3.8 and Figure 3.9. Solution state emission spectra of each of the functionalized scaffolds in DMSO are shown in Figure 3.19. Upon excitation at 310 nm, characteristic Yb^{III} emission in the NIR is observed for each scaffold with a maximum at 980 nm arising from the $^2F_{5/2} \rightarrow ^2F_{7/2}$ transition.

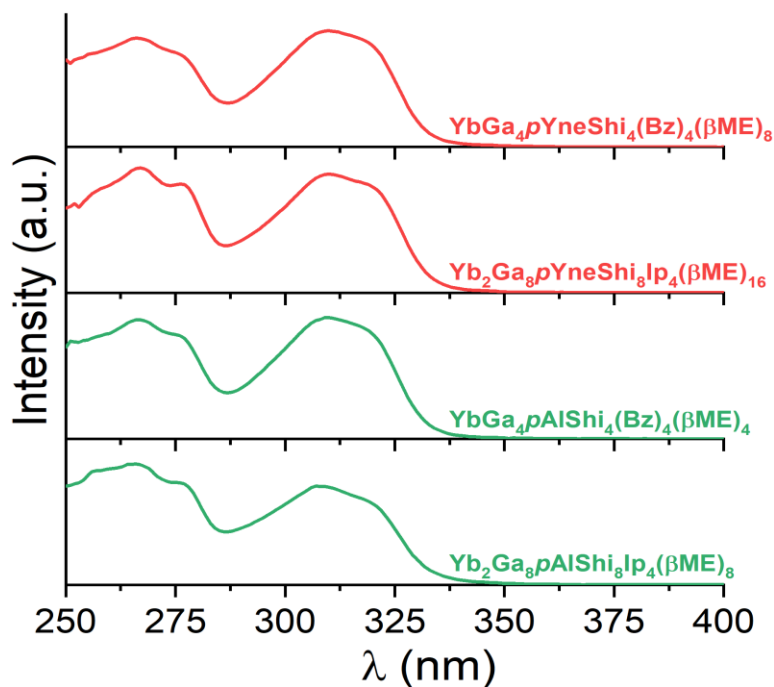


Figure 3.18 UV-Vis Absorbance spectra of $\text{YbGa}_4\text{pYneShi}_4(\text{benzoate})_4$, $\text{Yb}_2\text{Ga}_8\text{pYneShi}_8\text{Ip}_4$, $\text{YbGa}_4\text{pAlShi}_4(\text{benzoate})_4$, and $\text{Yb}_2\text{Ga}_8\text{pAlShi}_8\text{Ip}_4$ post β -mercaptoethanol coupling recorded at room temperature in DMSO at concentrations of 0.1 mg/mL.

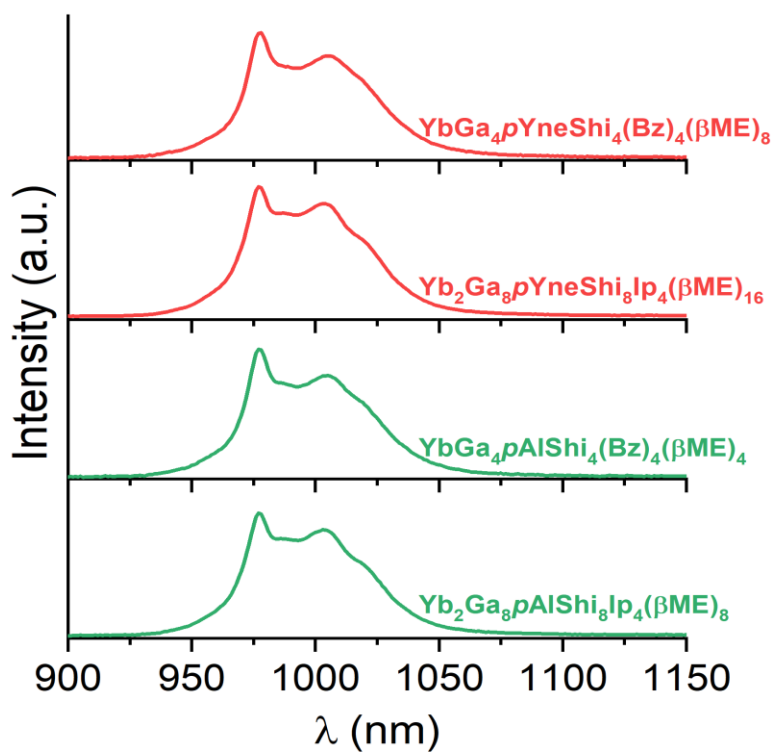


Figure 3.19 Solution state emission (λ_{ex} : 310 nm) spectra of $\text{YbGa}_4\text{pYneShi}_4(\text{benzoate})_4$, $\text{Yb}_2\text{Ga}_8\text{pYneShi}_8\text{Ip}_4$, $\text{YbGa}_4\text{pAlShi}_4(\text{benzoate})_4$, and $\text{Yb}_2\text{Ga}_8\text{pAlShi}_8\text{Ip}_4$ post β -mercaptoethanol coupling recorded at room temperature in DMSO at concentrations of 0.1 mg/mL.

3.3.3 Hyperboloidal Dendrimeric Metallacrowns (H-DMCs)

Synthetic Approaches to Prepare H-DMCs with $Yb_2Ga_8pYneShi_8Ip_4$. Three different approaches (UV light-catalyzed **Approach A**, UV light-catalyzed **Approach B**, and heat-catalyzed **Approach C**) were attempted to synthesize hyperboloidal DCMs with $Yb_2Ga_8pYneShi_8Ip_4$ as the core via thiol-yne coupling. Both **Approach A** and **Approach B** are UV-light catalyzed strategies, but utilizing different photoinitiators: 2,2-Dimethoxy-2-phenylacetophenone (DMPA) for **A**; and 4,4'-Bis(dimethylamino)benzophenone (Michler's Ketone) for **B**. **Approach C** is a thermally catalyzed approach where azobisisobutyronitrile (AIBN) was used as the radical initiator. The three approaches rely on thiol radical coupling to the MC core.

Figure 3.20 shows ESI-MS spectra of the different reaction conditions utilizing **Approach A**, where $Yb_2Ga_8pYneShi_8Ip_4$ and thiol-focal point PAMAM dendrons of G 1.0 were dissolved in degassed DMF, and then irradiated with UV light (365 nm) using DMPA as the photoinitiator. The reaction conditions (e.g. MC concentration, DMPA concentration, and reaction time) were changed for each of the shown spectra, and are detailed in Table 3.4. Utilizing **Approach A** yielded a maximum of six to eight couplings of G1.0 PAMAM dendron to the MC core with the following reaction conditions: 45 mg/mL reaction concentration, 40 equivalents of HS-G1.0 PAMAM dendron to MC, 0.32 equivalents of DMPA to MC, and two hours under UV light (365 nm) irradiation. Increasing reaction time under UV light or increasing photoinitiator concentration did not yield better results and, in fact, resulted in lower couplings of the dendron to the MC core. Similarly, decreasing MC concentration or decreasing photoinitiator concentration did not yield better results either. The worst results were seen when the amount of photoinitiator was reduced significantly (0.1 eq) or increased significantly (1.0 eq), where only one to four couplings of the dendron to the MC core were obtained. Thus, demonstrating the delicate reaction conditions needed for photocatalytic thiol-yne coupling. Furthermore, addition of more dendron and photoinitiator in an attempt to drive the reaction to completion did not yield more couplings. While only up to eight dendron couplings to the MC core were observed, no unreacted MC (i.e., MC with zero dendron couplings) was observed.

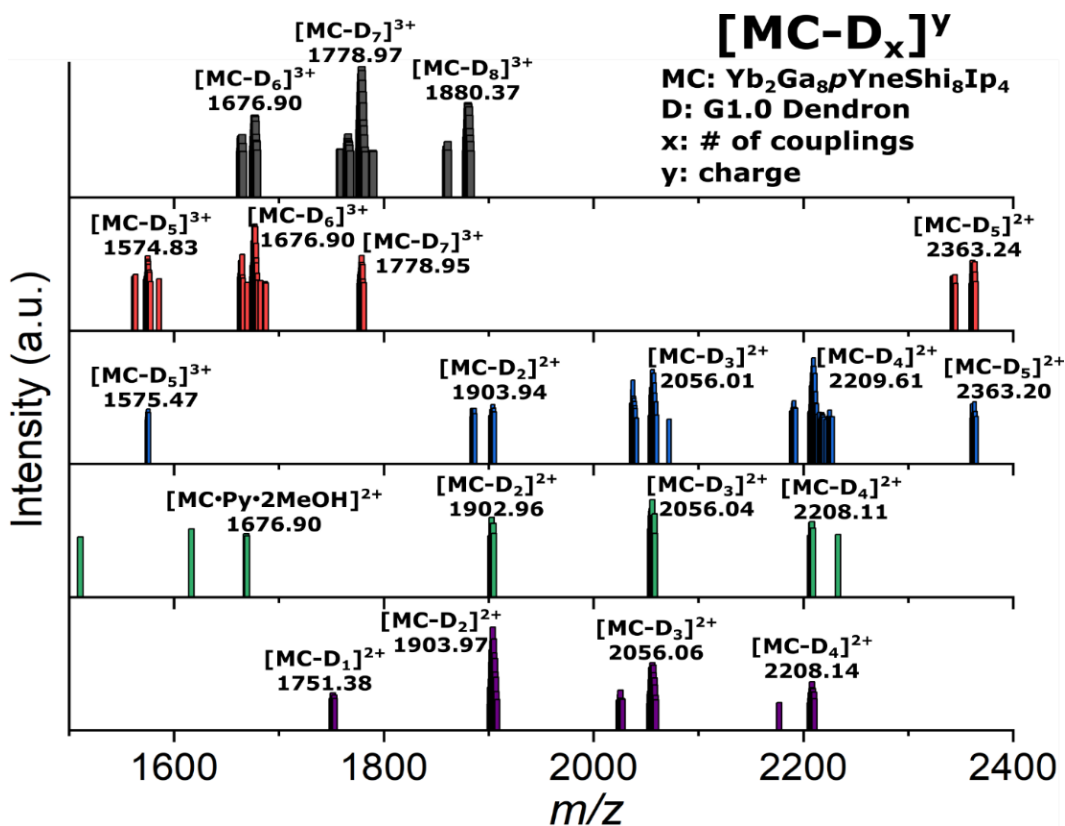


Figure 3.20. ESI-MS spectra of the synthetic trials to prepare hyperboloidal DMC with $\text{Yb}_2\text{Ga}_8\text{pYneShi}_8\text{Ip}_4$ MC cores and HS-G1.0 PAMAM dendrons under **Approach A**.

Table 3.4 Reaction conditions for coupling **HS-G1.0 PAMAM dendrons** to $\text{Yb}_2\text{Ga}_8\text{pYneShi}_8\text{Ip}_4$ under UV light-catalyzed **Approach A**. Each of the trials is color coded to match the ESI-MS results on Figure 3.20.

Plot	Concentration to MC (mg/mL)	HS G1.0 Dendron (eq)	DMPA (eq)	Reaction Time (hrs)
Gray	45	40	0.32	2
Red	4	40	0.32	2
Blue	45	40	0.5	4
Green	40	40	1.0	2
Purple	30	40	0.1	2

Shown in Figure 3.21 are the ESI-MS results of the synthetic trials to prepare DMCs using **Approach A** with $\text{Yb}_2\text{Ga}_8\text{pYneShi}_8\text{Ip}_4$ as the MC core, but with HS-G1.5 PAMAM dendrons and varying reaction conditions listed on Table 3.5. Under the best reaction condition utilizing **Approach A**, yielded a maximum of six to eight coupling of G1.5 PAMAM dendron to the MC core under the following reaction conditions: 3 mg/mL reaction concentration, 40 equivalents of HS-G1.5 dendron to MC, 1.0 eq of DMPA to MC, and two hours under UV light irradiation.

Attempts to improve results by increasing reaction times (4-14 hours), addition of more dendron and photoinitiator to drive reactions to completion, or longer reaction concentration (10 mg/mL) did not yield better results.

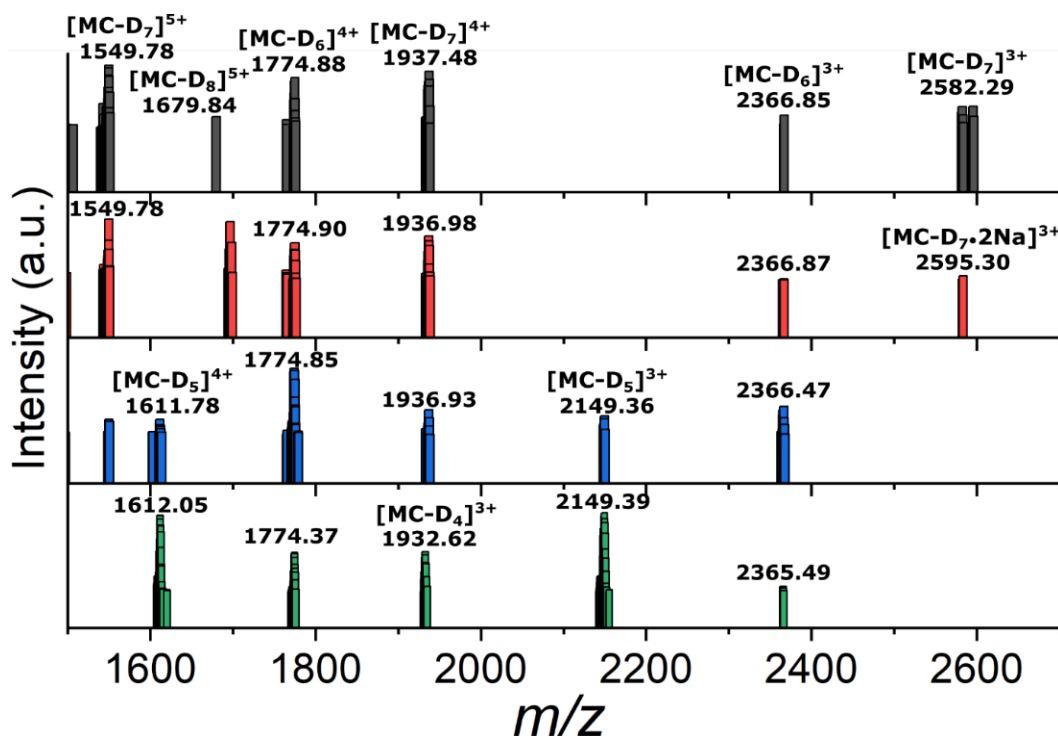


Figure 3.21. ESI-MS spectra of the synthetic trials to prepare hyperboloidal DMC with $\text{Yb}_2\text{Ga}_8\text{pYneShi}_8\text{Ip}_4$ MC cores and HS-G1.5 PAMAM dendrons under **Approach A**.

Table 3.5 Reaction conditions for coupling **HS-G1.5 PAMAM dendrons** to $\text{Yb}_2\text{Ga}_8\text{pYneShi}_8\text{Ip}_4$ under UV light-catalyzed **Approach A**. Each of the trials is color coded to match the ESI-MS results on Figure 3.21.

Plot	Concentration to MC (mg/mL)	HS G1.5 Dendron (eq)	DMPA (eq)	Reaction Time (hrs)
Gray	3	40	1.0	2
Red	10	40	0.32	14
Blue	4	40	0.5	4
Green	5	40	0.5	2

Shown in Figure 3.22 are the synthetic trials utilizing **Approach B** and **Approach C** in an effort to obtain complete coupling of sixteen G1.0 PAMAM dendrons to $\text{Yb}_2\text{Ga}_8\text{pYneShi}_8\text{Ip}_4$. However, in both cases incomplete coupling was observed by ESI-MS characterization. The reaction conditions (e.g. MC concentration, radical initiator concentration, and reaction time) were changed for each of the shown spectra, and are detailed in

Table 3.6. As seen on the top green plot, under **Approach B** (with Michler's ketone as the radical initiator) only four to six couplings of dendron to the MC core were observed. Just as with **Approach A**, no unreacted MC was seen by mass spectrometry; however, aside from the lower reactivity toward dendron thiol-yne coupling compared to **Approach A**, a strong discoloration of the reaction mixture was observed, likely due to the decomposition of the photoinitiator. After two hours under UV light irradiation, the reaction solution turned from colorless to bright yellow – something that was not observed under **Approach A** even after longer reaction times.

Next, the thermal-catalyzed **Approach C** (with AIBN as the radical initiator) was also investigated. It yielded poor coupling results as seen in the yellow and pink plots. Under varying AIBN concentration (0.32 eq vs 1.0 eq), and while keeping the rest of the reaction conditions constant (25 mg/mL reaction concentration, 40eq dendron to MC, and 3 hours at 80°C), very similar results were observed for both cases including the presence of unreactive MC, and an array of one to four dendron couplings to the MC core.

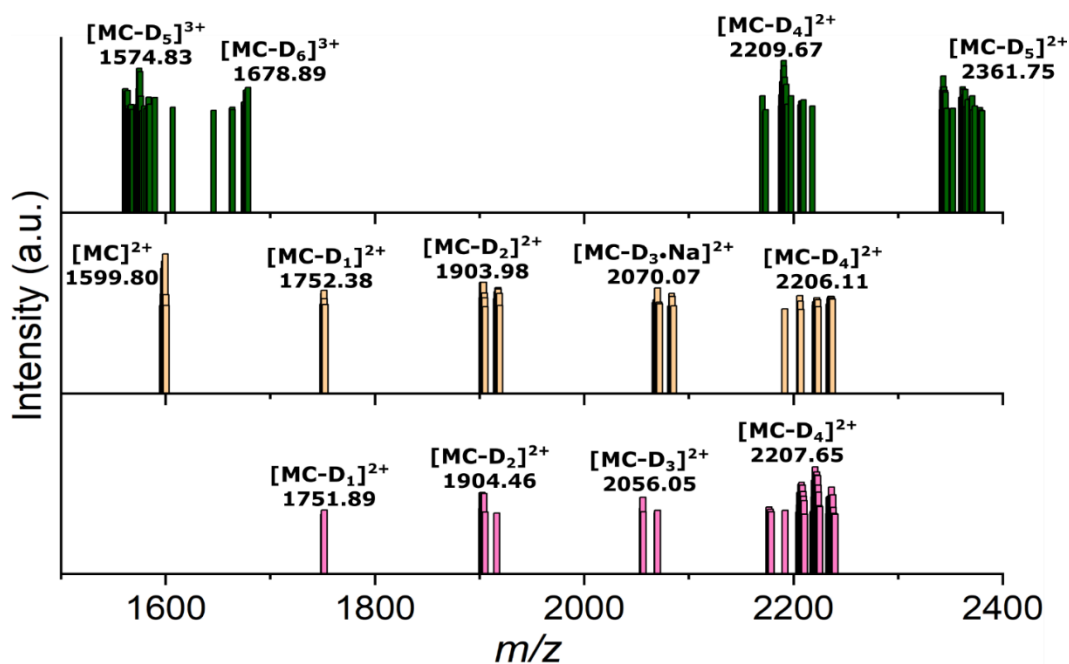


Figure 3.22 ESI-MS spectra of the synthetic trials to prepare hyperboloidal DMC with $\text{Yb}_2\text{Ga}_8\text{P}_7\text{YneShi}_8\text{Ip}_4$ MC cores and HS-G1.0 PAMAM dendrons under **Approach B** (Green) and **Approach C** (Yellow and Pink).

Table 3.6 Reaction conditions for coupling **HS-G1.0 PAMAM dendrons** to **Yb₂Ga₈PYneShi₈Ip₄** under UV light-catalyzed **Approach B (Green)** and heat-catalyzed **Approach C (Yellow and Pink)**. Each of the trials is color coded to match the ESI-MS results on Figure 3.22.

Plot	Concentration to MC (mg/mL)	HS G1.0 Dendron (eq)	Radical Initiator (eq)	Reaction Time (hrs)
Green	10	40	0.32	2
Yellow	25	40	0.32	3
Pink	25	40	1.0	3

Approach B was also employed for the coupling of HS-G1.5 PAMAM dendrons to Yb₂Ga₈PYneShi₈Ip₄ as seen in Figure 3.23, and with the different reaction details listed on Table 3.7. The two reactions conditions were only different in the amount of Michler's ketone photoinitiator added (0.32 eq vs. 4.0 equivalents), and both yielded similar results of six to eight dendron couplings per metallacrown. Compared to the results when coupling HS-G1.0 dendrons to the MC core, the number of couplings of HS-G1.5 increased. This observation suggests that the surface of the dendrons (-OMe for G1.5, vs. -NH₂ for G1.0) may play a role on the reactivity of the thiol-yne coupling. In both reaction trials, unreactive MC (i.e., MC with zero dendron couplings) was not observed, and the number of dendrons coupled to the MC is the same as when done with **Approach A** (with DMPA as the photo initiator). Yet, no more than eight maximum couplings were observed by ESI-MS. Furthermore, just as with the coupling trials with HS-G1.0 under this same approach, an obvious discoloration of the reaction mixture was seen. Investigation of the nature of the discoloration when implementing **Approach B** was not further pursued, primarily due to the lack of complete dendron coupling to the MC core, which would complicate isolation of the colored component.

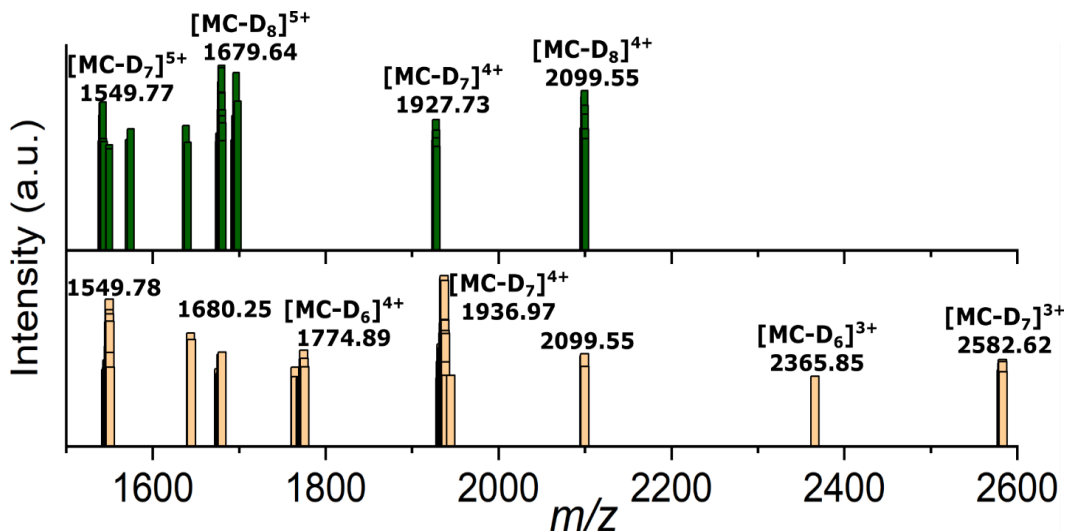


Figure 3.23 ESI-MS spectra of the synthetic trials to prepare hyperboloidal DMC with $\text{Yb}_2\text{Ga}_8\text{pYneShi}_8\text{Ip}_4$ MC cores and HS-G1.5 PAMAM dendrons under **Approach B**.

Table 3.7 Reaction conditions for coupling **HS-G1.5 PAMAM dendrons** to $\text{Yb}_2\text{Ga}_8\text{pYneShi}_8\text{Ip}_4$ under UV light-catalyzed **Approach B**. Each of the trials is color coded to match the ESI-MS results on Figure 3.23.

Plot	Concentration to MC (mg/mL)	HS G1.5 Dendron (eq)	Michler's Ketone (eq)	Reaction Time (hrs)
Olive	4	40	0.32	2
Yellow	3	40	4.0	2

Synthetic Approaches to Prepare H-DMCs with $\text{YbGa}_4\text{pAlShi}_4(\text{benzoate})_4$, $\text{Yb}_2\text{Ga}_8\text{pAlShi}_8\text{Ip}_4$, and $\text{Yb}_2\text{Ga}_8\text{mAlShi}_8\text{Ip}_4$. The reaction between $\text{YbGa}_4\text{pAlShi}_4(\text{benzoate})_4$ and HS-G1.0 PAMAM dendrons in degassed DMF, following irradiation with UV light (365 nm) with DMPA as the photoinitiator (**Approach A**), led to the formation of a dendrimeric metallacrown with a monomeric MC as the core. As seen in Figure 3.24 the ESI-MS of the reaction shows peaks corroborating the complete coupling of four dendrons to the MC core, and the lack of unreactive MC (m/z : 1759.94 or 1455.81). The reaction conditions are listed in Table 3.8. The dendrimeric metallacrowns were best characterized in positive ion mode, and can be seen in ESI-MS as a +2 charged complex. This differs from the unreacted $\text{YbGa}_4\text{pAlShi}_4(\text{benzoate})_4$ core which is best observed as a -1 charge complex in negative ion mode. This likely is due to the increasing number of internal amide and amine surface groups that can be more easily protonated during ESI-MS characterization.

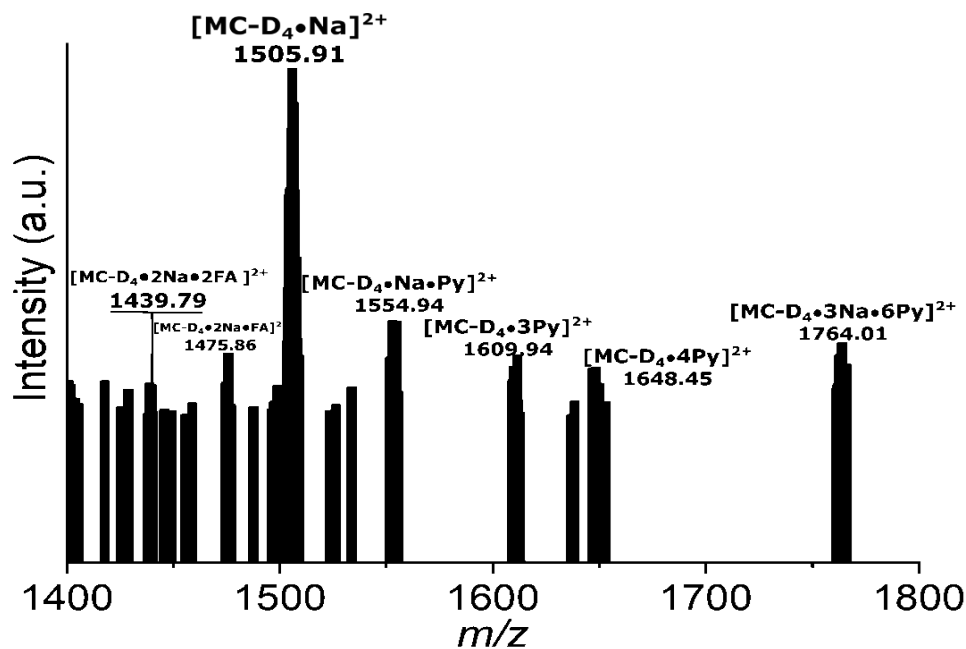


Figure 3.24 ESI-MS spectra of DMC G1.0 with YbGa₄Shi₄(benzoate)₄ MC core under **Approach A**.

Table 3.8 Reaction conditions for coupling HS-G1.0 PAMAM dendrons to YbGa₄pAlShi₄(benzoate)₄ under UV-light catalyzed **Approach A**.

Plot	Concentration to MC (mg/mL)	HS G1.5 Dendron (eq)	DMPA (eq)	Reaction Time (hrs)
Black	35	40	0.25	1

Approach A was also implemented for the coupling of HS-G0.5 dendrons to the dimeric Yb₂Ga₈pAlShi₈Ip₄ MC. Seen in Figure 3.25 and detailed on Table 3.9, are two different trials where the reaction concentration and reaction times were varied. In both cases, an array of dendron coupling to the MC core was observed – with four to eight couplings under the first reaction condition, and six to eight under the second condition where the reaction concentration was reduced and reaction time increased. Decreasing the reaction concentration or increasing reaction times even further did not yield better results. Addition of more thiol focal point dendron to the reaction did not increase the number of couplings to the MC core past six to eight.

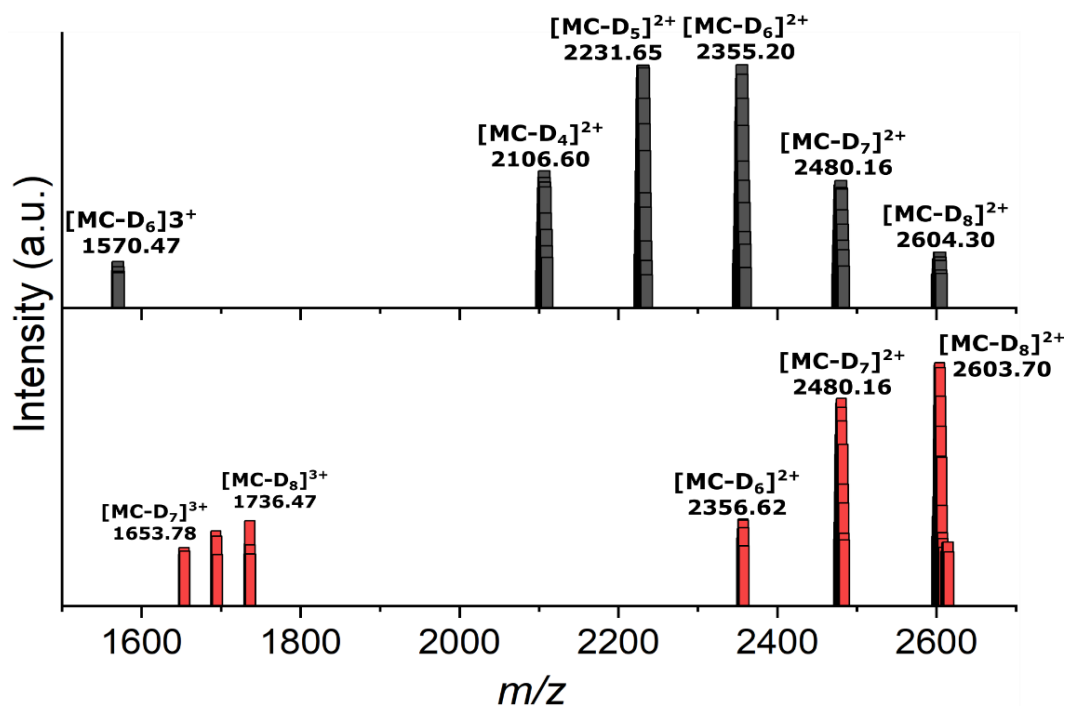


Figure 3.25 ESI-MS spectra of the synthetic trials to prepare hyperboloidal DMC with $\text{Yb}_2\text{Ga}_8\text{pAlShi}_8\text{Ip}_4$ MC cores and HS-G0.5 PAMAM dendrons under **Approach A**.

Table 3.9 Reaction conditions for coupling **HS-G0.5 PAMAM dendrons** to $\text{Yb}_2\text{Ga}_8\text{pAlShi}_8\text{Ip}_4$ under UV- light catalyzed Approach A. Each of the trials is color coded to match the ESI-MS results on Figure 3.25

Plot	Concentration to MC (mg/mL)	HS G0.5 Dendron (eq)	DMPA (eq)	Reaction Time (hrs)
Gray	50	80	0.5	2
Red	20	80	0.5	4

Under **Approach A**, the coupling of HS-G1.0 PAMAM dendrons to $\text{Yb}_2\text{Ga}_8\text{pAlShi}_8\text{Ip}_4$ MC was tested under varying reaction conditions listed in Table 3.10. As seen in Figure 3.26, the ESI-MS spectra of the four different reaction conditions display six to eight couplings of dendrons to the MC core in all cases. Increasing reaction times (0.5-4 hrs), DMPA equivalents (0.50-1.0 eq), or dendron equivalents (80-100eq) did not seem to have much influence on the amount of dendron couplings, as seen with the coupling of HS-G0.5 dendrons. The narrow distribution of HS-G1.0 dendron couplings to $\text{Yb}_2\text{Ga}_8\text{pAlShi}_8\text{Ip}_4$ is similar to the distribution shown in Figure 3.15 (bottom) and Figure 3.25 (bottom) were six to eight couplings of βME or HS-G0.5, respectively, are coupled to the MC core. Furthermore, no unreactive MC is seen by ESI-MS (m/z 1606.82²⁺), corroborating the formation of toroidal dendrimeric metallacrowns with partial to complete

dendron coupling to the MC core. The $\text{Yb}_2\text{Ga}_8\text{pAlShi}_8\text{Ip}_4$ G1.0 DMC reaction was then scaled up to batches of 30-50 mg of MC, purified by dialysis, and characterized by dynamic light scattering (DLS) and luminescence.

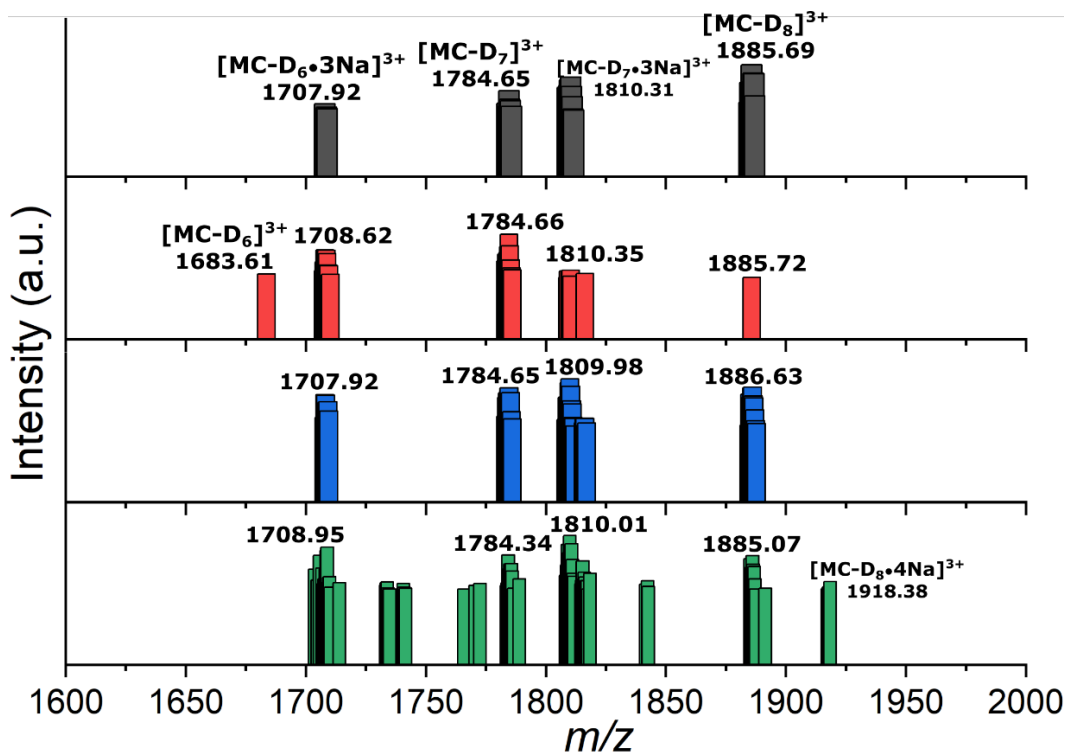


Figure 3.26 ESI-MS spectra of the synthetic trials to prepare hyperboloidal DMC with $\text{Yb}_2\text{Ga}_8\text{pAlShi}_8\text{Ip}_4$ MC cores and HS-G1.0 PAMAM dendrons under **Approach A**.

Table 3.10 Reaction conditions for coupling **HS-G1.0 PAMAM dendrons** to $\text{Yb}_2\text{Ga}_8\text{pAlShi}_8\text{Ip}_4$ under UV- light catalyzed **Approach A**. A. Each of the trials is color coded to match the ESI-MS results on Figure 3.26.

Plot	Concentration to MC (mg/mL)	HS G1.0 Dendron (eq)	DMPA (eq)	Reaction Time (hrs)
Gray	35	80	0.50	0.5
Red	35	80	0.50	1.0
Blue	35	80	1.0	2
Green	35	100	0.50	4

Dendron coupling (HS-G1.0) to the $\text{Yb}_2\text{Ga}_8\text{pAlShi}_8\text{Ip}_4$ MC was also investigated under **Approach A** and **Approach C**. Shown in Figure 3.27 and detailed in Table 3.11 are three different trials varying reaction concentrations (10-50 mg/mL) and lengths of reaction time (1-4hrs). A lower reactivity toward thiol-ene coupling was to be expected based on the results from βME

coupling to the same MC core (Figure 3.16); however, the broad distribution of dendron coupling ranging from one to seven, under varying conditions, was surprising. Increase of reaction concentration or reaction length under UV light did not yield significantly better results. Thus, only incomplete coupling of HS-G1.0 dendron to $\text{Yb}_2\text{Ga}_8\text{mAlShi}_8\text{Ip}_4$ was observed by ESI-MS.

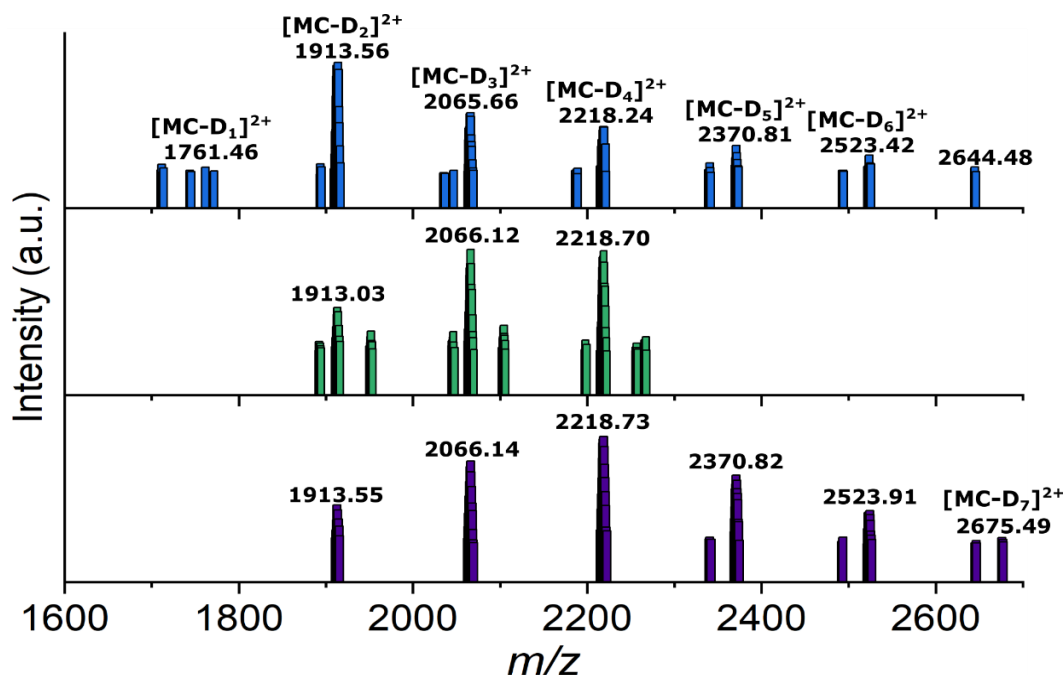


Figure 3.27 ESI-MS spectra of the synthetic trials to prepare hyperboloidal DMC with $\text{Yb}_2\text{Ga}_8\text{mAlShi}_8\text{Ip}_4$ MC cores and HS-G1.0 PAMAM dendrons under **Approach A**.

Table 3.11 Reaction conditions for coupling **HS-G1.0 PAMAM dendrons** to $\text{Yb}_2\text{Ga}_8\text{mAlShi}_8\text{Ip}_4$ under UV- light catalyzed **Approach A**.

Plot	Concentration to MC (mg/mL)	HS G1.5 Dendron (eq)	DMPA (eq)	Reaction Time (hrs)
Blue	10	80	0.5	4
Green	20	80	0.5	2
Purple	50	80	0.5	1

Approach C was also employed for the same MC and dendron generation to investigate if a non-photocatalytic approach was better suited for the meta-substituted MC. However, as seen in Figure 3.28 significantly worse results were observed – with a maximum of two dendron couplings and observable unreacted $\text{Yb}_2\text{Ga}_8\text{mAlShi}_8\text{Ip}_4$. Reaction conditions are listed on Table 3.12.

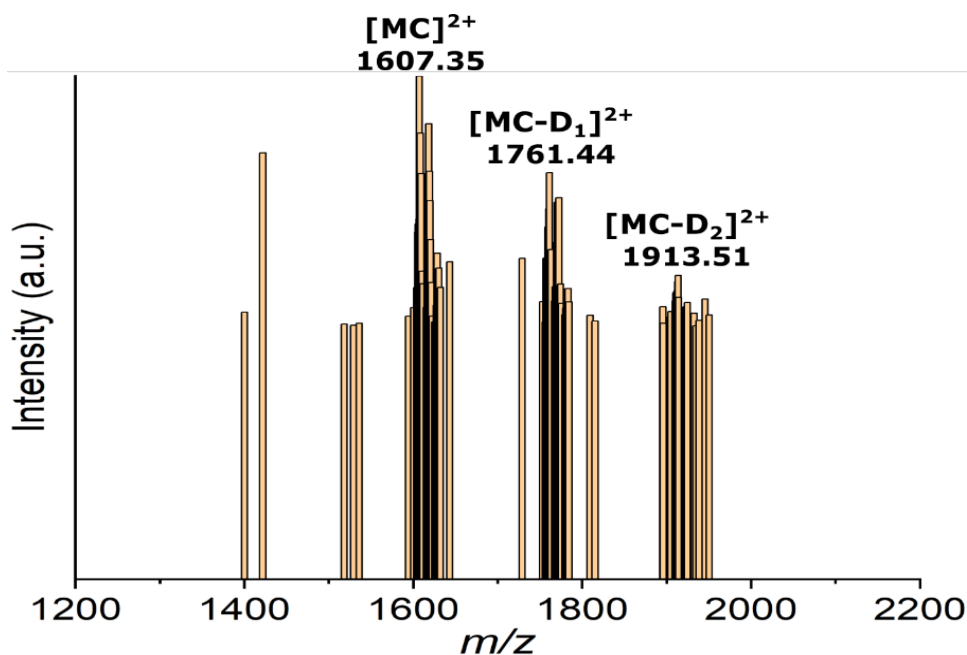


Figure 3.28 ESI-MS spectra of the synthetic trials to prepare hyperboloidal DMC with $\text{Yb}_2\text{Ga}_8\text{mAlShi}_8\text{Ip}_4$ MC cores and HS-G1.0 PAMAM dendrons under **Approach C**.

Table 3.12 Reaction conditions for coupling **HS-G1.0 PAMAM dendrons** to $\text{Yb}_2\text{Ga}_8\text{mAlShi}_8\text{Ip}_4$ under Heat-catalyzed Approach C.

Plot	Concentration to MC (mg/mL)	HS G1.0 Dendron (eq)	AIBN (eq)	Reaction Time (hrs)
Yellow	10	80	10	14

Characterization of $\text{Yb}_2\text{Ga}_8\text{pAlShi}_8\text{Ip}_4$ G1.0 DMC. Size distribution analysis of $\text{Yb}_2\text{Ga}_8\text{pAlShi}_8\text{Ip}_4$ metallacrown and G1.0 DMC in DMSO solutions using DLS are seen in Figure 3.29. The average hydrodynamic diameters (D_{av}), polydispersity indexes (PdI), and diffusion coefficients (D_c) of the MC and the DMC G1.0 are the following: D_{av} : 3.7 nm, PdI: 0.06, D_c : $1.30\text{e-}6 \text{ cm}^2\text{s}^{-1}$ for $\text{Yb}_2\text{Ga}_8\text{pAlShi}_8\text{Ip}_4$ MC; and D_{av} : 5.3 nm, PdI: 0.09, D_c : $9.09\text{e-}7 \text{ cm}^2\text{s}^{-1}$ for $\text{Yb}_2\text{Ga}_8\text{pAlShi}_8\text{Ip}_4$ G1.0 DMC. The increasing diameter and decreasing diffusion coefficients confirm that the DMC is larger in size, volume, and molecular weight. The lower intensity peak at higher diameters of the DMC plot (D_{av} : 43.5 nm, PdI: 0.04, D_c : $1.11\text{e-}7 \text{ cm}^2\text{s}^{-1}$) is likely the result of a small degree of aggregation in solution due to sample concentration ($\sim 3 \text{ mM}$), solvent interaction, or dendron interlinking between DMC molecules. The solution behavior of the G1.0 hyperboloidal-DMC was also investigated in a more aqueous environment. The DMC was diluted with water to a final solution composition of 99:1 $\text{H}_2\text{O}/\text{DMSO}$ (v/v%) at pH 7.5. The DLS plot in

Figure 3.30 shows that under such conditions, the H-DMC forms large aggregates (bigger and heavier particle) with an average hydrodynamic diameter of ~ 340 nm, a slightly broader polydispersity (0.12), and a smaller diffusion coefficient (D_c : $1.41 \times 10^{-8} \text{ cm}^2 \text{ s}^{-1}$).

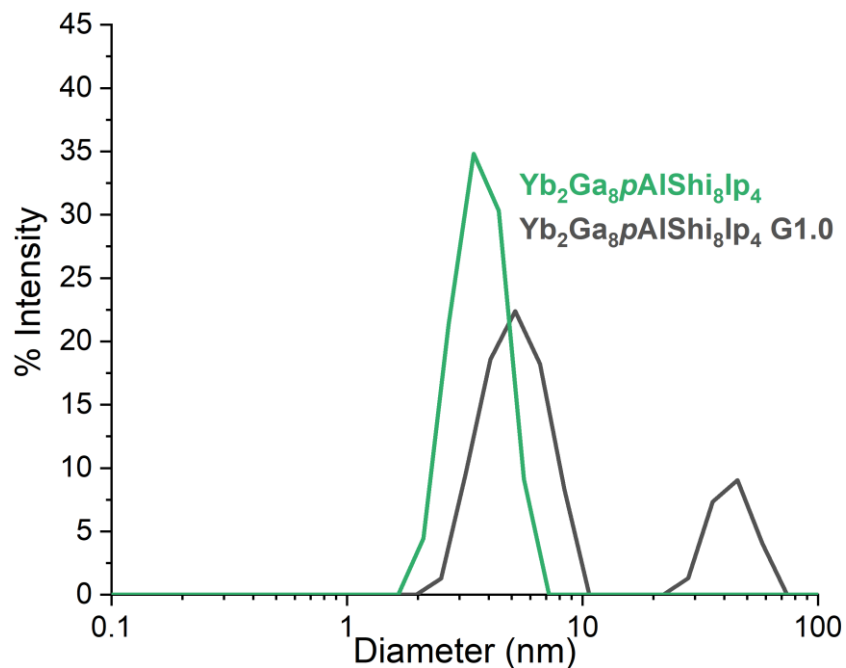


Figure 3.29 DLS size distribution of Yb₂Ga₈pAlShi₈Ip₄ MC and G1.0 DMC at 5 mg/mL and 3.2 mM, respectively, in DMSO and at room temperature.

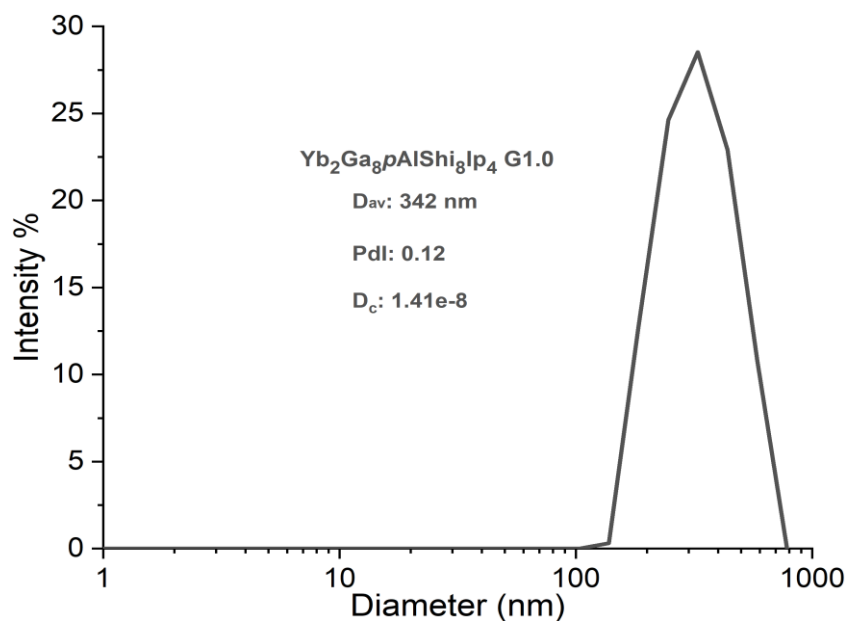


Figure 3.30 DLS size distribution of Yb₂Ga₈pAlShi₈Ip₄ G1.0 hyperboloidal-DMC at 34.1 μM solution in 99:1 H₂O:DMSO at room temperature and at pH: 7.5.

The UV-Vis absorbance of $\text{Yb}_2\text{Ga}_8\text{pAlShi}_8\text{Ip}_4$ G1.0 DMC shown in Figure 3.31, exhibit a broad absorption band attributed to the $\pi \rightarrow \pi^*$ transition located in the range of 250 – 340 nm. The spectra also show a low energy maximum at ~310 nm, just as with the unfunctionalized $\text{Yb}_2\text{Ga}_8\text{pAlShi}_8\text{Ip}_4$ MC. The energy of the ligand singlet (S^*), determined from the edge of the absorption spectra, is identical to that of the MC core with no dendrons coupled, and it is located at ~340 nm (29412 cm^{-1}). The similar absorbance profiles and intensities of the unfunctionalized MC and $\text{Yb}_2\text{Ga}_8\text{pAlShi}_8\text{Ip}_4$ G1.0 DMC suggest that the absorbance behavior is not affected by the addition of the dendrons to the MC core. The slight decrease in absorbance intensity of the $\text{Yb}_2\text{Ga}_8\text{pAlShi}_8\text{Ip}_4$ G1.0 DMC is due to the small difference in solution concentration between the two samples – 12 μM for the MC and 11 μM for the DMC.

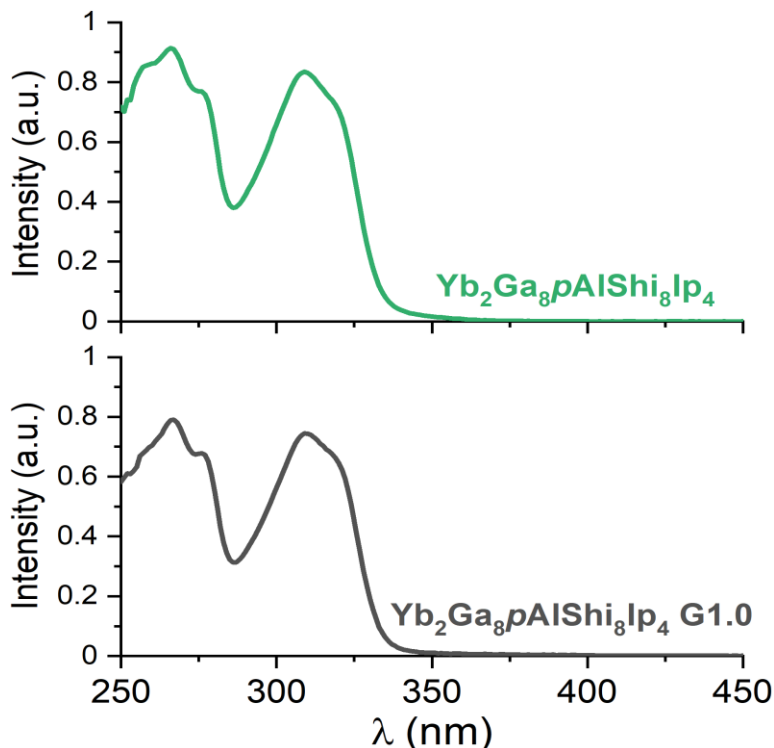


Figure 3.31 UV-Vis absorption spectrum of 12 μM $\text{Yb}_2\text{Ga}_8\text{pAlShi}_8\text{Ip}_4$ MC (top) and 11 μM $\text{Yb}_2\text{Ga}_8\text{pAlShi}_8\text{Ip}_4$ G1.0 DMC (bottom) dissolved in DMSO and at room temperature. Absorbance maxima for both compounds is at 310 nm with an extinction coefficient of $6.8 \times 10^4 \text{ M}^{-1}\text{cm}^{-1}$.

The excitation and emission spectra of $\text{Yb}_2\text{Ga}_8\text{pAlShi}_8\text{Ip}_4$ G1.0 DMC collected in DMSO at room temperature are shown in Figure 3.32. Solid state measurements were not collected so as to avoid undesired dendritic defects (e.g., trailing generations, oligomers, retro-Michael addition)

during sample concentration. The solution state excitation spectrum was collected upon monitoring the Yb^{III} emission at 980 nm, and showed broad ligand-centered bands up to 350 nm. Solution state emission upon excitation in the ligand-centered region at 320 nm exhibited characteristic Yb^{III} luminescent signals in the range of 900-1100 nm arising from the $^2F_{5/2} \rightarrow ^2F_{7/2}$ transition, and with a maximum at 980 nm. Luminescent lifetimes (τ_{obs}) and ligand-centered quantum yields (ϕ_{Yb}^L) in DMSO were also acquired and are summarized in Table 3.13. For the sake of comparison, the values for the unreacted MC (Yb₂Ga₈pAlShi₈Ip₄), the parent MC (Yb₂Ga₈Shi₈Ip₄), and the equivalent toroidal DMC (Yb₂Ga₈Shi₈Mip₄ G1.0) are also listed. Compared to the Yb₂Ga₈pAlShi₈Ip₄ core, the DMC has τ_{obs} and ϕ_{Yb}^L values that are ~ 1.4 and ~ 1.2 times higher, respectively. An improvement in both τ_{obs} and ϕ_{Yb}^L values compare to Yb₂Ga₈Shi₈Ip₄ also increased in the DMC by a factor of ~ 1.1 and ~ 1.2 , respectively. Interestingly, compared to the toroidal DMC of the same generation (Yb₂Ga₈Shi₈Mip₄ G1.0), τ_{obs} increased by a factor of ~ 1.1 , while ϕ_{Yb}^L decreased by ~ 0.9 .

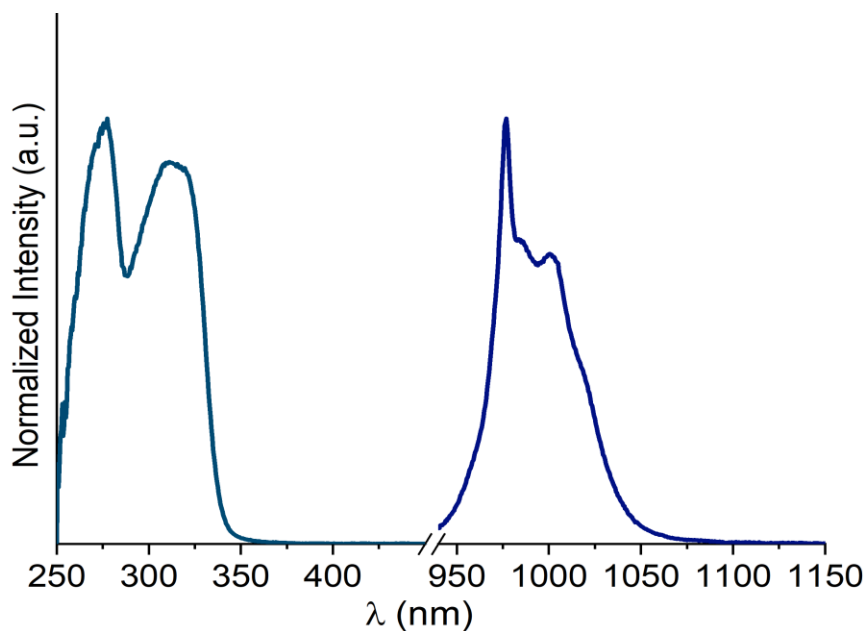


Figure 3.32 Corrected and normalized excitation (left, $\lambda_{\text{em}} = 980$ nm), and emission ($\lambda_{\text{ex}} = 320$ nm) spectra of 50 μM DMSO solution of Yb₂Ga₈pAlShi₈Ip₄ G1.0 DMC at room temperature.

Table 3.13 Luminescence lifetimes (τ_{obs}) and Yb^{III}-centered quantum yields collected under ligand excitation (ϕ_{Yb}^L)^a

Compound	Solvent	τ_{obs} [μs] ^b	ϕ_{Yb}^L [%] ^c
Yb ₂ Ga ₈ pAlShi ₈ Ip ₄ G1.0	DMSO	69.2(3)	8.7(2)
Yb ₂ Ga ₈ pAlShi ₈ Ip ₄	DMSO	49.9(7)	7.75(1)
Yb ₂ Ga ₈ Shi ₈ Ip ₄	DMSO	60.9(4)	7.56(2)
Yb ₂ Ga ₈ Shi ₈ Mip ₄ G1.0	DMSO	63.8(8)	9.38(2)

^a For samples 50 μM solutions in DMSO at room temperature, and with 2σ values between parentheses. Estimated experimental errors: τ_{obs} , $\pm 2\%$; Q_{Yb}^L , $\pm 10\%$. ^b Under excitation at 355 nm. ^c Under excitation at 320 nm.

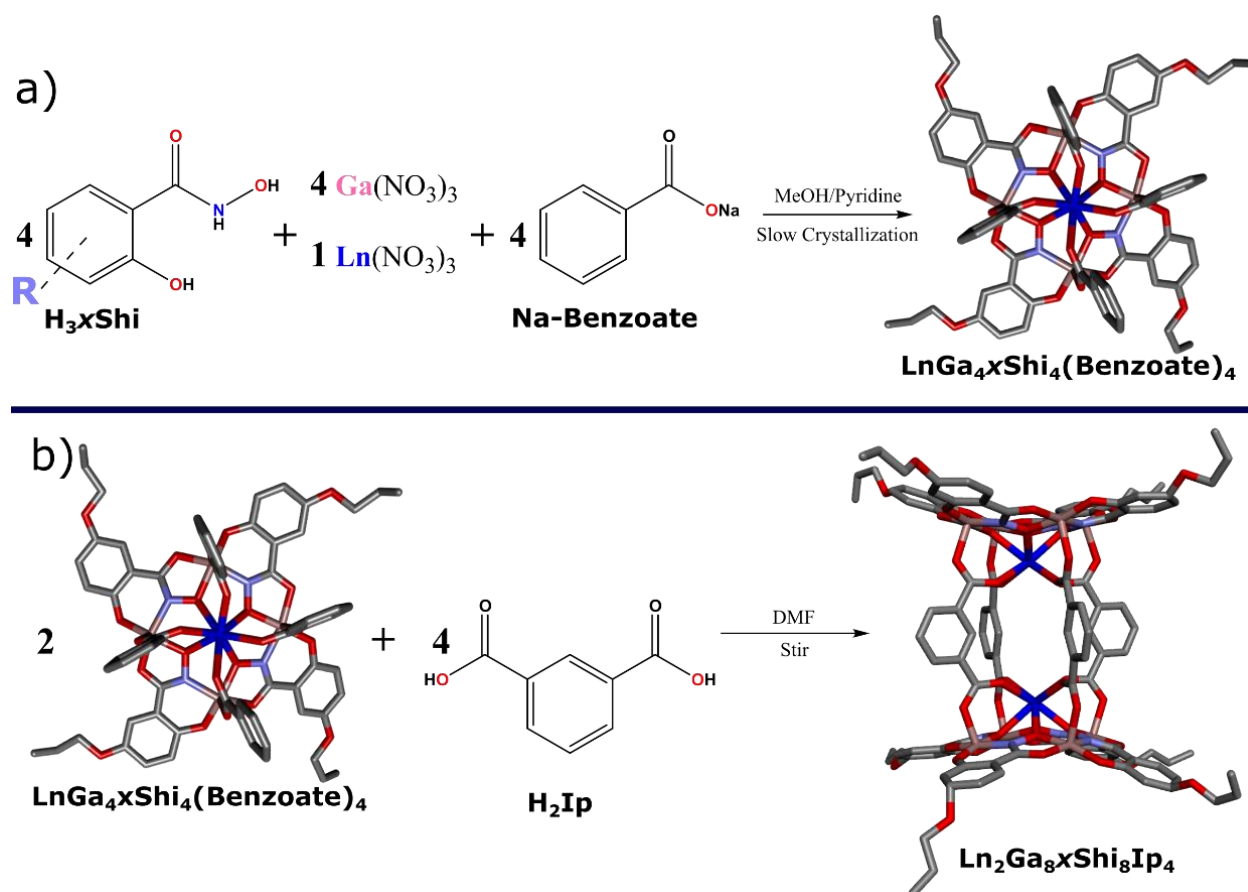
3.4 Discussion

3.4.1 Synthesis and Characterization of LnGa₄xShi₄(benzoate)₄ and Ln₂Ga₈xShi₈Ip₄ Metallacrowns (Ln: Yb^{III}, Sm^{III}, and Gd^{III}; x: pYne, mYne, pAl, and pAl)

The LnGa₄xShi₄(benzoate)₄ and Ln₂Ga₈xShi₈Ip₄ scaffolds represent the first metallacrowns with ring ligands capable of undergoing thiol-yne/ene photocatalytic addition. The monomeric LnGa₄xShi₄(benzoate)₄ derivatives were prepared through the reaction of H₃xShi and nitrate salts of Ga^{III} and Ln^{III} in solutions of methanol and pyridine, followed by the addition of sodium benzoates, as shown in Scheme 3.1 (top). The novel LnGa₄xShi₄(benzoate)₄ scaffolds are structurally similar to unsubstituted parent material LnGa₄Shi₄(benzoate)₄ previously reported by our group.¹⁰² Crystal structures of two of the analogues (LnGa₄pYneShi₄ and LnGa₄mAlShi₄) shown in Figure 3.4 corroborate that the meta- and para-substituted scaffolds are structurally similar, aside from the position of the functional group. Each of the four monomeric derivatives were prepared with Yb^{III}, Sm^{III}, and Gd^{III}. As for the dimeric scaffolds, Ln₂Ga₈xShi₈Ip₄ MCs was prepared by carboxylate substitution on the LnGa₄xShi₄(benzoate)₄ with isophthalic acid, as shown in Scheme 3.1 (bottom). This synthetic approach was adopted because of the relatively fast product formation over the typical slow evaporation approach used to prepare other Ln₂Ga₈Shi₈Ip₄ MC analogues.^{106,124} The substitution of the four benzoate ligands by four bridging isophthalic ligands is driven by the difference in pK_a between them – ~ 4.20 for benzoate, and ~ 3.46 , ~ 4.46 for isophthalate. Crystallographic data of the dimeric Ln₂Ga₈xShi₈Ip₄ MCs was not collected since the product was isolated as a powder and not as single crystals. However, the structure is expected to be analogous to the unsubstituted parent material Ln₂Ga₈Shi₈Ip₄ previously reported by our group.^{106,124} Just as with the monomeric counterparts, dimers were prepared with Yb^{III}, Sm^{III}, and

Gd^{III}; however, there is no reason to believe that the full range of Ln(III) ions that have previously been used for Ln₂Ga₈Shi₈Ip₄ MC cannot be prepared with these ligands.

In both the monomeric and dimeric MCs, the 12-MC_{Ga(III)N(xshi)-4} scaffolds have a slightly concave ring morphology, and contain four d¹⁰ Ga^{III} metal ions linked together by four xShi³⁻ ring ligands. The Ln^{III} ions are located at the center of each of the 12-MC_{Ga(III)N(xshi)-4} scaffolds and their eight-coordination is fulfilled by four oxime oxygens from the MC and the four carboxylate oxygens from the bridging ligands. In the case of the dimeric scaffolds, two 12-MC_{Ga(III)N(xshi)-4} are bridged together by the isophthalate bridges.



Scheme 3.1 a) Synthesis of LnGa₄xShi₄(benzoate)₄ from free ligands and metal salts via slow crystallization. b) Synthesis of Ln₂Ga₈xShi₈Ip₄ by carboxylate substitution of benzoate with H₂Ip on the monomeric MC. The same reaction scheme was used for all LnGa₄xShi₄(benzoate)₄ and Ln₂Ga₈xShi₈Ip₄ prepared with the four different ring ligands (H_{3p}/mYneShi and H_{3p}/mAlShi) and the three different Ln^{III} ions (Yb^{III}, Sm^{III}, and Gd^{III}).

Chemical compositions for all the monomeric and dimeric derivatives were further corroborated by ESI-MS and ¹H NMR (for the Sm^{III} analogues), as shown in Figure 3.2, Figure

3.6, and Appx. C Figures 41-43. With both characterization techniques, the exclusive presence of the MC scaffold was observed, thus confirming the composition and purity of the compounds. An important feature of $\text{LnGa}_4\text{xShi}_4(\text{Benzoate})_4$ characterization by ESI-MS is that it is common to see an array of five signals arising from the exchange of benzoate by formate ligands during data collection. This bridge ligand exchange during ESI-MS characterization arises from the solvent composition used to run the mass spectrometer (i.e. acetonitrile with 0.1% formic acid), and the susceptibility of benzoate bridging ligands to be substituted by carbonyl-based acids. This can often be avoided by careful rinsing of the instrument's lines with copious amounts of methanol. Yet, even after complete exchange of bridging ligands (i.e., $\text{LnGa}_4\text{xShi}_4(\text{Formate})_4$), the $12\text{-MC}_{\text{Ga(III)N(xshi)-4}}$ scaffold itself remains intact, and the purity of the sample can still be corroborated.

Looking at the isotopic distribution in each of the ESI-MS spectra, the overall charge of the monomeric and dimeric MCs was confirmed to be -1 and -2, respectively. Charge neutrality of the monomers is maintained with a single pyridinium ion, as confirmed by crystallographic data, while for the dimeric MCs, charge balance is expected to be maintained by two pyridinium ions. This model is corroborated by the presence of pyridine signals in the ^1H NMR spectra of these compounds. Furthermore, NMR characterization also corroborates the desired dimeric composition of $\text{Ln}_2\text{Ga}_8\text{xShi}_8\text{Ip}_4$ MCs with the presence of 2:1 integration ratios of $\text{xShi}^{-3}:\text{Ip}^{-2}$ ligands. Peak splitting of the bridging protons (labeled 17 and 19 on Figure 3.6) arises from the non-equivalence between the two $12\text{-MC}_{\text{Ga(III)N(xshi)-4}}$ scaffolds in the dimeric MC. This has been observed in the previously reported $\text{Ln}_2\text{Ga}_8\text{Shi}_8\text{Ip}_4$ ^{106,124} MC and in the $\text{Ln}_2\text{Ga}_8\text{Shi}_8\text{Mip}_4$ ¹²² described in Chapter 2.

The solution absorbance spectroscopy of $\text{LnGa}_4\text{xShi}_4(\text{benzoate})_4$ and $\text{Ln}_2\text{Ga}_8\text{xShi}_8\text{Ip}_4$ in DMSO demonstrate that para-substituted scaffolds have similar profiles, with absorbance between 250-340 nm, while the meta-substituted have absorbances between 250-360nm. These observations demonstrate that while the functional group class (alkene vs alkyne) does not seem to have much influence on the absorbance profile, the ring position does. This is seen as a red-shift of the lower energy maximum by 2846 cm^{-1} , and the S^* energy position by 2745 cm^{-1} when comparing *m*Yne/AlShi to *p*Yne/*p*AlShi MCs. Another observation is that while the absorbance energy is blue-shifted for the para-substituted MC, their extinction coefficients are ~1.3-1.8 times larger than those of the meta-substituted ligands. Therefore, there is an effect on the polarizability of the MC ligands based on the substituent position. Furthermore, a doubling in extinction

coefficient per molecule on going from the monomer to the dimer occurs, which is expected since the amount of ring ligand also doubles from $\text{LnGa}_4\text{xShi}_4(\text{benzoate})_4$ to $\text{Ln}_2\text{Ga}_8\text{xShi}_8\text{Ip}_4$.

As shown in Table 3.14, S^* states of each para-substituted and meta-substituted MC scaffolds have a favorable energy difference (ΔE) to the measured T^* states, with values close to $\sim 5000 \text{ cm}^{-1}$ that ensure efficient ligand intersystem crossing ($S^* \rightarrow T^*$). Compared to the values of the unfunctionalized parent MCs ($\text{GdGa}_4\text{Shi}_4$ and $\text{Gd}_2\text{Ga}_8\text{Shi}_8\text{Ip}_4$), the S^*-T^* ΔE of the new MCs are narrower. Thus, suggesting that the new scaffolds have more favorable $S^* \rightarrow T^*$ transitions. This is of great importance for Ln^{III} ion sensitization since the T^* state of the antenna is regarded as the main feeding level to the metal ion emissive state (Ln^*).¹³¹ Furthermore, to ensure appropriate Ln^{III} ion sensitization, a minimum ΔE of $2500\text{-}3000 \text{ cm}^{-1}$ between the T^* and Ln^* is required to ensure efficient energy transfer and minimize thermally activated back transfer events ($T^* \leftarrow \text{Ln}^*$). As seen on Table 3.14, each of the new MC scaffolds fulfills such requirements when Yb^{III} and Sm^{III} are used. Scaffolds prepared with Ln^{III} ions with emissive states larger than 18000 cm^{-1} ($< 540 \text{ nm}$) will likely undergo back transfer ($T^* \leftarrow \text{Ln}^*$). Thus, if MCs are prepared with lanthanide ions such as Tb^{III} , Dy^{III} , and Tm^{III} , quantum yields would be hindered by the $T^* \leftarrow \text{Ln}^*$ back transfer.

Table 3.14 Absorbance maximum (Abs_{max}) of MCs, energy levels of their singlet (S^*) triplet (T^*), and lanthanide (Ln^*) energies, and energy difference (ΔE) between states.

Compound	Abs_{max} (cm^{-1}) ^a	S^* (cm^{-1}) ^b	T^* (cm^{-1}) ^c	S^*-T^* ΔE (cm^{-1})	$T^*-\text{Yb}^*$ ^d ΔE (cm^{-1})	$T^*-\text{Sm}^*$ ^e ΔE (cm^{-1})
$\text{GdGa}_4\text{Shi}_4$ ^f	310	28571	22170	6401	11870	4270
$\text{GdGa}_4\text{pYneShi}_4$	310	29412	23450	5962	13150	5550
$\text{GdGa}_4\text{mYneShi}_4$	340	26667	21480	5187	11180	3580
$\text{GdGa}_4\text{pAlShi}_4$	310	29412	23360	6052	13060	5460
$\text{GdGa}_4\text{mAlShi}_4$	340	26667	21630	5037	11330	3730
$\text{Gd}_2\text{Ga}_8\text{Shi}_8\text{Ip}_4$ ^g	310	28650	21980	6670	11680	4080
$\text{Gd}_2\text{Ga}_8\text{pYneShi}_8\text{Ip}_4$	310	29412	--	--	--	--
$\text{Gd}_2\text{Ga}_8\text{mYneShi}_8\text{Ip}_4$	340	26667	21620	5047	11320	3720
$\text{Gd}_2\text{Ga}_8\text{pAlShi}_8\text{Ip}_4$	310	29412	22740	6672	12440	4840
$\text{Gd}_2\text{Ga}_8\text{mAlShi}_8\text{Ip}_4$	340	26667	21410	5257	11110	3510

^a Determined from the UV-Vis Absorbance spectrum DMSO solutions. ^b Determined as the edge of absorption spectrum of the corresponding ligand. ^c Determined as 0-0 transition of the phosphorescence spectrum of the corresponding Gd^{III} MC. ^d $E^{\text{Yb}}(^2\text{F}_{5/2}) = 10300 \text{ cm}^{-1}$. ^e $E^{\text{Sm}}(^4\text{G}_{5/2}) = 17900 \text{ cm}^{-1}$ ^f From *J. Am. Chem. Soc.* **2016**, 138, 5100-5109. ^g From *Chem. Eur. J.* **2018**, 24, 1031-1035.

Looking at the plotted S^* vs. T^* of each measured Gd^{III} -scaffold and the parent MCs in Figure 3.33, a consistent shift in energy between the two states is observed when going from the

monomeric to the dimeric scaffolds. This highlights the relatively small contribution of the bridging ligands to the triplet state of the scaffolds, with a 1-3% difference in triplet state going from the monomeric to the dimeric scaffold. Moreover, while in general the $S^* - T^*$ ΔE for the new MCs is smaller than that of the parent MCs, the *para*-substituted scaffolds have more energetic singlet and triplet states than both the parent and *meta*-substituted MCs. This further confirms that the functionalization position at the ring ligand has an important effect on the electronic properties of the scaffold. This could be of utility when designing MC scaffolds where delicate tuning of the optical properties can be done by changing the energy levels of the coordinating ligands, as it was recently shown by Salerno *et al.*^{120,178} with the white light emission of Dy^{III}-based MCs. This may be also useful for the design of MC as imaging probes where lower excitation energies are desired since they are both less harmful for biological systems and have much deeper penetration.¹⁷⁹

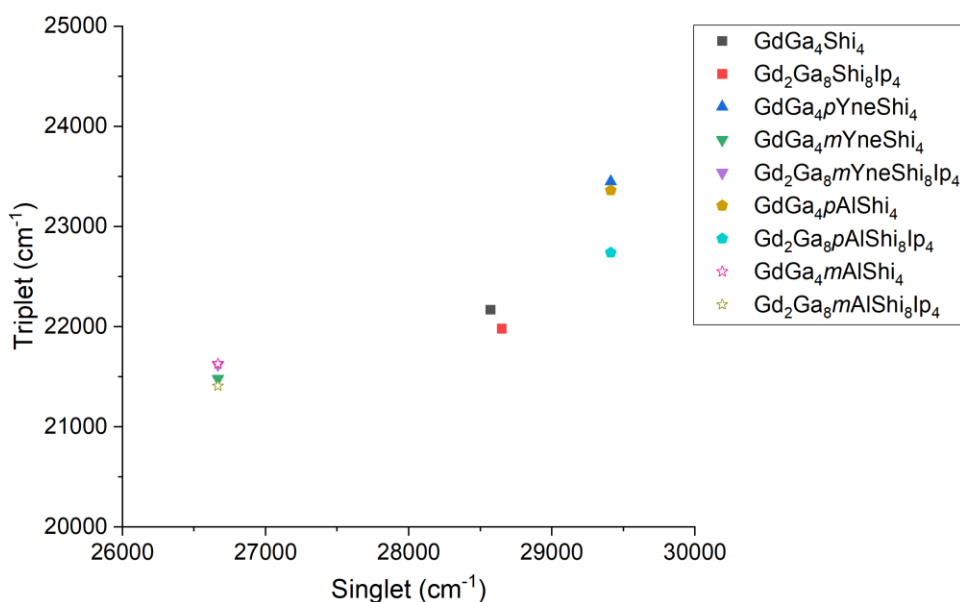


Figure 3.33 Plot of singlet energy vs. triplet energy for the parent MCs and all of the measured monomeric and dimeric Gd^{III}-MC with thiol-ene/yne appendages.

The Ln^{III}-centered photophysical properties, combined with the good spectral overlap between the absorbance and excitation spectra of the each of the LnGa_{4x}Shi₄(benzoate)₄ to Ln₂Ga_{8x}Shi₈Ip₄ MCs (as shown in Figure 3.8, Figure 3.9, Figure 3.11, and Figure 3.12), illustrates the favorable antenna effect of the ring ligands to the Ln^{III} ions. As for the emissive properties, upon excitation into the ligand centered bands at 320-360 nm, characteristic Sm^{III} and Yb^{III}

luminescence emission in the visible and NIR was observed in both solution and solid state.

Focusing on the solid state quantitative photophysical data of the Yb^{III}-MCs listed in Table 3.3, the data show that the τ_{obs} and ϕ_{Ln}^L are lower than the previously reported Yb^{III}-based MCs of the Ga-family. This drop in τ_{obs} and ϕ_{Ln}^L could be attributed to: *i*) the presence of pyridinium counter ions; and *ii*) the introduction of propyne (HC≡CCH₂OR) and propene (H₂C=CHCH₂OR) groups to the ring ligands. In the former, the N-H vibronic oscillators from the pyridinium counter ions could get close enough to the Ln^{III} center of the metallacrown to induce quenching of the luminescent signal. As seen by the values of τ_{obs} and ϕ_{Yb}^L for all of the scaffolds, this is more of an effect in the solid state than in solution, likely due to the dissociation/solvation of the pyridinium ions in DMSO which results in ϕ_{Ln}^L that are higher or very close to the values of the parent MCs. Furthermore, it is important to highlight that the parent Yb₂Ga₈Shi₈Ip₄¹²⁴ scaffold used to compare the τ_{obs} and ϕ_{Yb}^L values to the dimeric scaffolds in this thesis work has two sodium counterions instead of pyridinium cations. This observation demonstrates that the choice of counter ion has a very significant effect on the solid-state luminescence of metallacrowns. As for the latter point, the presence of the propyne (HC≡CCH₂OR) and propene (H₂C=CHCH₂OR) appendages with a certain degree of flexibility and numerous C-H oscillators can potentially be in close enough proximity to the Ln^{III} ion centers to promote luminescent quenching.

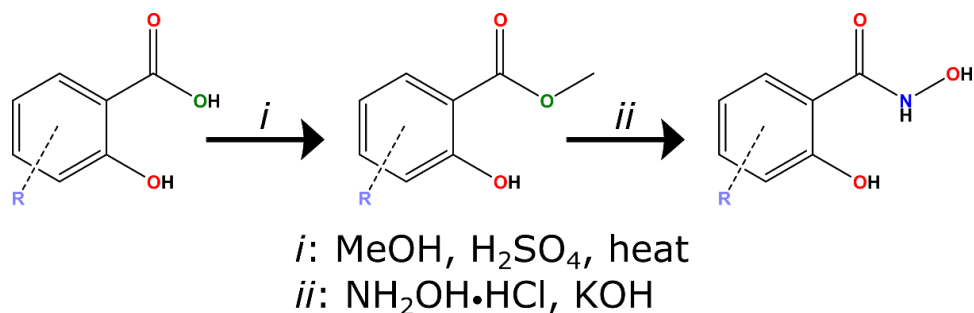
On the other hand, looking at the solution state ϕ_{Ln}^L values for all of the monomeric scaffolds, they have higher quantum yields than the parent YbGa₄Shi₄, with the YbGa₄pAlShi₄(benzoate)₄ MC having the highest ϕ_{Ln}^L recorded in DMSO among Yb^{III}-based MCs, as seen in Table 3.15. As for the dimeric scaffolds, the ϕ_{Ln}^L of the new MCs are very close or slightly higher than those of the parent Yb₂Ga₈Shi₈Ip₄. This suggests that the introduction of functional groups such as alkene and alkynes are not detrimental to the solution state luminescent emission, and in fact it results in higher quantum yields by positioning the T* of the ligands at more favorable distances from the S* as to ensure efficient energy transfer. Therefore, this work highlights the importance of careful ligand design to ensure attractive functionalization while still ensuring efficient luminescent sensitization.

Table 3.15 Luminescence lifetimes (τ_{obs}) and Yb^{III}-centered quantum yields (ϕ_{Ln}^L) in DMSO of MCs described in this chapter. Compounds have been listed in order of decreasing quantum yields, and divided between monomeric and dimeric scaffolds.

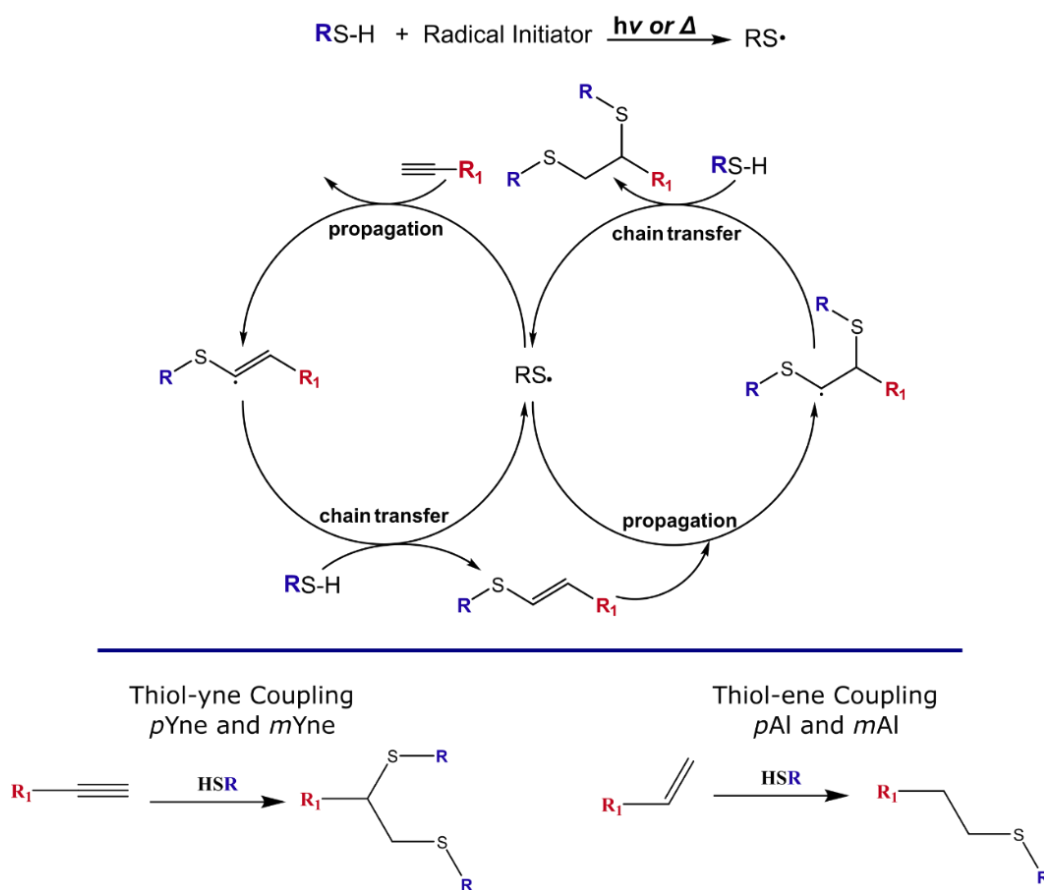
Compounds	τ_{obs} [μs]	ϕ_{Ln}^L [%]
YbGa ₄ pAlShi ₄	36(2)	8.10(7)
YbGa ₄ mAlShi ₄	47(2)	3.80(7)
YbGa ₄ mYneShi ₄	48(3)	3.73(9)
YbGa ₄ pYneShi ₄	34(1)	3.7(2)
YbGa ₄ Shi ₄	24(1)	2.2(1)
Yb ₂ Ga ₈ pAlShi ₄ Ip ₄	49.9(7)	7.75(1)
Yb ₂ Ga ₈ Shi ₈ Ip ₄	60.9(4)	7.56(3)
Yb ₂ Ga ₈ mAlShi ₄ Ip ₄	59(5)	7.46(7)
Yb ₂ Ga ₈ mYneShi ₄ Ip ₄	58(4)	7.3(2)
Yb ₂ Ga ₈ pYneShi ₄ Ip ₄	47.3(3)	6.26(6)

3.4.2 Small Molecule Functionalization of LnGa_xShi₄(benzoate)₄ and Ln₂Ga₈Shi₈Ip₄ Metallacrowns (Ln: Yb^{III} and Sm^{III}; x: pYne, mYne, pAl, and pAl)

Thiol active appendages were chosen as the functionalization sites of metallacrowns due to the relatively mild reaction condition required to perform the desired couplings. Given that the maleimide appendages in Ln₂Ga₈Shi₈Mip₄ scaffold were highly reactive toward both small molecule and thiol-focal point PAMAM dendrons, early attempts to incorporate such groups at the ring position were pursued. Unfortunately, due to the synthetic requirement to prepare the hydroxamic acids that template MC scaffolds, maleimide (and other highly reactive thiol coupling groups) could not be incorporated into the ring ligands. As seen in Scheme 3.2, the most common hydroxamic acid synthesis methodologies follow two basic steps: *i*) esterification of a carboxylic acid derivative; and *ii*) hydroxylation of the ester derivative. Esterification is often the least concerning step, as many functional groups are capable of withstanding such conditions, and reactions tend to have good yields after 5-10 hours. On the other hand, the hydroxylation step often requires long reaction times (7-10 days) in order to produce good yields. More importantly, if the functional group of interest can undergo Michael-addition reactions with primary amines, as in the case of maleimide and other thiol-active groups, hydroxamic acid synthesis is not feasible – especially if the functional group is more reactive than the ester site. Therefore, while maleimide and acrylate appendages could be incorporated into the hydroxamic acid precursors (i.e., ester precursor), their high reactivity towards both thiol- and amine-Michael addition inhibited the hydroxylation step.



Scheme 3.2 Basic steps for hydroxamic acid synthesis starting from a carboxylic acid derivative. Introduction of the functional group (**R**) must withstand both reaction steps. Oxygen atoms highlighted in green point out the location for hydroxylation. Oxygen atoms highlighted in red and nitrogen atoms in blue indicate the coordination sites for metallacrown formation.



Scheme 3.3 (Top) Radical mediated thiol-yne/ene coupling reaction to unsaturated C=C and C≡C bonds. Thiol-yne/ene addition start with the radical initiator producing thiol radicals, that can then enter the cycle addition. (Bottom) Thiol-yne coupling to *p*Yne and Yne and *m*Yne, where two thiols can be added per ring ligand. Thiol-ene coupling to *p*Al and *m*Al where one thiol per ring ligand is added.

In Michael addition reactions¹⁸⁰, strong nucleophiles (such as amino and mercapto groups) attack the β-carbon of α,β-unsaturated carbonyl groups, leading to the formation of a new N/S-C

bond. Therefore, during the second synthetic step, hydroxylamine is more likely to undergo Michael addition to the unsaturated C=C bond of maleimide and acrylate groups than undergo amidation at the ester position. Other synthetic methods to incorporate the hydroxamic acid site could be used so as to avoid amine-Michael addition (e.g., hydrogenation of *O*-benzylhydroximates);¹⁴⁵ however, a more careful selection of the functional group to be introduced would be required which would potentially limit their synthetic utility even further. Therefore, due to the lack of success to introduce a highly thiol-active maleimide and acrylate appendages, a compromise was made: incorporate less active thiol-active groups so that the functional appendage could tolerate the hydroxylamine synthetic step. To that end, four ring ligands were prepared ($H_3p/mYneShi$, and $H_3m/pAlShi$) and investigated towards thiol-yne/ene. While highly reactive thiol-coupling groups can undergo Michael addition via acid-base equilibrium or nucleophilic-catalyzed addition,^{180–182} less reactive thiol-coupling groups requires a more energetic approach.^{183,184} In this case, a photocatalytic radical-mediated thiol-yne/ene addition mechanism was employed. As shown in Scheme 3.3 (top), the radical initiator accelerates the reaction by producing thiol radicals that then can enter the thiol-yne/ene cycle addition.

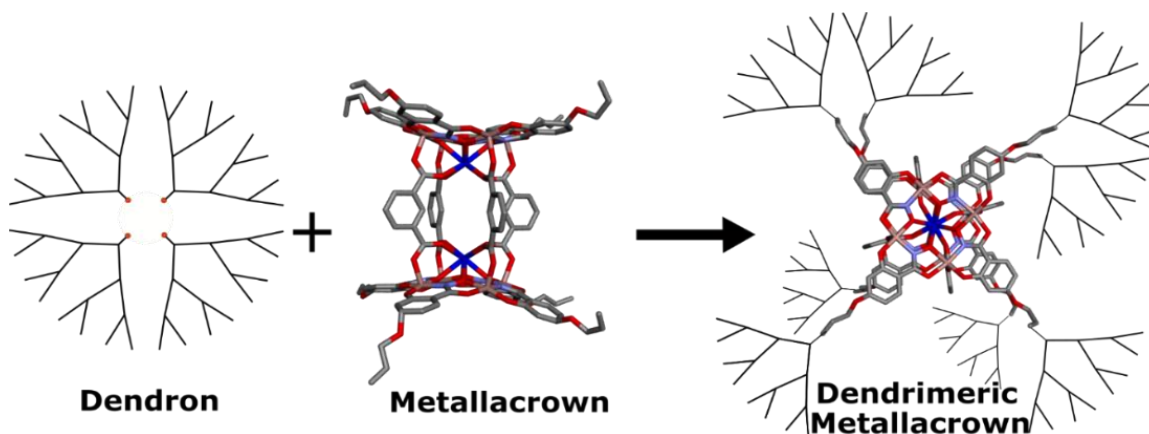
Using this approach, addition of β -mercaptoethanol to metallocrowns was carried out onto the four and eight appendages of $LnGa_{4x}Shi_4(benzoate)_4$ and $Ln_2Ga_{8x}Shi_8Ip_4$, respectively. As seen in Scheme 3.3 (bottom), for MCs templated with $H_3p/mYneShi$, up to two couplings per ring ligand can be expected, while for MCs templated with $H_3p/mAlShi$ a single thiol addition per ring is expected. Reactions were done by placing degassed DMF reaction solution under UV light (365 nm) in the presence 2,2-Dimethoxy-2-phenylacetophenone (DMPA) as the photoinitiator (radical initiator). For the monomeric MCs, complete coupling of four β ME was observed to $YbGa_{4p}Alshi_4$ and $YbGa_{4m}Alshi_4$. Partial to complete coupling was seen to $YbGa_{4p}Yneshi_4$ with six to eight β ME. As for coupling to $YbGa_{4m}Yneshi_4$, lower thiol-yne coupling reactivity was seen, with an array of zero to six couplings. Reaction to the dimeric MC scaffolds were also investigated. A slight improvement on the reactivity of $Yb_2Ga_{8m}Yneshi_8Ip_4$ was observed, with eleven to sixteen β ME coupled to the MC. Best results were seen with $Yb_2Ga_{8p}Yneshi_8Ip_4$ and $Yb_2Ga_{8p}Alshi_8Ip_4$, where partial to complete coupling of 14-16 and 6-8 β ME couplings were seen, respectively. Furthermore, the ESI-MS peaks for complete coupling on both of these metallocrowns were of highest intensity. Since the molecular weight and size of both MCs with partial and complete coupling would differ by only two β ME (~160 amu max), it is prudent to expect that the intensity

of the ESI-MS signal likely represents the density of population of each species. Thus, in both cases the most prominent species is the fully coupled $\text{Yb}_2\text{Ga}_8\text{pYneShi}_8\text{Ip}_4(\beta\text{ME})_{16}$ and $\text{Yb}_2\text{Ga}_8\text{pAlShi}_8\text{Ip}_4(\beta\text{ME})_8$.

Absorbance and fluorescence spectroscopy of $\text{Yb}_2\text{Ga}_8\text{pYneShi}_8\text{Ip}_4$ and $\text{Yb}_2\text{Ga}_8\text{pAlShi}_8\text{Ip}_4$ pre- and post- βME coupling demonstrate that the luminescent properties of the MC are not affected by small molecule coupling. As seen in Figure 3.18, the solution state absorbance of the four scaffolds have matching profiles. Likewise, luminescent emission shown in Figure 3.19 show characteristic Yb^{III} luminescence in each scaffold. Therefore, these results demonstrate the first example of successful photocatalyzed thiol-yne/ene coupling of small molecules to monomeric and dimeric metallacrowns. More importantly, these results also demonstrate that Ln^{III} sensitization by the MC is still observed after coupling reactions.

3.4.3 Hyperboloidal Dendrimeric Metallacrowns

After developing MC scaffolds capable of undergoing thiol-coupling at the ring ligands, and corroborating that the Ln^{III} sensitization was not detrimentally affected by such functionalization, the next step was to expand the novel field of dendrimeric metallacrowns. To this end, $\text{Ln}_2\text{Ga}_8\text{xShi}_8\text{Ip}_4$ MC were employed as the core of PAMAM dendrimers, as shown in Scheme 3.4 in order to develop a new class of dendrimeric metallacrowns with hyperboloidal shapes.



Scheme 3.4 Simplified representation of dendrimeric metallacrown preparation. Left, thiol-focal point dendron. Middle, model of $\text{Ln}^{\text{III}}_2[12\text{-MC}_{\text{Ga}(\text{III})\text{N}(\text{xshi})\text{-4}}]_2(\text{Ip})_4$ MC. Right, top view of hyperboloidal dendrimeric metallacrowns.

Thiol-focal point PAMAM dendrons were prepared in the same fashion as described in Chapter 2. Next, given the lower reactivity toward thiol coupling of MCs templated with

H₃myneShi, only MCs with the other three ligands were utilized in the trials to develop dendrimers. Chronologically, MCs with H₃pyneShi were first examined in an attempt to create a thiol-reactive scaffold. Thus, the first trials to develop DMC were exclusively attempted in Yb₂Ga_{8p}YneShi₈Ip₄ MCs. As detailed in the experimental and result sections, three radical-mediated approaches were utilized to obtain sixteen couplings of HS-G1 or 1.5 to a Yb₂Ga_{8p}YneShi₈Ip₄ core. **Approach A** resembles the photocatalytic approach utilized to couple βME to MCs. **Approach B** is also a photocatalytic reaction, but it utilizes 4,4'-Bis(dimethylamino)benzophenone (Michler's ketone) as the photoinitiator. Lastly, **Approach C** is a thermal radical-mediated approach that employed azobisisobutyronitrile (AIBN) as the radical initiator. The least successful approach was **Approach C**, since even after long reaction times and increasing equivalents of AIBN, it only yielded one to four coupling of HS-G1.0 to Yb₂Ga_{8p}YneShi₈Ip₄ MC core.

Both of the photocatalytic approaches yielded only slightly better results, with only partial coupling of six to eight HS-G1 to the Yb₂Ga_{8p}YneShi₈Ip₄ under **Approach A**, and seven to eight HS-G1.5 to the Yb₂Ga_{8p}YneShi₈Ip₄ core under **Approach B**. Attempts to improve the success rate by systematically modifying each of the reaction variables did not yield better results. Interestingly, **Approach B** yielded better results with G1.5 than with G1.0 (7-8 couplings, vs. 4-6, respectively). This suggests that the nature of the photoinitiator and the surface of the dendron (-OMe for G1.5 and -NH₂ for G1.0) may have an influence on the reactivity of the thiol-yne coupling. Additional synthetic trials were not done utilizing **Approach B** since a yellow discoloration due to photodecomposition of the Michler's ketone was observed in all trials.

Since for every ring ligand in Yb₂Ga_{8p}YneShi₈Ip₄ MCs, two thiol groups can be coupled, the synthesis of H-DMCs under **Approach A** only had 38-50% success rate with both G1.0 and G1.5 dendrons, as seen in Figure 3.20 and Figure 3.23. This could mean that some of the ring ligands in the MC core are undergoing a single or double dendron coupling events, while others are not coupling any dendrons at all. However, there is also the possibility that a second coupling to each of the ring ligands can be hindered by the relatively large size of the dendrons, which would render the success rate of the reaction to be 75-100% effective. In other words, while 14-16 βME can be coupled to a Yb₂Ga_{8p}YneShi₈Ip₄ (two thiols per ring ligand), the relatively larger size of the dendrons (G1.0 and G1.5 dendrons are 4-8 times more massive than βME) can impede the addition of a second dendron at the same ligand position. Nevertheless, in an effort to obtain

complete and effective dendron coupling to the MC cores, a second generation of ring ligands were investigated.

To this end, $H_3pAlShi$ and $H_3mAlShi$ ligands were synthesized. Given the success of βME thiol-ene coupling to $YbGa_4pAlShi_4$, coupling of HS-G1.0 dendrons to the monomeric MC was performed with the main goal to then form the dimeric scaffold by benzoate exchange with isophthalic acid. Shown in Figure 3.24 is the ESI-MS spectrum of $YbGa_4pAlShi_4$ metallacrown with complete coupling of four HS-G1.0 PAMAM dendrons. While this monomeric MC-cored DMC was not the main target behind this thesis work, it is still worth comparing some of its structural features with regular PAMAM dendrimers. Based on the crystal structure of the meta-substituted MC analogue and the previously measured diameters of PAMAM dendrimers,^{43,185} at G1.0 this monomeric MC-cored DMC is about the same diameter as G3.0 ethylenediamine (EDA)-cored PAMAM dendrimer. Additionally, the overall molecular weight of this G1.0 DMC (~3KDa by ESI-MS), is close to the molecular weight of a G2.0 PAMAM dendrimer. As for the overall shape, unlike the more globular PAMAM dendrimers, this DMC potentially has a flatter and disk-like shape. The non-globular shape, more massive luminescent core, and larger overall diameter at relatively low generations of this DMC scaffold, should alter the pharmacokinetic properties (e.g. longer retention time or cell uptake) from those of regular PAMAM dendrimers. Furthermore, this DMC is the closest analogue to metallodendrimers with porphyrin⁵² or cyclam⁸⁶ cores, where the core is made with a single well-defined macrocyclic scaffold capable of coordinating a metal ion at its center. The main difference between porphyrin- and cyclam-cored metallodendrimers and this DMC is that the MC core is capable of encapsulating and sensitizing lanthanide ion luminescence. Further luminescent characterization of this DMC was not performed for this thesis work, but is expected to efficiently sensitize lanthanide luminescence. Furthermore, it may also improve the overall solution stability of the MC core by limiting bridging dissociation in solution.

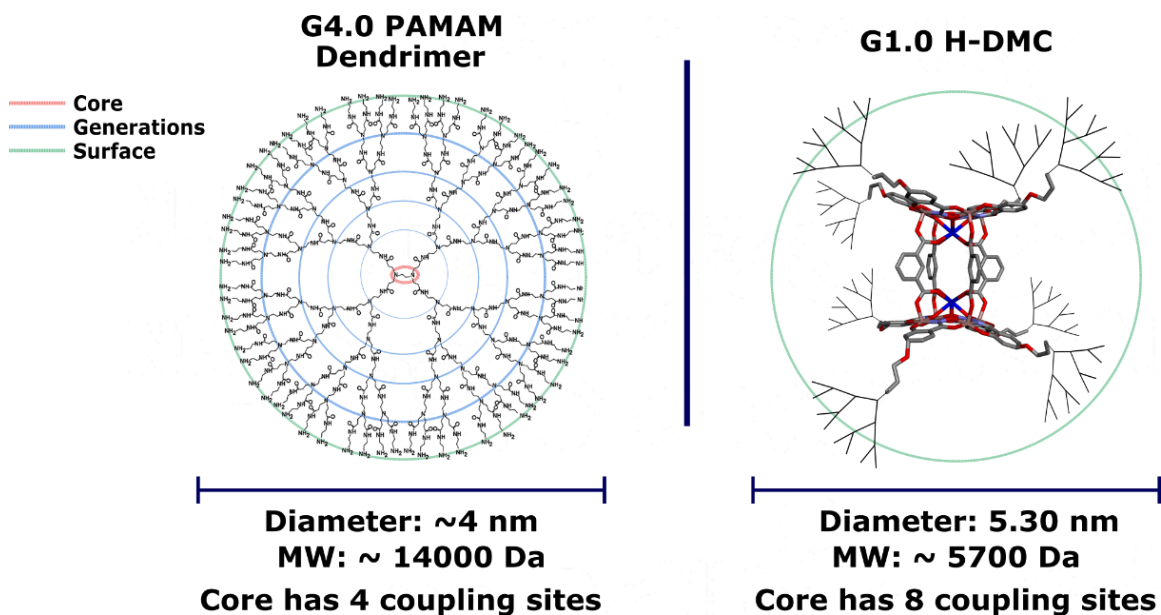
While exciting results were obtained, the formation of the dimeric scaffold by bridge exchange with this monomeric MC-cored DMC was not successful. This is probably due to the nature of the dendron, which has $-NH_2$ surfaces and internal amides that can interfere with the deprotonation of the isophthalic acid by the benzoates; thus, interfering with the bridge exchange events. It could also be due to the protecting effect of the dendron arms limiting bridge ligand dissociation. Furthermore, attempts to scale up the thiol-ene dendron coupling to $YbGa_4pAlShi_4$ yielded less favorable results, and very noisy ESI-MS spectra. This is likely due to the fact that

benzoates are good radical scavengers that can undergo radical addition.^{186,187} Thus, scaling up the reaction ultimately increases the concentration of benzoates, which then increases the chances of radical quenching and unwanted side reactions. This situation could be improved by using different carbonyl bridging ligands with lower reactivity towards radical formation, but this was not explored further since alternative approaches to make the dimeric DMC proved to be more successful.

The most successful dendron coupling reaction was achieved with $\text{Yb}_2\text{Ga}_8\text{pAlShi}_8\text{Ip}_4$ as the MC core, and HS-G1.0 PAMAM dendrons. As seen in Figure 3.26, under different reaction conditions and employing **Approach A**, similar results were observed. A narrow distribution of six to eight couplings of dendron per MC can be seen by ESI-MS, which translates into a 75-100% coupling success rate – a significant improvement to the 35-50% success rate with $\text{Yb}_2\text{Ga}_8\text{pYneShi}_8\text{Ip}_4$ MC. Scaling up of the reaction of $\text{Yb}_2\text{Ga}_8\text{pAlShi}_8\text{Ip}_4$ and HS-G1.0 PAMAM dendrons, from 1-5 mg for the trials to 20-40 mg, did not hinder the reactivity of the thiol-ene addition. This complex, which from here on will be referred to as $\text{Yb}_2\text{Ga}_8\text{pAlShi}_8\text{Ip}_4$ G1.0 DMC, was purified by dialysis against DMSO, and then further characterized by DLS and luminescence spectroscopy. Interestingly, the reaction of $\text{Yb}_2\text{Ga}_8\text{pAlShi}_8\text{Ip}_4$ with HS-G0.5 dendrons, which is a slightly smaller dendron, also yielded six to eight couplings. Similarly, as described earlier, βME coupling to the same MC also resulted in six to eight couplings. Thus, the increasing size of the thiol compounds (MW: HS G1.0 > HS G0.5 >> βME) is not the main culprit hindering the single thiol coupling to each of the MC rings. Potentially, 100% coupling rates of dendrons to the MC core could be achieved if more reactive thiol-ene groups were employed; however, as described earlier, the delicate synthetic requirements of the hydroxamic acid ligands can limit the available options for thiol-ene coupling.

As seen in Figure 3.5 and Figure 3.26, the characterization by ESI-MS of the $\text{Yb}_2\text{Ga}_8\text{pAlShi}_8\text{Ip}_4$ MC and $\text{Yb}_2\text{Ga}_8\text{pAlShi}_8\text{Ip}_4$ G1.0 H-DMC corroborated the expected increase in molecular weight between the two compounds. Interestingly, while the $\text{Yb}_2\text{Ga}_8\text{pAlShi}_8\text{Ip}_4$ MC is best characterized as a -2 species in negative ion mode, the $\text{Yb}_2\text{Ga}_8\text{pAlShi}_8\text{Ip}_4$ G1.0 H-DMC was better detected by the mass spectrometer as a +3 species in positive ion mode. This is due to the easy protonation of the $-\text{NH}_2$ surface groups of the DMC. DLS characterization of the $\text{Yb}_2\text{Ga}_8\text{pAlShi}_8\text{Ip}_4$ MC and the $\text{Yb}_2\text{Ga}_8\text{pAlShi}_8\text{Ip}_4$ G1.0 H-DMC in DMSO also confirmed the increase in size, showing an expansion in average hydrodynamic diameters (from 3.7 to 5.3 nm)

and slower diffusion coefficients (from $1.30\text{e-}6$ to $9.09\text{e-}7 \text{ cm}^2\text{s}^{-1}$). As for the structural difference between standard PAMAM dendrimers and hyperboloidal DMCs, at a given generation the DMC is much larger than PAMAM dendrimer of the same generation. For example, the $\text{Yb}_2\text{Ga}_8\text{pAlShi}_8\text{Ip}_4$ G1.0 DMC is predicted to be close in diameter to a standard G5.0 PAMAM dendrimer.⁴³ This is of synthetic importance since while PAMAM dendrimer defects (e.g, incomplete monomer addition, missing dendrons, or cyclization) can occur during dendrimer synthesis or due to sample concentration, such defects tend to increase with increasing dendrimer generation.^{4,12} Therefore, if a G5.0 EDA-cored PAMAM dendron is needed for its size (~ 5.5 nm in diameter), a G1.0 H-DMC could be used instead as they have similar diameters, but with the H-DMC having shorter dendron generation and thus a lower defect concentration. Similarly, $\text{Yb}_2\text{Ga}_8\text{pAlShi}_8\text{Ip}_4$ G1.0 H-DMC has as many surface groups as a larger G2.0 PAMAM dendrimer – sixteen compared to eight $-\text{NH}_2$ groups, respectively. Lastly, the molecular weight of G1.0 DMC as seen by mass spectrometry (~ 5.7 kDa) is comparable to that of a G2-3 PAMAM dendrimers.¹⁷³ Just as with toroidal DMCs (T-DMCs), the structural and physical difference of hyperboloidal DMCs arises from the much larger and heavier metallacrowns core compared to the regular EDA-cored PAMAM dendrimers, as seen in Scheme 3.5. As for the overall shape, dendrimers are known for adopting globular shapes in solution. By comparison, the hyperboloidal DMC, as the name indicates, could be described as a hyperboloid shaped (or hourglass) complex based on the site of dendron attachment. However, based on the narrow PDI values observed in DLS, in solution the DMC could potentially adopt a more spherical shape.



Scheme 3.5 Comparison between a G4 EDA-cored PAMAM dendrimer with a $\text{Ln}_2\text{Ga}_8\text{pAlShi}_8\text{Ip}_4$ MC highlighting that the MC has a diameter (measured by DLS) as large as a large PAMAM dendrimer. Also, the MC used as the core of H-DMC has twice as many coupling sites for dendron grow, compare to the EDA core in that only has four.

As shown in Figure 3.34, the polydispersity index (PdI) of the $\text{Yb}_2\text{Ga}_8\text{pAlShi}_8\text{Ip}_4$ G1.0 H-DMC (PdI:0.06) is significantly smaller than that of the $\text{Yb}_2\text{Ga}_8\text{Shi}_8\text{Mip}_4$ G1.0 T-DMC (PdI: 0.34), and closer to the values of standard PAMAM dendrimers (PdI: 0-0.1). This suggest that in DMSO solutions, hyperboloidal DMCs are more spherical than the T-DMCs – which are closer to a disk shape. Furthermore, through DLS one can investigate the aggregation behavior of particles in solution. As seen in Figure 3.34, while the presence of aggregates (peaks with smaller intensity at higher diameters) is observed in both DMCs, the H-DMC's aggregate peak is located at smaller diameters and has a much narrower width. This suggests that there is a smaller distribution in size of the aggregates and that they are much smaller than those of the T-DMC. This is of importance for the potential application of H-DMCs as imaging probes since aggregate formation in solution can heavily influence the pharmacokinetic behavior of the probe – e.g., hinder cell uptake.

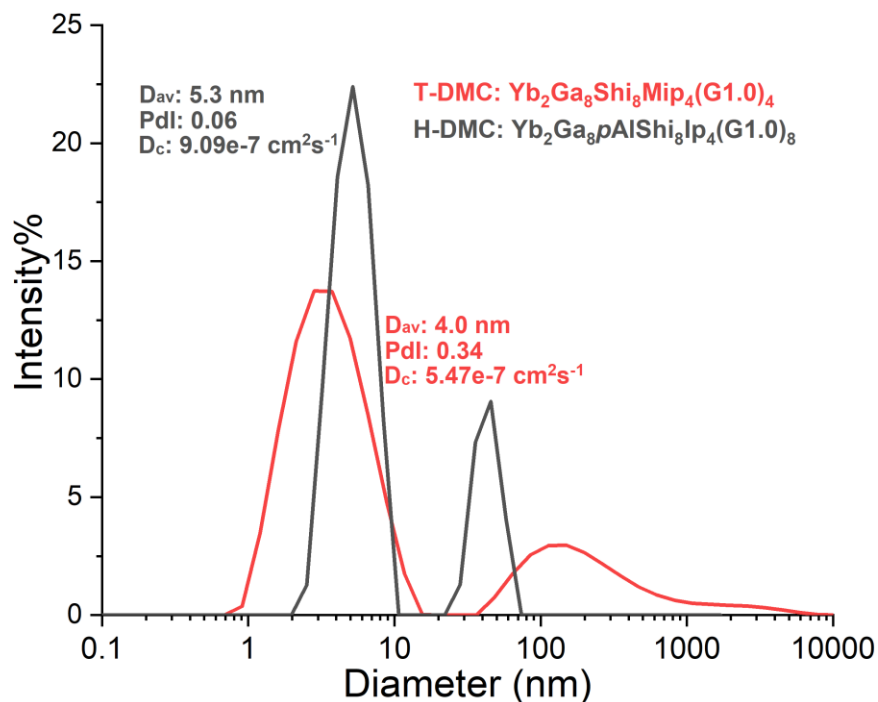


Figure 3.34 DLS size distribution of $\text{Yb}_2\text{Ga}_8\text{Shi}_8\text{Mip}_4 \text{ G1.0}$ T-DMC and $\text{Yb}_2\text{Ga}_8\text{pAlShi}_8\text{Ip}_4 \text{ G1.0}$ H-DMC in DMSO at room temperature.

To further investigate the H-DMC behavior in solution, DLS characterization was also performed in more aqueous environments ($\text{H}_2\text{O}:\text{DMSO}$, 99:1, v/v%). Just as with the previously described toroidal-DMC, the G1.0 hyperboloidal-DMC also showed solvent dependent aggregation behavior (Figure 3.30). Aggregates with an average diameter of $\sim 340 \text{ nm}$ were the only species seen by DLS, which suggest that the G1.0 H-DMC undergoes rapid self-aggregation in aqueous solutions. This can be problematic for their application as imaging agents, since depending on their size, large aggregates can hinder cellular internalization. More rigorous DLS experiments looking at the concentration dependence, pH dependence, solvent system dependence, or any other important parameters that influences aggregation would be of great importance in order to minimize the formation of large particles in solution, and be able to exploit the excellent luminescent properties of hyperboloidal-DMCs.

Another piece of information that can be subtracted from the DLS data is an approximation of the maximum number of solvent molecules encapsulated/associated to the DMC and the MC. This can be extrapolated from the density (ρ_m) of the measured sample by DLS, and comparing it to the expected density of the sample, which can be determined from the crystal structure of a given scaffold. Three assumptions would be made in the case of $\text{Yb}_2\text{Ga}_8\text{pAlShi}_8\text{Ip}_4$ MC and

Yb₂Ga₈pAlShi₈Ip₄ G1.0 H-DMC: *i*) the density of the Yb₂Ga₈pAlShi₈Ip₄ would be assumed to be same as the one measured for the Yb₂Ga₈Shi₈Ip₄ MC from crystallographic data¹⁰⁶ (ρ :1.445); *ii*) the density of the DMC is extrapolated from the difference in the measured values of the MC and the DMC, and the assumed MC density; and *iii*) the molecules associated/encapsulated are only DMSO (MW: 78 g/mol). Values to perform the calculations are listed in Table 3.16, and detailed step-by-step calculation are shown in Appendix B. With this approach, a reasonable estimation for the level of solvation of the MC and the H-DMC can be determined. An increase in the number of DMSO molecules associated with the H-DMC is to be expected since the addition of eight sets of dendrons arms also increases the number of cavities for solvent encapsulation. Comparing the number of solvent molecules encapsulated/associated to Yb₂Ga₈Shi₈Mip₄ G1.0 T-DMC (~20 DMSOs) and Yb₂Ga₈pAlShi₈Ip₄ G1.0 H-DMC, the latter has about three times as many DMSO molecules encapsulated and/or associated as the former. This seems reasonable since not only the amount of dendron arms per MC core doubles with the H-DMC, but also the position of the dendrons arms are in more favorable positions (“top” and “bottom” of the MC core) to encapsulate solvent molecules.

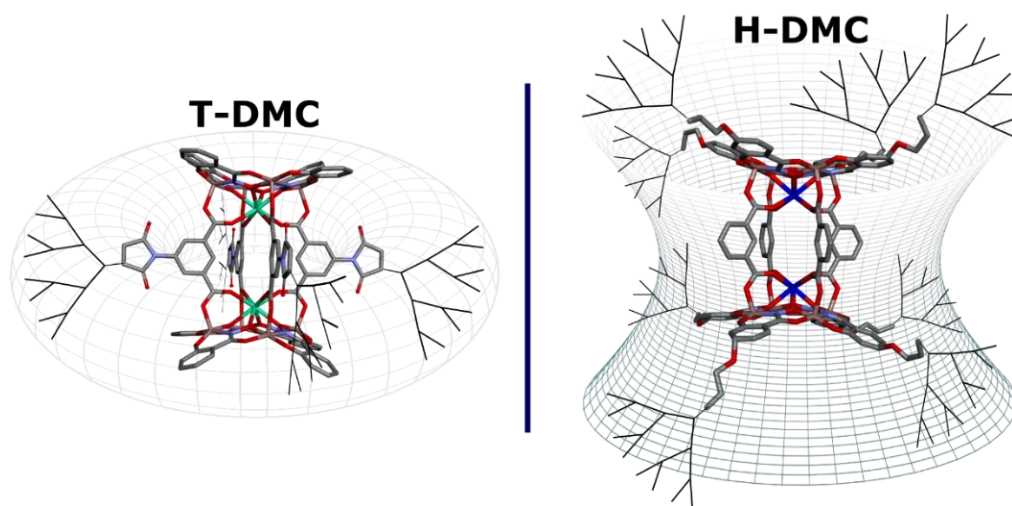
Table 3.16 Calculated solvent molecules encapsulated or associated with samples in DLS.

Sample	R ^a (nm)	V ^b (mL)	MW ^c (g/mol)	Mass ^d (g)	ρ_m^e (g/mL)	ρ (g/mL)	#DMSO molecules
MC	1.85	26.56e-21	3210	5.33e-21	0.20	1.445 ^f	35
DMC G1.0	2.65	77.95e-21	5660	9.40e-21	0.12	0.90	63

^a From DLS estimated hydrodynamic radius. ^b Volume assuming sample is a sphere; $V=3/4\pi R^3$. ^c From ESI-MS. ^d MW/Avogadro's number. ^e Calculated density. ^f From crystal structure.¹⁰⁶

Further comparison between H-DMC and T-DMCs demonstrates a significant reduction of reaction time for the preparation of DMCs when utilizing the photocatalyzed thiol-ene coupling approach. As described in Chapter 2, to prepare G1.0 T-DMCs, 5-7 days were necessary to obtain complete couplings of four dendrons to the MC core. In the case of photocatalyzed H-DMCs, only 0.5-1 hour of reaction time is necessary. However, T-DMC synthesis has the benefit of having 100% coupling success, and is more easily scalable – with ~250-500 mg of MC batch sizes. Yet, the rapid synthesis of smaller batch sizes (20-40 mg of MC) could potentially outweigh the significantly longer reaction times of T-DMCs. The next most significant difference between the two DMCs is their shape and number of dendrons coupled to the MC core, shown in Scheme 3.6.

As their name indicates and based on the site of dendron attachment, one could imagine the DMCs having a toroidal and hyperboloidal shape. The shape difference is also highlighted by the PdI difference in the DLS, which shows the T-DMC having a less globular shape in solution than H-DMCs. Since the number of dendron attachment sites to the MC core doubles from $\text{Ln}_2\text{Ga}_8\text{Shi}_8\text{Mip}_4$ to $\text{Ln}_2\text{Ga}_8p\text{AlShi}_8\text{Ip}_4$, the number of surface groups also doubles for a given generation. Therefore, while a $\text{Ln}_2\text{Ga}_8\text{Shi}_8\text{Mip}_4$ G1.0 T-DMC has a diameter of 4.00 nm and eight $-\text{NH}_2$ groups at the surface, a $\text{Ln}_2\text{Ga}_8p\text{AlShi}_8\text{Ip}_4$ G1.0 H-DMC's diameter is 5.30 nm and has sixteen surface groups. However, both DMCs are similar in the sense that they are both significantly larger and heavier than standard PAMAM dendrimers of the same generation.



Scheme 3.6 Simplified representation of toroidal dendrimeric metallacrown (T-DMC, left) and hyperboloidal dendrimeric metallacrown (H-DMC, right).

Unlike standard PAMAM dendrimers that required surface modification with organic chromophores or encapsulation of organic-based luminescent probes in order to have luminescent emissions, the MC core of $\text{Yb}_2\text{Ga}_8p\text{AlShi}_8\text{Ip}_4$ G1.0 H-DMC ensures that the complex is intrinsically luminescent – with emission in the NIR for this specific case. The photophysical properties of $\text{Yb}_2\text{Ga}_8p\text{AlShi}_8\text{Ip}_4$ G1.0 H-DMC were investigated, and compared to G1.0 T-DMC from Chapter 2 and other Yb^{III} -based metallacrowns. Based on Figure 3.31, absorption spectra of $\text{Yb}_2\text{Ga}_8p\text{AlShi}_8\text{Ip}_4$ G1.0 DMC exhibit similar $\pi \rightarrow \pi^*$ transition bands to those of the MC core, with an absorbance in the range of 250-340 nm, with a low-energy maximum at 310 nm ($\epsilon=6.8 \times 10^4 \text{ M}^{-1}$

$^1\text{cm}^{-1}$) and a S^* at 26667 cm^{-1} . Thus, it can be said that the incorporation of PAMAM dendrons to the ring ligand of the MC core does not seem to affect the scaffold's electronic properties. While the triplet state of the DMC was not measured, it is not expected to change much as the PAMAM dendrons are poor antennas for energy transfer.

Good overlap of the solution state absorbance and excitation spectra indicates effective energy absorbance and transfer by the MC core ring ligands to the Yb^{III} ions. Excitation at 320 nm exhibited characteristic Yb^{III} emission between 950-1150 nm, as seen in Figure 3.32. Photophysical data in the solution state detailed on Table 3.13, show that the τ_{obs} and ϕ_{Yb}^L values of the DMC are larger than both the $\text{Yb}_2\text{Ga}_8p\text{AlShi}_8\text{Ip}_4$ with no dendrons, and the $\text{Yb}_2\text{Ga}_8\text{Shi}_8\text{Ip}_4$ parent MC – $\tau_{\text{obs}}:\sim 1.4/\phi_{\text{Yb}}^L:\sim 1.12$ and $\tau_{\text{obs}}:1.1/\phi_{\text{Yb}}^L:\sim 1.2$ times higher, respectively. The increase in both values can be attributed to the added protection that the dendron arms offer to the MC core from solvent molecules, and the narrower $S^* \rightarrow T^*$ ΔE of the *para*-substituted MC core compared to the parent MC.

When compared to G1.0 T-DMC, an increase of $\tau_{\text{obs}}:\sim 1.4$ times, but a decrease of $\phi_{\text{Yb}}^L:\sim 0.9$ times was observed with the G1.0 H-DMC. The subtle decrease in quantum yield may be due to the position and solvent encapsulation of the dendrons, as seen in Scheme 3.6. In other words, while the dendritic shell helps protect the MC from the surrounding environment, it also forms cavities capable of encapsulating solvent molecules. Since the dendrons are positioned at the ring ligands, the solvent-filled cavities can be relatively close to the Ln^{III} ions. Furthermore, as shown by the DLS solvation calculations, H-DMCs can have a significantly larger number of solvent molecules encapsulated by the dendritic shell than T-DMCs. This is because the hyperboloidal scaffolds have twice as many dendron arms as the toroidal ones. Nonetheless, even with solvent-filled cavities, the DMCs have larger quantum yields than the MC core or parent MC alone; suggesting that solvents molecules in DMCs are kept farther away from the Ln^{III} ions. Overall, the high quantum yields of the $\text{Yb}_2\text{Ga}_8p\text{AlShi}_8\text{Ip}_4$ G1.0 DMC, long luminescent lifetimes, and NIR emission are exciting and encouraging results for the dendrimer and metallacrown fields.

While cell studies were not performed with the $\text{Yb}_2\text{Ga}_8p\text{AlShi}_8\text{Ip}_4$ G1.0 DMC, based on the DLS data in both DMSO and $\text{H}_2\text{O}/\text{DMSO}$ solutions, it can be expected that self-aggregation will hinder the effective cell uptake of G1.0 H-DMCs. Aqueous solubility is not likely the main perpetrator behind self-aggregation, since this G1.0 H-DMC has twice as many hydrophilic surface groups than the G1.0 T-DCM, which experience a smaller degree of aggregation in cells. Thus,

further DLS studies are necessary to better understand the mechanisms of self-aggregation, and to investigate the optimal conditions in aqueous solutions that would minimize the aggregation of the H-DMC. The great luminescent sensitization, attractive structural features, and the presence of twice as many dendrons as standard PAMAM dendrimers of the same generation, grant the investigation of the imaging behavior of hyperboloidal-DMCs worthwhile.

3.5 Conclusions

The work detailed in this chapter demonstrates the remarkable functionalization potential of luminescent metallacrowns, and excellent luminescent emissions of dendrimeric metallacrowns. In this chapter, I presented the synthetic incorporation of thiol-yne and thiol-ene groups to the ring ligands for monomeric $\text{LnGa}_{4x}\text{Shi}_4(\text{benzoate})_4$ and dimeric $\text{Ln}_2\text{Ga}_{8x}\text{Shi}_8\text{Ip}_4$ metallacrowns with four different ring ligands (H_3pYneShi , H_3mYneShi , H_3pAlShi , and H_3mAlShi), and three Ln^{III} ions (Yb^{III} , Sm^{III} , and Gd^{III}). The scaffolds were characterized by crystallography, ESI-MS, and NMR to corroborate chemical and structural composition. Photophysical characterization of each scaffold demonstrated that the presence of pyridinium and other vibrational quenchers near the Ln^{III} ions severely quenches the luminescent signal of the MCs in the solid state; however, in DMSO solutions, a significant increase in both lifetimes and quantum yields was seen for all compounds. The thiol-yne/ene functionalization ability of $\text{LnGa}_{4x}\text{Shi}_4(\text{benzoate})_4$ and $\text{Ln}_2\text{Ga}_{8x}\text{Shi}_8\text{Ip}_4$ metallacrowns was corroborated by coupling up to four, eight, or sixteen β -mercaptoethanol molecules to the four or eight thiol-yne/ene appendages of MCs via UV-light photocatalyzed thiol coupling. The Yb^{III} emission of the pre- and post- β ME coupling to MCs confirmed that the luminescent signal is not hindered by the thiol-yne/ene functionalization. This work represents the first incorporation of thiol active site to the ring of MCs, the first-time photocatalytic coupling reaction has been employed to MC, and the first-time up to sixteen molecules have been coupled to a single MC.

To advance the field of luminescent metallodendrimers, new Ln_2Ga_8 complexes were incorporated as the core of hyperboloidal-DMCs. I investigated the reaction conditions necessary to accomplish this, and while most of the new MC scaffolds prepared for this work successfully underwent thiol coupling with small molecules, only one of the new structures was able to be used as the core of hyperboloidal-DMCs. I was able to show the synthesis and characterization of a new type of dendrimeric metallacrown with $\text{Ln}_2\text{Ga}_{8p}\text{AlShi}_8\text{Ip}_4$ cores and PAMAM dendritic shells.

Furthermore, while the coupling success rate of $\text{Yb}_2\text{Ga}_8\text{pAlShi}_8\text{Ip}_4$ was shown to be 75-100%, the short reaction times and mild reaction conditions are to be highlighted. Compared to toroidal-DMCs that requires 5-10 days to fully react, synthesis of the hyperboloidal-DMC only requires 1 hour of reaction time. Furthermore, the number of couplings doubles compared to toroidal-DMCs.

ESI-MS and DLS studies corroborated the formation of the DMCs, while photophysical characterization demonstrated excellent sensitization and quantum yield of $\text{Yb}_2\text{Ga}_8\text{pAlShi}_8\text{Ip}_4$ G1.0 DMC in DMSO. Furthermore, the distinct structural features of DMCs, such as the hyperboloidal shape, large diameters, and high molecular weight with smaller generations, are interesting features that could be exploited in biological settings. With this work, I was able to expand the functionalization of MC while also exploiting their luminescent sensitization. Furthermore, I was able to demonstrate that MCs can be functionalized at the ring ligand position, and be employed as the core of dendrimeric metallocrowns.

Chapter 4

Bifunctional Luminescent Metallacrowns and Symmetric/Asymmetric Dendrimeric Metallacrowns

4.1 Introduction

The scaffolds developed in Chapter 2 ($\text{Ln}_2\text{Ga}_8\text{Shi}_4\text{Mip}_4$) and Chapter 3 ($\text{Ln}_2\text{Ga}_{8x}\text{Shi}_8\text{Ip}_4$) are clear examples of the synthetic functionalization capabilities of metallacrowns. The maleimide appendages of $\text{Ln}_2\text{Ga}_8\text{Shi}_4\text{Mip}_4$ were introduced by modification of the bridging ligands, yielding a scaffold with four maleimide groups capable of coupling to thiol moieties. As for $\text{Ln}_2\text{Ga}_{8x}\text{Shi}_8\text{Ip}_4$, a more delicate synthetic methodology was implemented, which culminated with the development of scaffolds with eight appendages capable of undergoing thiol-ene/yne photocatalytic addition. Both scaffolds represent the firsts MCs able to couple thiol-bearing molecules – either small ones like cysteamine or β -mercaptoethanol, or larger ones like PAMAM dendrimers. This functionalization led to the development of luminescent Ln_2Ga_8 MC-cored PAMAM DMCs with toroidal and hyperboloidal shapes, and some of the highest Yb^{III} quantum yields among MCs.

The systematic synthetic functionalization of Ln_2Ga_8 MCs shown in the previous two chapters has now enabled the development of luminescent bifunctional scaffolds with twelve points of attachment. Additionally, due to the significant difference in reactivity towards thiol coupling of each ligand appendage (maleimide $\gg\gg$ thiol-ene/yne), asymmetric coupling to the same MC core can also be achieved. Thus, these bifunctional MC can be interesting cores of luminescent metallodendrimers. For this chapter, I first describe the synthesis and characterization of bifunctional $\text{Ln}_2\text{Ga}_{8x}\text{Shi}_8\text{Mip}_4$ (x : $p/m\text{Al}$ and $p/m\text{Yne}$) metallacrowns. I then demonstrate the thiol-coupling capabilities of the MC at both ligands' positions with small molecules. Next, I follow this by presenting data on the formation of symmetric and asymmetric DMCs, as well as their characterization and photophysical properties. Lastly, I describe the development and

characterization of redshifted toroidal-DMCs. The DMCs described in this chapter are labeled as “symmetric” (S-DMC) if both the ring and bridging ligands are coupled to the same PAMAM generation dendron, and “asymmetric” or Janus (Janus-DMC) if two different dendron generation or molecule are orthogonally coupled. Altogether, this last data chapter combines the two sites for thiol functionalization in a Ln_2Ga_8 metallacrown, and exploits both its coupling capabilities and photophysical properties.

4.2 Experimental

4.2.1 Chemical and Materials

All reagents and chemicals were purchased from commercial sources and used without further purification. Some chemicals have been omitted from the following listing wherever the starting materials are the same as those described on previous chapters. Cysteamine hydrochloride (Alfa Aesar, 98+%), Extra dry dichloromethane (**DCM**, Acros, 99.9%), Trifluoro acetic acid (**TFA**, Fisher, Peptide synthesis grade), Trityl chloride (Acros, 98%), Chloroform (Fisher, ACS grade), Sodium hydroxide (Fisher, ACS grade), Magnesium sulfate anhydrous (Fisher), D-(+)-Biotin (Alfa Aesar, 98+%), N-hydroxysuccinimide (**NHS**, eMolecules), *N,N'*-Dicyclohexylcarbodiimide (**DCC**, Sigma Aldrich, 99%), *N,N*-dimethylformamide (**DMF**, Fisher, Sequencing grade), Diethyl ether (Fisher), *N,N*-Diethylethanamine (**TEA**, Sigma Aldrich, 99+%), Ethyl acetate (Fisher, ACS grade), Dichloromethane (Fisher, ACS grade), Triethylsilane (TCl, 98+%), Toluene (LabChem, ACS grade), Petroleum ether (Fisher, ACS grade), Anhydrous methanol (Sigma Aldrich, 99.8%), ethanolamine (Sigma Aldrich, >99%), Anhydrous potassium carbonate (Fisher, Certified ACS), Gallium (III) nitrate hydrate (Acros, 99.9998%), Ytterbium nitrate pentahydrate (Sigma Aldrich, 99.9%), Sodium benzoate (Fisher), Pyridine (Fisher, ACS certified), β -Mercapto ethanol (Fisher), 2,2-Dimethoxy-2-phenylacetophenone (**DMPA**, Sigma, 99%), 4-(Dimethylamine)pyridine (**DMAP**, Acros, 99%), Dialysis membrane Spectra/Por 7 (MWCO 3.5 kDa, regenerated cellulose), Dimethyl sulfoxide (Fisher, HPLC grade), Dimethyl sulfoxide- d_6 0.03% TMS (Acros, 99.9%), NanoStar Disposable MicroCuvette (Wyatt), LED Emitter UV 365 nm flat lens (Digikey), AC/DC Wall mount adapter (Digikey), Computer fan (Newark), and Aluminum foil tape (Newark).

4.2.2 General Characterization Methods

Electrospray Ionization Mass Spectrometry (ESI-MS) was performed on an Agilent 6230 TOF HPLC-MS in negative or positive ion mode with fragmentation voltage of 250-350V. Samples were prepared by dissolving approximately 0.5-1 mg of compound in 2 mL of HPLC grade methanol. Samples of 5-10 μ L were manually injected. Methanol was employed as eluent in negative ion, and acetonitrile with 0.1% formic acid in positive ion. The flow rate was 0.5-1 mL/min. Data were processed with Agilent MassHunter Qualitative Analysis Software.

CHN elemental analysis was performed in a Carlo Erba 1108 elemental analyzer and a PerkinElmer 2400 elemental analyzer by Atlantic Microlab.

^1H NMR spectra were acquired on a 400 MHz Varian MR400 or 500 MHz Varian VNMRS500 NMR Spectrometer. Samples were prepared in Chloroform- d , Dimethyl sulfoxide- d_6 , or Methanol- d_4 , and spectra were processed using MestraNOVA software.

Dynamic Light Scattering (DLS) was performed on a DynaPro NanoStar instrument at 25°C with a scattering angle of 90°. Samples were prepared by dilution in DMSO, followed by centrifugation for five minutes at twelve thousand rpm. Scans were done with five second acquisition time set and twenty runs. Data was plotted using OriginPro 2020 software.

4.2.3 UV Photocatalytic Setup

UV-light catalyzed thiol-yne and -ene coupling of small molecules and dendrons to metallacrown was done using the set up (LED Box) shown below in Figure 4.1. The LED Box and lid (not shown in the picture) were made using fiberboard, and all of its interior was coated with aluminum tape or foil as to increase light reflectance. An aluminum coating was chosen for its high reflectivity (>85%) in the UV region¹⁷⁷ and its low cost. The light source is a UV LED emitter with a 15 Watts of output power and a narrow emission at 365 nm. To avoid overheating of the LED emitter, a copper metal plate was used as a heat sink with a computer fan placed in the back to expel hot air. Vials with samples were placed at 5-7 cm from the light source.

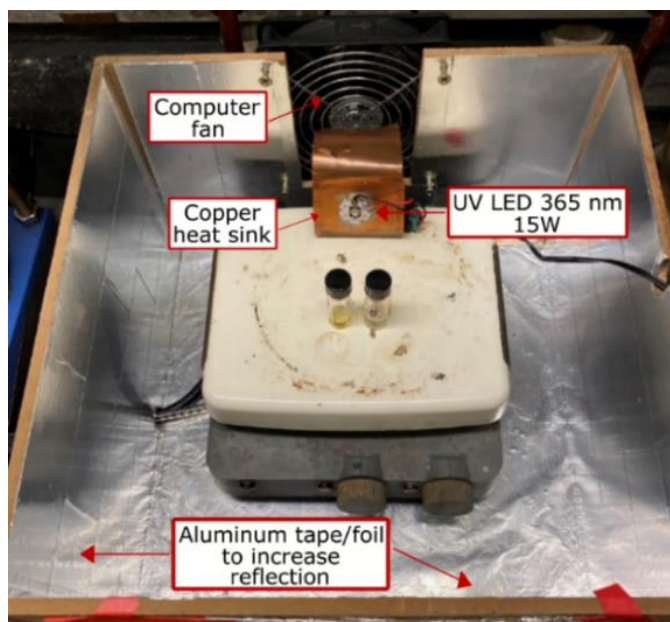


Figure 4.1 Photograph of LED Box highlighting key components. Coupling reaction using this set up were performed by covering the box with a lid (not shown in picture) and placing the assembly inside a hood.

4.2.4 Synthetic Procedures

I now describe the synthetic procedures followed in this chapter. All reactions were completed under aerobic conditions and at room temperature, unless otherwise noted. Characterization figures (ESI-MS, NMR, and DLS) not shown under the result section can be found in Appendix (Appx.) D.

Metallacrown bridge and ring ligands:

Synthetic procedures and characterization of *5-maleimidoisophthalic acid* (H_2Mip), *N,2-dihydroxy-4-(prop-2-yn-1-yloxy)benzamide* ($H_3pYneShi$), *N,2-dihydroxy-5-(prop-2-yn-1-yloxy)benzamide* ($H_3mYneShi$), *4-(allyloxy)-N,2-dihydroxybenzamide* ($H_3pAlShi$), and *5-(allyloxy)-N,2-dihydroxybenzamide* ($H_3mAlShi$) are detailed in Chapter 2 and 3.

YbGa₄xShi₄(Benzoate)₄ Metallacrowns:

*General synthesis procedure for Yb[12-MC_{Ga(III)N(xShi)}-4](benzoate)₄(pyridinium)(pyridine)₂(MeOH)₂ metallacrowns (x: *pYne*, *mYne*, *pAl*, and *mAl*).* Monomeric metallacrowns were prepared in the same fashion as described in Chapter 3.

Yb₂Ga₈xShi₈Mip₄ Metallacrowns:

*General synthesis procedure for Yb₂[12-MC_{Ga(III)N(xshi)-4}]₂(Mip)₄ metallacrowns (x: pAl, mAl, and pYne.; shorthand: **Ln₂Ga₈xShi₄Mip₄**). Dimeric metallacrowns were prepared in the same fashion as in Chapter 2, but with LnGa₄xShi₄(benzoate)₄ as the monomeric MC. Products were pale orange to yellow powders. The synthetic yields were 70-85% based on the metallacrown.*

*Yb₂Ga₈pAlShi₈Mip₄. MS (Figure 4.2, ESI): *m/z* calcd. for Yb₂Ga₈C₁₂₈H₈₄N₁₂O₅₆: 1794.85 [M]²⁻; found 1795.77 [M]²⁻. Elemental analysis calcd. (%) for Yb₂Ga₈C₁₄₃H₁₂₇N₁₅O₇₀Na: C 41.63, H 3.10, N 5.09; found: C 41.61, H 3.08, N 5.04.*

*Yb₂Ga₈mAlShi₈Mip₄. MS (Figure Appx. D76, ESI): *m/z* calcd. for Yb₂Ga₈C₁₂₈H₈₄N₁₂O₅₆: 1794.85 [M]²⁻; found 1795.77 [M]²⁻. Elemental analysis calcd. (%) for Yb₂Ga₈C₁₃₆H₁₁₃N₁₄O₆₈Na₃: C 40.79, H 2.84, N 4.90; found: C 40.74, H 2.84, N 4.79.*

*Yb₂Ga₈pYneShi₈Mip₄. (Figure Appx. D77, ESI): *m/z* calcd. for Yb₂Ga₈C₁₂₈H₆₈N₁₂O₅₆: 1787.29 [M]²⁻; found 1787.70 [M]²⁻. Elemental analysis calcd. (%) for Yb₂Ga₈C₁₄₀H₁₀₄N₁₅O₇₀Na₃: C 41.12, H 2.56, N 5.14; found: C 41.11, H 2.56, N 5.14.*

*Yb₂Ga₈mYneShi₈Mip₄. (Figure Appx. D78, ESI): *m/z* calcd. for Yb₂Ga₈C₁₂₈H₆₈N₁₂O₅₆: 1787.29 [M]²⁻; found 1787.78 [M]²⁻. Elemental analysis calcd. (%) for Yb₂Ga₈C₁₁₂H₇₆N₁₄O₅₅Na₂: C 45.58 H 2.95 N 5.28; found: C 45.46, H 2.94, N 5.24.*

Small molecule coupling to Yb₂Ga₈xShi₈Mip₄:

General coupling procedure of β-Mercaptoethanol (βME) to Yb₂Ga₈xShi₈Mip₄ (x: pAl, mAl, and pYne). The coupling reaction was done by dissolving the metallacrown (10-30 mg, 1 eq), βME (100 eq), and 2,2-Dimethoxy-2-phenylacetophenone (DMPA, 1.0 eq) in degassed DMF to a concentration of 35 mg/mL to the MC mass. The reaction mixture was sealed with a septum lid and then flushed with N₂ (g) for a minimum of 10 minutes. After this time, the reaction lid was wrapped with parafilm to ensure a complete seal, and placed in the LED Box for four hours. The reaction was monitored by ESI-MS. Once finished, the reaction solution was concentrated with a stream of N₂ (g) prior to purification. The dried product was then rinsed with copious amount of water to yield a light-to bright-yellow powder that was dried under vacuum at room temperature overnight (>80% yield, post purification).

*Yb₂Ga₈pAlShi₈Mip₄(βME)₁₂₋₁₁. MS (Figure 4.5 (top), ESI): *m/z* calcd. for Yb₂Ga₈C₁₅₂H₁₅₆N₁₂O₆₈S₁₂: 2263.43 [M]²⁻; found: 2263.33 [M]²⁻. *m/z* calcd. for*

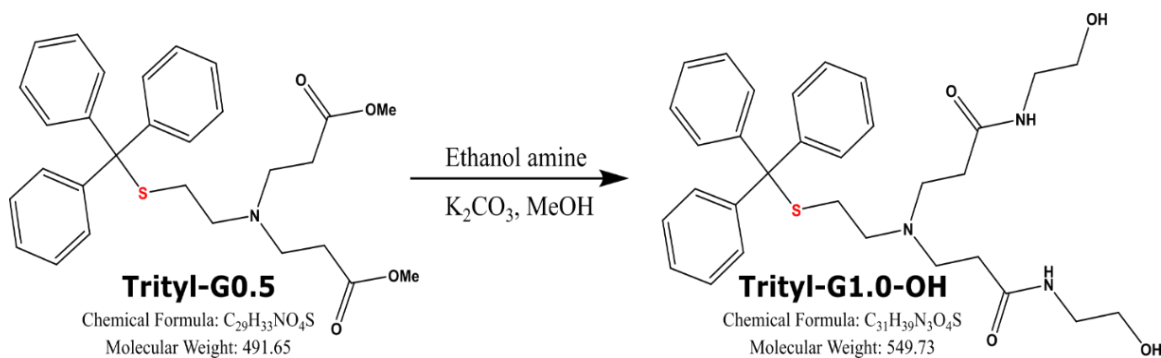
$\text{Yb}_2\text{Ga}_8\text{C}_{150}\text{H}_{150}\text{N}_{12}\text{O}_{67}\text{S}_{11}$: 2224.43 $[\text{M}]^{-2}$; found: 2225.33 $[\text{M}]^{-2}$.

$\text{Yb}_2\text{Ga}_8\text{mAlShi}_8\text{Mip}_4(\beta\text{ME})_{12-11}$. MS (Figure 4.6 (top), ESI): m/z calcd. for $\text{Yb}_2\text{Ga}_8\text{C}_{152}\text{H}_{158}\text{N}_{12}\text{O}_{69}\text{S}_{12}$: 2272.44 $[\text{M}\cdot\text{H}_2\text{O}]^{-2}$; found: 2250.93 $[\text{M}\cdot\text{H}_2\text{O}]^{-2}$. m/z calcd. for $\text{Yb}_2\text{Ga}_8\text{C}_{150}\text{H}_{156}\text{N}_{12}\text{O}_{70}\text{S}_{11}$: 2250.94 $[\text{M}\cdot 3\text{H}_2\text{O}]^{-2}$; found: 2250.93 $[\text{M}\cdot 3\text{H}_2\text{O}]^{-2}$.

$\text{Yb}_2\text{Ga}_8\text{pYneShi}_8\text{Mip}_4(\beta\text{ME})_{20-18}$. MS (Figure 4.7 (top), ESI): m/z calcd. for $\text{Yb}_2\text{Ga}_8\text{C}_{168}\text{H}_{188}\text{N}_{12}\text{O}_{76}\text{S}_{20}$: 2567.92 $[\text{M}]^{-2}$; found: 2566.93 $[\text{M}]^{-2}$. m/z calcd. for $\text{Yb}_2\text{Ga}_8\text{C}_{166}\text{H}_{182}\text{N}_{12}\text{O}_{75}\text{S}_{19}$: 2528.42 $[\text{M}]^{-2}$; found: 2528.93 $[\text{M}]^{-2}$. m/z calcd. for $\text{Yb}_2\text{Ga}_8\text{C}_{165}\text{H}_{184}\text{N}_{12}\text{O}_{75}\text{S}_{18}$: 2506.94 $[\text{M}\cdot\text{MeOH}]^{-2}$; found: 2505.42 $[\text{M}\cdot\text{MeOH}]^{-2}$.

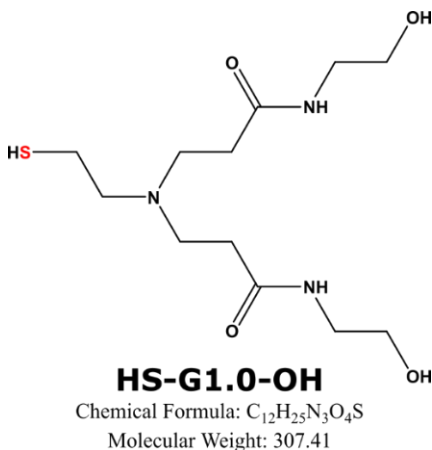
Thiol focal point PAMAM dendrons:

General synthesis, protection, and deprotection procedures of thiol focal PAMAM dendrons of different generations (HS-GX; X: 0.5-1.5) are detailed in the experimental section of Chapter II. Freshly deprotected dendrons were used for the coupling reactions to metallocrowns. A modified G1.0 -OH dendron with hydroxyl surface groups was also prepared, and the synthesis is described below.



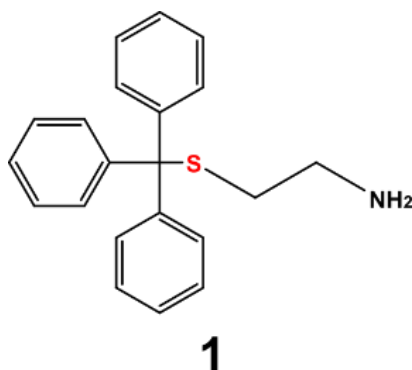
Trityl-G1.0-OH dendron was prepared by first dissolving *Trityl-G0.5 dendron* (3.93 g, 8.0 mmol, 1 eq) in anhydrous methanol (20 mL), followed by the addition of ethanolamine (5.0 mL, 80 mmol, 10 eq) and anhydrous potassium carbonate (11.07 g, 80 mmol, 10 eq). The reaction mixture was then stirred at room temperature for four days. After this time, the reaction solution was filtered and then concentrated using a rotary evaporator at 35°C . The product was redissolved in water (150 mL) and then neutralized to pH~7 with concentrated HCl. The aqueous solution was then extracted thrice with chloroform (3 x 50 mL), dried over magnesium sulfate, and concentrated once again under reduced pressure at 35°C . The product was a clear yellow oil (80% yield). ^1H

NMR (Figure Appx. D79, 400 MHz, CD₃OD) δ 7.34 (d, $J = 7.7$ Hz, 6H), 7.24 (t, $J = 7.5$ Hz, 6H), 7.18 (d, $J = 7.3$ Hz, 3H), 3.52 (t, $J = 5.8$ Hz, 4H), 3.21 (t, $J = 5.8$ Hz, 4H), 2.54 (t, $J = 6.7$ Hz, 4H), 2.32 (s, 4H), 2.22 (t, $J = 6.7$ Hz, 4H).



HS-G1.0-OH dendron was prepared by dissolving *Trityl-G1.0-OH dendron* (1.10 g, 2.0 mmol, 1 eq) in 20 mL of dry DCM. TFA (2.30 mL, 30.0 mmol, 15 eq) was added to the solution slowly while stirring and with N₂ (g) blowing over the flask. This was followed by the one-shot addition of triethylsilane (2.40 mL, 15.0 mmol, 7.5 eq). The reaction was left stirring at room temperature for four hours under N₂ (g) atmosphere. The solvent was removed under reduced pressure at a maximum of 35°C, followed by trituration with petroleum ether five times (5 x 20 mL) for fifteen minutes each. Final product was once again dried under reduced pressure, yielding a white oil (~75% yield) that was stored at -80°C. ¹H NMR (Figure Appx. D80, 400 MHz, CD₃OD) δ 3.63 (d, $J = 5.9$ Hz, 2H), 2.80 (s, 2H), 2.74 (d, $J = 5.7$ Hz, 2H), 2.65 (s, 4H), 2.58 (d, $J = 7.2$ Hz, 2H), 2.49 (d, $J = 9.8$ Hz, 2H), 2.16 – 2.09 (m, 2H), 1.98 (s, 4H).

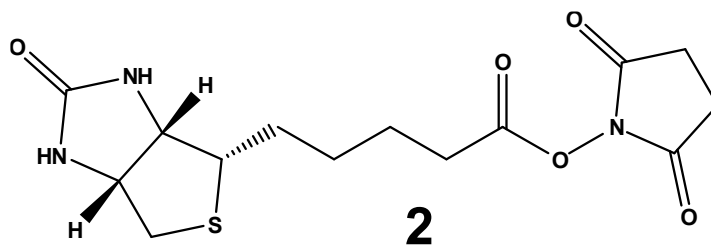
Biotin-thiol synthesis procedure:



Chemical Formula: C₂₁H₂₁NS

MW: 319.47 g/mol

2-(tritylthio)ethanamine (**1**), was prepared by adding anhydrous dichloromethane (DCM) (15 mL) to cysteamine hydrochloride (1.14 g, 10 mmol) under N₂ (g), and placed in an ice bath. Then, while stirring TFA (2 mL) was added to the mixture dropwise, followed by the addition of trityl chloride (2.79 g, 10 mmol) at once. The solution turned dark yellow, and was stirred under N₂ (g) atmosphere at 0°C for 2 hours. After this time, the reaction solution was concentrated under reduced pressure, and then redissolved in chloroform (10 mL). While vigorously stirring the redissolve reaction, 10 M NaOH (3 mL) was added to it, and stirred at room temperature for one hour. The reaction solution turned clear and was then extracted with 3 x 10 mL chloroform. The organic layers were combined, and then washed with 3 x 10 mL brine. Finally, the organic layer was dried over anhydrous MgSO₄, and concentrated to yield a colorless oil (2.99 g, 94% yield, 98% pure). ¹H NMR (Figure Appx. D81, 500 MHz, CDCl₃) δ 7.51 (d, 6H), 7.30 (t, *J* = 8.8, 6.8 Hz, 6H), 7.23 (t, 3H), 2.57 (t, *J* = 6.6 Hz, 2H), 2.35 (t, *J* = 6.6 Hz, 2H), 1.47 (s, 2H).

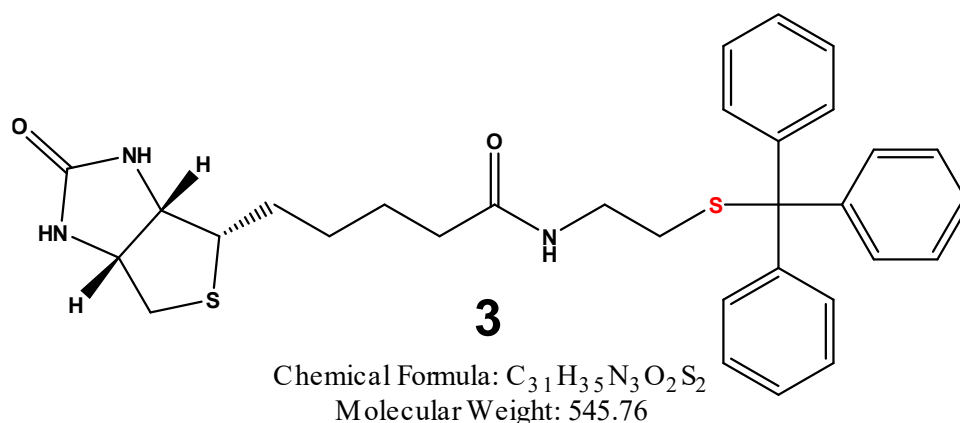


Chemical Formula: C₁₄H₁₉N₃O₅S

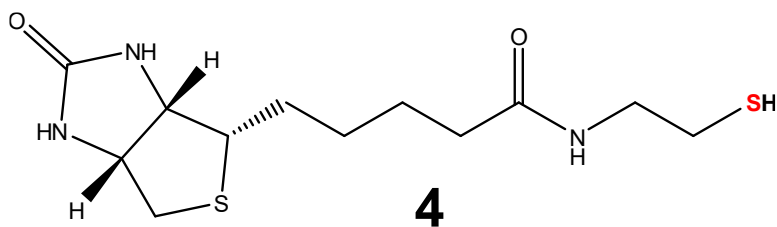
Molecular Weight: 341.38

Biotin N-hydroxysuccinimide Ester (**2**) was prepared by first warming up DMF (30 mL) to 60°C, and then using it to dissolve D-(+)-Biotin (2.00 g, 8.2 mmol) and N-hydroxysuccinimide

(0.94 g, 8.2 mmol). Then, while stirring, *N,N'*-Dicyclohexylcarbodiimide was added, and the reaction mixture was stirred overnight at room temperature. After this time, the reaction was filtered, and the precipitates rinsed with DMF and discarded. The filtrate was concentrated under pressure at 40°C using a rotary evaporator. The leftover solid product was triturated thrice with diethyl ether for 10 minutes at the time, and then filtered to yield white powder as the final product (95% yield, 93% pure). ¹H NMR (Figure Appx. D82, 400 MHz, dms_o-d₆) δ 6.42 (s, 1H), 6.36 (s, 1H), 4.34 – 4.26 (m, 1H), 4.14 (ddd, *J* = 7.8, 4.4, 1.8 Hz, 1H), 3.10 (ddd, *J* = 8.1, 6.4, 4.3 Hz, 1H), 2.87 – 2.80 (m, 1H), 2.81 (s, 4H), 2.79 (s, 0H), 2.71 – 2.63 (m, 2H), 2.58 (d, *J* = 12.4 Hz, 1H), 1.72 – 1.16 (m, 6H).



5-((3*aS*,4*S*,6*aR*)-2-oxohexahydro-1*H*-thieno[3,4-*d*]imidazol-4-yl)-*N*-(2-(tritylthio)ethyl)pentanamide (**3**) was prepared by dissolving **1** (2.99 g, 9.4 mmol), **2** (3.30 g, 9.37 mmol), and triethylamine (2.60 mL, 18.7 mmol) in DMF (50 mL) for 36 hours at room temperature. After this time, DMF was removed under reduce pressure at 40°C using a rotary evaporator. The product was then redissolved in ethyl acetate (50 mL) and wash thrice with distilled water (3 x 25 mL). Organic layer was dried over magnesium sulfate and concentrated under reduce pressure. Product was a clear to light yellow oil (90% yield). ¹H NMR (Figure Appx. D83, 400 MHz, dms_o-d₆) δ 7.88 (t, *J* = 5.8 Hz, 1H), 7.38 – 7.28 (m, 12H), 7.27 – 7.22 (m, 3H), 6.42 (d, *J* = 2.3 Hz, 1H), 6.36 (s, 1H), 4.27 (dd, *J* = 7.7, 5.1 Hz, 1H), 4.08 (ddd, *J* = 7.8, 4.5, 1.8 Hz, 1H), 3.38 (dd, *J* = 14.7, 7.7 Hz, 9H), 3.04 (ddd, *J* = 8.6, 6.2, 4.4 Hz, 1H), 2.97 (q, *J* = 6.7 Hz, 2H), 2.78 (dd, *J* = 12.5, 5.1 Hz, 1H), 2.56 (d, *J* = 12.4 Hz, 1H), 2.18 (t, *J* = 7.0 Hz, 2H), 2.04 – 1.96 (m, 2H), 1.61 – 1.19 (m, 6H).



Chemical Formula: $C_{12}H_{21}N_3O_2S_2$
Molecular Weight: 303.44

N-(2-mercaptoethyl)-5-((3*aS*,4*S*,6*aR*)-2-oxohexahydro-1*H*-thieno[3,4-*d*]imidazol-4-yl)pentanamide (**4**, Biotin-thiol) was prepared by dissolving **3** (1.00 g, 1.83 mmol) in anhydrous DMC (40 mL) and placing it in an ice bath. While stirring and with N_2 (g) blowing over the container, TFA (40 mL) was added dropwise, followed by the addition in one shot of triethylsilane (4.15 mL, 2.6 mmol). The reaction was then stirred for four hours at room temperature. After this time, the reaction was concentrated under reduced pressure at 30°C in a rotary evaporator. The product was then redissolved in toluene (30 mL) and concentrated again under reduced pressure. Once again the product was redissolved in dichloromethane (30 mL) and concentrated under reduced pressure. The product was then triturated thrice with pet. Ether (3 x 30 mL) for 15 minutes each time. Finally, product was redissolved in DCM and concentrated under reduced pressure one last time. Product was a white powder (96% yield, >90% pure). 1H NMR (Figure Appx. D84, 500 MHz, CD_3OD) δ 4.50 (dd, $J = 7.9, 4.8$ Hz, 1H), 4.31 (dd, $J = 7.9, 4.5$ Hz, 1H), 3.33 (t, $J = 7.1$ Hz, 2H), 3.21 (dt, $J = 9.9, 5.2$ Hz, 1H), 2.93 (dd, $J = 12.8, 5.0$ Hz, 1H), 2.71 (d, $J = 12.8$ Hz, 1H), 2.60 (td, $J = 6.9, 1.6$ Hz, 2H), 2.41 – 2.20 (m, 2H), 1.83 – 1.22 (m, 6H).

Dendrimeric Metallacrown (DMC) synthesis and purification:

This section details the different synthetic reaction explored in order to synthesize symmetric and asymmetric DMCs with $Ln_2Ga_8mYneShi_8Ip_4$ and $Ln_2Ga_8pAlShi_8Ip_4$ as the MC core.

Purification details: MC cores first reacted with HS-G0.5 or HS-Biotin were purified by rinsing a concentrated solution with copious amount of water, followed by overnight drying under vacuum at room temperature. For samples with longer dendrons (HS-G1.0 or G1.5), purification was done using RC dialysis bags with a MWCO of 3.5 kDa, and with DMSO as the dialysate. To start, DMC samples were concentrated slowly with a stream of N_2 (g) as to remove the initial DMF, and then redissolved with DMSO to the same initial concentration. The volume of dialysate

was 200 times the volume of the sample inside the dialysis bag. To avoid dialysis bag decomposition, new bags were used every 24 hours, and dialysate was also exchanged daily. Mass spectra of the samples were taken daily to monitor the removal of free dendron. Once the dendron peak was not observed by ESI-MS, the dialysis was stopped, and the sample was slowly concentrated to about ¼ of the original volume with a stream of N₂ (g). Sample concentration was determined by UV-Vis spectrometry by using the extinction coefficient of the metallacrown core prior dendron coupling. *It is important to avoid complete removal of all the solvent, or temperatures above 35°C so as to avoid defect formation. DMCs were stored as DMSO solutions for further characterization.*

Synthesis procedure of Symmetric G0.5 DMC with Yb₂Ga₈pAlShi₈Mip₄ MC: DMC synthesis was done in two steps. First, Yb₂Ga₈pAlShi₈Mip₄ (10-15 mg, 1 eq) was dissolved in degassed DMF to a concentration of 50 mg/mL based on the MC mass. This was followed by the addition of HS-G0.5 (20 eq) and DMAP (1 eq). The reaction mixture was then flushed with N₂ (g) for a minimum of 10 minutes, and then stirred for three days at room temperature. After purification, the product was light yellow powder that was immediately used for the next step. For the second step, the G0.5 DMC was redissolved in the same initial amount of degassed DMF. Then, HS-G0.5 (100 eq) and DMPA (1 eq) were added, and the reaction mixture was flushed with N₂ (g) for a minimum of 10 minutes before sealing it and placing it in the LED Box for two hours. The reaction was monitored by ESI-MS, and if partial coupling was observed, attempts to drive the reaction to completion were made by adding ½ of the initial dendron and DMPA concentration to the mixture, and stirring for two more hours as previously described. Once finished, the reaction solution was concentrated with a stream of N₂ (g) prior to purification by dialysis. Final product was a clear light-yellow solution with an >70% yield post purification. The product was stored as a DMSO solution at room temperature.

Yb₂Ga₈pAlShi₈Mip₄(G0.5)₄: MS (Figure 4.9 (top), ESI): *m/z* calcd. for Yb₂Ga₈C₁₆₈H₁₆₀N₁₆O₇₂S₄: 2293.56 [M]⁻²; found: 2294.53 [M]⁻².

S-DMC Yb₂Ga₈pAlShi₈Mip₄(G0.5)₁₂₋₁₀: MS (Figure 4.9 (bottom), ESI): *m/z* calcd. for Yb₂Ga₈C₂₄₈H₃₁₇N₂₄O₁₀₄S₁₂: 2194.66 [M]⁺³; found: 2195.62 [M]⁺³. *m/z* calcd. for Yb₂Ga₈C₂₃₈H₃₀₂N₂₃O₁₀₂S₁₁: 2124.30 [M]⁺³; found: 2123.92 [M]⁺³. *m/z* calcd. for Yb₂Ga₈C₂₂₈H₂₈₃N₂₂O₉₈S₁₀: 2040.60 [M•2H₂O]⁺³; found: 2041.90 [M•2H₂O]⁺³.

Synthesis procedure of Asymmetric (Janus) DMCs with Ln₂Ga₈pAlShi₈Mip₄ MC cores: two different types of Janus DMCs were prepared with either dendrons of different generations (G1.0/G0.5) or with Biotin and G1.0 dendron coupled to either the ring or bridge position of a dimeric MC core. Each set of reaction conditions are described below.

Janus DMC with G1.0 and G0.5 dendrons: DMC synthesis was done in two steps. First, Yb₂Ga₈pAlShi₈Mip₄ (25-35 mg, 1 eq) was dissolved in degassed DMF to a concentration of 10 mg/mL based on the MC mass. This was followed by the addition of HS-G1.0 (20 eq) and DMAP (1 eq). The reaction mixture was then flushed with N₂ (g) for a minimum of 10 minutes, and then stirred for five days at room temperature. Once complete coupling to the bridge ligands was corroborated by ESI-MS, the reaction mixture was first degassed with N₂ (g) for 15 minutes, followed by the addition of HS-G0.5 (100 eq) and DMPA (1 eq). Once again, the solution was flushed with N₂ (g) for a minimum of 10 minutes before sealing it and placing it in the LED Box for two hours. The reaction was monitored by ESI-MS, and if partial coupling was observed, attempts to drive the reaction to completion were made by adding ½ of the initial dendron and DMPA concentration to the mixture, and stirring for two more hours as previously described. Once finished, the reaction solution was concentrated with a stream of N₂ (g) prior to purification by dialysis. Final product was a clear amber solution with an ~75% yield post purification based on UV-Vis concentration. The product was stored as a DMSO solution at room temperature.

Yb₂Ga₈pAlShi₈Mip₄(G1.0)₄: MS (Figure 4.10 (top), ESI): *m/z* calcd. for Yb₂Ga₈C₁₇₆H₁₉₆N₃₂O₆₄S₄: 2407.24 [M]⁺²; found: 2408.21 [M]⁺².

Janus-DMC Yb₂Ga₈pAlShi₈Mip₄(G1.0)₄(G0.5)₇₋₄: MS (Figure 4.10 (bottom), ESI): *m/z* calcd. for Yb₂Ga₈C₂₄₆H₃₃₀N₃₉O₉₂S₁₁: 2186.74 [M]⁺³; found: 2187.73 [M]⁺³. *m/z* calcd. for Yb₂Ga₈C₂₃₆H₃₁₁N₃₈O₈₈S₁₀: 2104.04 [M]⁺³; found: 2105.70 [M]⁺³. *m/z* calcd. for Yb₂Ga₈C₂₂₆H₂₉₂N₃₇O₈₄S₉: 2020.33 [M]⁺³; found: 2021.00 [M]⁺³. *m/z* calcd. for Yb₂Ga₈C₂₁₆H₂₇₅N₃₆O₈₁S₈: 1943.64 [M•H₂O]⁺³; found: 1945.93 [M•H₂O]⁺³.

Janus DMC with G1.0 dendrons at the ring ligands, Biotin at the bridge ligands, and a Yb₂Ga₈pAlShi₈Mip₄ MC core: DMC synthesis was done in two steps. First, Yb₂Ga₈xAlShi₈Mip₄ (10-15 mg, 1 eq), HS-Biotin (**4**, 40 eq) and DMPA (1.5 eq) were dissolved in degassed DMF to a

concentration of 50 mg/mL based on the MC mass. The reaction mixture was then stirred at room temperature for six days. Once complete coupling of four biotin to the MC was confirmed by ESI-MS, the solvent was removed with a stream of N₂ (g). The solid was then washed with copious amounts of methanol to yield a purple to dark pink powder that was dried under vacuum overnight. Then, the biotinylated MC was dissolved in degassed DMF to a concentration of 35 mg/mL based on the MC mass, followed by the addition of HS-1.5 (100 eq) and DMPA (1 eq). The solution mixture was flushed with N₂ (g) for a minimum of 10 minutes before being sealed, and placed in the LED Box for two hours. If partial dendron coupling was observed by ESI-MS, attempts to drive the reaction to completion were made by adding ½ of the initial dendron and DMPA concentration to the mixture, and stirring for two more hours as previously described. Once finished, the reaction solution was concentrated with a stream of N₂ (g) prior to purification by dialysis against DMSO. Final product was a solution clear faint yellow solution with an overall >70% yield post purification based on UV-Vis concentration. The product was stored as a DMSO solution at room temperature.

Yb₂Ga₈pAlShi₈Mip₄(Biotin)₄: MS (Figure 4.12 (top), ESI): *m/z* calcd. for Yb₂Ga₈C₁₇₆H₁₆₈N₂₄O₆₄S₈: 2401.06 [M]⁻²; found: 2402.93 [M]⁻².

Janus-DMC Yb₂Ga₈pAlShi₈Mip₄(Biotin)₄(G1.0)₈₋₅: MS (Figure 4.12 (bottom), ESI): *m/z* calcd. for Yb₂Ga₈C₂₇₂H₃₈₉N₆₄O₈₀S₁₆: 2416.89 [M]⁺³; found: 2413.74 [M]⁺³. *m/z* calcd. for Yb₂Ga₈C₂₆₀H₃₆₂N₅₉O₇₈ S₁₅: 2315.16 [M]⁺³; found: 2313.74 [M]⁺³. *m/z* calcd. for Yb₂Ga₈C₂₄₈H₃₃₅N₅₄O₇₆S₁₄: 2213.43 [M]⁺³; found: 2213.02 [M]⁺³. *m/z* calcd. for Yb₂Ga₈C₂₃₆H₃₁₀N₄₉O₇₅S₁₃: 2118.0 [M•H₂O]⁺³; found: 2118.60 [M•H₂O]⁺³.

Janus DMC with Biotin at the ring ligands and G1.0 dendrons at the bridge ligands Janus DMC with biotin at the ring ligands, G1.0 dendrons at the bridge ligands, and a Yb₂Ga₈pAlShi₈Mip₄ MC core: The first reaction step followed the same procedure described above, where HS-G1.0 dendrons were coupled to the maleimide appendages of Yb₂Ga₈pAlShi₈Mip₄. The only difference being that the MC was dissolved with DMF to a concentration of 30 mg/mL based on the MC mass. Then, without further purification, the reaction mixture was degassed with N₂ (g) for 15 minutes, followed by the addition of HS-Biotin (**4**, 80 eq) and DMPA (0.5 eq). The reaction as then with N₂ (g) for a minimum of 10 minutes before being

sealed, and placed in the LED Box for two hours. If partial biotin coupling was observed by ESI-MS, attempts to drive the reaction to completion were made by adding the initial concentration of HS-Biotin and DMPA, and stirring for two more hours as previously described. Once finished, the reaction was concentrated with a stream of N₂ (g) prior to purification by dialysis against DMSO. Final product was a clear light orange solution with an overall >75% yield post purification based on UV-Vis concentration. The product was stored as a DMSO solution at room temperature.

Yb₂Ga₈pAlShi₈Mip₄(G1.0)₄: MS (Figure 4.10 (top), ESI): *m/z* calcd. for Yb₂Ga₈C₁₇₆H₁₉₆N₃₂O₆₄S₄: 2407.24 [M]⁺²; found: 2408.21 [M]⁺².

Janus-DMC Yb₂Ga₈pAlShi₈Mip₄(G1.0)₄(Biotin)₈: (Figure 4.14, ESI): *m/z* calcd. for Yb₂Ga₈C₂₇₂H₃₆₅N₅₆O₈₀S₂₀: 2414.12 [M]⁺³; found: 2414.05 [M]⁺³. *m/z* calcd. for Yb₂Ga₈C₂₆₀H₃₄₄N₅₃O₇₈S₁₈: 2313.08 [M]⁺³; found: 2313.36 [M]⁺³. *m/z* calcd. for Yb₂Ga₈C₂₄₈H₃₂₃N₅₀O₇₆S₁₆: 2212.04 [M]⁺³; found: 2212.05 [M]⁺³.

Toroidal DMCs with red-shifted ring ligands: Synthesis and purification of DCMs with Yb₂Ga₈*m*YneShi₈Mip₄ MC cores and three different generations (G1.0, G1.0 -OH, and G1.5) was done in the same fashion as described in Chapter two. Reaction details were Yb₂Ga₈*m*AlShi₈Mip₄ (0.010 mmol, 1 eq), HS-G1.0 (0.20 mmol, 20 eq), and DMAP (0.010 mmol, 1 eq) dissolved in degassed DMF to a concentration of 10 mg/mL based on the MC mass. Solutions were stirred for five days with HS-G1.0 dendrons and seven days for HS-G1.5. After purification and concentration, the final products were clear light orange solution with an overall >80% yield post purification based on UV-Vis concentration. The products were stored as DMSO solutions at room temperature.

*Redshifted-DMC Yb₂Ga₈*m*YneShi₈Mip₄ (G1.0)₄*: MS (Figure 4.19A, ESI): *m/z* calcd. for Yb₂Ga₈C₁₇₆H₁₇₆N₃₂O₆₄S₄: 2398.16 [M]⁻²; found: 2398.15 [M]⁻².

*Redshifted-DMC Yb₂Ga₈*m*YneShi₈Mip₄ (G1.0 -OH)₄*: (Figure 4.19B, ESI): *m/z* calcd. for Yb₂Ga₈C₁₇₆H₁₇₂N₂₄O₇₂S₄: 2403.11 [M]⁺²; found: 2404.11 [M]⁺².

*Redshifted-DMC Yb₂Ga₈*m*YneShi₈Mip₄ (G1.5)₄*: MS (Figure 4.19C, ESI): *m/z* calcd. for Yb₂Ga₈C₂₄₀H₂₇₇N₃₂O₉₆S₄: 2058.65 [M]⁺³; found: 2059.62 [M]⁺³.

4.2.5 Luminescence Studies

Solution state absorbance was collected using a Cary 100Bio UV-Vis spectrometer in absorbance mode. Samples were prepared by dissolving them in 3 mL of DMSO with a final concentration of 1-25 μM . Data were processed using OriginPro 2020 software.

Photophysical measurements were performed by Dr. Svetlana Eliseeva at the Centre de Biophysique Moléculaire, Orleans, France. Luminescence data of MCs were collected on freshly prepared solutions in DMSO or in the solid state placed into 2.4 mm i.d. quartz capillaries, while DMC samples were diluted to 50 μM solutions and only recorded in solution state. Emission and excitation spectra were measured on a Horiba-Jobin-Yvon Fluorolog 3 spectrofluorimeter equipped with either a visible photomultiplier tube (PMT) (220-800 nm, R928P; Hamamatsu), a NIR solid-state InGaAs detector cooled to 77 K (800-1600 nm, DSS-IGA020L; ElectroOptical Systems, Inc., USA), or a NIR PMT (950-1650 nm, H10330-75; Hamamatsu). All spectra were corrected for the instrumental functions. Luminescence lifetimes were determined under excitation at 355 nm provided by a Nd:YAG laser (YG 980; Quantel). Luminescent signals were detected in the visible or NIR ranges with a R928 or H10330-75 PMTs connected to the iHR320 monochromator (Horiba Scientific), respectively. The output signals from the detectors were fed into a 500 MHz bandpass digital oscilloscope (TDS 754C; Tektronix) and transferred to a PC for data processing with the Origin 8 software. Luminescence lifetimes are reported as the average of three or more independent measurements. Quantum yields were determined with a Fluorolog 3 spectrofluorimeter based on the absolute method using an integration sphere (GMP SA). Each sample was measured several times varying the position of samples. Estimated experimental error for the determination of quantum yields is estimated as $\sim 10\%$. Details on the instrument set up to measure quantum yields is described in the experimental section of Chapter 2, under luminescent studies.

4.2.6 Cell Studies

Cell studies were performed and interpreted by Dr. Guillaume Collet at the Centre de Biophysique Moléculaire, Orleans, France.

Cell culture: HeLa cells (human cervical cancer cells collected from Henrietta Lacks) were cultured in EMEM medium (Sigma) supplemented with 10% (vol:vol) fetal bovine serum (FBS, Sigma), 100 U/mL penicillin (Sigma), and 100 $\mu\text{g}/\text{mL}$ streptomycin (Sigma). Cells were routinely

cultured at 37 °C in a humidified incubator in a 95% air/5% CO₂ atm and passaged by detaching cells with trypsin/EDTA 0.25% (Gibco). HeLa cells were seeded in an eight chambers Lab-Tek (1.0 borosilicate coverglass system) at 10 000 cells/chamber in a final volume of 400 μL of complete EMEM medium. After 48 h, cell culture medium was removed and after three washes with 500 μL of saline (9 g/L NaCl), Yb₂Ga₈Shi₈Mip₄ DMC was added to cells at a dilution of 100 μM in saline with 1 % DMSO (vol:vol) for 2 hours of incubation. Prior collecting images, HeLa cells were washed three times with 500 μL of saline. For the microscopy imaging, HeLa cells were kept in 200 μL of OptiMEM (Gibco) without phenol red, supplemented with 2% (vol:vol) fetal bovine serum (FBS, Sigma), 100 U/mL penicillin (Sigma), and 100 μg/mL streptomycin (Sigma).

Optical microscopy imaging: Epifluorescence microscopy was performed with an inverted Nikon Eclipse Ti microscope equipped with an EMCCD Evolve camera from Photometrics. The Nikon Intensilight C-HGFIE mercury-halide lamp was used as the excitation source. For imaging of Yb₂Ga₈Shi₈Mip₄ DMC, the Yb^{III} signal was observed using the following set of filters: a 377 nm with 50 nm bandwidth in the pass band excitation filter, a 506 nm dichroic beam splitter, and a long pass 785 nm emission filter. Fluorescent images were obtained with Nikon Plan Fluor 40x objective after two seconds of exposure time. An Okolab incubation chamber adapted to the microscope allowed the incubation parameters to be maintained at a constant 37 °C with a humidified atmosphere of 95% air/5% CO₂. All microscopy images were acquired and processed with Nikon NIS Elements AR software.

4.3 Results

4.3.1 Ln₂Ga₈xShi₈Mip₄ Metallacrowns

Synthesis and physical characterization of Ln₂Ga₈xShi₈Mip₄. The reaction between LnGa₄xShi₄(Benzoate)₄ (Ln = Yb^{III}; x: *p*Yne, *m*Yne, *p*Al, and *m*Al) and 5-maleimidoisophthalic acid (H₂Mip) in DMF led to the formation of Ln₂Ga₈xShi₈Mip₄ with the general formula Ln₂[12-MC_{Ga(III)N(xshi)-4}]₂(Mip)₄. Solids were collected as crystalline powder material, and characterized by ESI-MS and elemental analysis. As seen in Figure 4.2, the ESI-MS spectrum of Yb₂Ga₈*p*AlShi₈Mip₄ is consistent with the MC structure, and displays an isotopic separation of 0.5 *m/z*, corroborating the intrinsic -2 charge of the metallacrown. The extra peaks in the ESI-MS at higher *m/z* values are due to solvent adducts (water and/or methanol), while the one at lower *m/z* is due to the loss of an ether allyl group, likely due to the high voltage potential (350 V) at which

the mass spectrometer was operated. ESI-MS spectra of scaffolds prepared with each of the four ring ligands (*p*YneShi, *m*YneShi, *p*AlShi, and *m*AlShi), can be found in Appendix D Figures 76-78.

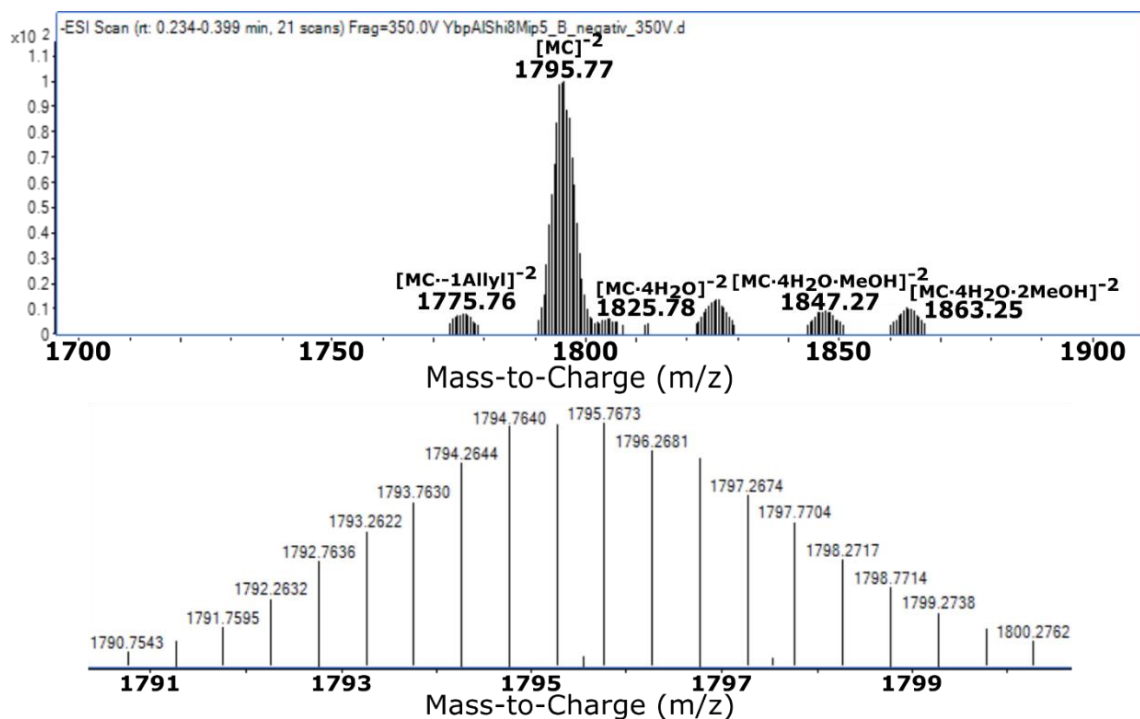


Figure 4.2 (Top) ESI-MS of $\text{Yb}_2\text{Ga}_8\text{pAlShi}_8\text{Mip}_4$ metallacrown in negative ion mode. (Bottom) expansion of the major peak corroborating the -2 isotopic distribution of the complex.

Photophysical properties of $\text{Yb}_2\text{Ga}_8\text{Shi}_8\text{Mip}_4$. Absorption spectra of each of the four MC scaffolds collected in DMSO are shown in Figure 4.3. The *para*-substituted MCs have $\pi \rightarrow \pi^*$ transitions located between 250-340 nm, with a low-energy maximum located at ~ 310 nm and absorption coefficients of $\epsilon_{p\text{Yne}(310\text{nm})} = 7.86 \times 10^4 \text{ M}^{-1}\text{cm}^{-1}$ for $\text{Yb}_2\text{Ga}_8\text{pYneShi}_8\text{Mip}_4$ and $\epsilon_{p\text{Al}(310\text{nm})} = 8.67 \times 10^4 \text{ M}^{-1}\text{cm}^{-1}$ for $\text{Yb}_2\text{Ga}_8\text{pAlShi}_8\text{Mip}_4$. The *meta*-substituted scaffolds have their $\pi \rightarrow \pi^*$ transitions located between 250-360 nm, with their low-energy maximum red-shifted to ~ 340 nm. Their extinction coefficients are reduced compared to the *para*-substituted scaffold, with values of $\epsilon_{m\text{Yne}(337\text{nm})} = 4.36 \times 10^4 \text{ M}^{-1}\text{cm}^{-1}$ for $\text{Yb}_2\text{Ga}_8\text{mYneShi}_8\text{Mip}_4$ and $\epsilon_{m\text{Al}(341\text{nm})} = 4.62 \times 10^4 \text{ M}^{-1}\text{cm}^{-1}$ for $\text{Yb}_2\text{Ga}_8\text{mAlShi}_8\text{Mip}_4$. The energy positions of the ligands' singlet states (S^*), determined from the edge of the absorption spectra, are located at ~ 340 nm (29412 cm^{-1}) for the MCs templated with *p*YneShi and *p*AlShi, and at ~ 380 nm (26667 cm^{-1}) for the MCs with *m*YneShi and *m*AlShi.

These values are similar to those of the parent $\text{Ln}_2\text{Ga}_8\text{xShi}_8\text{Ip}_4$ MCs described in Chapter 3. The triplet state (T^*) energy of the scaffolds was not measured, but are likely to be close to those of the parent $\text{Ln}_2\text{Ga}_8\text{xShi}_8\text{Ip}_4$ MCs introduced in Chapter 3. This is expected because, as shown in Chapter 2, the bridging ligands have minimal influence on the overall T^* energy levels of MCs – such as in the case of $\text{Ln}_2\text{Ga}_8\text{Shi}_8\text{Ip}_4$ (T^* : 21980 cm^{-1}) and $\text{Ln}_2\text{Ga}_8\text{Shi}_8\text{Mip}_4$ (T^* : 23280 cm^{-1}) where the only difference was the type of bridging ligand (H_2Ip vs. H_2Mip) which corresponds to a 5.7% difference between T^* values. Thus, the T^* of the MC in this chapter are as follows: 463 nm (21620 cm^{-1}) for $\text{Ln}_2\text{Ga}_8\text{mYneShi}_8\text{Mip}_4$; 440 nm (22740 cm^{-1}) for $\text{Ln}_2\text{Ga}_8\text{pAlShi}_8\text{Mip}_4$; and 467 nm (21410 cm^{-1}) for $\text{Ln}_2\text{Ga}_8\text{mAlShi}_8\text{Mip}_4$. Due to the difficulty to obtain enough crystalline product for analysis, data for $\text{Gd}_2\text{Ga}_8\text{pYneShi}_8\text{Mip}_4$ metallacrowns was not collected.

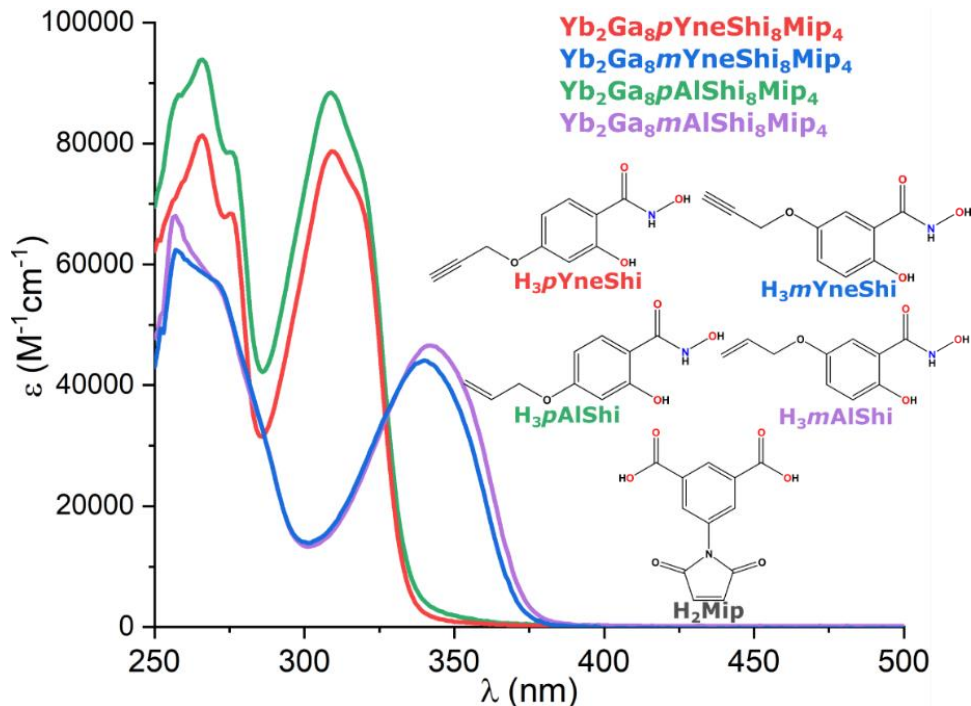


Figure 4.3 UV-Vis absorbance spectra of $\text{Yb}_2\text{Ga}_8\text{xShi}_8\text{Mip}_4$ (x : *pYne*, *mYne*, *pAl*, and *mAl*) recorded at room temperature in DMSO at concentrations of 8.5-10.5 μM .

Solution and solid-state excitation and emission of $\text{Yb}_2\text{Ga}_8\text{pAlShi}_8\text{Mip}_4$ and $\text{Yb}_2\text{Ga}_8\text{mYneShi}_8\text{Mip}_4$ show once again that the MC scaffold, regardless of functionalization, is able to sensitize lanthanide luminescence. As seen on Figure 4.4, the excitation spectra in the solid state and in DMSO solutions collected upon monitoring the Yb^{III} -centered emission at 980 nm show broad ligand-centered bands up to 350-400 nm for $\text{Yb}_2\text{Ga}_8\text{pAlShi}_8\text{Mip}_4$, and up to 380-430

nm for $\text{Yb}_2\text{Ga}_8m\text{YneShi}_8\text{Mip}_4$. Due to saturation effects,¹⁵⁷ a slight expansion of the excitation bands is observed for the solid-state data compared to the solution data. As for the luminescent emission in both solid and solution state, upon excitation in the ligand centered region (320 nm or 375 nm), characteristic Yb^{III} emission is observed (920-1100 nm) from the $^2\text{F}_{5/2} \rightarrow ^2\text{F}_{7/2}$ transition with both metallacrowns. The luminescent lifetimes (τ_{obs}) and the lanthanide's quantum yields upon ligand excitation (φ_{Ln}^L) were also measured, and are summarized in Table 4.1. For the sake of comparison, values of other previously reported Yb^{III} -MCs are also shown – including the MC parent materials introduced in Chapters 2 and 3. Biexponential decay is observed with both of $\text{Yb}_2\text{Ga}_8p\text{AlShi}_8\text{Mip}_4$ and $\text{Yb}_2\text{Ga}_8m\text{YneShi}_8\text{Mip}_4$ in the solid state, while in solution only the former has biexponential decay. In all cases of biexponential decay, the dominant contribution came from the slower decay. The τ_{obs} of $\text{Yb}_2\text{Ga}_8p\text{AlShi}_8\text{Mip}_4$ are ~ 1.7 times longer in solution than in solid state. While for $\text{Yb}_2\text{Ga}_8m\text{YneShi}_8\text{Mip}_4$ solution τ_{obs} values are ~ 3.3 times longer. As for the MCs' φ_{Ln}^L , the solution state values for $\text{Yb}_2\text{Ga}_8p\text{AlShi}_8\text{Mip}_4$ are ~ 4.8 times larger than in the solid state. Similarly, the φ_{Ln}^L of $\text{Yb}_2\text{Ga}_8m\text{YneShi}_8\text{Mip}_4$ in solution is ~ 13.0 times larger. Compared to each other, while the *meta*-substituted MC has longer τ_{obs} values in both solid state and solution, the *para*-substituted MC has higher φ_{Ln}^L in both states.

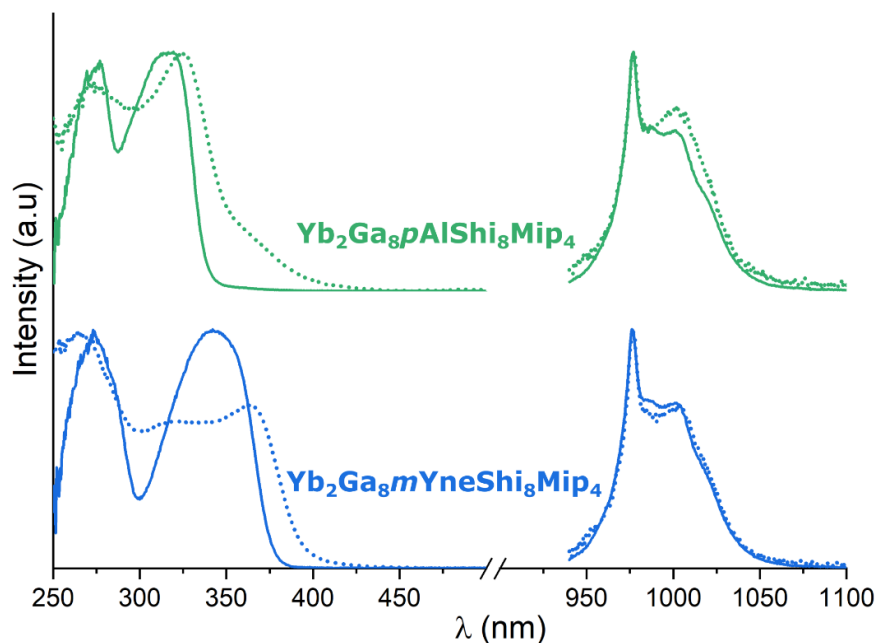


Figure 4.4 Corrected and normalized excitation (left, λ_{em} : 980 nm) and emission (right, λ_{ex} : 320–375 nm) spectra of $\text{Yb}_2\text{Ga}_8p\text{AlShi}_8\text{Mip}_4$ and $\text{Yb}_2\text{Ga}_8m\text{YneShi}_8\text{Mip}_4$ in the solid state (dashed traces) and 50 μM solutions in DMSO (solid traces) at room temperature.

Table 4.1 Luminescence lifetimes (τ_{obs}) and Yb^{III}-centered quantum yields collected under ligand excitation (ϕ_{Yb}^L)^a

Compound	State/Solvent	τ_{obs} [μs] ^b	τ_{av} [μs] ^c	ϕ_{Ln}^L [%] ^d
Yb ₂ Ga _{8p} AlShi ₈ Mip ₄	Solid	16.7(3) : 78(1)% 6.0(2) : 22(1)%	15.7(3)	0.553(4)
	DMSO	53.4(7) : 92(1)% 13(1) : 8(1)%	52.5(9)	4.96(6)
Yb ₂ Ga _{8m} YneShi ₈ Mip ₄	Solid	20.5(5) : 85(2)% 5.8(1) : 15(2)%	19.8(4)	0.28(2)
	DMSO	65.1(8) : 100%	--	3.63(5)
Yb ₂ Ga ₈ Shi ₈ Mip ₄	Solid	23.2(3) : 89.8(4)% 4.75(7) : 10.2(4)%	22.7(8)	0.126(3)
	DMSO	48.7(6) : 84.6(5)% 6.9(2) : 15.4(5)%	45.3(9)	2.78(6)
Yb ₂ Ga _{8p} AlShi ₈ Ip ₄	Solid	23.2(3)	--	1.37(8)
	DMSO	53.5 : 65(1)% 8.4(1) : 35(1)%	49.9(7)	7.75(1)
Yb ₂ Ga _{8m} YneShi ₈ Ip ₄	Solid	20.1(2) : 83(3)% 5.4(3):27(3)%	19.4(3)	1.59(5)
	DMSO	58(4) : 100%	--	7.3(2)

^a For samples in the solid state or for 50 μM solutions in DMSO, at room temperature, 2σ values between parentheses. Estimated experimental errors: τ_{obs} , $\pm 2\%$; Q_{Yb}^L , $\pm 10\%$. ^b Under excitation at 355 nm. If biexponential decay was observed, population parameters $P_i = \frac{B_i \tau_i}{\sum_{i=1}^n B_i \tau_i}$ in % are given after the colon. ^c Lifetime averages calculated as: $\tau_{\text{av}} = \frac{\sum_i B_i \tau_i^2}{\sum_i B_i \tau_i}$. B_i are the population parameters given in % after the lifetime values. ^d Quantum yield under excitation at 320-360 nm.

Comparing the τ_{obs} and ϕ_{Yb}^L values of the parent Yb₂Ga₈Shi₈Mip₄ MC without any ring functionalization, the new Yb₂Ga_{8p}AlShi₈Mip₄ MC has larger values in solution (~ 1.2 and ~ 1.8 times, respectively), while in solid state the τ_{obs} is smaller (~ 0.7 times) and the ϕ_{Yb}^L is larger (~ 4.4 times). However, comparing it to the parent Yb₂Ga_{8p}AlShi₈Ip₄ MC that is only functionalized at the ring position, the τ_{obs} in solution and solid state of the new Yb₂Ga_{8p}AlShi₈Mip₄ are very similar, while a more significant difference is observed in the ϕ_{Yb}^L values – with a $\sim 36\%$ decrease in solution and a $\sim 60\%$ decrease in the solid state. As for the *meta*-substituted MC, a similar trend is observed. Comparing the τ_{obs} and ϕ_{Yb}^L values of Yb₂Ga_{8m}YneShi₈Mip₄ to the parent Yb₂Ga₈Shi₈Mip₄ MC, the solution values are both ~ 1.3 times larger, while in the solid state τ_{obs} is ~ 0.9 times shorter and ϕ_{Yb}^L is ~ 2.2 times higher for the bifunctionalized MC. When compared to the monofunctionalized Yb₂Ga_{8m}YneShi₈Ip₄, τ_{obs} in solution and solid state are very similar, while the ϕ_{Yb}^L values decrease in both solution (by $\sim 50\%$) and solid state (by $\sim 72\%$).

4.3.2 Ln₂Ga_{8x}Shi₈Mip₄ Functionalization

Small molecule coupling to Ln₂Ga_{8x}Shi₈Mip₄. The reaction between Yb₂Ga_{8x}Shi₈Mip₄ and

β -mercaptoethanol (β ME) in the presence of DMPA and UV light, led to the symmetric coupling of up to twelve (four at the bridge and the eight at ring ligands) or twenty (four at the bridge and sixteen at ring ligands) equivalents of the small molecule onto the MC core. The thiol coupling to the $\text{Yb}_2\text{Ga}_8p\text{AlShi}_8\text{Mip}_4$ and $\text{Yb}_2\text{Ga}_8m\text{AlShi}_8\text{Mip}_4$ MCs was done via thiol-maleimide and thiol-ene coupling, while $\text{Yb}_2\text{Ga}_8p\text{YneShi}_8\text{Mip}_4$ underwent thiol-maleimide and thiol-yne addition. The $\text{Ln}_2\text{Ga}_8m\text{YneShi}_8\text{Mip}_4$ MC was not investigated for bifunctional coupling since the templating ring ligands (H_3mYeShi) were shown to be the least reactive toward thiol coupling in Chapter 3.

The desired product was collected as a bright yellow powder that was characterized by ESI-MS and UV-Vis absorbance spectroscopy. Shown in Figure 4.5 and Figure 4.6 are the ESI-MS spectra of the thiol-ene coupling to the *para*- and *meta*-substituted $\text{Yb}_2\text{Ga}_8x\text{Shi}_8\text{Mip}_4$ MCs. In both cases, a narrow distribution of eleven to twelve couplings of β ME to the MC are observed. As for the coupling to $\text{Yb}_2\text{Ga}_8p\text{YneShi}_8\text{Mip}_4$, Figure 4.7 shows a distribution of eighteen to twenty β ME couplings. Just as previously observed with the parent $\text{Ln}_2\text{Ga}_8x\text{Shi}_8\text{Ip}_4$ MCs only functionalized at the ring position, the scaffold templated with *p*YneShi and *m*AlShi ring ligands seem to be slightly less reactive toward thiol addition than the MCs with *p*AlShi ring ligands. Lastly, the UV-Vis absorbance spectra of the three scaffolds taken after thiol coupling shown in Figure 4.8, display profiles similar to the MCs prior to functionalization. The absorbance spectra display $\pi \rightarrow \pi^*$ transition bands extending up to 340 or 360 nm, with absorbance maxima (λ_{max}) located at about 310 nm for the *para*-substituted MCs, and about 340 nm for the *meta*-substituted MC.

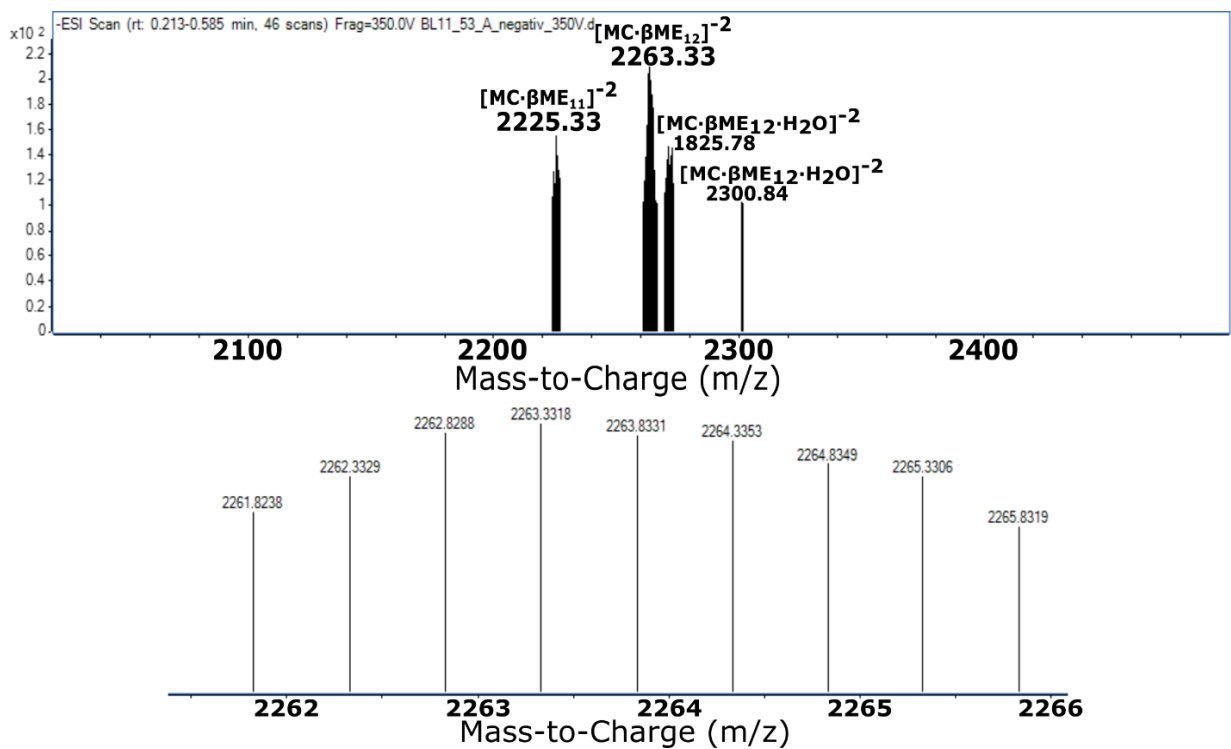


Figure 4.5 (Top) ESI-MS of Yb₂Ga₈pAlShi₈Mip₄βME₁₂₋₁₁ metallacrown in negative ion mode. (Bottom) expansion of the major peak corroborating the -2 isotopic distribution of the complex.

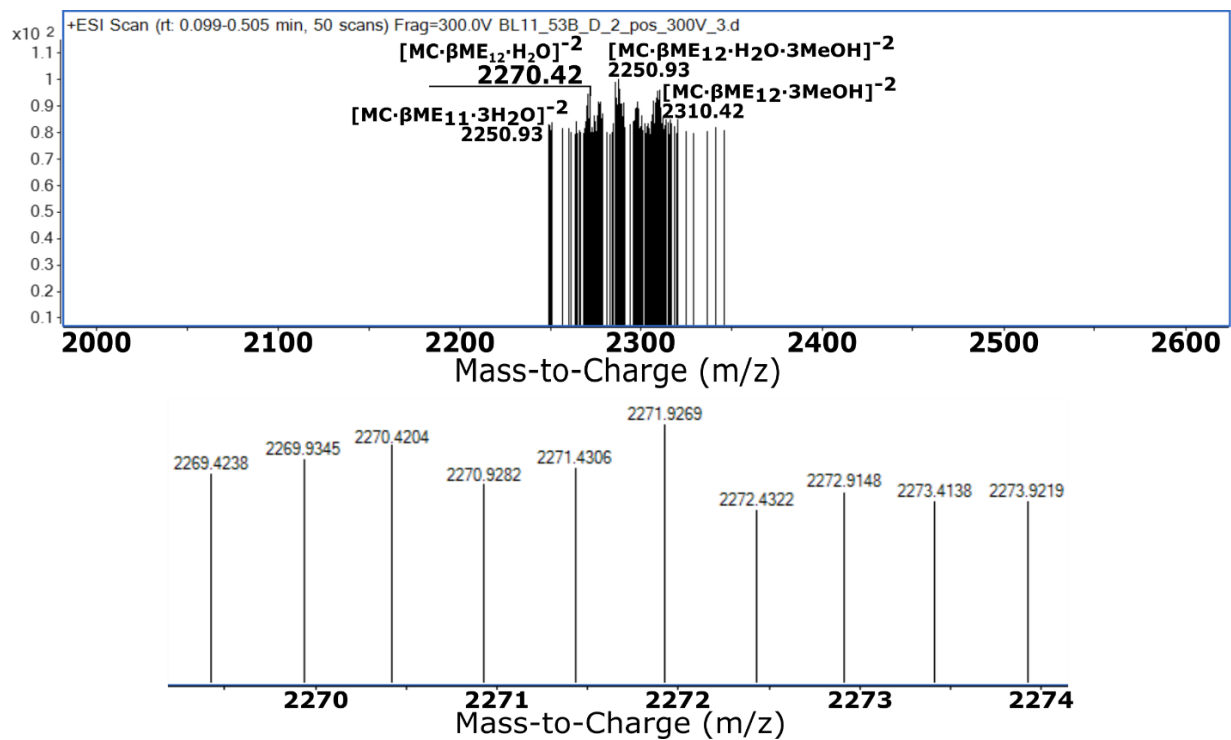


Figure 4.6 (Top) ESI-MS of Yb₂Ga₈mAlShi₈Mip₄βME₁₂₋₁₁ metallacrown in negative ion mode. (Bottom) expansion of the major peak corroborating the -2 isotopic distribution of the complex.

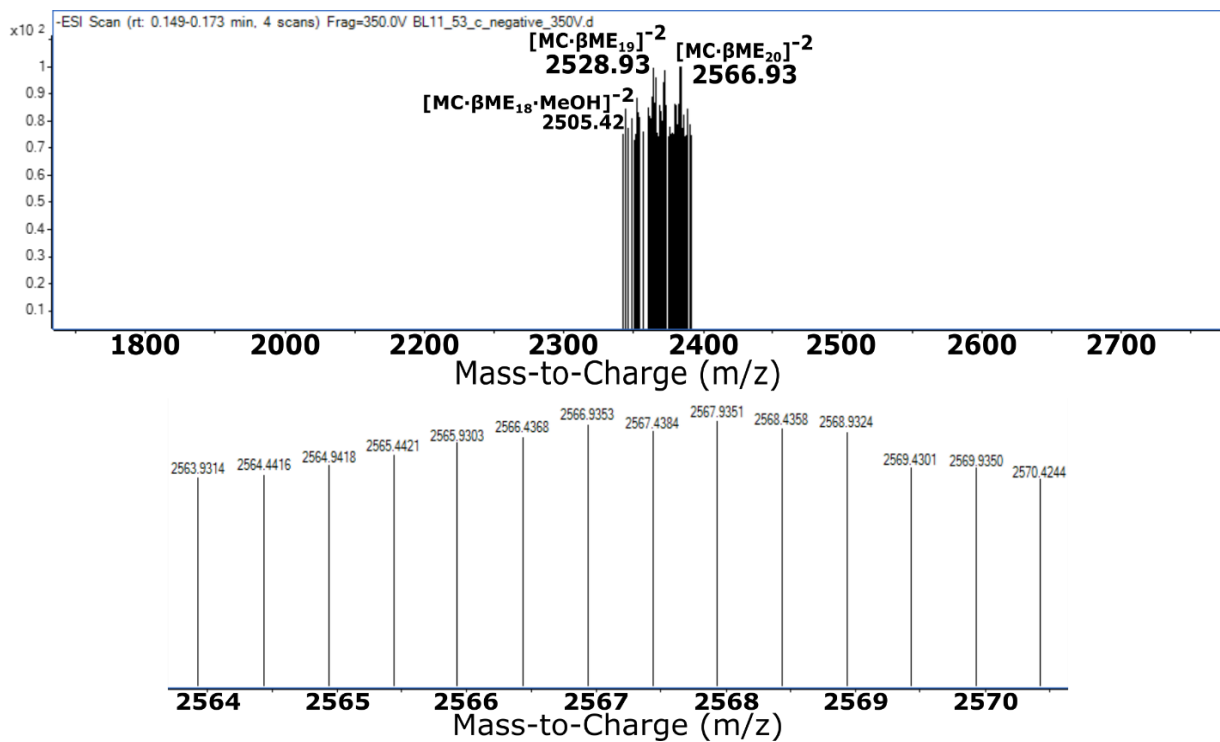


Figure 4.7 (Top) ESI-MS of $\text{Yb}_2\text{Ga}_8p\text{YneShi}_8\text{Mip}_4\beta\text{ME}_{20-18}$ metallacrown in negative ion mode. (Bottom) expansion of the major peak corroborating the -2 isotopic distribution of the complex.

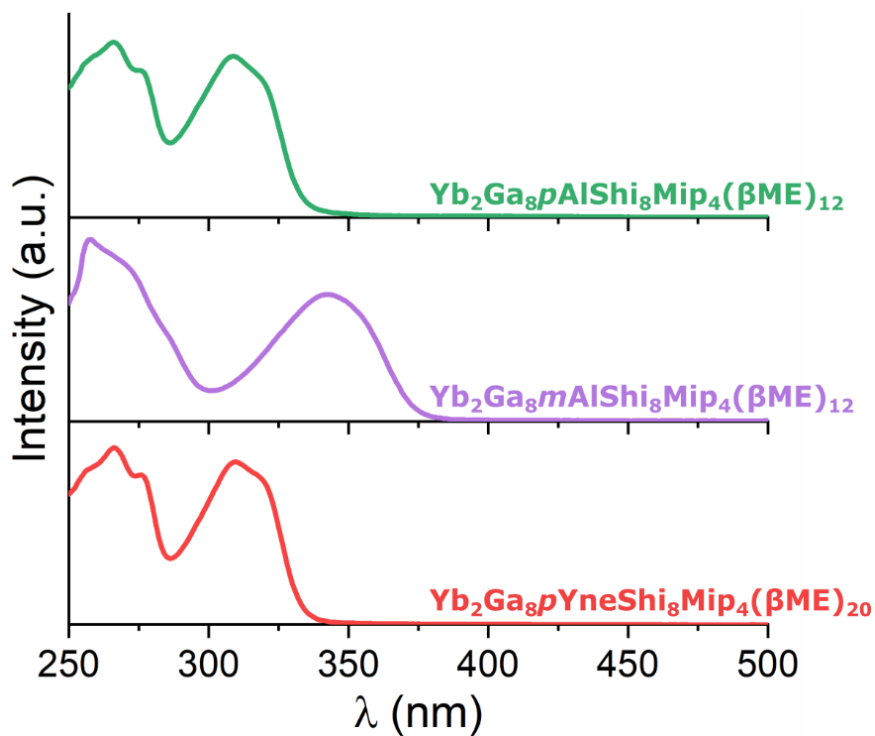


Figure 4.8 UV-Vis Absorbance spectra of $\text{Yb}_2\text{Ga}_8p\text{AlShi}_8\text{Mip}_4$, $\text{Yb}_2\text{Ga}_8m\text{AlShi}_8\text{Mip}_4$, and $\text{Yb}_2\text{Ga}_8p\text{YneShi}_8\text{Mip}_4$ post symmetric β -mercaptoethanol coupling recorded at room temperature in DMSO at concentrations of 10-18 μM .

4.3.3 Symmetric and Asymmetric Dendrimeric Metallacrowns

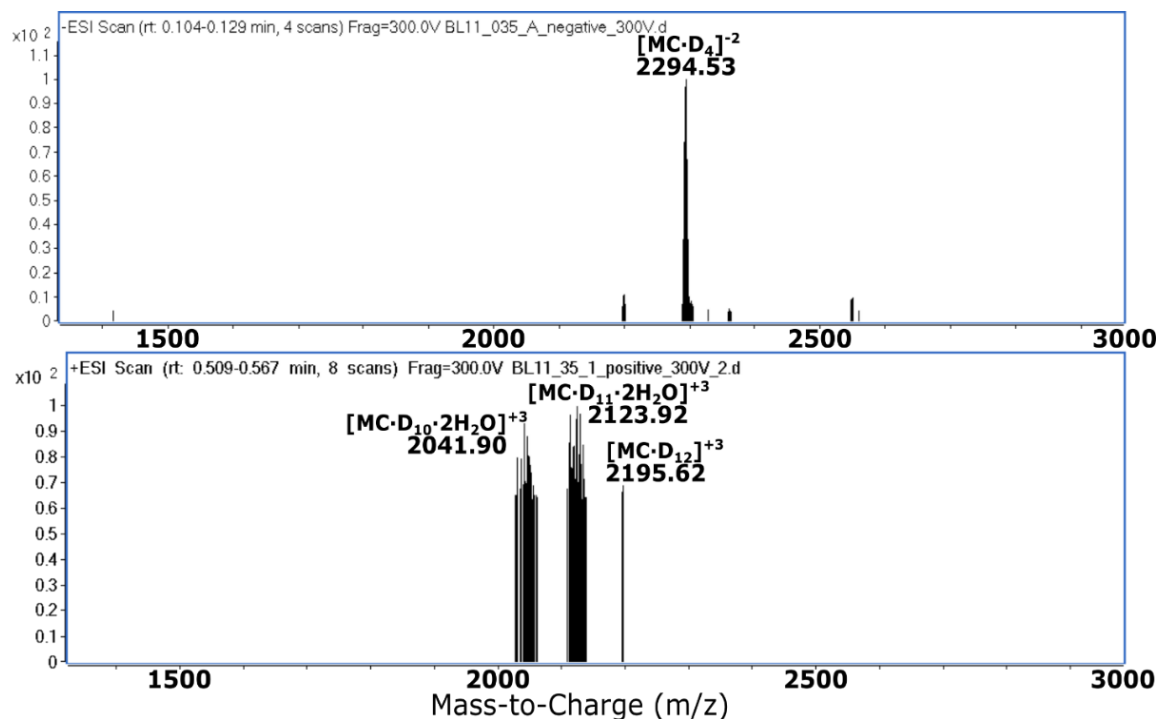


Figure 4.9 (Top) ESI-MS of $\text{Yb}_2\text{Ga}_8\text{pAlShi}_8\text{Mip}_4 (\text{G}0.5)_4$ DMC in negative ion mode. Dendrons (D_x) are only coupled to the four maleimide appendages of the metallacrown core. (Bottom) ESI-MS of $\text{Yb}_2\text{Ga}_8\text{pAlShi}_8\text{Mip}_4 (\text{G}0.5)_{12-10}$ in positive ion mode. This time, G0.5 dendrons are attached to both the maleimide appendages and the ring ligands of the MC core.

Synthesis of G0.5 Symmetric-DMCs with PAMAM dendrons. The reaction between $\text{Yb}_2\text{Ga}_8\text{pAlShi}_8\text{Mip}_4$, excess of thiol-focal point G0.5 (HS-G0.5) PAMAM dendron, and one equivalent of DMPA in degassed DMF led to the formation of a G0.5 PAMAM toroidal dendrimeric metallacrown (T-DMC). As seen in Figure 4.9 (top), the ESI-MS shows the coupling of four G0.5 dendrons to the MC core, which, under the employed reaction conditions, are expected to be only coupled to the maleimide bridging ligands. After purification, the bright yellow product was re-dissolved in DMF and reacted with more HS-G0.5 in the presence of DMPA and UV light. This led to the formation of new S-DMCs with up to twelve dendron couplings. As shown in Figure 4.9 (bottom), the photocatalytic reaction of the G0.5 T-DMC added six to eight more G0.5 dendrons to the ring ligands of the MC core. Both the bridge and ring ligands of the $\text{Yb}_2\text{Ga}_8\text{pAlShi}_8\text{Mip}_4$ MC core demonstrated similar reactivity towards thiol coupling as in its parent materials ($\text{Yb}_2\text{Ga}_8\text{Shi}_8\text{Mip}_4$ and $\text{Yb}_2\text{Ga}_8\text{pAlShi}_8\text{Ip}_4$), with complete coupling of four dendrons to the bridging ligands, and 75-100% coupling success to the ring ligands.

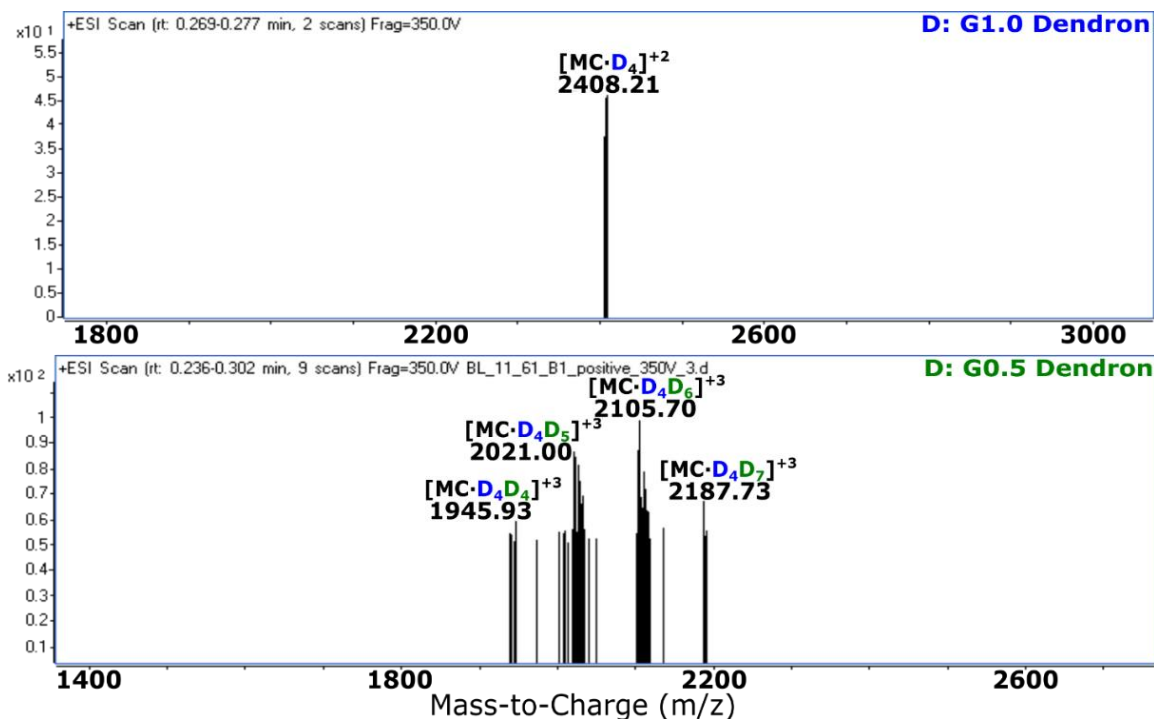


Figure 4.10 (Top) ESI-MS of $\text{Yb}_2\text{Ga}_8\text{pAlShi}_8\text{Mip}_4$ (**G1.0**)₄ DMC, and (Bottom) $\text{Yb}_2\text{Ga}_8\text{pAlShi}_8\text{Mip}_4$ (**G1.0**)₄ (**G0.5**)₇₋₄ in positive ion mode. **G1.0** dendrons are only coupled to the four maleimide appendages, while the **G0.5** dendrons are coupled only to the ring ligands of the MC core.

Synthesis of G1.0/G0.5 Janus-DMC with PAMAM dendrons. Asymmetric functionalization was achieved by exploiting the differential reactivity of the bridging and ring ligands. First, a G1.0 T-DCM was prepared by reacting $\text{Yb}_2\text{Ga}_8\text{pAlShi}_8\text{Mip}_4$ with HS-G1.0 PAMAM dendrons and DMPA in DMF. As corroborated by ESI-MS shown in Figure 4.10 (top), only four G1.0 dendrons are attached to the MC core, and due to the high reactivity of the maleimide appendages, it is reasonable to expect that the dendrons only coupled to the bridging ligands. Next, photocatalytic addition of HS-G0.5 dendrons to the G1.0 $\text{Yb}_2\text{Ga}_8\text{pAlShi}_8\text{Mip}_4$ DMC was done in the presence of DMPA and UV-light. This led to the formation of a new Janus-DMC with up to eleven dendrons coupled to the MC core. As shown in Figure 4.10 (bottom), the photocatalytic step added four to seven G0.5 dendrons to the ring ligands of the MC core. Just as with the symmetric G0.5 DMC described above, the bridge ligand of the bifunctionalized MC core seems to be similar to that of the parent MC. However, the ring ligands seem to be slightly less reactive – with a 50-88% coupling success.

The UV-Vis absorbance of the G1.0/G0.5 Janus-DMC with a $\text{Yb}_2\text{Ga}_8\text{pAlShi}_8\text{Mip}_4$ core is shown in Figure 4.11. The spectrum exhibits a broad absorption band at 250-340 nm due to the

$\pi \rightarrow \pi^*$ transition of the MC core. The spectrum also shows a low energy maximum at ~ 310 nm and a S^* is located at ~ 340 nm (29412 cm^{-1}), just as with the unfunctionalized $\text{Yb}_2\text{Ga}_8\text{pAlShi}_8\text{Mip}_4$ core. The similar absorbance profiles and intensities of the unfunctionalized MC and the Janus-DMC confirm that the absorbance behavior is not affected by the addition of dendrons to the MC core.

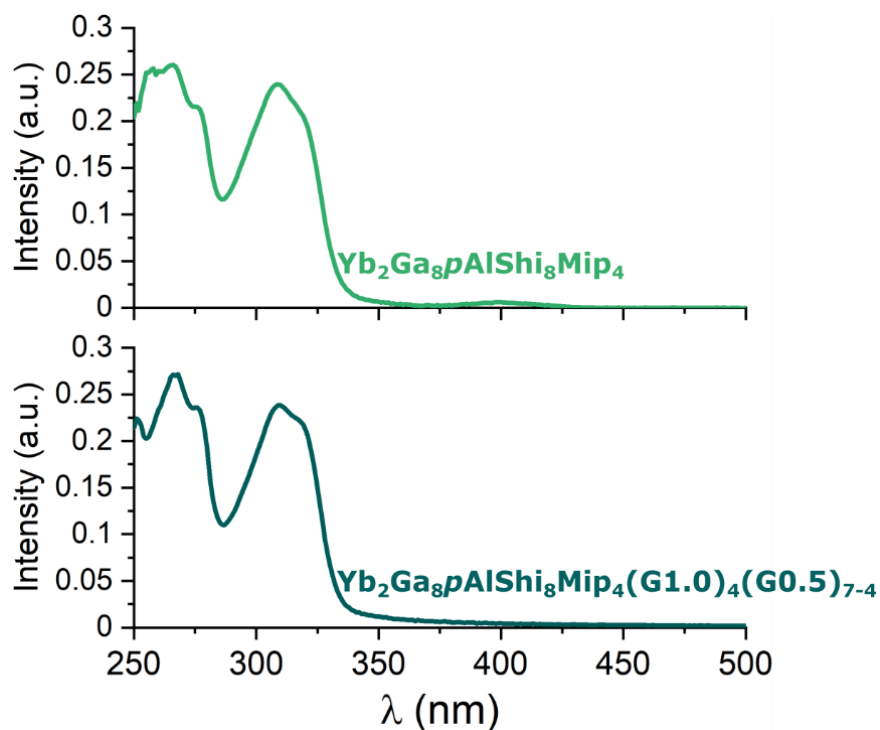


Figure 4.11 UV-Vis absorption spectra of $2.60 \mu\text{M}$ $\text{Yb}_2\text{Ga}_8\text{pAlShi}_8\text{Mip}_4$ MC (top) and $2.75 \mu\text{M}$ $\text{Yb}_2\text{Ga}_8\text{pAlShi}_8\text{Mip}_4(\text{G}1.0)_4(\text{G}0.5)_{7-4}$ Janus-DMC (bottom) dissolved in DMSO and at room temperature. Absorbance maxima for both compounds is at 310 nm with an extinction coefficient of $8.67 \times 10^4 \text{ M}^{-1}\text{cm}^{-1}$. The slight decrease in absorbance intensity of the Janus-DMC is due to the small difference in solution concentration between the two samples.

Synthesis and characterization of biotinylated Janus-DMC with G1.0 PAMAM dendrons.

Once again, asymmetric functionalization was implemented in a $\text{Yb}_2\text{Ga}_8\text{pAlShi}_8\text{Mip}_4$ MC where biotin (Bt) groups were first coupled to the maleimide bridging ligands of a $\text{Yb}_2\text{Ga}_8\text{pAlShi}_8\text{Mip}_4$. The reaction of the MCs with biotin in the presence of DMAP, led to the formation of $\text{Yb}_2\text{Ga}_8\text{pAlShi}_8\text{Mip}_4(\text{Bt})_4$, as seen on Figure 4.12 (top). Complete coupling of four equivalents of biotin to the MC core was observed by ESI-MS. After purification, the light purple product was re-dissolved in DMF, and reacted with HS-G1.0 PAMAM dendrons under UV-light. The photocatalytic addition of the thiol-focal point dendrons to the pre-biotinylated MC core resulted

in the coupling of five to eight dendrons to MC, as seen at the bottom of Figure 4.12 (bottom). Compared to the G0.5 S-DMC, this new complex, $\text{Yb}_2\text{Ga}_8\text{pAlShi}_8\text{Mip}_4(\text{Bt})_4(\text{G1.0})_{8-5}$, seems to have slightly lower reactivity towards thiol-ene coupling at the ring positions. Thus, a broader distribution of ring couplings (five to eight, vs. six to eight) is observed with this Janus-DMC. The UV-Vis absorbance spectrum show similar profiles to those of the unfunctionalized MC cores, as seen in Figure 4.13, with $\pi \rightarrow \pi^*$ transitions located between 250-340 nm, with a low-energy maximum located at ~310 nm and S^* located at ~340 nm (29412 cm^{-1}).

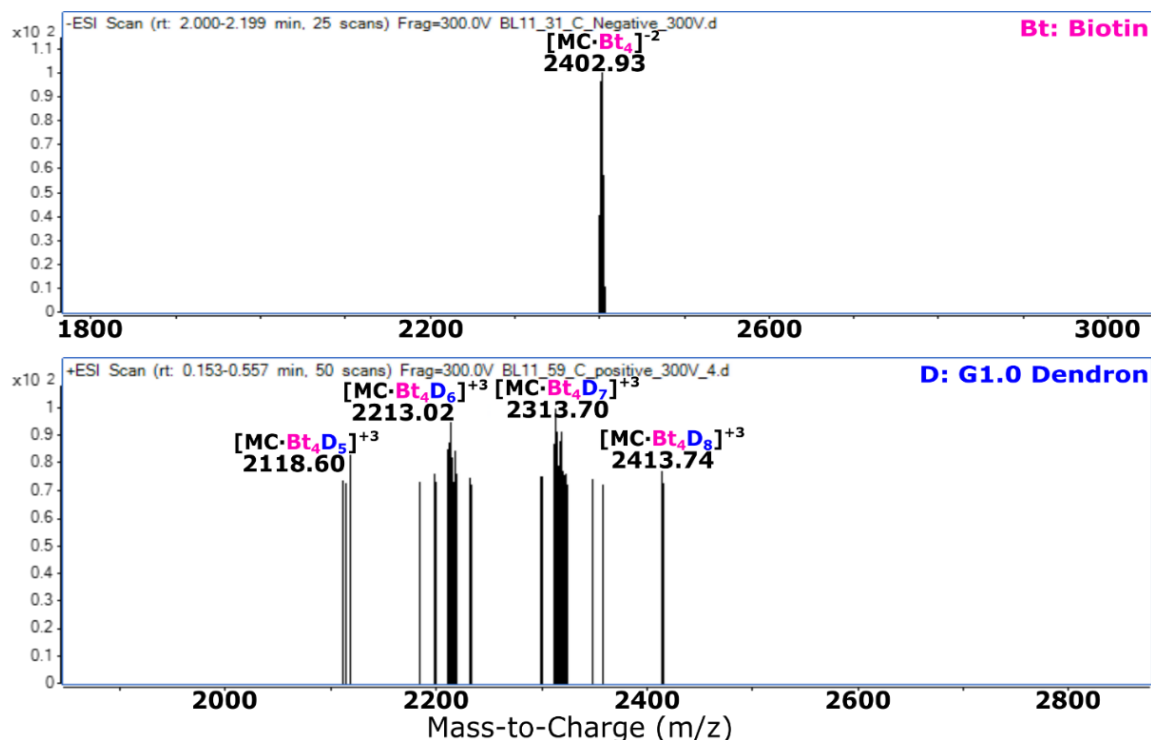


Figure 4.12 ESI-MS of $\text{Yb}_2\text{Ga}_8\text{pAlShi}_8\text{Mip}_4(\text{Bt})_4$ DMC in negative ion mode, and (Bottom) $\text{Yb}_2\text{Ga}_8\text{pAlShi}_8\text{Mip}_4(\text{Bt})_4(\text{G1.0})_{8-5}$ in positive ion mode. Biotin groups are only coupled to the four maleimide appendages, while the G1.0 dendrons are coupled only to the ring ligands of the MC core.

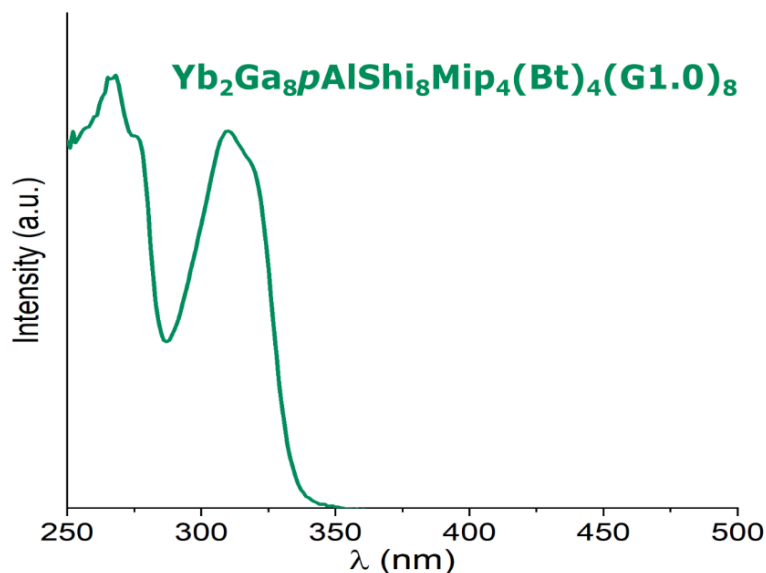


Figure 4.13 Absorption spectra of 2.64 μM $\text{Yb}_2\text{Ga}_8\text{pAlShi}_8\text{Mip}_4(\text{G1.0})_4(\text{Bt})_{8.5}$ Janus-DMC dissolved in DMSO and at room temperature. Absorbance maximum located at 310 nm with an extinction coefficient of $8.67 \times 10^4 \text{ M}^{-1}\text{cm}^{-1}$.

A different configuration of biotinylated Janus-DMC was also investigated, by first preparing a T-DMC with G1.0 PAMAM dendrons in the presence of DMAP in DMF. Once complete coupling of four dendrons to the MC core was achieved and corroborated by ESI-MS, the next step was the addition of biotin to the ring ligands. This was done by photocatalytic reaction of the G1.0 T-DMC with thiol-Biotin (HS-Bt), in the presence of DMPA and UV-light (365 nm). This led to the formation of a Janus-DMC with four G1.0 dendrons coupled to the bridging ligands, and up to eight biotins groups coupled to the ring ligands of the MC core – $\text{Yb}_2\text{Ga}_8\text{pAlShi}_8\text{Mip}_4(\text{G1.0})_4(\text{Bt})_{8.6}$, as seen in Figure 4.14. Both the ring and the bridging ligands of the bifunctionalized core exhibited similar reactivity as the parent materials ($\text{Yb}_2\text{Ga}_8\text{Shi}_8\text{Mip}_4$ and $\text{Yb}_2\text{Ga}_8\text{pAlShi}_8\text{Ip}_4$) toward thiol-coupling. By ESI-MS, it can be seen that the Janus-DMC is better characterized in positive ion more, with isotopic distributions corresponding to +3 and +4 charged species. The numerous internal amine and surface amine of the dendrons allow for multiple protonation states of the complex.

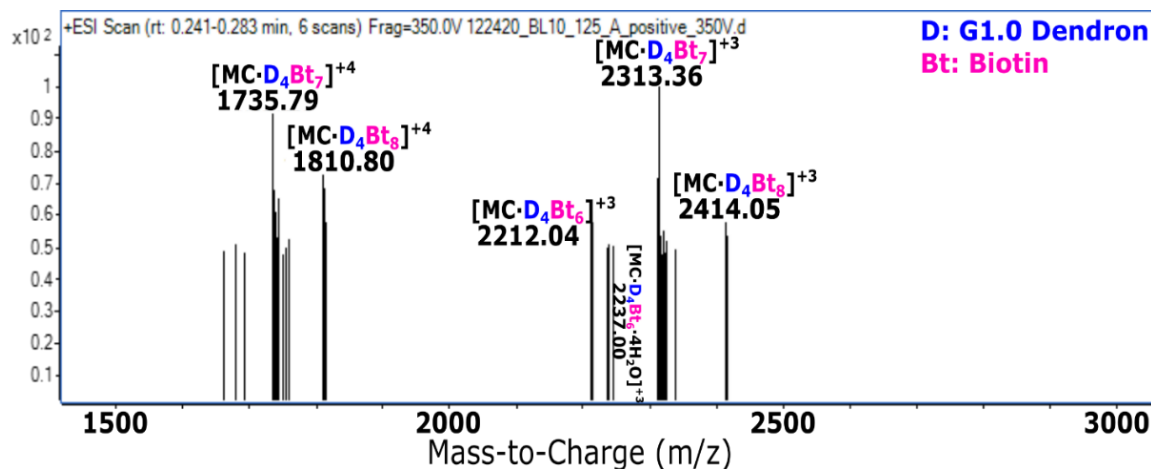


Figure 4.14 ESI-MS of $\text{Yb}_2\text{Ga}_8\text{pAlShi}_8\text{Mip}_4(\text{G1.0})_4(\text{Bt})_{8-6}$ DMC in positive ion mode. G1.0 dendrons are only coupled to the four maleimide appendages, while the Biotin groups are coupled only to the ring ligands of the MC core.

Size distribution analysis of the $\text{Yb}_2\text{Ga}_8\text{pAlShi}_8\text{Mip}_4(\text{G1.0})_4(\text{Bt})_8$ Janus-DMC in DMSO using DLS is shown in Figure 4.15. The average hydrodynamic diameters (D_{av}), polydispersity indexes (PDI), and diffusion coefficients (D_c) of the Janus-DMC are the following: D_{av} : 3.69 nm, PDI: 0.19, and D_c : $5.93 \times 10^{-7} \text{ cm}^2\text{s}^{-1}$. The complex shows moderate polydispersity, but with no observable aggregates in DMSO solutions. This is a change from G1.0 H-DMC and G1.0 T-DMC, where low intensity aggregates were observed (D_c : ~100 nm and 40 nm, respectively). In order to investigate the solution behavior in more aqueous environment, the Janus-DMC was dissolved with 99:1 H_2O :DMSO v/v% (4.6 μM final concentration). The DLS plot shown in Figure 4.16, displays two peaks. The smaller signal has a D_{av} value of 4.0 nm which matches closely the one in DMSO solutions signifying the presence of a single Janus-DMC unit. This first peak also has a narrower PDI: 0.04, which matches closely the PDI value of standard PAMAM dendrimers (PDI: 0-0.1) by DLS. A peak of larger diameter (D_{av} : 60.0 nm), smaller diffusion coefficient (D_c : $6.99 \times 10^{-8} \text{ cm}^2\text{s}^{-1}$), and a narrower polydispersity (PDI: 0.07) is also observed, which indicates the presence of bigger and heavier particles due to sample aggregation in more aqueous environments.

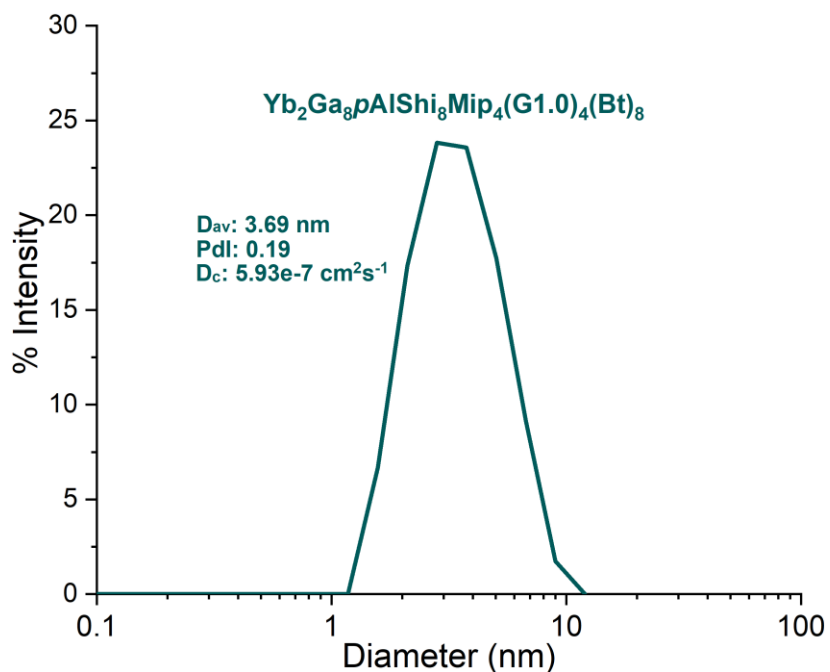


Figure 4.15 DLS size distribution of Yb₂Ga₈pAlShi₈Mip₄(G1.0)₄(Bt)₈ Janus-DMC at 1.5 μM solution in DMSO at room temperature.

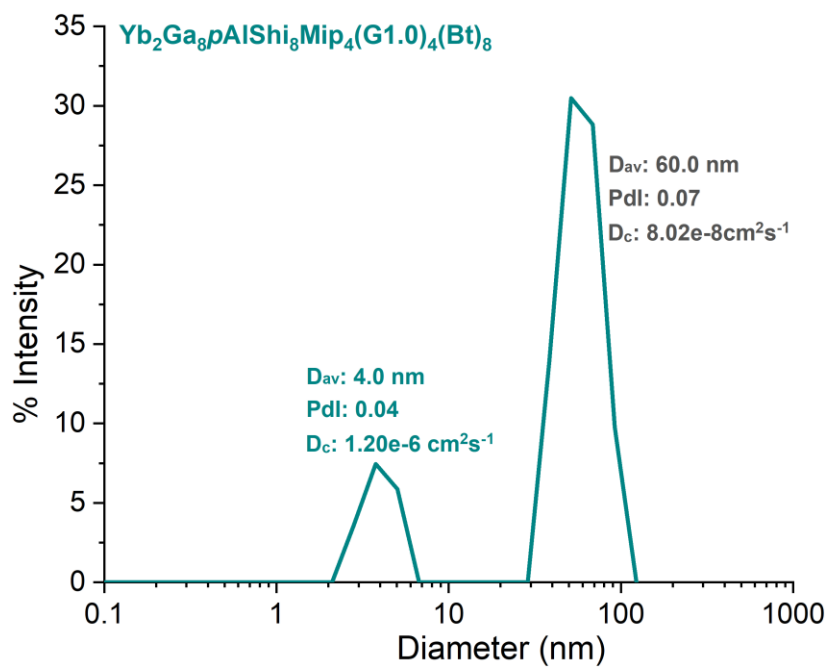


Figure 4.16 DLS size distribution of Yb₂Ga₈pAlShi₈Mip₄(G1.0)₄(Bt)₈ Janus-DMC at 4.6 μM solution in 99:1 H₂O:DMSO at room temperature and at pH: 7.5.

The UV-Vis absorbance spectrum of Yb₂Ga₈pAlShi₈Mip₄(G1.0)₄(Bt)₈₋₆ Janus-DMC

shown in Figure 4.17, exhibit a similar profile to that of the unfunctionalized metallacrown core and the G1.0/G0.5 Janus-DMC described above, with a $\pi \rightarrow \pi^*$ bands between 250-340 nm; λ_{max} at 310 with an ϵ : $8.67 \times 10^4 \text{ M}^{-1} \text{ cm}^{-1}$; and the S^* located at $\sim 340 \text{ nm}$ (29412 cm^{-1}). Shown in Figure 4.18 is the solution state excitation and emission spectra of this DMC dissolved in DMSO. Emission characterization upon excitation in the ligand-centered region at 320 nm exhibited characteristic Yb^{III} luminescent at 900-1100 nm arising from the $^2F_{5/2} \rightarrow ^2F_{7/2}$ transition, and with a maximum at 980 nm. Excitation spectra was collected upon monitoring the Yb^{III} emission at 980 nm, and showed broad ligand-centered bands up to 350 nm. Luminescent lifetimes (τ_{obs}) and ligand-centered quantum yields ($\phi_{\text{Yb}}^{\text{L}}$) in DMSO were also acquired and are summarized in Table 4.2. For the sake of comparison, the values for the unreacted MC core ($\text{Yb}_2\text{Ga}_8\text{pAlShi}_8\text{Mip}_4$), and the equivalent toroidal-DMC ($\text{Yb}_2\text{Ga}_8\text{Shi}_8\text{Mip}_4$ G1.0) and hyperboloidal-DMC ($\text{Yb}_2\text{Ga}_8\text{pAlShi}_8\text{Ip}_4$ G1.0) are also listed. Compared to the MC core, the Janus-DMC has a monoexponential decay with a τ_{obs} that is ~ 1.15 times higher. Additionally, a significant improvement in the $\phi_{\text{Yb}}^{\text{L}}$ of the DMC is observed with a ~ 1.5 times increase compared to the MC core. When compared to the G1.0 T-DMC and the H-DMC, the new Janus-DMC has a τ_{obs} values that is similar to that of the T-DMC and slightly shorter than of the H-DMC. As for the $\phi_{\text{Yb}}^{\text{L}}$, this Janus-DMC has the lowest quantum yield, followed by the H-DMC, and with the T-DMC having the highest value of all dendrimeric metallacrowns. Yet, the quantum yield of the Janus-DMC is still among the highest compared to other Yb^{III} -based MCs.

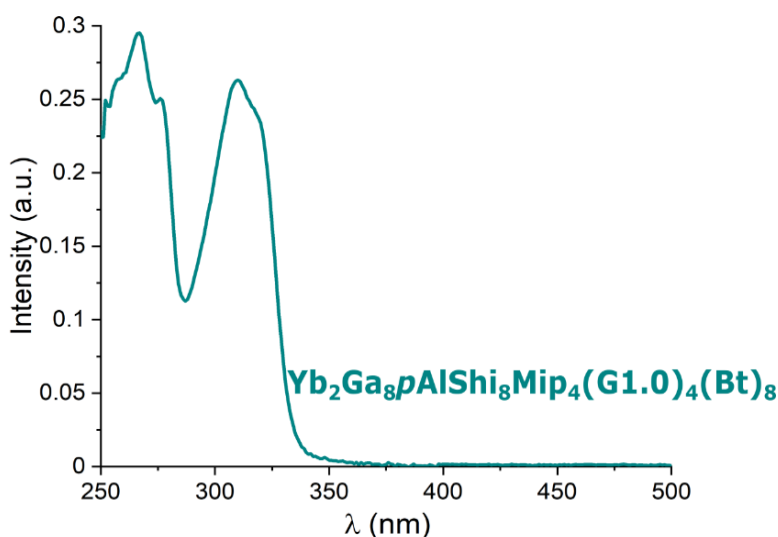


Figure 4.17 UV-Vis absorption spectrum of $3.4 \mu\text{M}$ $\text{Yb}_2\text{Ga}_8\text{pAlShi}_8\text{Mip}_4(\text{G1.0})_4(\text{Bt})_{8-6}$ Janus-DMC dissolved in DMSO and at room temperature. Absorbance maximum at 310 nm with an extinction coefficient of $8.67 \times 10^4 \text{ M}^{-1} \text{ cm}^{-1}$.

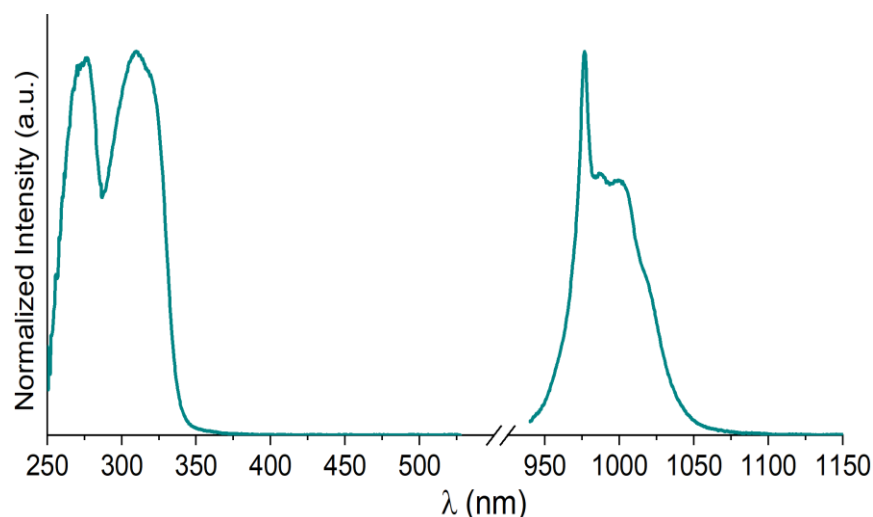


Figure 4.18 Corrected and normalized excitation (left, $\lambda_{em} = 980$ nm), and emission ($\lambda_{ex} = 320$ nm) spectra of 50 μ M DMSO solution of $\text{Yb}_2\text{Ga}_8\text{pAlShi}_8\text{Mip}_4(\text{G1.0})_4(\text{Bt})_8$ Janus-DMC at room temperature.

Table 4.2 DMSO solution luminescence lifetimes (τ_{obs}) and Yb^{III} -centered quantum yields collected under ligand excitation (ϕ_{Yb}^L)^a

Compound	τ_{obs} [μ s] ^b	τ_{av} [μ s]	ϕ_{Yb}^L [%] ^c
$\text{Yb}_2\text{Ga}_8\text{pAlShi}_8\text{Mip}_4(\text{G1.0})_4(\text{Bt})_8$	61.5(2) : 100%	--	7.41(5)
$\text{Yb}_2\text{Ga}_8\text{pAlShi}_8\text{Mip}_4$	43.4(7) : 92(1)% 13(1) : 8(1)%	53.5(9)	4.96(6)
$\text{Yb}_2\text{Ga}_8\text{Shi}_8\text{Mip}_4(\text{G1.0})_4$	63.8(8) : 100%	--	9.38(2)
$\text{Yb}_2\text{Ga}_8\text{pAlShi}_8\text{Ip}_4(\text{G1.0})_8$	69.2(3) : 100%	--	8.7(2)

^a For samples 50 μ M solutions in DMSO at room temperature, and with 2σ values between parentheses. Estimated experimental errors: τ_{obs} , $\pm 2\%$; Q_{Yb}^L , $\pm 10\%$. ^b Under excitation at 355 nm. ^c Under excitation at 320 nm.

4.3.4 Redshifted Toroidal Dendrimeric Metallacrowns

Synthesis and characterization of redshifted-DMCs with PAMAM dendrons. The reaction between $\text{Yb}_2\text{Ga}_8m\text{YneShi}_8\text{Mip}_4$, excess thiol-focal point PAMAM dendrons, and DMPA in degassed DMF led to the formation of toroidal dendrimeric metallacrowns of three different generations (G:1.0, 1.0 -OH, and 1.5) and with redshifted absorbance maxima, from here on referred to as redshifted-DMCs. The products were purified by dialysis and characterized by ESI-MS to corroborate complete coupling of only four dendrons to the maleimide appendages of the MC core, as shown in Figure 4.19. Structural imperfection arising from synthetic protocols or ESI-MS characterization can be seen as peaks with smaller m/z values. The lack of more dendron couplings to the MC core, and the proven low reactivity towards thiol-yne coupling of the $m\text{YneShi}$

ring ligands helps corroborate that dendrons are exclusively coupled to the maleimide appendages.

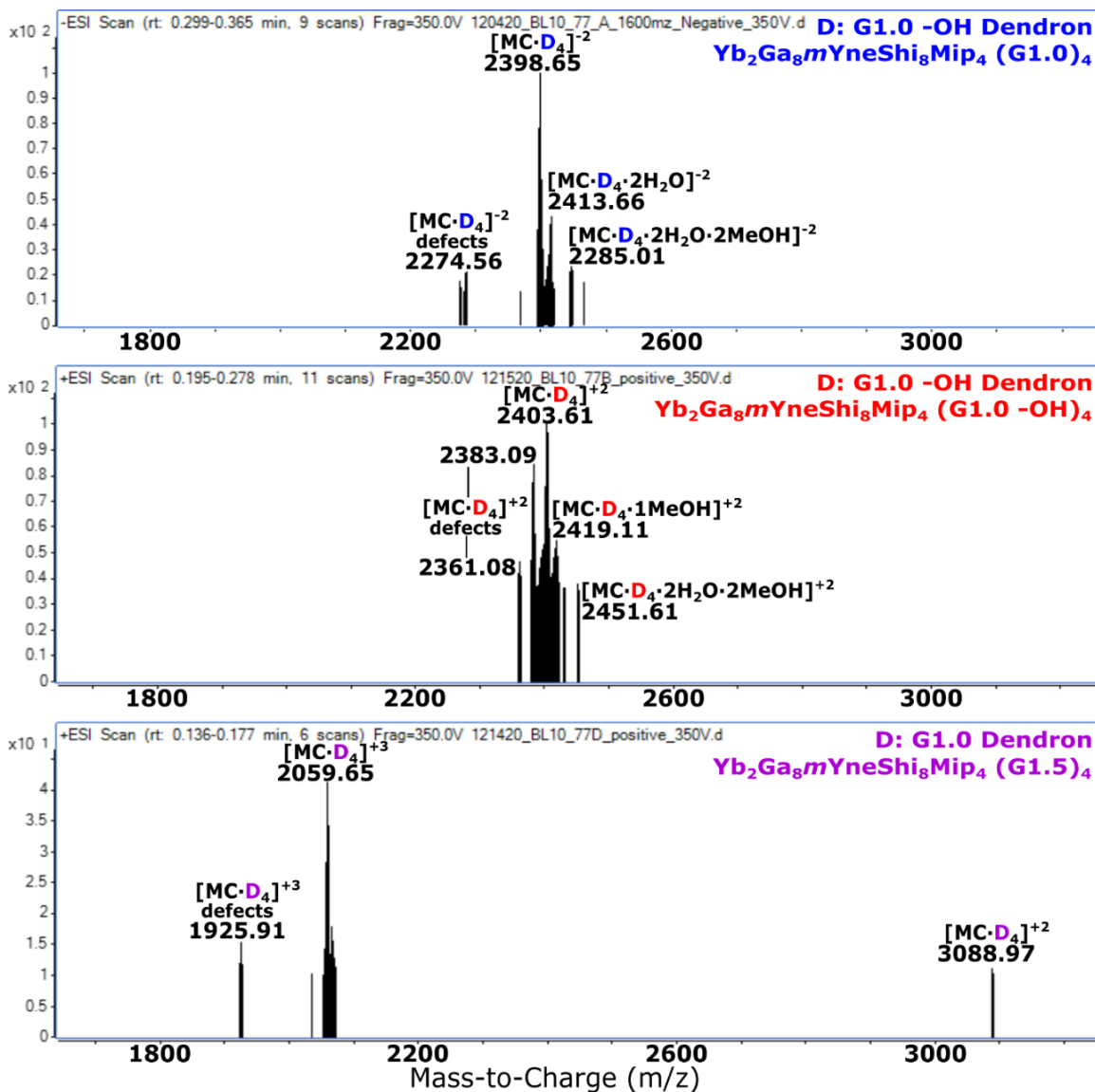


Figure 4.19 Normalized ESI-MS spectra of DMCs with $\text{Yb}_2\text{Ga}_8\text{mYneShi}_8\text{Mip}_4$ cores and G: 1.0, 1.0 -OH, and 1.5 in methanol solutions. Dendrons are only coupled to the maleimide appendages of the MC core.

Shown in Figure 4.20 is the size distribution analysis of the three redshifted T-DMCs in DMSO using DLS. The average measured hydrodynamic diameters (D_{av}), polydispersity indices (PdI), and diffusion coefficients (D_c) of each redshifted T-DMC are the following: D_{av} : 3.4 nm, PdI: 0.48, D_c : $6.43\text{e-}7 \text{ cm}^2\text{s}^{-1}$ for $\text{Yb}_2\text{Ga}_8\text{mYneShi}_8\text{Mip}_4$ G1.0; D_{av} : 3.46 nm, PdI: 0.22, D_c : $6.32\text{e-}7 \text{ cm}^2\text{s}^{-1}$ for $\text{Yb}_2\text{Ga}_8\text{mYneShi}_8\text{Mip}_4$ G1.0 -OH; and D_{av} : 3.76 nm, PdI: 0.08, D_c : $5.82\text{e-}7 \text{ cm}^2\text{s}^{-1}$ for $\text{Yb}_2\text{Ga}_8\text{mYneShi}_8\text{Mip}_4$ G1.5. The increasing diameters and decreasing D_c values confirm the

increase in size, volume, and weight of each complex. The G1.0 redshifted-DMC shows moderate polydispersity that is comparable to that of the original T-DMC in Chapter 2. But with the added difference that the aggregate signal at higher diameter is of significant intensity. As for the G1.0 -OH and G1.5 redshifted-DMCs, they have narrower polydispersities which seems to highlight the difference in surface interaction with the surrounding solvent (i.e., -NH₂, -OH, and -OMe).

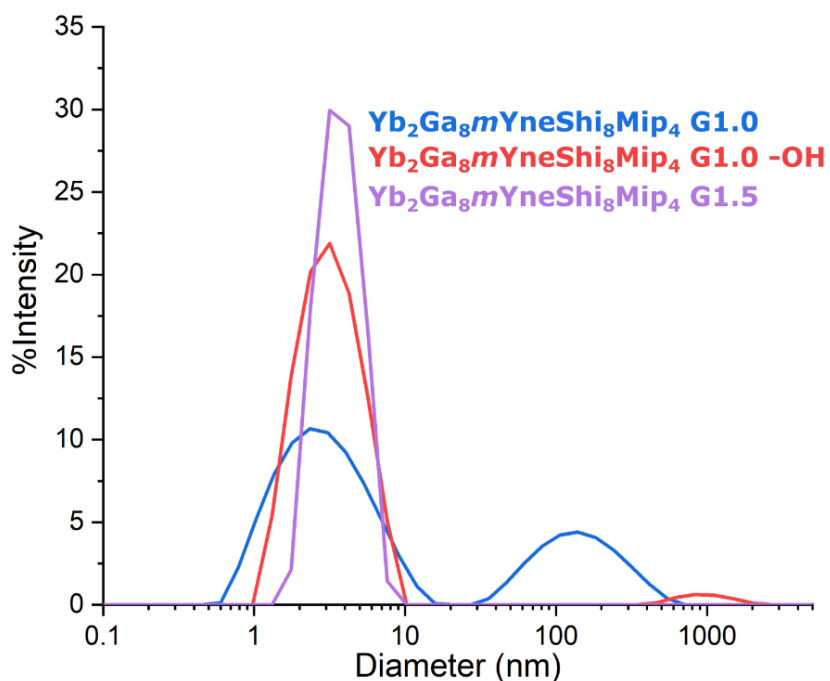


Figure 4.20 DLS size distribution of Yb₂Ga₈mYneShi₈Mip₄ T-DMC with G1.0, 1.0 -OH, and 1.5 at 1.5 μM concentrations dissolved in DMSO at room temperature.

To investigate the solution behavior of each complex in more aqueous environments, each of the three new redshifted-DMCs were dissolved with 99:1 H₂O:DMSO v/v%, and characterized by DLS. Shown in Figure 4.21 are the DLS size distribution plots which demonstrates that G1.0 and G1.0 -OH DMCs form large aggregates in more aqueous solutions, while the G1.5 DMC behaves very differently. From the DLS results, the G1.0 -OH complex also evidently forms large and polydisperse aggregates more readily. The very different behavior between these complexes likely arises from the difference in surface interaction with the more aqueous environment (i.e., -NH₂ and -OH for G1.0, and -OMe for G1.5). The average measured hydrodynamic diameters, polydispersity indices (PdI), and diffusion coefficients (D_c) of each redshifted T-DMC are the following: D_{av}: 107 and 385 nm, PdI: 0.15 and 0.17, D_c: 7.53e-8 and 1.25e-8 cm²s⁻¹ for

Yb₂Ga₈mYneShi₈Mip₄ G1.0; D_{av}: 64 and 96 μm, PdI: 1.4 and 14, D_c: 4.5 and 5043 e-8 cm²s⁻¹ for Yb₂Ga₈mYneShi₈Mip₄ G1.0 -OH; and D_{av}: 5.8 nm, PdI: 0.34, D_c: 8.3 e-7 cm²s⁻¹ for Yb₂Ga₈mYneShi₈Mip₄ G1.5.

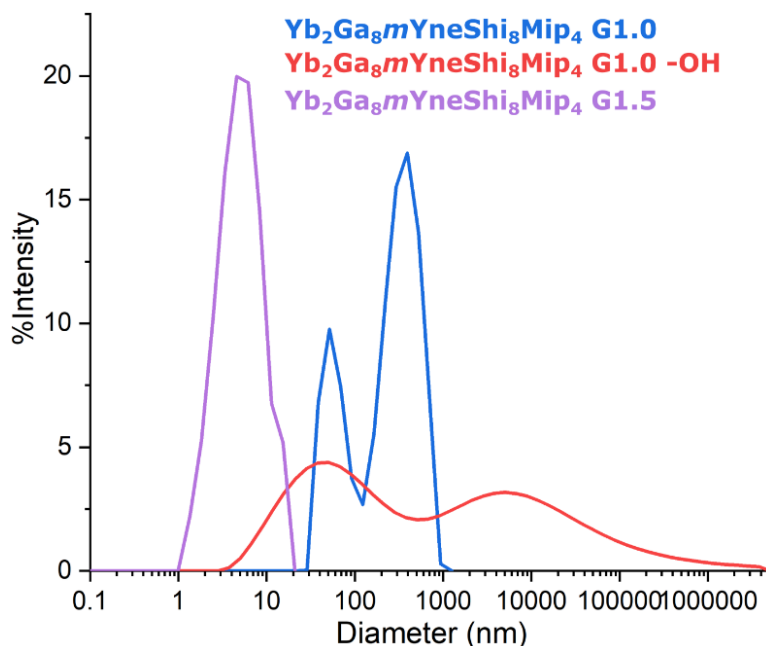


Figure 4.21 DLS size distribution of Yb₂Ga₈mYneShi₈Mip₄ T-DMC with G1.0 (50.4 μM) , 1.0 -OH (27.5 μM) , and 1.5 (15 μM) in 99:1 H₂O:DMSO at room temperature and at pH: 7.5.

The UV-Vis absorbance spectra of the three redshifted-DMCs in DMSO are shown in Figure 4.22. An expected shift to longer wavelengths is observed when compared to the *para*-substituted MC and DMCs. The absorbance spectra show $\pi \rightarrow \pi^*$ bands located between 250-360 nm, with a low energy maximum at ~340 nm, and with the S* energy located at ~380 nm (26667 cm⁻¹). As with the other DMCs, the absorbance profiles of these complexes and the unfunctionalized MC core are similar. Solution state excitation and emission spectra of each of these compounds in DMSO were also collected and are shown in Figure 4.23. Upon excitation at 340 nm, characteristic Yb^{III} luminescent signals arising from the ²F_{5/2} → ²F_{7/2} transition were observed between 900-1100 nm, and with a maximum at 980 nm. Excitation spectra was collected upon monitoring the Yb^{III} emission at 980 nm, and showed broad ligand-centered bands up to 375 nm that overlap well with the absorbance spectra.

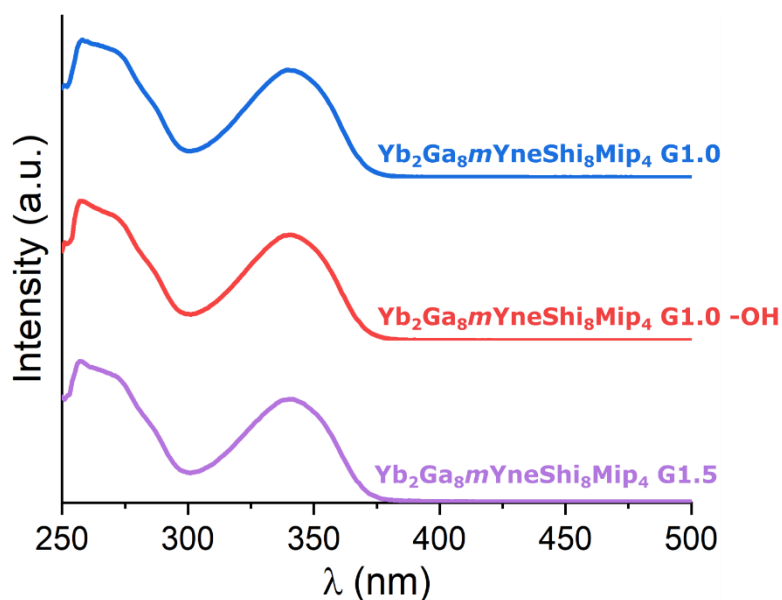


Figure 4.22 UV-Vis absorption spectra of redshifted T-DMCs $\text{Yb}_2\text{Ga}_8m\text{YneShi}_8\text{Mip}_4$ G1.0 (25.1 μM), 1.0 -OH (19.7 μM), and 1.5 (9.36 μM) dissolved in DMSO and at room temperature. Absorbance maxima at 340 nm and with an extinction coefficient of $4.36 \times 10^4 \text{ M}^{-1}\text{cm}^{-1}$.

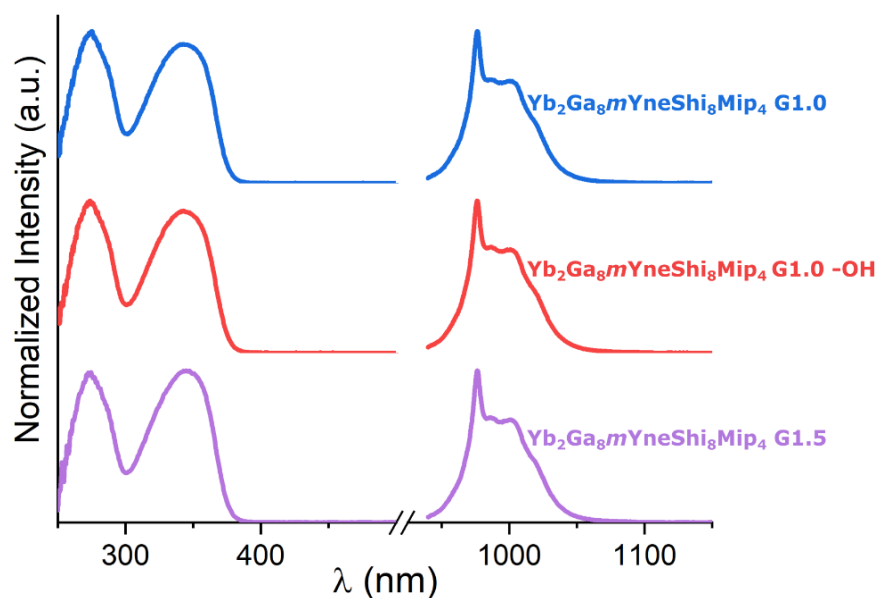


Figure 4.23 Corrected and normalized excitation (left, $\lambda_{\text{em}} = 980 \text{ nm}$), and emission ($\lambda_{\text{ex}} = 320 \text{ nm}$) spectra of 50 μM DMSO solution of redshifted T-DMC $\text{Yb}_2\text{Ga}_8m\text{YneShi}_8\text{Mip}_4$ G1.0, G1.0 -OH, and G1.5 at room temperature.

Luminescent lifetimes (τ_{obs}) and ligand-centered quantum yields (ϕ_{Yb}^L) in DMSO were also acquired and are summarized in Table 4.3. For comparison, the values of the MC core ($\text{Yb}_2\text{Ga}_8m\text{YneShi}_8\text{Mip}_4$) and the equivalent toroidal-DMCs ($\text{Yb}_2\text{Ga}_8\text{Shi}_8\text{Mip}_4$ G1.0 and G1.5) are also listed. The three redshifted-DMCs have monoexponential decays with relatively similar τ_{obs}

value. The ϕ_{Yb}^L are also very similar, with a $\sim 0.7\%$ decreased in value between the G1.0 -OH and G1.0 compounds, and a steeper decrease of $\sim 7\%$ with the G1.5 DMC. Yet, compared to the unfunctionalized MC core, the three new DMCs have between ~ 2.3 - 2.4 times higher ϕ_{Yb}^L values, once again demonstrating that the quenching effects of the maleimide appendages are eliminated upon thiol coupling. When comparing each of the three DMCs to the $Yb_2Ga_8mYneShi_8Ip_4$, a 10-17% increase in quantum yields and 8-12% elongation of the lifetimes is observed. Compared to the original T-DMCs with unfunctionalized ring ligands (Shi), the τ_{obs} of the redshifted-DMCs are slightly longer, while a $\sim 10\%$ reduction in ϕ_{Yb}^L is observed in all three cases.

Table 4.3 DMSO solution luminescence lifetimes (τ_{obs}) and Yb^{III} -centered quantum yields collected under ligand excitation (ϕ_{Yb}^L)^a

Compound	τ_{obs} [μs] ^b	ϕ_{Yb}^L [%] ^c
$Yb_2Ga_8mYneShi_8Ip_4$	58(4)	7.3(2)
$Yb_2Ga_8mYneShi_8Mip_4$	65.1(8)	3.63(5)
$Yb_2Ga_8mYneShi_8Mip_4$ G1.0	64(2)	8.77(7)
$Yb_2Ga_8mYneShi_8Mip_4$ G1.0 -OH	66(2)	8.83(8)
$Yb_2Ga_8mYneShi_8Mip_4$ G1.5	63(1)	8.18(4)
$Yb_2Ga_8Shi_8Mip_4$ G1.0	63.8(8)	9.38(2)
$Yb_2Ga_8Shi_8Mip_4$ G1.5	62.9(3)	9.02(8)

^a For samples 50 μM solutions in DMSO at room temperature, and with 2σ values between parentheses. Estimated experimental errors: τ_{obs} , $\pm 2\%$; ϕ_{Yb}^L , $\pm 10\%$. ^b Under excitation at 355 nm. ^c Under excitation at 340 nm.

The three redshifted-DCMs $Yb_2Ga_8mYneShi_8Mip_4$ G1.0, 1.0 -OH, and 1.5 were used to investigate their ability to label cells. To this end, HeLa cells were incubated for two hours with each of the compounds dissolved in cell culture media (99:1 OptiMEM:DMSO v/v%) to a final concentration of 50.4 μM , 27.5 μM , and 15 μM , respectively. Epifluorescence microscopy images of the cells exhibited Yb^{III} luminescent signals arising from the core of each DMC; however, as seen in Figure 4.24 the three DMCs show significant aggregation and localization at the surface of the cells. Substrate interaction can be seen with the G1.0 -OH DMC, which is seen as bright dots outside the cell area. Yet, strong luminescent signals in the NIR from each of the DMCs is observed resulting from non-specific interactions of the aggregates at the surface of living HeLa cells.

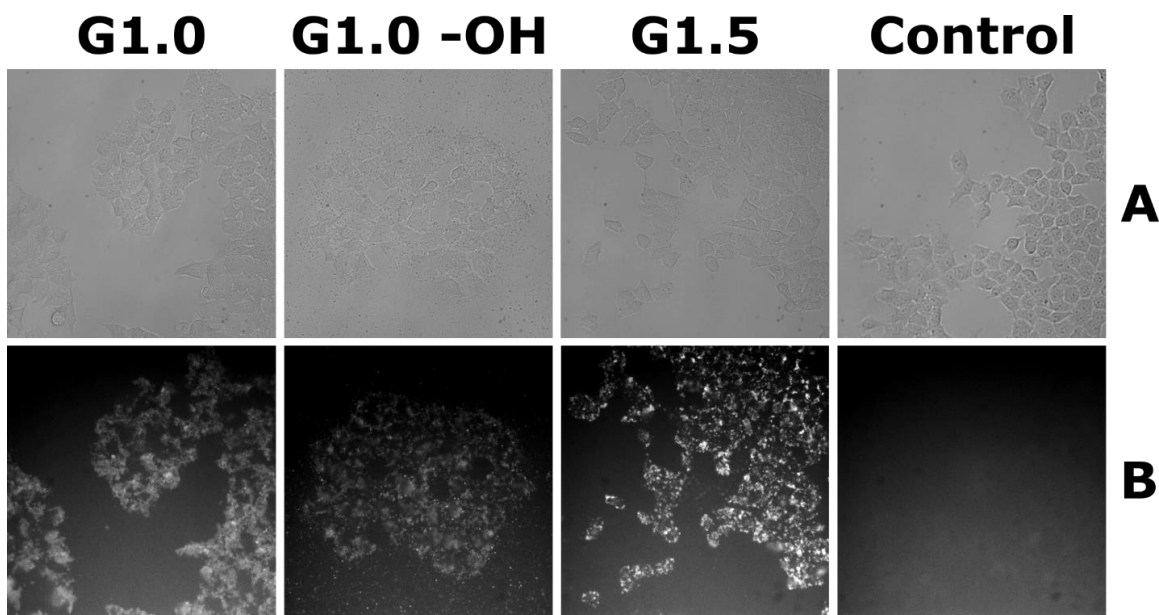


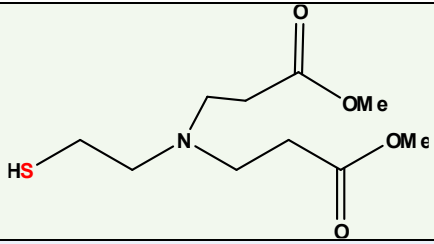
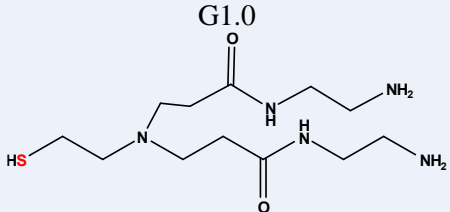
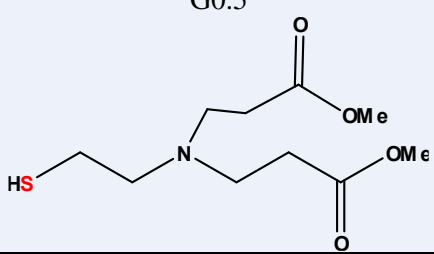
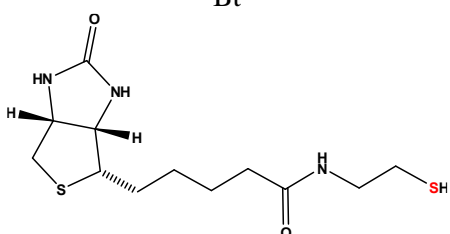
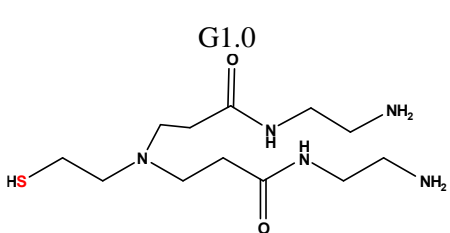
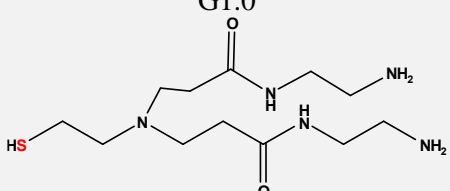
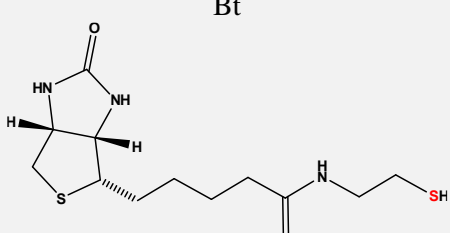
Figure 4.24 Microscopy images of HeLa cells incubated with $\text{Yb}_2\text{Ga}_8\text{mYneShi}_8\text{Mip}_4$ G1.0, 1.0 -OH, 1.5 T-DMC in cell culture media solution with 1% DMSO. A) Brightfield image, and B) NIR epifluorescence image ($\lambda_{\text{ex}} = 377\text{nm}$, band pass 50nm; $\lambda_{\text{em}} = 785\text{nm}$, long pass; 2s of exposure).

4.4 Discussion

To aid with the discussion of all the different molecules prepared for this chapter, Table 4.4 lists them all, with a visual description of the coupled thiol-groups and a brief description on the coupling configuration.

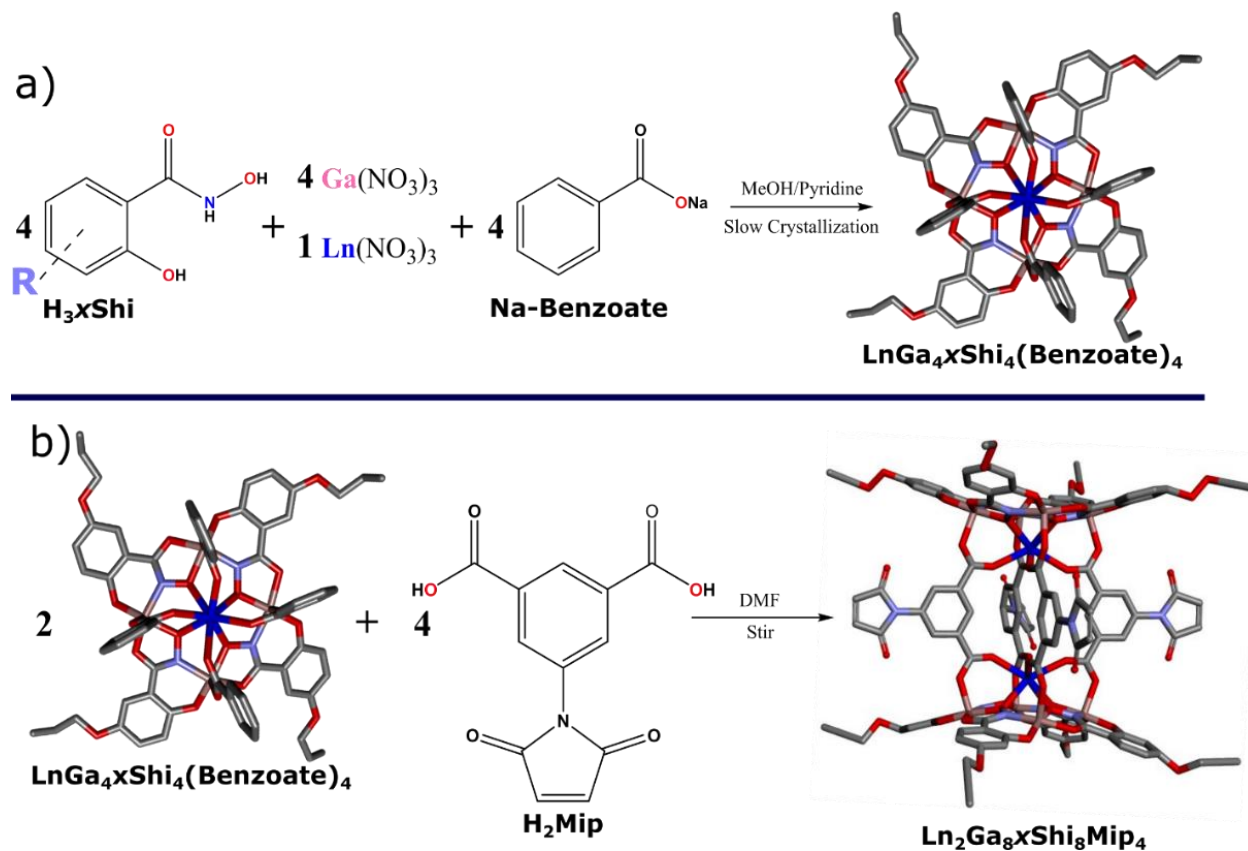
Table 4.4 List of MC and DMC prepared for this chapter. Each of the different classifications are highlighted with different color, with the small molecule coupling in yellow, S-DMC in green, Janus-DMC in blue, biotinylated Janus-DMCs in gray and white, and the redshifted-DMCs in orange.

Compound	Thiol group(s)	Comments
$\text{Yb}_2\text{Ga}_8\text{pYneShi}_8\text{Mip}_4$ (βME) ₁₂		Small molecule coupled to all of the twelve-ligand positions in the Yb_2Ga_8 MC.
$\text{Yb}_2\text{Ga}_8\text{pAlShi}_8\text{Mip}_4$ (βME) ₁₂		
$\text{Yb}_2\text{Ga}_8\text{mAlShi}_8\text{Mip}_4$ (βME) ₁₂		
$\text{Yb}_2\text{Ga}_8\text{pAlShi}_8\text{Mip}_4$ (G0.5) ₁₂	G0.5	G0.5 dendrons coupled to all of the twelve-ligand positions of the MC core, yielding a G0.5 S-DMC.

		
$\text{Yb}_2\text{Ga}_8\text{pAlShi}_8\text{Mip}_4$ $(\text{G1.0})_4(\text{G0.5})_8$	<p>G1.0</p> 	<p>G1.0 dendrons coupled to the bridging ligands, and G0.5 dendrons coupled to the ring ligands of the MC core. This yielded a G1.0/G0.5 Janus-DMC with PAMAM dendrons coupled to all of the twelve-ligand positions.</p>
	<p>G0.5</p> 	
$\text{Yb}_2\text{Ga}_8\text{pAlShi}_8\text{Mip}_4$ $(\text{Bt})_4(\text{G1.0})_8$ $\text{Yb}_2\text{Ga}_8\text{mAlShi}_8\text{Mip}_4$ $(\text{Bt})_4(\text{G1.0})_8$	<p>Bt</p> 	<p>Biotin (Bt) groups coupled to the bridging ligands, and G1.0 dendrons coupled to the ring ligands of the MC core. This yielded a biotinylated Janus-DMC.</p>
	<p>G1.0</p> 	
$\text{Yb}_2\text{Ga}_8\text{pAlShi}_8\text{Mip}_4$ $(\text{G1.0})_4(\text{Bt})_8$	<p>G1.0</p> 	<p>G1.0 dendrons coupled to the bridging ligands, and Biotin (Bt) groups coupled to the ring ligands of the MC core. This yielded a biotinylated Janus-DMC.</p>
	<p>Bt</p> 	

$\text{Yb}_2\text{Ga}_8m\text{YneShi}_8\text{Mip}_4$ (G1.0) ₄		Dendrons were coupled only at the bridging ligands of MC cores, yielding redshifted-DMCs.
$\text{Yb}_2\text{Ga}_8m\text{YneShi}_8\text{Mip}_4$ (G1.0-OH) ₄		
$\text{Yb}_2\text{Ga}_8m\text{YneShi}_8\text{Mip}_4$ (G1.5) ₄		

4.4.1 Synthesis, Characterization, and Small Molecule Functionalization of $\text{Ln}_2\text{Ga}_8x\text{Shi}_8\text{Mip}_4$ (Ln: Yb^{III} ; x : $p\text{Yne}$, $m\text{Yne}$, $p\text{Al}$, and $p\text{Al}$)



Scheme 4.1 a) Synthesis of $\text{LnGa}_4x\text{Shi}_4(\text{benzoate})_4$ from free ligands and metal salts via slow crystallization. b) Synthesis of $\text{Ln}_2\text{Ga}_8x\text{Shi}_8\text{Mip}_4$ by carboxylate substitution of benzoate with H_2Mip on the monomeric MC.

The $\text{Ln}_2\text{Ga}_{8x}\text{Shi}_8\text{Mip}_4$ scaffolds represents the first class of bifunctional metallacrowns capable of undergoing thiol coupling at the bridging ligands (via thiol-maleimide addition) and at the ring ligands (via thiol-ene/-yne photocatalytic addition). As shown in Scheme 4.1, the four set of dimeric MC scaffolds were prepared by carboxylate substitution on monomeric $\text{LnGa}_{4x}\text{Shi}_4(\text{benzoate})_4$ scaffolds with 5-maleimide isophthalic acid (H_2Mip). As described in Chapter 3, monomeric MCs were obtained as crystals through the reaction of H_3xShi , sodium benzoate, and $\text{Ga}^{\text{III}}/\text{Ln}^{\text{III}}$ nitrate salts in solutions of methanol and pyridine. Substitution of the benzoate bridging ligands by 5-maleimide isophthalic acid yielded the dimeric metallacrowns that were characterized by ESI-MS and elemental analysis. Crystallographic data of the dimeric $\text{Ln}_2\text{Ga}_{8x}\text{Shi}_8\text{Mip}_4$ MCs was not collected since the product was isolated as a powder and not as single crystals. However, the structures are expected to be analogues to the unsubstituted parent material $\text{Ln}_2\text{Ga}_8\text{Shi}_8\text{Ip}_4$ previously reported by our group,^{106,124} and structurally similar to the monomeric $\text{LnGa}_{4x}\text{Shi}_4(\text{benzoate})_4$ described in Chapter 3. Thus, the MCs can be generally described as two $12\text{-MC}_{\text{Ga}(\text{III})\text{N}(x\text{shi})-4}$ bridged together by four Mip^{-2} bridging ligands, leading to the formation of MCs with twelve points of attachments (four at bridges and eight at the ring ligands). Just like with the other scaffold described in Chapter 2 and 3, these bifunctional MC can be prepared with other Ln^{III} ions, but emphasis was placed on Yb^{III} due to its interesting NIR emissions. Chemical compositions for all the dimeric derivatives were further corroborated by elemental analysis and ESI-MS, with the purity of the dimeric MCs confirmed by the lack of monomeric MC peaks in the mass spectra. Charge neutrality is likely achieved with two pyridinium counter ions, as it is in the case of the analogue $\text{Ln}_2\text{Ga}_{8x}\text{Shi}_8\text{Ip}_4$ MC described in Chapter 3.

The solution absorbance spectroscopy of each $\text{Ln}_2\text{Ga}_{8x}\text{Shi}_8\text{Mip}_4$ MC dissolved in DMSO corroborates that the *para*-substituted scaffolds ($\text{Ln}_2\text{Ga}_{8p}\text{AlShi}_8\text{Mip}_4$ and $\text{Ln}_2\text{Ga}_{8p}\text{YneShi}_8\text{Mip}_4$) have similar profiles with absorbance between 250-340 nm, while the *meta*-substituted have ($\text{Ln}_2\text{Ga}_{8m}\text{AlShi}_8\text{Mip}_4$ and $\text{Ln}_2\text{Ga}_{8m}\text{YneShi}_8\text{Mip}_4$) absorbances between 250-380nm. The absorbance profiles of the four bifunctionalized MC scaffolds are similar to those of $\text{Ln}_2\text{Ga}_{8x}\text{Shi}_8\text{Ip}_4$ where only the ring ligands are functionalized, corroborating that the added functional group at the bridge ligands does not change the absorbance profiles. Therefore, the singlet energy values of these new bifunctional MCs are the same as of the monosubstituted. Similarly, while the triplet state levels were not measured for these new MCs, their values are

expected to be close to those of the monofunctionalized $\text{Gd}_2\text{Ga}_8\text{xShi}_8\text{Ip}_4$ MCs (Table 3.14). Thus, the new bifunctional MC scaffolds are expected to have favorable energy gaps between their singlet and triplet states ($\sim 5000\text{ cm}^{-1}$) and the triplet and Ln^{III} ion emissive state to ensure good intersystem crossing ($\text{S}^* \rightarrow \text{T}^*$ and $\text{T}^* \rightarrow \text{Ln}^*$).

Photophysical characterization of bifunctional MCs. As seen in Figure 4.3 and Figure 4.4, the Ln^{III} -centered photophysical properties, combined with the good spectral overlap between the absorbance and excitation spectra of the each of the Yb^{III} -based MC scaffolds, illustrates the favorable antenna effect of the ring ligands to the Yb^{III} ions. As for the emissive properties, upon excitation into the ligand centered bands at 320-360 nm, characteristic Yb^{III} luminescence emission in the NIR was observed in both solution and solid state. Quantitative photophysical data listed in Table 4.1 show that the $\phi_{\text{Yb}}^{\text{L}}$ values of the bifunctionalized $\text{Yb}_2\text{Ga}_8\text{pAlShi}_8\text{Mip}_4$ and $\text{Yb}_2\text{Ga}_8\text{mYneShi}_8\text{Mip}_4$ MCs are significantly lower than those of the monofunctionalized $\text{Yb}_2\text{Ga}_8\text{pAlShi}_8\text{Ip}_4$ and $\text{Yb}_2\text{Ga}_8\text{mYneShi}_8\text{Ip}_4$ MC analogues. This behavior was also observed when comparing the $\text{Yb}_2\text{Ga}_8\text{Shi}_8\text{Ip}_4$ to $\text{Yb}_2\text{Ga}_8\text{Shi}_8\text{Mip}_4$ in Chapter 2 due to the well-known^{160,161} quenching effects of unsubstituted maleimide groups. Fortunately, such quenching effects are improved once the C=C bonds becomes saturated by thiol coupling. Something important to highlight is that while the decrease in quantum yield between $\text{Yb}_2\text{Ga}_8\text{Shi}_8\text{Ip}_4$ and the monofunctionalized $\text{Yb}_2\text{Ga}_8\text{Shi}_8\text{Mip}_4$ was $\sim 97\%$ in solid state and $\sim 63\%$ in DMSO solutions, a smaller difference is seen when comparing the unfunctionalized $\text{Yb}_2\text{Ga}_8\text{Shi}_8\text{Ip}_4$ and bifunctionalized MCs: for $\text{Yb}_2\text{Ga}_8\text{pAlShi}_8\text{Mip}_4$ there is a $\sim 60\%/\sim 36\%$ decrease in solid/solution state; and there is a $\sim 82\%/\sim 50\%$ decrease in solid/solution state for $\text{Yb}_2\text{Ga}_8\text{mYneShi}_8\text{Mip}_4$. Thus, emphasizing the importance and ability to improve the photophysical properties of MCs through synthetic modification.

Small molecule coupling to bifunctional MCs. The ability of $\text{Yb}_2\text{Ga}_8\text{pAlShi}_8\text{Mip}_4$, $\text{Yb}_2\text{Ga}_8\text{mAlShi}_8\text{Mip}_4$, and $\text{Yb}_2\text{Ga}_8\text{pYneShi}_8\text{Mip}_4$ to undergo thiol coupling was investigated by photocatalytic addition of β -mercaptoethanol (β ME). The $\text{Yb}_2\text{Ga}_8\text{mYneShi}_8\text{Mip}_4$ MC was not investigated since in Chapter 3 it was shown that scaffolds with *mYneShi* ring ligands were the least reactive towards thiol coupling.

Maleimide groups do not require the highly energetic photocatalytic approach to yield efficient thiol-couplings. This is because thiol-maleimide addition is driven by the withdrawing effects of the two carbonyl groups, along with the enhanced reactivity of the alkene site due to ring

strain, ultimately rendering maleimide appendages with very high thiol-coupling reactivities. On the other hand, thiol-ene/yne addition to propargyl and allyl ether does not require photocatalyzed radical addition due to their much lower reactivity for thiol-coupling. Therefore, given the significant difference in reactivity of both thiol-active groups in the bifunctional MC, the addition of thiols can be done in two steps: first to the maleimide bridging ligands, and then to the ring ligands via radical-addition.

In the case of the small molecule coupling to the three MC scaffolds, *in situ* addition of β ME under photocatalytic conditions (UV light and DMPA as the photoinitiator) yielded scaffolds with up to twelve β MEs coupled to $\text{Yb}_2\text{Ga}_8p\text{AlShi}_8\text{Mip}_4$ and $\text{Yb}_2\text{Ga}_8m\text{AlShi}_8\text{Mip}_4$, and up to twenty to $\text{Yb}_2\text{Ga}_8p\text{YneShi}_8\text{Mip}_4$. As seen in Figure 4.5-4.7, partial to mostly complete coupling was observed with the three MCs, with eleven to twelve couplings to both $\text{Yb}_2\text{Ga}_8p\text{AlShi}_8\text{Mip}_4$ and $\text{Yb}_2\text{Ga}_8m\text{AlShi}_8\text{Mip}_4$ (~92-100% coupling success), and eighteen to twenty β MEs coupled to $\text{Yb}_2\text{Ga}_8p\text{YneShi}_8\text{Mip}_4$ (90-100% coupling success). Similar reactivity behavior toward small molecule coupling was observed with these three bifunctional MCs as previously shown for the MC functionalized only at the bridge or ring positions. Thus, it is prudent to assume that the thiol-maleimide addition at the bridge ligand went to completion, while addition to the ring ligands via radical thiol-ene or -yne was slightly less reactive, but mostly effective.

As described in Chapter 2 with the analogous $\text{Yb}_2\text{Ga}_8\text{Shi}_8\text{Mip}_4$ MC, thiol addition to the bridging ligands of $\text{Yb}_2\text{Ga}_8x\text{Shi}_8\text{Mip}_4$ MCs can occur at either of two carbon positions in the maleimide's C=C bond. Thus, such thiol-coupling results in the formation of two different isomers per appendage, with each having 180° of rotational freedom. This means that each of the four maleimide appendages of a $\text{Yb}_2\text{Ga}_8x\text{Shi}_8\text{Mip}_4$ MC can each have four possible configurations once coupled to thiol-bearing groups. While each species could possess different physical and optical properties, at this point there is no method for separating each of these distinct complexes. Therefore, for the remainder of this work, coupling to the maleimide bridging ligands is treated as if it corresponds to a single isomer. As for the thiol-ene/yne coupling to the ring ligands, such additions have been shown to have high anti-Markovnikov regioselectivity.^{182,188}

The UV-Vis absorbance spectra profiles in DMSO solutions of the MCs pre- and post- β ME coupling are identical. Similar results were observed for the MC scaffolds with small molecules coupled exclusively at the ring ligands or at the bridge ligands. Therefore, this shows that the addition of small molecules does not affect the absorbance behavior of the MC cores, and

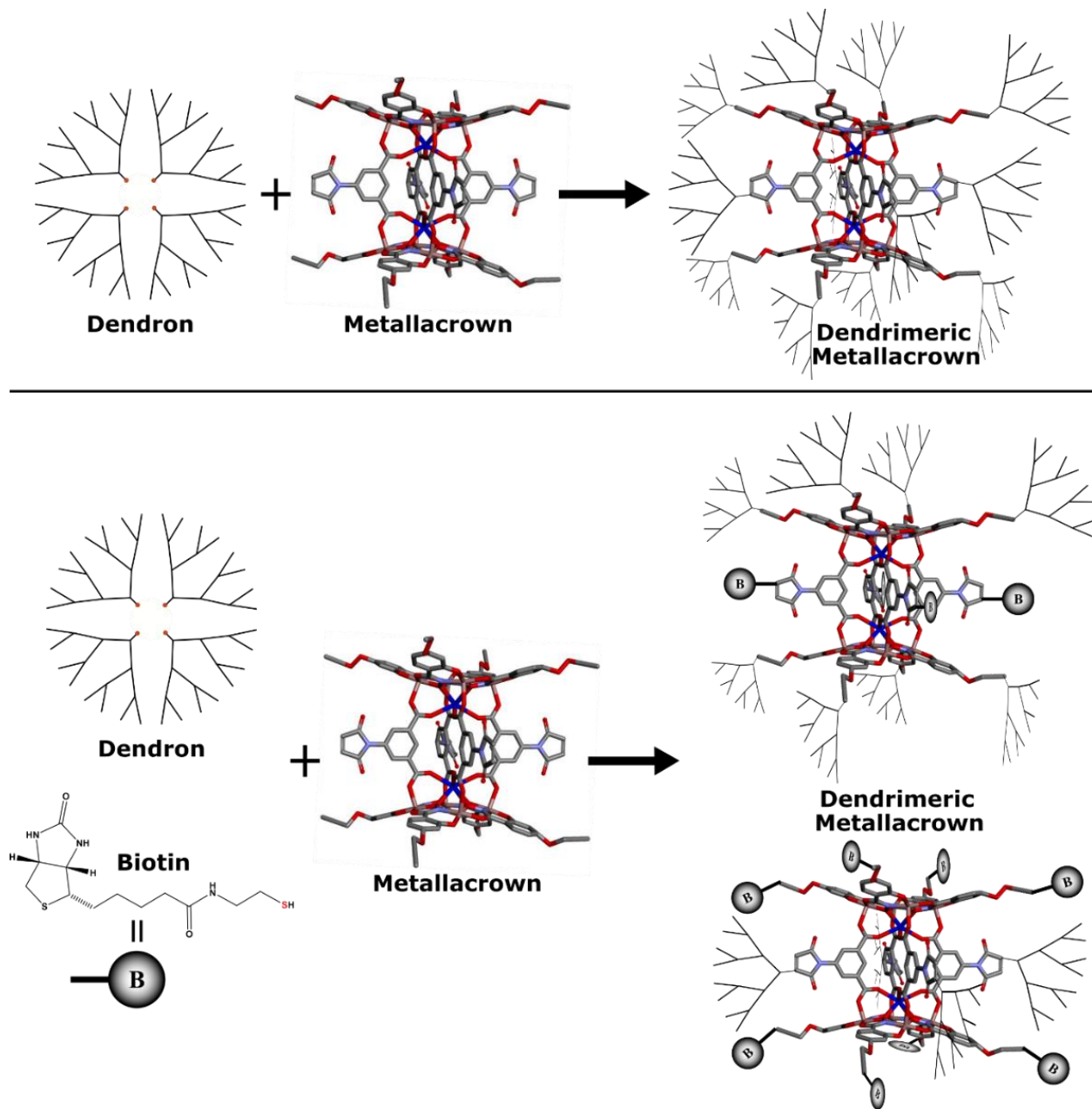
that in general, bifunctional MCs have similar absorption behaviors as the other two monofunctionalized MCs. While excitation and emission spectra were not collected for the β ME-functionalized MCs, it is prudent to expect that good luminescent sensitization will be observed. This is based on the fact that the cysteamine-functionalized $\text{Sm}_2\text{Ga}_8\text{Shi}_8\text{Mip}_4$ and β ME-functionalized $\text{Yb}_2\text{Ga}_8\text{Shi}_8\text{Ip}_4$ MC analogues, exhibited excellent Ln^{III} sensitization post-small molecule coupling. Therefore, altogether these results demonstrate the first example of combined thiol-maleimide and photocatalyzed thiol-yne/ene coupling of small molecules to bifunctional metallacrowns.

4.4.2 Symmetric and Asymmetric (Janus Dendrimeric Metallacrowns)

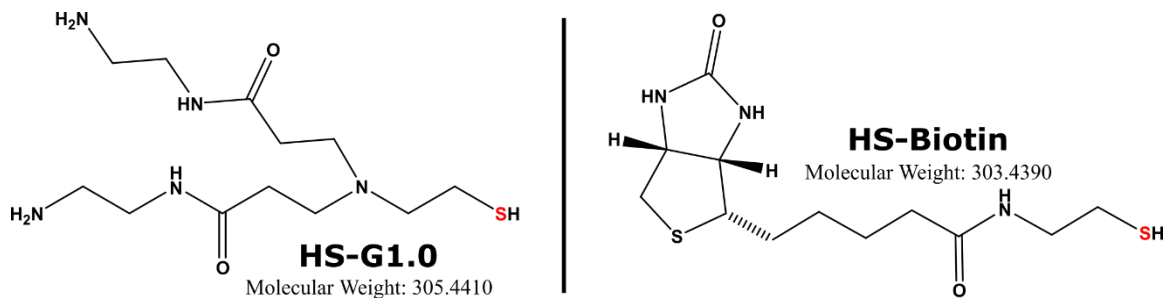
After developing MC scaffolds capable of undergoing thiol-coupling at the bridge and ring ligands, the next step was to further exploit the bifunctional MC in order to expand both the fields of dendrimers and dendrimeric metallacrowns (DMCs). To this end, $\text{Yb}_2\text{Ga}_8\text{AlShi}_8\text{Mip}_4$ MCs were employed as the core of PAMAM dendrimers, as shown in Scheme 4.2, as to develop a new class of DMCs with symmetric and asymmetric dendritic shells or targeting groups. The DMCs labeled as “symmetric” (S-DMC) represents complexes where both ligand sites of a MC core were coupled with dendrons of the same generation. As for the asymmetric DMCs (Janus-DMCs), they described complexes where either two different dendron generations, or mixture of dendrons and biotin groups that are coupled orthogonally, i.e., with one species at the ring and another at the bridging ligands.

Symmetric and asymmetric dendron addition to the MC core was performed in two steps, with thiol-maleimide coupling as the first step, followed by thiol-ene photocatalytic addition. Thiol-focal point PAMAM dendrons were prepared in the same fashion as described in Chapter 2. Based on the finding from Chapter 3, only $\text{Yb}_2\text{Ga}_8\text{AlShi}_8\text{Mip}_4$ MCs were investigated as the core of these new DMCs to ensure high coupling success rates. Similarly, only thiol focal point dendrons of generation 0.5 and 1.0 were utilized. To make biotinylated Janus DMCs, thiol focal point biotin was synthesized and coupled exclusively at either the ring or the bridging ligands, while G1.0 dendrons were coupled at the orthogonal ligand positions. Biotin was chosen as the target biomolecule to make Janus DMCs since it is of similar size and weight as a HS-G1.0 PAMAM dendrons, as seen in Scheme 4.3. Additionally, its incorporation onto DMCs could

render the complexes with interesting biological activity, such as high tumor specificity and strong affinity to avidin and streptavidin.¹⁸⁹



Scheme 4.2 Simplified representation of symmetric and Janus dendrimeric metallacrown preparation (Top). Left, thiol-focal point dendron. Middle, model of $\text{Ln}^{\text{III}}_2[12\text{-MC}_{\text{Ga(III)N}(\text{xshi})\text{-4}}]_2(\text{Mip})_4$ MC. Right, DMC with twelve dendrons attached to the MC core. Compounds with the same dendron generation are described as symmetric-DMCs, while if different dendron generation, then they are described as Janus-DMCs. (Bottom). Left, thiol-focal point dendron and biotin. Middle, model of $\text{Ln}^{\text{III}}_2[12\text{-MC}_{\text{Ga(III)N}(\text{xshi})\text{-4}}]_2(\text{Mip})_4$ MC. Right, biotinylated Janus-DMC with dendrons and biotin groups placed orthogonally to each other. Depending on the order of addition, two different Janus-DMCs can be prepared.

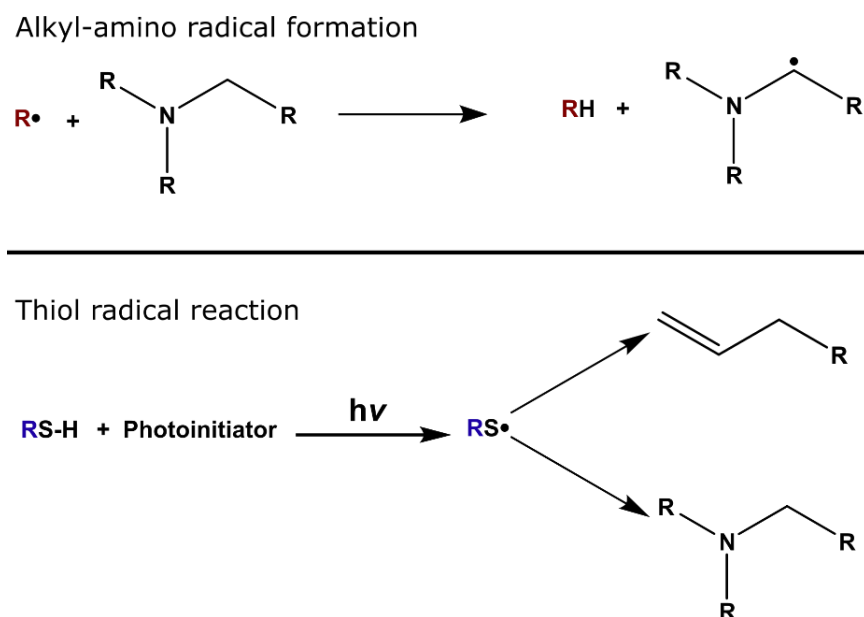


Scheme 4.3 Thiol focal point G1.0 dendrimer and biotin. Both molecules are relatively the same size and length, and have very similar molecular weights.

Symmetric dendrimeric metallacrowns. A G0.5 S-DMC was prepared with $\text{Yb}_2\text{Ga}_8\text{pAlShi}_8\text{Mip}_4$ as the MC core. Shown in Figure 4.9, a narrow distribution of ten to twelve G0.5 couplings to the MC core can be seen by ESI-MS. This translates to an overall ~83-100% coupling success rate of PAMAM dendrons to the $\text{Yb}_2\text{Ga}_8\text{pAlShi}_8\text{Mip}_4$ core. While compared to the small molecule coupling to the same MC, a ~8.3% decrease in coupling reactivity is observed with the dendrons, this still represents the first dendrimeric metallacrown and Ln^{III} -based dendrimer with twelve couplings. Furthermore, this DMC represents one of the few examples among both dendrimers and metallodendrimers with cores capable of having twelve dendrons per core. The other two known examples are by Finikova *et al.*¹⁹⁰ with a porphyrin-cored dendrimer with twelve poly(ester-amide) dendrons attached to both the *meso*- and pyrrole- β positions. While the second is by Dijkstra *et al.*¹⁹¹ with a dodecakis(pincer) compounds made out of an aromatic core connected by twelve dimethylamine-pincer palladium dendrons via ether bond. Therefore, this G0.5 S-DMC is a clear proof of concept that bifunctional MCs can be used as the core of dendrimers.

An attempt was made to prepare a G1.0 S-DMC by following the same reaction steps as with the G0.5 complex. While the dendron addition to the maleimide appendages yielded the expected product (four dendrons coupled to the MC-core), the photocatalytic addition of HS-G1.0 did not yield the final G1.0 S-DMC. By ESI-MS, only up to two dendron couplings to the ring ligands were observed. *In situ* addition of dendrons to the unfunctionalized $\text{Yb}_2\text{Ga}_8\text{pAlShi}_8\text{Mip}_4$ MC (as done previously with the small molecule addition) did not yield better results. Since the synthesis of G0.5 S-DMC yielded far better results, the poor reactivity observed when preparing the G1.0 S-DMC is likely due to the high concentration of amine groups present in the reaction. This can be explained by the fact that the amine groups ($-\text{NR}_3$ and $-\text{NH}_2$) in PAMAM dendrons

can become radical co-initiators (synergist) in photocatalytic reactions.^{192–194} As seen in Scheme 4.4, in such cases, the C-H group next to the amine group becomes an excellent hydrogen donor, and thus a new and very reactive alkyl-amino radical is formed by hydrogen abstraction. The highly reactive alkyl-amino radical can potentially then react with itself or the MC core. But in a more detrimental and likely scenario, thiol radicals can do the hydrogen extraction of the amine groups, and no longer enter the thiol-ene radical addition cycle – thus explaining the low reactivity of formation of G1.0 S-DMCs. However, while this DMC preparation was unsuccessful, based on the favorable results of both the small molecule- and G0.5 dendron-coupling to $\text{Yb}_2\text{Ga}_8\text{pAlShi}_8\text{Mip}_4$ MCs, suggest that dendron generations or dendron families with fewer or no amine groups could be used to make S-DMCs in the same fashion.



Scheme 4.4 (Top) Alkyl-amino radical formation with amine group in the presence of radical groups through hydrogen abstraction from the adjacent C-H bond to the nitrogen. (Bottom) Thiol radical reactions possibilities in the presence of alkene and amine groups. Deactivation of the thiol radical by hydrogen abstraction of amine groups may be the main culprit behind the low reactivity of MC core with HS-G1.0 PAMAM dendrimers.

Janus dendrimeric metallacrowns. To further investigate the bifunctionality of $\text{Yb}_2\text{Ga}_8\text{pAlShi}_8\text{Mip}_4$ and the unequal reactivity towards thiol-coupling of the templating ligands, Janus dendrimers with two different PAMAM dendron generations (G1.0 and G0.5) were investigated. First, HS-G1.0 dendrons were coupled to the MC core to form a $\text{Yb}_2\text{Ga}_8\text{pAlShi}_8\text{Mip}_4$ (G1.0)₄ DMC. Once the complete coupling of four dendrons was confirmed by ESI-MS,

photocatalytic addition of HS-G0.5 dendrons was attempted. As seen in Figure 4.10, incomplete coupling to the MC core was obtained, with a broad distribution of eight to eleven dendrons coupled to the MC core, and an overall ~67-92% coupling success. The relatively lower coupling reactivity of this Janus-DMC was attributed once again to the presence of a high number of amine groups (-NR₃ and -NH₂). In this case, after the successful coupling of G1.0 dendrons to the Yb₂Ga_{8p}AlShi₈Mip₄, the photocatalysis addition of G0.5 dendrons was attempted without removal of the excess G1.0 dendron. A large excess of dendron (20 eq) is necessary to drive the DMC coupling reaction to completion, and in this case the leftover dendron excess is also the source of a large amount of amine groups.

Purification of DMCs is best done with dialysis against DMSO since it allows for the removal of excess unreacted dendron under mild conditions and without sample concentration. As described in Chapter 2, complete concentration of DMC solutions (and any PAMAM dendrimer in general) leads to the formation of defects (e.g., retro-Michael addition or lactam formation), and severe sample aggregation. Thus, dialysis seemed to be the best purification method for DMCs. However, through dialysis, sample volume increases as each sample component (DMC, excess dendron, DMSO) move towards equilibrium in both side of the dialysis membrane. This represents an issue since as described in the synthetic trials in Chapter 3, photocatalytic thiol addition to the MCs is highly sensitive towards the solution concentration. To this end a compromise was taken, and the addition of HS-G0.5 dendron to Yb₂Ga_{8p}AlShi₈Mip₄(G1.0)₄ was done without purification. From the lack of high dendron coupling success for this Janus-DMC, it is obvious that removal of excess PAMAM dendron is necessary; however, this will require the exploration of alternative purification techniques. Alternatively, as suggested earlier, utilizing a different dendron family with fewer or no amine groups (e.g., bis-MPA or PGLSA-OH) would likely improve the coupling success rate of Janus-DMCs by minimizing the hindering effects of high amine concentrations during photocatalytic thiol-ene coupling.

Nonetheless, while not perfect, the coupling of two different generation dendrimers to the same MC core was done without further synthetic modification, such as protection or deprotection steps of the core prior adding the second dendron, as it is commonly done with standard Janus dendrimers synthesis.^{25,195} Additionally, this DMC synthesis attempt was also another proof of concept that asymmetric coupling is achievable with the bifunctional Yb₂Ga_{8p}AlShi₈Mip₄ MC core.

Biotinylated Janus dendrimeric metallacrowns. While addition of PAMAM dendrons to the twelve coupling sites of a $\text{Yb}_2\text{Ga}_8\text{pAlShi}_8\text{Mip}_4$ MC core may face some synthetic challenges, interesting Janus-DMCs can still be prepared by placing the dendrons and target molecules at orthogonal ligand positions. To this end, two types of biotinylated Janus-DMCs were attempted: $\text{Yb}_2\text{Ga}_8\text{pAlShi}_8\text{Mip}_4(\text{Bt})_4(\text{G1.0})_8$ and $\text{Yb}_2\text{Ga}_8\text{pAlShi}_8\text{Mip}_4(\text{G1.0})_4(\text{Bt})_8$. With the former having four biotin groups at the bridging ligands and eight G1.0 dendrons at the ring ligands, and the latter having four G1.0 dendrons and eight biotins at the bridge and ring ligands, respectively.

$\text{Yb}_2\text{Ga}_8\text{pAlShi}_8\text{Mip}_4(\text{Bt})_4(\text{G1.0})_8$ Janus-DMCs were prepared by first coupling biotin to the maleimide appendages. After purification and corroborating the desired product by ESI-MS, photocatalytic addition of HS-G1.0 to the ring ligands was done. As seen in Figure 4.12, a total of nine to twelve couplings to the MC cores was obtained, which translates to an overall 75-100% success coupling rate. While complete coupling of biotin to the MC core was obtained, partial to complete addition of five to eight G1.0 dendrons to the ring ligands was observed. While not perfect, the coupling success rate of this Janus-DMC is higher than the G1.0/G0.5 Janus-DMC, with ~67-92% coupling success rate. This supports the idea that a smaller concentration of amine groups in solution improves the overall coupling reactivity of the photocatalytic step, and the possibility that other dendron families could improve the coupling success rate of the photocatalytic step of Janus-DMCs.

The orthogonal configuration was also investigated where first a $\text{Yb}_2\text{Ga}_8\text{pAlShi}_8\text{Mip}_4(\text{G1.0})_4$ DMC was prepared, followed by the photocatalytic addition of thiol-biotin. Coupling of four dendrons, and six to eight biotin groups to the MC core was corroborated by ESI-MS, as seen in Figure 4.14. A high success rate of coupling (~83-100%) was observed, which is comparable to that of the symmetric G0.5 DMC, and higher than the Janus G0.5/G1.0 DMC. Furthermore, compared to the $\text{Yb}_2\text{Ga}_8\text{pAlShi}_8\text{Ip}_4$ G1.0 H-DMC, this $\text{Yb}_2\text{Ga}_8\text{pAlShi}_8\text{Mip}_4(\text{G1.0})_4(\text{Bt})_8$ Janus-DMC has the same coupling reactivity to the ring ligands, with both having six to eight thiol groups coupled to the ring ligands of the MC core. This complex was purified by dialysis against DMSO, and then further characterized by DLS and luminescence spectroscopy.

As seen in Figure 4.2 and Figure 4.14, the characterization by ESI-MS of the $\text{Yb}_2\text{Ga}_8\text{pAlShi}_8\text{Mip}_4$ MC and the $\text{Yb}_2\text{Ga}_8\text{pAlShi}_8\text{Mip}_4(\text{G1.0})_4(\text{Bt})_8$ Janus-DMC corroborate the expected increase in molecular weight with the added dendrons and biotin groups to the MC core.

As seen with other DMCs, while the ESI-MS of the MC core is best observed as a -2 species in negative mode, the $\text{Yb}_2\text{Ga}_8\text{pAlShi}_8\text{Mip}_4(\text{G1.0})_4(\text{Bt})_8$ Janus-DMC was better detected by the mass spectrometer as a +3 and +4 species in positive ion mode. This is due to the numerous protonation sites that both the dendron and the biotin groups have. The DLS size distribution of the DMC in DMSO shows that while this compound is mildly polydisperse, no aggregates are observed. This is different from T-DMC and H-DMCs with G1.0 dendrons, as seen in Figure 4.25, and of special interest since large aggregate in solution can heavily influence behavior of the complex – e.g., hinder cell uptake or retard diffusion rates. This Janus-DMC seem to share similar diameters (~4 nm) and polydispersity as the T-DMC (PdI: ~0.2) which can be attributed to fact that the dendrons in both DMCs are coupled to the bridging ligands. The larger polydispersity of the Janus-DMC compared to the H-DMCs is likely due to the presence of isomers arising from the two different coupling sites in a maleimide appanage. Such isomers can be interpreted as a measure of low homogeneity by the DLS, and as a result, yield large polydispersity values.

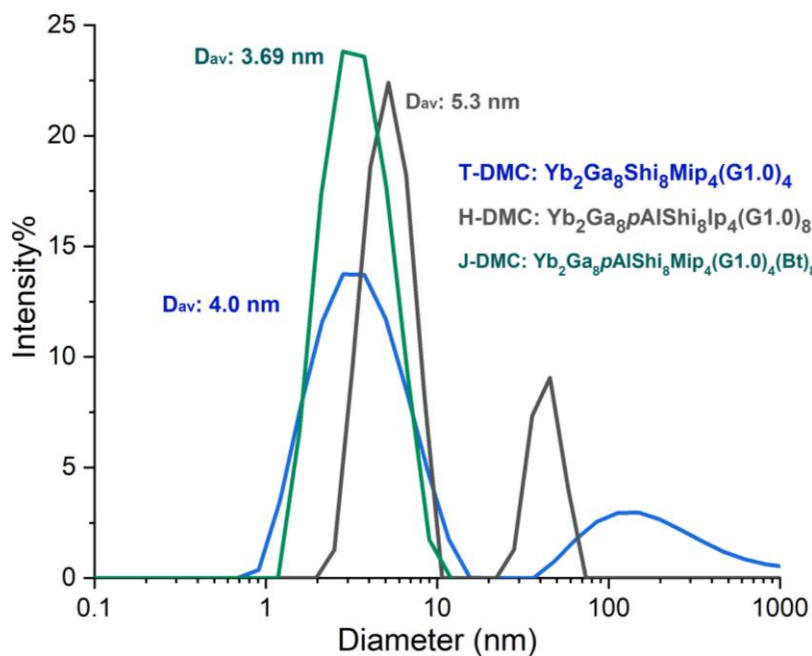


Figure 4.25 DLS size distribution comparing $\text{Yb}_2\text{Ga}_8\text{pAlShi}_8\text{Mip}_4(\text{G1.0})_4(\text{Bt})_8$ J-DMC, $\text{Yb}_2\text{Ga}_8\text{Shi}_8\text{Mip}_4(\text{G1.0})_4$ T-DMC and $\text{Yb}_2\text{Ga}_8\text{pAlShi}_8\text{Ip}_4(\text{G1.0})_8$ H-DMC in DMSO at room temperature.

As seen in Figure 4.26, when comparing the size distribution plots of the same set of G1.0 DMCs in more aqueous environments (99:1, $\text{H}_2\text{O}:\text{DMSO}$ v/v%), it can be seen that while the three DMCs tend to form aggregates, the $\text{Yb}_2\text{Ga}_8\text{pAlShi}_8\text{Mip}_4(\text{G1.0})_4(\text{Bt})_8$ J-DMC has the smallest

aggregates in diameter, while both the T-DMC and H-DMC seem to have similar sized ones. What these results are suggesting is that the biotin groups at the ring positions are aiding to keep the average hydrodynamic diameter of the aggregates smaller compared to the other two G1.0 DMCs. This behavior should influence the pharmacokinetic properties of $\text{Yb}_2\text{Ga}_8\text{pAlShi}_8\text{Mip}_4(\text{G1.0})_4(\text{Bt})_8$ Janus-DMCs differently, and likely positively, compared to the other two DMC of the same generation. While cell studies were not performed for this particular Janus-DMC, based on the DLS results in both DMSO and water/DMSO, it could be expected that cell uptake of the $\text{Yb}_2\text{Ga}_8\text{pAlShi}_8\text{Mip}_4(\text{G1.0})_4(\text{Bt})_8$ Janus-DMC would be likely as good as with the $\text{Yb}_2\text{Ga}_8\text{Shi}_8\text{Mip}_4$ G1.0 T-DMC (where cell internalization was achieved). Additionally, the presence of the numerous biotin groups may also help improve the cell uptake of the DMC.

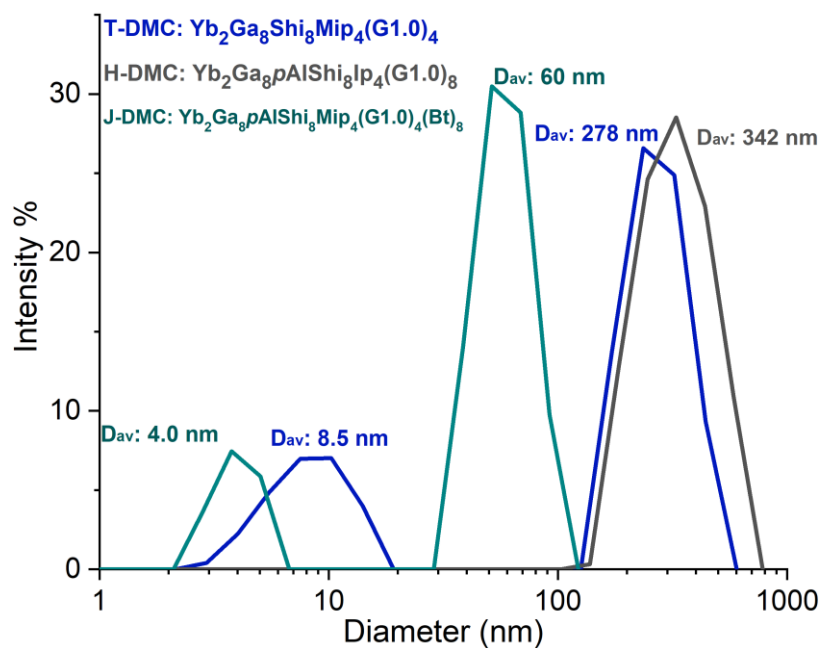
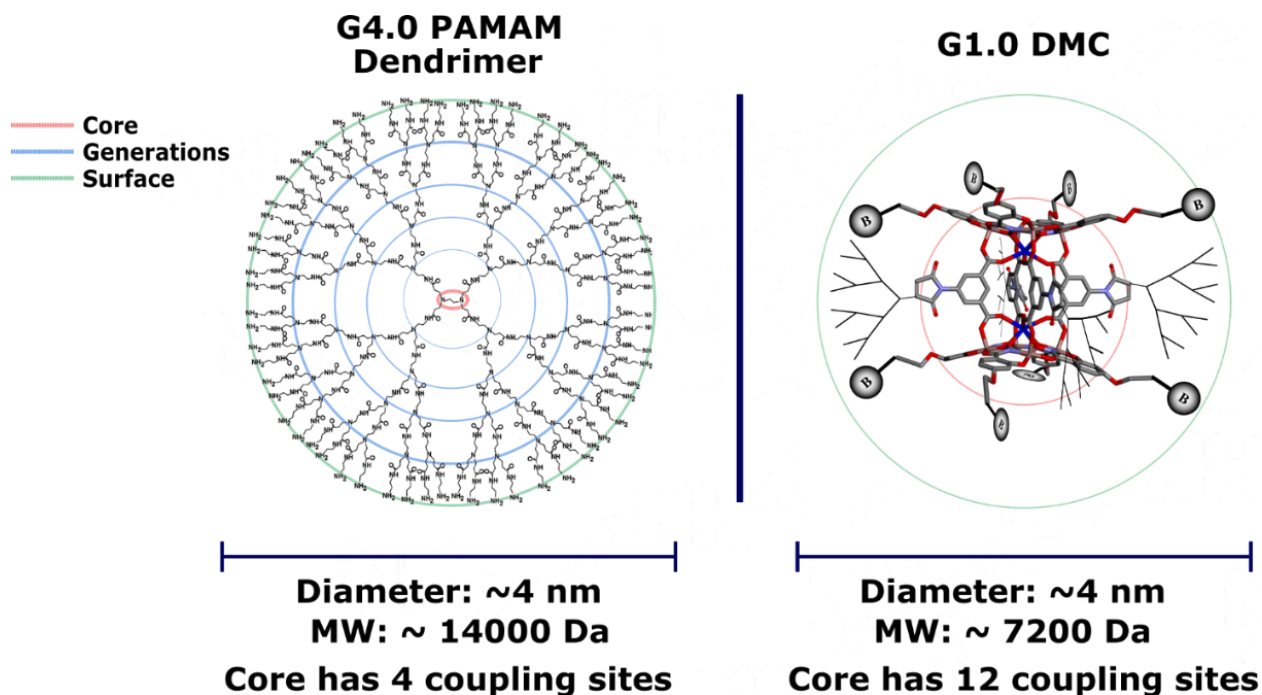


Figure 4.26 DLS size distribution comparing $\text{Yb}_2\text{Ga}_8\text{pAlShi}_8\text{Mip}_4(\text{G1.0})_4(\text{Bt})_8$ J-DMC, $\text{Yb}_2\text{Ga}_8\text{Shi}_8\text{Mip}_4$ G1.0 T-DMC and $\text{Yb}_2\text{Ga}_8\text{pAlShi}_8\text{Ip}_4$ G1.0 H-DMC in solution in 99:1 H_2O :DMSO at room temperature and at pH: 7.5.

Both the ESI-MS and DLS data highlight the structural and morphological difference of regular PAMAM dendrimers and the biotinylated Janus-DMC. At the same G1.0 dendrimer generation, the Janus-DMC is about 1.7 times larger than the standard a G1.0 PAMAM dendrimer, and as large in diameter as a G3-4 PAMAM dendrimer.^{43,196} Additionally, the molecular weight of $\text{Yb}_2\text{Ga}_8\text{pAlShi}_8\text{Mip}_4(\text{G1.0})_4(\text{Bt})_8$ Janus-DMC by mass spectroscopy (~7.2 kDa) is comparable to that of a G3.0 PAMAM dendrimer (~7 kDa). Thus, as seen in Scheme 4.5, the Janus-DMC

reaches larger diameters and is more massive with smaller generations. Lastly, the $\text{Yb}_2\text{Ga}_8\text{pAlShi}_8\text{Mip}_4(\text{G1.0})_4(\text{Bt})_8$ J-DMC has the same number of surface groups as a standard G1.0 PAMAM dendrimer (eight $-\text{NH}_2$ total), but also eight biotin groups at a well-defined location. A more obvious difference is observable when comparing the other biotinylated G1.0 Janus-DMC, which has twice as many surfaces group as a standard G1.0 PAMAM dendrimer and four biotin groups. When making such comparisons with the symmetric G0.5 DMC, the number of surface groups in the DMC is three times as many as a PAMAM dendrimer of the same generation.

Just as with T-DMCs and H-DMCs, the structural and physical differences between the biotinylated J-DMC and regular PAMAM dendrimers is due to their core. While PAMAM dendrimers are normally prepared with ethylenediamine groups as the core (~ 0.38 nm in diameter), the core of the DMCs in this work is significantly larger and more massive. Also, the $\text{Yb}_2\text{Ga}_8\text{pAlShi}_8\text{Mip}_4$ MC core has a total of twelve sites for dendron coupling while the ethylenediamine core only has four. As for the overall shape, the DMCs described here are likely to have a more spherical conformations, especially with symmetric dendron coupling to both of the ligand positions.

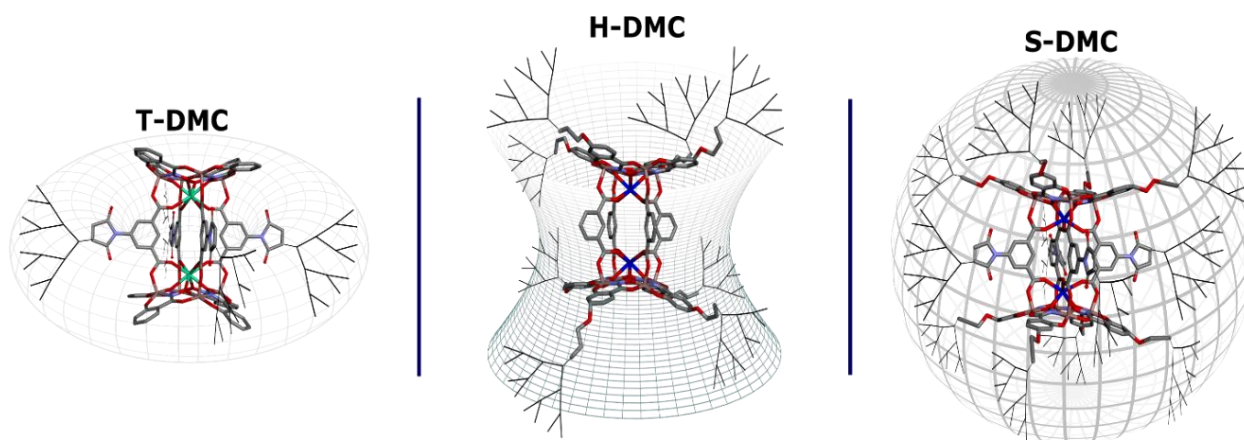


Scheme 4.5 Comparison between a G4.0 EDA-cored PAMAM dendrimer with a G1.0 $\text{Ln}_2\text{Ga}_8\text{pAlShi}_8\text{Mip}_4$ DMC highlighting that the DMC has a diameter (measured by DLS) as large as a large PAMAM dendrimer. Also, the MC used as the core of DMC has three times as many coupling sites for dendron grow, compare to the EDA core in PAMAM dendrimers that only has four.

Additionally, dendrimer functionalization generally occurs by modifying the numerous surface groups with the desired molecule (e.g., chromophore, antigen, target drug). This often results in low control on the concentration and position of the appended groups, especially with large dendrimer that have a high number of surface groups. Therefore, the added benefit of a MC-cored dendrimers versus regular dendrimers is that the MC offers a much higher control on both the number of appendages and their coupling position. Like in the case of both biotinylated Janus-DMCs, the biotin groups can be exclusively couple to either the bridging ligands, adding four biotins per DMC, or at the ring ligands, adding up to eight groups per DMC. This kind of control over the position and number of targeted molecules are qualities sought after in the development of nanomaterial and biological imaging probes.²³

Unlike luminescent PAMAM dendrimers that rely on surface modification or encapsulation of luminescent chromophores, DMCs are intrinsically luminescent due to their Ln^{III}-based MC cores. The photophysical properties of Yb₂Ga_{8p}AlShi₈Mip₄(G1.0)₄(Bt)₈ J-DMC were investigated, and compared to G1.0 T-DMC and H-DMC from Chapter 2 and 3, and other Yb^{III}-based metallacrowns. As seen in Figure 4.17 absorption spectra of Yb₂Ga_{8p}AlShi₈Mip₄(G1.0)₄(Bt)₈ Janus-DMC exhibit similar $\pi \rightarrow \pi^*$ transition bands to those of the MC core, with an absorbance in the range of 250-340 nm. This suggest that the incorporation of both dendrons and biotin groups do not hinder the MC core's electronic properties. Furthermore, the good overlap of the solution state absorbance and excitation spectra indicates effective energy absorbance and transfer by the MC core to the Yb^{III} ions. Excitation at 320 nm exhibited the expected characteristic Yb^{III} emission between 950-1150 nm, as seen Figure 4.18. Photophysical data in the solution state detailed on Table 4.1, show that the τ_{obs} and ϕ_{Yb}^L values of the DMC are larger than the Yb₂Ga_{8p}AlShi₈Mip₄ with no dendrons. This confirms once again that the quenching effects of the maleimide appendages are eliminated once they are bound to thiol groups. Compared to the original dimeric Yb₂Ga₈Shi₈Ip₄ MC (ϕ_{Yb}^L : 7.56%), the G1.0 T-DMC (ϕ_{Yb}^L : 9.38%) and the G1.0 H-DMC (ϕ_{Yb}^L : 8.7%), the Yb₂Ga_{8p}AlShi₈Mip₄(G1.0)₄(Bt)₈ Janus-DMC quantum yield in solution (7.41%) is very close that of the Yb₂Ga₈Shi₈Ip₄, but lower than the two other DMCs. The 15-20% decreased in quantum yield of the Janus-DMC compared to the other two could be a combination of the position of the functionalities – i.e., coupling at the ring ligands was shown to result in a ~7% reduction in quantum yield when comparing T-DMC and H-DMC (Scheme 4.6); or, due to the higher number of solvent molecules encapsulated by the Janus-DMC

since this complex has twelve couplings which are likely to increase the number of solvent molecules close to the MC core. As shown before by DLS calculations, the H-DMC (which has eight couplings per MC) had a significantly larger number of solvent molecules encapsulated by the dendritic shell than T-DMCs. Thus, it would not be surprising if that is the main reason behind the drop in ϕ_{Yb}^L when the MC core has more couplings. Nonetheless, the overall high quantum yield, long luminescent lifetimes, NIR emission of $\text{Yb}_2\text{Ga}_8\text{pAlShi}_8\text{Mip}_4(\text{G1.0})_4(\text{Bt})_8$ J-DMC, along with its well-defined synthetic control over the position and concentration of secondary groups (i.e., biotin) are exciting results for lanthanide-based luminescent scaffolds and the dendrimer field in general.



Scheme 4.6 Simplified representation of toroidal dendrimeric metallacrown (T-DMC, left) and hyperboloidal dendrimeric metallacrown (H-DMC, middle), and the newest dendrimeric metallacrowns introduced in this chapter (S-DMC, right).

4.4.3 Redshifted Dendrimeric Metallacrowns (Redshifted-DMCs)

Lastly, while the MCs templated with mYneShi ring ligands did not have efficient reactivities towards thiol coupling, their less energetic absorbance maxima were still exploited to develop redshifted-DMCs. Lower energy absorbances are an important factor when developing imaging agents since to be truly used as biological probes, the excitation of the probe should not be harmful to the system under study. To this end, three redshifted-DMCs were prepared with G1.0, G1.0 -OH, and G1.5 PAMAM dendrons exclusively coupled to the bridging ligands of $\text{Yb}_2\text{Ga}_8\text{mYneShi}_8\text{Mip}_4$ MC cores. The G1.0 -OH dendron is similar size and molecular weight to a regular G1.0 dendron, with the only difference being the hydroxyl surface groups. Since a certain degree of aggregation was observed with the $\text{Yb}_2\text{Ga}_8\text{Shi}_8\text{Mip}_4$ G1.0 T-DMC, it was of interest to

investigate whether the hydrophilic hydroxyl surface groups would behave differently. As seen in Figure 4.19 and Figure 4.20, ESI-MS and DLS characterization of each of the three Red T-DMCs corroborated both the complete coupling of only four dendrons per MC core, and increasing molecular weights and hydrodynamic diameters. While DLS characterization in DMSO showed that the G1.0 -OH and 1.5 DMC undergo little or no aggregation, the G1.0 T-DMC showed a significant degree of aggregation. Further DLS investigation under more aqueous environments, shown in Figure 4.21, demonstrated that both G1.0 and G1.0 -OH DMC form aggregates of large diameters, with the latter having the broadest range of aggregate size and high polydispersity. On the other hand, the smallest aggregates formed with the G1.5 DMC (D_{av} : ~6 nm), which is likely due to the hydrophobic interactions of its surface groups (-OME) with the surrounding environment. Furthermore, when compared to the original G1.0 T-DMC (Figure 4.26, blue), the aggregates of the G1.0 and 1.0 -OH redshifted-DMCs are of significantly larger hydrodynamic diameters. Since the main difference between the standard T-DMCs and the new DMCs is the ring ligands, the alkyl ether group on the MC core worsen aggregation behavior in solution.

This is further corroborated during the incubation of HeLa cells with the three new redshifted-DMCs. As shown in Figure 4.24, the cell experiments demonstrated that the three DMCs localized at the surface of the cells, which greatly differs from incubation with G1.0 T-DMC which showed internalization by the cells. These experiments highlight the delicate balance between acquiring optimal pharmacokinetic properties (e.g., solubility and cell uptake), while also fulfilling the photophysical requirements (e.g., bright emissions, with low energy excitations). While no cell uptake of the DMC was observed, strong Yb^{III} luminescent signals were detected with the three redshifted-DMC from non-specific interactions of the aggregates on the surface of living HeLa cells.

More detailed luminescent characterization of the three redshifted-DMCs showed that their absorbance profiles are similar to that of the unfunctionalized core, with a low-energy maximum at 340 nm. Good overlap between the absorption and excitation spectra in solution also suggest effective energy transfer from the antennas in the MC core to the Yb^{III} ions. Emission spectra showed characteristic Yb^{III} emission between 950-1150 nm for the three Red T-DMCs. Photophysical characterization of each DMC in solution showed similar monoexponential decay and quantum yields between 8.18-8.83%. The original T-DMC still has the largest quantum yields (8.73-9.38%) among all the different DMCs described in this thesis. The slightly lower ϕ_{Yb}^L of the

redshifted-DMCs could be due to the alkyl ether groups ($\text{HC}\equiv\text{CCH}_2\text{OR}$) in the ring ligands. Since these appendages have a certain degree of flexibility and numerous C-H oscillators, they could be quenching some of the luminescent signal of the MC core. Yet, these DMCs' quantum yields are among the largest compared to other Yb^{III} -based MCs in solution. The enhanced photophysical values are attributed to the presence of the dendritic shell. This is corroborated by comparing the quantum yield of $\text{Yb}_2\text{Ga}_8m\text{YneShi}_8\text{Ip}_4$ (7.3%) to the three redshifted-DMCs, where a 10-17% increase in quantum yield is observed. Once again, the photophysical and functionalization potential of MC core were combined to develop DMCs with excellent quantum yields and emissions in the NIR.

4.5 Conclusions

The work presented in this chapter illustrates that the photophysical properties of Ln^{III} -based MCs and their remarkable functionalization potential can be combined to develop a new class of luminescent metallodendrimer. In this chapter, I developed a series of Yb^{III} -based bifunctional metallacrowns capable of undergoing symmetric and asymmetric coupling on to the same MC core. I did this by combining the synthetic work and coupling methodologies developed in Chapter 2 and 3. The bifunctional MCs were characterized by ESI-MS and elemental analysis to corroborate chemical and structural composition, and by UV-VIS and fluorescence spectroscopy to study their luminescent behavior. Functionalization ability of $\text{Yb}_2\text{Ga}_8x\text{Shi}_8\text{Mip}_4$ (x : *pAl*, *mAl*, and *pyne*) was corroborated by coupling up to twelve or twenty β -mercaptoethanol molecules to the templating ligands of MCs via UV-light photocatalyzed thiol coupling. This work represents the first incorporation of thiol active sites to both the ring and bridging ligands of MCs, and the first-time up to twenty molecules have been coupled to a single MC core. Furthermore, as it was discussed in Chapter 2, the incorporation of thiol groups to the maleimide appendages can yield an array of isomers combinations since each maleimide appanage can yield two different isomers upon thiol coupling. Therefore, if the chirality of the system can be synthetically controlled, or the diastereomers separated, interesting polarizable luminescent studies and biological studies could be investigated.

Once the coupling capabilities of the bifunctional MC were demonstrated, $\text{Yb}_2\text{Ga}_8p\text{AlShi}_8\text{Mip}_4$ MCs were used as the core of dendrimeric metallacrowns with twelve points of attachment. Symmetric incorporation of G0.5 to the MC core to yield

$\text{Yb}_2\text{Ga}_8\text{pAlShi}_8\text{Mip}_4(\text{G}0.5)_{12}$ S-DMC was highly successful. However, incorporation of the longer G1.0 dendron did not yield such results. This is likely due to the presence of numerous amine group that can interfere with the photocatalytic step of the synthesis. Nonetheless, the successful synthesis of G0.5 S-DMC represents an important advance in the field of dendrimers, since before this work, only two examples of dendrimers with twelve couplings site were known. Furthermore, other dendrimer families that have no amine groups, but still share the same biocompatible properties of PAMAM dendrimer, could be coupled to the MC core in the same fashion.

Next, asymmetric or Janus DMCs were prepared. The first one was prepared with G1.0 and G0.5 dendrons coupled to the bridge and ring ligands, respectively. While the low coupling success (~60-80%) of such DMC was attributed to the high concentration of amine groups, it opened-up the possibility to perform asymmetric coupling by taking advantage of the different reactivity of the bridge and ring ligands. To this end, two biotinylated Janus-DMCs were prepared, with the $\text{Yb}_2\text{Ga}_8\text{pAlShi}_8\text{Mip}_4(\text{G}1.0)_4(\text{Bt})_8$ Janus-DMC further characterized for its luminescent properties. ESI-MS and DLS studies corroborated the formation of the $\text{Yb}_2\text{Ga}_8\text{pAlShi}_8\text{Mip}_4(\text{G}1.0)_4(\text{Bt})_8$ Janus-DMC, while photophysical characterization demonstrated excellent sensitization and quantum yield of the scaffold in DMSO solutions. Furthermore, the distinct structural features these DMCs, such as more spherical shape compared to T-DMC and H-DMC, their large diameters and high molecular weight with smaller generations, are appealing properties that can have interesting pharmacokinetic advantages over regular PAMAM dendrimers. Additionally, DMCs are intrinsically luminescent, and the MC core offer excellent control of the position and number of coupled target molecules.

Lastly, redshifted-DMCs were also prepared with the least reactive ring ligands (H_3mYneShi). While it was unfortunate that $m\text{YneShi}$ ligands had very little reactivity towards thiol coupling, this lack of reactivity was exploited to make redshifted-DMCs. Since long generation T-DMC (>G1.0) require preparation times up to 10 days in the presence of a large excess of PAMAM dendrons, the low reactivity of $m\text{YneShi}$ comes in handy to ensure that dendron coupling only occurs at the bridging ligands, even after long reaction times. To this end G1.0, G1.0-OH, G1,5 redshifted-DMC were prepared. ESI-MS and DLS studies corroborated the formation of each of the three DMCs. Luminescent characterization of the three DMCs showed both efficient Yb^{III} sensitization, and quantum yields in solution that are among the highest among Yb^{III} -based MCs. Cell studies demonstrated excellent Ln^{III} sensitization, as well as robust stability in cell

culture conditions, but no cell uptake likely due to aggregation. Despite the lack of cell uptake, these are promising results since either the dendritic shell, the MC core, or the cell studies conditions can be further optimized to yield better results – e.g, longer dendrimers, different dendrimer families, different buffer conditions.

With this work, I was able to expand the functionalization of MCs by making bifunctional scaffolds capable of undergoing symmetric and asymmetric functionalization, while also exploiting their luminescent sensitization. Furthermore, I was able to demonstrate that such MCs can be utilized as the core of dendrimeric metallacrowns. Additionally, bifunctional MCs offer the possibility of designing Janus-DMCs with attractive biomolecules or target agents (such as small peptides), and antennas to further redshift the excitation energy. Thus, altogether, with this work I have contributed to the diversification of metallacrown and dendrimer design.

Chapter 5

Conclusions and Future Work

This thesis focuses on the development of dendrimeric metallacrowns (DMCs) from lanthanide-based metallacrown-cores (MCs). Metallacrowns have been shown to be especially suitable at exploiting the luminescent properties of lanthanides; however, their limited solubility and solution stability in aqueous environments has limited their application as imaging probes. Similarly, current luminescent dendrimers lack robust photostability since they rely on the coupling of organic chromophores, but are known to have excellent biocompatibility. To overcome these drawbacks, while also exploiting their individual properties, dendrimers were built from luminescent MC-cores. In this work, the functionalization of Ln_2Ga_8 MCs at the bridging ligands (Chapter 2), the ring ligands (Chapter 3), and both (Chapter 4) positions was investigated to combine the properties of dendrimers and MCs, creating a new class of metallodendrimers with exceptional luminescent properties. The four major contributions of this thesis toward this end are now discussed.

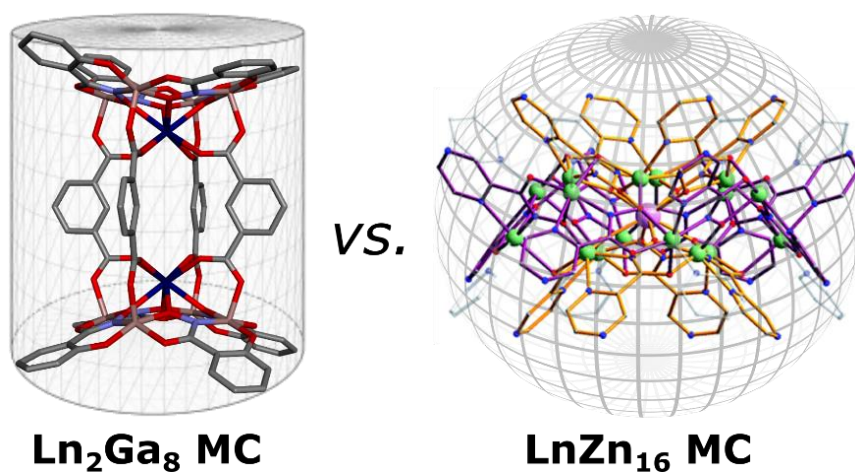
5.1 Preparation of DMCs

The foremost contribution of this thesis is the preparation of dendrimeric metallacrowns. This first required the synthetic incorporation of thiol-active sites to the templating ring and bridging ligands of Ln_2Ga_8 MCs, the corroboration of thiol-coupling reactivity, and the optimization of the reaction conditions for DMC synthesis. Synthetic functionalization of the isophthalate bridging ligands was the most straightforward, and allowed the incorporation of highly reactive thiol-active groups. Functionalization of the ring ligands, however, was more challenging and required the inclusion of less reactive thiol-coupling appendages. Due to the difference in reactivity, coupling reaction conditions differed greatly between ligands, so much so that a photocatalytic approach for the coupling at the ring ligands of Ln_2Ga_8 MCs had to be pioneered. For the preparation of DMCs, optimization of the reaction conditions based on ligand

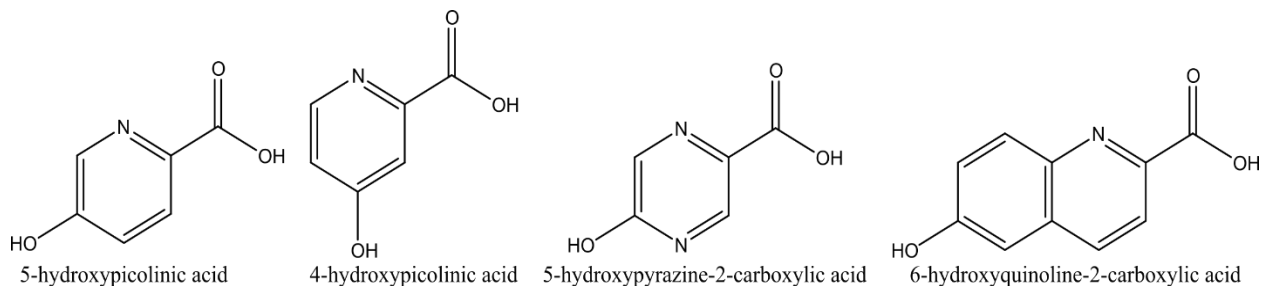
functionalization and DMC type was essential. For toroidal-DMCs, reaction length was dependent on the size and length of the PAMAM dendrons. For hyperboloidal-DMCs, synthesis was highly dependent on reaction concentration and the class and position of the functional group at the rings. As for the symmetric- and Janus-DMCs, their preparation depended on the previous optimization of the reaction conditions for T-DMCs and H-DMCs

Altogether, this demonstrates that through synthetic modification of the templating ligands, metallocrowns can be used as the core of dendrimers that range between those offering simple shapes and compositions, to those nanomaterials that are highly complex, asymmetric, and chiral.

This work supports the idea that other metallocrown scaffolds could be used as the core of dendrimers. It will be insightful to develop new DMCs from the luminescent LnZn_{16} metallocrown given that it has a more globular shape than Ln_2Ga_8 MCs (Scheme 5.1); it can be intrinsically soluble in water when made with H_2PyzHa ; it can label and simultaneously fix and counterstain HeLa cells;^{128,129} and has sixteen points of attachment, which would make it the dendrimer with the highest number of dendrons per core. Furthermore, the incorporation of the dendritic shell should improve the water solubility of the LnZn_{16} MC-core, as well as enhance its luminescent properties by protecting the Ln^{III} ion from solvent molecules. Similar synthetic methodologies described in Chapter 3 could be used to functionalize LnZn_{16} MCs with allyl appendages using the commercially available ligands shown in Scheme 5.2, and photocatalytic addition protocols can be employed for the coupling of dendrons.



Scheme 5.1 Overall shape difference between the more cylindrical Ln_2Ga_8 MC and the more spherical (globular) LnZn_{16} MC. The LnZn_{16} MC also has a higher number of templating ligands (16) that can be functionalized with thiol-active groups to serve as MC cores for future DMCs.



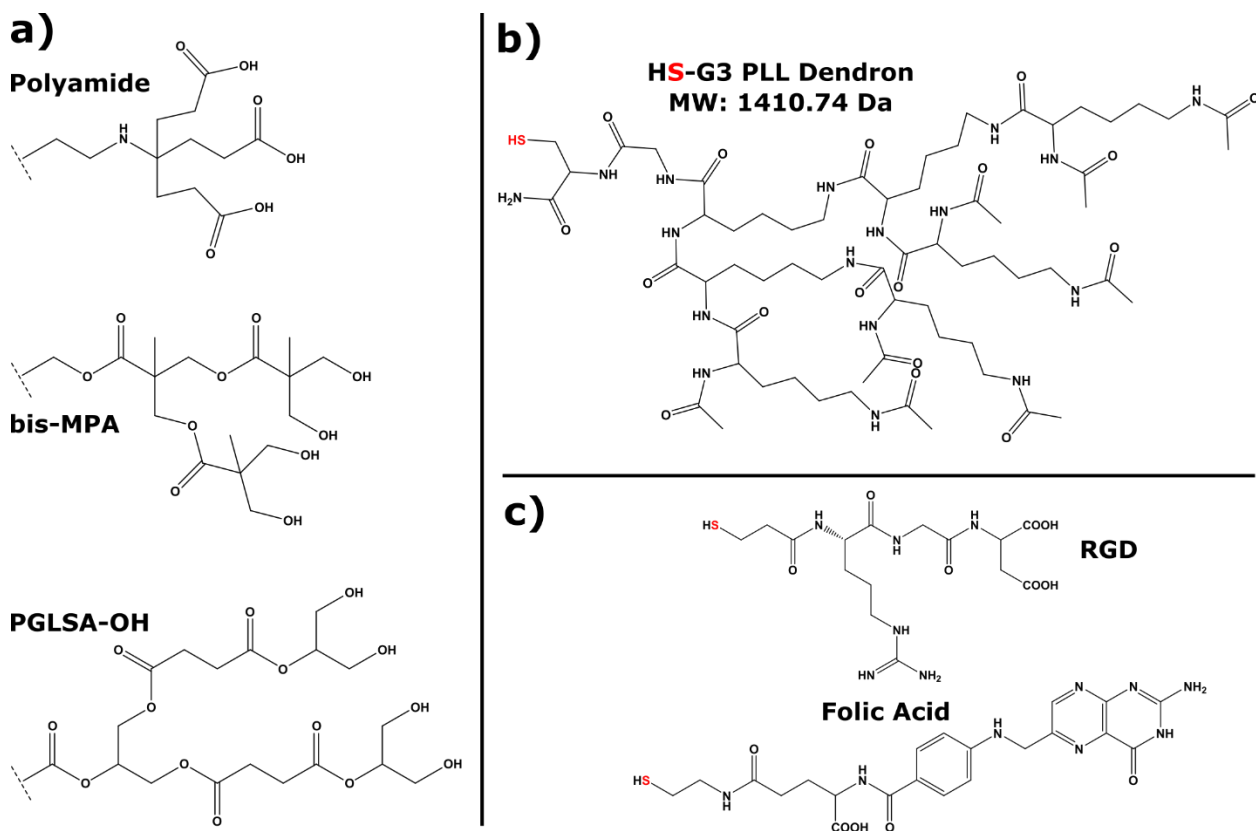
Scheme 5.2 Commercially available starting material for the incorporation of thiol-ene appendages and subsequent formation of thiol active LnZn_{16} metallacrowns.

Having shown the successful asymmetric synthesis of biotinylated Janus-DMCs with bifunctionalized Ln_2Ga_8 MC-cores, other diverse DMCs could be developed. In the case of Janus-DMCs, these could be made by using two different dendron families at each ligand position to exploit the individual properties of each family and the optical properties of the MC-core. For best results, the dendron attached at the ring ligand should have few or no amine sites, as to avoid unwanted amine radical formation during the photocatalytic step. For example, Janus-DMCs could be made with PAMAM dendrons at the bridging ligands and any of the dendrons shown in Scheme 5.3a coupled at the ring ligands.

Additionally, peptide-based dendrons, such as Poly-L-lysine (PLL) appendages, could also be used as the dendritic shell of DMCs. PLL dendrons, known for their intrinsically antiangiogenic¹⁹⁷ and microbicidal²⁸ properties, were initially studied alongside PAMAM dendrons to prepare DMCs. Thiol-focal point G3.0 PLL dendrons, shown in Scheme 5.3b, were prepared and purified by commonly employed solid-phase peptide synthesis approaches used in the Pecoraro group.^{198–201} Initial studies corroborated the HS-PLL dendron coupling reactivity to the maleimide appendages of functionalized isophthalic acid ligands; however, coupling to the Ln_2Ga_8 MC core was not achieved under the same reaction conditions necessary to prepared PAMAM toroidal-DMCs (i.e., based catalyzed conditions). Thus, it will be worthwhile to alter the reaction conditions to prepared PLL-based DMCs, and investigate both the luminescent and pharmacokinetic behavior of DMCs prepared with this peptide derived dendritic shells.

Furthermore, Janus-DMCs could also be prepared with other biomolecules of interest of size similar to biotin (Scheme 5.3c) and with PAMAM dendrons at the bridging ligands. To improve cell uptake through the hydrophilic bilayer, cell-penetrating peptides (CPP) such as arginine-glycine-aspartate (RGD) peptide could be coupled to the DMC. Similarly, coupling of

transporter groups that resembled specific endogenous substrate on cells, such as folic acid, could be photocatalytically attached to Janus-DMCs to improve the overall intracellular delivery. In general, a diverse variety of Janus-DMCs with attractive optical and physical properties can be made by exploiting the well-controlled addition of thiol-bearing molecules/dendrons to bifunctionalized MC-cores as demonstrated in this thesis.



Scheme 5.3 (a) Suggested dendrons for photocatalytic addition at the ring ligands of Janus-DMCs. These dendrons are selected for their low concentration of amine site that can hinder the photocatalytic thiol-addition. (b) Thiol-focal point Poly-L-lysine dendron. (c) Two proposed target molecules that can be easily synthesized (RGD) or are commercially available (FA) to make Janus-DMCs.

5.2 Effect of functional group position

Another important contribution of this thesis work is the discovery that the optical properties of the templating ring ligands of MCs are affected by the position of functional groups. This part of the work required the functionalization at the *para* and *meta* position of salicylhydroxamic acid derivatives, and their subsequent photophysical characterization. Functionalization was done with propargyl- and allyl-ether groups that were intended to be used

as thiol-active sites, but similar effects are expected from other functional groups appended to such ring positions. Absorbance spectroscopy and photophysical characterization of each of the MCs demonstrated an interesting trend based on functionalization position. The *para*-substituted MCs had high extinction coefficients, highly energetic singlet and triplet energies, and large energy differences between the singlet and triplet energies. With the *meta*-substituted MCs, the opposite was observed. The plot shown in Figure 5.1 illustrates the trend on singlet and triplet energy of LnGa₄ and Ln₂Ga₈ metallacrowns synthetically functionalized at the *meta*- or *para*-position (this work) and of previous metallacrowns prepared with commercially available ring ligands.

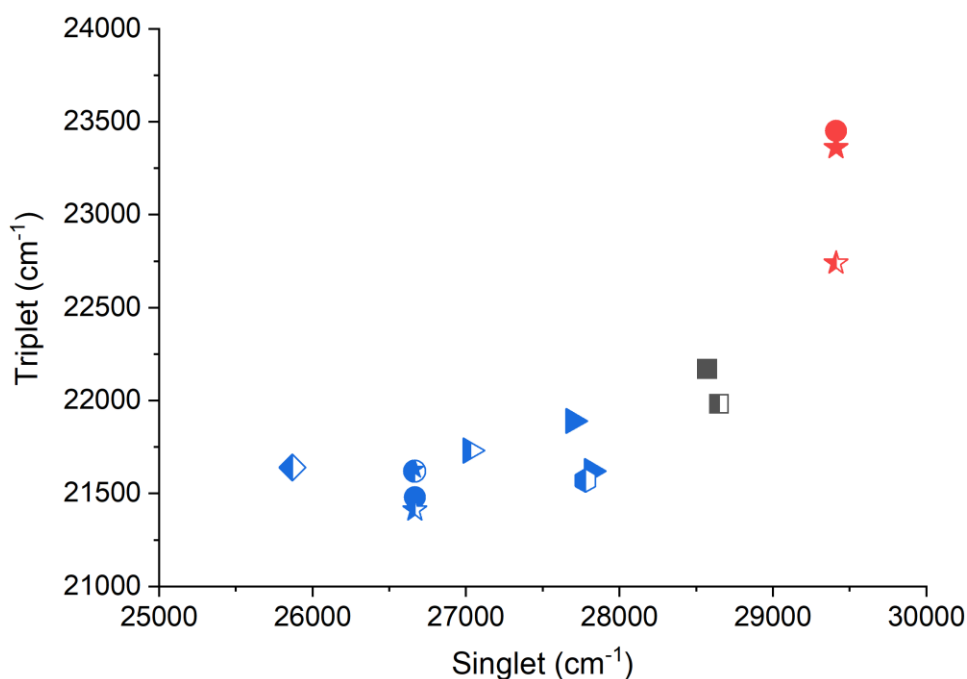


Figure 5.1 Plot of singlet vs. triplet energies of synthetically functionalized metallacrowns prepared for this thesis (GdGa₄*p*YneShi₄, GdGa₄*m*YneShi₄, GdGa₄*p*AlShi₄, GdGa₄*m*AlShi₄, Gd₂Ga₈*m*YneShi₈, Gd₂Ga₈*p*AlShi₈, Gd₂Ga₈*m*AlShi₈), and previously reported scaffolds (GdGa₄Shi₄, GdGa₄Cl-Shi₄, GdGa₄Br-Shi₄, Gd₂Ga₈Shi₈, Gd₂Ga₈I-Shi₈, Gd₂Ga₈MoShi₈, and Gd₂Ga₈MeShi₈)^{102,106,124,178} with appendages at the *para*- and *meta*-positions. *Para*-substituted MCs are in red, *meta*-substituted are in blue, and unsubstituted are in gray. LnGa₄ are depicted with filled symbols, while Ln₂Ga₈ scaffolds are half-filled. Legend: unsubstituted MCs with rectangles (Shi); propargyl-appended MCs with circles (*p/m*YeneShi); allyl-appended MCs with stars (*p/m*AlShi); halogenated-appended MCs with triangles (*x*-Shi); alkoxy-appended MC with a diamond (MoShi); and methyl-appended MC with a hexagon (MeShi).

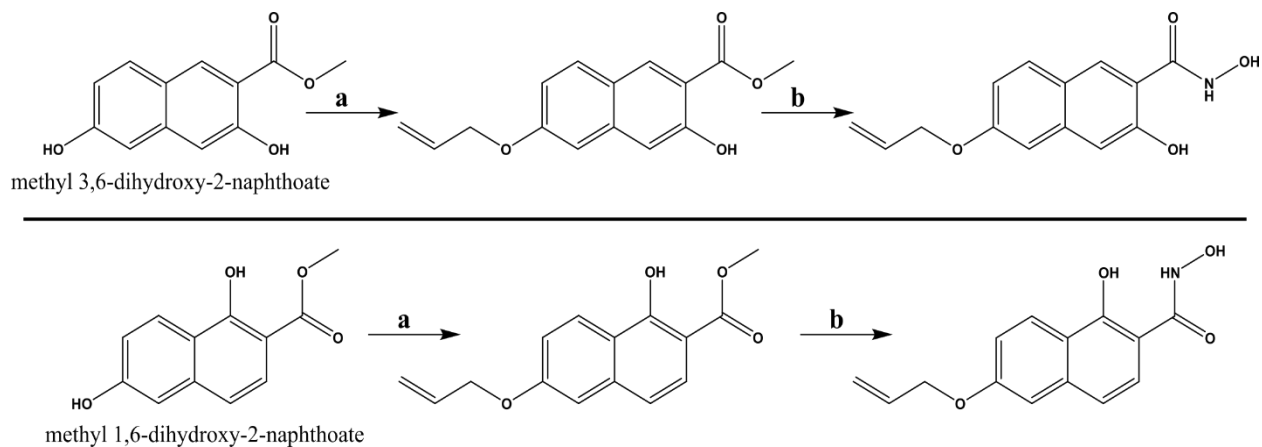
Serendipitously, MCs with functional groups (e.g., halogens, alkyls, alkoxy) have been mainly prepared with *meta*-substituted ring ligands. But now two well-defined trends can be defined based on the position of the appended groups on the ring ligands. The first is that *meta*-substitution influences the optical properties of MCs by having less energetic singlet and triplet

energies than the unsubstituted and *para*-substituted ring ligands. The second is that the singlet-triplet energy gaps are the most pronounced for the *para*-substituted and unsubstituted scaffolds, followed by the *meta*-halogenated, and with the *meta*-alkyl ether MCs having smallest energy gaps. These ligand-centric effects have important implications for the design of MCs as imaging probes and as luminescent materials as a whole. Therefore, if for a given application highly energetic triplet states and large extinction coefficients are desired, then functionalization at the *para*-position would yield the best optical results as long as high energy excitations are also not detrimental for such application. However, for imaging purposes, the *meta*-position should be pursued since lower energy excitations are less harmful to biological systems and also have deeper tissue penetration.¹⁷⁹ Unfortunately, dendron coupling at the *meta*-substituted MC cores was less effective than at the *para*-substituted cores. Thus, a better understanding of the electronic influences of the functionalization position on coupling reactivity might provide the necessary answers to fully exploit these optical trends.

Future work on DMC synthesis might include investigating the effects of ligand functionalization and photocatalytic addition reactivity. This will enable better utilization of the *meta*-substituted MCs as viable DMC cores. The light source wavelength, currently UV 365 nm, may be a critical factor in the observed reactivity trend. Thus, one approach might be to utilize a visible light photocatalytic approach for thiol-ene addition, which has been shown to work well with small molecule and polymer synthesis.^{183,184,202} Optimization of the reaction conditions and photoinitiator (radical initiator) of choice will be of utmost importance. Additionally, a shift from PAMAM dendrimers may be also necessary since amine groups are often used as co-photoinitiator during visible light photocatalytic reactions. Dendrimer families like the ones shown in Scheme 5.3 can be good alternatives to PAMAM, as they have no (or few) amine sites and are water soluble.

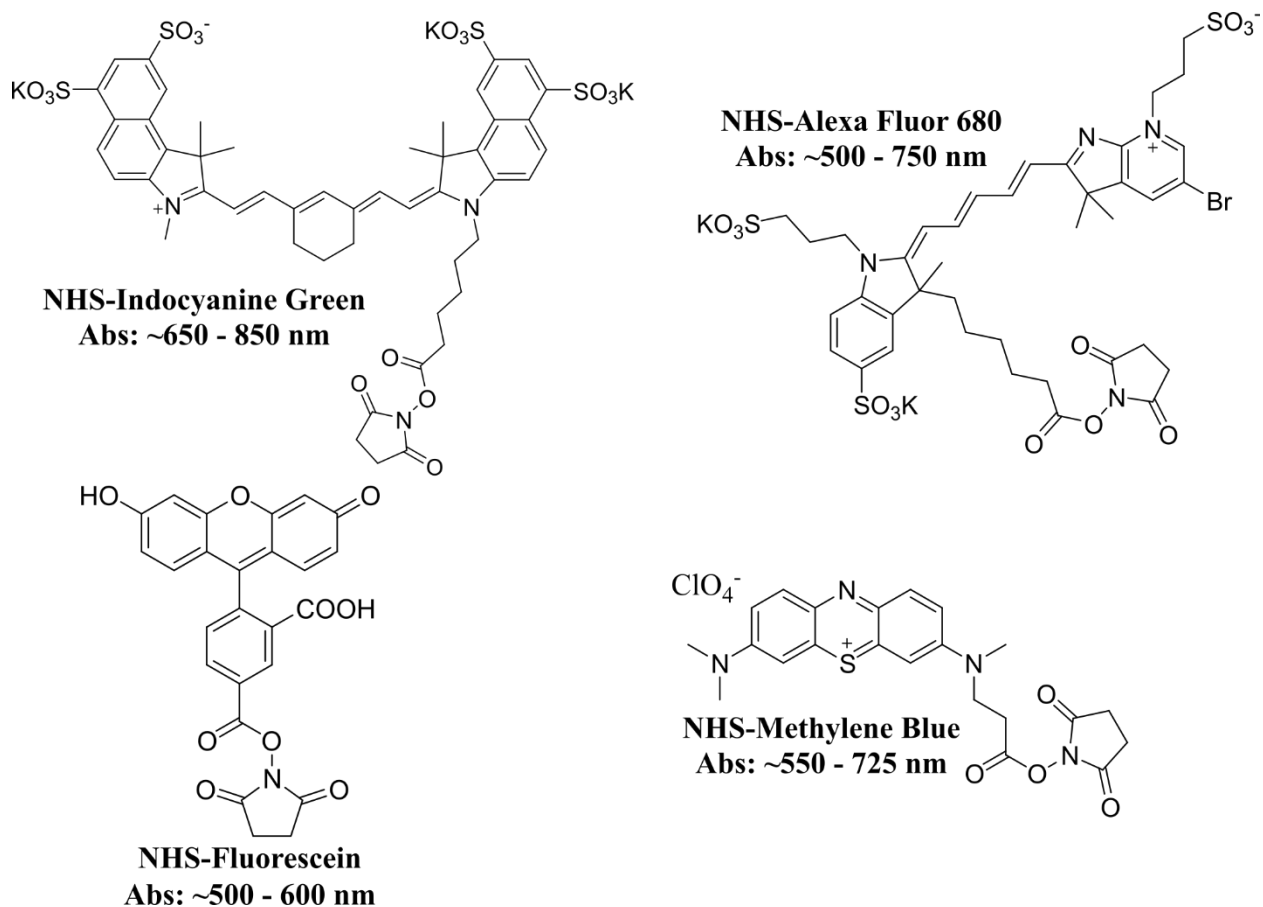
Another alternative to make DMCs with lower excitation energies is to functionalize more conjugated ring ligands at the *para*-position. Ln₂Ga₈ MCs have been previously prepared with 3-hydroxy-2-naphthalene hydroxamic acids (H₃nha) and exhibited excitation energies up to 430 nm (S*: 23300 and T*: 18150 cm⁻¹).¹¹⁹ Thus, naphthalene hydroxamic acid derivatives functionalized at the *para*-position could be prepared to redshift the absorbance of DMCs while also ensuring efficient dendron-coupling reactivity. Functionalization in such conjugated systems has not been investigated before, thus photophysical studies of a pre-dendron-coupled metallacrown will also

be necessary to ensure that the triplet and singlet energies are at favorable positions for effective Ln sensitization. Scheme 5.4 shows two commercially available naphthalene derivatives that could be synthetically modified to incorporate allyl-appendages for thiol-ene coupling in the same manner as was shown in Chapter 3.



Scheme 5.4 Synthetic plan to prepare *para*-substituted naphthalene hydroxamic acid derivatives with thiol-ene appendages. Reagents and conditions based on synthetic work in Chapter 3: (a) allyl bromide, potassium carbonate, acetone, and reflux; (b) hydroxylamine hydrochloride, potassium hydroxide, and methanol.

Potentially, even longer excitation wavelengths (>450 nm) could be pursued by coupling additional antennas to the ring or bridging ligands of Janus-DMCs with PAMAM dendrons on the orthogonal ligand position. Commercially available antennas, like the ones shown on Scheme 5.5, could be functionalized to have thiol-focal points in a similar fashion as thiol-biotin (Chapter 4). If coupled to the ring ligands, it would be insightful to investigate if the ligand position (*para* vs. *meta*) has an effect on the energy absorbance and transfer of the antenna to the MC. On the other hand, if coupled to the bridging ligands, adequate energy transfer would need to be confirmed through extensive photophysical characterization. Finally, synthetic investigation of the optimal Janus-DMC coupling configuration (ring vs. bridge), as well as on the optimal number of coupled-antennas per MC core, will be required to ensure efficient preparation and luminescent sensitization.



Scheme 5.5 Potential antennas that could be appended to the ring or bridging ligands of Janus-DMC to lower the overall excitation energy.

5.3 Enhancement of luminescence

A third contribution of this thesis work was the enhancement of the luminescent properties (i.e., longer luminescent lifetimes and higher quantum yields) of MCs through the addition of dendritic shells. This was observable through the photophysical characterization of each DMC (toroidal, hyperboloidal, and asymmetric), which demonstrated that after the incorporation of dendrons, quantum yield values increased significantly compared to each of the MC cores alone. Additionally, in all cases (except with the Janus-DMC), the DMCs had better quantum yield and longer lifetimes in DMSO than any other Yb^{III}-based MC previously reported, as seen in Table 5.1.

It was also observed that, when comparing each of the three classes of DMC prepared with G1.0 PAMAM dendrons coupled at different ligand positions, the quantum yields decreased with increasing number of dendrons. Dendron size (i.e., generation) had a similar effect on the quantum

yield of Toroidal-DMCs. This behavior was attributed to the better encapsulation of solvent molecules by the DMCs with increasing number of couplings or generation size (i.e., toroidal-DMC = 4, hyperboloidal-DMC = 8, and Janus-DMC = 12). Therefore, through the photophysical analysis performed in this thesis work, it was confirmed that dendrimeric metallacrowns are capable of both exploiting and enhancing the optical properties of metallacrowns, which makes DMCs a new class of intrinsically luminescent metallodendrimers. Furthermore, based on the photophysical data, in terms of quantum yield alone toroidal-DMCs would make the best luminescent probes (Figure 5.2a). On the other hand, in terms of luminescent intensity (brightness) which is the product of quantum yield and extinction coefficient, Janus-DMC would be superior (Figure 5.2b). Thus, future work must take into consideration the observed dependence that DMC configuration (i.e., toroidal vs. hyperboloidal vs. Janus) has on the overall optical parameters of the scaffolds when designing new DMCs as luminescent probes.

Table 5.1 Luminescent parameters of Yb^{III}-based MCs and DMCs collected under ligand excitation (ϕ_{Ln}^L).

Compound	Solvent	Lifetime ^a [μ s]	ϕ_{Yb}^L ^b [%]	Brightness [x10 ⁴]
YbGa ₄ Shi ₄	DMSO	24(1)	2.2(1)	--
Yb ₂ Ga ₈ Shi ₈ Ip ₄	DMSO	60.9(4)	7.56(3)	30.2
Yb₂Ga₈Shi₈Mip₄	DMSO	45.3(9)	2.78(6)	11.4
Yb ₂ Ga ₈ Shi ₈ Mip ₄ G0.5	DMSO	62.3(4)	7.03(1)	28.8
Yb ₂ Ga ₈ Shi ₈ Mip ₄ G1.0	DMSO	63.8(8)	9.38(2)	38.5
Yb ₂ Ga ₈ Shi ₈ Mip ₄ G1.5	DMSO	62.9(3)	9.02(8)	37.0
Yb ₂ Ga ₈ Shi ₈ Mip ₄ G2.0	DMSO	63.6(4)	8.73(8)	35.8
Yb₂Ga_{8p}AlShi₈	DMSO	49.9(7)	7.75(1)	29.5
Yb ₂ Ga _{8p} AlShi ₈ Ip ₄ G1.0	DMSO	69.2(3)	8.7(2)	33.1
Yb₂Ga_{8p}AlShi₈Mip₄	DMSO	52.5(9)	4.96(6)	43.2
Yb ₂ Ga _{8p} AlShi ₈ Mip ₄ (G1.0) ₄ (Bt) ₈	DMSO	61.5(2)	7.41(5)	64.5
Yb₂Ga_{8m}YneShi₈Mip₄	DMSO	65.1(8)	3.63(5)	16.0
Yb ₂ Ga _{8m} YneShi ₈ Mip ₄ G1.0	DMSO	64(2)	8.77(7)	38.6
Yb ₂ Ga _{8m} YneShi ₈ Mip ₄ G1.0 -OH	DMSO	66(2)	8.83(8)	38.9
Yb ₂ Ga _{8m} YneShi ₈ Mip ₄ G1.5	DMSO	63(1)	8.18(4)	36.0

Each of the MC and DMC classes/families are highlighted in different colors, with the standard Ga-MCs in yellow, Toroidal-DMCs in blue, Hyperboloidal-DMC in green, Janus-DMC in purple, and redshifted-DMCs in orange. MC-cores of each DMC class are bolded. ^a Under excitation at 355 nm. ^b Under excitation at 320-360 nm.

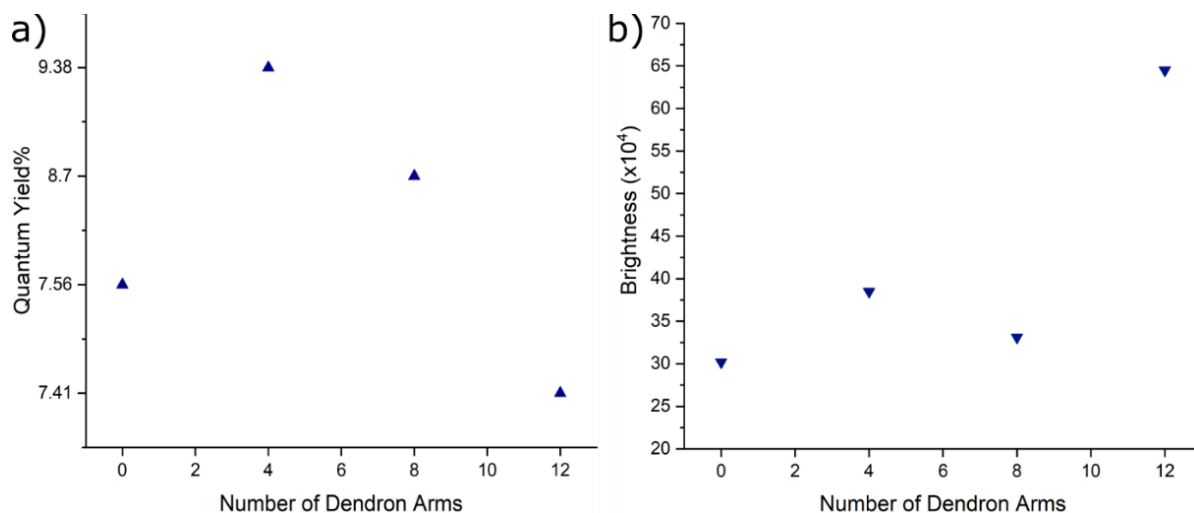


Figure 5.2 Plots showing dependence of DMC configuration on quantum yield (a) and brightness (b). $\text{Yb}_2\text{Ga}_8\text{Shi}_8\text{Ip}_4$ represents a MC with zero dendron arms and with no ring/bridge functionalization, Toroidal-DMC has four dendron arms, Hyperboloidal-DMC has eight dendron arms, and Janus-DMC has twelve dendron arms. Data used to make both plots was collected in DMSO solutions and with G1.0 PAMAM DMCs only.

It is also worthwhile to give a brief comparison of the DMCs studied in this thesis with existing luminescent probes. In particular, a comparison can be made to organic- and other lanthanide-based probes. For the sake of this discussion, only complexes with NIR emissions are considered. Organic luminescent probes tend to be relatively small, have high extinction coefficients, and can display high solubility and stability in aqueous environments. However, they are not photostable, tend to have short luminescent lifetimes, and have narrow Stokes shifts. DMCs, on the other hand, have the enhanced photostability and optical properties of their Ln^{III} -based MC cores, and have the capability of undergoing synthetic functionalization at the MC core or at the dendritic shell, which offers the possibility of developing multimodal compounds. As for other Ln^{III} -based luminescent probes, such as cyclam- or porphyrin-based complexes, they have been shown to be able to sensitize lanthanide ion luminescence, and in many cases also have high water solubility. However, their preparation and synthetic modification are often difficult and tend to have relatively low yields. Furthermore, the same cyclam or porphyrin scaffold is almost never able to sensitize a broad range of Ln^{III} -ions, and tend to have multiple vibrational oscillators at close proximity to the metal ion center that significantly decrease the overall quantum yields of the scaffolds. On the contrary, the MC-core of DMCs has no vibrational oscillators at close proximity to the Ln^{III} -ions, and the dendritic shell further protects the core from non-radiative quenching by solvents molecules. In addition, both MCs and DMCs can withstand more

sophisticated synthetic functionalization without affecting their luminescent properties. Below in Table 5.2 are shown some examples of NIR-emitting luminescent probes reported in the past few years with notable photophysical properties. It is important to keep in mind that due to the differences in measurement methodology of the quantum yields (absolute method using a integration sphere and comparative method using a known luminescent standard),^{131,156} and the dissimilarities in solvent systems, a direct comparison of DMCs to each of these scaffolds cannot be made. However, it does offer a good overview of the fact that DMCs are competitive luminescent probes (Table 5.1) not only due to their photophysical properties but also due to their better functionalization potential and ability to further exploit the properties of the dendritic shell.

Table 5.2 List of NIR-emitting probes reported in the past five years with attractive photophysical properties and investigated for cell imaging.

Compound	Solvent	Lifetime	Quantum Yield [%]	Extinction coefficient [$M^{-1}cm^{-1}$]	Brightness
Indocyanine Green ^{203,204}	DMSO	1.11 ns	12	4.1×10^4	49×10^4
Methylene Blue ²⁰⁵	DMSO	--	80	6.7×10^4	540×10^4
Alexa Fluor 680	PBS Buffer	1.2 ns	23	22×10^4	506×10^4
AIEgen10 (HL3) ²⁰⁶	Water	--	11.7	0.93×10^4	10.9×10^4
F ₁₅ TPPYb-H (Yb-2) ²⁰⁷	DMSO	20.2 μ s	3.5	--	--
[Yb(dppz)(ttfa) ₃] (Yb-4)	Water:DMF (98:2)	15.7 μ s	0.107	6.8×10^4	0.7×10^4
PAN-DOTA(Yb) ²⁰⁸	DMSO	--	0.054	--	--

5.4 Cellular uptake

Lastly, through this work it was demonstrated that cellular uptake of DMCs was dependent on the dendron surface, ring hydrophobicity, self-aggregation behavior and the overall water solubility of the complex. This conclusion was reached by performing cell studies with toroidal- and redshifted-DMCs of different generations. Cell studies performed with toroidal-DMCs suggested that the surface groups have a strong influence on their cell uptake, with the G1.0 DMCs (with -NH₂ groups at the surface) being internalized by HeLa cells, while G0.5- and G1.5-DMCs

(with -OMe groups at the surface) only bind to the cell membrane. By comparison, cell studies with G1.0 and G1.5 redshifted-DMCs showed no observable internalization even with dendrons with -OH or -NH₂ surfaces, and such behavior was attributed to the more hydrophobic *mYneShi* templating ring ligands. Furthermore, in all cases a degree of sample aggregation at the cell membrane was observed. Through dynamic light scattering (DLS) characterization in both DMSO and H₂O/DMSO (99:1 v/v%) solutions, it was determined that aggregation behavior of DMCs is solvent dependent, with a larger degree of aggregation observed in the more aqueous solutions. It was also observed that in H₂O/DMSO, DMCs with -OMe surface groups had the least degree of aggregation, compared to DMCs with -NH₂ or -OH surface groups. Thus, these results and the cell images suggest that G1.0 DMCs undergo self-aggregation in solution, while G1.5/G0.5 aggregate at the cell surfaces. Lastly, no cell studies would have been possible without the increased solubility in aqueous solutions that the dendric shell offered to the MC core.

Altogether these findings have four major implications for the design and application of DMCs as viable imaging agents. First, self-aggregation will hinder cell uptake by creating particles that are too large for effective cell internalization. Second, incompatible surfaces will promote aggregation at the cell surface and inhibit uptake. Third, ring hydrophobicity will hinder cell uptake even with surfaces that are compatible with the cell membrane. And fourth, water solubility and stability of DMCs are a key parameters for cell studies. Therefore, through cell studies and DLS experiments done for this thesis, factors that control the effectiveness of DMCs as imaging agents were determined.

Future work may require a better understanding of the mechanism of self-aggregation of DMCs in more aqueous environments, and how to mitigate it without compromising effective cell uptake. This will likely involve more comprehensive DLS studies to look at the degree of self-aggregation as a function of DMC concentration and shape, temperature, pH, and cell medium to offer a better insight into DMC behavior during cell incubation and to optimize cell study parameters. A synthetic approach that can be explored to reduce self-aggregation and increase cell uptake would be the preparation of Janus-DMCs with, for example, G1.5 and G1.0 PAMAM dendrons appended orthogonally. The G1.0 dendrons would ensure surface compatibility at the cell membrane for effective internalization, while the G1.5 dendrons would help mitigate the self-aggregation in solution. Similarly, CPP such as RGD (Scheme 5.3b) could be appended orthogonally to G1.5 dendrons in a Janus-DMC for the same purpose. Investigation of the optimal

configuration (i.e., G1.5 appended at the bridges or at the rings) will be also required. Additionally, these Janus-DMC examples might also mitigate the hindering effects of hydrophobic ring ligands by effective coupling of dendrons or targeted molecules at the ring appendages. As mentioned earlier, for optimal imaging potential *meta*-substituted ring ligands or the proposed *para*-substituted naphthalene ring ligands (Scheme 5.4) should be employed as the templating ligands for the MC cores of the proposed Janus-DMCs.

5.5 Summary

This thesis has described the development of intrinsically luminescent dendrimeric metallacrowns by exploiting the functionalization potential of the templating ligands of lanthanide-based metallacrowns. Previous work on luminescent MCs has mainly focused on the enhancement of their optical properties (e.g., absorbance redshifting or higher number of antennas) that required minimal or no synthetic modification of the templating ligands. With this thesis, it was shown that common organic synthesis protocols such as the Williamson ether synthesis, or more sophisticated synthetic approaches such as photocatalyzed thiol-ene coupling, can be used to expand the functionalization of MCs. This work additionally clarified the requirements for the careful design of synthetic protocols for ligand preparation and metallacrown functionalization, while also highlighting the relationship between synthetic modification and overall optical properties of MCs.

From this work, dendrimeric metallacrowns have been established as a new class of metallodendrimers that combines the properties of both metallacrowns and dendrimers. For the dendrimer field, the benefit of having an intrinsically luminescent core means that further functionalization with organic chromophores is no longer necessary. Additionally, the Ln^{III}-based luminescence of the MC core also offers higher photostability and a variety of emission wavelengths in both the visible and NIR. For metallacrowns, the addition of a dendritic shell has both improved their water solubility and stability, as well as enhanced their luminescent properties. Thus, combining the fields of dendrimers and metallacrowns has resulted in the creation of dendritic compounds with intrinsic luminescent behavior and with the highest Yb^{III} quantum yields among MCs and NIR emitters. Furthermore, it has opened up the door to the development of a wide range of compounds due to the variety of dendrimer families and the numerous MCs that can be functionalized to be the core of dendrimers. In this way, this thesis has only scratched the

surface of what type of dendrimeric metallacrowns can be prepared and their applications as luminescent probes.

In conclusion, this thesis yielded thirteen new metallacrown scaffolds capable of undergoing thiol addition at both or either ligand position, four new classes of luminescent dendrimeric metallacrowns (toroidal-, hyperboloidal, symmetrical, and Janus-DMCs), and a better understanding of the synthetic requirements for modifying metallacrowns to expand their application as imaging probes.

Appendices

Appendix A Supplemental Information for Chapter 2

¹H NMR Spectra *Bridge ligand NMRs:*

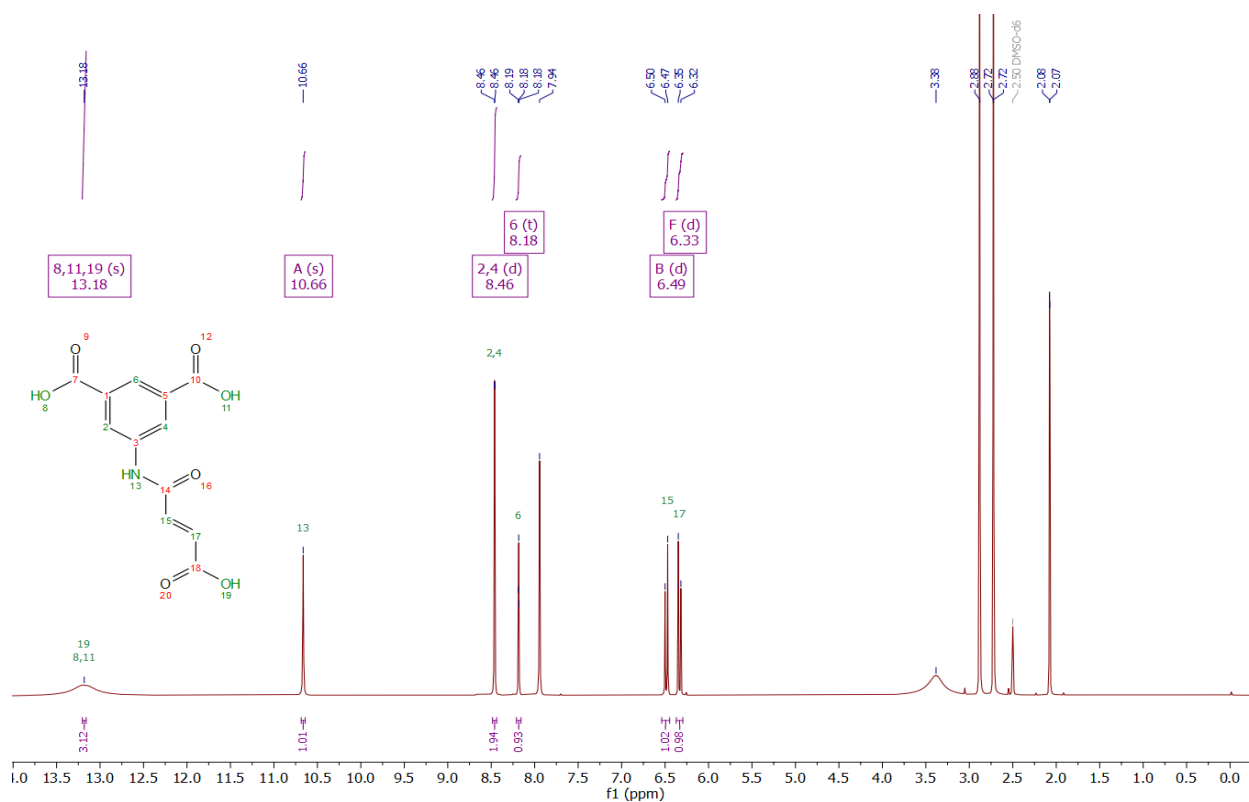


Figure A1 ¹H NMR spectrum of 5-(3-carboxylacrylamide)isophthalic acid. Unlabeled peaks are left over solvent molecule, such as acetone, DMF, and water.

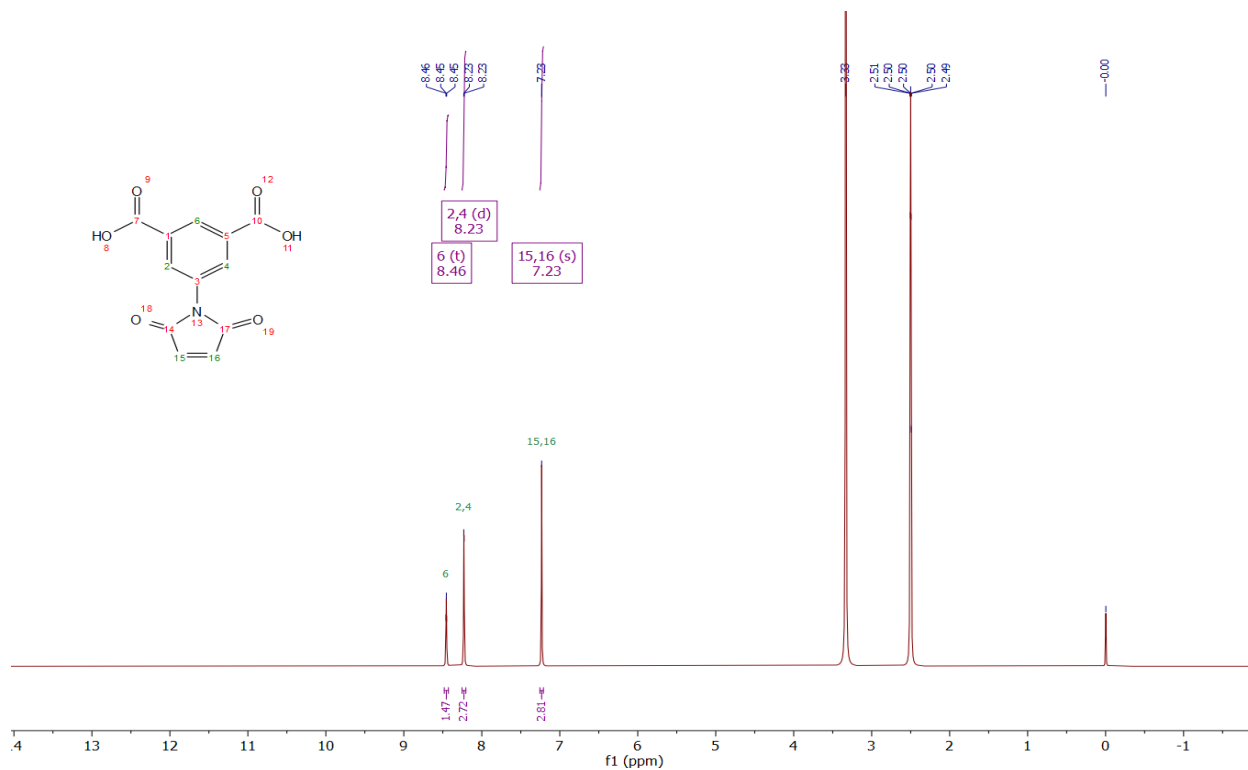


Figure A2 ^1H NMR spectrum of 5-maleimideisophthalic acid. Unlabeled peaks are left over solvent molecule, such as water.

Metallacrown NMR

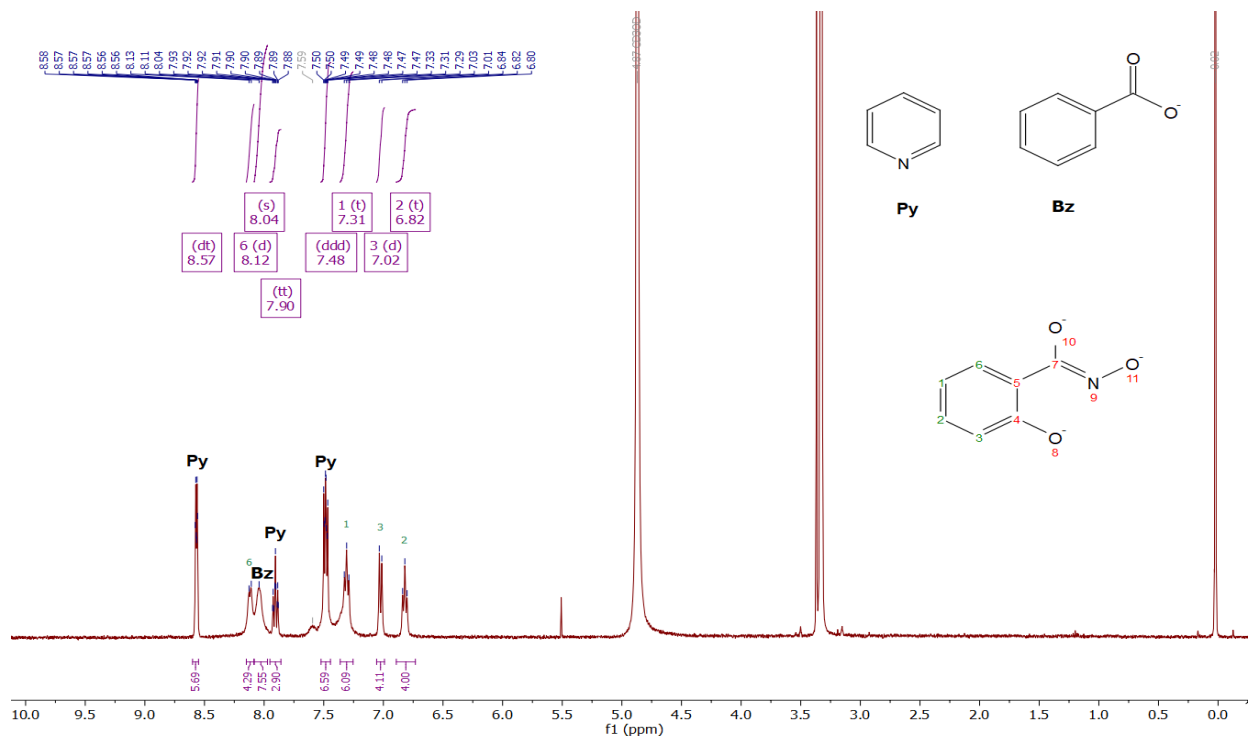


Figure A3 ^1H NMR spectrum of $\text{YbGa}_4\text{Shi}_4(\text{benzoate})_4$. Labeled peaks are from ring ligand. Pyridine and benzoate peaks labeled separately. Unlabeled peaks are solvents.

Trityl-protected dendron NMRs:

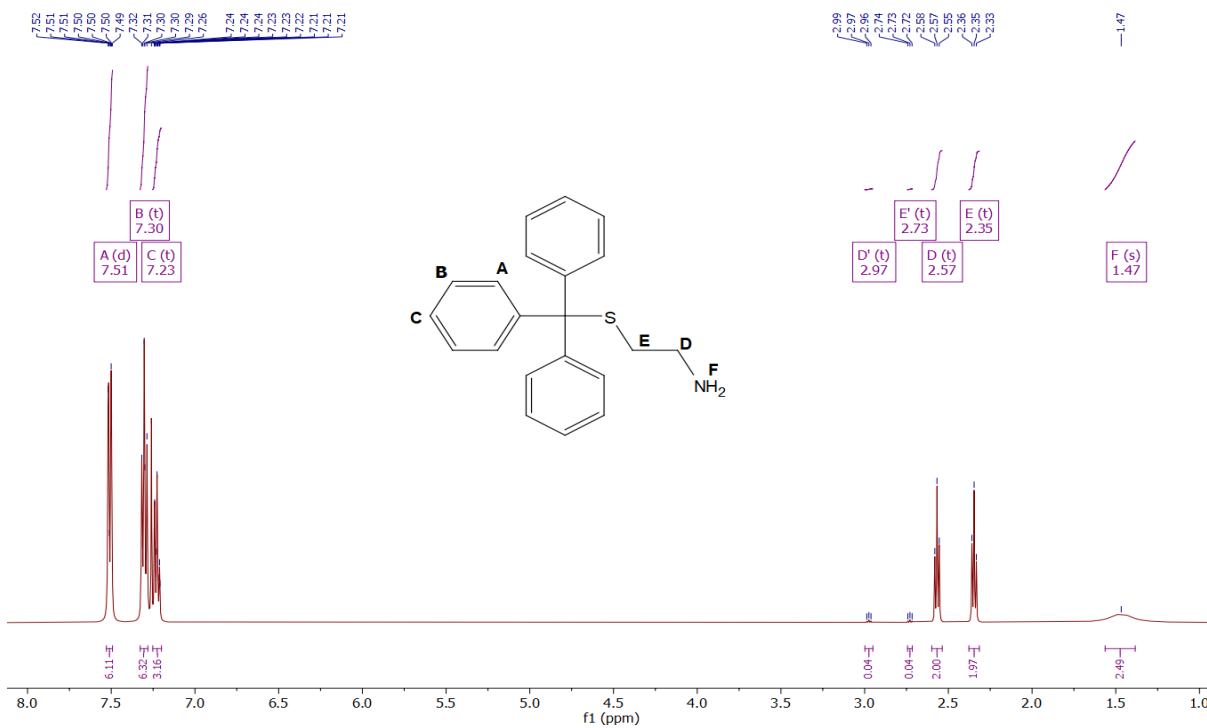


Figure A4 ¹H NMR spectrum of **1**. Small impurity peaks at 2.73 ppm and 2.97 ppm are from cystamine byproduct (~2%).

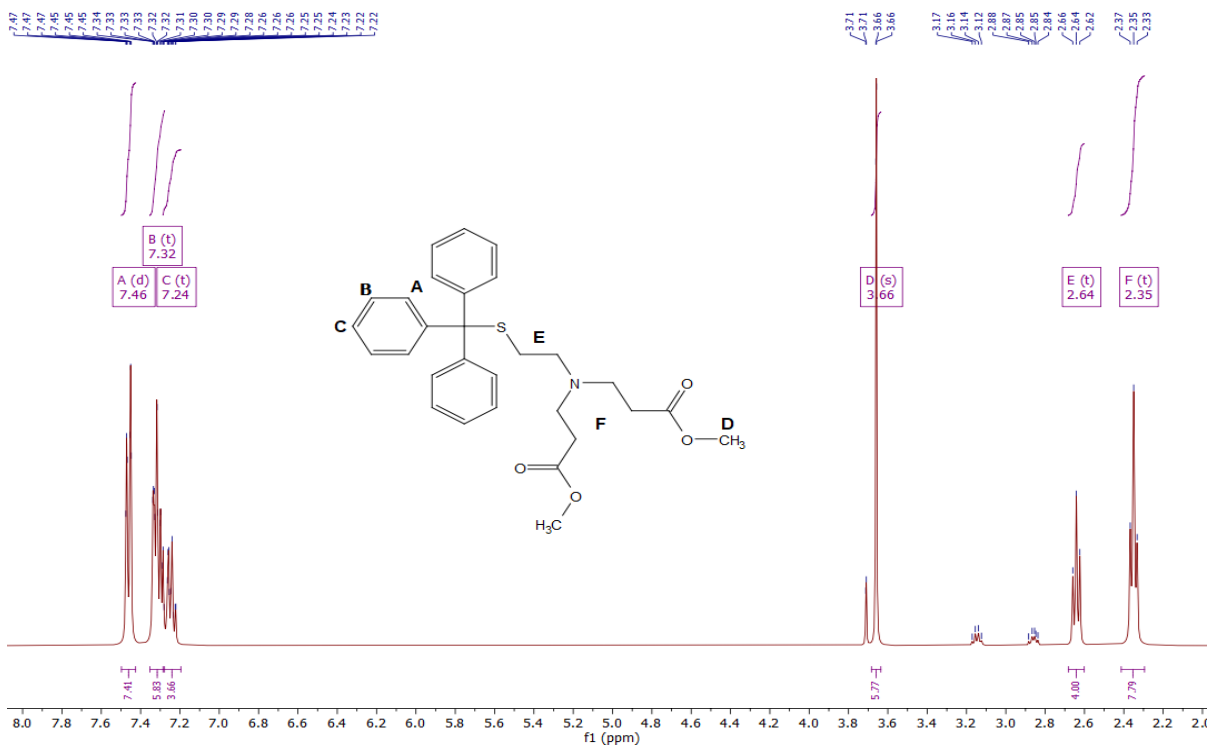


Figure A5 ¹H NMR spectrum of **2**. Small impurity peaks at 2.80-3.20 ppm and 3.70 ppm are from disulfide byproduct (~5%).

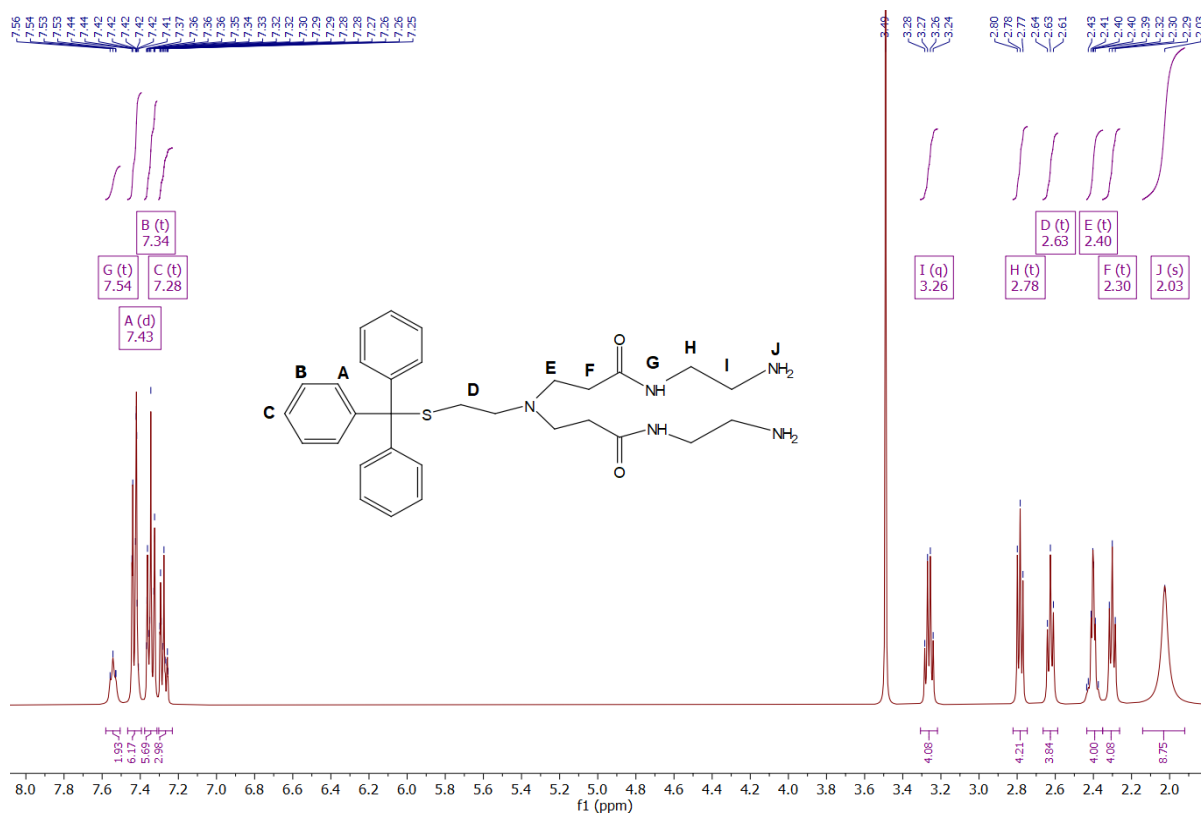


Figure A6 ^1H NMR spectrum of 3.

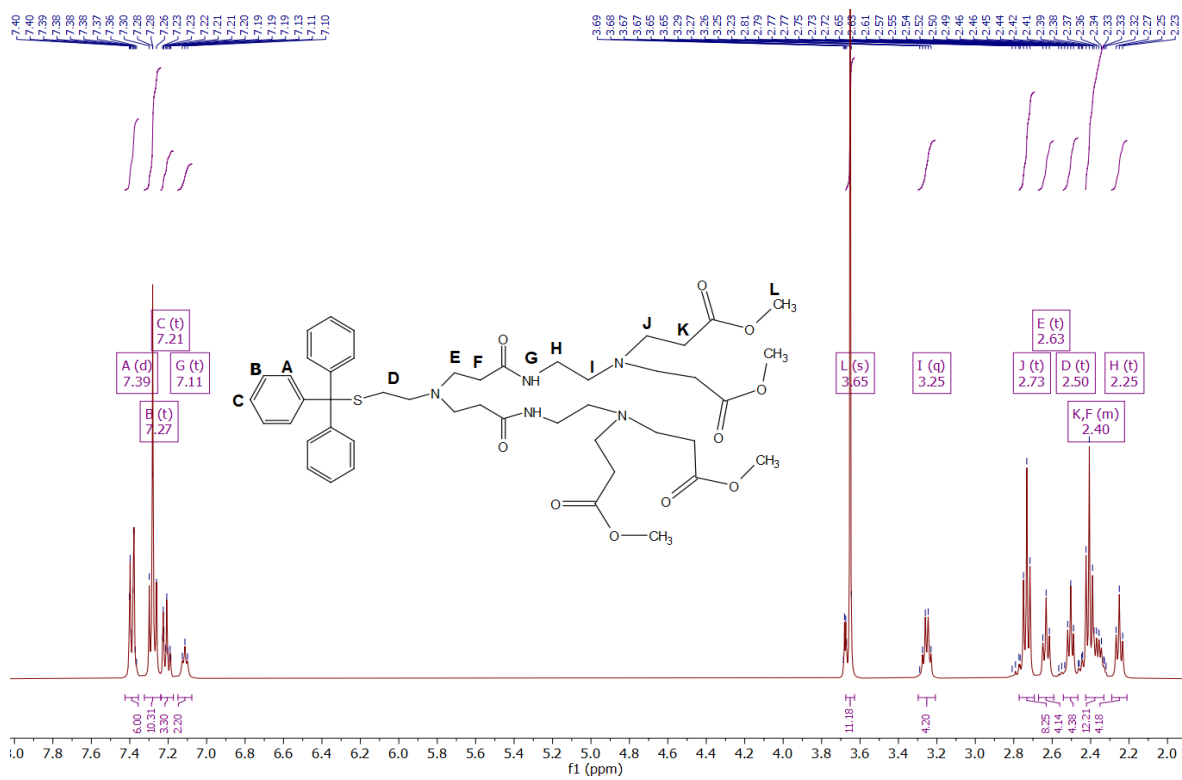


Figure A7 ^1H NMR spectrum of 4.

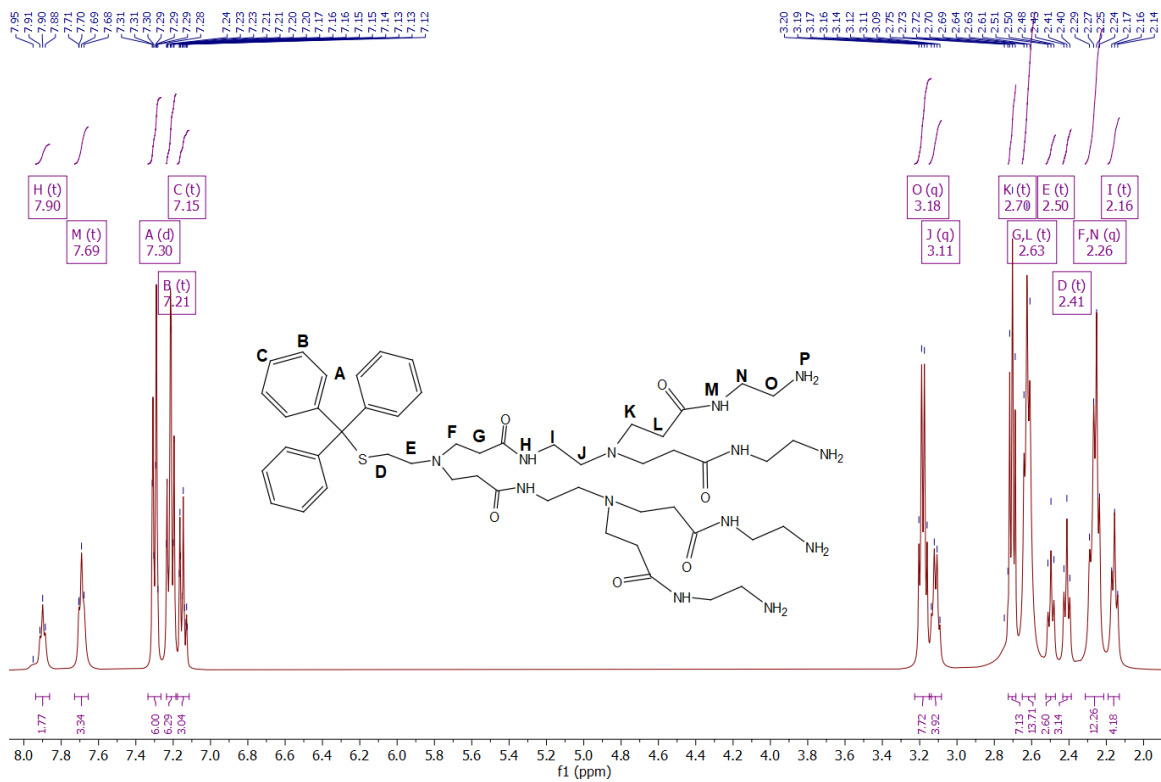


Figure A8 ¹H NMR spectrum of **5**.

Deprotected HS-Dendron NMRs:

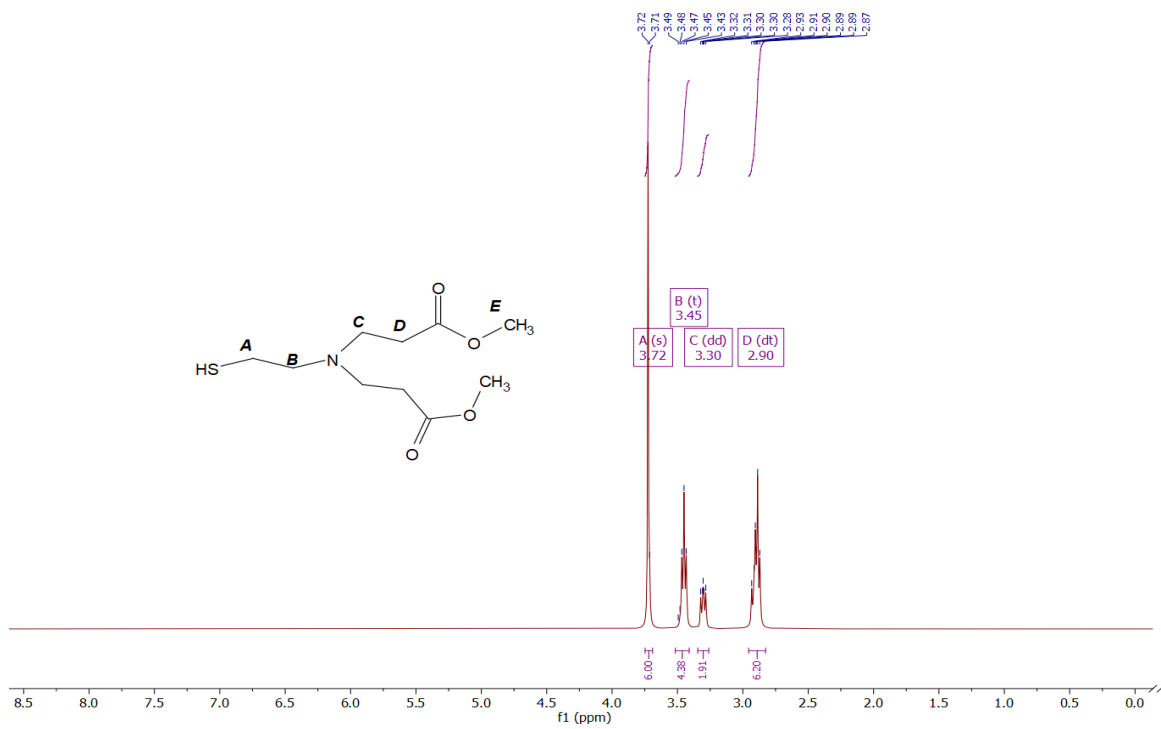


Figure A9 ¹H NMR spectra of deprotected **6**.

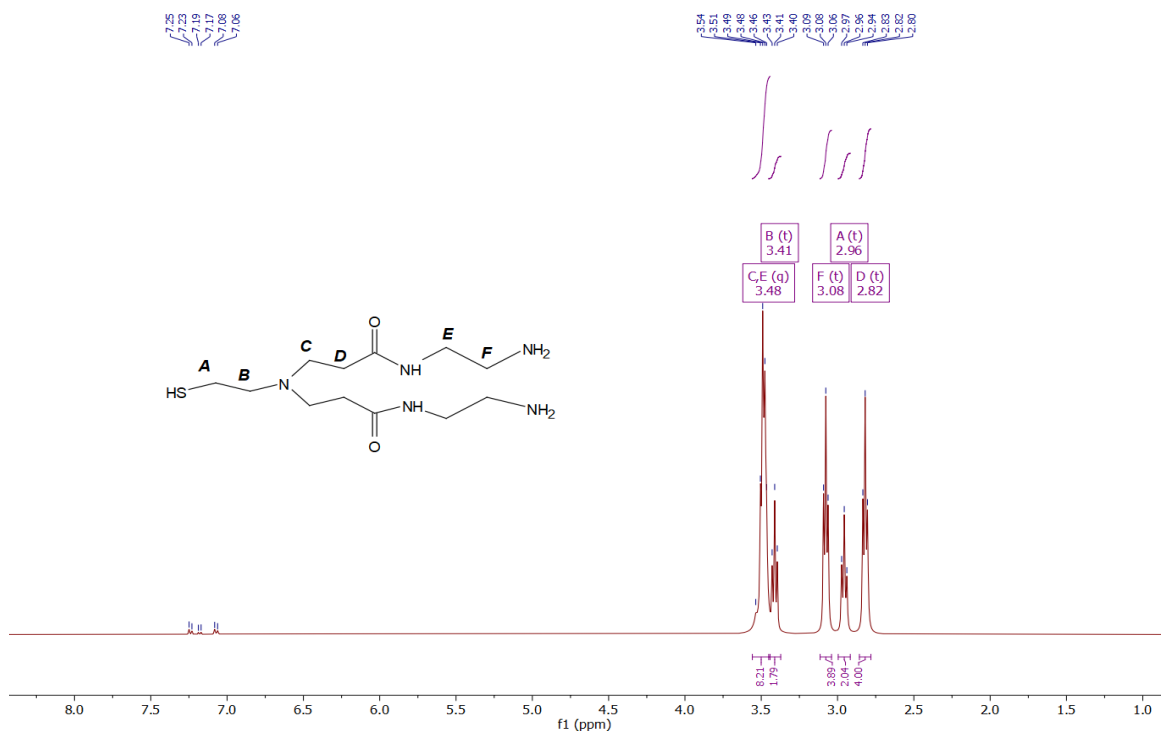


Figure A10 ^1H NMR spectra of deprotected **7**. Left over trityl salt seen between 7.00-7.50 ppm accounts for $\leq 1\%$.

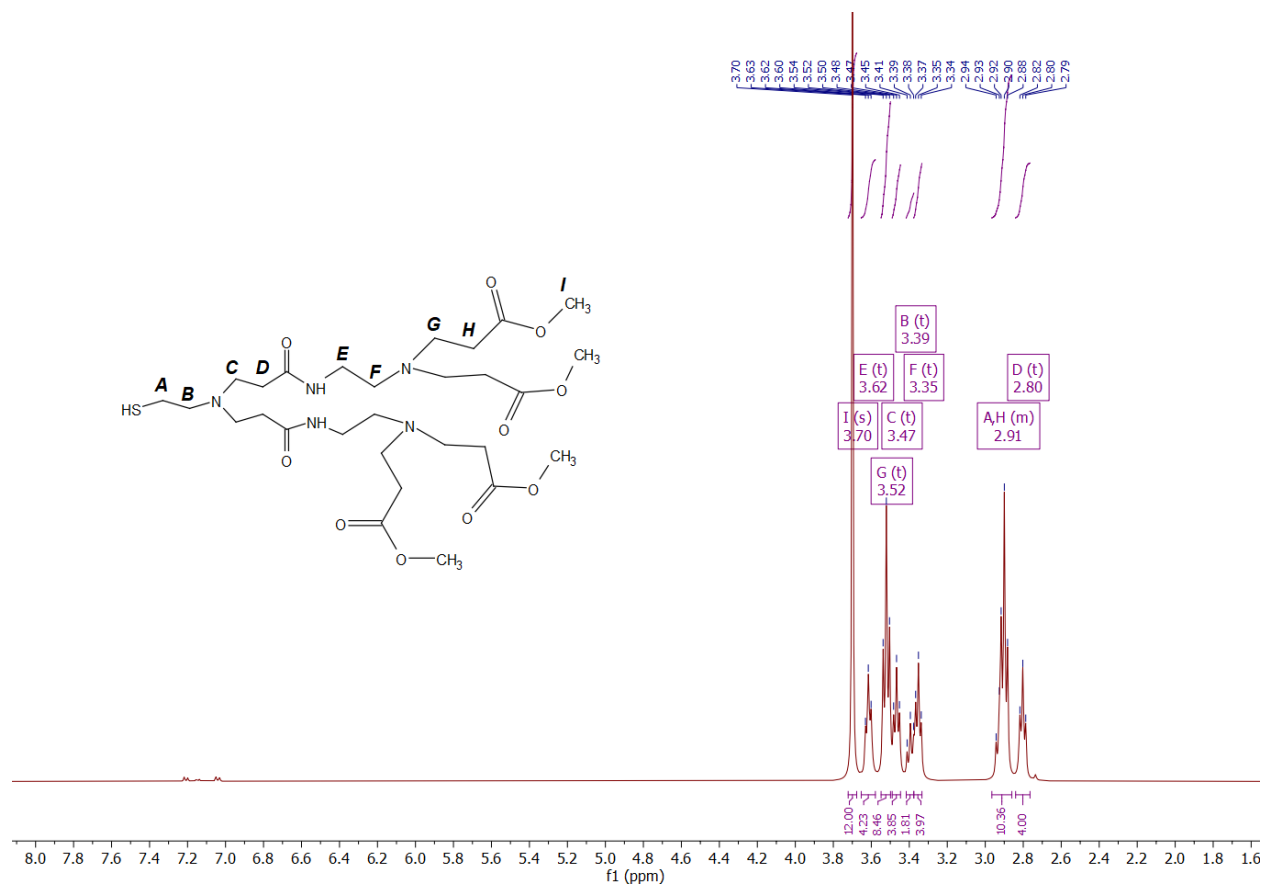
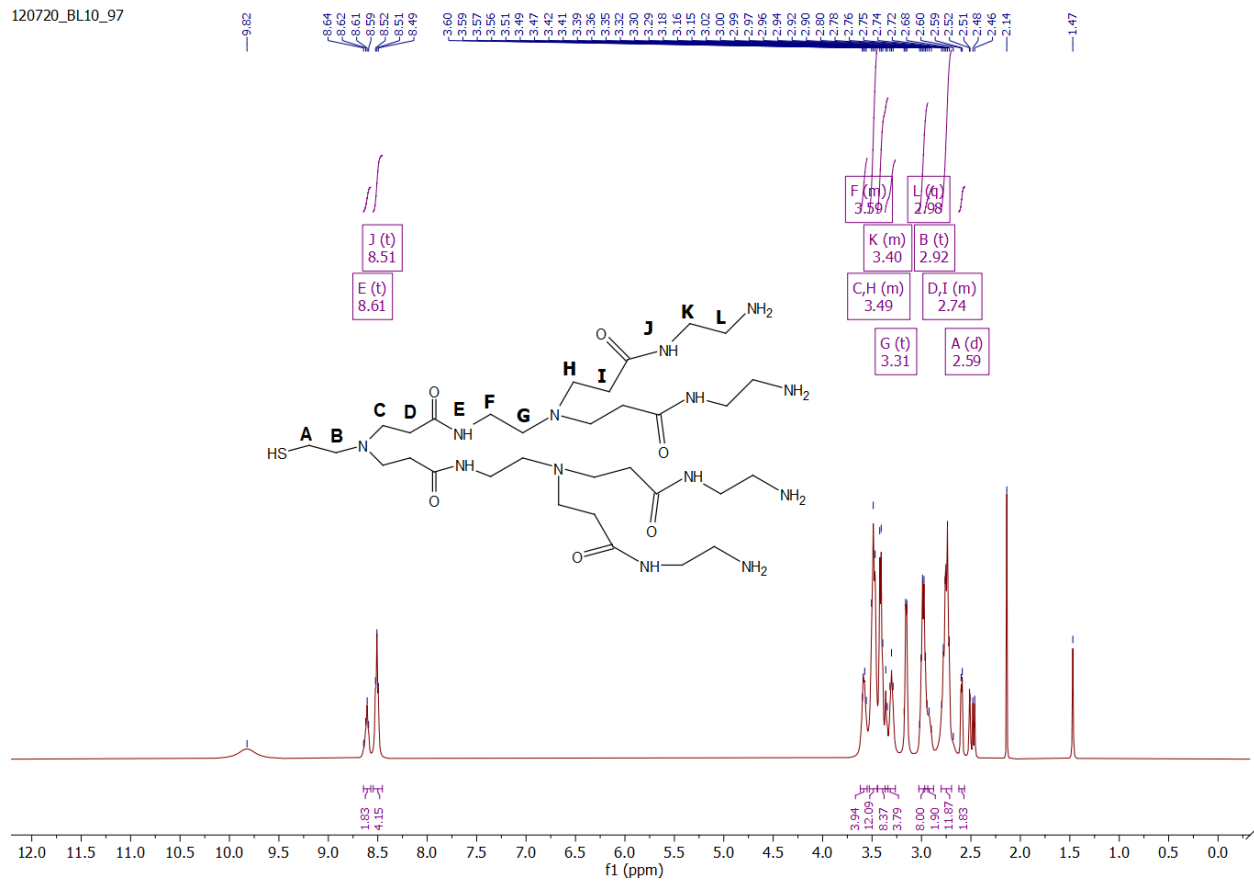


Figure A11 ^1H NMR spectra of deprotected **8**. Left over trityl salt seen between 7.00-7.50 ppm accounts for $\leq 1\%$.

Figure A12 ^1H NMR spectra of deprotected **9**.

ESI-MS Spectrum

LnGa₄Shi₄(benzoate)₄ MC ESI-MS:

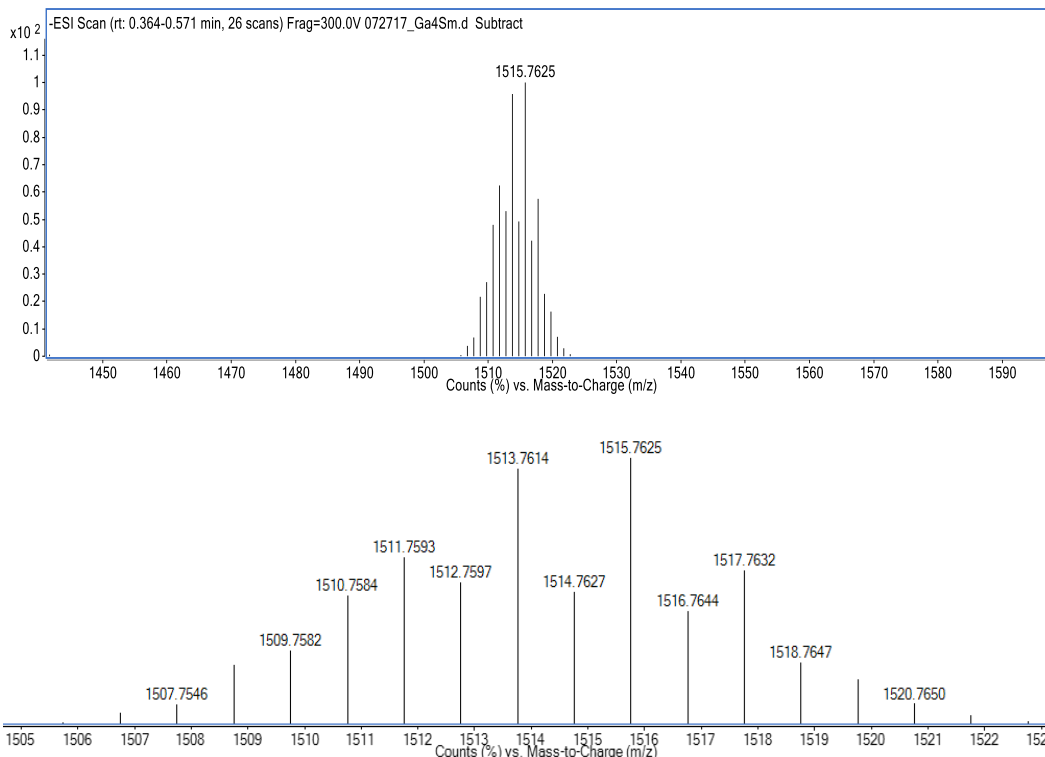


Figure A13 (Top) ESI-MS of SmGa₄Shi₄(benzoate)₄ metallacrown in negative ion. (Bottom) -1 isotopic distribution.

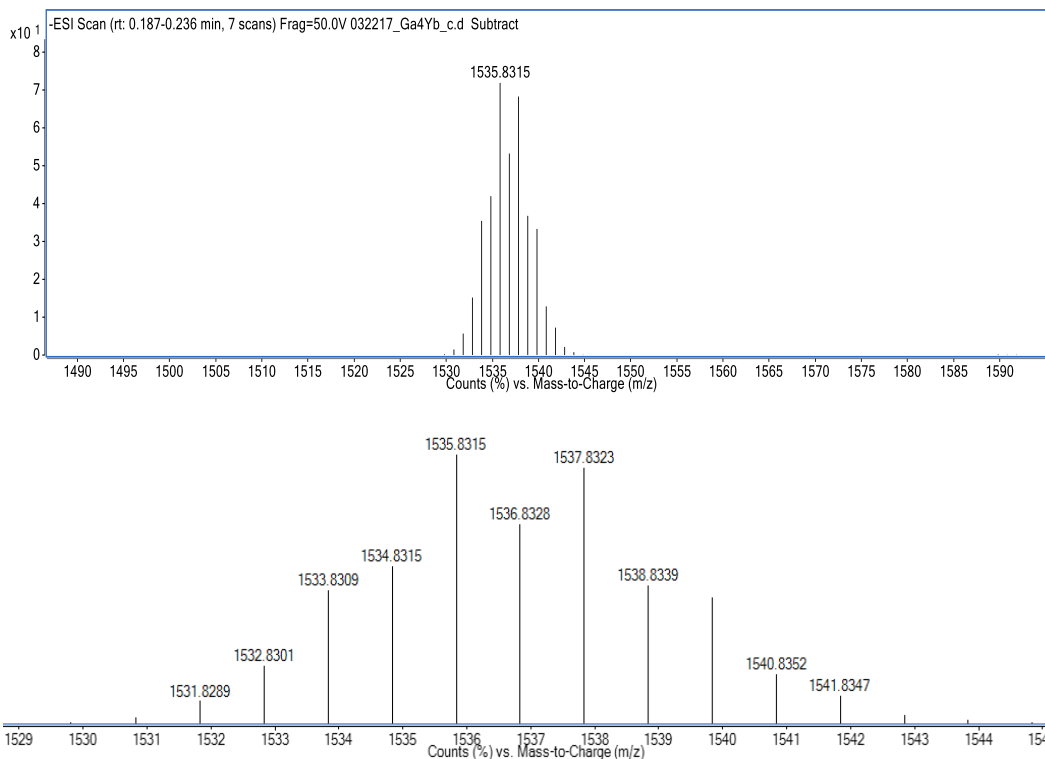


Figure A14 (Top) ESI-MS of YbGa₄Shi₄(benzoate)₄ metallacrown in negative ion. (Bottom) -1 isotopic distribution.

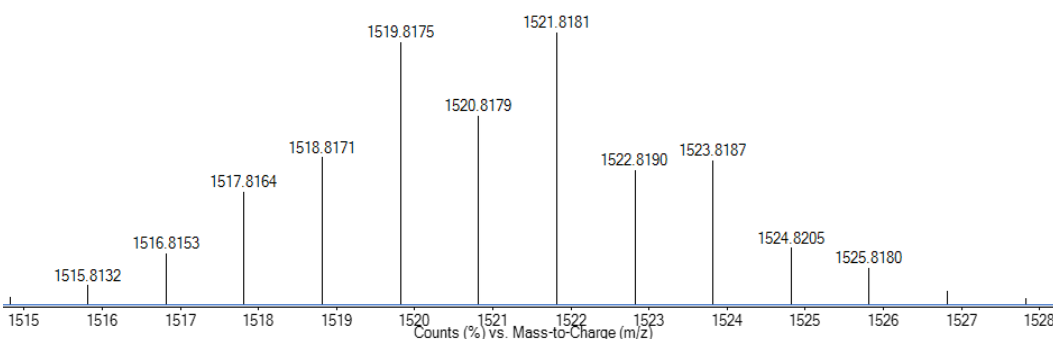
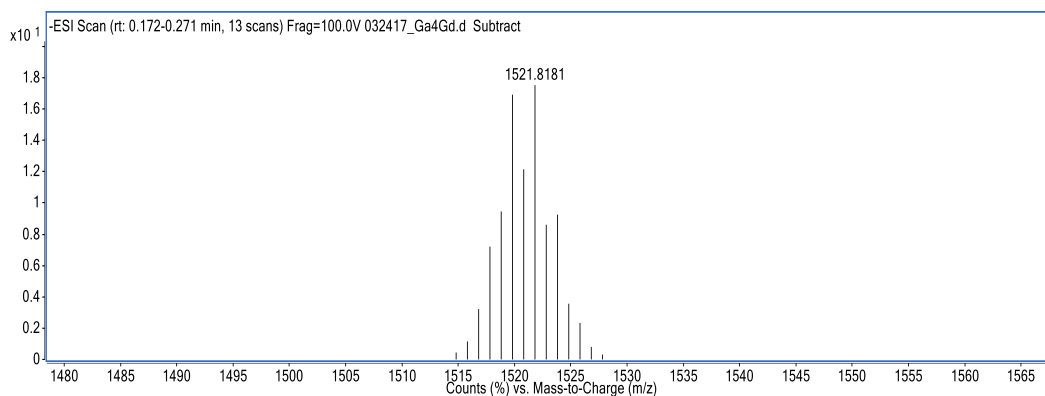


Figure A15 (Top) ESI-MS of GdGa₄Shi₄(benzoate)₄ metallacrown in negative ion. (Bottom) -1 isotopic distribution.

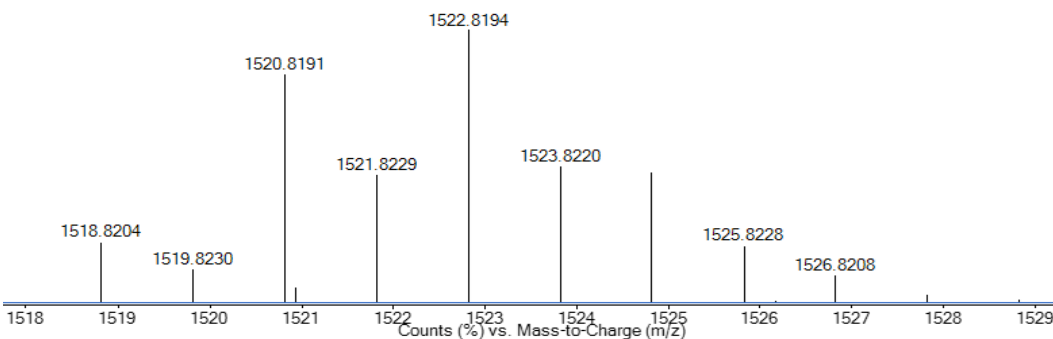
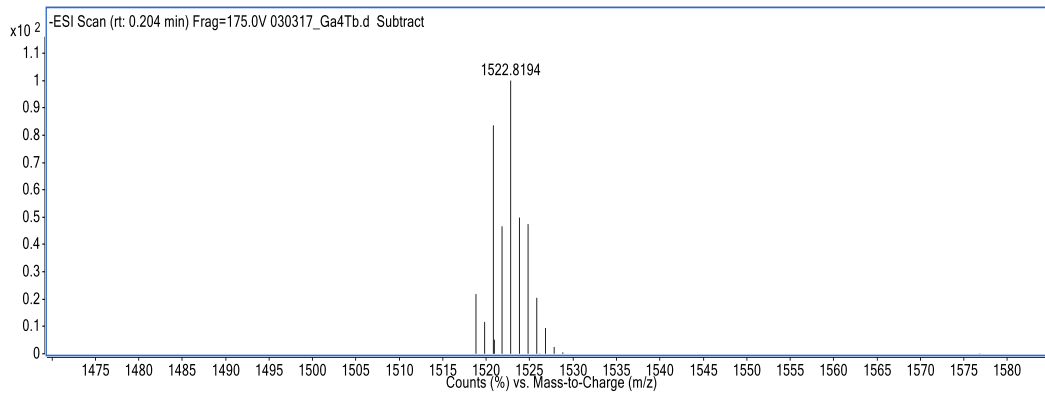
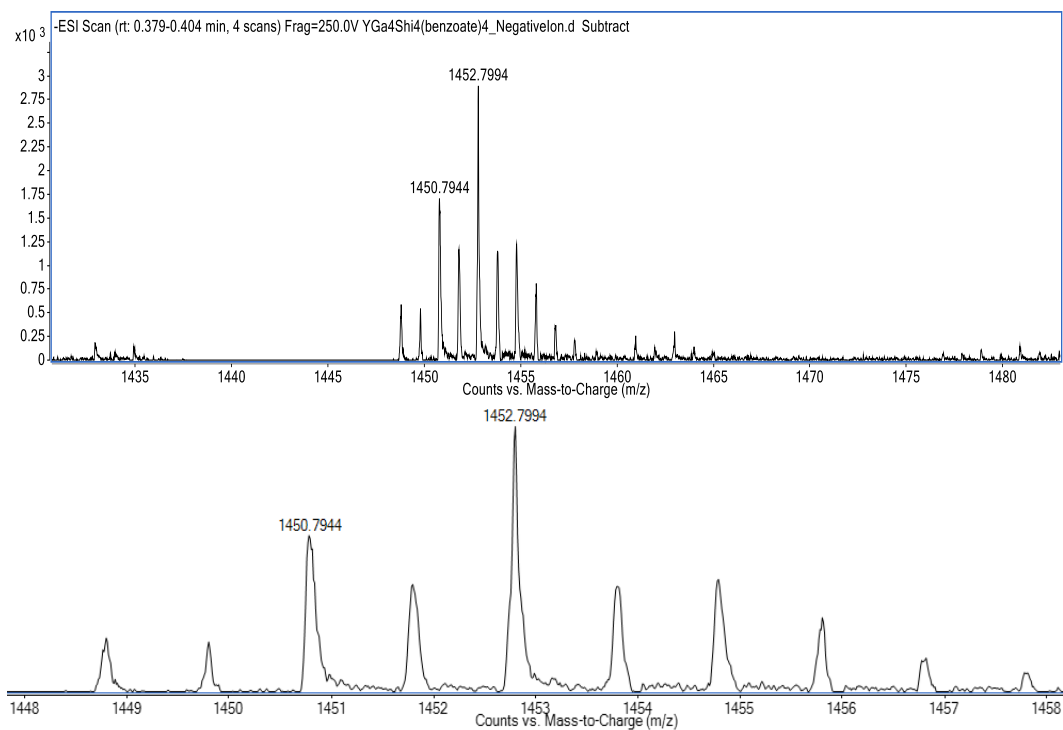
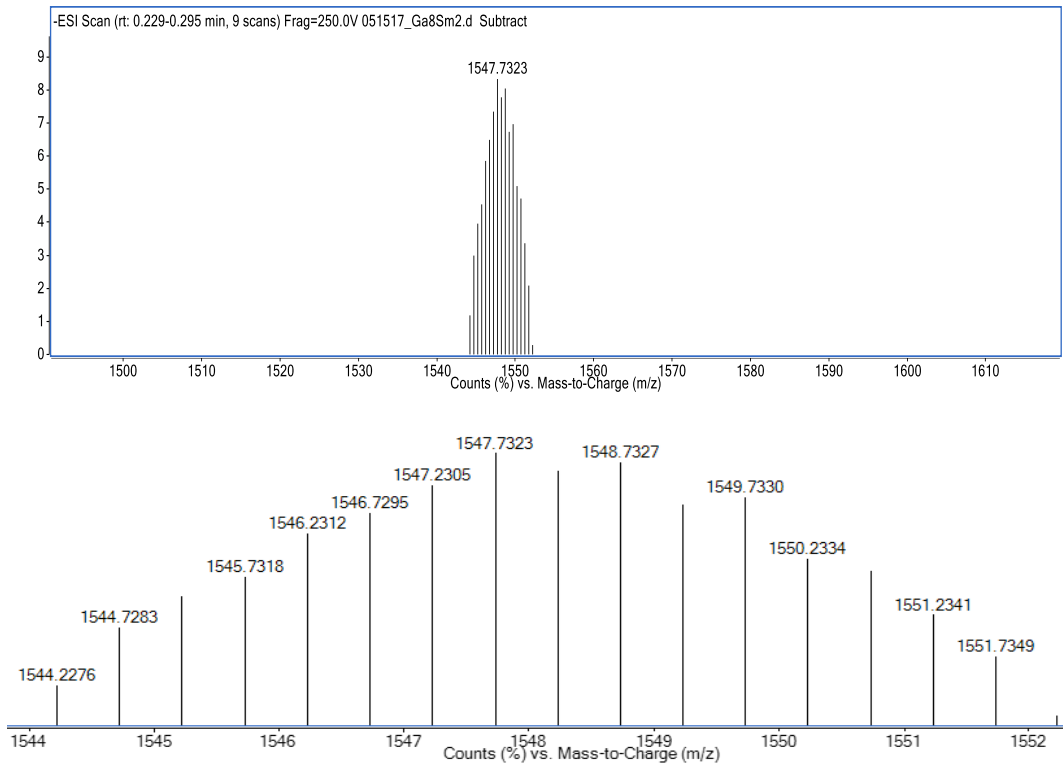


Figure A16 (Top) ESI-MS of TbGa₄Shi₄(benzoate)₄ metallacrown in negative ion. (Bottom) -1 isotopic distribution.



$\text{Ln}_2\text{Ga}_8\text{Shi}_8\text{Mip}_4$ MC ESI-MS:



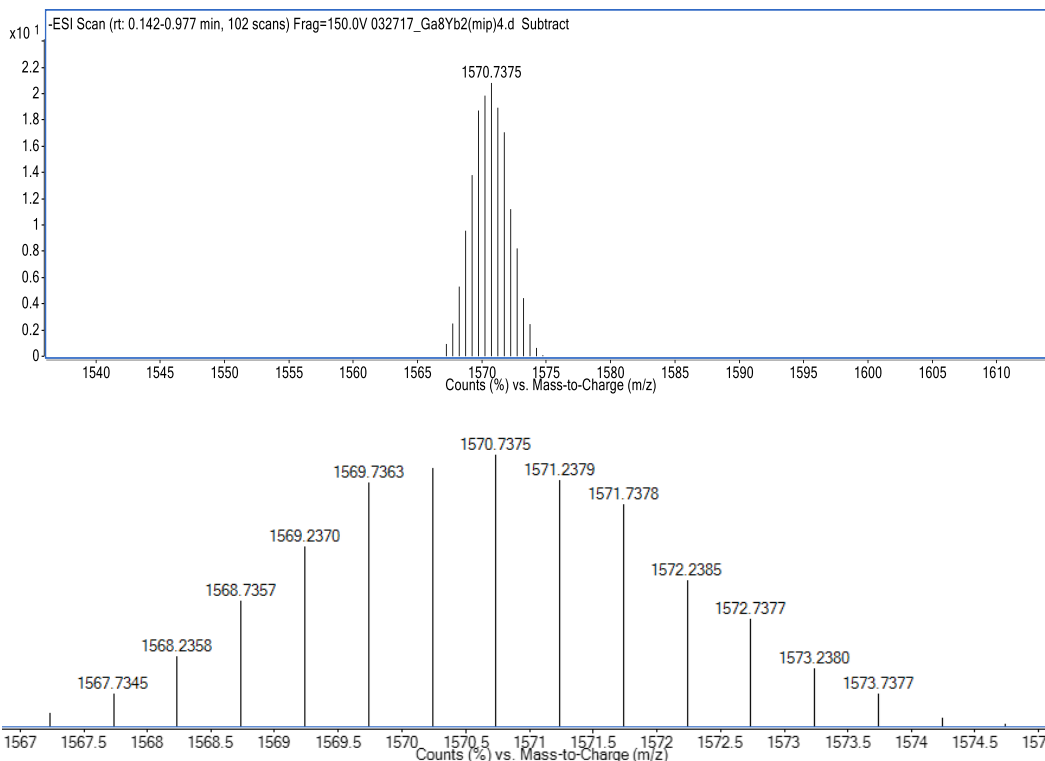


Figure A19 (Top) ESI-MS of $\text{Yb}_2\text{Ga}_8\text{Shi}_8\text{Mip}_4$ metallacrown in negative ion. (Bottom) -2 isotopic distribution.

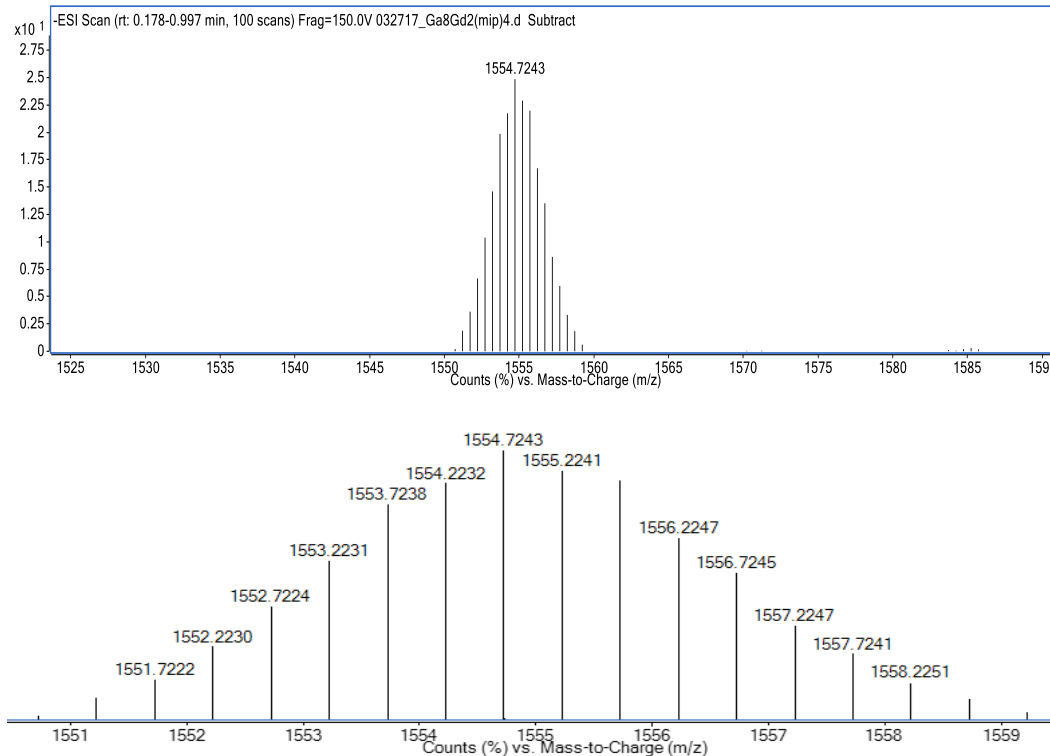


Figure A20. (Top) ESI-MS of $\text{Gd}_2\text{Ga}_8\text{Shi}_8(\text{Mip})_4$ metallacrown in negative ion. (Bottom) -2 isotopic distribution.

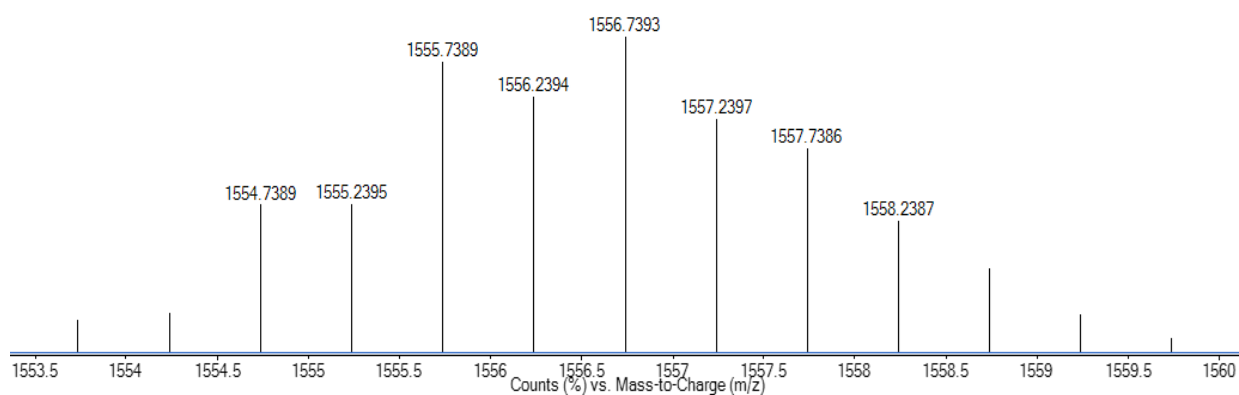
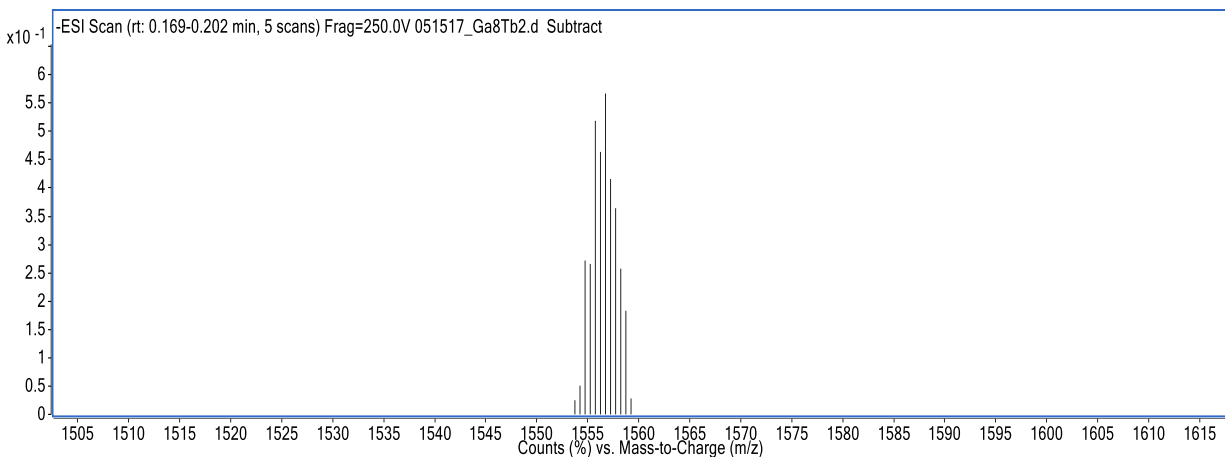


Figure A21. (Top) ESI-MS of $Tb_2Ga_8Shi_8(Mip)_4$ metallacrown in negative ion. (Bottom) -2 isotopic distribution.

Ln₂Ga₈Shi₈Mip₄ DMC ESI-MS:

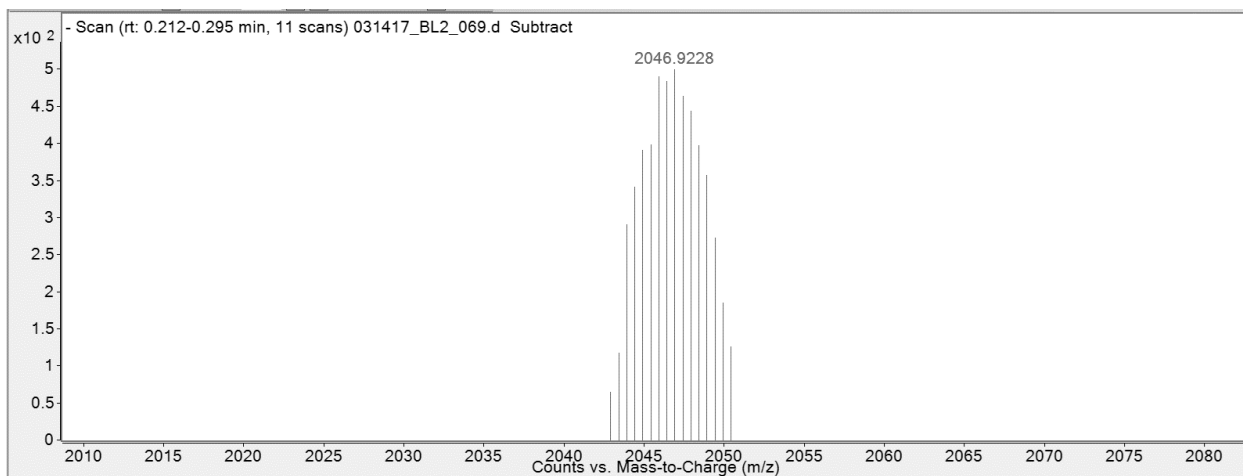


Figure A22 ESI mass spectrum of $Sm_2Ga_8Shi_8(Mip)_4$ G0.5 dendrimeric metallacrown in negative ion.

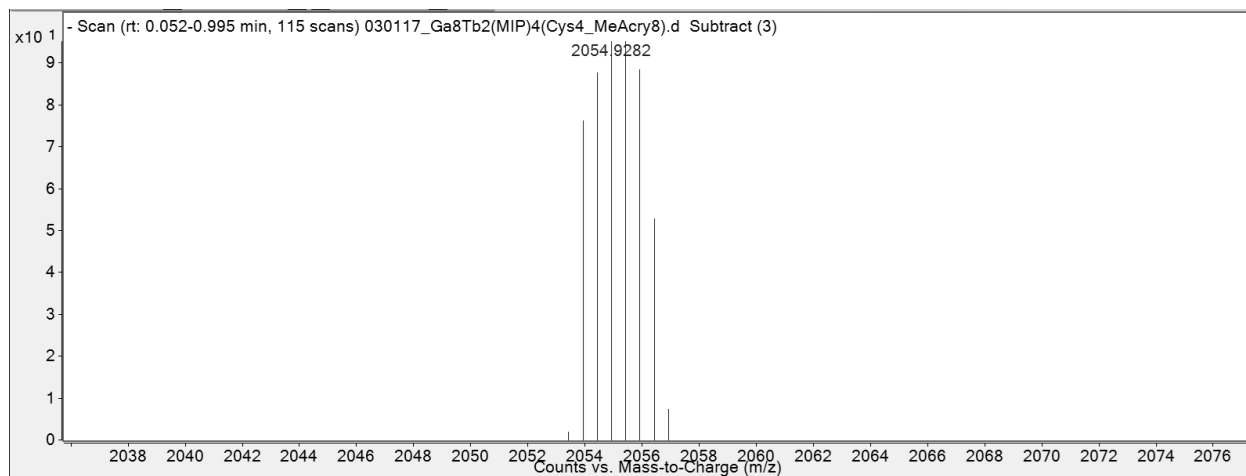


Figure A23 ESI mass spectrum of $Tb_2Ga_8Shi_8(Mip)_4 G0.5$ dendrimeric metallacrown in negative ion.

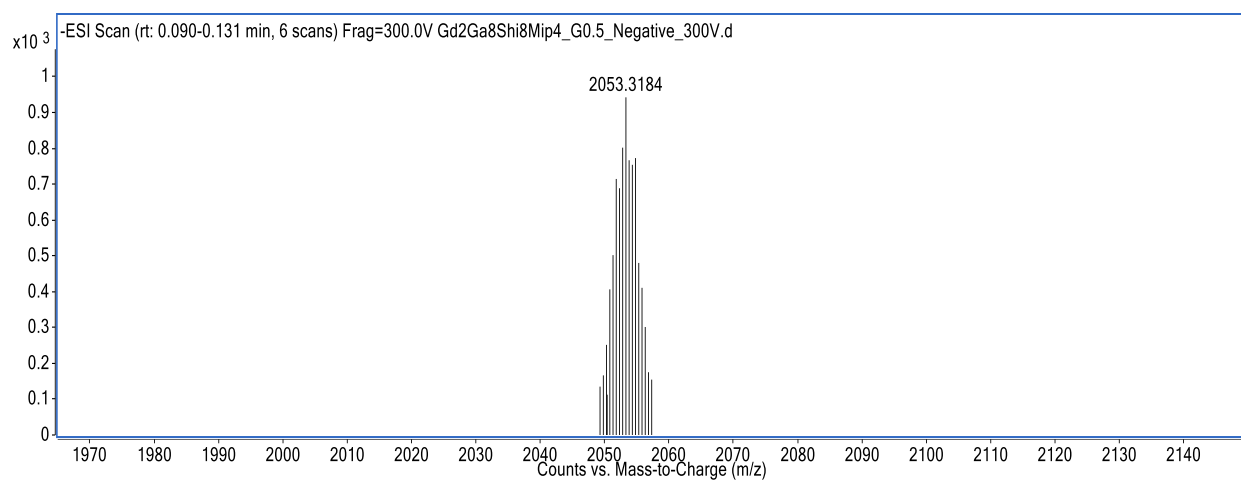


Figure A24 ESI mass spectrum of $Gd_2Ga_8Shi_8(Mip)_4 G0.5$ dendrimeric metallacrown in negative ion.

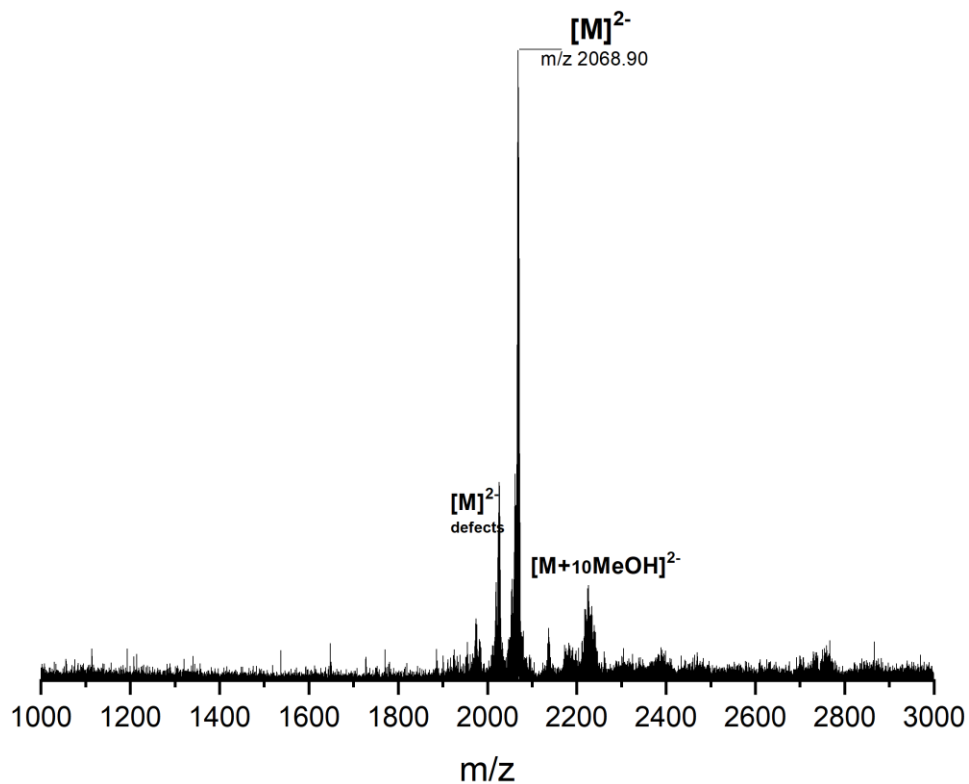


Figure A25 ESI mass spectrum of $\text{Yb}_2\text{Ga}_8\text{Shi}_8(\text{Mip})_4$ G0.5 dendrimeric metallacrown in negative ion.

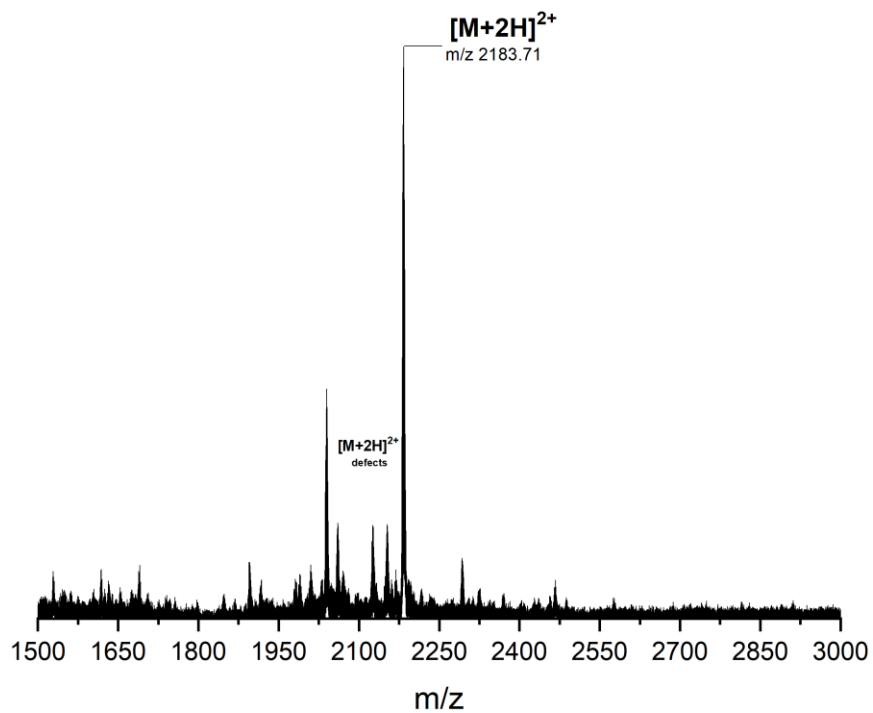


Figure A26. ESI mass spectrum of $\text{Yb}_2\text{Ga}_8\text{Shi}_8(\text{Mip})_4$ G1.0 dendrimeric metallacrown in positive ion.

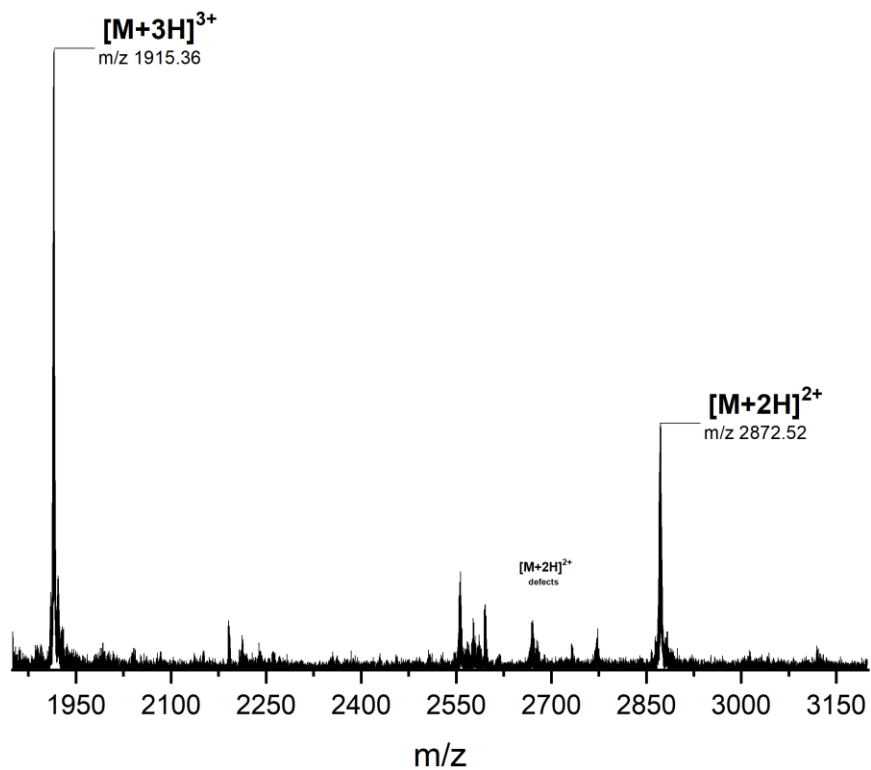


Figure A27 ESI mass spectrum of $\text{Yb}_2\text{Ga}_8\text{Shi}_8(\text{Mip})_4$ G1.5 dendrimeric metallacrown in positive ion.

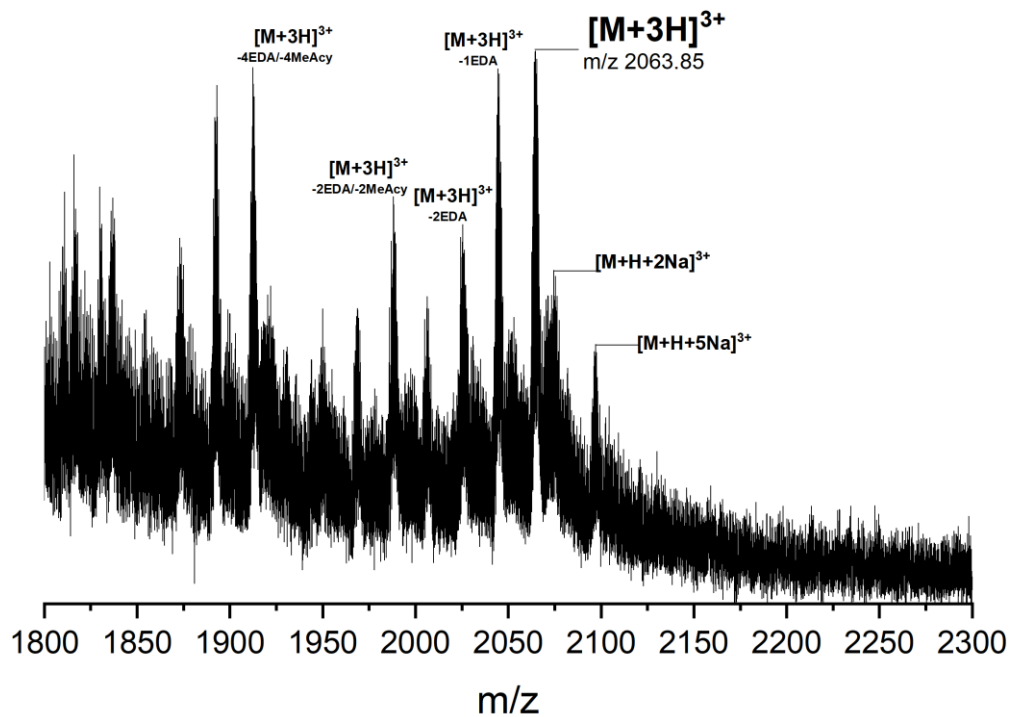


Figure A28 ESI mass spectrum of $\text{Yb}_2\text{Ga}_8\text{Shi}_8(\text{Mip})_4$ G2.0 dendrimeric metallacrown in positive ion.

UV-VIS Spectrum

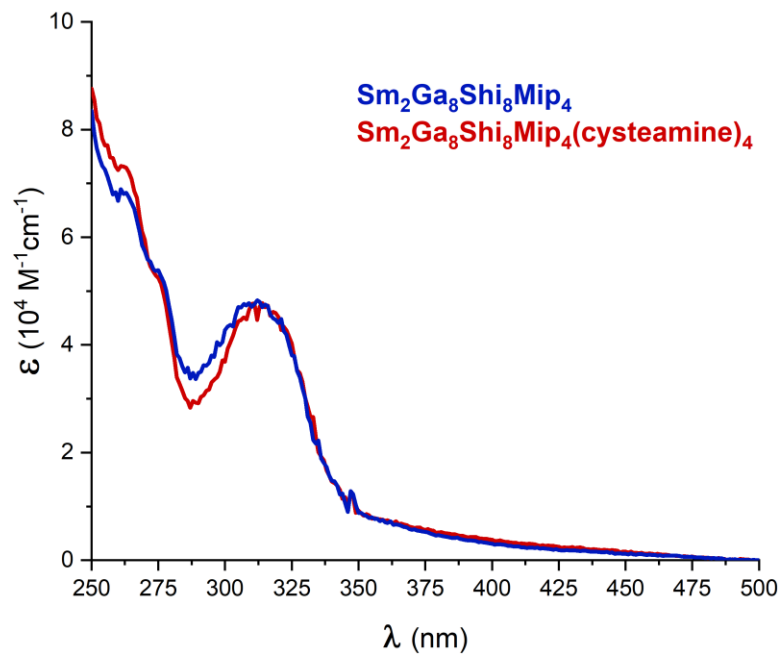


Figure A29 UV-Vis absorbance spectra in MeOH of $\text{Sm}_2\text{Ga}_8\text{Shi}_8\text{Mip}_4$ prior and after cysteamine coupling in at room temperature and with 2-3 μM concentrations.

Appendix B

Calculations for the Estimation of Encapsulated/Associated Solvent Molecules to MCs and DMCs by DLS

Dendrimers are known for being excellent at encapsulating molecules within their shells.^{209,210} Likewise, some solvent molecules have been shown to coordinate to the ring metals templating MCs.^{101,102} Thus, it can be expected that in solution, numerous solvent molecules can be encapsulated or associated within the dendritic shell of DMCs. The following workup of DLS data was done in order to estimate the maximum number of solvent molecules encapsulates/associated within dendrimeric metallocrowns. An important assumption being made for this is that the effective volume in solution (MC+solvent or DMC+solvent) measured by DLS is identical to the volume of the complex in the solid state (MC or DMC). Based on this, the following steps described below were taken.

First, with the average hydrodynamic radius (R) measured by DLS, the volume (V) of the uncoupled MC core was determined using

$$V = \frac{3}{4}\pi R^3 . \quad (1)$$

Then, the mass of the complex was determined by dividing the molecular weight of the MC (determined by ESI-MS) by Avogadro's number,

$$mass = \frac{MW_{MC}}{Avogadro's\#} = \frac{(m/Z)(Z)}{6.022 \times 10^{23}} , \quad (2)$$

where m/z is the value recorded by ESI-MS and Z is the MC's charge number. Finally, the density in solution of the MC core ($\rho_{m\ MC}$) was calculated by

$$\rho_{m\ MC} = \frac{mass}{V} . \quad (3)$$

As for the determination of the number of solvent molecules encapsulated/associated with the MC, the following equation was used:

$$\# \text{ Solvent molecules} = \frac{\Delta MW}{MW_{\text{solvent}}} = \frac{MW_{MC}}{MW_{\text{solvent}}} \left(\frac{\rho_{MC} - \rho_{m MC}}{\rho_{MC}} \right). \quad (4)$$

Where ΔMW is the difference between the effective molecular weight of the MC in solution (MC+solvent) and the molecular weight in the solid state (MC); MW_{solvent} is the molecular weight of the solvent, in this case DMSO (78 g/mol); and ρ_{MC} is the density of the MC in the solid state, ideally determined for its crystal structure. For this case, since the crystallography data was not collected for the MC cores in this thesis, the density values for the parent $\text{Yb}_2\text{Ga}_8\text{Si}_8\text{I}_4$ MC was used instead ($\rho_{MC}:1.445$),¹⁰⁶ which should be expected to be slightly larger than the actual density value for the MC cores. Thus, Equation 4 establishes that there is a proportionality between the change in density and the change in molecular weight between the solution (MC+solvent) and the solid state (MC), based on the previously stated assumption that the volume in solution and in solid state are the same.

Next, to estimate the number of solvent molecules in the DMCs the assumption that the ratio of the measured density in solution and in the solid state is constant for both the MC core and each of its DMCs, which is described with the following equation:

$$\frac{\rho_{MC}}{\rho_{m MC}} = \frac{\rho_{DMC}}{\rho_{m DMC}}. \quad (5)$$

Thus, the $\rho_{m DMC}$ for a given DMC can be calculated with Equations 1-3, to then determine the ρ_{DMC} values with Equation 5. Finally, the number of solvent molecules for a given DMC can be calculated using Equation 4 with the molecular weight and density values for the DMC.

It is important to remember that since several assumptions were made for these calculations, that the number of solvent molecules encapsulated/associated with a given MC or DMC are just estimations. A second solution state technique, such as DOSY NMR, could be used in conjunction to DLS to corroborate the solvent encapsulation estimation.

Appendix C Supplemental Information for Chapter 3

^1H NMR Spectra

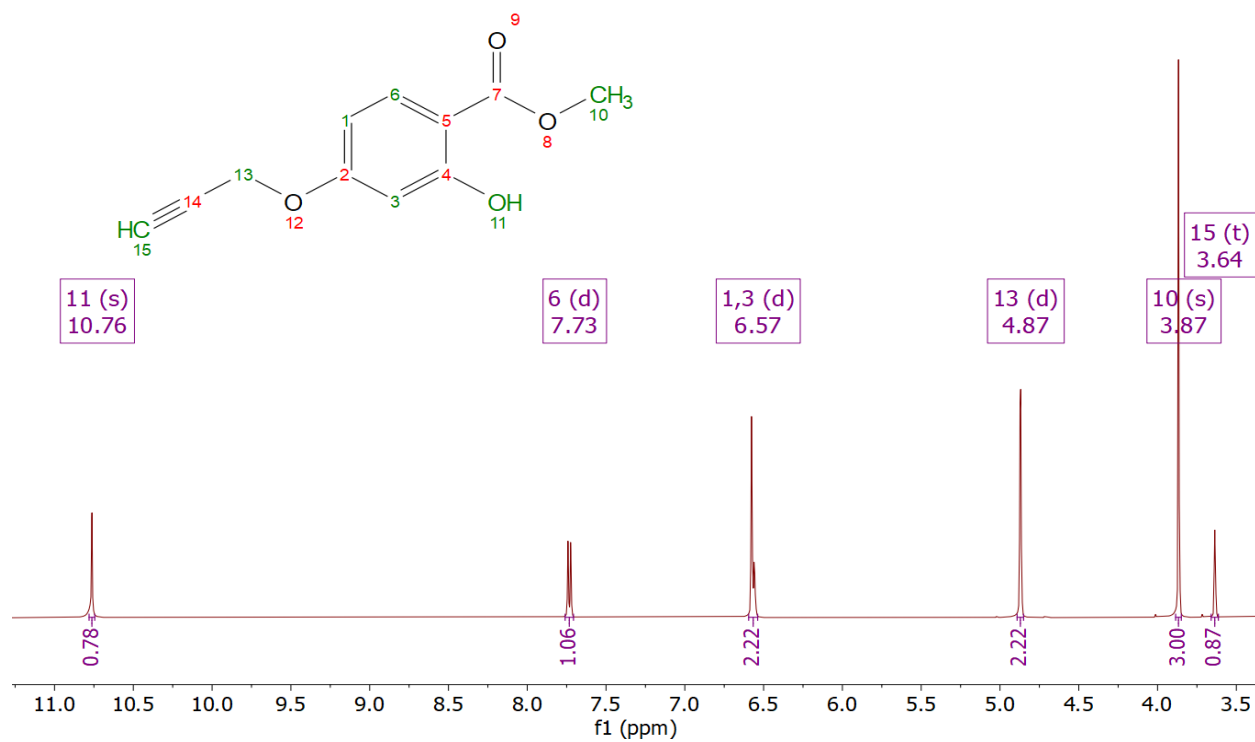


Figure C30 ^1H NMR spectrum of Methyl 2-hydroxy-4-(prop-2-yn-1-yloxy)benzoate (1)

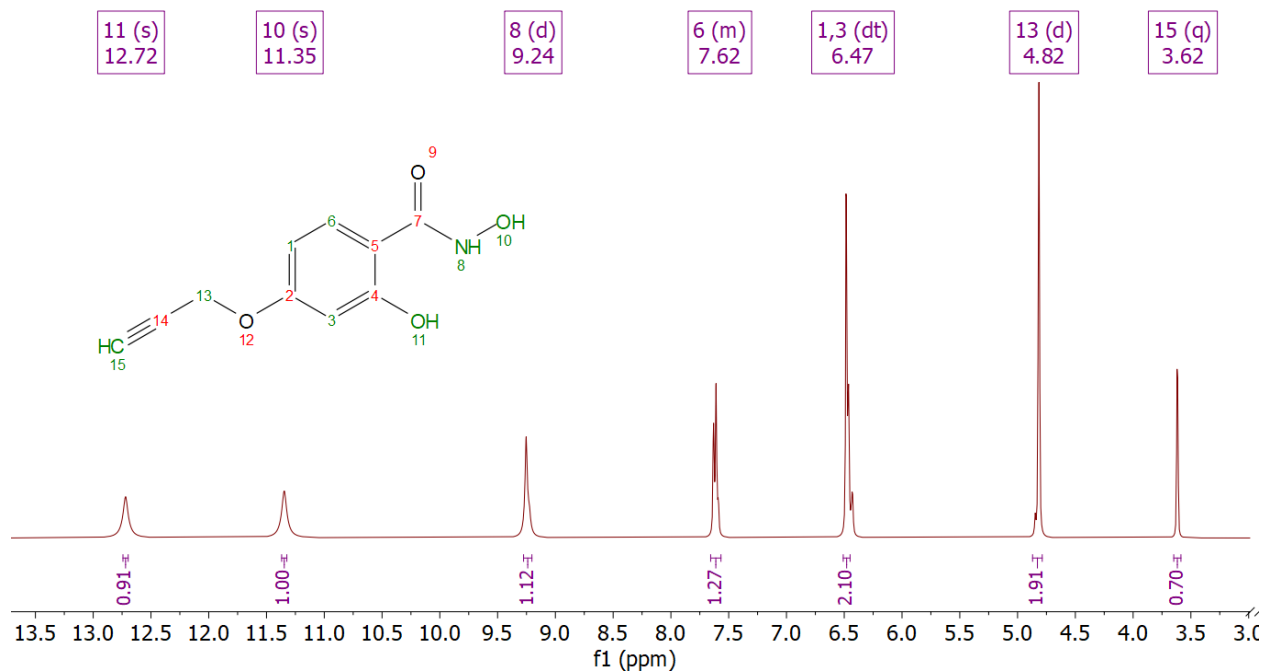


Figure C31 ^1H NMR spectrum of N,2-dihydroxy-4-(prop-2-yn-1-yloxy)benzamide (pYneShi, 2).

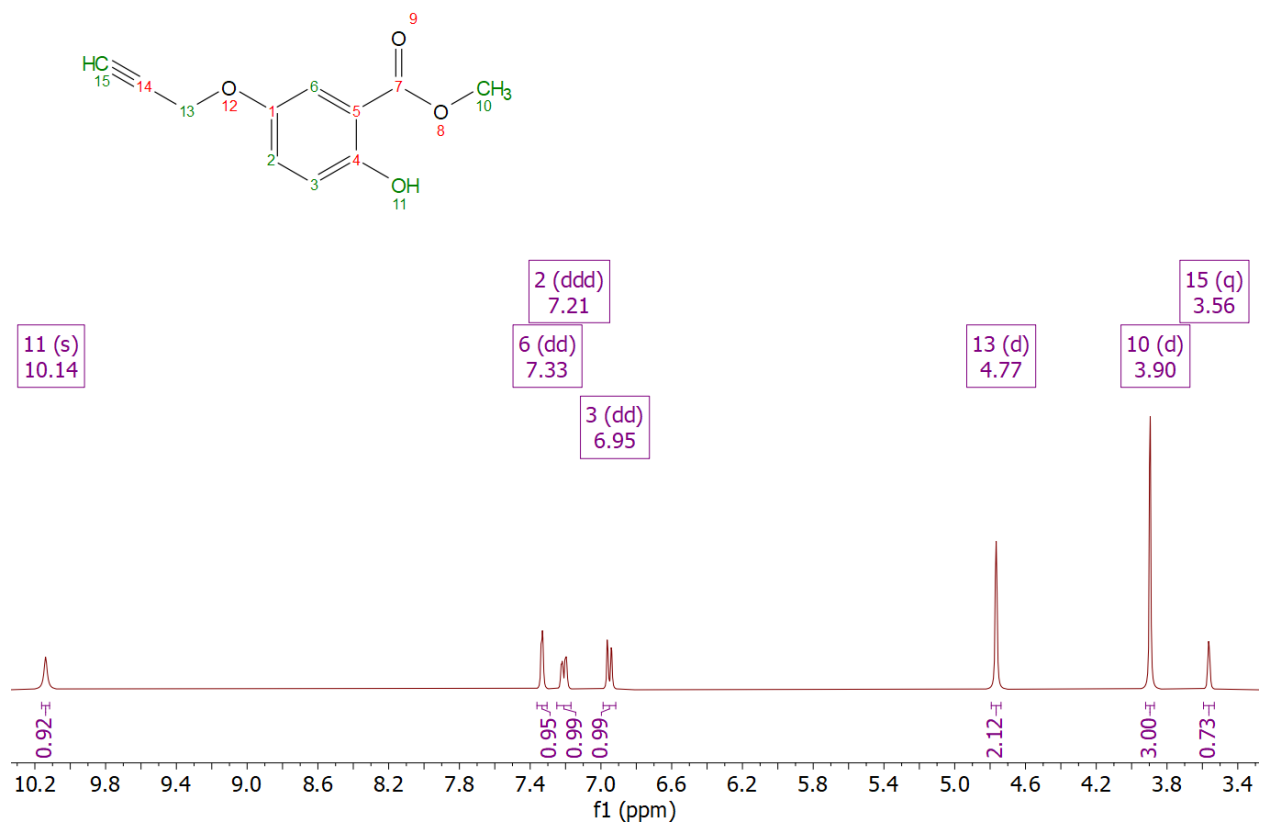


Figure C32 ^1H NMR spectrum of Methyl 2-hydroxy-5-(prop-2-yn-1-yloxy)benzoate (3).

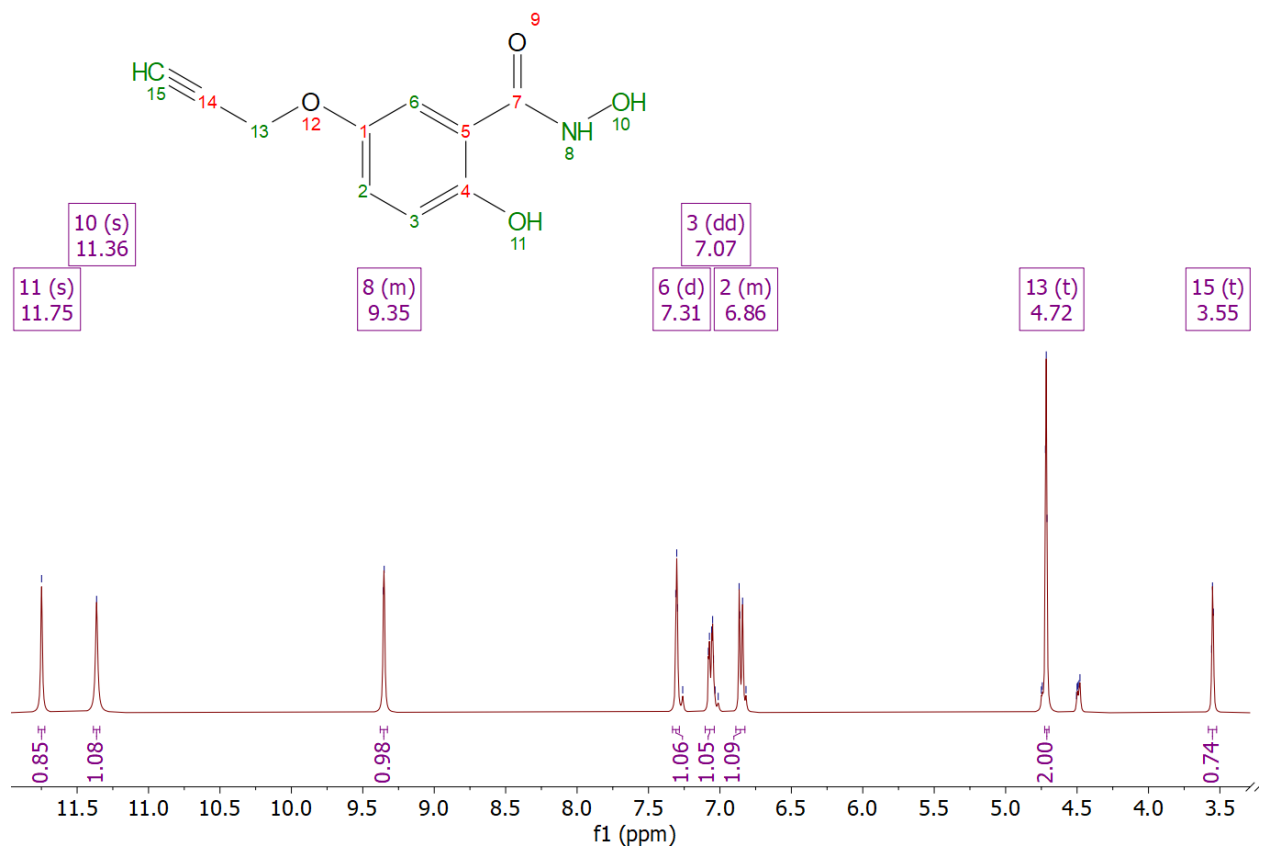


Figure C33 ^1H NMR spectrum of N,2-dihydroxy-5-(prop-2-yn-1-yloxy)benzamide (mYneShi, 4).

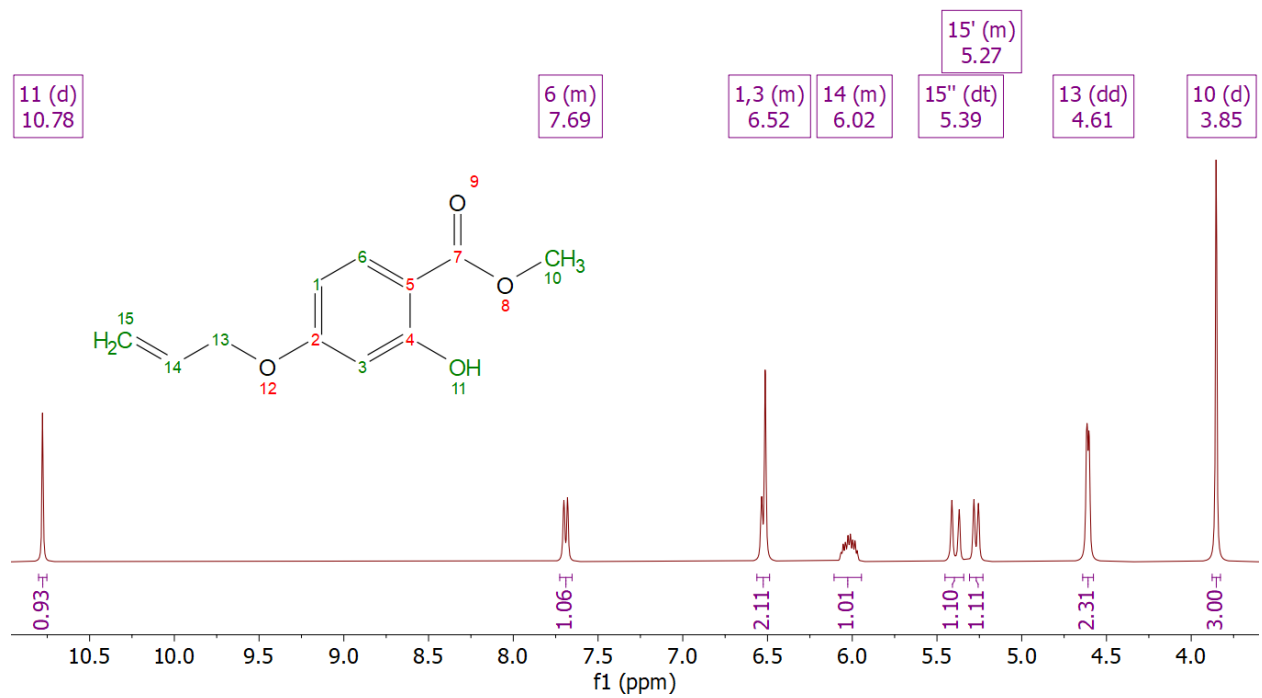


Figure C34 ^1H NMR spectrum of Methyl 4-(allyloxy)-2-hydroxybenzoate (5).

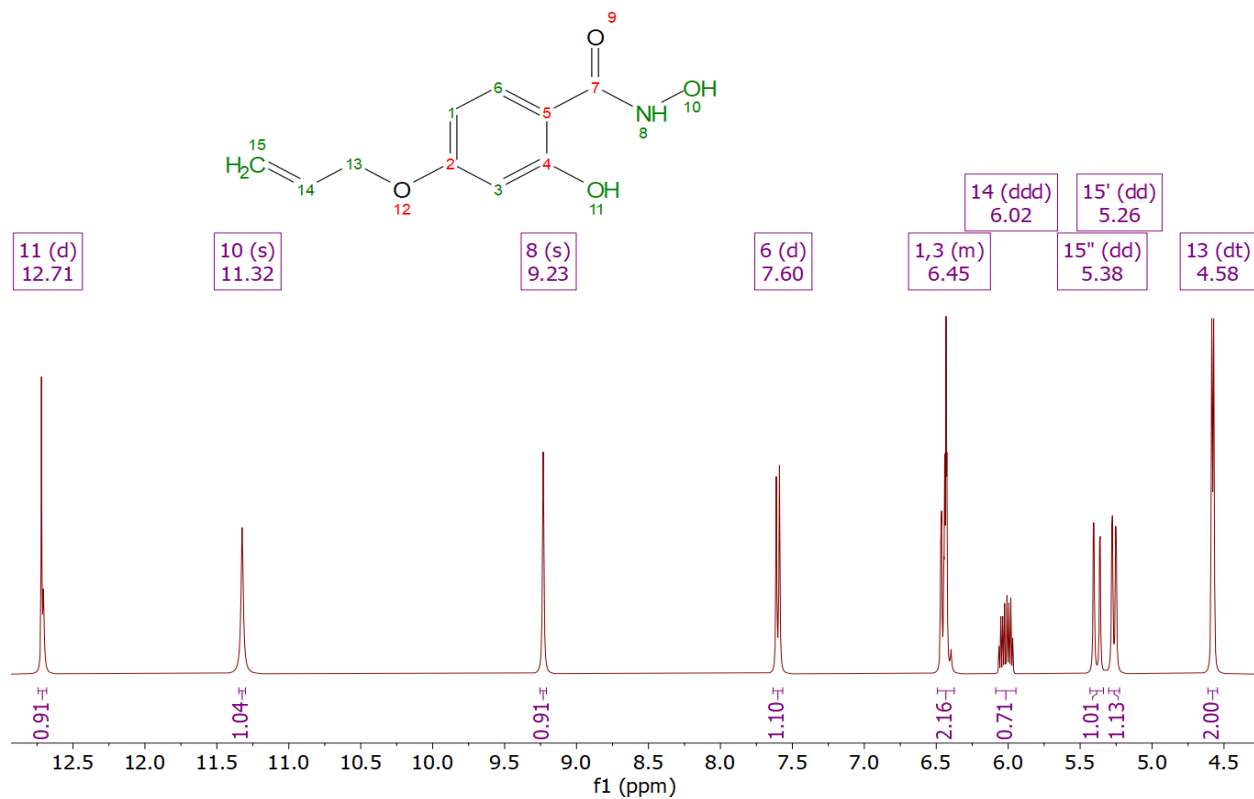


Figure C35 ^1H NMR spectrum of 4-(allyloxy)-N,2-dihydroxybenzamide (pAlShi, 6).

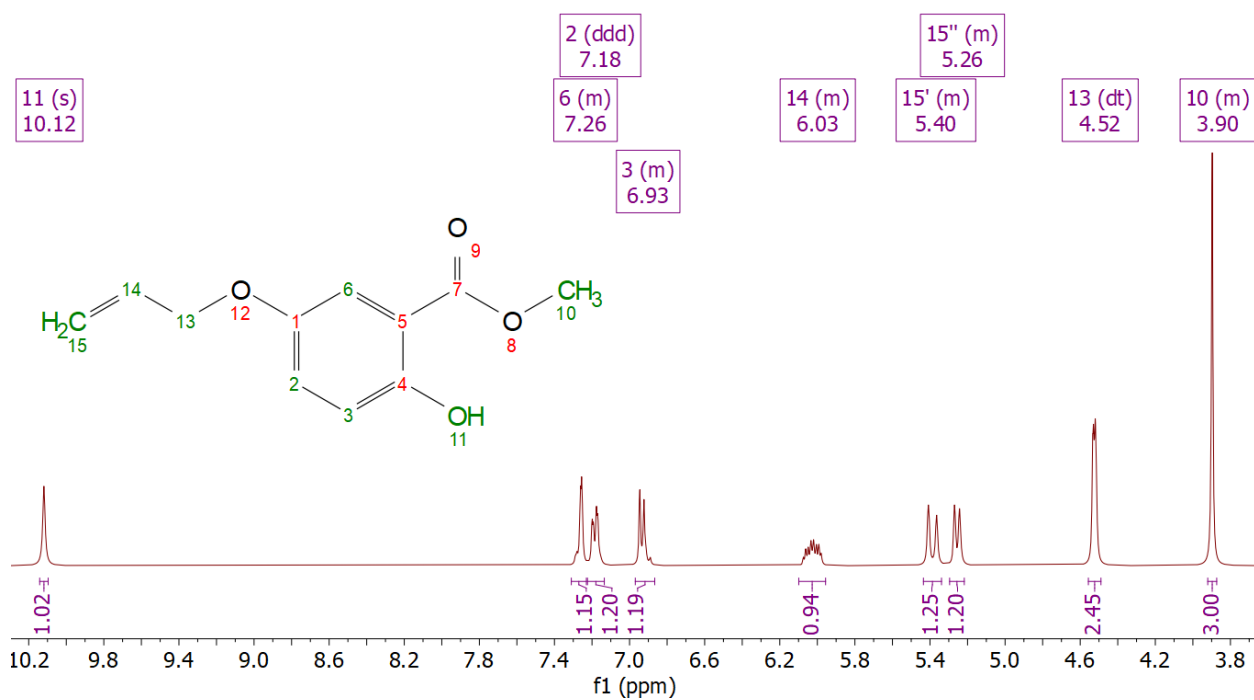


Figure C36 ^1H NMR spectrum of Methyl 5-(allyloxy)-2-hydroxybenzoate (7).

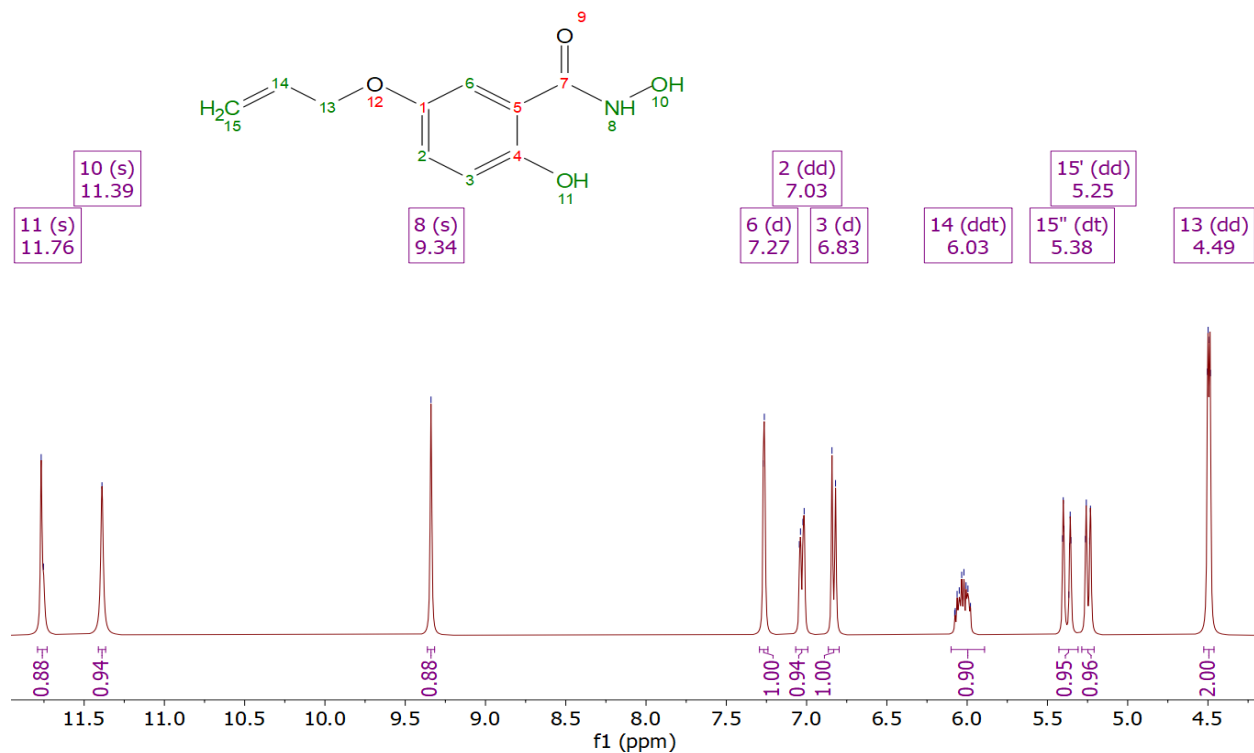


Figure C37 ^1H NMR spectrum of 5-(allyloxy)-N,2-dihydroxybenzamide (mAlShi, 8)

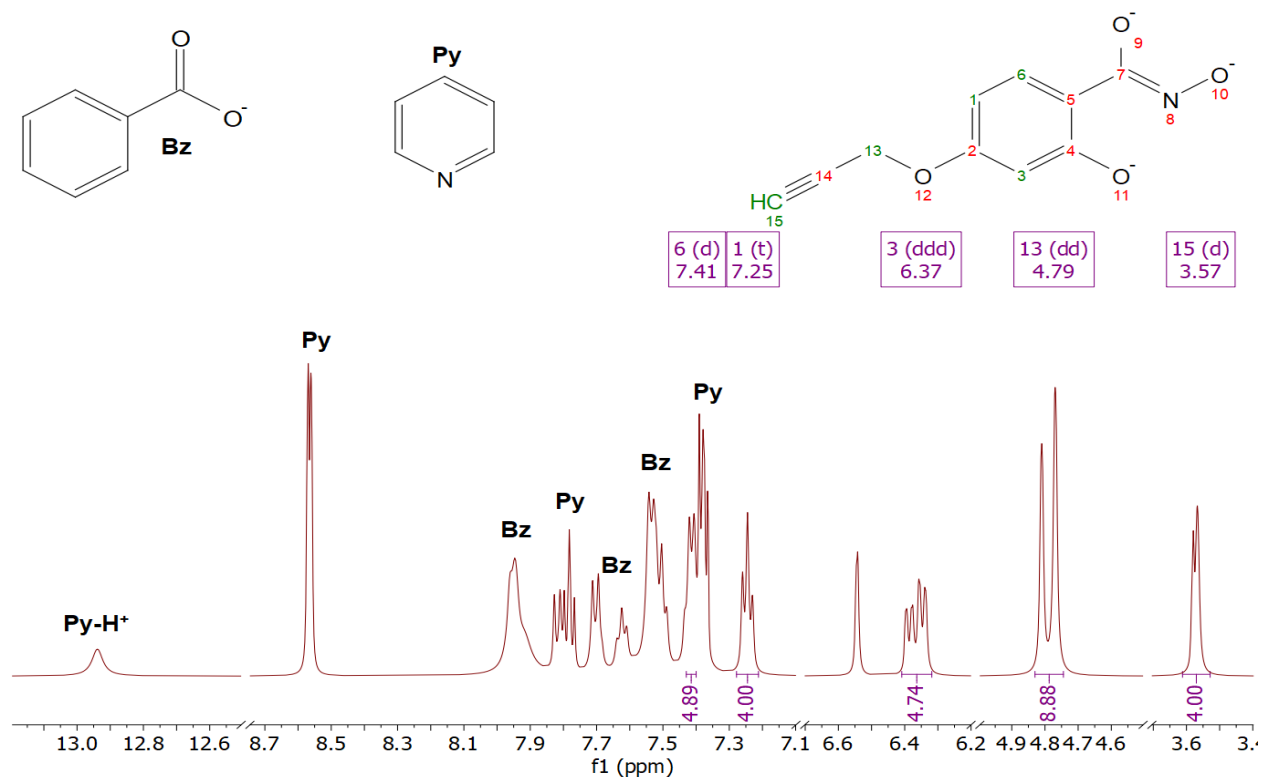


Figure C38 ^1H NMR spectrum of $\text{SmGa}_4\text{PyneShi}_4(\text{Benzoate})_4$ in d_6 -DMSO. Labeled peaks from the ring ligands. Pyridine peaks labeled separately.

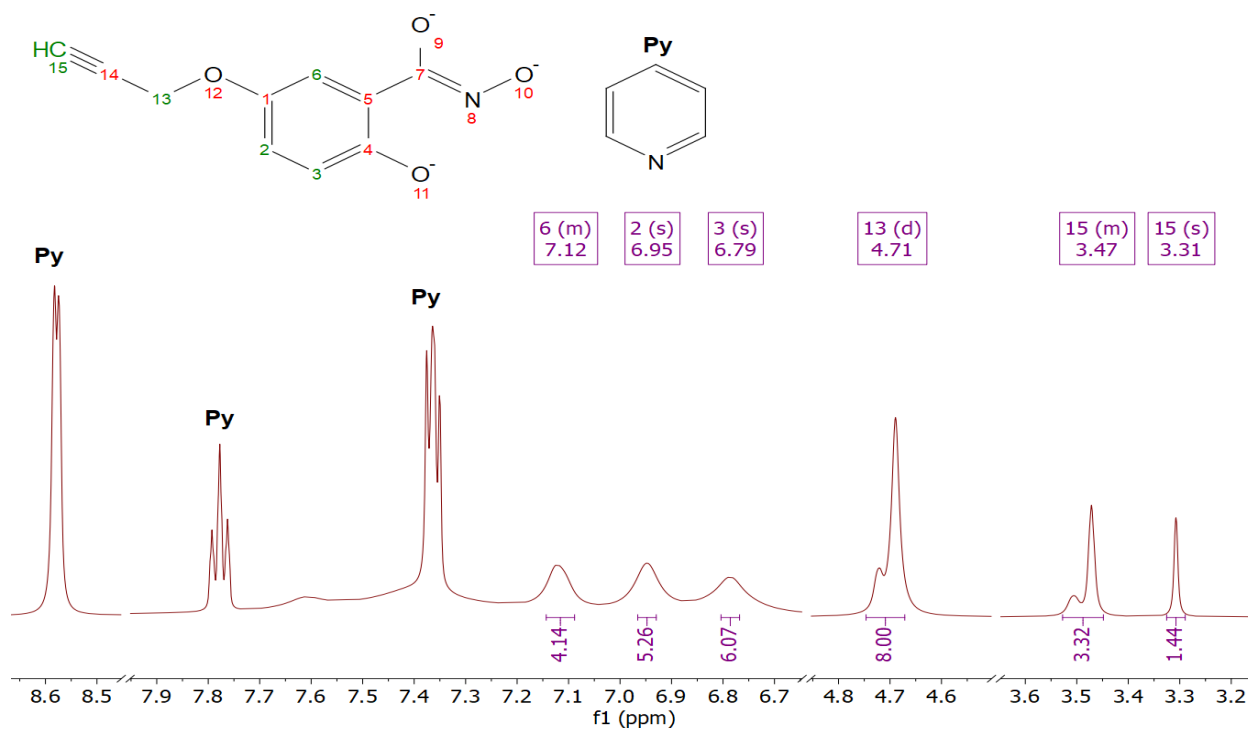


Figure C39 ^1H NMR spectrum of $\text{SmGa}_4m\text{YneShi}_4(\text{Benzoate})_4$ in d_6 -DMSO. Labeled peaks from the ring ligands. Pyridine peaks labeled separately.

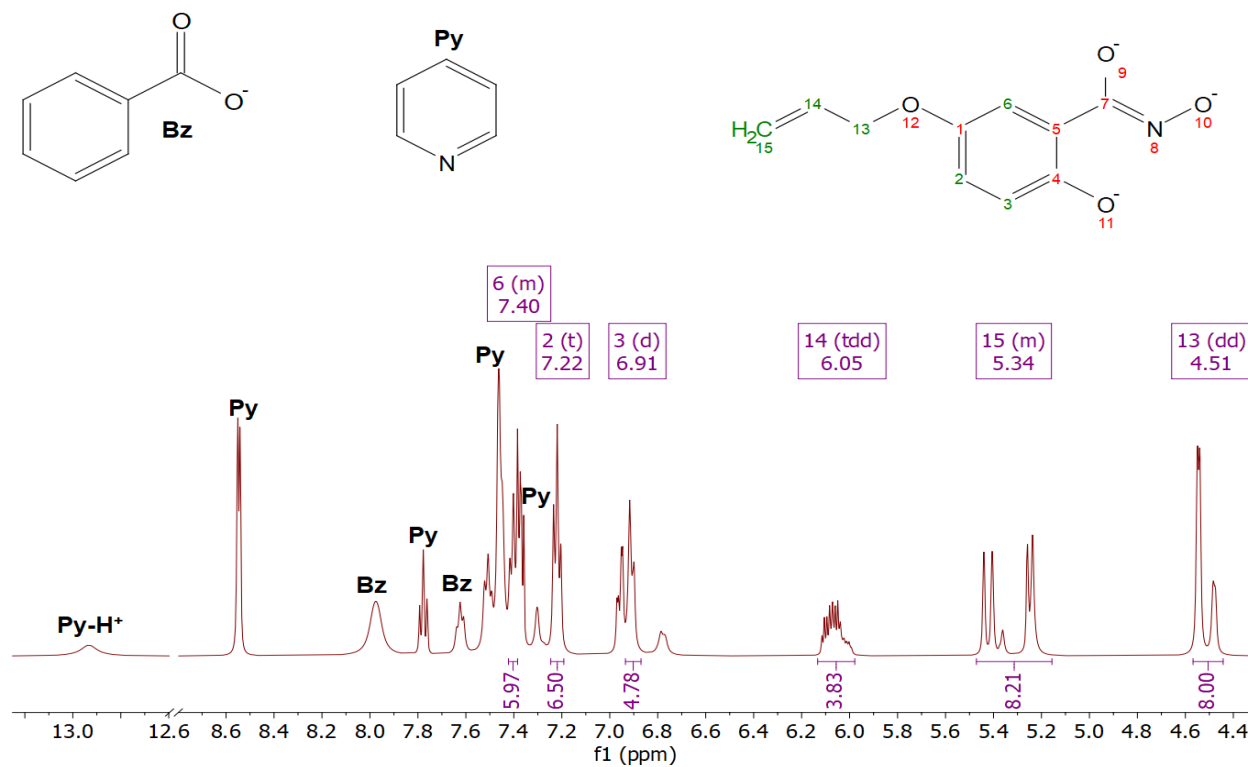


Figure C40 ^1H NMR spectrum of $\text{SmGa}_4m\text{AlShi}_4(\text{Benzoate})_4$ in d_6 -DMSO. Labeled peaks from the ring ligands. Pyridine and benzoate peaks labeled separately.

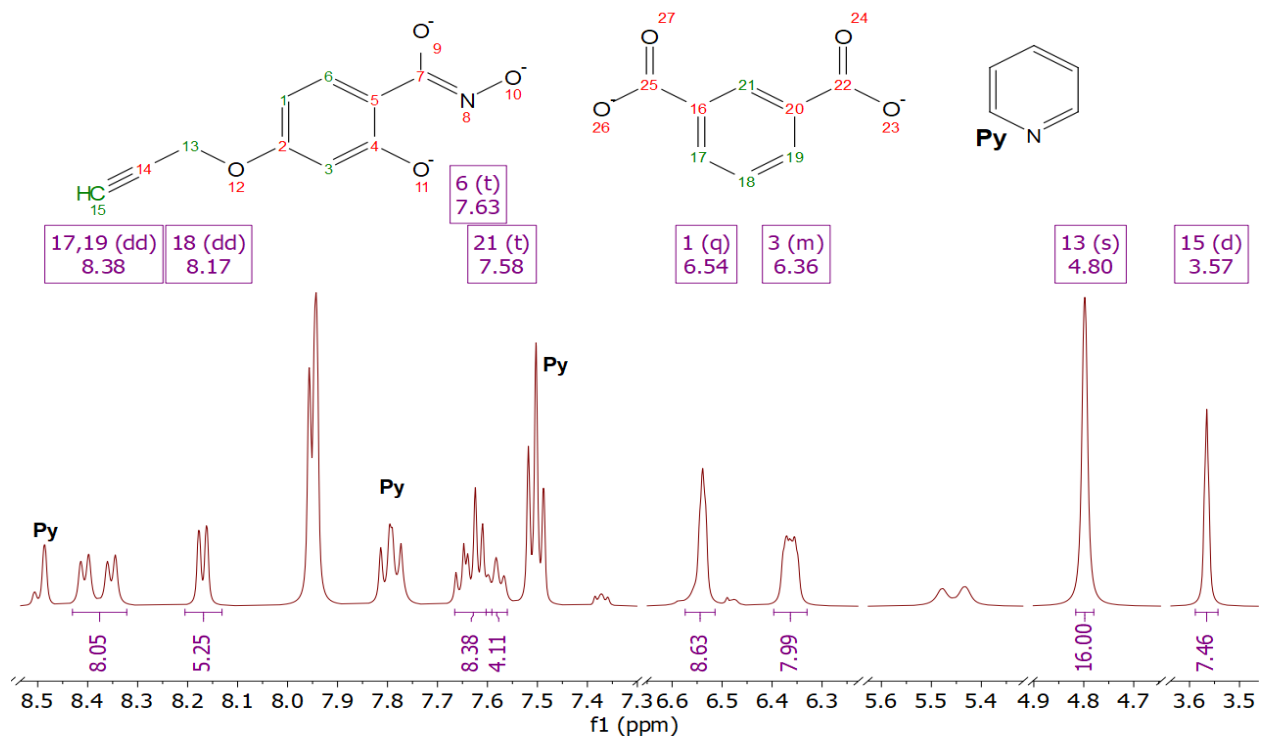


Figure C41 ^1H NMR spectrum of $\text{Sm}_2\text{Ga}_8\text{pYneShi}_8\text{Ip}_4$ in d_6 -DMSO. Labeled peaks from the ring and bridge ligands. Pyridine peaks labeled separately.

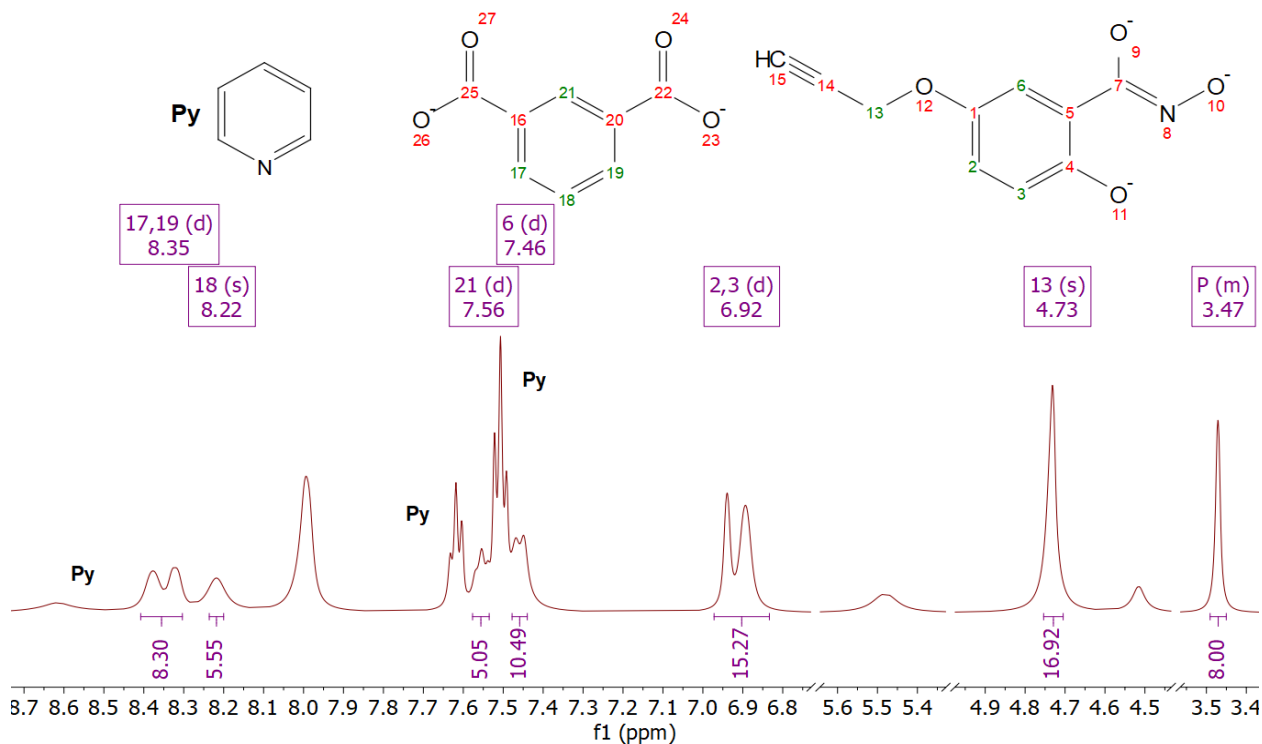


Figure C42 ^1H NMR spectrum of $\text{Sm}_2\text{Ga}_8\text{mYneShi}_8\text{Ip}_4$ in d_6 -DMSO. Labeled peaks from the ring and bridge ligands. Pyridine peaks labeled separately.

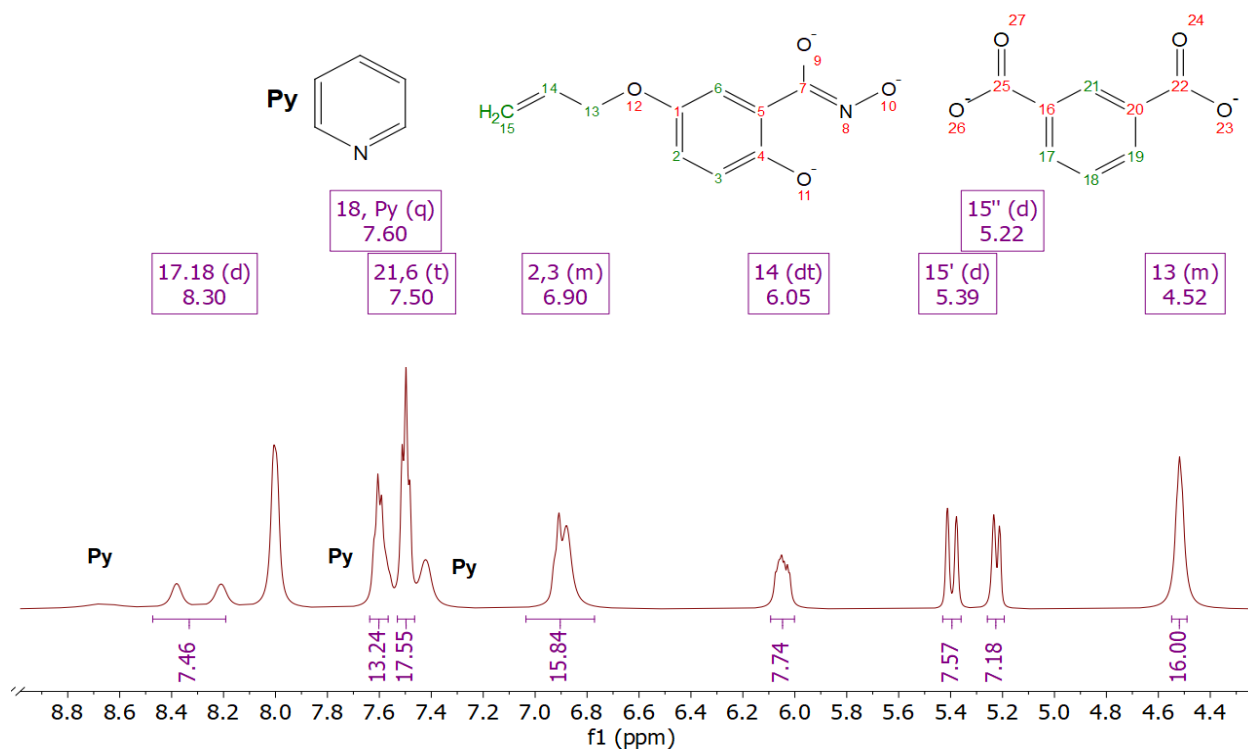


Figure C43 ^1H NMR spectrum of $\text{Sm}_2\text{Ga}_8m\text{AlShi}_8\text{Ip}_4$ in d_6 -DMSO. Labeled peaks from the ring and bridge ligands. Pyridine peaks labeled separately.

ESI Mass Spectra

$\text{LnGa}_4x\text{Shi}_4$ Metallacrowns ($\text{Ln}: \text{Yb}^{\text{III}}, \text{Sm}^{\text{III}}, \text{and } \text{Gd}^{\text{III}}$; $x: p\text{Yne}, m\text{Yne}, p\text{Al}, \text{and } m\text{Al}$)

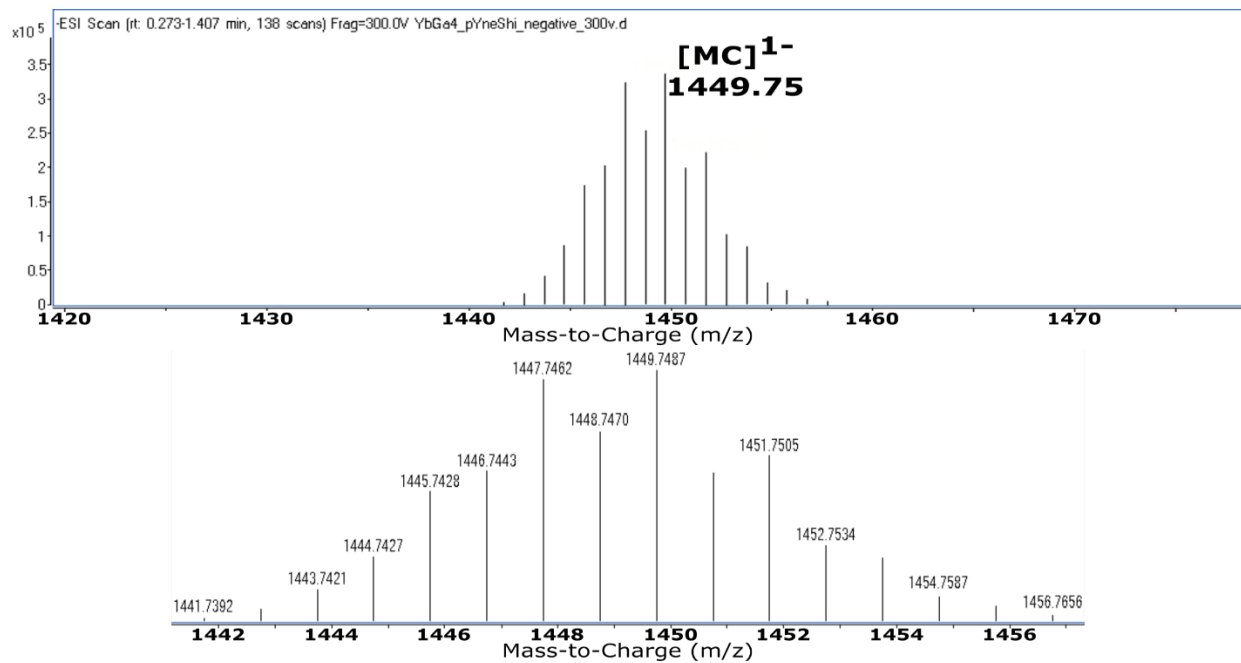


Figure C44 (Top) ESI-MS of $\text{YbGa}_4p\text{YneShi}_4(\text{Formate})_4$ MC in negative ion. (Bottom) -1 isotopic distribution.

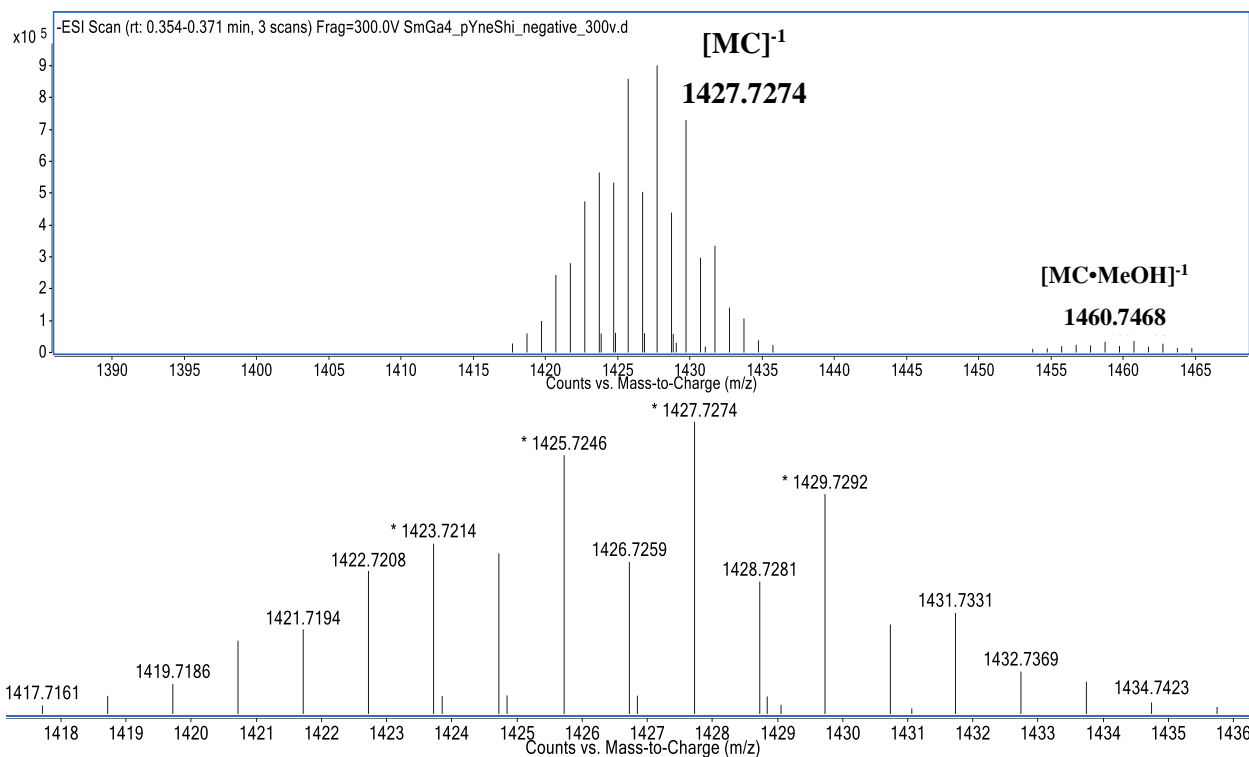


Figure C45 (Top) ESI-MS of SmGa₄pYneShi₄(Formate)₄ MC in negative ion. (Bottom) -1 isotopic distribution.

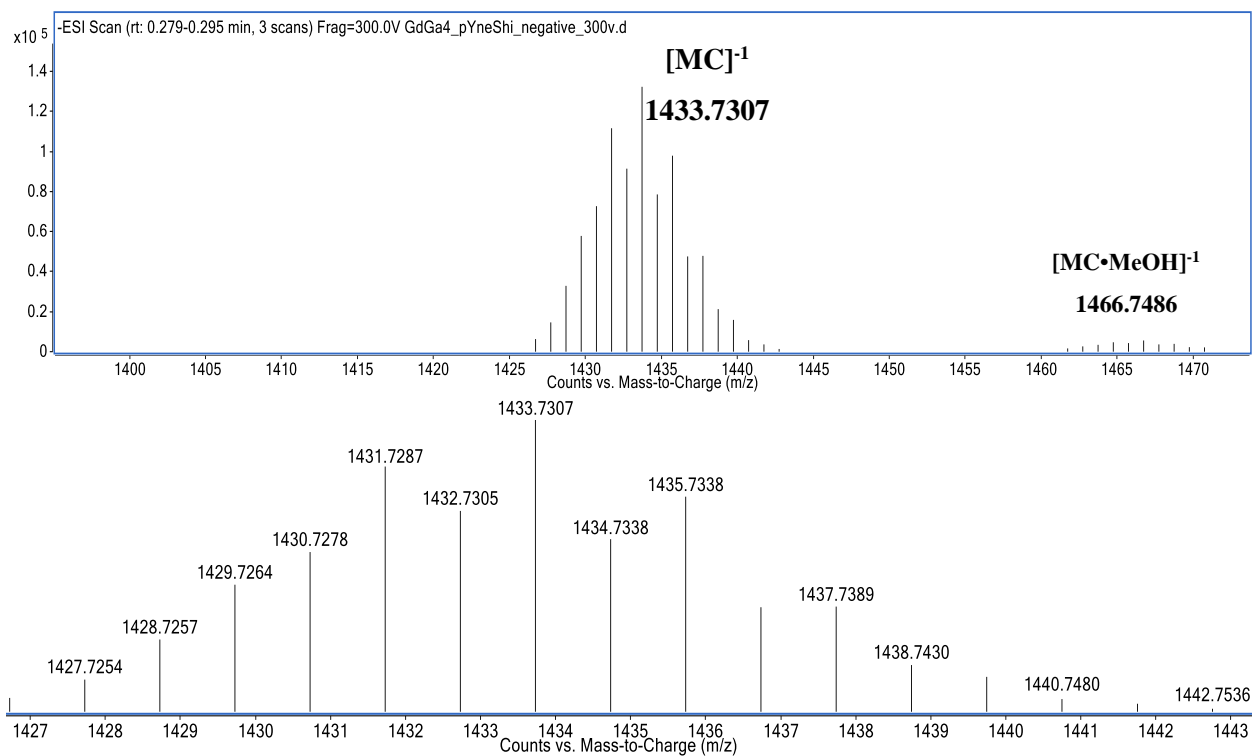


Figure C46 (Top) ESI-MS of GdGa₄pYneShi₄(Formate)₄ MC in negative ion. (Bottom) -1 isotopic distribution.

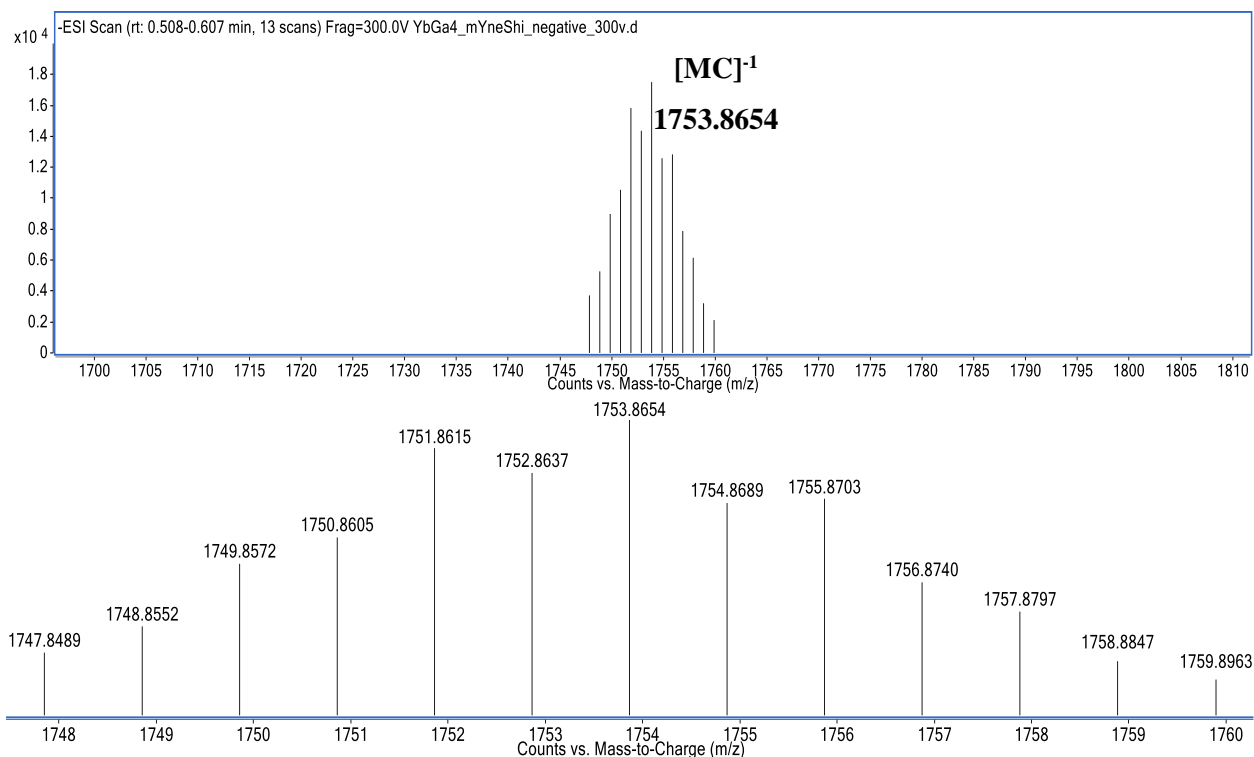


Figure C47 (Top) ESI-MS of YbGa₄mYneShi₄(Benzoate)₄ MC in negative ion. (Bottom) -1 isotopic distribution.

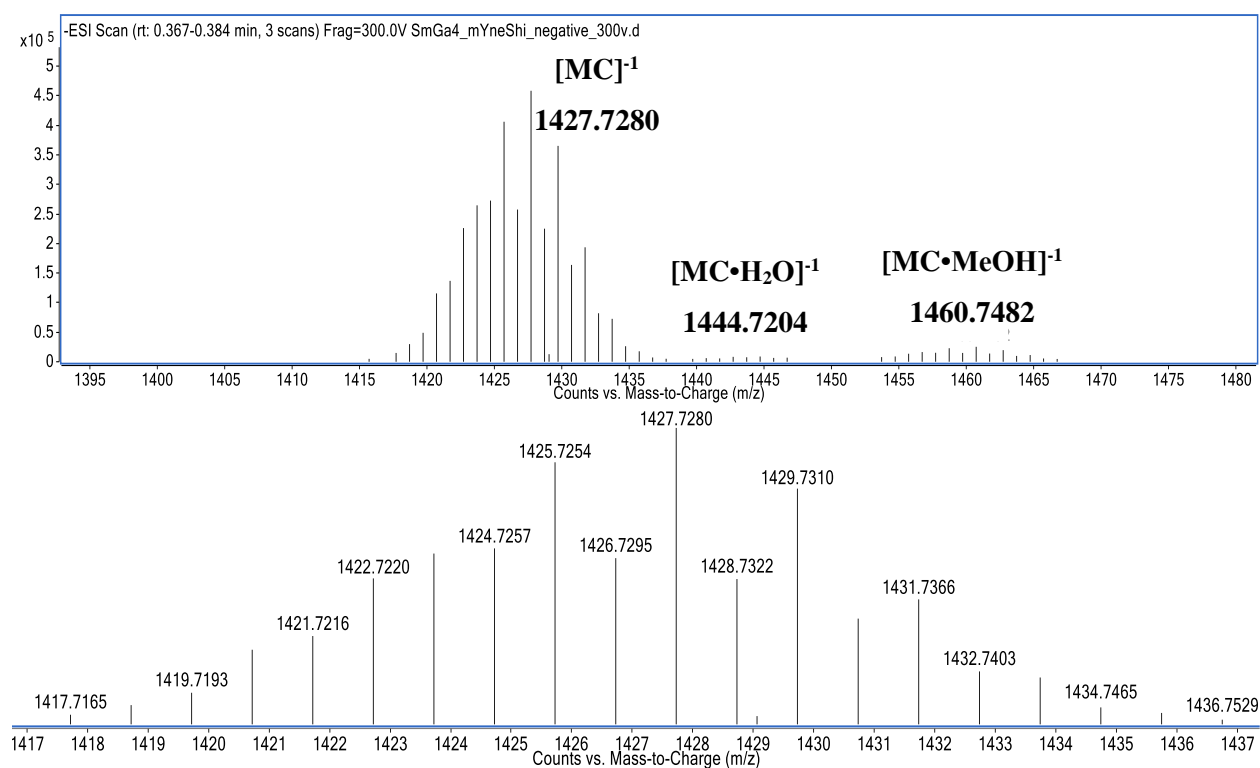


Figure C48 (Top) ESI-MS of SmGa₄mYneShi₄(Formate)₄ MC in negative ion. (Bottom) -1 isotopic distribution.

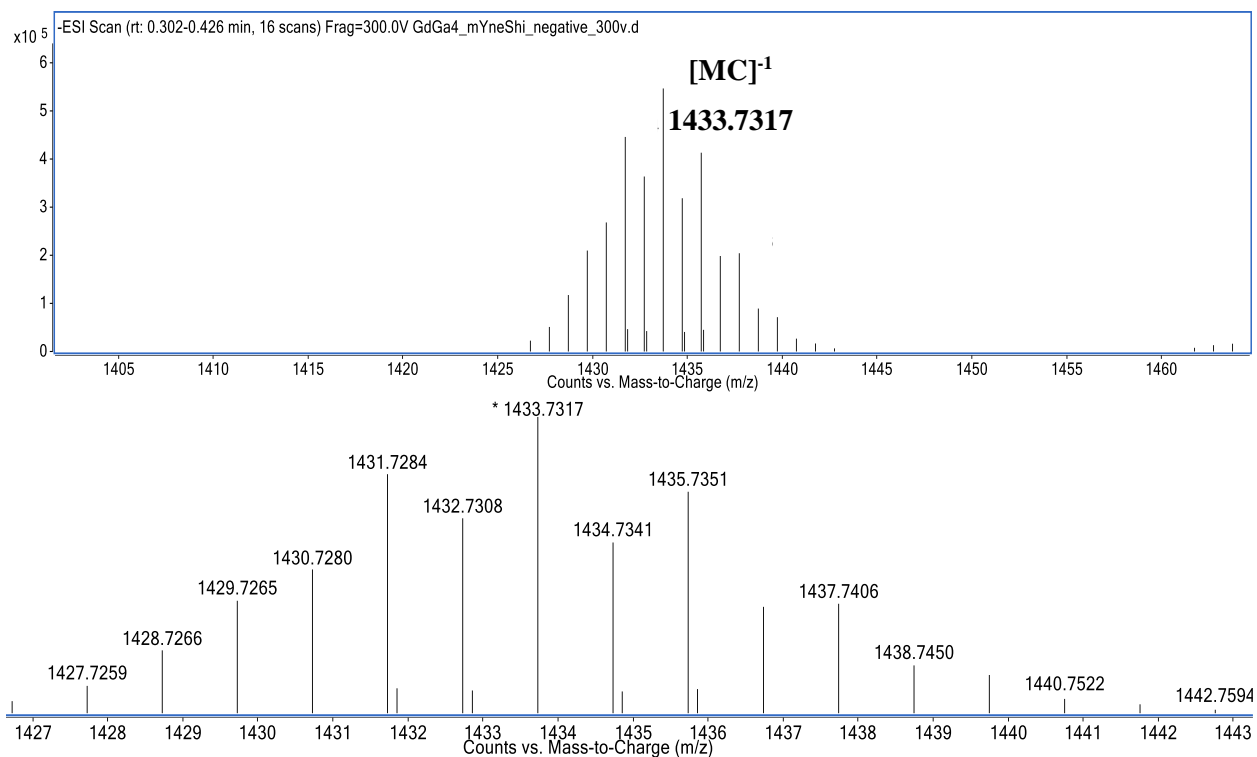


Figure C49 ESI-MS of GdGa₄mYneShi₄(Formate)₄ MC in negative ion. (Bottom) -1 isotopic distribution.

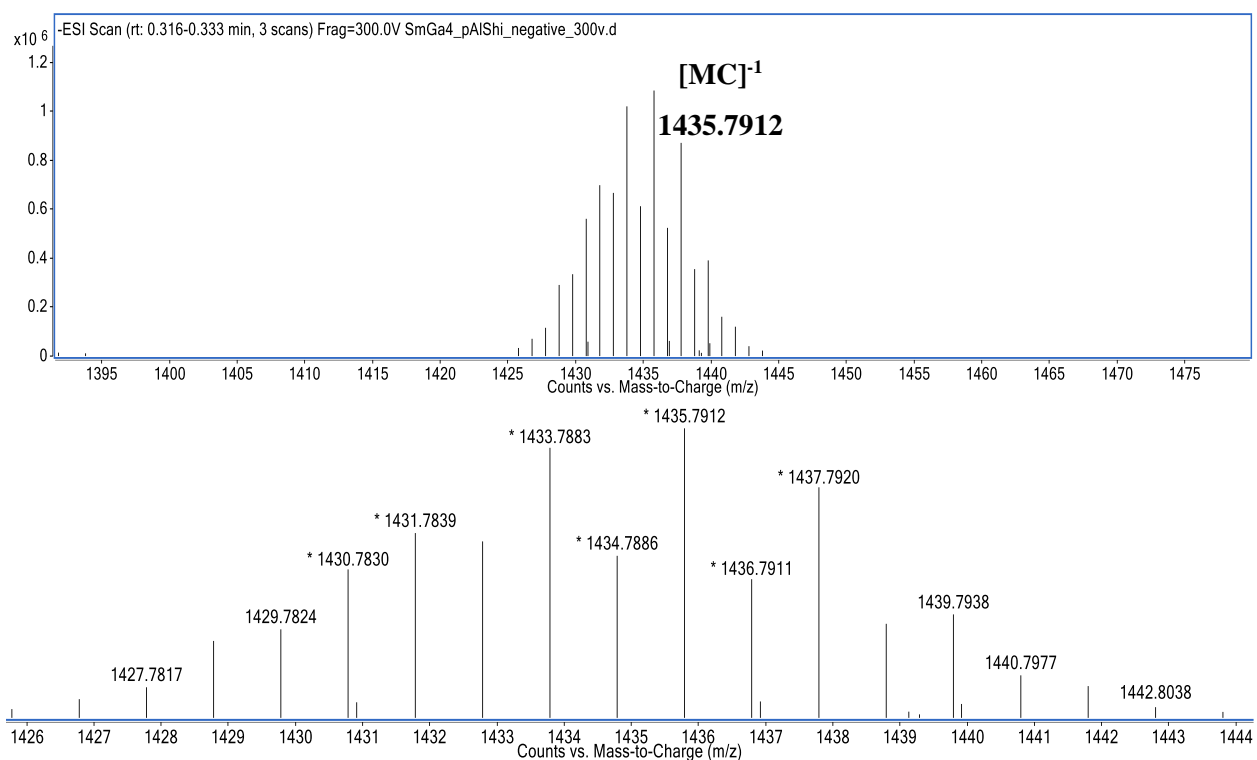


Figure C50 (Top) ESI-MS of SmGa₄pAlShi₄(Formate)₄ MC in negative ion. (Bottom) -1 isotopic distribution.

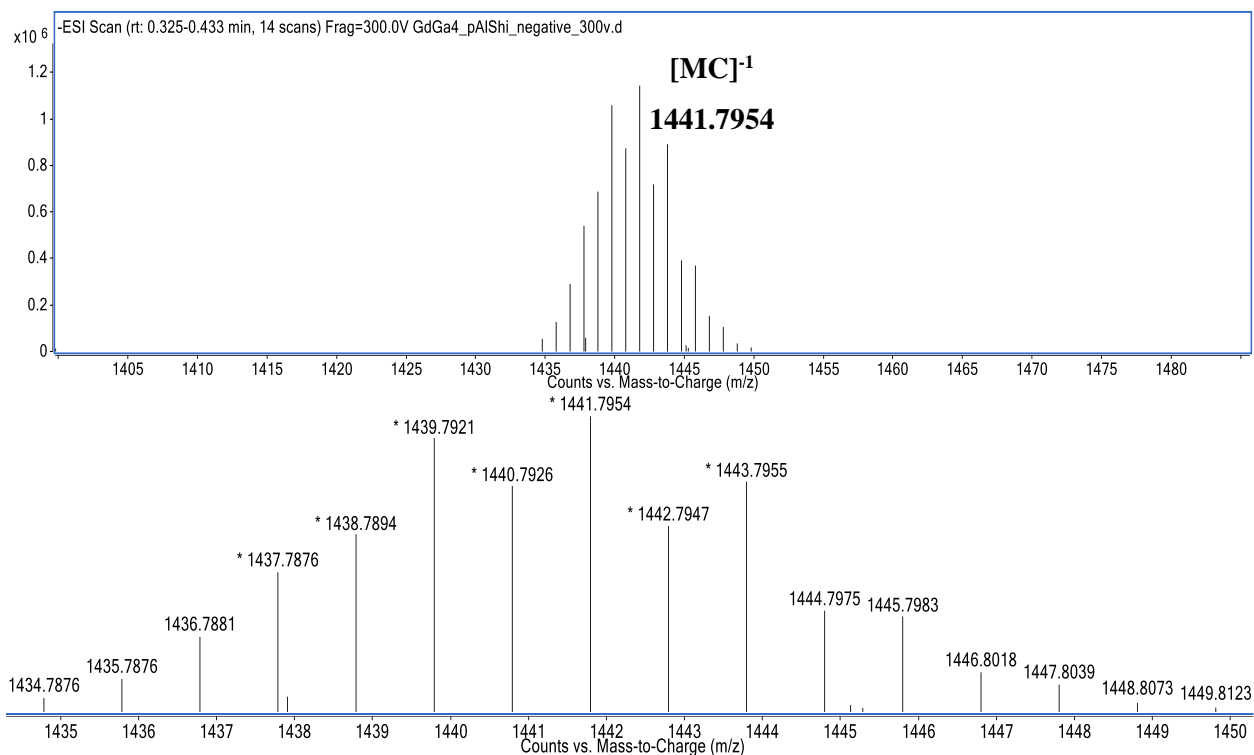


Figure C51 (Top) ESI-MS of GdGa₄pAlShi₄(Formate)₄ MC in negative ion. (Bottom) -1 isotopic distribution.

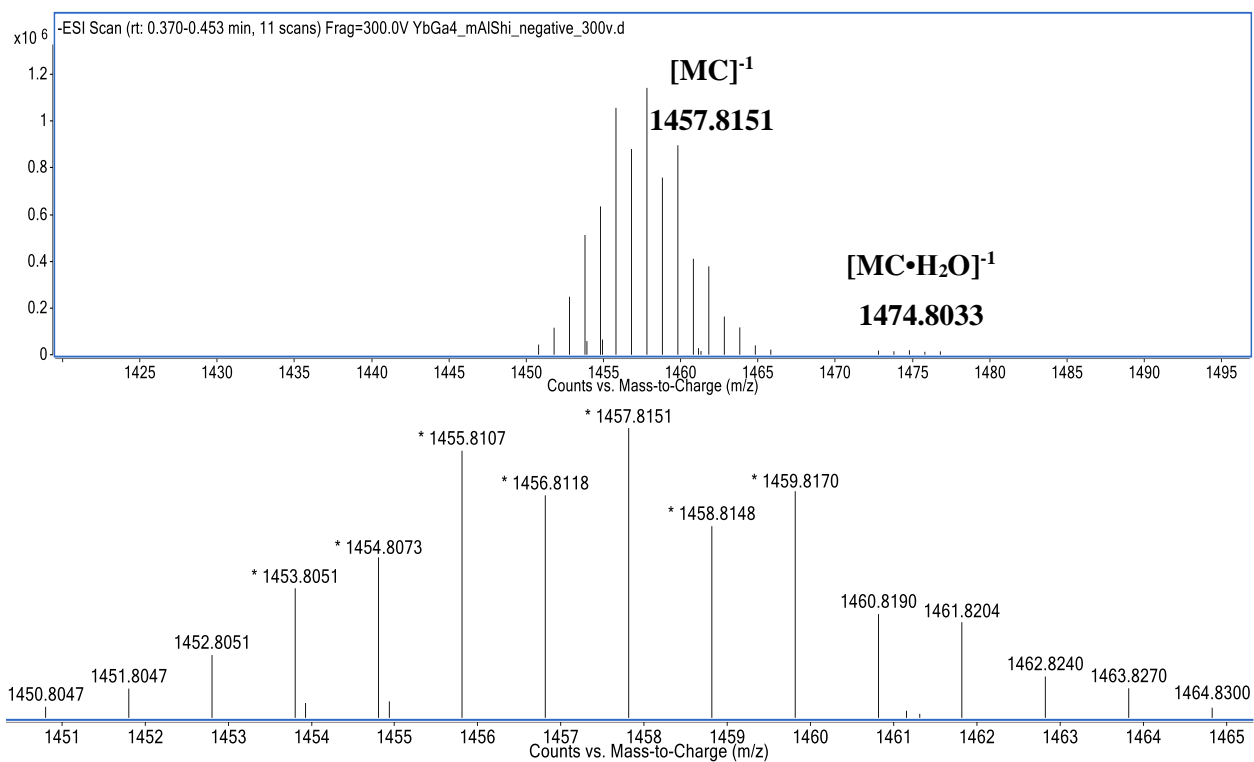


Figure C52 (Top) ESI-MS of YbGa₄mAlShi₄(Formate)₄ MC in negative ion. (Bottom) -1 isotopic distribution.

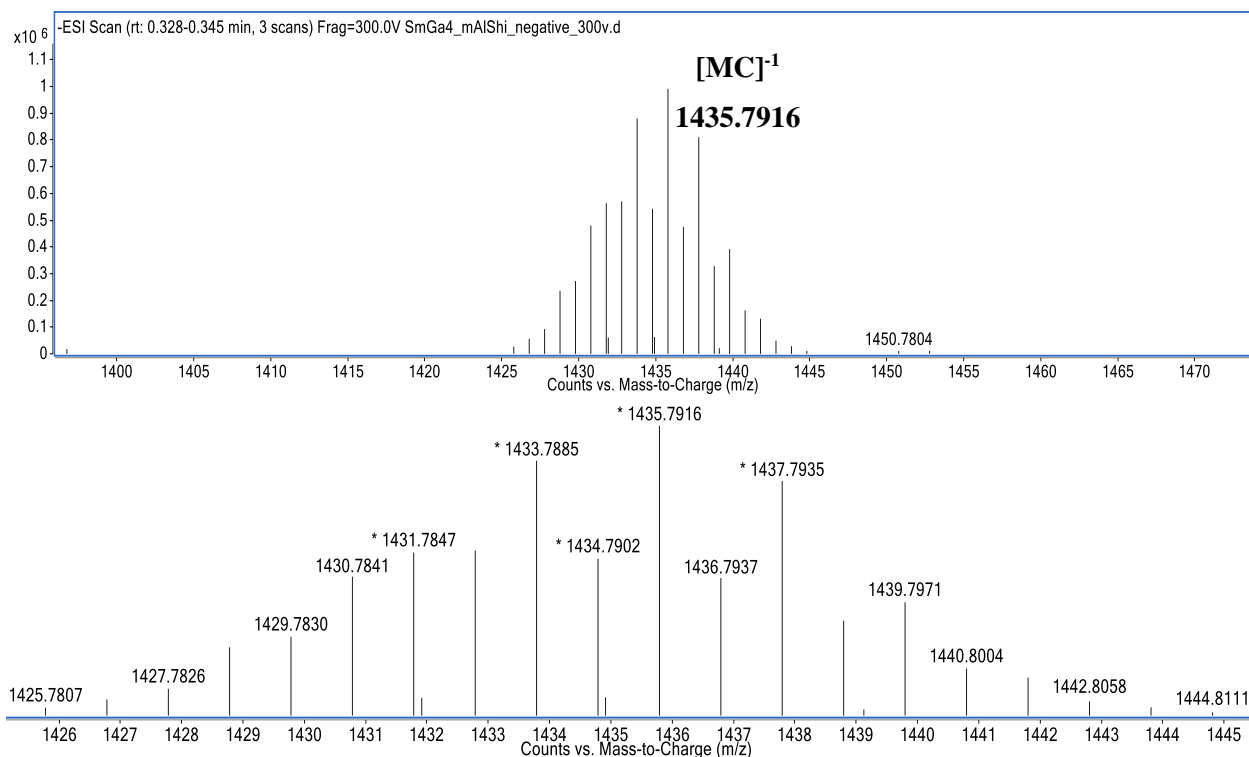


Figure C53 (Top) ESI-MS of SmGa₄mAlShi₄(Formate)₄ MC in negative ion. (Bottom) -1 isotopic distribution.

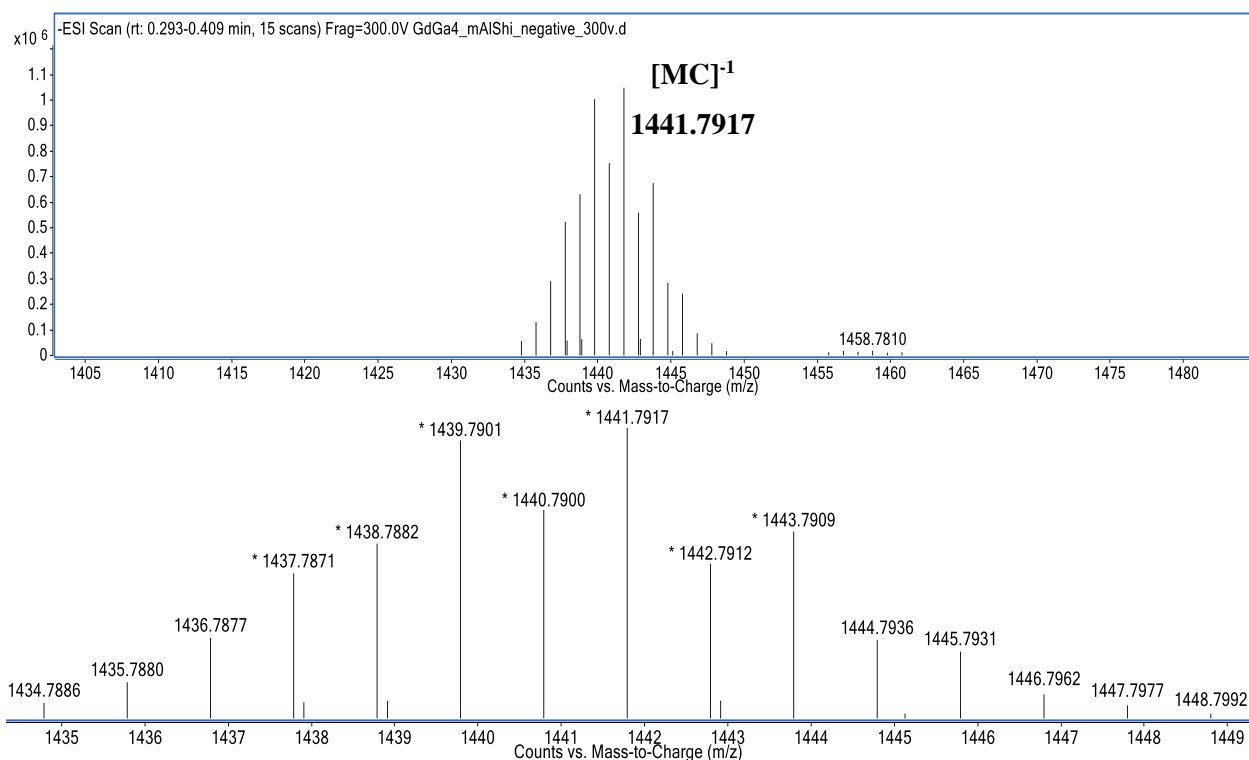


Figure C54 (Top) ESI-MS of GdGa₄mAlShi₄(Formate)₄ MC in negative ion. (Bottom) -1 isotopic distribution.

Ln₂Ga₈xShi₈Ip₄ Metallacrowns (Ln: Yb^{III}, Sm^{III}, and Gd^{III}; x: pYne, mYne, pAl, and mAl)

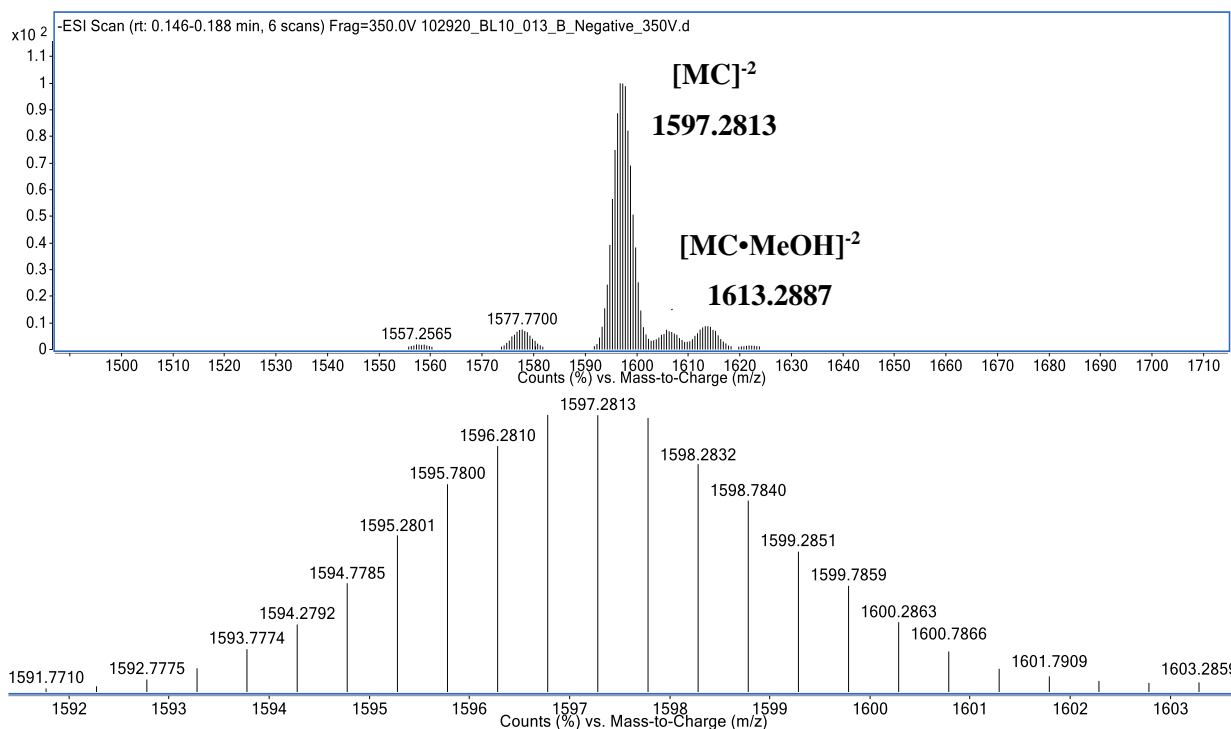


Figure C55 (Top) ESI-MS of Yb₂Ga₈pYneShi₈Ip₄ MC in negative ion. (Bottom) -2 isotopic distribution.

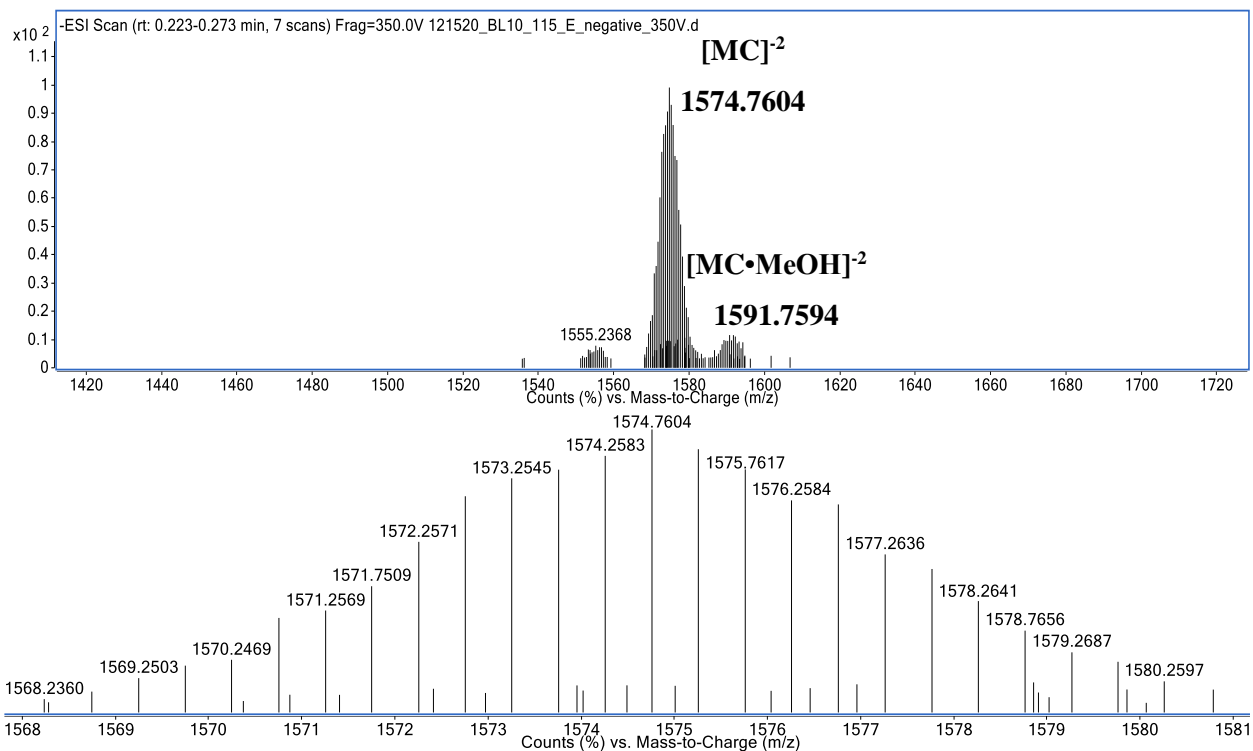


Figure C56 (Top) ESI-MS of Sm₂Ga₈pYneShi₈Ip₄ MC in negative ion. (Bottom) -2 isotopic distribution.

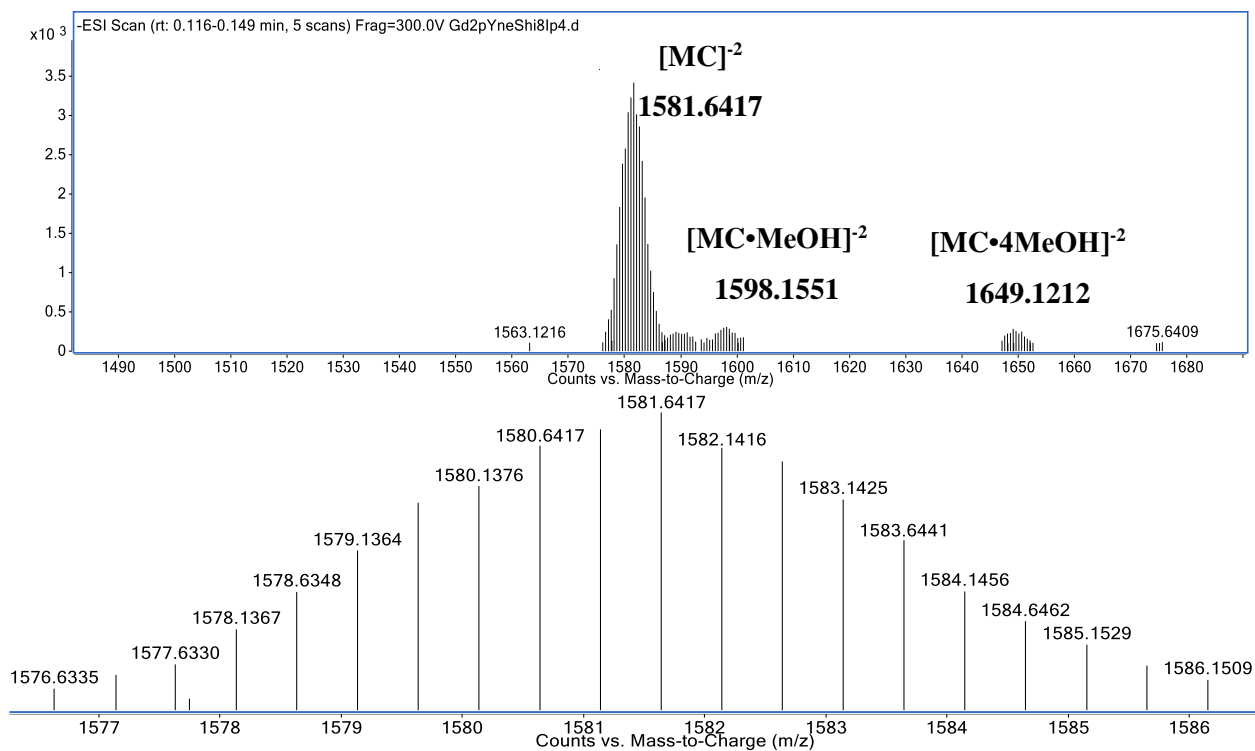


Figure C57. (Top) ESI-MS of $Gd_2Ga_8pYneShi_8Ip_4$ MC in negative ion. (Bottom) -2 isotopic distribution.

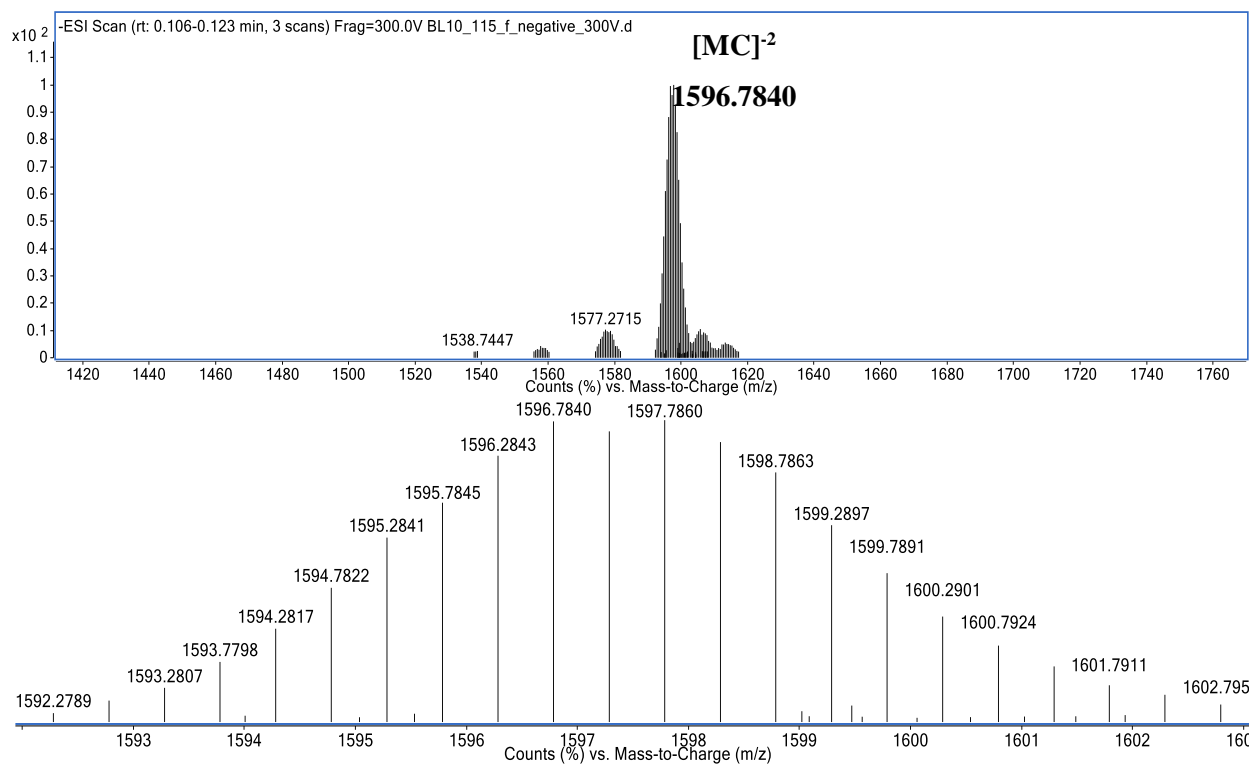


Figure C58 ESI-MS of $Yb_2Ga_8mYneShi_8Ip_4$ MC in negative ion. (Bottom) -2 isotopic distribution.

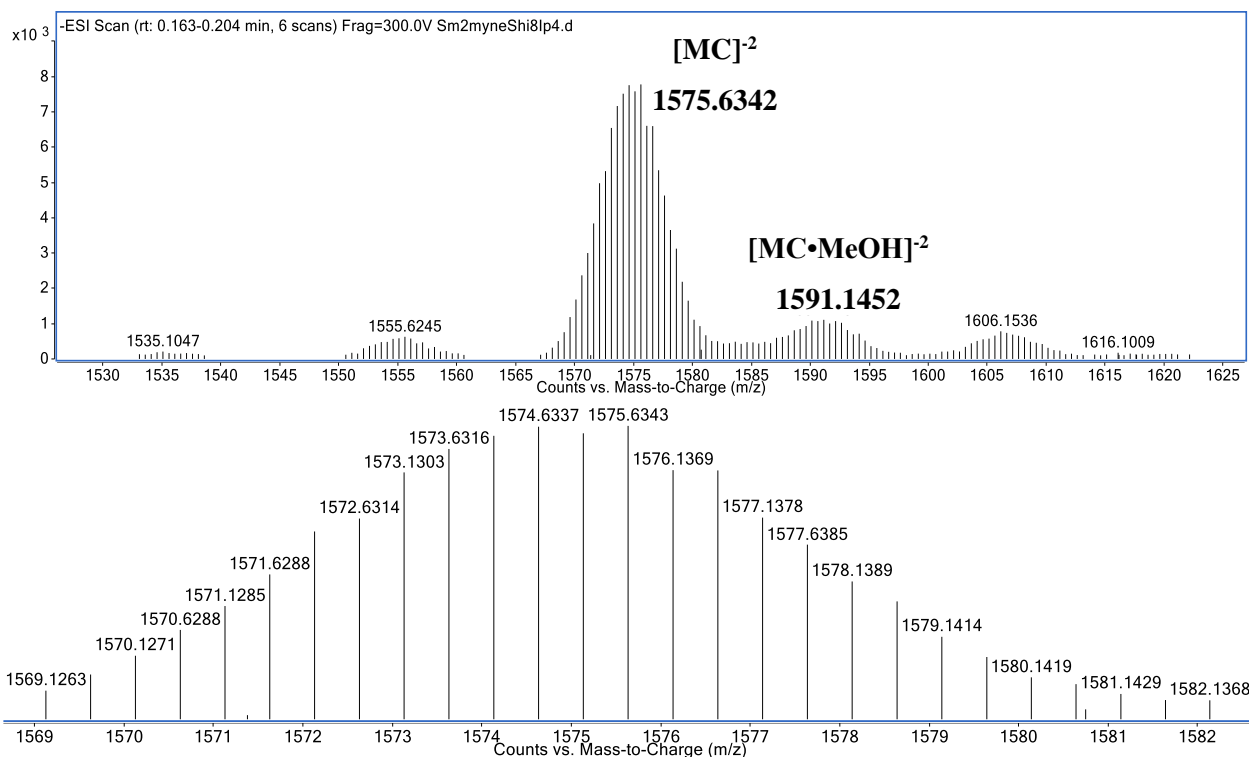


Figure C59 ESI-MS of Sm₂Ga₈mYneShi₈Ip₄ MC in negative ion. (Bottom) -2 isotopic distribution.

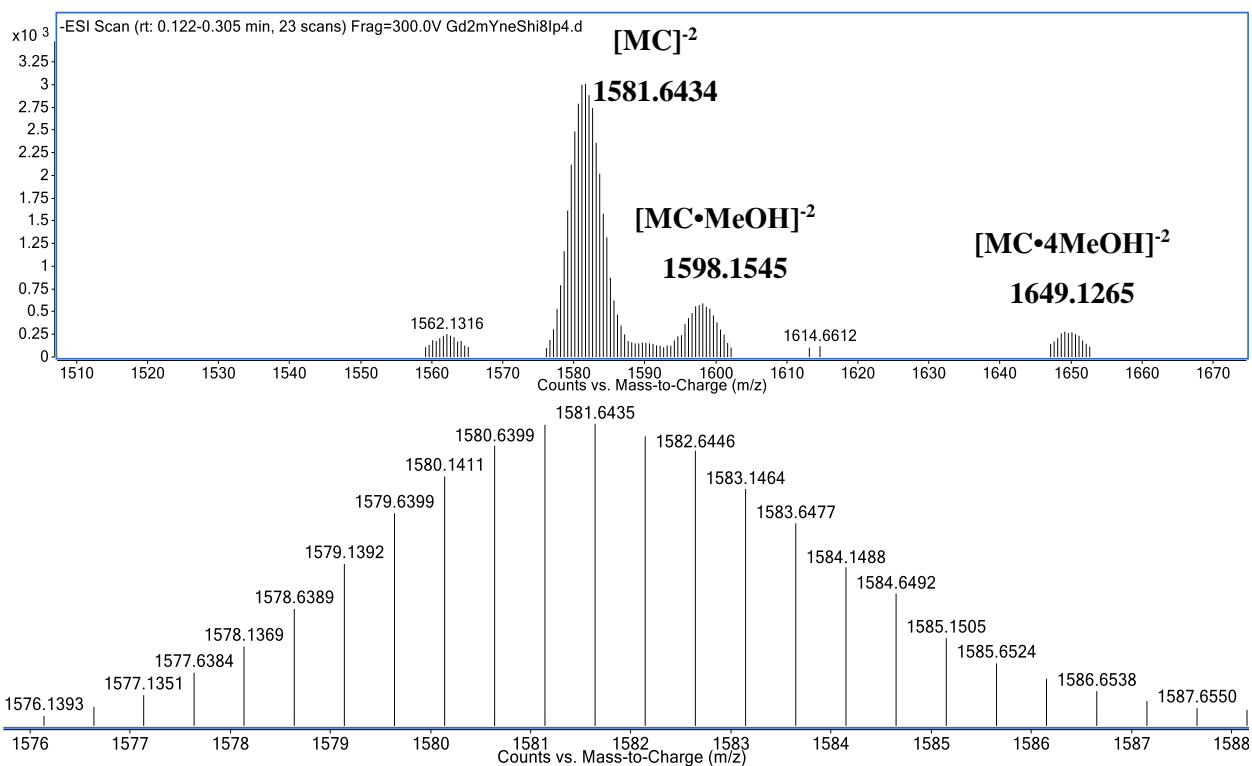


Figure C60 ESI-MS of Gd₂Ga₈mYneShi₈Ip₄ MC in negative ion. (Bottom) -2 isotopic distribution.

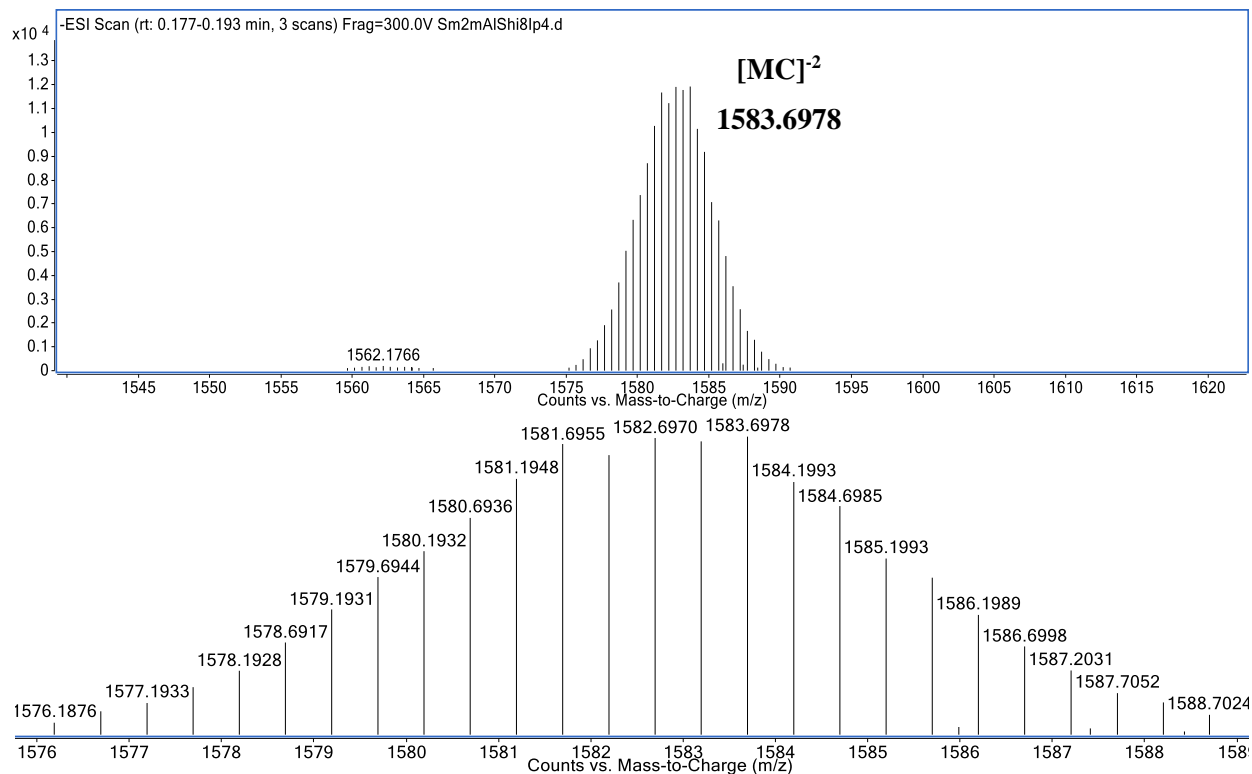


Figure C61 (Top) ESI-MS of Sm₂Ga₈pAlShi₈Ip₄ MC in negative ion. (Bottom) -2 isotopic distribution.

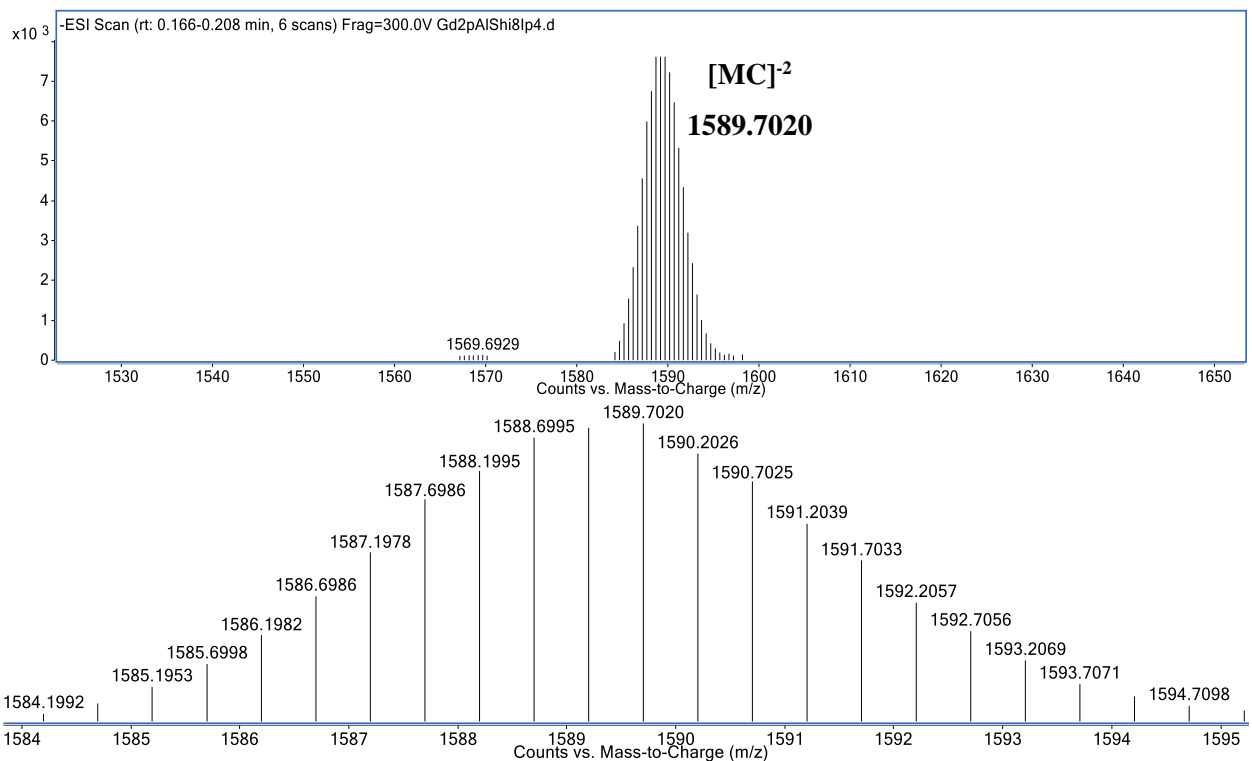


Figure C62 (Top) ESI-MS of Gd₂Ga₈pAlShi₈Ip₄ MC in negative ion. (Bottom) -2 isotopic distribution.

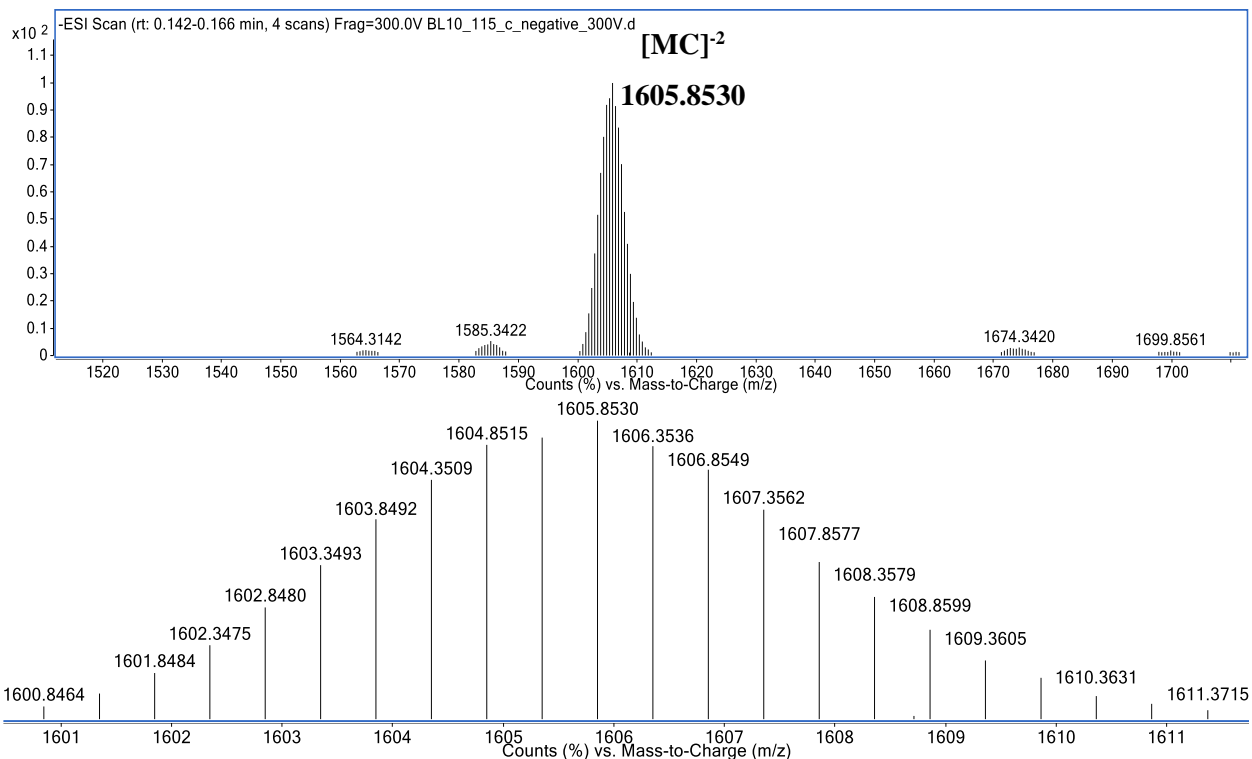


Figure C63 (Top) ESI-MS of Yb₂Ga_{8m}AlShi₈Ip₄ MC in negative ion. (Bottom) -2 isotopic distribution.

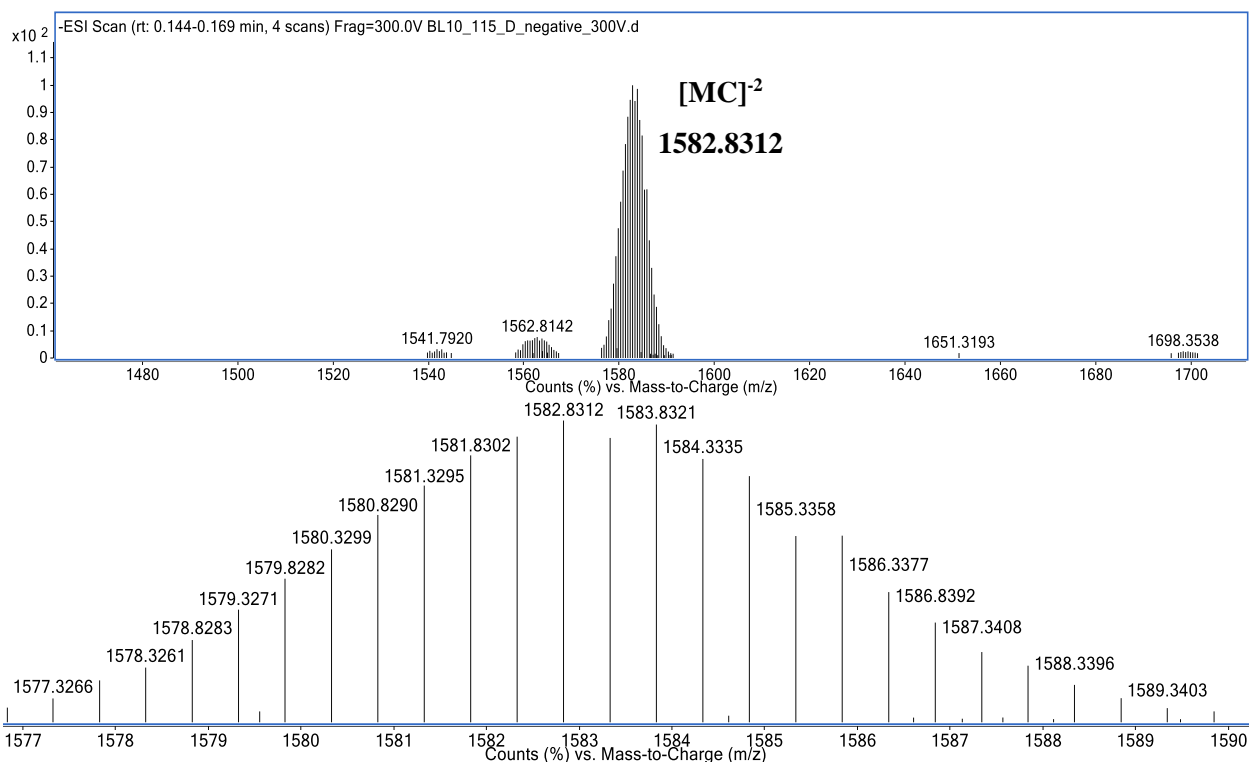
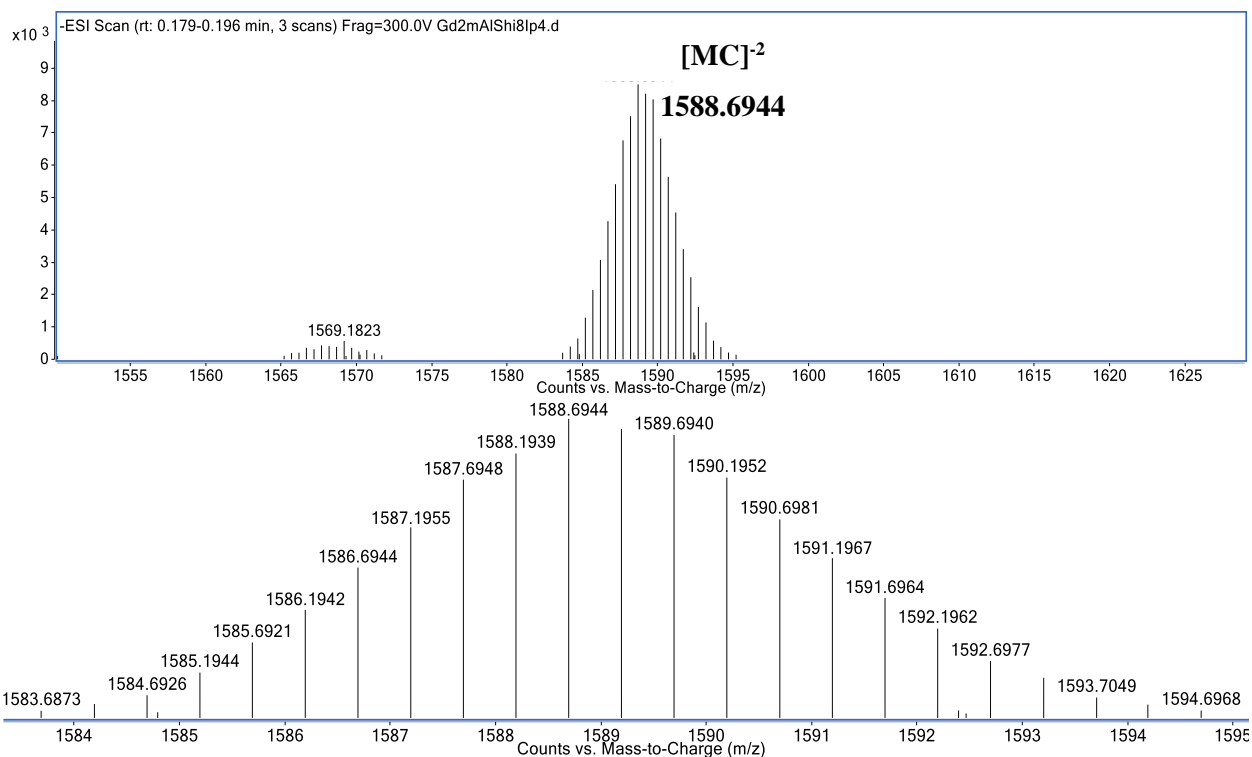
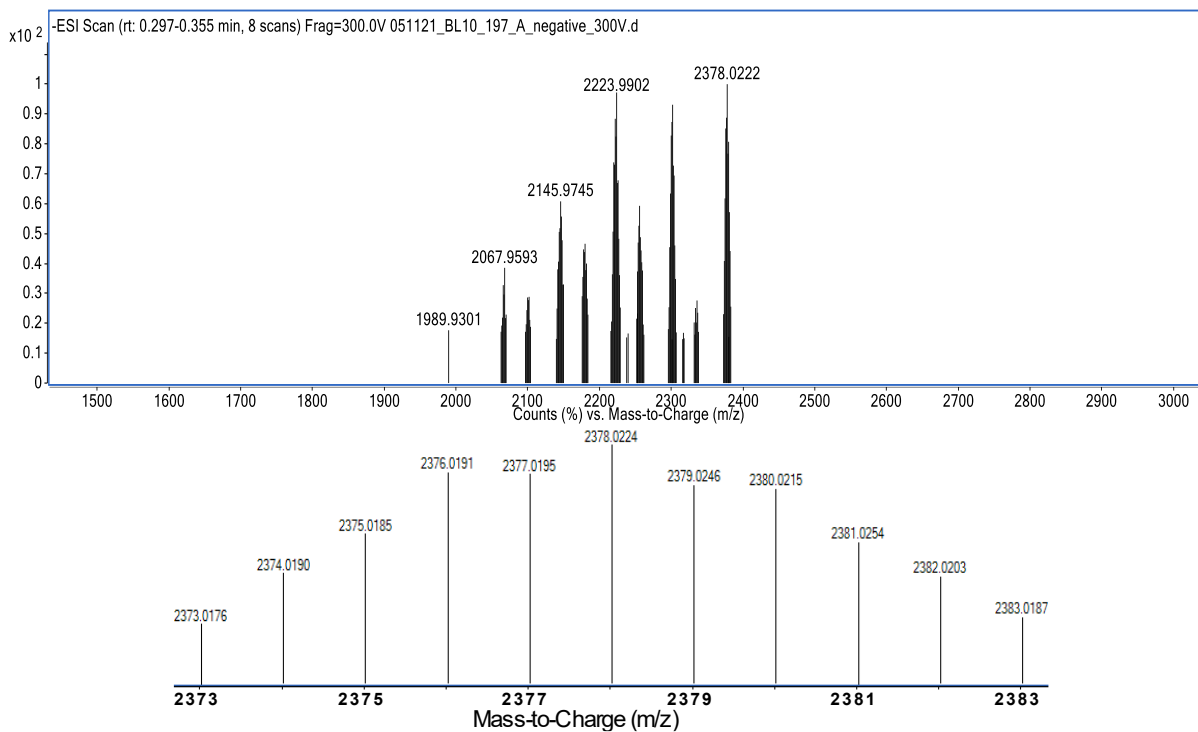


Figure C64 (Top) ESI-MS of Sm₂Ga_{8m}AlShi₈Ip₄ MC in negative ion. (Bottom) -2 isotopic distribution.



Coupling of β -mercaptoethanol to $LnGa_xShi_4(benzoate)_4$ Metallacrowns ($Ln: Yb^{III}$ and Sm^{III} ; $x: pYne, mYne, pAl,$ and mAl)



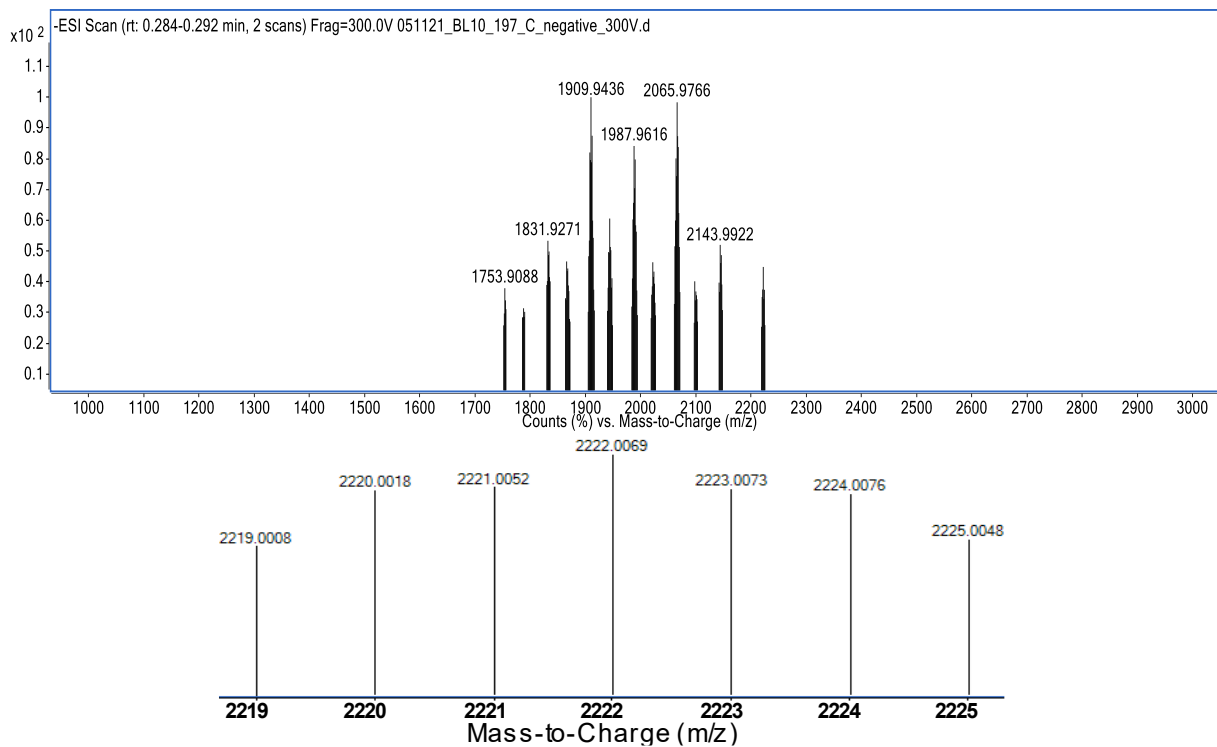


Figure C67 ESI-MS of $\text{YbGa}_4\text{mYneShi}_4(\beta\text{ME})_{6-4}$ in negative ion. (Bottom) -1 isotopic distribution.

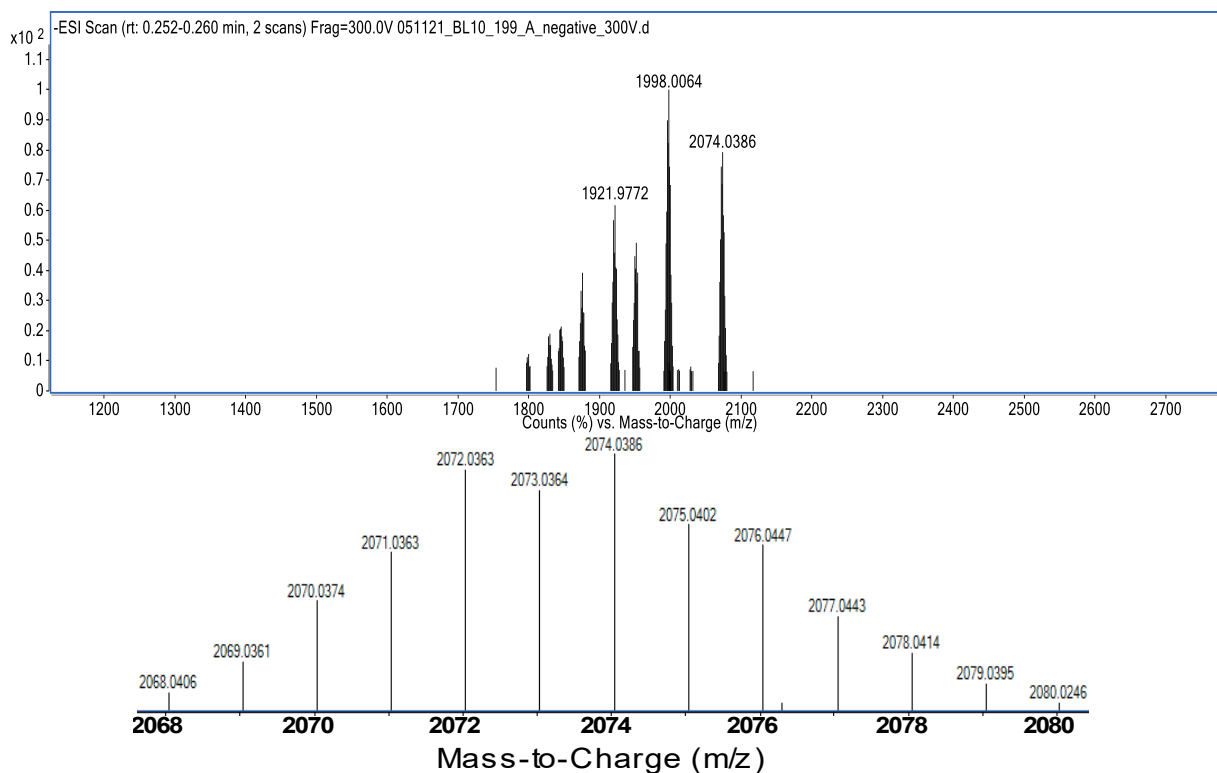


Figure C68 ESI-MS of $\text{YbGa}_4\text{pAlShi}_4(\beta\text{ME})_4$ in negative ion. (Bottom) -1 isotopic distribution.

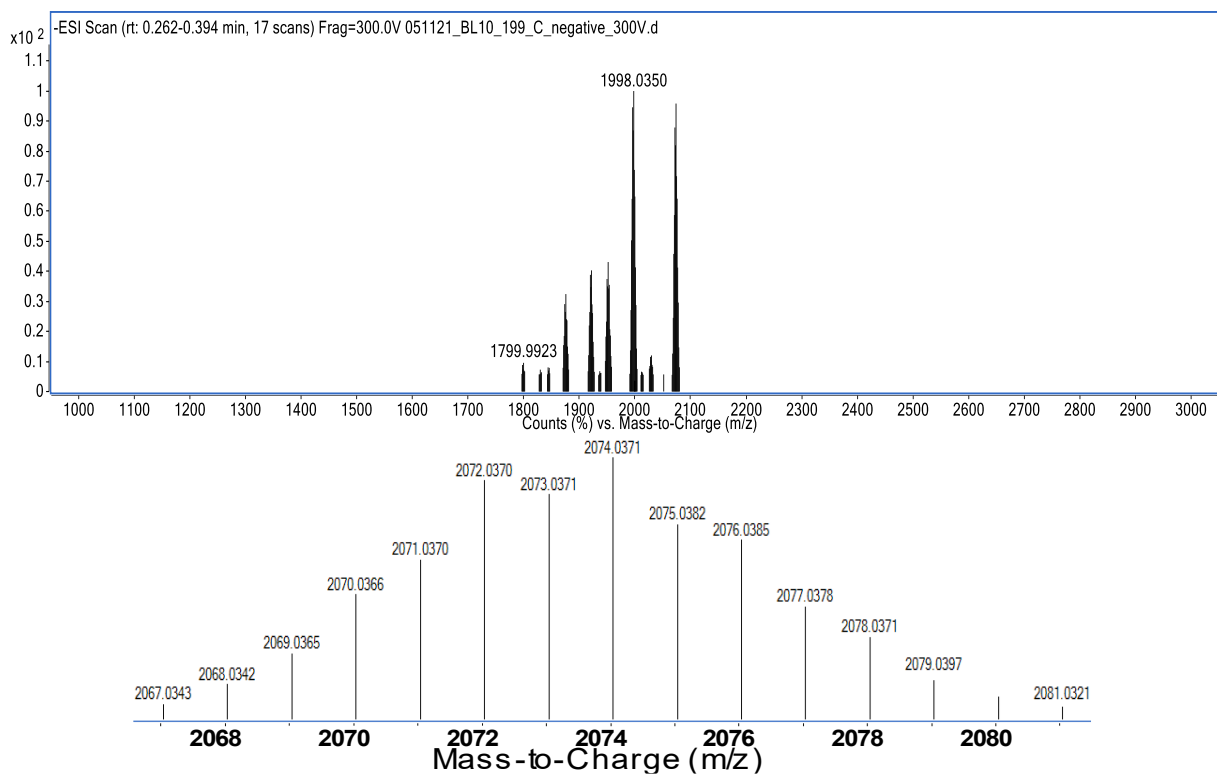
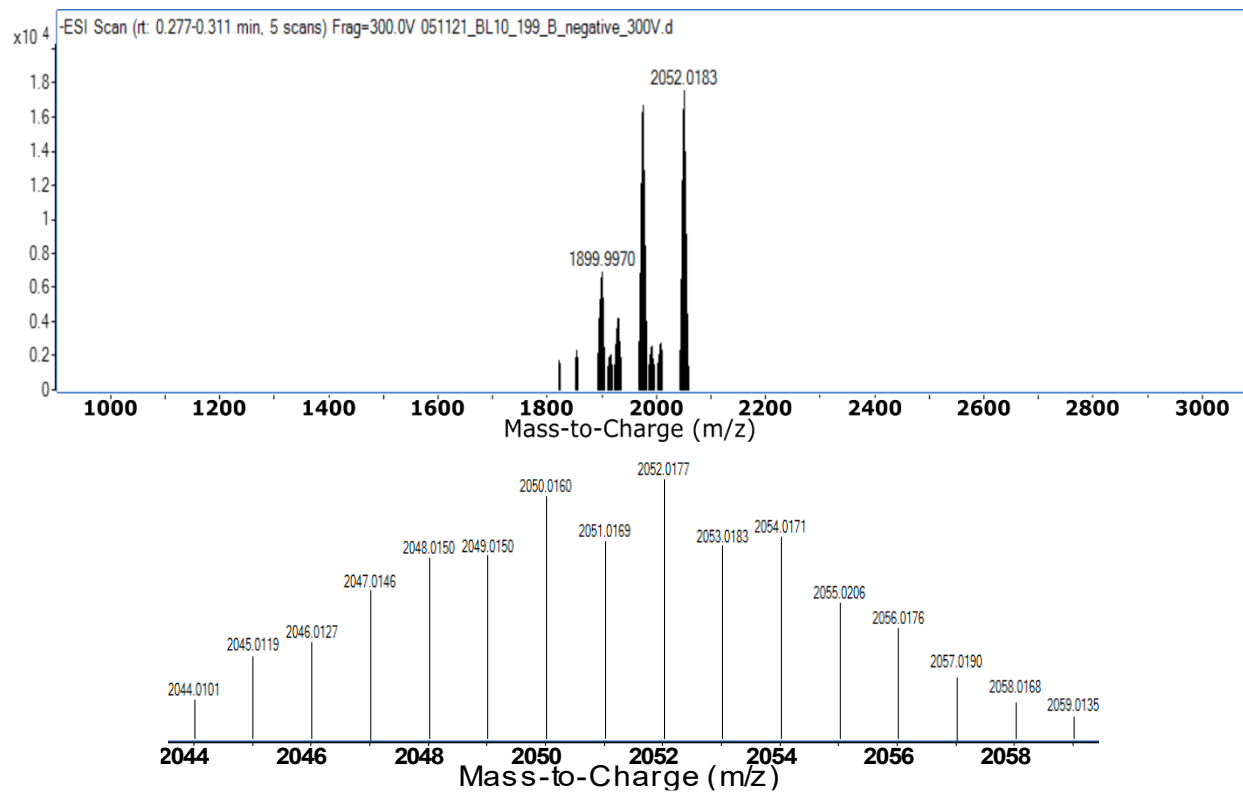


Figure C69 ESI-MS of $\text{YbGa}_4\text{mAlShi}_4(\beta\text{ME})_4$ in negative ion. (Bottom) -1 isotopic distribution.



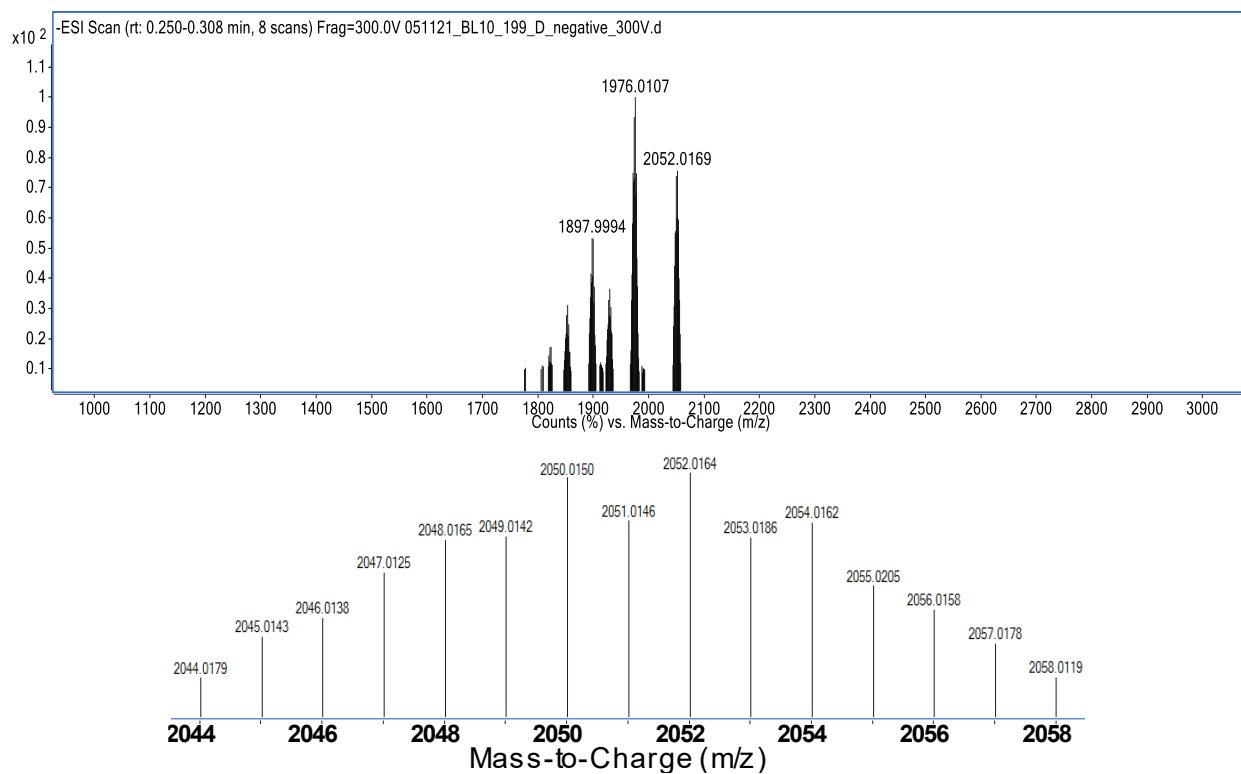


Figure C71. ESI-MS of $\text{SmGa}_4\text{mAlShi}_4(\beta\text{ME})_4$ in negative ion. (Bottom) -1 isotopic distribution.

Coupling of β -mercaptoethanol to $\text{Ln}_2\text{Ga}_8\text{xShi}_8\text{Ip}_4$ MCs ($\text{Ln}:\text{Yb}^{\text{III}}$; x : pYne, mYne, pAl, and mAl)

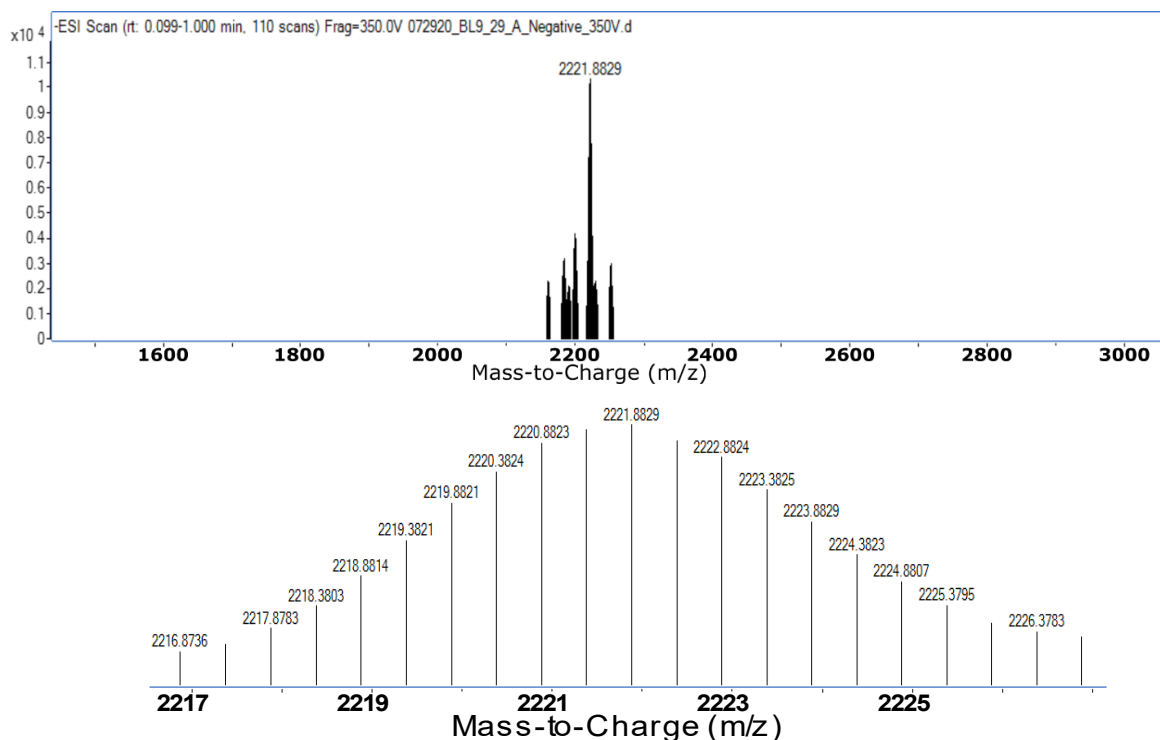


Figure C72. ESI-MS of $\text{Yb}_2\text{Ga}_8\text{pYneShi}_8\text{Ip}_4(\beta\text{ME})_{16-14}$ in negative ion. (Bottom) -2 isotopic distribution.

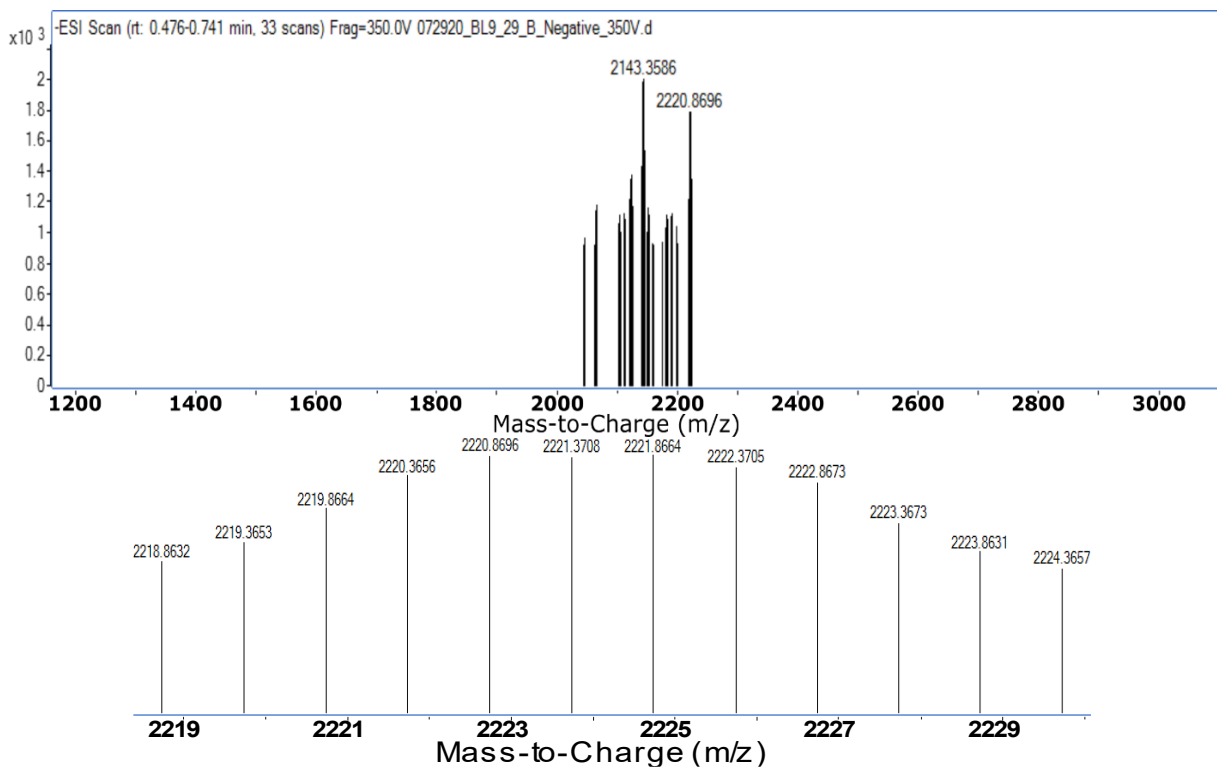


Figure C73 ESI-MS of $\text{Yb}_2\text{Ga}_8\text{mYneShi}_8\text{Ip}_4(\beta\text{ME})_{16-11}$ in negative ion. (Bottom) -2 isotopic distribution.

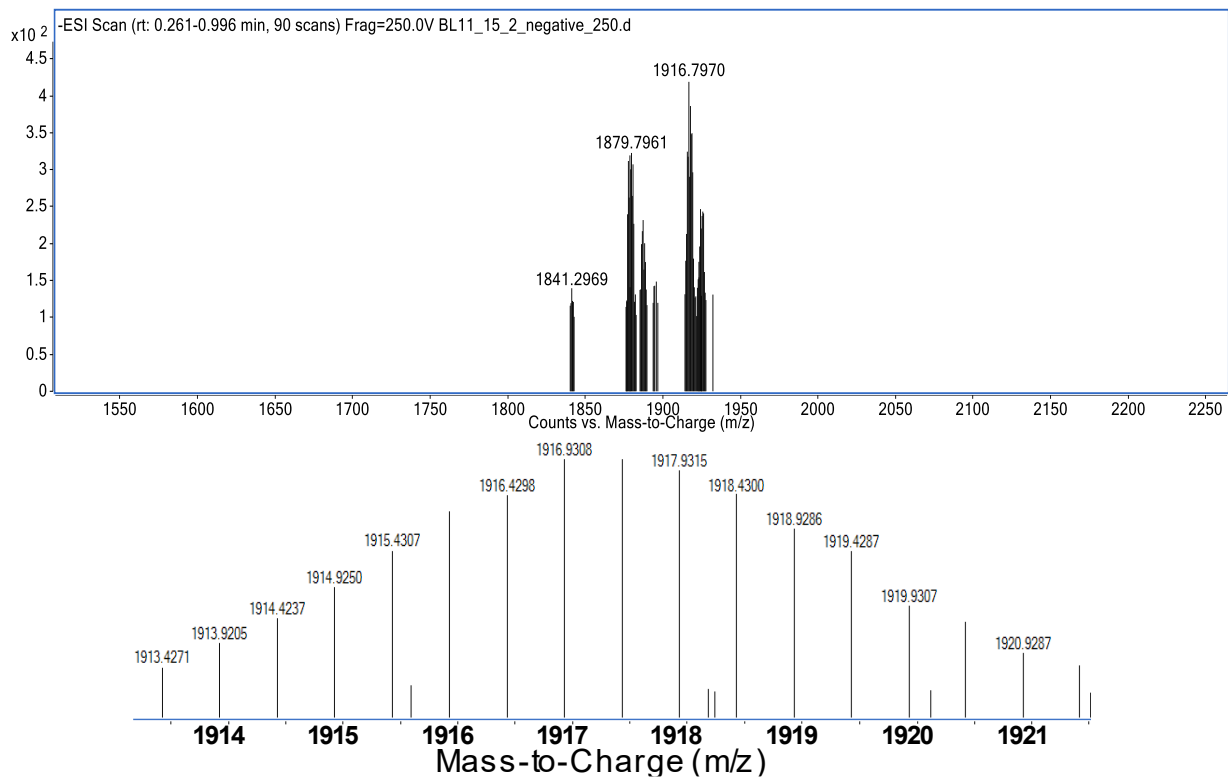


Figure C74 ESI-MS of $\text{Yb}_2\text{Ga}_8\text{pAlShi}_8\text{Ip}_4(\beta\text{ME})_{8-6}$ in negative ion. (Bottom) -2 isotopic distribution.

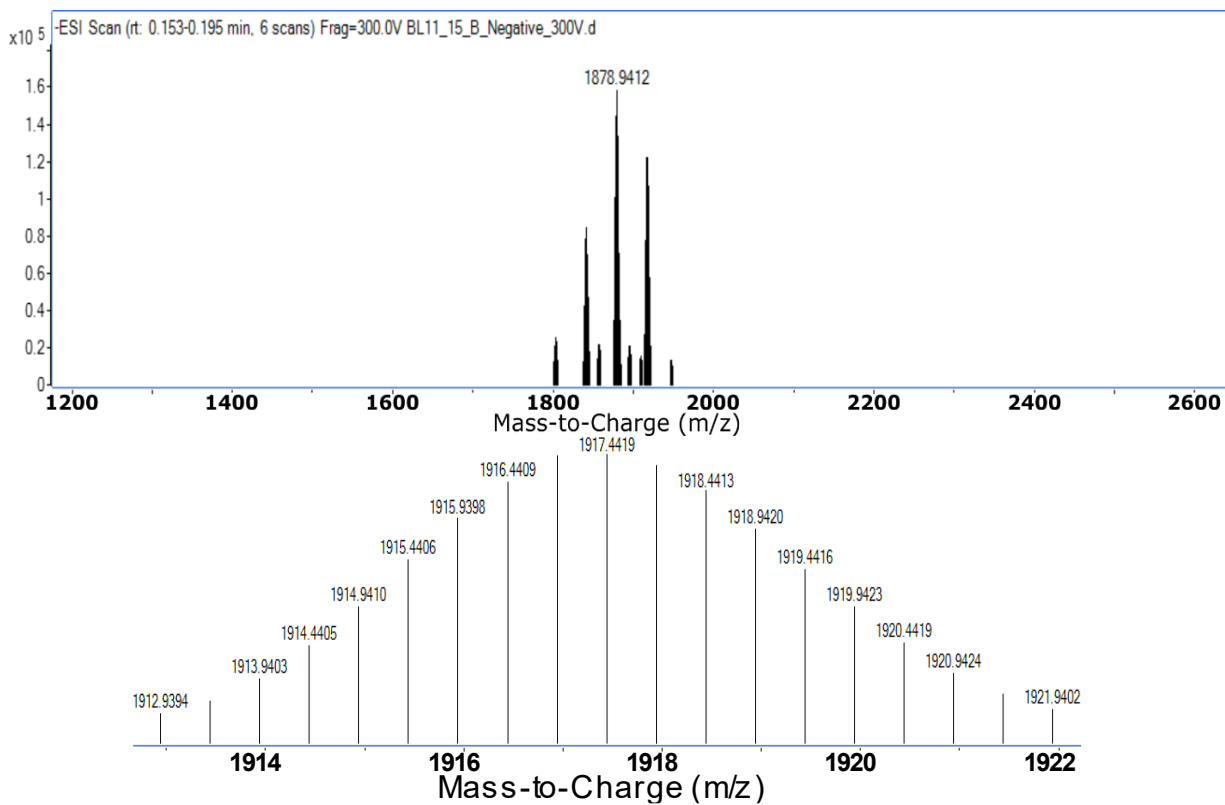


Figure C75 ESI-MS of $\text{Yb}_2\text{Ga}_8\text{mAlShi}_3\text{Ip}_4(\beta\text{ME})_{8.5}$ in negative ion. (Bottom) -2 isotopic distribution.

Appendix D Supplemental Information for Chapter 4

ESI Mass Spectra

*Ln*₂Ga₈xShi₈Mip₄ Metallacrowns (*Ln*: Yb^{III} and Gd^{III}; *x*: mAl and pYne)

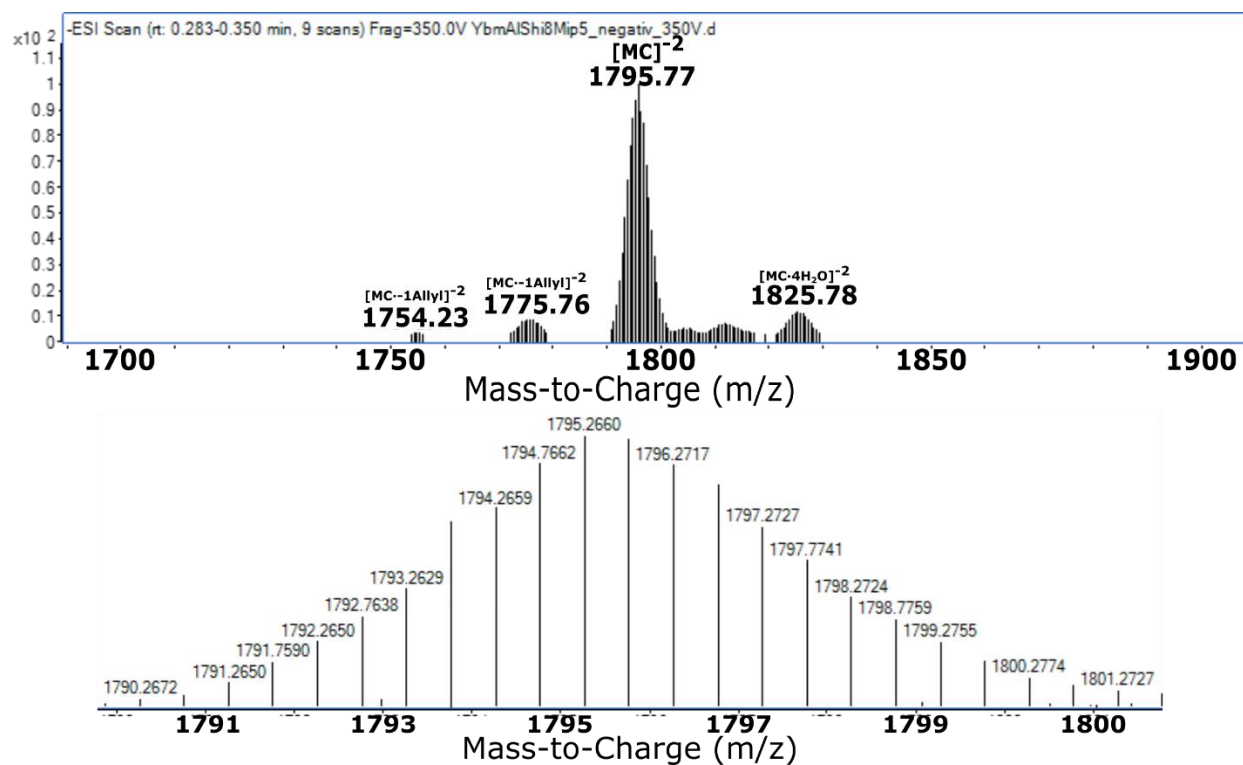


Figure D76 (Top) ESI-MS of Yb₂Ga₈mAlShi₈Mip₄ MC in negative ion. (Bottom) expansion of the major peak corroborating the -2 isotopic distribution of the complex.

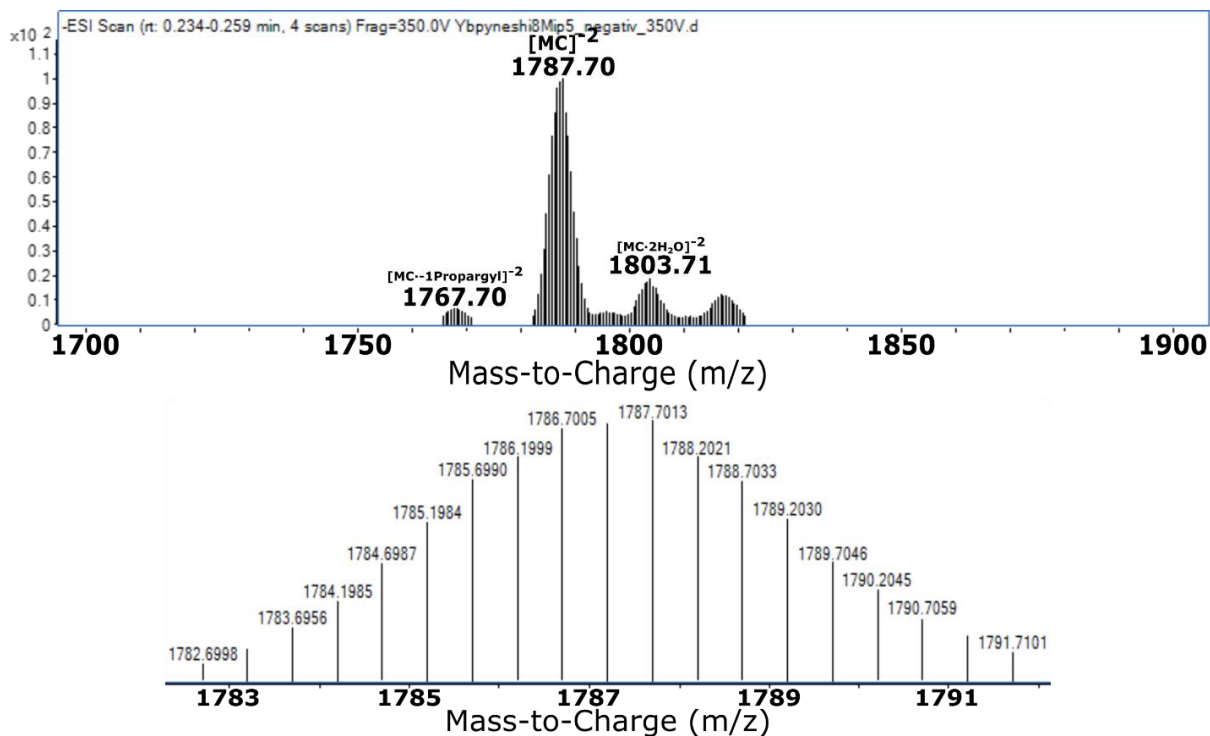


Figure D77 (Top) ESI-MS of Yb₂Ga₈pYneShi₈Mip₄ MC in negative ion. (Bottom) expansion of the major peak corroborating the -2 isotopic distribution of the complex.

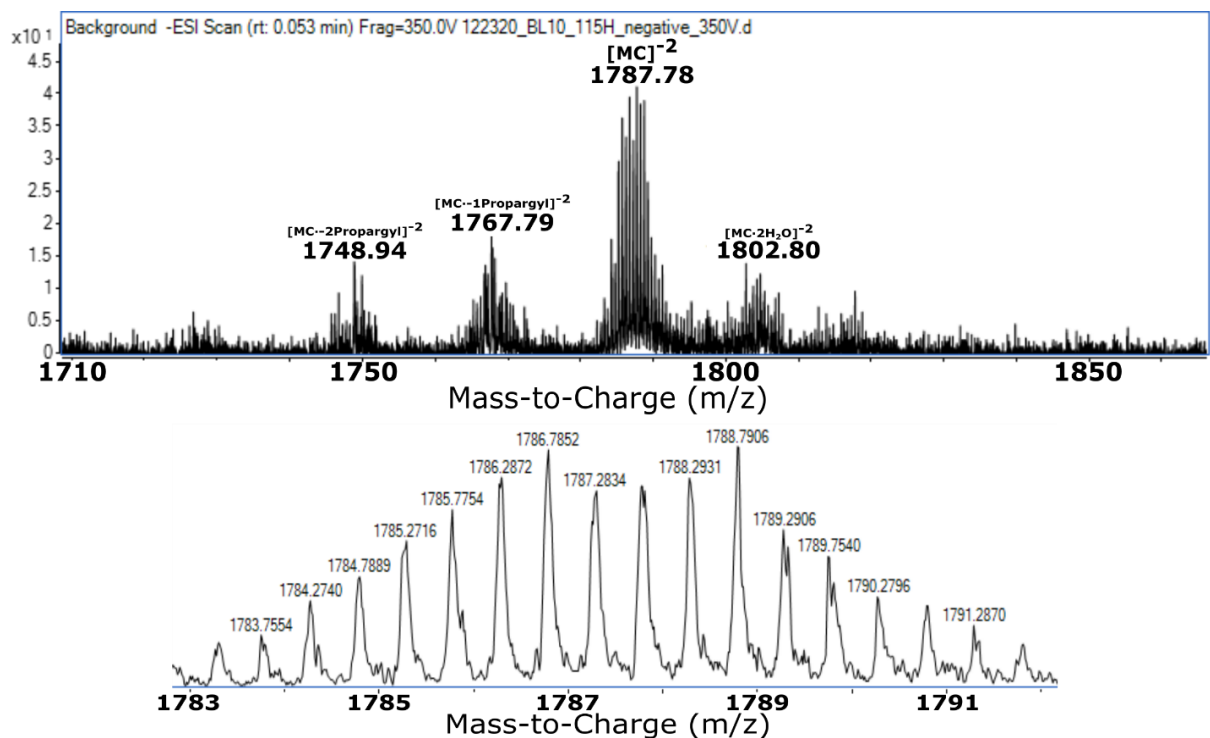


Figure D78 (Top) ESI-MS of Yb₂Ga₈mYneShi₈Mip₄ MC in negative ion. (Bottom) expansion of the major peak corroborating the -2 isotopic distribution of the complex.

¹H NMR Spectra

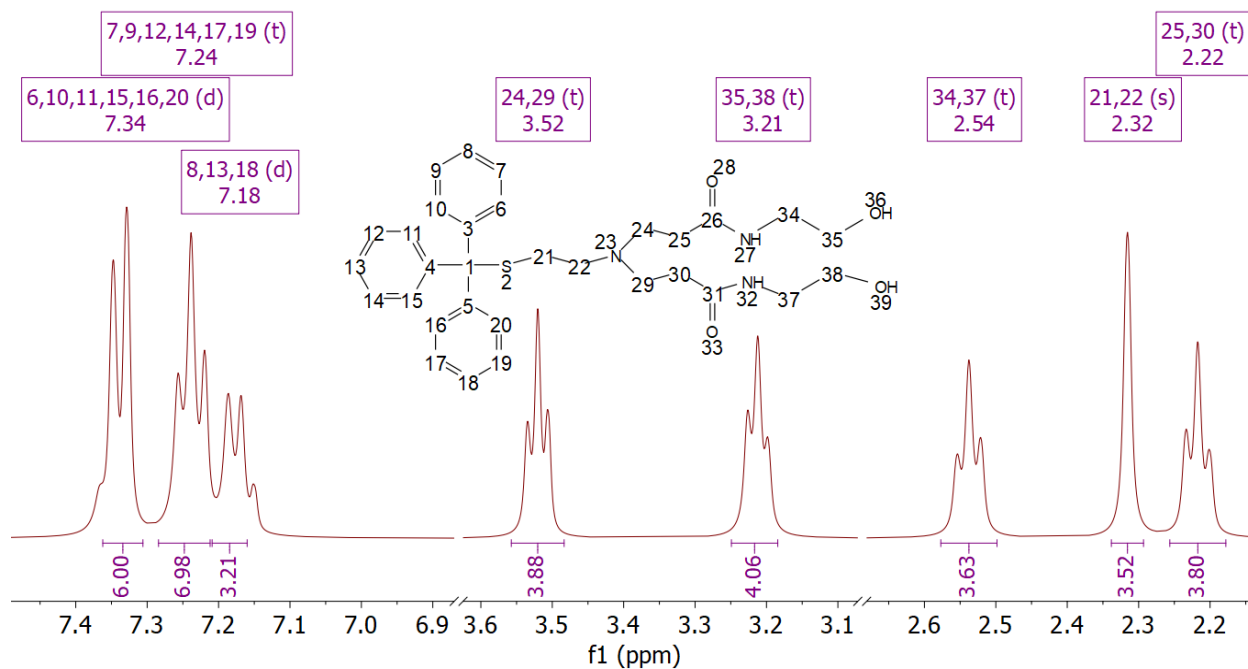


Figure D79 ¹H NMR spectrum of Trityl-G1.0-OH dendron.

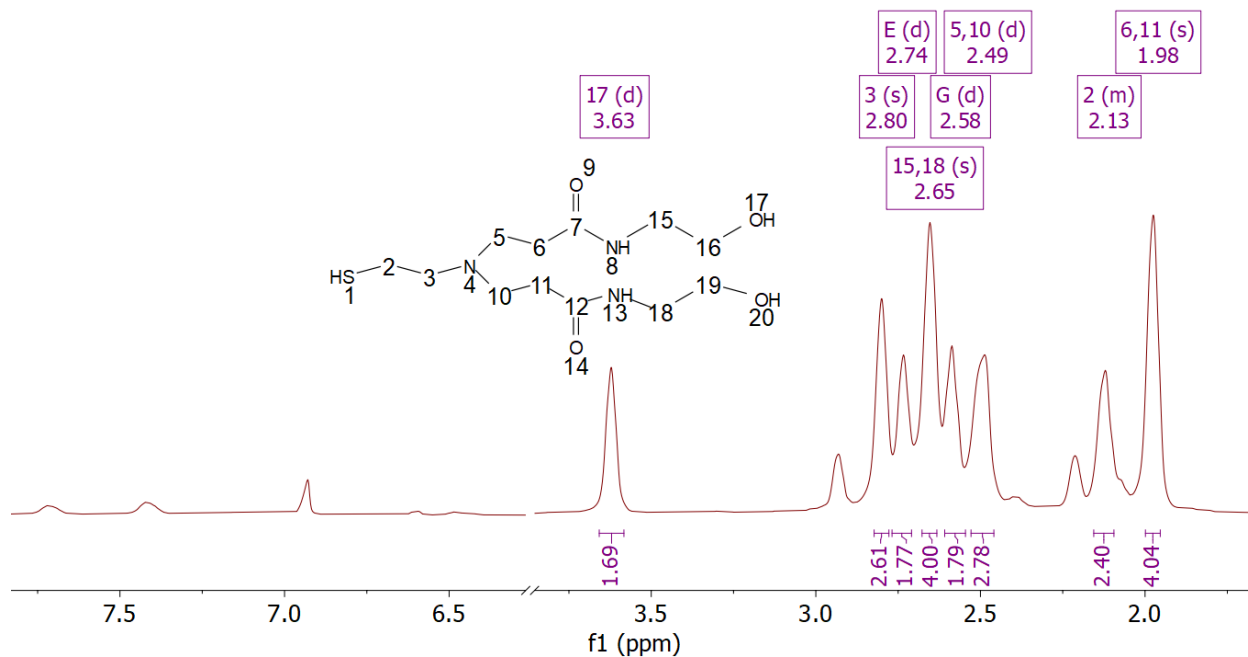


Figure D80 ¹H NMR spectrum of HS-G1.0-OH dendron. Signals at ~6.9-7.7 ppm are left over trityl salt.

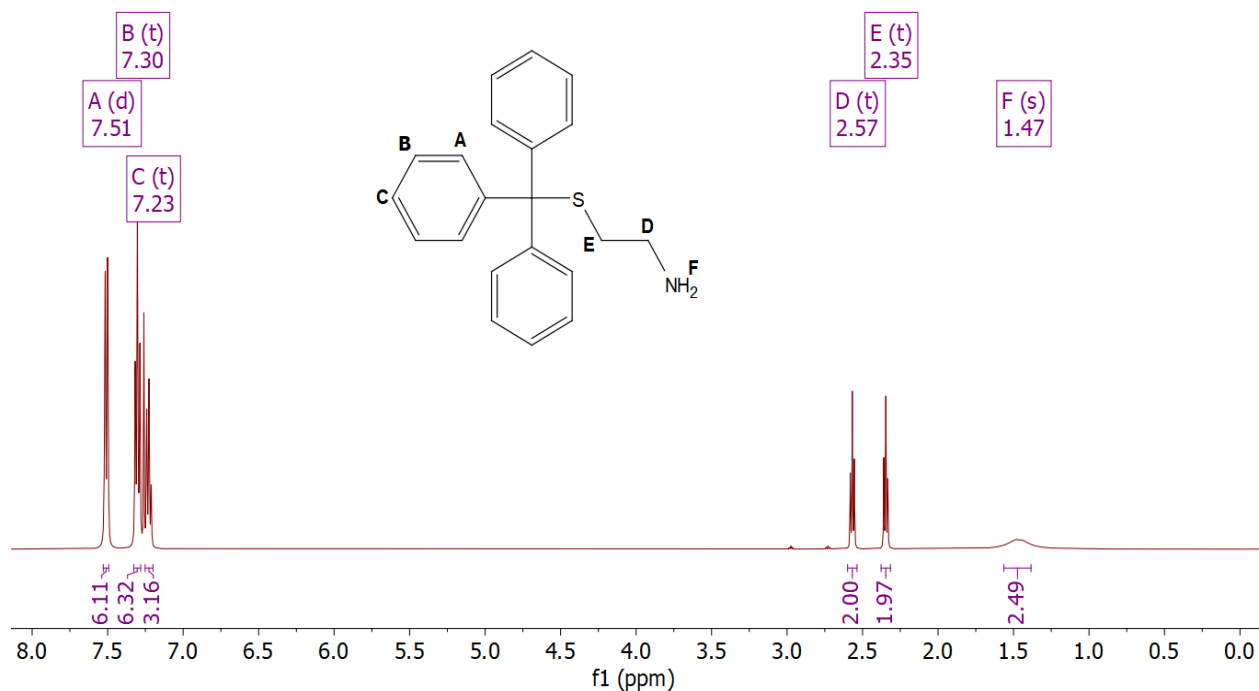


Figure D81 ¹H NMR spectrum of **1**. Small impurity peaks at 2.73 ppm and 2.97 ppm are from cystamine byproduct (~2%).

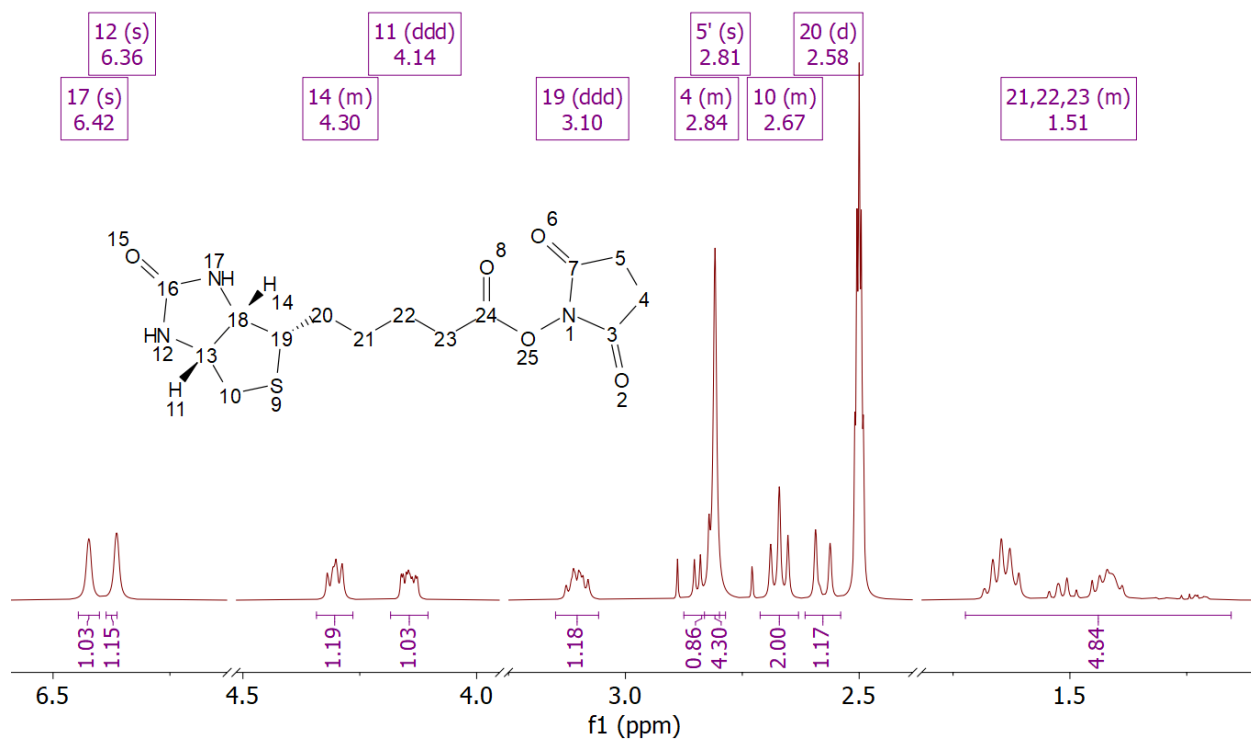


Figure D82 ¹H NMR spectrum of **2**. Unlabeled peaks at 2.50 ppm, 2.73 ppm, and 2.89 ppm are from dms₂-d₆ and leftover DMF.

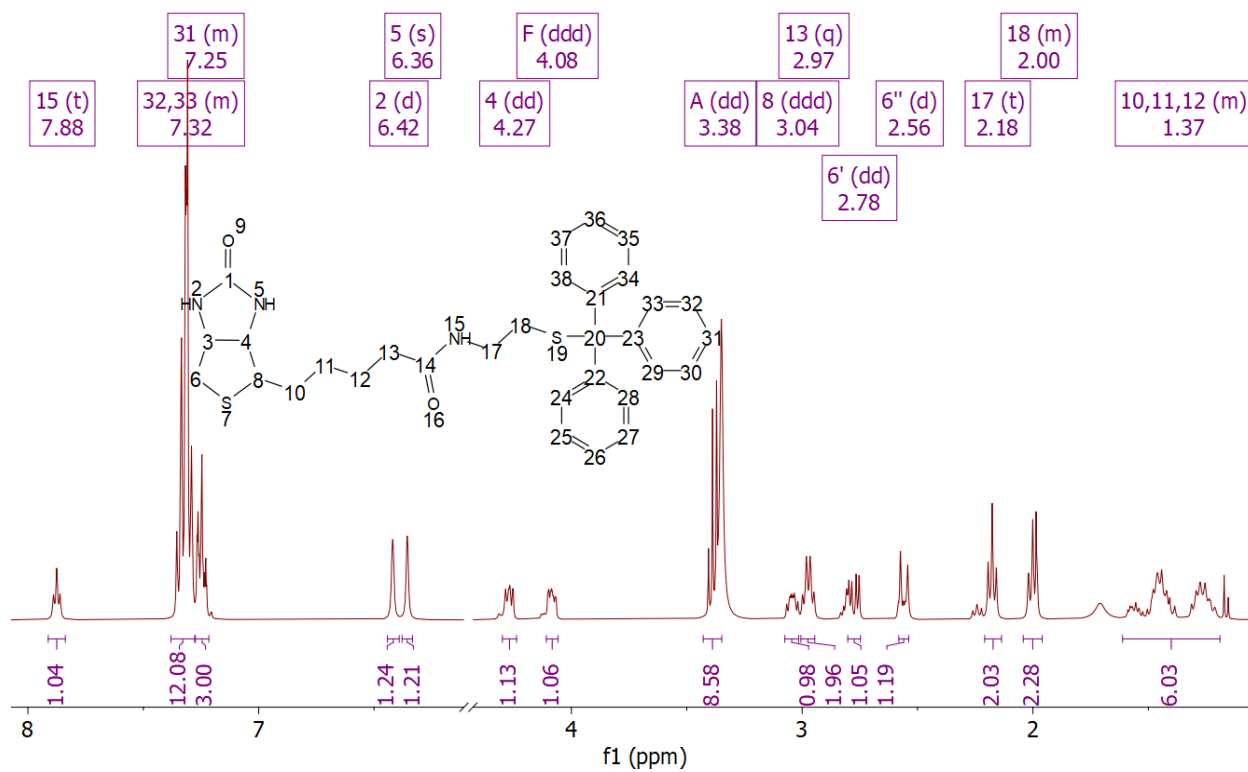


Figure D83 ¹H NMR spectrum of **3**.

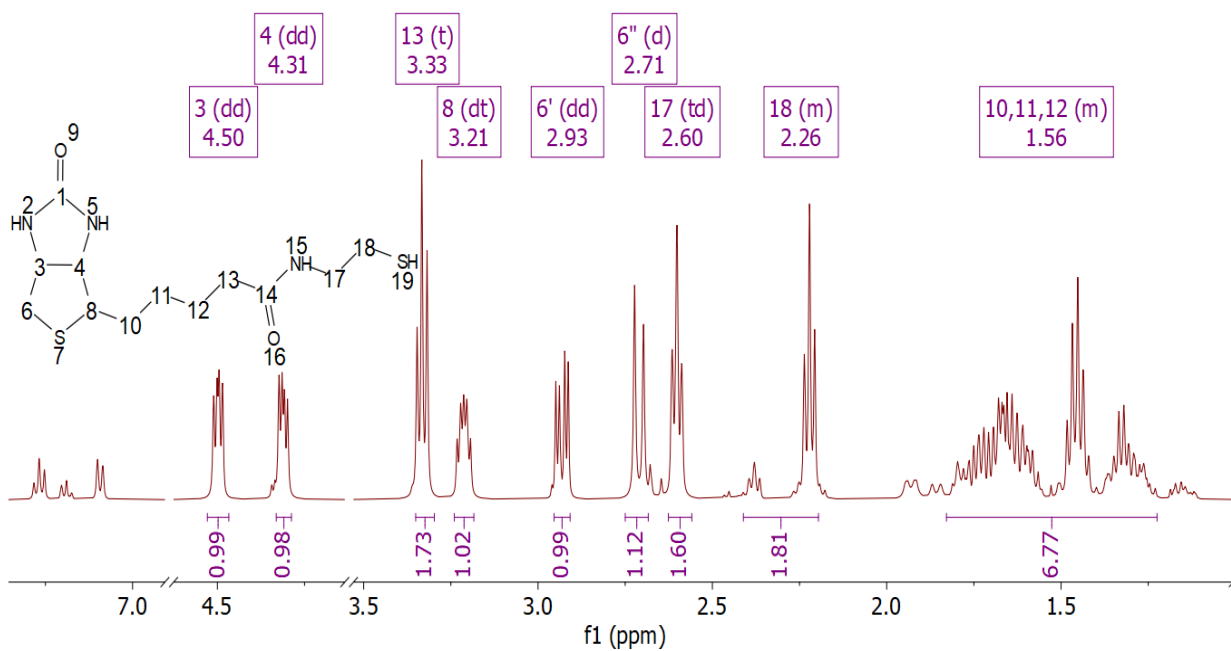


Figure D84 ¹H NMR spectrum of **3**. Peaks at above 7.0 ppm are residual trityl salt.

Bibliography

1. Donald A. Tomalia, Jørn B. Christensen, U. B. *Dendrimer, Dendron, and Dendritic Polymers: Discovery, Applications, and the Future*. (Cambridge University Press, 2012).
2. Buhleier, E., Wehner, W. & Vogtle, F. 'Cascade' and 'Nonskid-Chain-like' Syntheses of Molecular Cavity Topologies. *Synthesis (Stuttg)*. 155–158 (1978).
3. Tomalia, D. A. *et al.* A new class of polymers: Starburst-dendritic macromolecules. *Polym. J.* **17**, 117–132 (1985).
4. Mintzer, M. A. & Grinstaff, M. W. Biomedical applications of dendrimers: A tutorial. *Chem. Soc. Rev.* **40**, 173–190 (2011).
5. Hermanson, G. T. Dendrimers and Dendrons. in *Bioconjugate Techniques (Third edition)* 351–386 (2013). doi:<http://dx.doi.org/10.1016/B978-0-12-382239-0.00008-X>.
6. Grayson, S. M. & Fréchet, J. M. J. J. Convergent dendrons and dendrimers: From synthesis to applications. *Chem. Rev.* **101**, 3819–3867 (2001).
7. Maiti, P. K., Çağın, T., Wang, G. & Goddard, W. A. Structure of PAMAM dendrimers: Generations 1 through 11. *Macromolecules* **37**, 6236–6254 (2004).
8. Van Dongen, M. A., Desai, A., Orr, B. G., Baker, J. R. & Banaszak Holl, M. M. Quantitative analysis of generation and branch defects in G5 poly(amidoamine) dendrimer. *Polymer (Guildf)*. **54**, 4126–4133 (2013).
9. Hawker, C. J. & Fréchet, J. M. J. Preparation of Polymers with Controlled Molecular Architecture. A New Convergent Approach to Dendritic Macromolecules. *J. Am. Chem. Soc.* **112**, 7638–7647 (1990).
10. Gupta, U. & Perumal, O. Dendrimers and Its Biomedical Applications. in *Natural and Synthetic Biomedical Polymers* (eds. Kumbar, S. G. & Laurencin, C. T.) 243–257 (2014). doi:10.1016/B978-0-12-396983-5.00016-8.
11. Walter, M. V. & Malkoch, M. Simplifying the synthesis of dendrimers: Accelerated approaches. *Chem. Soc. Rev.* **41**, 4593–4609 (2012).
12. Lyu, Z., Ding, L., Huang, A. Y. T., Kao, C. L. & Peng, L. Poly(amidoamine)dendrimers: covalent and supramolecular synthesis. *Mater. Today Chem.* **13**, 34–48 (2019).
13. Astruc, D., Boisselier, E. & Ornelas, C. Dendrimers designed for functions: From physical, photophysical, and supramolecular properties to applications in sensing, catalysis, molecular electronics, photonics, and nanomedicine. *Chem. Rev.* **110**, 1857–1959 (2010).
14. Lee, C. C., Mackay, J. A., Fréchet, J. M. J. & Szoka, F. C. Designing dendrimers for biological applications. *Nat. Biotechnol.* **23**, 1517–1526 (2005).
15. Denkwalter, R. G., Kolc, J. F. & Lukasavage, W. J. MACROMOLECULAR HIGHLY BRANCHED HOMOGENEOUS COMPOUND. (1983).
16. de Brabander-van den Berg, E. M. M. & Meijer, E. W. Poly(propyleneimine) Dendrimers: Large-Scale Synthesis by Heterogeneously Catalyzed Hydrogenations. *Angew. Chemie Int. Ed. English* **32**, 1308–1311 (1993).
17. Malmström, E., Johansson, M. & Hult, A. Hyperbranched Aliphatic Polyesters.

- Macromolecules* **28**, 1698–1703 (1995).
18. Grinstaff, M. W. Biodendrimers: New Polymeric Biomaterials for Tissue Engineering. *Chem. - A Eur. J.* **8**, 2838 (2002).
 19. Newkome, G. R., Yao, Z. Q., Baker, G. R. & Gupta, V. K. Cascade Molecules: A New Approach to Micelles. *J. Org. Chem.* **50**, 2003–2004 (1985).
 20. Chen, H. T., Neerman, M. F., Parrish, A. R. & Simanek, E. E. Cytotoxicity, hemolysis, and acute in vivo toxicity of dendrimers based on melamine, candidate vehicles for drug delivery. *J. Am. Chem. Soc.* **126**, 10044–10048 (2004).
 21. Turnbull, W. B. & Stoddart, J. F. Design and synthesis of glycodendrimers. *Rev. Mol. Biotechnol.* **90**, 231–255 (2002).
 22. Gillies, E. R. & Frechet, J. M. J. Dendrimers and dendritic polymers in drug delivery. *Drug Discov. Today* **10**, 35–43 (2005).
 23. Jiao, M. *et al.* Recent advancements in biocompatible inorganic nanoparticles towards biomedical applications. *Biomater. Sci.* **6**, 726–745 (2018).
 24. Xiao, Q. *et al.* Janus dendrimersomes coassembled from fluorinated, hydrogenated, and hybrid Janus dendrimers as models for cell fusion and fission. *Proc. Natl. Acad. Sci. U. S. A.* **114**, E7045–E7053 (2017).
 25. Caminade, A.-M., Laurent, R., Delavaux-Nicot, B. & Majoral, J.-P. “Janus” dendrimers: syntheses and properties. *New J. Chem.* **36**, 217–226 (2012).
 26. Duncan, R. & Izzo, L. Dendrimer biocompatibility and toxicity. *Adv. Drug Deliv. Rev.* **57**, 2215–2237 (2005).
 27. Jain, K., Kesharwani, P., Gupta, U. & Jain, N. K. Dendrimer toxicity: Let’s meet the challenge. *Int. J. Pharm.* **394**, 122–142 (2010).
 28. Patravale, V., Dandekar, P. & Jain, R. Clinical trials industrial aspects. in *Nanoparticulate Drug Delivery* 191–207 (Elsevier, 2012). doi:10.1533/9781908818195.191.
 29. Singh, P. Dendrimers and their applications in immunoassays and clinical diagnostics. *Biotechnol. Appl. Biochem.* **48**, 1 (2007).
 30. Yamamoto, K., Imaoka, T., Tanabe, M. & Kambe, T. New Horizon of Nanoparticle and Cluster Catalysis with Dendrimers. *Chem. Rev.* **120**, 1397–1437 (2020).
 31. Reek, J. N. H., Arévalo, S., van Heerbeek, R., Kamer, P. C. J. & van Leeuwen, P. W. N. M. Dendrimers in Catalysis. *Adv. Catal.* **49**, 71–151 (2006).
 32. Méry, D. & Astruc, D. Dendritic catalysis: Major concepts and recent progress. *Coord. Chem. Rev.* **250**, 1965–1979 (2006).
 33. Balzani, V. *et al.* Dendrimers based on photoactive metal complexes. Recent advances. *Coord. Chem. Rev.* **219–221**, 545–572 (2001).
 34. Balzani, V., Ceroni, P., Maestri, M., Saudan, C. & Vicinelli, V. Luminescent Dendrimers. Recent Advances. in *Dendrimers V. Topics in Current Chemistry* 159–191 (2003). doi:10.1007/b11010.
 35. D’Ambruoso, G. D. & McGrath, D. V. Energy harvesting in synthetic dendrimer materials. in *Advances in Polymer Science* vol. 214 87–147 (Springer, Berlin, Heidelberg, 2008).
 36. Nishiyama, N. *et al.* Light-harvesting ionic dendrimer porphyrins as new photosensitizers for photodynamic therapy. *Bioconjug. Chem.* **14**, 58–66 (2003).
 37. Li, J. & Liu, D. Dendrimers for organic light-emitting diodes. *J. Mater. Chem.* **19**, 7584–7591 (2009).
 38. Lo, S. C. & Burn, P. L. Development of dendrimers: Macromolecules for use in organic light-emitting diodes and solar cells. *Chemical Reviews* vol. 107 1097–1116 (2007).

39. Kopidakis, N. *et al.* Bulk heterojunction organic photovoltaic devices based on phenyl-cored thiophene dendrimers. *Appl. Phys. Lett.* **89**, 103524 (2006).
40. Schulz, G. L. *et al.* Synthesis and photovoltaic performance of pyrazinoquinoxaline containing conjugated thiophene-based dendrimers and polymers. *Macromolecules* **46**, 2141–2151 (2013).
41. Jiang, D. L. & Aida, T. Morphology-dependent photochemical events in aryl ether dendrimer porphyrins: Cooperation of dendron subunits for singlet energy transduction. *J. Am. Chem. Soc.* **120**, 10895–10901 (1998).
42. Sadamoto, R., Tomioka, N. & Aida, T. Photoinduced electron transfer reactions through dendrimer architecture. *J. Am. Chem. Soc.* **118**, 3978–3979 (1996).
43. Fox, L. J., Richardson, R. M. & Briscoe, W. H. PAMAM dendrimer - cell membrane interactions. *Adv. Colloid Interface Sci.* **257**, 1–18 (2018).
44. Esfand, R. & Tomalia, D. A. Poly(amidoamine) (PAMAM) dendrimers: From biomimicry to drug delivery and biomedical applications. *Drug Discov. Today* **6**, 427–436 (2001).
45. Boas, U., Christensen, J. B. & Heegaard, P. M. H. *Dendrimers in Medicine and Biotechnology. Dendrimers in Medicine and Biotechnology* (Royal Society of Chemistry, 2007). doi:10.1039/9781847552679.
46. Kéri, M. *et al.* Beware of phosphate: Evidence of specific dendrimer-phosphate interactions. *Phys. Chem. Chem. Phys.* **19**, 11540–11548 (2017).
47. Tang, Y.-H., Ya-Ting Huang, A., Chen, P.-Y., Chen, H.-T. & Kao, C.-L. Metallodendrimers and Dendrimer Nanocomposites. *Curr. Pharm. Des.* **17**, 2308–2330 (2011).
48. Sanz del Olmo, N., Carloni, R., Ortega, P., García-Gallego, S. & de la Mata, F. J. Metallodendrimers as a promising tool in the biomedical field: An overview. in *Advances in Organometallic Chemistry* vol. 74 1–52 (Elsevier Inc., 2020).
49. Caminade, A. M., Hameau, A., Turrin, C. O., Laurent, R. & Majoral, J. P. Dendritic metal complexes for bioimaging. Recent advances. *Coordination Chemistry Reviews* vol. 430 213739 (2021).
50. Govender, P., Therrien, B. & Smith, G. S. Bio-Metallodendrimers - Emerging Strategies in Metal-Based Drug Design. *Eur. J. Inorg. Chem.* **2012**, 2853–2862 (2012).
51. Helms, B. & Fréchet, J. M. J. The dendrimer effect in homogeneous catalysis. *Adv. Synth. Catal.* **348**, 1125–1148 (2006).
52. Li, W. S. & Aida, T. Dendrimer porphyrins and phthalocyanines. *Chem. Rev.* **109**, 6047–6076 (2009).
53. Bergamini, G., Marchi, E. & Ceroni, P. Metal ion complexes of cyclam-cored dendrimers for molecular photonics. *Coordination Chemistry Reviews* vol. 255 2458–2468 (2011).
54. Garfias-Gonzalez, K. I. *et al.* High fluorescent porphyrin-PAMAM-fluorene dendrimers. *Molecules* **20**, 8548–8559 (2015).
55. Ceroni, P., Bergamini, G., Marchioni, F. & Balzani, V. Luminescence as a tool to investigate dendrimer properties. *Prog. Polym. Sci.* **30**, 453–473 (2005).
56. Kawa, M., Fréchet, J. M. J., and, M. K. & Jean M. J. Fréchet*, ‡. Self-assembled lanthanide-cored dendrimer complexes: Enhancement of the luminescence properties of lanthanide ions through site-isolation and antenna effects. *Chem. Mater.* **10**, 286–296 (1998).
57. Foucault-Collet, A., Shade, C. M., Nazarenko, I., Petoud, S. & Eliseeva, S. V. Polynuclear Sm III Polyamidoamine-Based Dendrimer: A Single Probe for Combined Visible and Near-Infrared Live-Cell Imaging. *Angew. Chemie Int. Ed.* **53**, 2927–2930 (2014).
58. Cross, J. P., Lauz, M., Badger, P. D. & Petoud, S. Polymetallic lanthanide complexes with

- PAMAM-naphthalimide dendritic ligands: Luminescent lanthanide complexes formed in solution. *J. Am. Chem. Soc.* **126**, 16278–16279 (2004).
59. Vicinelli, V. *et al.* Luminescent lanthanide ions hosted in a fluorescent polylysine dendrimer. Antenna-like sensitization of visible and near-infrared emission. *J. Am. Chem. Soc.* **124**, 6461–6468 (2002).
 60. Scott, R. W. J., Wilson, O. M. & Crooks, R. M. Synthesis, characterization, and applications of dendrimer-encapsulated nanoparticles. *J. Phys. Chem. B* **109**, 692–704 (2005).
 61. Yamamoto, K. Dendrimer complexes: Fine control of metal assembly in macromolecules. *J. Polym. Sci. Part A Polym. Chem.* **43**, 3719–3727 (2005).
 62. Newkome, G. R., Yoo, K. S., Kim, H. J. & Moorefield, C. N. Routes to Metallodendrimers: Synthesis of Isomeric Neutral Metallomacromolecules Based on Bis(2,2':6',2''-terpyridine)ruthenium(II) Connectivity. *Chem. - A Eur. J.* **9**, 3367–3374 (2003).
 63. Li, W. S., Jiang, D. L., Suna, Y. & Aida, T. Cooperativity in chiroptical sensing with dendritic zinc porphyrins. *J. Am. Chem. Soc.* **127**, 7700–7702 (2005).
 64. Oh, J. B., Kim, Y. H., Nah, M. K. & Kim, H. K. Inert and stable erbium(III)-cored complexes based on metalloporphyrins bearing aryl-ether dendron for optical amplification: Synthesis and emission enhancement. *J. Lumin.* **111**, 255–264 (2005).
 65. Govender, P., Pai, S., Schatzschneider, U. & Smith, G. S. Next generation photoCORMs: Polynuclear tricarbonylmanganese(I)- functionalized polypyridyl metallodendrimers. *Inorg. Chem.* **52**, 5470–5478 (2013).
 66. Viñas, C., Teixidor, F. & Núñez, R. Boron clusters-based metallodendrimers Metallodendrimers Special Issue. *Inorganica Chim. Acta* **409**, 12–25 (2014).
 67. Andolina, C. M., Klemm, P. J., Floyd, W. C., Fréchet, J. M. J. & Raymond, K. N. Analysis of lanthanide complex dendrimer conjugates for bimodal NIR and MRI imaging. *Macromolecules* **45**, 8982–8990 (2012).
 68. Zhang, K. Y., Liu, H. W., Fong, T. T. H., Chen, X. G. & Lo, K. K. W. Luminescent dendritic cyclometalated iridium(III) polypyridine complexes: Synthesis, emission behavior, and biological properties. *Inorg. Chem.* **49**, 5432–5443 (2010).
 69. Govender, P., Riedel, T., Dyson, P. J. & Smith, G. S. Higher generation cationic N,N-ruthenium(II)-ethylene-glycol-derived metallodendrimers: Synthesis, characterization and cytotoxicity. *J. Organomet. Chem.* **799–800**, 38–44 (2015).
 70. Sommerfeld, N. S. *et al.* Low-Generation Polyamidoamine Dendrimers as Drug Carriers for Platinum(IV) Complexes. *Eur. J. Inorg. Chem.* **2017**, 1713–1720 (2017).
 71. Ornelas, C., Ruiz Aranzaes, J., Cloutet, E., Alves, S. & Astruc, D. Click Assembly of 1,2,3-Triazole-Linked Dendrimers, Including Ferrocenyl Dendrimers, Which Sense Both Oxo Anions and Metal Cations. *Angew. Chemie* **119**, 890–895 (2007).
 72. Choi, M.-S., Aida, T., Yamazaki, T. & Yamazaki, I. Dendritic Multiporphyrin Arrays as Light-Harvesting Antennae: Effects of Generation Number and Morphology on Intramolecular Energy Transfer. *Chem. - A Eur. J.* **8**, 2667 (2002).
 73. Diallo, A. K., Ornelas, C., Salmon, L., Ruiz Aranzaes, J. & Astruc, D. “Homeopathic” Catalytic Activity and Atom-Leaching Mechanism in Miyaura-Suzuki Reactions under Ambient Conditions with Precise Dendrimer-Stabilized Pd Nanoparticles. *Angew. Chemie Int. Ed.* **46**, 8644–8648 (2007).
 74. Sun, C. *et al.* DOTA-Branched Organic Frameworks as Giant and Potent Metal Chelators. *J. Am. Chem. Soc.* **142**, 198–206 (2020).
 75. McMahon, M. T. & Bulte, J. W. M. Two decades of dendrimers as versatile MRI agents : a

- tale with and without metals. *Nanomed Nanobiotechnol* **10**, 1416 (2018).
76. Kojima, C. *et al.* Dendrimer-based MRI contrast agents: The effects of PEGylation on relaxivity and pharmacokinetics. *Nanomedicine Nanotechnology, Biol. Med.* **7**, 1001–1008 (2011).
 77. Daniel, M. C., Ruiz, J., Blais, J. C., Daro, N. & Astruc, D. Synthesis of five generations of redox-stable pentamethylamidoferrocenyl dendrimers and comparison of amidoferrocenyl- and pentamethylamidoferrocenyl dendrimers as electrochemical exoreceptors for the selective recognition. *Chem. - A Eur. J.* **9**, 4371–4379 (2003).
 78. Plevoets, M., Vögtle, F., De Cola, L. & Balzani, V. Supramolecular dendrimers with a [Ru(bpy)₃]²⁺ core and naphthyl peripheral units. *New J. Chem.* **23**, 63–69 (1999).
 79. Vögtle, F. *et al.* Dendrimers with a photoactive and redox-active [Ru(bpy)₃]²⁺-type core: Photophysical properties, electrochemical behavior, and excited-state electron-transfer reactions. *J. Am. Chem. Soc.* **121**, 6290–6298 (1999).
 80. Everse, J. Heme Proteins. in *Encyclopedia of Biological Chemistry: Second Edition* 532–538 (Elsevier Inc., 2013). doi:10.1016/B978-0-12-378630-2.00015-3.
 81. Jiang, D. L. & Aida, T. A dendritic iron porphyrin as a novel haemoprotein mimic: Effects of the dendrimer cage on dioxygen-binding activity. *Chem. Commun.* 1523–1524 (1996) doi:10.1039/cc9960001523.
 82. Matos, M. S. *et al.* Effect of core structure on photophysical and hydrodynamic properties of porphyrin dendrimers. *Macromolecules* **33**, 2967–2973 (2000).
 83. Yoriko Tomoyose *et al.* Aryl Ether Dendrimers with an Interior Metalloporphyrin Functionality as a Spectroscopic Probe: Interpenetrating Interaction with Dendritic Imidazoles. *Macromolecules* **29**, 5236–5238 (1996).
 84. Kimura, M., Shiba, T., Muto, T., Hanabusa, K. & Shirai, H. Intramolecular energy transfer in 1,3,5-phenylene-based dendritic porphyrins. *Macromolecules* **32**, 8237–8239 (1999).
 85. Jeong, Y. H., Yoon, H. J. & Jang, W. D. Dendrimer porphyrin-based self-assembled nano-devices for biomedical applications. *Polym. J.* **44**, 512–521 (2012).
 86. Saudan, C. *et al.* Dendrimers with a cyclam core. Absorption spectra, multiple luminescence, and effect of protonation. *Tetrahedron* **59**, 3845–3852 (2003).
 87. Saudan, C. *et al.* Dendrimers as ligands. Formation of a 2:1 luminescent complex between a dendrimer with a 1,4,8,11-tetraazacyclotetradecane (cyclam) core and Zn²⁺. *J. Am. Chem. Soc.* **125**, 4424–4425 (2003).
 88. Saudan, C. *et al.* Cyclam-based dendrimers as ligands for lanthanide ions. *Dalt. Trans.* 1597–1600 (2004) doi:10.1039/B403664F.
 89. Bergamini, G. *et al.* Dendrimers based on a bis-cyclam core as fluorescence sensors for metal ions. *J. Mater. Chem.* **15**, 2959–2964 (2005).
 90. Gu, T., Whitesell, J. K. & Fox, M. A. Intramolecular charge transfer in 1:1 Cu(II)/pyrenylcyclam dendrimer complexes. *J. Phys. Chem. B* **110**, 25149–25152 (2006).
 91. Branchi, B. *et al.* Metal ion driven formation of a light-harvesting antenna investigated by sensitized luminescence and fluorescence anisotropy. *Chem. Commun.* **46**, 3571–3573 (2010).
 92. Balzani, V., Bergamini, G., Ceroni, P. & Marchi, E. Designing light harvesting antennas by luminescent dendrimers. *New Journal of Chemistry* vol. 35 1944–1954 (2011).
 93. Chow, C. Y., Trivedi, E. R., Pecoraro, V. & Zaleski, C. M. Heterometallic Mixed 3d - 4f Metallacrowns: Structural Versatility, Luminescence, and Molecular Magnetism. *Comments Inorg. Chem.* **35**, 214–253 (2015).

94. Lutter, J. C., Zaleski, C. M. & Pecoraro, V. L. Metallacrowns: Supramolecular Constructs With Potential in Extended Solids, Solution-State Dynamics, Molecular Magnetism, and Imaging. in *Advances in Inorganic Chemistry* (eds. Eldik, R. van & Puchta, R.) vol. 71 177–246 (Academic Press, 2018).
95. Mezei, G., Zaleski, C. M. & Pecoraro, V. L. Structural and Functional Evolutions of Metallacrowns. *Chem. Rev.* **107**, 4933–5003 (2007).
96. Lah, M. S. & Pecoraro, V. L. Isolation and characterization of {MnII[MnIII(salicylhydroximate)]4(acetate)2(DMF)6}.cntdot.2DMF: an inorganic analog of M2+(12-crown-4). *J. Am. Chem. Soc.* **111**, 7258–7259 (1989).
97. Cao, F. *et al.* Family of mixed 3d-4f dimeric 14-metallacrown-5 compounds: Syntheses, structures, and magnetic properties. *Inorg. Chem.* **52**, 10747–10755 (2013).
98. Wang, K. *et al.* A series of 3D metal organic frameworks based on [24-MC-6] metallacrown clusters: structure, magnetic and luminescence properties. *Dalt. Trans.* **43**, 12989 (2014).
99. Pavlishchuk, A. V. *et al.* A Triple-Decker Heptadecanuclear (CuII)15(CrIII)2 Complex Assembled from Pentanuclear Metallacrowns. *Eur. J. Inorg. Chem.* **2010**, 4851–4858 (2010).
100. Azar, M. R. *et al.* Controllable formation of heterotrimetallic coordination compounds: Systematically incorporating lanthanide and alkali metal ions into the manganese 12-metallacrown-4 framework. *Inorg. Chem.* **53**, 1729–1742 (2014).
101. Jankolovits, J., Andolina, C. M., Kampf, J. W., Raymond, K. N. & Pecoraro, V. L. Assembly of near-infrared luminescent lanthanide host(host-guest) complexes with a metallacrown sandwich motif. *Angew. Chemie - Int. Ed.* **50**, 9660–9664 (2011).
102. Chow, C. Y. *et al.* Ga3+/Ln3+ Metallacrowns: A Promising Family of Highly Luminescent Lanthanide Complexes That Covers Visible and Near-Infrared Domains. *J. Am. Chem. Soc.* **138**, 5100–5109 (2016).
103. Jankolovits, J., Kampf, J. W. & Pecoraro, V. L. Solvent dependent assembly of lanthanide metallacrowns using building blocks with incompatible symmetry preferences. *Inorg. Chem.* **53**, 7534–7546 (2014).
104. Jankolovits, J., Kampf, J. W. & Pecoraro, V. L. Isolation of Elusive Tetranuclear and Pentanuclear M(II)- Hydroximate Intermediates in the Assembly of Lanthanide [15-Metallacrown-5] Complexes. *Inorg. Chem.* **52**, 5063–5076 (2013).
105. Seda, S. H., Janczak, J. & Lisowski, J. Synthesis and reactivity of copper(II) metallacrowns with (S)-phenylalanine and 2-picolinehydroxamic acids. *Inorganica Chim. Acta* **359**, 1055–1063 (2006).
106. Nguyen, T. N. *et al.* One-Step Assembly of Visible and Near-Infrared Emitting Metallacrown Dimers Using a Bifunctional Linker. *Chem. - A Eur. J.* **24**, 1031–1035 (2018).
107. Jankolovits, J., Lim, C. S., Mezei, G., Kampf, J. W. & Pecoraro, V. L. Influencing the size and anion selectivity of dimeric Ln 3+[15-Metallacrown-5] compartments through systematic variation of the host side chains and central metal. *Inorg. Chem.* **51**, 4527–4538 (2012).
108. Soo Lah, M. & Pecoraro, V. L. Development of Metallacrown Ethers: A New Class of Metal Clusters. *Comments Inorg. Chem.* **11**, 59–84 (1990).
109. Pecoraro, V. L. *et al.* *Metallacrowns: A new class of molecular recognition agents. Progress in Inorganic Chemistry, Volume 45* vol. 45 (1996).
110. Cutland, A. D., Halfen, J. A., Kampf, J. W. & Pecoraro, V. L. Chiral 15-metallacrown-5 complexes differentially bind carboxylate anions [2]. *Journal of the American Chemical*

- Society* vol. 123 6211–6212 (2001).
111. Sgarlata, C., Giuffrida, A., Trivedi, E. R., Pecoraro, V. L. & Arena, G. Anion Encapsulation Drives the Formation of Dimeric GdIII[15-metallacrown-5]3+ Complexes in Aqueous Solution. *Inorg. Chem.* **56**, 4771–4774 (2017).
 112. Boron, T. T., Kampf, J. W. & Pecoraro, V. L. A mixed 3d-4f 14-metallacrown-5 complex that displays slow magnetic relaxation through geometric control of magnetoanisotropy. *Inorg. Chem.* **49**, 9104–9106 (2010).
 113. Zaleski, C. M., Depperman, E. C., Kampf, J. W., Kirk, M. L. & Pecoraro, V. L. Synthesis, structure, and magnetic properties of a large lanthanide-transition-metal single-molecule magnet. *Angew. Chemie Int. Ed.* **43**, 3912–3914 (2004).
 114. Happ, P., Plenck, C. & Rentschler, E. 12-MC-4 metallacrowns as versatile tools for SMM research. *Coord. Chem. Rev.* **289**, 238–260 (2015).
 115. Zaleski, C. M., Depperman, E. C., Kampf, J. W., Kirk, M. L. & Pecoraro, V. L. Using LnIII[15-MCCuII(N)(S)-pheHA-5]3+ Complexes To Construct Chiral Single-Molecule Magnets and Chains of Single-Molecule Magnets. *Inorg. Chem.* **45**, 10022–10024 (2006).
 116. Chow, C. Y. *et al.* Assessing the exchange coupling in binuclear lanthanide(III) complexes and the slow relaxation of the magnetization in the antiferromagnetically coupled Dy2 derivative. *Chem. Sci.* **6**, 4148–4159 (2015).
 117. Lutter, J. C., Eliseeva, S. V., Kampf, J. W., Petoud, S. & Pecoraro, V. L. A Unique Ln III {[3.3.1]Ga III Metallacryptate} Series That Possesses Properties of Slow Magnetic Relaxation and Visible/Near-Infrared Luminescence. *Chem. - A Eur. J.* **24**, 10773–10783 (2018).
 118. Trivedi, E. R. *et al.* Highly Emitting Near-Infrared Lanthanide ‘Encapsulated Sandwich’ Metallacrown Complexes with Excitation Shifted Toward Lower Energy. *J. Am. Chem. Soc.* **136**, 1526–1534 (2014).
 119. Salerno, E. V. *et al.* Visible, near-infrared, and dual-range luminescence spanning the 4F series sensitized by a gallium(III)/lanthanide(III) metallacrown structure. *J. Phys. Chem. A* **124**, 10550–10564 (2020).
 120. Eliseeva, S. V., Salerno, E. V., Lopez Bermudez, B. A., Petoud, S. & Pecoraro, V. L. Dy3+White Light Emission Can Be Finely Controlled by Tuning the First Coordination Sphere of Ga3+/Dy3+Metallacrown Complexes. *J. Am. Chem. Soc.* **142**, 16173–16176 (2020).
 121. Salerno, E. V. *et al.* [Ga3+8Sm3+2, Ga3+8Tb3+2] Metallacrowns are Highly Promising Ratiometric Luminescent Molecular Nanothermometers Operating at Physiologically Relevant Temperatures. *Chem. - A Eur. J.* **26**, 13792–13796 (2020).
 122. Lutter, J. C., Lopez Bermudez, B. A., Nguyen, T. N., Kampf, J. W. & Pecoraro, V. L. Functionalization of luminescent lanthanide-gallium metallacrowns using copper-catalyzed alkyne-azide cycloaddition and thiol-maleimide Michael addition. *J. Inorg. Biochem.* **192**, 119–125 (2019).
 123. Rajczak, E., Pecoraro, V. L. & Juskowiak, B. Sm(iii)[12-MC_{Ga(III)shi}-4] as a luminescent probe for G-quadruplex structures. *Metallomics* **9**, 1735–1744 (2017).
 124. Lutter, J. C. *et al.* Iodinated Metallacrowns: Toward Combined Bimodal Near-Infrared and X-Ray Contrast Imaging Agents. *Chem. – A Eur. J.* **26**, 1274–1277 (2020).
 125. Trivedi, Evan R.; Pecoraro, Vincent L.; Eliseeva, Svetlana V.; Petoud, Stéphane; Jankolovits, Joseph; Foucault-Collet, Alexandra; Martinic, I. Metallacrown complexes and methods of making the same, Patents US20160215001A1, US10174057B2. (2019).

126. Trivedi, Evan R.; Pecoraro, Vincent L.; Eliseeva, Svetlana V.; Petoud, Stéphane; Chow, Chun Y.; Nguyen, Tu Ngoc; Lutter, Jacob Charles; Martinic, I. Ln(III) and Ga(III) metallacrown complexes, Patent WO2016166380A1. (2016).
127. Pecoraro, V. L., Lopez Bermudez, B. A., Eliseeva, S. V. & Petoud, S. Dendrimeric Metallacrowns. (2019).
128. Martinić, I., Eliseeva, S. V., Nguyen, T. N., Pecoraro, V. L. & Petoud, S. Near-Infrared Optical Imaging of Necrotic Cells by Photostable Lanthanide-Based Metallacrowns. *J. Am. Chem. Soc.* **139**, 8388–8391 (2017).
129. Martinić, I. *et al.* Near-infrared luminescent metallacrowns for combined in vitro cell fixation and counter staining. *Chem. Sci.* **8**, 6042–6050 (2017).
130. Binnemans, K. Lanthanide-based luminescent hybrid materials. *Chem. Rev.* **109**, 4283–4374 (2009).
131. Bünzli, J.-C. G. & Eliseeva, S. V. Basics of Lanthanide Photophysics. in *Lanthanide Luminescence: Photophysical, Analytical and Biological Aspects* 1–45 (2010). doi:10.1007/4243_2010_3.
132. Sabbatini, N., Guardigli, M. & Lehn, J.-M. M. Luminescent lanthanide complexes as photochemical supramolecular devices. *Coord. Chem. Rev.* **123**, 201–228 (1993).
133. Uh, H. & Phane Petoud, S. Novel antennae for the sensitization of near infrared luminescent lanthanide cations. *C. R. Chim.* **13**, 668–680 (2010).
134. Bünzli, J. G. On the design of highly luminescent lanthanide complexes. *Coord. Chem. Rev.* **293–294**, 19–47 (2015).
135. Petoud, S. *et al.* Influence of charge-transfer states on the Eu(III) luminescence in mononuclear triple helical complexes with tridentate aromatic ligands. *J. Lumin.* **82**, 69–79 (1999).
136. D’Aléo, A. *et al.* Efficient sensitization of europium, ytterbium, and neodymium functionalized tris-dipicolinate lanthanide complexes through tunable charge-transfer excited states. *Inorg. Chem.* **47**, 10258–10268 (2008).
137. Carnall, W. T., Fields, P. R. & Rajnak, K. Electronic energy levels of the trivalent lanthanide aquo ions. IV. Eu 8+. *J. Chem. Phys.* **49**, 4424–4442 (1968).
138. Carnall, W. T., Fields, P. R. & Rajnak, K. Electronic energy levels of the trivalent lanthanide aquo ions. III. Tb3+. *J. Chem. Phys.* **49**, 4412–4423 (1968).
139. Martinić, I., Eliseeva, S. V. & Petoud, S. Near-infrared emitting probes for biological imaging: Organic fluorophores, quantum dots, fluorescent proteins, lanthanide(III) complexes and nanomaterials. *J. Lumin.* **189**, 19–43 (2017).
140. Lutter, J. C. Refining Lanthanide Luminescence in Metallacrowns by Systematic Alteration of Hydroxamate Ligands. (The University of Michigan, 2018).
141. Bünzli, J.-C. G. & Eliseeva, S. V. Lanthanide NIR luminescence for telecommunications, bioanalyses and solar energy conversion. *J. Rare Earths* **28**, 824–842 (2010).
142. Zhang, J., Badger, P. D., Geib, S. J. & Petoud, S. Sensitization of near-infrared-emitting lanthanide cations in solution by tropolonate ligands. *Angew. Chem. Int. Ed. Engl.* **44**, 2508–12 (2005).
143. Melan, M. A. Overview of cell fixation and permeabilization. *Methods in molecular biology (Clifton, N.J.)* vol. 34 55–66 (1994).
144. Monti, D. M. *et al.* Biocompatibility, uptake and endocytosis pathways of polystyrene nanoparticles in primary human renal epithelial cells. *J. Biotechnol.* **193**, 3–10 (2015).
145. Marzaroli, V. *et al.* Three-Dimensional Porous Architectures Based on Mn II/III Three-

- Blade Paddle Wheel Metallacryptates. *Cryst. Growth Des.* **19**, 1954–1964 (2019).
146. Fabbri, D. *et al.* Iodinated X-ray contrast agents: Photoinduced transformation and monitoring in surface water. *Sci. Total Environ.* **572**, 340–351 (2016).
 147. Plenk, C., Krause, J., Beck, M. & Rentschler, E. Rational linkage of magnetic molecules using click chemistry. *Chem. Commun.* **51**, 6524–6527 (2015).
 148. McKetty, M. H. The AAPM/RSNA Physics Tutorial for Residents: X-ray Attenuation. *Radiographics* **18**, 151–163 (1998).
 149. Schilz, M. & Plenio, H. A guide to sonogashira cross-coupling reactions: The influence of substituents in aryl bromides, acetylenes, and phosphines. *J. Org. Chem.* **77**, 2798–2807 (2012).
 150. Iwai, K. *et al.* Single-Crystalline Optical Microcavities from Luminescent Dendrimers. *Angew. Chemie* **132**, 12774–12779 (2020).
 151. Tomalia, D. A. *et al.* Non-traditional intrinsic luminescence: inexplicable blue fluorescence observed for dendrimers, macromolecules and small molecular structures lacking traditional/conventional luminophores. *Progress in Polymer Science* vol. 90 35–117 (2019).
 152. Eggeling, C., Widengren, J., Rigler, R. & Seidel, C. A. M. Photobleaching of Fluorescent Dyes under Conditions Used for Single-Molecule Detection: Evidence of Two-Step Photolysis. *Anal. Chem.* **70**, 2651–2659 (1998).
 153. Diaspro, A., Chirico, G., Usai, C., Ramoino, P. & Dubrucki, J. Photobleaching. in *Handbook of Biological Confocal Microscopy* (ed. Pawley, J. B.) 690–702 (Springer, 2006).
 154. Pitois, C., Hult, A. & Lindgren, M. Lanthanide-cored fluorinated dendrimer complexes: Synthesis and luminescence characterization. *J. Lumin.* **111**, 265–283 (2005).
 155. Pillai, Z. S. *et al.* Dendrimers as Nd³⁺ ligands: Effect of Generation on the Efficiency of the Sensitized Lanthanide Emission. *Chem. - An Asian J.* **8**, 771–777 (2013).
 156. Mello, J. C. de, Wittmann, H. F. & Friend, R. H. An improved experimental determination of external photoluminescence quantum efficiency. *Adv. Mater.* **9**, 230–232 (1997).
 157. de Mello Donegá, C., Meijerink, A. & Blasse, G. Saturation effects in the excitation spectra of rare-earth ions. *J. Lumin.* **62**, 189–201 (1994).
 158. Northrop, B. H., Frayne, S. H. & Choudhary, U. Thiol–maleimide ‘click’ chemistry: evaluating the influence of solvent, initiator, and thiol on the reaction mechanism, kinetics, and selectivity. *Polym. Chem.* **6**, 3415 (2015).
 159. Carnall, W. T., Eieids, P. R. & Rajnak, K. Electronic energy levels of the trivalent lanthanide aquo ions. II. Gd³⁺. *J. Chem. Phys.* **49**, 4407–4411 (1968).
 160. Mabire, A. B. *et al.* Aminomaleimide fluorophores: a simple functional group with bright, solvent dependent emission. *Chem. Commun. (Camb)*. **51**, 9733–9736 (2015).
 161. Xie, Y. *et al.* Rational design of substituted maleimide dyes with tunable fluorescence and solvafluorochromism. *Chem. Commun.* **54**, 3339–3342 (2018).
 162. Tomalia, D. A., Huang, B., Swanson, D. R., Brothers, H. M. & Klimash, J. W. Structure control within poly(amidoamine) dendrimers: size, shape and regio-chemical mimicry of globular proteins. *Tetrahedron* **59**, 3799–3813 (2003).
 163. Wängler, C. *et al.* PAMAM Structure-Based Multifunctional Fluorescent Conjugates for Improved Fluorescent Labelling of Biomacromolecules. *Chem. - A Eur. J.* **14**, 8116–8130 (2008).
 164. Wängler, C. *et al.* Multimerization of cRGD peptides by click chemistry: Synthetic strategies, chemical limitations, and influence on biological properties. *ChemBioChem* **11**, 2168–2181 (2010).

165. Demattei, C. R., Huang, B. & Tomalia, D. A. Designed Dendrimer Syntheses by Self-Assembly of Single-Site, ssDNA Functionalized Dendrons. *Nano Lett* **4**, 771–777 (2004).
166. Huang, B. & Tomalia, D. A. Dendronization of gold and CdSe/cdS (core–shell) quantum dots with tomalia type, thiol core, functionalized poly(amidoamine) (PAMAM) dendrons. *J. Lumin.* **111**, 215–223 (2005).
167. Kantner, T. & Watts, A. G. Characterization of Reactions between Water-Soluble Trialkylphosphines and Thiol Alkylating Reagents: Implications for Protein-Conjugation Reactions. *Bioconjug. Chem.* **27**, 2400–2406 (2016).
168. Getz, E. B., Xiao, M., Chakrabarty, T., Cooke, R. & Selvin, P. R. A comparison between the sulfhydryl reductants tris(2- carboxyethyl)phosphine and dithiothreitol for use in protein biochemistry. *Anal. Biochem.* **273**, 73–80 (1999).
169. McCarney, E. R., Breaux, C. J. & Rendle, P. M. Measurement of the hydrodynamic radii of PEE-G dendrons by diffusion spectroscopy on a benchtop NMR spectrometer. *Magn. Reson. Chem.* **58**, 641–647 (2020).
170. Leith, D. Drag on nonspherical objects. *Aerosol Sci. Technol.* **6**, 153–161 (1987).
171. Majoros, I. J., zs Keszler, B., Woehler, S., Bull, T. & Baker, J. R. Acetylation of Poly(amidoamine) Dendrimers. *Macromolecules* **36**, 5526–5529 (2003).
172. Fritzing, B. & Scheler, U. Scaling behaviour of PAMAM dendrimers determined by diffusion NMR. *Macromol. Chem. Phys.* **206**, 1288–1291 (2005).
173. Müller, R., Laschober, C., Szymanski, W. W. & Allmaier, G. Determination of molecular weight, particle size, and density of high number generation PAMAM dendrimers using MALDI-TOF-MS and nES-GEMMA. *Macromolecules* **40**, 5599–5605 (2007).
174. Menjoge, A. R., Kannan, R. M. & Tomalia, D. A. Dendrimer-based drug and imaging conjugates: design considerations for nanomedical applications. *Drug Discov. Today* **15**, 171–185 (2010).
175. Salatin, S., Maleki Dizaj, S. & Yari Khosroushahi, A. Effect of the surface modification, size, and shape on cellular uptake of nanoparticles. *Cell Biol. Int.* **39**, 881–890 (2015).
176. Bräse, S., Gil, C., Knepper, K. & Zimmermann, V. Organic azides: An exploding diversity of a unique class of compounds. *Angewandte Chemie - International Edition* vol. 44 5188–5240 (2005).
177. Shingu, A. & Ooyagi, M. Aluminum foil for ultraviolet light reflecting materials and methods for producing same. (2017).
178. Salerno, E. V. Synthetic and spectroscopic investigation of ligand field effects in molecular ion complexes. (University of Michigan, 2021).
179. Eliseeva, S. V. & Bünzli, J.-C. G. Lanthanide luminescence for functional materials and bio-sciences. *Chem. Soc. Rev.* **39**, 189–227 (2009).
180. Nair, D. P. *et al.* The Thiol-Michael addition click reaction: A powerful and widely used tool in materials chemistry. *Chemistry of Materials* vol. 26 724–744 (2014).
181. Northrop, B. H. & Coffey, R. N. Thiol-ene click chemistry: Computational and kinetic analysis of the influence of alkene functionality. *J. Am. Chem. Soc.* **134**, 13804–13817 (2012).
182. Hoyle, C. E., Lowe, A. B. & Bowman, C. N. Thiol-click chemistry: a multifaceted toolbox for small molecule and polymer synthesis. *Chem. Soc. Rev.* **39**, 1355–1387 (2010).
183. Allegranza, M. L., Thompson, A. M., Kloster, A. J. & Konkolewicz, D. Photocatalyzed thiol–alkene coupling: Mechanistic study and polymer synthesis. *J. Polym. Sci. Part A Polym. Chem.* **57**, 1931–1937 (2019).

184. Keylor, M. H., Park, J. E., Wallentin, C. J. & Stephenson, C. R. J. Photocatalytic initiation of thiol-ene reactions: Synthesis of thiomorpholin-3-ones. *Tetrahedron* **70**, 4264–4269 (2014).
185. Tomalia, D. A. Birth of a new macromolecular architecture: Dendrimers as quantized building blocks for nanoscale synthetic polymer chemistry. *Prog. Polym. Sci.* **30**, 294–324 (2005).
186. Wu, C., De Visscher, A. & Gates, I. D. Reactions of hydroxyl radicals with benzoic acid and benzoate. *RSC Adv.* **7**, 35776–35785 (2017).
187. Haseloff, R. F., Blasig, I. E., Meffert, H. & Ebert, B. Hydroxyl radical scavenging and antipsoriatic activity of benzoic acid derivatives. *Free Radic. Biol. Med.* **9**, 111–115 (1990).
188. Sinha, A. K. & Equbal, D. Thiol–Ene Reaction: Synthetic Aspects and Mechanistic Studies of an Anti-Markovnikov-Selective Hydrothiolation of Olefins. *Asian Journal of Organic Chemistry* vol. 8 32–47 (2019).
189. Ren, W. X. *et al.* Recent development of biotin conjugation in biological imaging, sensing, and target delivery. *Chem. Commun.* **51**, 10403–10418 (2015).
190. Finikova, O. *et al.* Porphyrin and tetrabenzoporphyrin dendrimers: Tunable membrane-impermeable fluorescent pH nanosensors. *J. Am. Chem. Soc.* **125**, 4882–4893 (2003).
191. Dijkstra, H. P. *et al.* Shape-persistent nanosize organometallic complexes: Synthesis and application in a nanofiltration membrane reactor. *J. Org. Chem.* **68**, 675–685 (2003).
192. Buschow, K. H., Jürgen Cahn, R. W., Flemings, M. C., Ilschner, B. & Kramer, Edward J. Mahajan, S. Photoinitiators and Photopolymerization. in *Encyclopedia of Materials - Science and Technology* 6947 (Elsevier, 2001).
193. Capaldo, L. & Ravelli, D. Hydrogen Atom Transfer (HAT): A Versatile Strategy for Substrate Activation in Photocatalyzed Organic Synthesis. *European Journal of Organic Chemistry* vol. 2017 2056–2071 (2017).
194. Bartling, H., Eisenhofer, A., König, B. & Gschwind, R. M. The Photocatalyzed Aza-Henry Reaction of N-Aryltetrahydroisoquinolines: Comprehensive Mechanism, H•- versus H+-Abstraction, and Background Reactions. *J. Am. Chem. Soc.* **138**, 11860–11871 (2016).
195. Ropponen, J., Nummelin, S. & Rissanen, K. Bisfunctionalized Janus Molecules. *Org. Lett.* **6**, 2495–2497 (2004).
196. Taghavi Pourianazar, N., Mutlu, P. & Gunduz, U. Bioapplications of poly(amidoamine) (PAMAM) dendrimers in nanomedicine. *J. Nanoparticle Res.* **16**, 2342 (2014).
197. Gorain, B. *et al.* Dendrimers as Effective Carriers for the Treatment of Brain Tumor. *Nanotechnology-Based Target. Drug Deliv. Syst. Brain Tumors* 267–305 (2018) doi:10.1016/B978-0-12-812218-1.00010-5.
198. Tolbert, A. E. *et al.* Heteromeric three-stranded coiled coils designed using a Pb(ii)(Cys)₃ template mediated strategy. *Nat. Chem.* **2020 124 12**, 405–411 (2020).
199. Koebeke, K. J. *et al.* The pH-Induced Selectivity Between Cysteine or Histidine Coordinated Heme in an Artificial α -Helical Metalloprotein. *Angew. Chemie* **133**, 4020–4024 (2021).
200. Peacock, A. F. A., Hemmingsen, L. & Pecoraro, V. L. Using diastereopeptides to control metal ion coordination in proteins. *Proc. Natl. Acad. Sci. U. S. A.* **105**, 16566–16571 (2008).
201. Lu, Y. Design and engineering of metalloproteins containing unnatural amino acids or non-native metal-containing cofactors. *Curr. Opin. Chem. Biol.* **9**, 118–126 (2005).
202. Xu, J. & Boyer, C. Visible Light Photocatalytic Thiol–Ene Reaction: An Elegant Approach for Fast Polymer Postfunctionalization and Step-Growth Polymerization. (2015) doi:10.1021/ma502460t.

203. Berezin, M. Y., Lee, H., Akers, W. & Achilefu, S. Near Infrared Dyes as Lifetime Solvatochromic Probes for Micropolarity Measurements of Biological Systems. *Biophys. J.* **93**, 2892–2899 (2007).
204. Yuan, B., Chen, N. & Zhu, Q. Emission and absorption properties of indocyanine green in Intralipid solution. *J. Biomed. Opt.* **9**, 497 (2004).
205. Shahinyan, G. A., Amirbekyan, A. Y. & Markarian, S. A. Photophysical properties of methylene blue in water and in aqueous solutions of dimethylsulfoxide. *Spectrochim. Acta Part A Mol. Biomol. Spectrosc.* **217**, 170–175 (2019).
206. Li, Y. *et al.* Novel NIR-II organic fluorophores for bioimaging beyond 1550 nm. *Chem. Sci.* **11**, 2621–2626 (2020).
207. Zhang, T. *et al.* Water-Soluble Mitochondria-Specific Ytterbium Complex with Impressive NIR Emission. *J. Am. Chem. Soc.* **133**, 20120–20122 (2011).
208. K, A., T, T., Y, K., K, S. & H, S. NIR fluorescent ytterbium compound for in vivo fluorescence molecular imaging. *Luminescence* **25**, 19–24 (2010).
209. Fréchet, J. M. J. Dendrimers and supramolecular chemistry. *Proc. Natl. Acad. Sci. U. S. A.* **99**, 4782–4787 (2002).
210. Beezer, A. E. *et al.* Dendrimers as potential drug carriers; encapsulation of acidic hydrophobes within water soluble PAMAM derivatives. *Tetrahedron* **59**, 3873–3880 (2003).